LIÈGE université
Sciences Appliquées

Piezoelectric Digital Vibration Absorbers for Multimodal Vibration Mitigation of Complex Mechanical Structures

A thesis submitted in partial fulfillment of the requirements
for the degree of Doctor of Philosphy (Phd) in Engineering Science

by

Ghislain RAZE

Supervisor: Gaëtan KERSCHEN

DOCTORAL COLLEGE IN AEROSPACE AND MECHANICS

FEBRUARY 2021

Members of the Examination Committee

Prof. Christophe Collette (President of the Committee)
University of Liège (Liège, Belgium), Université Libre de Bruxelles (Brussels, Belgium)

Prof. Gaëtan Kerschen (Supervisor)
University of Liège (Liège, Belgium)

Prof. Li Cheng
Hong Kong Polytechnic University (Hong Kong, China)

Prof. Arnaud Deraemaeker
Université Libre de Bruxelles (Brussels, Belgium)

Prof. Grigorios Dimitriadis
University of Liège (Liège, Belgium)

Prof. Paolo Gardonio
Università di Udine (Udine, Italy)

Prof. Jan Høgsberg
Technical University of Denmark (Lyngby, Denmark)

Abstract

Engineering structures are becoming lighter and more complex to accommodate the ever-increasing demand for performance and to comply with stringent environmental regulations. This trend comes with several challenges, one of which is the increased susceptibility to high-amplitude vibrations. These vibrations can be detrimental to structural performance and lifetime, and may sometimes even threaten safety. Passive and active vibration reduction techniques can provide a solution to this issue. Among the possibilities, piezoelectric damping is an attractive option, due to its compact and lightweight character, its reduced cost and its tunability. This technique uses the ability of a piezoelectric transducer to transform part of its mechanical energy into electrical energy. The converted energy can then be dissipated by connecting a shunt circuit to the transducer. However, the difficulty of realizing such circuits limits the broad applicability of piezoelectric shunting.

This doctoral thesis investigates the potential of replacing the electrical circuit comprising classical components such as resistors and inductors by a digital unit and a current source, thereby creating a digital vibration absorber (DVA). Virtually any circuit can be emulated with a digital controller, providing this approach with an extreme versatility for vibration mitigation of complex mechanical structures. In this regard, the DVA is first analyzed in terms of power consumption and stability of the controlled system. Then, effective and easy-to-use tuning approaches for the control of multiple structural modes either with passive electrical circuits or a DVA are proposed, namely a *passivity-based tuning* of shunt circuits, a *modal-based synthesis* of electrical networks interconnecting multiple piezoelectric transducers, and a numerical norm-homotopy optimization resulting in an *all-equal-peak design*. These techniques are eventually applied and adapted to real-life structures with potentially complex dynamics. Specifically, effective vibration mitigation is demonstrated on structures exhibiting nonlinear behaviors and high modal density.

Acknowledgements

First and foremost, my thanks go to my advisor, Gaëtan Kerschen, for accepting me as a PhD candidate, for his constant help, advice, enthusiasm, support and availability, especially over the last few weeks.

I would also like to thank Christophe Collette, not only for accepting the role of president of the jury of this thesis, but also for his help and guidance throughout my research project.

I am thankful to the members of my jury, Profs. Li Cheng, Arnaud Deraemaeker, Grigorios Dimitriadis, Paolo Gardonio and Jan Høgsberg, for accepting to participate in the examination committee of this doctoral thesis.

While working on the Maveric project, I was fortunate to meet a number of colleagues with whom I shared a common objective. I am grateful for that, because it made these years less solitary than (I guess) normally are. Special thanks to Jenni, Guoying, Ahmad and Jean-François for being such motivated and motivating people to work with. I also want to acknowledge my lab and department colleagues for making my work environment so pleasant. In particular, Jenni, Martin, Nicolas, Gaëtan, Denis and Thibaut, thank you very much for all these nice times spent together.

I had the chance to collaborate with people from other institutions during my PhD. Thanks to Boris Lossouarn for sharing his extensive knowledge on piezoelectric damping and his expertise in experimental testing. I value very much the discussions we had. I am indebted to my colleagues from HEPL, Valéry Broun, Andy Jadoul and Sylvain Guichaux, to whom I owe most of my experimental results, thanks to their help in building the digital absorbers used in this work. I also want to thank Arnaud Deraemaeker, whose shared knowledge on finite element modeling of piezoelectric structures was extremely helpful.

This work could not have been possible without the financial support of the service public de Wallonie (SPW), with a grant for the Maveric project (WALInnov grant 1610122). I want to express my gratitude to all the people who were involved to make this project a reality, and to those who accepted it, trusted us and supported us financially.

Last but not least, I want to thank my friends, roommate and family for their support and affection over these years. This is invaluable for me.

Contents

Introduction

The aerospace industry is facing new challenges regarding competitiveness and performance in a global market economy. Sustainability and the global threats of climate change are also key concerns. In Europe, the Flighpath 2050 document [1] lists guidelines for the years to come to maintain and extend industrial leadership, meet societal and market needs, ensure safety and security, and protect the environment. Drastic reductions in the environmental impact of aviation are envisioned therein. To meet these stringent requirements, innovative projects were recently proposed by leading industries such as Airbus with the ZEROe aircraft project [2]. Technology developments and sustainable aviation fuels are expected to play a role of up to 30% and 60% in these reductions, respectively [3]. Short-term technology advances can be realized through the improvement of engines, aerodynamics and flight controls, and through the use of lighter structures.

Using lightweight structures leads to a number of challenges, one of them being their increased susceptibility to vibration coming from their increased flexibility. Large-amplitude motions are an issue for several reasons. First, structural failure may occur due to overloading or high-cycle fatigue. Second, structural nonlinear behavior can be triggered, which can lead to sudden and often unexpected changes in the response of the structure. Other aspects such as precision in positioning and comfort can be a concern depending on the application. Special precaution must be taken at the design stage of a mechanical part to avoid resonances. If this is not possible due to, e.g., conflicting design objectives, or if vibration problems appear in later design stages, other means should be used to prevent the harmful action of vibrations. In this respect, numerous vibration mitigation techniques have been developed over the years.

Vibration mitigation

Vibration mitigation can pursue different objectives, such as stiffening, damping and isolation [4]. In this thesis, the aim is to improve the damping of a *host structure*, i.e., reducing the vibratory amplitude at its resonances by energy dissipation or counteracting forces. To achieve this goal, several means are possible.

Tuned mass damper

One of the most famous means for vibration mitigation is the tuned mass damper (TMD), which was invented by Frahm more than a century ago [5] using a small auxiliary body to counteract the vibrations of a larger body. The working principle of this *vibration absorber* is to match its resonance frequency to that of its host structure. By destructive interference, the targeted resonance frequency can be completely suppressed in the controlled host. This however comes at the expense of two additional resonances, and a large amplitude of vibration of the TMD at the host resonance frequency. Ormondroyd and Den Hartog [6] added a damper to this device (see Figure 1(a)) and Brock [7] proposed a particular value of the absorber damping coefficient to approximately

minimize the maximum amplitude (i.e., the H_∞ norm) of the forced response of the controlled structure. Those developments, gathered in Den Hartog's book [8], laid down the foundations of the *equal-peak design* because the controlled receptance exhibits two peaks of (approximately) equal amplitude, usually much lower than that of the uncontrolled structure, as illustrated in Figure 1(b). Nearly one century after the invention of the TMD, Nishihara and Asami [9] found the exact analytical solution to the H_∞-optimization problem by minimizing the maximum value of the receptance under the assumption that the latter exhibits two peaks of equal amplitude (i.e., an exact equal-peak design). TMDs are used in a wide range of civil and mechanical engineering applications, and reviews on the subject can be found, e.g., in [10, 11].

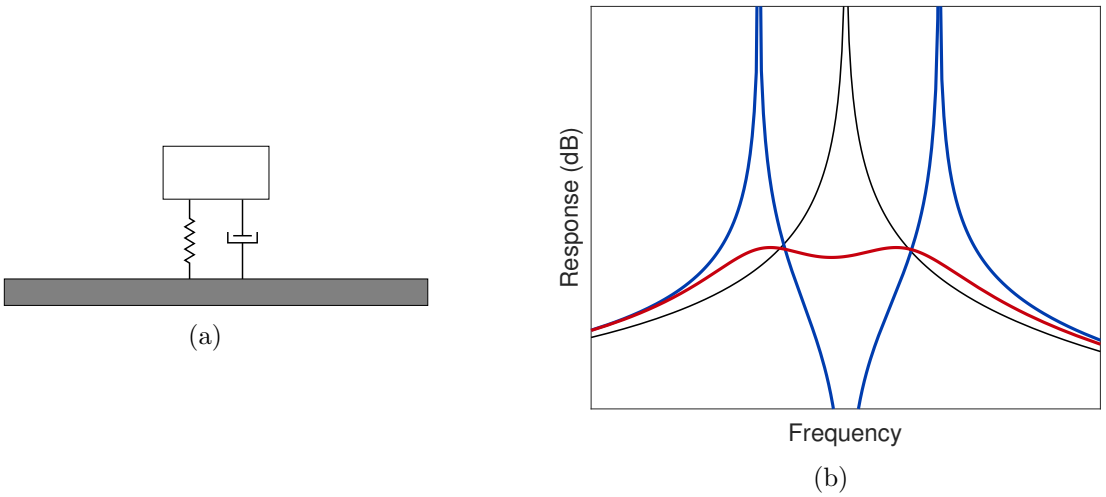

(a) (b)

Figure 1: Schematic representation of a structure with a TMD (a) and typical vibratory response of the structure without TMD (—), and with an undamped (—) and damped (—) TMD (b).

Piezoelectric vibration absorber

Piezoelectric shunt damping is an alternative vibration mitigation means that was invented by Forward [12], and the seminal work of Hagood and von Flotow [13] laid the grounds of the theoretical tuning approach used nowadays. A piezoelectric transducer bonded to a vibrating structure is strained by the vibrations and converts part of its mechanical energy into electrical energy. This electrical energy can then be dissipated in properly-tuned circuits that connect the electrodes of the transducers, as shown in Figure 2(a). Piezoelectric shunt damping is an appealing vibration mitigation technique for its compact and potentially lightweight character, its high bandwidth, its reduced cost and its possibility of fine-tuning [14]. By contrast with TMDs, piezoelectric absorbers do not require the addition of a moving mass to the structure. These features make this approach attractive for aerospace applications [15–18]. The main downsides of piezoelectric transducers are their brittleness (for piezoceramic materials), their limited temperature working range and the high voltages they can exhibit.

The circuit which connects the electrodes of the transducer is called a *shunt*. Various types of shunts were proposed in the literature. The most famous are the resistive and resonant shunts. The resistive shunt is constituted of a mere resistor that dissipates the electrical energy by Joule's effect [13]. A resonant shunt is created with the

connection of a resistor with an inductor, either in series [13] or in parallel [19]. The inductor resonates with the inherent capacitance of the piezoelectric material at a specific frequency, largely enhancing the electrical dissipation in the resistor. As a consequence, a properly-tuned resonant shunt is generally much more efficient than a resistive shunt in terms of vibration reduction, see Figure 2(b). However, the resonant shunt has to be *tuned* to a frequency close to that of the host structure. If the latter changes for any reason, the performance of a resonant shunt may be severely degraded. The resonant shunt thus has a broad similarity with the TMD, being both efficient vibration mitigation means conditioned upon their precise tuning.

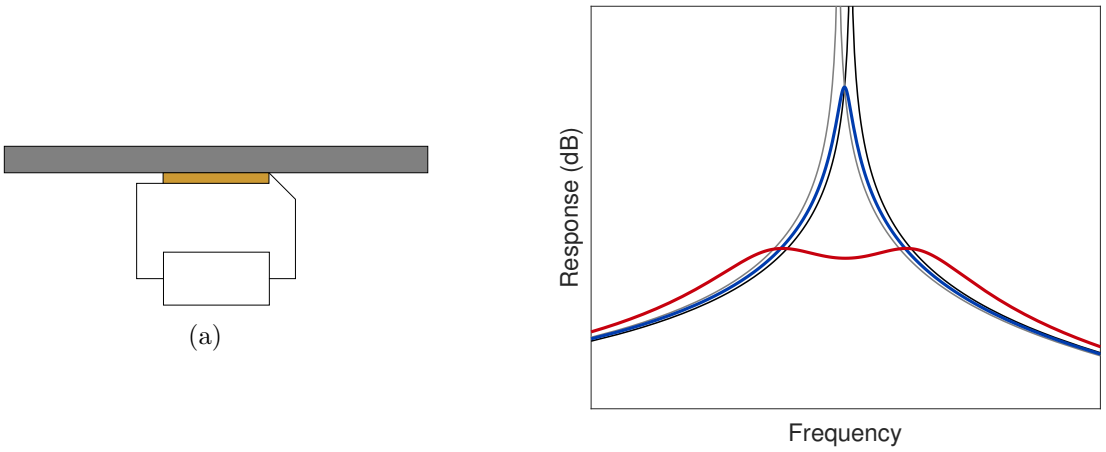

(a) (b)

Figure 2: Schematic representation of a structure with a shunted piezoelectric transducer (a) and typical vibratory response of the structure with a piezoelectric transducer with electrodes in open-circuit (—), short-circuit (—), or connected to a resistive (—) or resonant (—) shunt (b).

Since its inception, the field of piezoelectric shunt damping has largely grown, and numerous alternative solutions to the classical resistive and resonant shunts were proposed in the literature. The interested reader may refer to various reviews on the subject [20–22].

Digital vibration absorber

When it comes to the practical realization of a resonant piezoelectric vibration absorber, a number of challenges have to be overcome. The first difficulty is the large inductance value (typically hundreds of Henries) required for structures with low resonance frequencies. Although physical inductors with such high inductance values were realized [23], they are not commercially available. A common workaround is to use synthetic inductors or gyrators, but they come with non-ideal characteristics, such as frequency-dependent resistance [24]. Finally, some shunt circuits may not be simple to realize, because they would require numerous or complex electrical components.

To address these issues, a *synthetic impedance* was proposed by Fleming et al [25]. A digital signal processing unit together with a current source make the realization of an arbitrary impedance possible, as schematized in Figure 3. This however comes at the expense of a non-fully-passive absorber (because the analog and digital electronics need power) and at the risk of creating instabilities (because the system contains active elements).

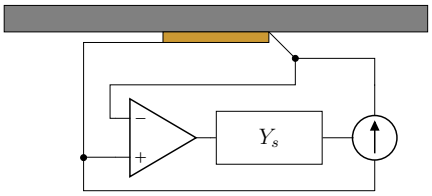

Figure 3: Schematic representation of a structure with a piezoelectric transducer connected to a synthetic impedance.

Other vibration mitigation techniques

The two aforementioned approaches are far from forming an extensive list of vibration mitigation techniques. They both belong to passive control, in which additional damping is brought to a host structure by coupling it with an additional device that dissipates energy. Other mechanical vibration absorbers such as the tuned liquid damper [26], tuned viscoelastic damper [27], nonlinear energy sink (NES) [28] and acoustic black hole (ABH) [29] use vibrating auxiliary devices or parts of the structure to absorb energy, similarly to the TMD. Some approaches make use of materials with high material damping like viscoelastic matrials [27]. Passive control system using transducers are also common and include electromagnetic shunt damping [30] or magnetostrictive materials [31], to name a few. The advantages of passive control are the guaranteed stability of the controlled system and the absence for power requirements, which additionally makes this approach fail-safe.

Semi-active control means work similarly to passive control, but can adapt the characteristics of the auxiliary device in order to meet specific needs. For instance, piezoelectric transducers can be switched on capacitive loads in order to adjust the resonance frequency of a structure away from that of an external excitation [32]. Semi-active control can achieve similar performance to passive control but is generally more robust due to its adaptive nature.

Alternatively, active vibration control can be used. With this approach, the state of the host structure is determined with sensors, and the structure is acted upon via actuators. The driving signals for the actuators are determined by the sensed signals and control laws, which can be synthesized with analog or digital electronics [33]. In structural vibration control, common control laws include direct velocity feedback [34], positive position feedback (PPF) [35–37] and integral force feedback [38, 39], to name a few. By contrast with passive control, active control does require power for operation, and is not a fail-safe approach. However, active control generally allows for better performance and is much more versatile.

Finally, hybrid control takes on the advantages of passive and active control. A hybrid control system generally consists in a passive device augmented with an active control apparatus. Examples of hybrid control systems include hybrid TMDs [40] and hybrid piezoelectric [41–43] and electromagnetic [44, 45] shunts. The active control part is used to achieve better performance, whereas the passive device guarantees a minimum performance and eases the power requirements on the active system. It can be a fail-safe approach, because in the event of a power failure, the passive part of the control system can still work.

Bladed structures in aircraft engines

One of the target applications of this doctoral thesis is a bladed structure used in aircraft engines. Turbofan engines are used in a large proportion of commercial and military aircraft. A celebrated example is the CFM56 depicted in Figure 4. These engines contain a number of bladed structures which rotate at high speeds.

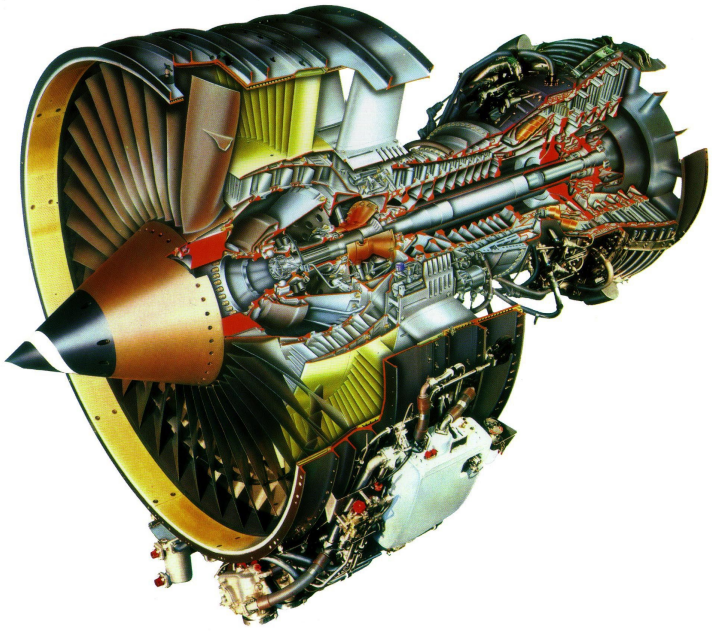

Figure 4: Cutaway drawing of a CFM56 engine, reproduced from [46].

Emergence of integrally bladed structures

Bladed structures are traditionally manufactured as assemblies, as depicted in Figure 5(a). The separately-manufactured blades are attached to the disk through root-fixing features, either axially or circumferentially. The disk is required to support the centrifugal blade load.

The progress of manufacturing techniques enabled the industrial production of monolithic structures, thereby removing the need for fastenings and connectors. This in turn entails great savings in terms of weight, which makes this type of new designs very attractive for the aerospace industry. This has motivated the appearance of integrally bladed parts such as bladed disks (BLISKs) (Figure 5(b)) or bladed drums (BluMs). These parts can be realized by machining the disk/drum, and friction welding of the blades. On the one hand, BLISKs and BluMs feature several advantages over their assembled counterparts, including weight savings of the order of 25%, improved aerodynamic efficiency, and suppression of the fretting fatigue occuring at the blade/disk attachment (which is one of the common modes of failure [47]). On the other hand, these structures are expensive to produce and repair, and may require exhaustive quality control [48].

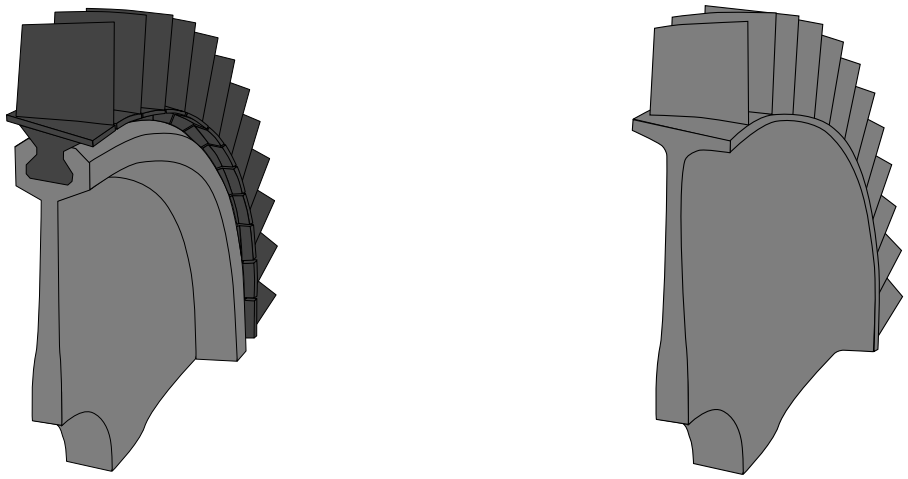

(a) (b)

Figure 5: Quarters of bladed disks in turbomachines: classical assembly (a) and BLISK (b).

Vibration problems in turbomachinery

Aircraft engines constitute a harsh environment for their mechanical components. Dynamic loadings such as out-of-balance forces and lack of axisymmetry in the airflow coming from upstream obstacles create vibrations that can cause structural failure through fatigue or overloading. The consequences can be dramatic, especially on rotating components, because they are associated with out-of-balance forces and debris expulsion [49]. Dynamic phenomena such as forced resonance must be avoided, and this is generally accounted for in early design phases by changing the mechanical design of the part, for instance.

In addition to these severe conditions, other phenomena peculiar to nominally cyclic symmetric structures can also accelerate the blade failure. One of them is called *mistuning* and originates from the lack of perfect cyclic symmetry in the structure stemming from manufacturing tolerances or in-operation wear. Localization of the resonant modes to a few blades can occur because of this mistuning. As a result, a few blades may vibrate with a very large amplitude and fail quickly due to high-cycle fatigue [50].

Combining the low structural damping of BLISKs and BluMs, the presence of mistuning and the dynamical loading conditions makes these parts prone to early failure, and vibration mitigation means should then be used to allow for a broad and safe deployment of such parts. The harsh environment limits the possible solutions [51]. Industrial state-of-the-art methods use friction damping [52] and/or viscoelastic damping [53], but the past decades have witnessed a growing interest for piezoelectric shunt damping [54].

Contributions of the thesis

This doctoral research was funded in the frame of a WALInnov project named Maveric. This project aims to develop smart vibration absorbers for aerospace structures, and, in particular, for the BluM in Figure 6 used in low-pressure compressors of aero-engines manufactured by Safran Aero Boosters. In this respect, the ability of passive and active

vibration mitigation techniques to damp the resonances of this structure is assessed. The eventual goal of this project is to demonstrate the action of these smart vibration absorbers in laboratory conditions (i.e., bring the concept to the technology readiness level (TRL) 4).

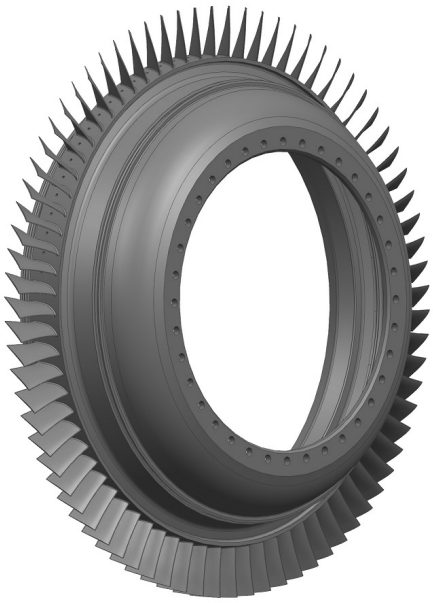

Figure 6: BluM of a low-pressure compressor manufactured by Safran Aero Boosters.

In this context, this thesis focuses on passive control solutions. Due to its exceptional versatility, the DVA was deemed to be a potential candidate for such an application. The main purpose of this work is thus to lay down solid theoretical and computational foundations for effective vibration mitigation of complex structures such as a BluM using a DVA.

In the first part of this thesis, Chapter 1 analyzes the DVA. The architecture of this apparatus is detailed in terms of hardware and software. The consequences of using elements that need to be powered in the DVA are also studied. Figures on its power consumption are given. The effects of sampling delays are characterized and are shown to be the cause of potential instabilities. A method is proposed to counteract these instabilities by simple modifications of the emulated shunt circuit.

The second part is constituted of Chapters 2, 3 and 4 and proposes new tuning strategies for the control of multiple structural resonances with piezoelectric vibration absorbers. Chapter 2 focuses on piezoelectric damping with a single transducer using shunt circuits with multiple branches. A three-step *passivity-based design procedure* is proposed. The first step concerns the identification of the piezoelectric structure. Generic specifications on the shunt circuits are then derived. Finally, the values of the electrical components making up the circuit are tuned. This approach is numerically verified and experimentally validated. In Chapter 3, multiple piezoelectric transducers are interconnected by an electrical network. A *modal-based synthesis* of the network is proposed, i.e., the network's behavior is specified in terms of its electrical modal properties. These properties are optimized to provide effective multimodal damping while guaranteeing the possible realization of the network with passive electrical elements. Finally, Chapter 4 proposes a robust numerical *norm-homotopy* optimization method to tune the characteristics of

piezoelectric vibration absorbers (realized either with circuits or networks) in order to minimize the H_∞ norm of a transfer function. The typical outcome is an *all-equal-peak design*, where all peaks of the transfer function at hand are equated in amplitude.

In the final part, Chapters 5 and 6 are concerned with the application of piezoelectric damping to complex structures. Chapter 5 outlines the detrimental effects of structural nonlinearities on the performance of tuned vibration absorbers. A remedy is to use an absorber which is itself nonlinear, and its realization is eased by the use of a DVA. This strategy is also extended to the control of multiple nonlinear resonances. Chapter 6 applies and adapts the previously-studied control approaches to bladed assemblies. To accurately represent the dynamics of such structures with models of tractable size, a modified Craig-Bampton model-order reduction approach is proposed. A hybrid control strategy tailored to the control of multiple families of modes with closely-spaced frequencies is developed. Effective vibration mitigation is then demonstrated on a bladed rail and a BluM.

Finally, conclusions regarding the completed research and the associated contributions to the field are drawn. A discussion of the ways in which this research may be extended is also given.

1 A digital vibration absorber

Abstract

This chapter presents a practical realization of a digital vibration absorber and discusses the purpose of its electronic components. The equivalence of a digital absorber and a piezoelectric shunt is experimentally demonstrated. The notion of passivity, as understood in this work, is discussed. Figures on power consumption entailed by the presence of electronic components are given from theoretical predictions and experimental measurements. Finally, the issue of stability of the digitally-controlled electromechanical system is tackled. Systems with low electromechanical coupling are shown to be prone to delay-induced instabilities, and a stabilization procedure is proposed to mitigate them.

1.1 Introduction

Piezoelectric shunt damping was originally proposed by Forward [12], and formalized by Hagood and von Flotow [13]. Its working principle is based on the transduction capability of piezoelectric materials: a piezoelectric transducer is able to convert a part of its mechanical energy into electrical energy. The latter can be dissipated by connecting a so-called shunt circuit to the electrodes of the transducer. A common type of shunt circuit is a resonant one, composed of a resistor and an inductor, arranged either in series or in parallel. The realization of this circuit may be challenging for several reasons. The first one is that the required inductance may be impractically large. The second reason is that the performance of the piezoelectric shunt is highly sensitive to the values of the electrical components. Any misevaluation or time variation of the system characteristics will result in sub-optimal performance, rectified by time-consuming manual modifications of the electrical parameters.

Fleming et al [25, 55] introduced the concept of synthetic impedance as an alternative solution. The combination of a digital signal processor with a current source makes it possible to realize an arbitrary impedance. The synthetic impedance is an attractive option to realize shunt damping circuits owing to its flexibility. This nonetheless comes at the expense of the need for powering the digital unit and its associated electronics. Since it was proposed, implementing piezoelectric shunt damping with a digital vibration absorber (DVA) has received rather limited attention. Fleming et al [56] and Pliva et al [57] developed architectures using pulse width modulation (PWM) in order to simplify the driving electronics. Giorgio [58] and Rosi [59] used digital controllers to validate their theoretical developments on shunt damping with electrical networks. Matten et al [60, 61], Necasek et al [62, 63] and Silva [64] investigated various electronic architectures to implement a DVA, and discussed how to set up its analog and digital parts. Dal Bo et al [65] configured a digital unit to realize vibration absorber with swept and switched characteristics. Recently, this concept was applied to metamaterials by Sugino et al [66] and Yi et al [67].

In the aforementioned works, the implications of implementing a passive control law with an electronic (thus active) control system were not thoroughly discussed. The purpose of this chapter is to present the working principles of a DVA, and to analyze the effects of its non-passive character. The main interest of the DVA, i.e., the flexibility it provides, will be a key point in the remainder of this thesis: it will enable the implementation of shunt circuits possessing numerous electrical elements (Chapters 2, 3 and 4) and with nonlinear elements (Chapter 5). All these aspects can enhance the performance of the control system in the cases discussed therein.

This chapter is organized as follows. Theoretical reminders on piezoelectric shunt damping are given in Section 1.2. Practical realizations of the digital absorber are then presented in Section 1.3. The presence of electronic components raises three issues. The first one is to determine whether the control system is to be considered either as passive or as active. This is discussed in Section 1.4. The power consumption of the electronics is addressed in Section 1.5. Finally, the stability of the controlled system is assessed in Section 1.6. Conclusions on the DVA are drawn in Section 1.7.

1.2 Reminders on piezoelectric structures and piezoelectric shunt damping

This section provides reminders on important notions used throughout this thesis. Section 1.2.1 reviews the basics of piezoelectric structures through their mechanical and electrical models, and then introduces the effective electromechanical coupling factor and the dynamic capacitance. Section 1.2.2 reviews the mechanisms of shunt damping achieved with various shunt circuits.

1.2.1 Single-degree-of-freedom structure coupled to a piezoelectric transducer

A single-degree-of-freedom (SDoF) structure coupled to a massless piezoelectric rod shown in Figure 1.1 is studied as a representative example. Although it is a rather simple apparatus, it can be used to understand the salient features of more complex piezoelectric structures, as shall be shown in Chapter 2. The rod is composed of a homogeneous piezoelectric material and possesses two thin electrodes (of negligible mechanical characteristics) at its ends. The piezoelectric structure and transducer are represented in Figure 1.1(a) and Figure 1.1(b), respectively.

To derive the governing equations of the system, the constitutive equations of linear piezoelectric materials in Voigt notation [68] are recalled (where Einstein summation convention on repeated indices is used):

$$\begin{aligned} \sigma_k &= c_{kl}^E \varepsilon_l - e_{pk} E_p \\ D_k &= e_{kp} \varepsilon_p + \epsilon_{kl}^\varepsilon E_l \end{aligned} \tag{1.1}$$

where σ_k (ε_k) is the k^{th} component of the Voigt stress (strain) vector and D_k and E_k are the k^{th} components of the electric displacement field and electric field, respectively. c_{kl}^E represents Hooke's matrix at constant electric field and $\epsilon_{kl}^\varepsilon$ the permittivity at

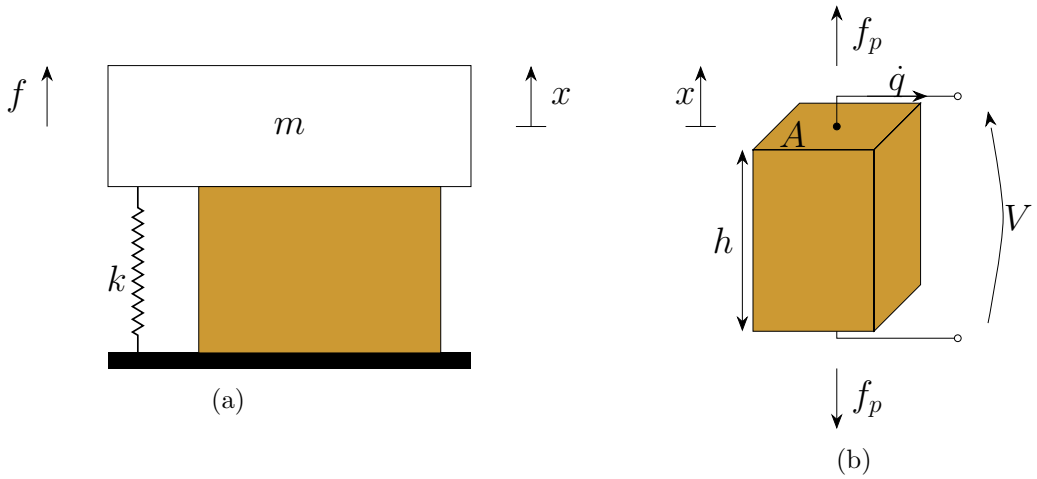

Figure 1.1: SDoF structure to which is bonded a piezoelectric rod (a) and schematic representation of the piezoelectric rod (b).

constant strain. The first mechanical and second electrical equations are coupled through a matrix e_{kp}. In the notation used herein, superscripts ε, σ and E denote a quantity at constant strain, stress and electric field, respectively (corresponding to superscripts S, T and E in [68], respectively).

Assuming that the expansion and polarization directions coincide with the axis of the rod (which is conventionally called the 3-direction), these constitutive equations reduce to

$$\begin{aligned} \sigma_3 &= c_{33}^E \varepsilon_3 - e_{33} E_3 \\ D_3 &= e_{33} \varepsilon_3 + \epsilon_{33}^\varepsilon E_3 \end{aligned}, \tag{1.2}$$

The integration of these equations over the volume of the rod (of thickness h along direction 3 and cross-section A) and division by its thickness leads to

$$\begin{aligned} f_p &= k_{p,sc} x + \gamma_p V \\ q &= \gamma_p x - C_p^\varepsilon V \end{aligned}, \tag{1.3}$$

where the macroscopic variables

$$f_p = \sigma_3 A, \qquad x = \varepsilon_3 h, \qquad V = -E_3 h, \qquad q = D_3 A, \tag{1.4}$$

represent the force acting on the transducer, its stroke, the voltage across its electrodes and the charge flowing through them, respectively. The macroscopic constants

$$k_{p,sc} = \frac{A c_{33}^E}{h}, \qquad \gamma_p = \frac{A e_{33}}{h}, \qquad C_p^\varepsilon = \frac{A \epsilon_{33}^\varepsilon}{h}, \tag{1.5}$$

are the stiffness of the transducer when its electrodes are short-circuited, a piezoelectric coupling constant and the piezoelectric capacitance at constant strain (also called blocked capacitance), respectively. The piezoelectric transducer is then integrated within a structure, symbolically represented as a spring-mass system of stiffness k and mass m. The transducer is bonded between the mass and the ground, in parallel to the spring, as shown in Figure 1.2(a). Introducing the structural stiffness when the piezoelectric transducer is short-circuited $k_{sc} = k_{p,sc} + k$, the governing

equations of the so-formed piezoelectric structure read

$$\begin{cases} m\ddot{x} + k_{sc}x + \gamma_p V = f \\ \gamma_p x - C_p^{\varepsilon} V = q \end{cases}. \tag{1.6}$$

Terms $\gamma_p x$ and $\gamma_p V$ are manifestations of the direct and converse piezoelectric effects, respectively. The time derivation of the second line of Equation (1.6) is equivalent to Kirchhoff's current law (KCL), which indicates that the electrical behavior of the transducer is modeled as an ideal current source ($\gamma_p \dot{x}$) placed in parallel with a capacitor (of capacitance C_p^{ε}). This is Norton's equivalent representation [69], which is shown in Figure 1.2(b).

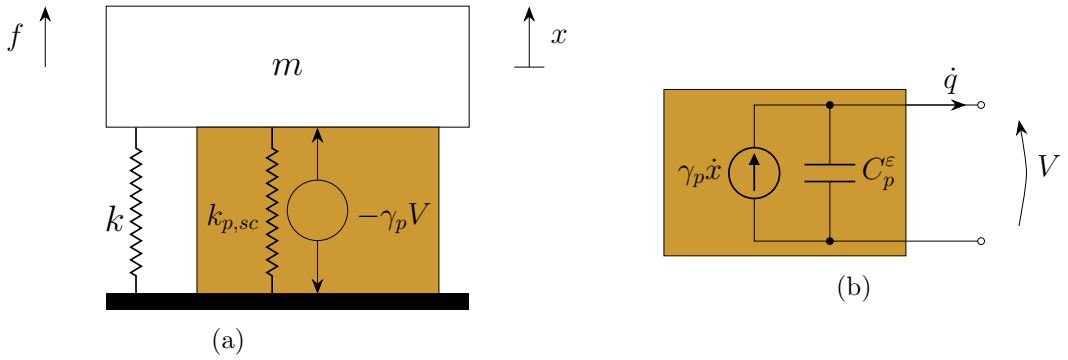

Figure 1.2: SDoF structure to which is bonded a piezoelectric rod: mechanical representation (a) and Norton equivalent electrical representation (b).

When the electrodes of the transducer are short-circuited, $V = 0$ and the structure behaves as a SDoF oscillator of stiffness of k_{sc}. A short-circuit resonance frequency can be defined as

$$\omega_{sc} = \sqrt{\frac{k_{sc}}{m}} \tag{1.7}$$

When the electrodes are left in open circuit, $q = 0$ and thus, using the second line of Equation (1.6)

$$V = \frac{\gamma_p}{C_p^{\varepsilon}} x. \tag{1.8}$$

Inserting this relation in the first line of Equation (1.6),

$$m\ddot{x} + k_{sc}x + \gamma_p V = m\ddot{x} + k_{sc}x + \frac{\gamma_p^2}{C_p^{\varepsilon}} x = m\ddot{x} + k_{oc}x = f, \tag{1.9}$$

in which

$$k_{oc} = k_{sc} + \frac{\gamma_p^2}{C_p^{\varepsilon}} \tag{1.10}$$

is the structural stiffness when the transducer is open-circuited. Hence, the electrical boundary conditions applied to the electrodes of the transducer play a significant role in the mechanical behavior of the structure it is bonded to.

Equation (1.6) uses the piezoelectric charge and voltage as independent and dependent variables, respectively. The dual representation is equally valid. From Equation (1.6), the following equivalent set of governing equations can be obtained:

$$\begin{cases} m\ddot{x} + k_{oc}x - \theta_p q = f \\ \theta_p x - \dfrac{1}{C_p^{\varepsilon}} q = V \end{cases}, \tag{1.11}$$

where

$$\theta_p = \gamma_p / C_p^{\varepsilon}. \tag{1.12}$$

With this representation, the electrical behavior of the transducer is modeled as an ideal voltage source ($\theta_p x$) in series with a capacitor (of capacitance C_p^{ε}), i.e., by Thévenin's equivalent model [69]. The representation of the system based on Equation (1.11) is shown in Figure 1.3.

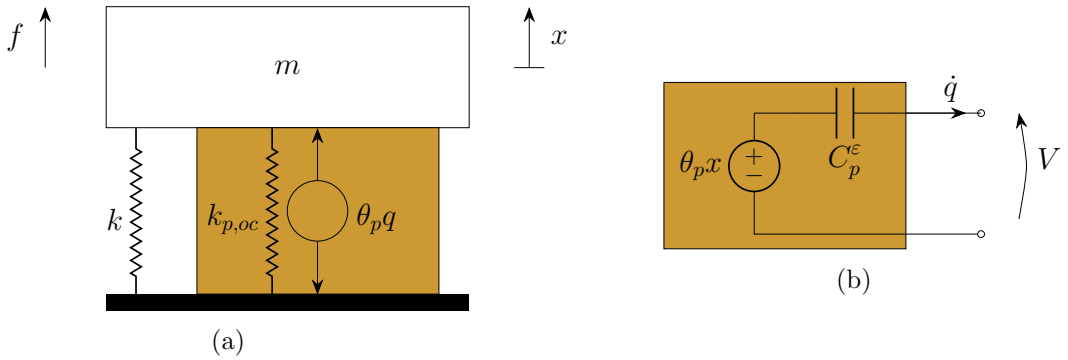

Figure 1.3: SDoF structure to which is bonded a piezoelectric rod: mechanical representation (a) and Thévenin's equivalent electrical representation (b).

An open-circuit resonance frequency can be defined as

$$\omega_{oc} = \sqrt{\frac{k_{oc}}{m}}. \tag{1.13}$$

1.2.1.1 Electromechanical coupling factors

The foregoing discussion highlighted the impact of the electrical boundary conditions on the mechanical behavior of the system, which is an indication of its electromechanical coupling. To characterize quantitatively this coupling, dimensionless coupling factors are generally used [70].

The quasi-static loading-unloading cycle represented in Figure 1.4 is considered. The electrodes of the piezoelectric transducer are initially short-circuited. A quasi-static loading f is applied to the system which reaches a deformed configuration $x = f/k_{sc}$. The energy stored into the system is then equal to the mechanical work provided by the external force, i.e.,

$$E_{sc} = \int_0^f x df = \int_0^f \frac{f}{k_{sc}} df = \frac{1}{2}\frac{f^2}{k_{sc}} \tag{1.14}$$

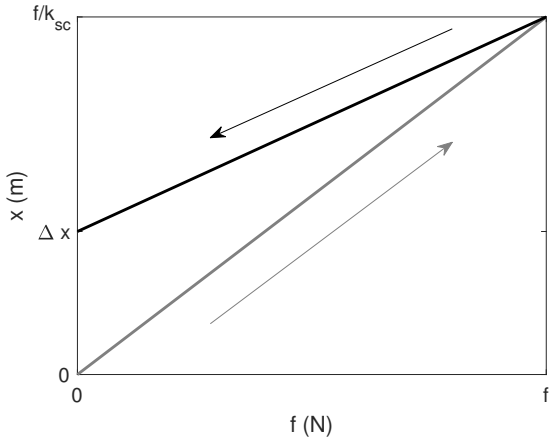

Figure 1.4: Quasi-static loading cycle of a piezoelectric structure: loading with a short-circuited transducer (—) and unloading with an open-circuited transducer (—).

The electrodes of the transducer are then disconnected, and the load is consecutively brought to zero. The energy restored by the system can be computed as

$$-E_{oc} = \int_f^0 x df = \int_f^0 \frac{f}{k_{oc}} df = -\frac{1}{2}\frac{f^2}{k_{oc}} \tag{1.15}$$

and because $k_{oc} > k_{sc}$, there is a residual deformation

$$\Delta x = \left(\frac{1}{k_{sc}} - \frac{1}{k_{oc}}\right) f \tag{1.16}$$

and a residual energy, equal to the difference of the two aforementioned energies, remains in the system.

Because of the direct piezoelectric effect, there is charge accumulation at the electrodes, which induces a potential difference between them. This potential difference indicates that the transducer has converted part of its strain energy into electrical energy while being unloaded. If the electrodes of the transducer were connected back, this residual energy would be dissipated, and the transducer would go back to its undeformed state.

The dimensionless effective electromechanical coupling factor (EEMCF) K_c is defined from a normalized version of this residual energy[1] as

$$K_c^2 = \frac{E_{sc} - E_{oc}}{E_{oc}} = \frac{\frac{1}{2}\frac{f^2}{k_{sc}} - \frac{1}{2}\frac{f^2}{k_{oc}}}{\frac{1}{2}\frac{f^2}{k_{oc}}} = \frac{k_{oc} - k_{sc}}{k_{sc}} \tag{1.18}$$

[1] A different energy may be used to normalize the EEMCF, leading to another definition

$$(K_c')^2 = \frac{E_{sc} - E_{oc}}{E_{sc}} = \frac{\omega_{oc}^2 - \omega_{sc}^2}{\omega_{oc}^2} = \frac{K_c^2}{1 + K_c^2}. \tag{1.17}$$

This definition is more commonly used in works treating the material aspects of piezoelectric structures [68, 70–73], whereas the definition used in this thesis is commonly used in the area of piezoelectric shunt damping [13, 74–77]. The name given to the EEMCF also varies from one author to another, but it is always aimed at representing electromechanical coupling with a dimensionless number.

The EEMCF measures the strength of the piezoelectric coupling in the system. In terms of parameters given in Equations (1.6) and (1.11), the EEMCF is given by

$$K_c^2 = \frac{\gamma_p^2}{k_{sc} C_p^\varepsilon} = \frac{\theta_p^2 C_p^\varepsilon}{k_{sc}}. \tag{1.19}$$

Dividing the numerator and denominator in Equation (1.18) by the structural mass m and using the resonance frequencies defined in Equations (1.7) and (1.13), the EEMCF can also be expressed as

$$K_c^2 = \frac{\omega_{oc}^2 - \omega_{sc}^2}{\omega_{sc}^2}. \tag{1.20}$$

This expression enables a rather straightforward experimental evaluation of the EEMCF, for instance by performing two modal tests with the transducer short-circuited and open-circuited and identifying the corresponding resonance frequencies, without the need for any model. This is advantageous, since models are associated with uncertainties coming from the material parameters[2], boundary conditions, mechanical [78, 79] and electrical [72] impact of the bonding layer between the transducer and the structure, and unmodelled three-dimensional effects [80], to name a few.

1.2.1.2 Dynamic capacitance

Equation (1.6) can be Laplace transformed to yield

$$\begin{cases} (ms^2 + k_{sc})x + \gamma_p V_p = f \\ \gamma_p x - C_p^\varepsilon V = q \end{cases}, \tag{1.22}$$

where s is Laplace's variable. Assuming the host is unforced ($f = 0$), a dynamic relation between the piezoelectric charge and voltage can be found as

$$\frac{q}{V} = -C_p^\varepsilon \left(\frac{1}{C_p^\varepsilon} \frac{\gamma_p^2}{ms^2 + k_{sc}} + 1 \right) = -C_p^\varepsilon \left(\frac{\omega_{oc}^2 - \omega_{sc}^2}{s^2 + \omega_{sc}^2} + 1 \right) = -C_p^\varepsilon \frac{s^2 + \omega_{oc}^2}{s^2 + \omega_{sc}^2} = C_p(s). \tag{1.23}$$

This equation features the *dynamic capacitance* measured from the electrodes of the transducer $C_p(s)$, wherein a constant capacitance C_p^ε is dynamically modulated. This dynamic modulation comes from the electromechanical interaction of the transducer with the structure, and is strongest near the structural resonance frequencies. Namely, we

[2] The EEMCF is not to be confused with the material coupling factor [68]

$$k_{33}^2 = \frac{e_{33}^2}{\epsilon_{33}^\varepsilon c_{33}^E + e_{33}^2} = \frac{k_{p,oc} - k_{p,sc}}{k_{p,oc}} \neq \frac{k_{p,oc} + k - (k_{p,sc} + k)}{k_{p,sc} + k} = K_c^2. \tag{1.21}$$

The EEMCF is a property of an electromechanical system (structure *and* transducer), whereas the material coupling factor is a sole property of the material used in the transducer. The former is smaller than the latter (excepted in very specific cases [70]), especially when the structure is stiffer than the transducer; $K_c' = k_{33}$ when the sole piezoelectric transducer is considered ($k = 0$). In general, the EEMCFs of typical piezoelectric structures are small, of the order of 0.1 or less.

note that the short-circuit and open-circuit resonance frequencies are the poles and zeros frequencies of the dynamic capacitance, respectively.

Figure 1.5 plots the magnitude of a typical Bode plot of a dynamic capacitance. The interest of evaluating this transfer function is that the two frequencies ω_{sc} and ω_{oc} as well as the capacitance C_p^ε can be determined with a single test, thereby providing all the required parameters to tune a shunt circuit, as shall be shown. Moreover, this test only involves electrical measurements, which are generally easier to perform than measurements of mechanical quantities.

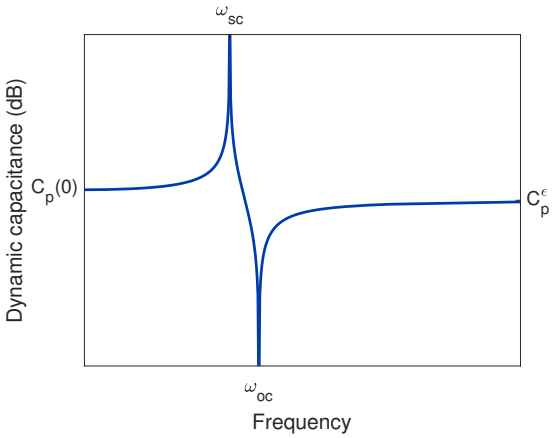

Figure 1.5: Dynamic capacitance magnitude of a piezoelectric transducer bonded to an SDoF structure.

The static value ($s = 0$) of the dynamic capacitance in Equation (1.23)

$$C_p(0) = C_p^\varepsilon \frac{\omega_{oc}^2}{\omega_{sc}^2} = C_p^\varepsilon \left(1 + K_c^2\right) \tag{1.24}$$

is smaller than the piezoelectric capacitance at constant stress or the free capacitance C_p^σ, but larger than the piezoelectric capacitance at constant strain C_p^ε, because

$$C_p^\varepsilon \leq C_p(0) = C_p^\varepsilon \left(1 + \frac{\gamma_p^2}{C_p^\varepsilon k_{sc}}\right) = C_p^\varepsilon \left(1 + \frac{\gamma_p^2}{C_p^\varepsilon \left(k + k_{p,sc}\right)}\right) \leq C_p^\varepsilon \left(1 + \frac{\gamma_p^2}{C_p^\varepsilon k_{p,sc}}\right) = C_p^\sigma \tag{1.25}$$

This stems from the fact that if a quasi-static voltage is applied to the transducer, it may store energy under electrical form and under mechanical form with the direct piezoelectric effect, but not as much as if it was completely free because of the stiffness of the structure. If the voltage is applied at high frequencies, inertia impedes mechanical motion, and energy can only be stored under electrical form, as if the transducer was blocked. Thus, in a completely analogous way as the change in stiffness provoked by different electrical boundary conditions, a change in mechanical boundary conditions changes the apparent capacitance of the piezoelectric transducer.

1.2.2 Shunt damping

A piezoelectric transducer is able to convert part of its mechanical energy imparted by the vibrations of its host. In an attempt to dissipate this energy, one may use electrical dissipative elements such as resistors. By connecting a resistor to the electrodes of the

transducer, a *shunt circuit* is thus created. The effect brought by the dissipation of electrical energy generally is the reduction of the vibration amplitude in the controlled structure, i.e., the shunted piezoelectric transducer exerts a force on the structure which is similar to a damping force. The performance of the control system can be enhanced by the use of more complex circuits. Namely, if the shunt circuit contains an inductor, it is possible to make it resonate with the inherent capacitance of the piezoelectric transducer and hence to enhance the energy dissipation in the resistor, which eventually results in better vibration mitigation. The purpose of this section is to review the basic mechanisms of these shunt circuits.

The electrical parameters of the shunt circuit can be tuned for optimal performance according to some metric. The most common performance measures are the H_∞ norm of the receptance (optimization under harmonic forcing), the H_2 norm of the receptance (optimization under broadband forcing) and the real part of the closed-loop system's poles (optimization of the transient response). The optimal parameters according to these different metrics are in general slightly different [75, 81]. Some tuning procedures use a combination of these objectives, such as the balanced calibration proposed by Høgsberg and Krenk [82], where the poles of the electromechanical system are set with equal (but not maximal) modal damping, and the frequency responses of the structure and the absorber are flat in the vicinity of the resonance. In this thesis, the H_∞ norm of the receptance is the considered performance index.

1.2.2.1 Resistive shunt damping

In order to dissipate the electrical energy generated by the vibrations through the direct piezoelectric effect, a resistor could be connected to the electrodes of the transducer, as shown in Figure 1.6. This approach was first pursued by Forward [12] and later formalized by Hagood and von Flotow [13] and Thomas et al [75].

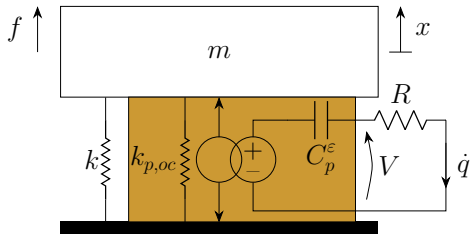

Figure 1.6: SDoF piezoelectric structure controlled by a resistive shunt.

By Ohm's law, connecting a resistor of resistance R to the transducer imposes a relation between the voltage and the charge as

$$V = R\dot{q} \tag{1.26}$$

which, when inserted into Equation (1.11), gives the coupled system

$$\begin{cases} m\ddot{x} + k_{oc}x - \theta_p q = f \\ R\dot{q} + \dfrac{1}{C_p^\varepsilon} q - \theta_p x = 0 \end{cases} \tag{1.27}$$

The frequency response function (FRF) of the system can be computed with the Laplace transform of these equations, and the subsequent insertion of the electrical equation into the mechanical one, yielding

$$\frac{x}{f} = \frac{1}{ms^2 + k_{oc} - \theta_p^2 \dfrac{1}{Rs + \dfrac{1}{C_p^\varepsilon}}} = \frac{Rs + \dfrac{1}{C_p^\varepsilon}}{(ms^2 + k_{oc})\left(Rs + \dfrac{1}{C_p^\varepsilon}\right) - \theta_p^2}. \tag{1.28}$$

The FRFs of the system controlled by a resistive shunt with various resistances are shown in Figure 1.7(a). Using a zero resistance is equivalent to a short-circuit, whereas using an infinite resistance is equivalent to an open-circuit. With finite resistances, the energy dissipated by the resistor results in a damping effect on the structure.

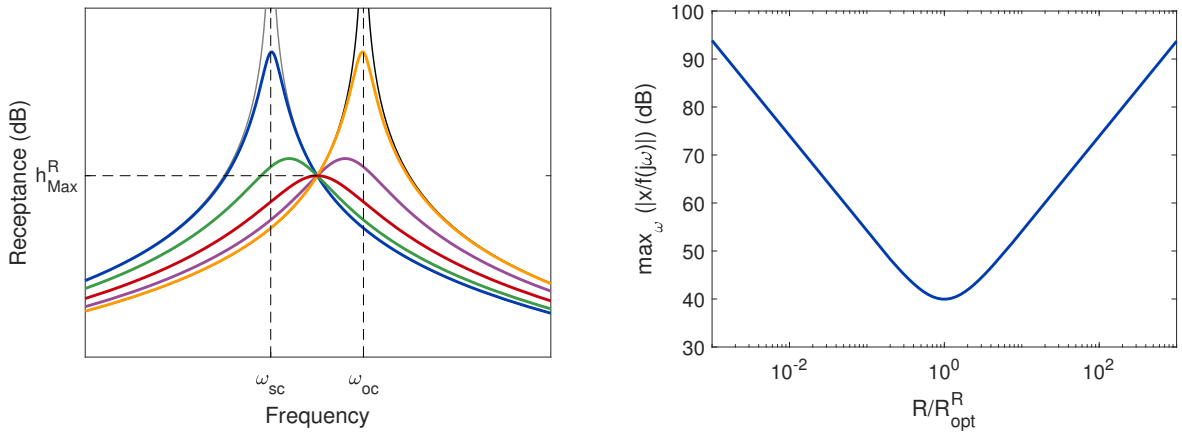

(a) (b)

Figure 1.7: FRF of the structure with a short-circuited transducer (—), with an open-circuited transducer (—) and with a resistive shunt: $R = 0.1R^R_{opt}$ (—), $R = 0.5R^R_{opt}$ (—), $R = R^R_{opt}$ (—), $R = 2R^R_{opt}$ (—) and $R = 10R^R_{opt}$ (—) (a) ; maximum amplitude of the FRF for various resistances (b).

Looking closely at the FRFs in Figure 1.7(a), one can observe that all of them pass through a fixed point. Thomas et al [75] used this fact to find the resistance that makes this fixed point a maximum of the FRF

$$R^R_{opt} = \frac{1}{C_p^\varepsilon \omega_{sc} \sqrt{1 + K_c^2/2}}. \tag{1.29}$$

The corresponding maximum amplitude is then given by

$$h^R_{Max} = \frac{2}{k_{sc} K_c^2} \tag{1.30}$$

Figure 1.7(b) compares the maximum amplitude of the FRFs obtained for various values of the resistance. Clearly, the optimal value given by Equation (1.29) yields the minimum maximum amplitude under harmonic forcing.

1.2.2.2 Resonant shunt damping: series RL shunt

Resistive shunt damping is a rather simple technique but generally offers limited vibration reduction. This is due to the generally low value of the EEMCF. It is however possible to enhance the reduction using fully passive means thanks to the use of an inductor. Hagood and von Flotow [13] proposed to place an inductor in series with the resistor, as depicted in Figure 1.8. The presence of the inductor cancels the inherent reactance of the piezoelectric transducer at one specific frequency, which makes the effect of the shunt circuit equivalent to pure mechanical damping at that frequency. Connecting a series RL

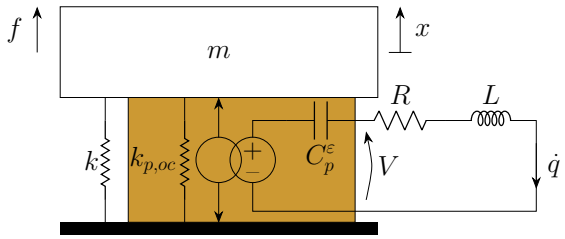

Figure 1.8: SDoF piezoelectric structure controlled by a series RL shunt.

shunt circuit to the piezoelectric transducer induces an electrical relation given by

$$V = L\ddot{q} + R\dot{q} \tag{1.31}$$

which, in the frequency domain, reads

$$sq = Y_s(s)V = \frac{1}{Ls + R}V, \tag{1.32}$$

where Y_s is the shunt admittance. When inserted into Equation (1.11), Equation (1.31) gives the coupled system's governing equations

$$\begin{cases} m\ddot{x} + k_{oc}x - \theta_p q = f \\ L\ddot{q} + R\dot{q} + \dfrac{1}{C_p^\varepsilon}q - \theta_p x = 0 \end{cases}. \tag{1.33}$$

The FRF of the controlled structure can be computed from the Laplace transform of these equations as

$$\frac{x}{f} = \frac{1}{ms^2 + k_{oc} - \theta_p^2 \dfrac{1}{Ls^2 + Rs + \dfrac{1}{C_p^\varepsilon}}} = \frac{Ls^2 + Rs + \dfrac{1}{C_p^\varepsilon}}{(ms^2 + k_{oc})\left(Ls^2 + Rs + \dfrac{1}{C_p^\varepsilon}\right) - \theta_p^2} \tag{1.34}$$

Figure 1.9 displays several FRFs for various values of inductance and resistance. Interestingly, Equation (1.34) indicates that if $R = 0$, at the electrical resonance frequency

$$\omega_e = \sqrt{\frac{1}{C_p^\varepsilon L}}, \tag{1.35}$$

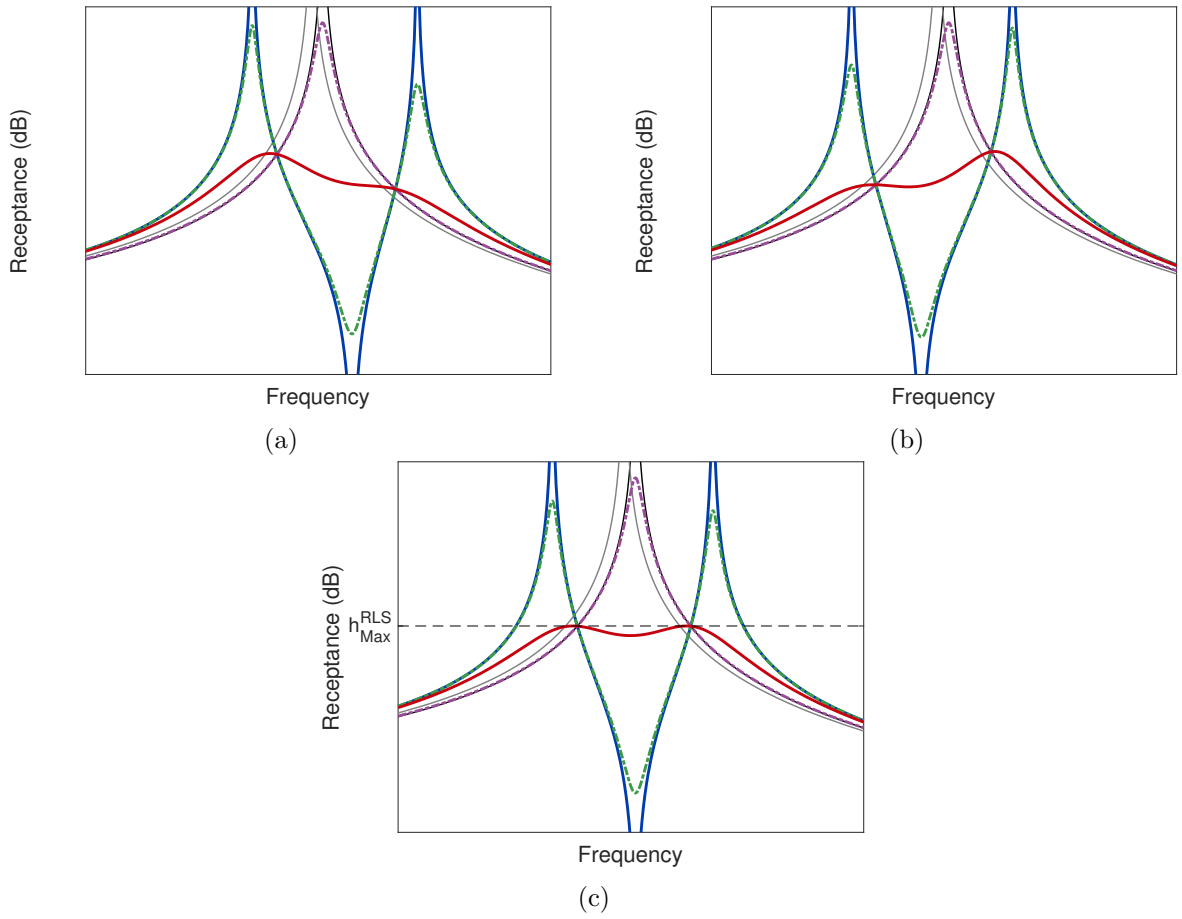

Figure 1.9: FRF of the structure with a short-circuited transducer (—), with an open-circuited transducer (—) and with a series RL shunt: $L = 0.95L_{opt}^{RLS}$ (a), $L = 1.05L_{opt}^{RLS}$ (b) and $L = L_{opt}^{RLS}$ (c) ; $R = 0$ (—), $R = 0.1R_{opt}^{RLS}$ (- - -), $R = R_{opt}^{RLS}$ (—), $R = 10R_{opt}^{RLS}$ (- - -).

the FRF is zero: the electrical resonance interferes destructively with the vibrations of the mechanical system. However, Figure 1.9 shows that this comes at the expense of two new undamped resonance peaks. This undesirable feature (in terms of H_∞ norm) can be mitigated with the use of a nonzero resistance.

Similarly to what was observed for a resistive shunt, it can be seen from Figure 1.9 that there exist so-called fixed points which, for a given inductance, belong to all FRFs. A way to tune the inductance is thus to make these fixed points equal in amplitude. There are then multiple ways to set the resistance. Hagood and von Flotow [13] proposed to set it such that the FRF amplitude at the electrical resonance frequency be equal to that of the fixed points, thereby obtaining a relatively flat FRF. Yamada et al [74] tuned it so that the fixed points be the maxima of the FRF. It is not possible to simultaneously make these two points maxima for a given resistance, and a mean-square average of the values making either fixed point a maximum was chosen as a practical choice of the resistance. Thomas et al [75] simplified the resulting expression with a truncated Taylor series in K_c.

The fixed-point method is based on fixed points which are only approximations of the true peaks of the FRF, and the resulting H_∞ norm is somewhat suboptimal. Obtaining the exact solution to the H_∞ norm minimization problem is a rather cumbersome task, but

closed-form solutions have been found in [81, 83]. Introducing an intermediate parameter

$$r = \frac{\sqrt{64 - 16K_c^2 - 26K_c^4} - K_c^2}{8}, \tag{1.36}$$

The optimal inductance and resistance yielding equal peaks with the exact same amplitude are

$$L_{opt}^{RLS} = \frac{4K_c^2 + 4}{3K_c^2 - 4r + 8} \frac{1}{\omega_{oc}^2 C_p^\varepsilon} = \frac{1}{\delta^2(K_c)\omega_{oc}^2 C_p^\varepsilon} \tag{1.37}$$

and

$$R_{opt}^{RLS} = \frac{2\sqrt{2\left(K_c^2+1\right)\left[27K_c^4 + K_c^2(80-48r) - 64(r-1)\right]}}{\left(5K_c^2+8\right)\sqrt{3K_c^2 - 4r + 8}} \frac{1}{\omega_{oc} C_p^\varepsilon} = \frac{2\zeta(K_c)}{\delta(K_c)\omega_{oc} C_p^\varepsilon}, \tag{1.38}$$

respectively. We note that $\delta(K_c) \overset{K_c \ll 1}{\approx} 1$, that is, the electrical resonance is very close to the open-circuit mechanical one.

Using the intermediate parameter defined in Equation (1.36), the peaks' amplitude is

$$h_{Max}^{RLS} = \frac{1}{k_{sc}\sqrt{1-r^2}} \approx \frac{\sqrt{2}}{k_{sc}K_c} + O(K_c). \tag{1.39}$$

The approximate truncated Puiseux series shows that an RL shunt results in a maximum vibration amplitude which scales with K_c^{-1}. In contrast, that with a resistive shunt scales with K_c^{-2} (Equation (1.30)), which owing to the smallness of the EEMCF can much larger. However, an issue of resonant shunts is highlighted by Figures 1.9(a) and 1.9(b): for a mere 5% error in the inductance value, the two peaks of the FRF can become seriously unbalanced. This sensitivity highlights the need for a precise tuning of the electrical frequency to that of the mechanical system for proper operation.

1.2.2.3 Resonant shunt damping: parallel RL shunt

Instead of placing the inductor in series with the resistor in the shunt circuit, the former may be placed in parallel with the latter, as in Figure 1.10. This particular arrangement was proposed by Forward [12] and Wu [19] and also exploits an electrical resonance for efficient vibration mitigation.

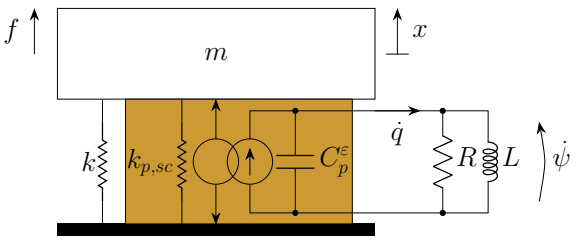

Figure 1.10: SDoF piezoelectric structure controlled by a parallel RL shunt.

The following quantities

$$\psi = \int_0^t V(\tau)d\tau, \qquad G = \frac{1}{R}, \qquad B = \frac{1}{L}, \tag{1.40}$$

are introduced as the flux linkage, the conductance of the resistor and the reluctance of the inductor, respectively. The connection of a parallel RL shunt circuit imposes the following relation between the current and the flux linkage

$$\dot{q} = G\dot{\psi} + B\psi. \tag{1.41}$$

Inserting this relation into Equation (1.6) yields the governing equations

$$\begin{cases} m\ddot{x} + k_{sc}x + \gamma_p\dot{\psi} = f \\ C_p^{\varepsilon}\ddot{\psi} + G\dot{\psi} + B\psi - \gamma_p\dot{x} = 0 \end{cases}. \tag{1.42}$$

Equations (1.33) and (1.42) are similar, and so are the performance of these two approaches [81, 84, 85]. Differences however exist when tuning the electrical parameters, especially the resistances. The tuning approaches are similar to those of the series RL shunt, namely, fixed points exist for the parallel RL shunt as well, which gives a way to determine the inductance. As for the resistance, Wu [19] equated the amplitude of the FRF at the electrical resonance frequency to that of the fixed points and Yamada et al [74] used the mean-square value of the resistances making the fixed-points maxima of the FRF. The exact H_∞-optimal solution was found by Ikegame et al [81] after noting the similarity with the problem of series RC shunts for electromagnetic transducers found by Tang et al [86]. The optimal formulae are obtained by first computing the series of coefficients

$$\begin{aligned}
b_0 &= 64 & b_1 &= -16K_c^2 \\
b_2 &= -64 + 16K_c^2 + 11K_c^4 & b_3 &= 2K_c^2(8 - K_c^2)(2 - K_c^2) \\
b_4 &= -2K_c^4(2 - K_c^2) & & \\
a_6 &= 27(b_0b_3^2 + b_1^2b_4) - 9b_2(b_1b_3 + 8b_0b_4) + 2b_2^3 & a_5 &= 12b_0b_4 - 3b_1b_3 + b_2^2 \\
a_4 &= \sqrt[3]{\frac{\sqrt{a_6^2 - 4a_5^3} + a_6}{2}} & a_3 &= \frac{1}{2}\sqrt{\frac{b_1^2}{b_0^2} + \frac{4(a_4^2 + a_5 - 2b_2a_4)}{3b_0a_4}} \\
a_2 &= -\frac{8b_0^2b_3 - 4b_0b_1b_2 + b_1^3}{4b_0^3a_3} & a_1 &= \frac{3b_1^2a_4 - 2b_0(4b_2a_4 + a_4^2 + a_5)}{6b_0^2a_4}
\end{aligned} \tag{1.43}$$

and finally,

$$r = -\frac{b_1}{4b_0} + \frac{a_3}{2} + \frac{\sqrt{a_1 + a_2}}{2} \tag{1.44}$$

and the optimal reluctance B and conductance G are given by

$$B_{opt}^{RLP} = \frac{2r - K_c^2 + \sqrt{16r^2 - 4rK_c^2 + K_c^4}}{6}\omega_{sc}^2C_p^{\varepsilon} = \nu^2(K_c)\,\omega_{sc}^2C_p^{\varepsilon} \tag{1.45}$$

and

$$G_{opt}^{RLP} = \frac{1}{2}\sqrt{\frac{1}{r}\frac{(r-1)(3r - 2K_c^2)}{2r + K_c^2 - \sqrt{16r^2 - 4rK_c^2 + K_c^4}}}\sqrt{B_{opt}^{RLP}C_p^{\varepsilon}} = 2\varsigma(K_c)\,\nu(K_c)\,\omega_{sc}C_p^{\varepsilon}, \tag{1.46}$$

respectively.

1.2.2.4 Other piezoelectric shunting techniques

The techniques presented above form the basics of piezoelectric shunt damping, but are far from constituting an extensive list of existing approaches. A few extensions are discussed hereafter.

A first extension is to use shunt circuit composed of more elements in the attempt to control multiple structural modes. This aspect is treated in Chapter 2.

Shunts circuits can be used in combination with a negative capacitance. In this approach invented by Forward [87], an active element implementing the behavior of a capacitor with negative capacitance is connected to the piezoelectric transducer. The introduction of this negative capacitance results in an increase in the EEMCF of the system (and thus in damping performance) through the modification of the short- and/or open-circuit resonance frequencies [88, 89]. This improvement comes at the expense of a necessarily active component.

Another approach using electromechanical coupling for vibration mitigation is the so-called switch damping approach, wherein the piezoelectric electrodes are connected to an electrical switch. Based on the features of a control signal, the switch either disconnects the electrodes or connects them. The connection can either be a short-circuit [90], a resistor [91], an inductor [92], a negative capacitance [93], or even a voltage source [94]. Although the switch is an active electronic component, this approach can be realized with low-power electronics to be self-powered [95]. This technique can however present issues when applied to structures with multiple modes: the excitation induced by the switching sequence can excite higher-frequency modes, which in turn can perturb the signals driving this sequence, resulting in loss of performance [96].

1.3 Purpose and practical realization of a digital absorber

Shunt damping is an attractive approach but may present practical issues. Among them, the main ones are listed below.

(i) Large inductances may be required. A commonly-used type of piezoelectric transducer is the piezoelectric patch. Typically, capacitances of piezoelectric patches are few tens nF and for low frequencies below a thousand Hz the required inductance is of the order of the Henry (H) or greater. Such high inductances are generally not commercially available. They can be realized using custom-made inductors [23, 97], but the inductance value may come at the expense of high associated series resistance, large weight and size or unwanted nonlinear behavior of the component [98]. Another approach uses the so-called synthetic inductors made with electronic amplifiers and realized either with Riordan gyrators [99] or Antoniou's generalized-impedance convertor circuit [100]. These circuits allow for fine tuning of the inductance, but are no longer passive and show non-ideal characteristics such as frequency-dependent resistance [24].

(ii) Vibration mitigation performance is very sensitive to the electrical parameters. In general, this implies that if a first test shows some misadjustments in the

electrical parameters, the corresponding components have to be manually modified or replaced, which may be a time-consuming procedure prone to manipulation errors. Besides, the host system's characteristics may change with time due to varying environmental conditions, which leads to a detuning of the absorber and performance loss.

(iii) Functional properties of the absorber (e.g., for multimodal or nonlinear control) most often require more electrical components, and some of them may not easily be found.

(iv) Piezoelectric transducers typically exhibit high voltages across their electrodes. Analog electrical circuits will require passive and/or active components to comply with such high voltage ranges.

Fleming et al [25] introduced the concept of synthetic impedance, for which the shunt circuit is replaced by an electronic circuit that mimics the desired impedance. The circuit is composed of analog electronic components that are to be connected to a piezoelectric transducer, and a digital unit. Issue (iv) is still present for the DVA, but can be mitigated with the use of a reduced number of high-voltage components (whereas in analog circuits, nearly every electrical component should be high-voltage). Issues (i) to (iii) are solved by the fact that the digital unit can be programmed to emulate virtually any circuit, regardless of its complexity. Modifications to this circuit are readily made by simple changes in the software of the digital unit. The synthetic impedance is not to be confused with the aforementioned synthetic inductor. In order to avoid any confusion, the terms *digital impedance* or *digital admittance* shall rather be used in this work. Similarly, a piezoelectric absorber made with such a digital impedance is called *DVA*.

A DVA can work in two ways to mimic an electrical circuit: it may either work as an electrical admittance (from a measure of the voltage across the electrodes of the transducer, the DVA injects a current) or as an electrical impedance (from a measure of the current flowing through the transducer, the DVA imposes a voltage). These two concepts can identically be referred to as immittance. Depending on its working mode, the electrical architecture of the DVA may vary, but in either case it comprises three basic building blocks:

1. A **sensing element** able to read the state of the transducer (either measure its voltage or current) and convert it to a suitable input signal for the next block.
2. A **digital processing unit** such as a microcontroller unit (MCU) or a digital signal processor (DSP) able to emulate a desired input-output (I/O) relation. The key feature of the DVA lies in this unit, because it enables the possibility to emulate any immittance by proper programming.
3. An **actuating element** able to impose the desired output (either voltage or current) to the piezoelectric transducer.

The arrangement of these building blocks is schematically depicted in the block diagrams in Figure 1.11.

In this work, digital absorbers sensing voltages and injecting currents (i.e., implementing an admittance) are preferred over their counterparts. This configurations has two

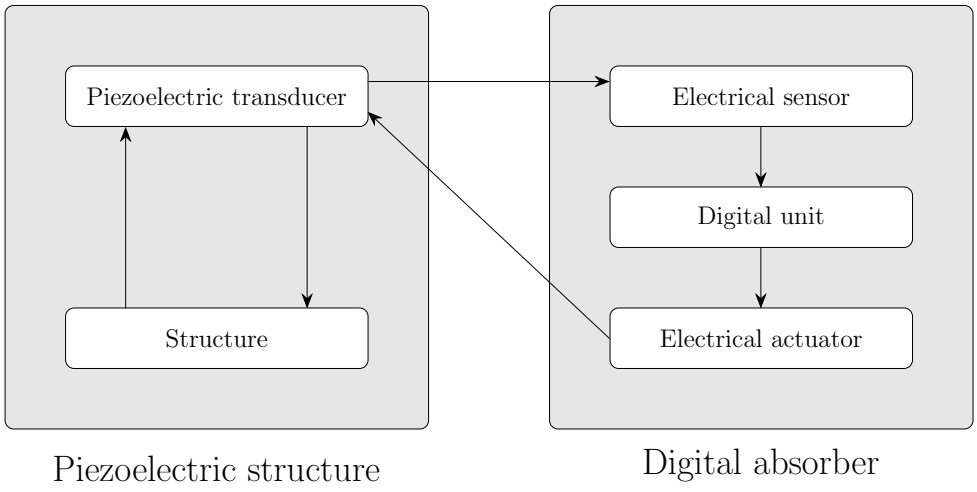

Figure 1.11: General schematics of a piezoelectric structure controlled by a DVA.

advantages [20]. The first one is that charge (or current) actuation substantially reduces hysteresis compared to voltage actuation [101]. The second reason is that most admittances to be realized are proper transfer functions (they possess more poles than zeros), and the impedances are thus improper transfer functions, which cannot be implemented as such [102].

1.3.1 Hardware

Between the transducer and the digital unit, there must be analog electronics. This stems from two main reasons. The first one is that piezoelectric transducers can output large voltages (cases considered in this work went up to hundreds of volts) whereas digital units generally work with low voltages (typically less than 10 V). The second one is that the digital unit may not be able to inject the desired current into the transducer by itself. The analog electronics thus play the role of an interface between the digital unit and the transducer.

A schematic view of the analog circuit used in this work is featured in Figure 1.12. The circuit serves the same purpose as described by Fleming et al [25] and is very close to what was proposed by Matten et al [60, 61].

The general working principles of the board are first explained and are followed by more detailed explanations discussing the settings of the board. It is assumed that every operational amplifier (OpAmp) behaves ideally, that is, they have an infinite input impedance, infinite open-loop gain and zero output impedance [103]. In other words, it can be assumed that the voltages of their inverting ($-$) and noninverting ($+$) inputs are equal, and that no current flows through them.

The transducer's voltage V is measured with a voltage divider made of R_1 and R_2. The OpAmp OA1 is a follower which outputs a fraction of the patch voltage αV, where

$$\alpha = \frac{R_2}{R_1 + R_2}. \tag{1.47}$$

A constant offset voltage ΔV_{in} is followed by OA2 to comply with the input voltage range of the analog-to-digital converter (ADC) of the MCU. OA3 is a summing amplifier that

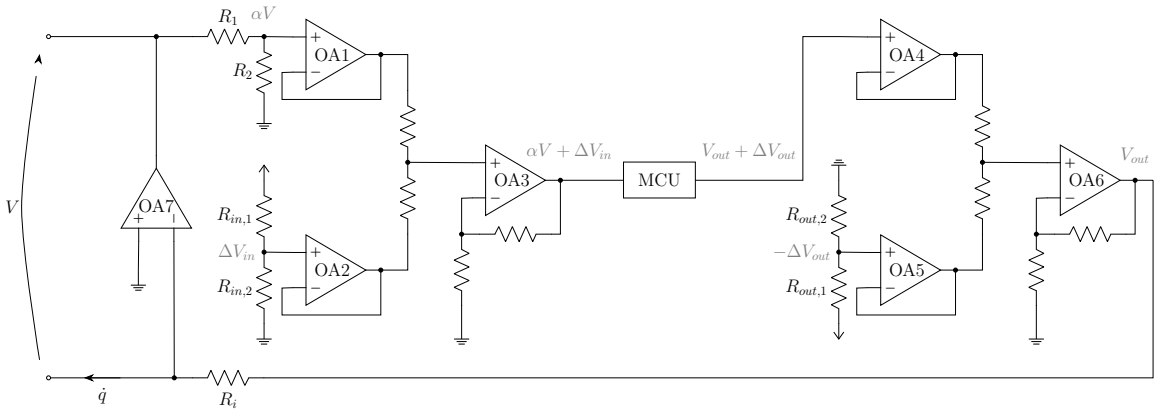

Figure 1.12: Layout of the DVA. The port to the left is to be connected to the piezoelectric transducer.

sums the two voltages and outputs $\alpha V + \Delta V_{in}$. The MCU computes the I/O relation to inject the desired current and sends a voltage signal with its digital-to-analog converter (DAC) to OA4, which is used as a buffer. Since the output voltage range of the MCU may not be symmetric with respect to the circuit ground, another offset voltage $-\Delta V_{out}$ coming from OA5 is added to the output signal by OA6. This results in an output voltage signal V_{out} proportional to the current to be injected in the transducer. This voltage signal is imposed on one terminal of the resistor R_i, while the other one is maintained to a virtual ground by OA7. Thus, the current injected into the piezoelectric patch is V_{out}/R_i.

The input voltage of the MCU must lie in a certain range comprised between $V_{ADC,min}$ and $V_{ADC,max}$ in order to avoid permanent damage. According to Figure 1.12, this input voltage depends on the division ratio α, the piezoelectric voltage V and the input offset voltage ΔV_{in}. Assuming that the piezoelectric voltage maximum amplitude is V_{max}, i.e., $V \in [-V_{max}, V_{max}]$, the maximum and minimum voltages at the ADC are

$$V_{ADC,max} = \alpha V_{max} + \Delta V_{in} \tag{1.48}$$

and

$$V_{ADC,min} = -\alpha V_{max} + \Delta V_{in}, \tag{1.49}$$

respectively. Consequently, α and ΔV_{in} can be found as

$$\alpha = \frac{V_{ADC,max} - V_{ADC,min}}{2V_{max}} \tag{1.50}$$

and

$$\Delta V_{in} = \frac{V_{ADC,max} + V_{ADC,min}}{2}, \tag{1.51}$$

respectively. A more conservative approach is to choose α smaller than given in Equation (1.50) in order to have safety margins. When $V_{ADC,max} = -V_{ADC,min}$ the voltage reference given by OA2 and the summing action of OA3 are not needed.

Similarly, the output voltage range should be shared equally between positive and negative ranges. The output voltage of the MCU is comprised between $V_{DAC,min}$ and $V_{DAC,max}$. Consequently, the output offset voltage should be

$$\Delta V_{out} = \frac{V_{DAC,max} + V_{DAC,min}}{2}. \tag{1.52}$$

When $V_{DAC,max} = -V_{DAC,min}$ the voltage reference given by OA5 and the summing action of OA6 are not needed. In case OA2, OA3, OA5 and OA6 are not needed, the analog circuit reduces to that given in Fleming et al [25].

OpAmps cannot in general have their input or output pins subjected to voltages outside of the range of their supply. For OpAmps 1 to 6, this is not a stringent constraint, as the order of magnitude of the voltages they are subjected to is identical to that of the MCU. However, OA7 is directly connected to the electrodes of the piezoelectric transducer and its output is at V, which might potentially be large. This particular OpAmp must thus be chosen accordingly. In response to issue (iv), this is the only component that needs to work with high voltages, as mentioned in [25].

The last parameter to be set in the analog circuit is the resistance of the current injector R_i. This parameter is discussed in the next section, since it may depend on the software implementation.

1.3.2 Software

The MCUs used in this work are Arduino, whose programming can be fairly straightforward thanks to the MATLAB support packages for Arduino hardware. The user essentially has to draw a block diagram in MATLAB Simulink representing the action of the DVA. A C-code is then automatically generated, compiled and downloaded to the MCU by the support packages.

Figure 1.13 represents the software working principles as a block diagram. With the Arduino, the ADC reads a voltage level and translates it into an unsigned integer number. This integer is reconverted to a floating point number representing a voltage level by the gain g_{in}. An offset ΔV_{in} is added to compensate for the input voltage offset generated by the analog circuit. The shifted and scaled signal is processed according to the desired I/O relation Y_s, the synthesized shunt circuit admittance [25]. It is then amplified by a gain g whose purpose is explained hereafter. The output signal is passed through a saturation operator to avoid integer overflow at the DAC. Finally, the output signal is shifted (by ΔV_{out}) and scaled (by g_{out}) back to an unsigned integer to be fed to the DAC.

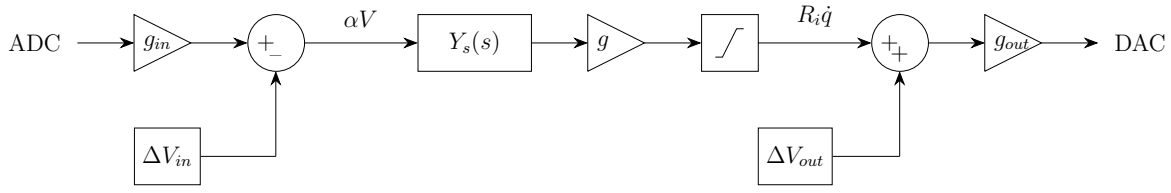

Figure 1.13: Block diagram representation of the software emulating a digital admittance $Y_s(s)$.

If the minimum and maximum values of the ADC outputs are $N_{ADC,min}$ and $N_{ADC,max}$ and correspond to an input voltage $V_{ADC,min}$ and $V_{ADC,max}$ respectively, the input gain g_{in} can be set to transform the input unsigned integer signal to an input voltage signal:

$$g_{in} = \frac{V_{ADC,max} - V_{ADC,min}}{N_{ADC,max} - N_{ADC,min}}. \tag{1.53}$$

Similarly, if the minimum and maximum values that can be fed to the DAC are $N_{DAC,min}$ and $N_{DAC,max}$ and correspond to an output voltage $V_{DAC,min}$ and $V_{DAC,max}$ respectively,

$$g_{out} = \frac{N_{DAC,max} - N_{DAC,min}}{V_{DAC,max} - V_{DAC,min}}. \tag{1.54}$$

Special care has to be taken when using the admittance block Y_s due to the fact that the digital unit works at a discrete rate. A discussion on this is made in Section 1.6.

If properly tuned, every voltage offset from the analog circuit should be compensated by an offset in the software. The remaining parameter to tune is the gain g whose purpose is to ensure the consistency of the I/O relation with a shunt circuit from the point of view of the transducer. If the offsets are perfectly compensated, the current $i = \dot{q}$ injected into the transducer should be

$$i(s) = \frac{1}{R_i} V_{out}(s) = \frac{g\alpha}{R_i} Y_s(s) V(s), \tag{1.55}$$

where s is the Laplace variable. Equation (1.55) shows that if the emulated shunt circuit is to mimic the desired admittance, the following consistency condition should be ensured

$$\frac{g\alpha}{R_i} = 1 \tag{1.56}$$

Which gives a final relation that fully specifies the characteristics of the DVA. Among the two remaining parameters g and R_i, one can be chosen freely, while the other is set to comply with Equation (1.56). Two approaches can then be followed, given an emulated admittance Y_s.

The first approach consists in setting R_i so that the full DAC voltage range is used concurrently with the full ADC voltage range. Under the assumption that the piezoelectric voltage amplitude is V_{max}, the maximum current is given by

$$i_{max} = H_\infty \left\{ Y_s(s) \right\} V_{max} \tag{1.57}$$

where $H_\infty \{\cdot\}$ is an operator giving the H_∞ norm, i.e., the maximum value over the frequency range

$$H_\infty \left\{ Y_s(s) \right\} = \max_\omega \left| Y_s(j\omega) \right|. \tag{1.58}$$

Consequently, the maximum output voltage amplitude should be

$$V_{out,max} = R_i i_{max} \tag{1.59}$$

The DAC voltage should cover this range of voltages added to ΔV_{out}, thus

$$V_{DAC,min} = -V_{out,max} + \Delta V_{out} \tag{1.60}$$

and

$$V_{DAC,max} = V_{out,max} + \Delta V_{out} \tag{1.61}$$

Combining Equations (1.57), (1.59), (1.60) and (1.61) yields an optimal value for the current injector resistance

$$R_i = \frac{V_{DAC,max} - V_{DAC,min}}{2 H_\infty \left\{ Y_s(s) \right\} V_{max}} \tag{1.62}$$

The gain g may then be determined from Equation (1.56). This approach has the advantage to make optimal use of the DAC range. An issue is that R_i becomes dependent on the emulated admittance; changing the latter hence requires hardware modifications which reintroduces issue (iii).

The second approach is thus to keep R_i to a fixed arbitrary value and compute g accordingly (Equation (1.56)). R_i should be chosen smaller than the optimal value given in Equation (1.62) considering any admittance Y_s to be emulated. Too low a resistance is however undesirable, as a smaller range of the DAC will be used. Moreover, the current injected in the transducer will be more sensitive to the output voltage noise of OA6 in Figure 1.12.

1.3.3 Experimental validation

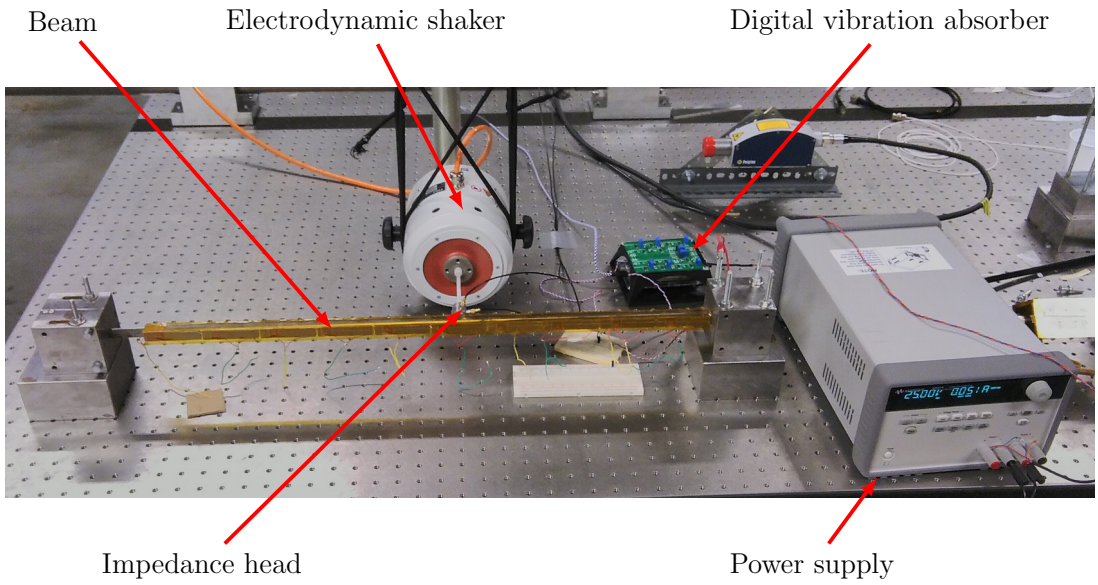

Figure 1.14: Picture of the experimental setup.

The action of the DVA was experimentally demonstrated on a clamped-free steel beam with a clamped thin lamina attached to its free end, as shown in Figure 1.14. When it undergoes large relative deformation, the thin lamina can cause an overall hardening nonlinear structural behavior. Up until Chapter 5, the excitation amplitude applied to the structure will be low enough so as to neglect this nonlinear effect; the structure is thus assumed to behave linearly. It was excited at middle span by an electrodynamic shaker (TIRA TV 51075). An impedance head (DYTRAN 5860B) was used to measure the force applied to the structure and the corresponding acceleration. The measurements were recorded by an acquisition system (LMS Scadas Mobile).

The beam is 700mm long and has a cross-sectional area of 14mm×14mm. It is covered over its whole length with pairs of 2mm-thick PSI-5A4E piezoelectric patches, each pair being placed on either side of the beam, as represented in Figure 1.15(a). The beam and each pair form a bimorph where the two patches are poled in opposite directions. Their electrodes are connected in parallel, thereby forming an electromechanical cell of the beam depicted in Figure 1.15(b). More details about the experimental setup can be found in [104].

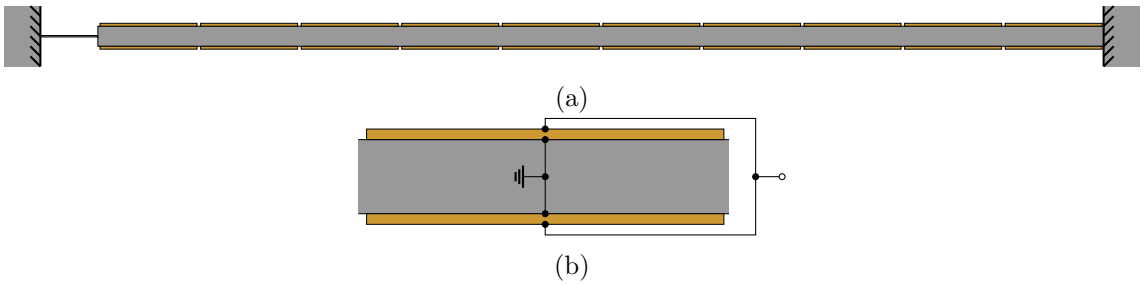

Figure 1.15: Schematic representation of the piezoelectric beam in top view (a) and close-up on an electromechanical cell of the beam (b).

By connecting cells in parallel, it is possible to form an equivalent transducer with a different electromechanical coupling than that of a single cell. Figure 1.16 depicts the EEMCFs with the first bending mode of the beam experimentally measured by connecting various numbers of cells closest to the clamped edge. The EEMCF first increases with this number, because the combined action of the patches increases the control authority over the structure. However, the modal strains induced in the patches can have different signs, and charge cancellation starts to occur when this number becomes too large, resulting in a decrease in the EEMCF. Figure 1.16 indicates that the number of parallel connections maximizing the EEMCF with the first bending mode is four. However, it was chosen to connect the five cells closest to the clamped end in parallel to mitigate the resonant vibrations around the first beam mode (leaving the five other cells in open circuit) in order to obtain results comparable to [104] with a near-optimal EEMCF.

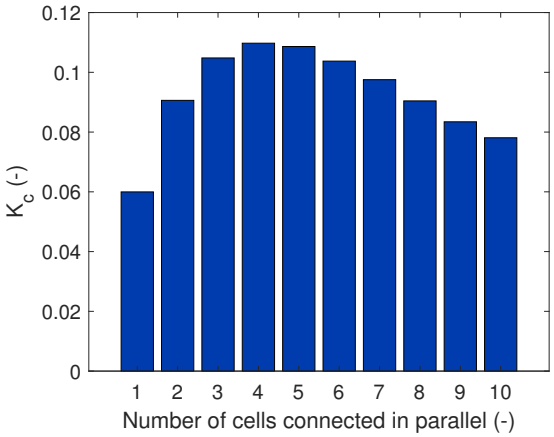

Figure 1.16: EEMCFs of the parallel connection of various numbers of cells closest to the clamped edge with the first bending mode of the beam.

Figure 1.17(a) shows a picture of the DVA, where the analog circuit realized with a printed circuit board (PCB) and the MCU are visible. Figure 1.17(b) offers a top view of the PCB. The PCB contains twice the circuit schematized in Figure 1.12. In Figure 1.17(b), the operational amplifiers (OPA 454 from Texas Instruments [105]) labeled with Ui or $U(i+7)$ $(i = 1, \cdots, 7)$ correspond to OAi in Figure 1.12. The blue potentiometers are used to easily set up R_1, $R_{in,1}$, $R_{out,1}$ and R_i.

To identify the system, the FRFs of the beam when the patches are short-circuited or open-circuited were measured. These FRFs, noted x/f and obtained with a low-level broadband excitation, are displayed in Figure 1.18.

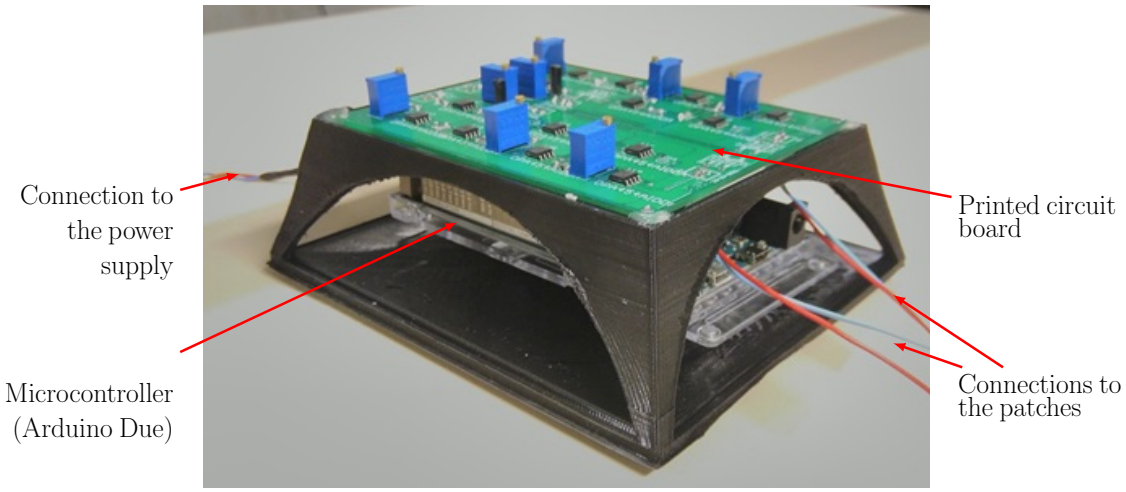

(a)

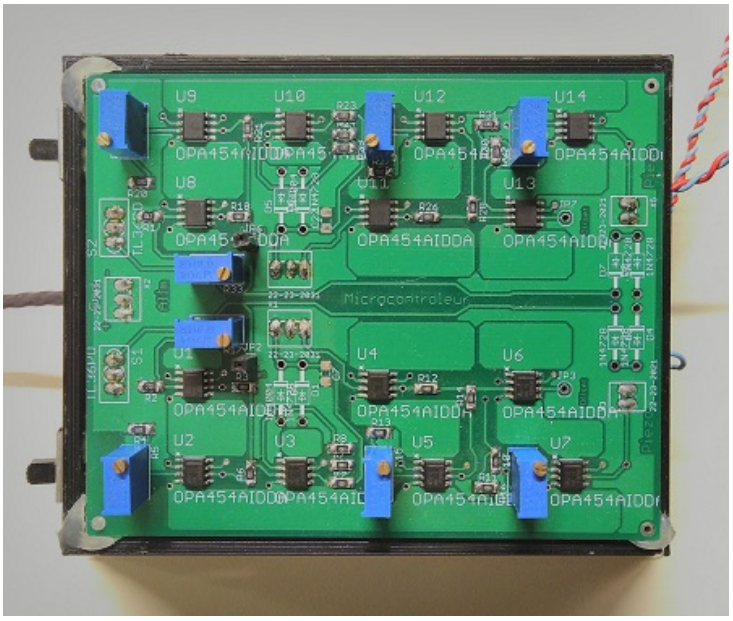

(b)

Figure 1.17: Pictures of the DVA: general view of the DVA (a) and top view of the PCB (b).

The peaks of these FRFs gave an estimation of the short- and open-circuit resonance frequencies. The piezoelectric capacitance was then measured with a multimeter (FLUKE 177). From these parameters, the optimal resistance of a resistive shunt was computed from Equation (1.29), and the optimal inductance and resistance of a series RL shunt were computed using Equations (1.37) and (1.38), respectively. All these parameters are reported in Table 1.1.

Parameter	f_{sc}	f_{oc}	K_c	C_p^{ε}	R_{opt}^{R}	R_{opt}^{RLS}	L_{opt}^{RLS}
Value	31.08Hz	31.29Hz	0.116	245nF	20 854Ω	2 961Ω	105.7H

Table 1.1: Parameters of the experimental setup.

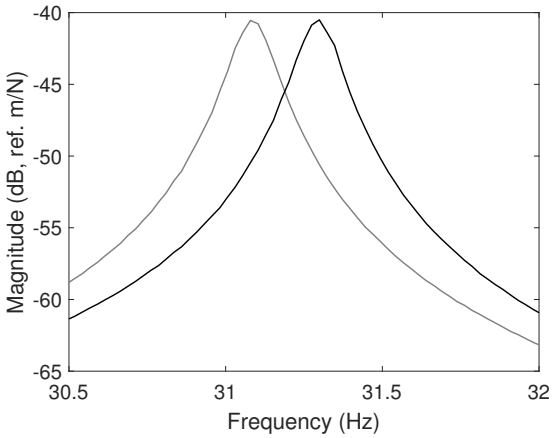

Figure 1.18: Experimental FRFs of the beam with short-circuited (—) and open-circuited (—) patches.

The DVA was powered with $\pm 25V$ by an external power supply (Keysight E3647A), and the MCU was programmed in order to mimic a desired admittance, with a sampling frequency of 10kHz. The parameters of the PCB were set according to the procedure exposed in Section 1.3.1, and the resistance of the current injector $R_i = 268.3\Omega$ was measured with a multimeter. At first, to validate the equivalence between a shunt circuit and the DVA, a resistive shunt was considered, since its realization with passive resistors is easily done. From series connections of available resistors, the resistance of the analog resistive shunt was measured at $20.51k\Omega$. The resulting FRF is compared to that obtained with the DVA emulating a resistive shunt in Figure 1.19. The two FRFs are very close, which confirms that the DVA can be used as a substitute to a shunt circuit and that its parameters are tuned correctly. It should be noted that unlike the case featured in Figure 1.7, the peak of the FRF with a resistive shunt is not coincident with the intersection of the short-circuit and open-circuit curves. This is solely due to the presence of structural damping in the host structure.

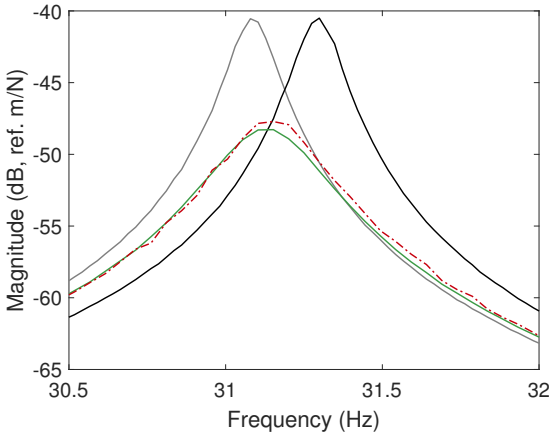

Figure 1.19: Experimental FRFs of the beam with short-circuited (—) and open-circuited (—) patches, analog resistive shunt (—) and digital resistive shunt (-·-·-).

A series RL shunt was then implemented with the DVA. Figure 1.20 gives the experimental FRFs of the structure for various values of R and L, and is to be compared to Figure 1.9. This parametric study is rather straightforward to implement, since it only requires to

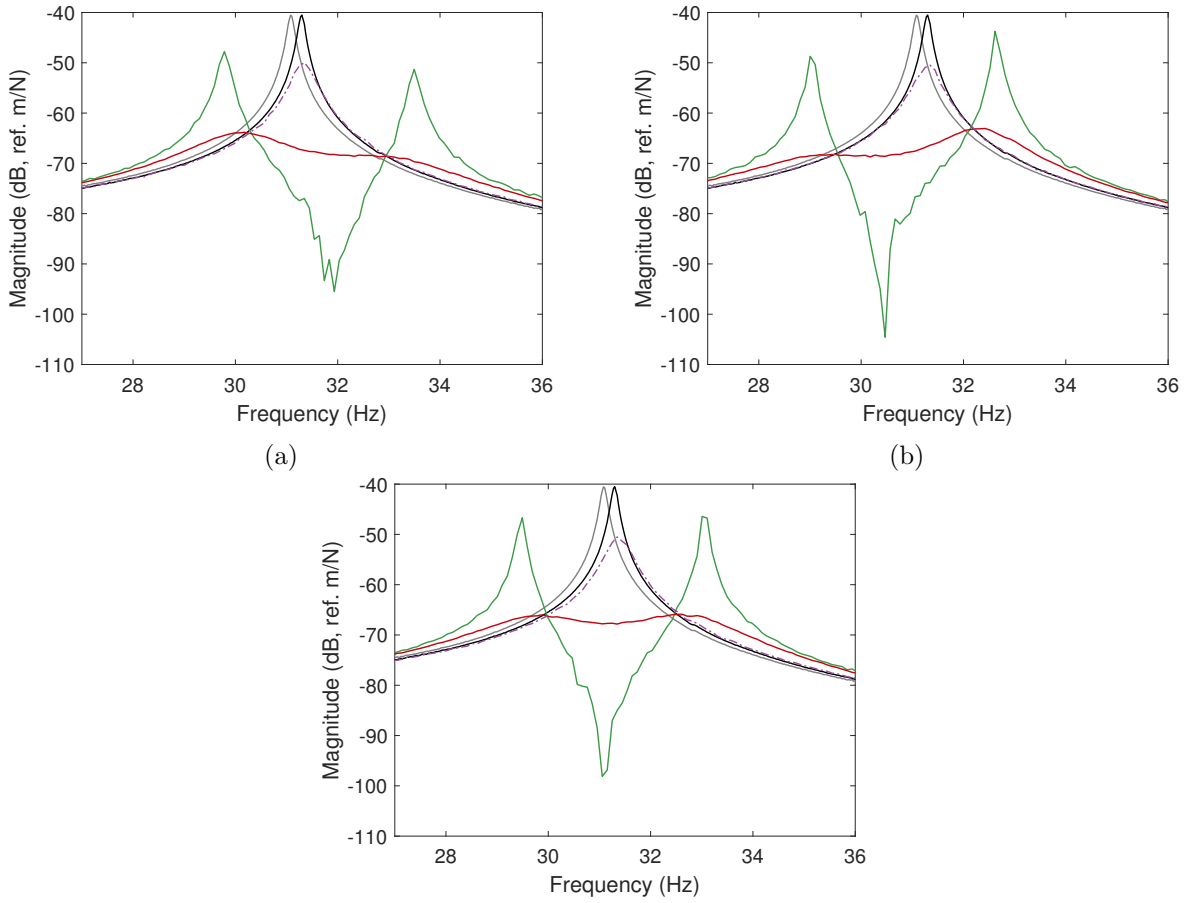

Figure 1.20: Experimental FRF of the beam with short-circuited (—) and open-circuited patches (—), and a series RL shunt: $L = 0.95L_{opt}^{RLS}$ (a), $L = 1.05L_{opt}^{RLS}$ (b) and $L = L_{opt}^{RLS}$ (c) ; $R = 0.1R_{opt}^{RLS}$ (—), $R = R_{opt}^{RLS}$ (—), $R = 10R_{opt}^{RLS}$ (- - -).

change the values of R and L in MATLAB Simulink files before measuring a FRF. Clearly, the DVA is able to emulate the desired shunt circuit.

1.4 Passivity

So far, the ability of the DVA to mimic a piezoelectric shunt was demonstrated. However, since the circuit made of purely passive components was replaced by an electronic circuit, the question of whether one is dealing with an active or a passive control system may be raised. The concept of passivity itself thus has to clearly be defined.

In this work, the term passivity may hold two meanings:

1. **The passivity of the control system**, i.e., the fact that the actual realization of the control system requires no external power supply for operation.

2. **The passivity of the control law**, i.e., the equivalence between the action of the control system on the plant and a passive control system.

The first meaning is purely related to the implementation of the control system, and, since the DVA possess both analog and digital electronics that require to be powered for operation, it is not a passive control system.

The passivity of the control law is determined based on energy concerns and only makes sense if the sensed and actuated quantities are energetically conjugate (e.g., position and force or charge and voltage). The theoretical conditions given in [106, 107] are based on the requirement that a passive system should not be able to supply more energy than the amount it initially stores plus the amount it received between this initial time and the current time. When used to implement passive shunt circuits, the DVA theoretically implements a passive control law.

It is then legitimate to wonder why one should implement passive control laws if a non-passive control system is used. A first advantage of such approach is the theoretically guaranteed stability of the controlled system with infinite gain margin [108]. Another advantage is that there exists a large body of literature on passive piezoelectric shunt damping, where tuning rules are relatively simple and allow a physical interpretation of the action of the controller. From a different point of view, the DVA could also be used as a fast prototyping device, for instance to validate theoretical tuning laws (which is one of its main use in this thesis). Despite the approach followed in this thesis, nothing prevents the use of the DVA as an active controller, as pursued in [60, 61, 109].

In the previous sections, an ideal DVA was considered, i.e., an absorber which is able to perfectly mimic a passive shunt circuit. The DVA nonetheless has two non-ideal characteristics that distinguish it from a passive shunt circuit. The first one is the non-passivity of the control system, which entails power consumption. This aspect is discussed in Section 1.5. The second non-ideal characteristic is the introduction of time delays in the system, due to the very nature of the digital unit. The consequences of such delays are investigated in Section 1.6.

1.5 Power consumption

Because of the presence of digital and analog electronics, the DVA needs to be powered. The purpose of this section is to explain how this power can be computed and to give some figures on power consumption.

Going back to the schematic representation of the DVA in Figure 1.12, two power-consuming elements can be identified: the operational amplifiers and the digital unit. The total power consumed by the DVA is simply the sum of the power consumed by these components.

The power consumption of the MCU can be estimated by [110]

$$P_{\text{MCU}} = P_{\text{MCU,Static}} + P_{\text{MCU,Dynamic}} = V_{CC,MCU} I_{CC,MCU} + \beta_{MCU} C_L V_{CC,MCU}^2 f_{CPU} \quad (1.63)$$

where $V_{CC,MCU}$ is the supply voltage, $I_{CC,MCU}$ the quiescent current, β_{MCU} is the activity factor, C_L is the load capacitance (it can also integrate the CMOS power-dissipation capacitance, and is generally determined from measurements, see [111] for more details) and f_{CPU} is the clock frequency at which the digital unit is operating. The static power $P_{\text{MCU,Static}}$ is consumed as soon as the digital unit is powered (even when it is idling), and the dynamic power $P_{\text{MCU,Dynamic}}$ is consumed when the digital unit is active.

The analog electronics consume a power which can be computed from the operating characteristics of the absorber. This power can be broken down into two parts. The first one is the quiescent power, i.e., the power consumed when the absorber is powered but not used to damp a structure. The additional power required to operate as an absorber is the useful power.

1.5.1 Power consumed by an operational amplifier

Figure 1.21(a) represents an OA whose output is connected to a load and to a power supply, and Figure 1.21(b) represents a model used to compute the power in this system [112]. The two impedances inside the OpAmp are used to model the output push-pull stage of the OpAmp [103], whereas the power consumption of the remainder of the electronics is abstracted out in the quiescent current.

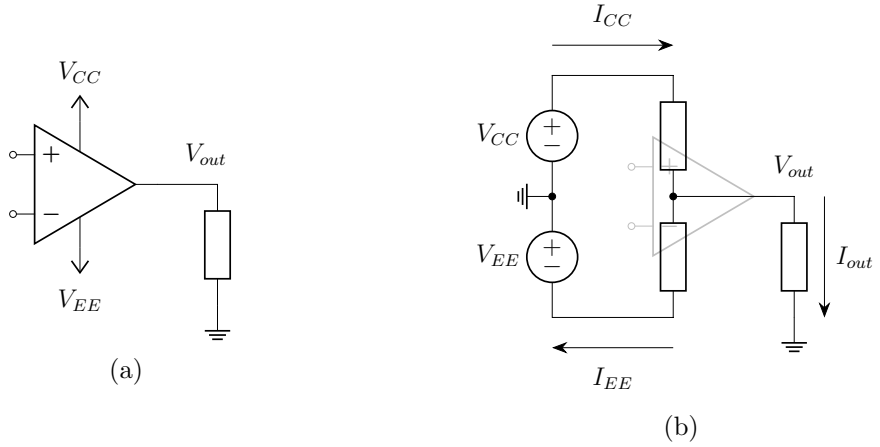

Figure 1.21: Model of an OpAmp connected to a load: electrical diagram (a) and equivalent model for power consumption assessment (b).

Applying KCL, the currents are related by

$$I_{out} = I_{CC} - I_{EE}. \tag{1.64}$$

The instantaneous power in the system can be computed as the sum of the powers in each impedance. The latter are given by the product of the current flowing through the impedances times the voltage drop across them.

$$P = I_{CC}(V_{CC} - V_{out}) + I_{EE}(V_{out} - V_{EE}) + (I_{CC} - I_{EE})V_{out} = I_{CC}V_{CC} - I_{EE}V_{EE} \tag{1.65}$$

The first two terms in the first equality represent the instantaneous power in the OpAmp, while the last one represents the instantaneous power in the load. The second equality states that the power consumed by the OpAmp and the load must be equal to the supplied power.

The OpAmp is generally supplied with a constant current called quiescent current I_Q. In addition, the power supply must supply the current sourced ($I_{out} > 0$) or sinked ($I_{out} < 0$) to the load. Owing to the internal mechanisms of the OpAmp (not detailed here but explained in [103]), sourced current comes from the positive

power supply rail (V_{CC}), whereas sinked current flows to the negative rail (V_{EE}). The supplied currents then take the conditional form

$$\begin{cases} I_{CC} = I_Q + I_{out} \qquad I_{EE} = I_Q \qquad \text{if } I_{out} \geq 0 \\ I_{CC} = I_Q \qquad I_{EE} = I_Q - I_{out} \quad \text{if } I_{out} \leq 0 \end{cases} \tag{1.66}$$

Inserting these expressions into Equation (1.65) yields another way of expressing the OpAmp power

$$P = \begin{cases} I_Q(V_{CC} - V_{EE}) + I_{out}V_{CC} & \text{if } I_{out} \geq 0 \\ I_Q(V_{CC} - V_{EE}) + I_{out}V_{EE} & \text{if } I_{out} \leq 0 \end{cases} \tag{1.67}$$

In either case, the first term featured in the expression of power in Equation (1.67) is the quiescent power consumed by the OpAmp, whereas the second one is the power needed to supply the current I_{out} to the load.

1.5.2 Power budget for a digital absorber

In the sequel, it is assumed that the OpAmps are powered by symmetric supplies, i.e.,

$$V_{CC,i} = -V_{EE,i}, \tag{1.68}$$

where subscript i refers to a particular OpAmp. Under this assumption, the power consumed by the OpAmp given in Equation (1.67) simplifies to

$$P_i(t) = 2I_{Q,i}V_{CC,i} + |I_{out,i}(t)|V_{CC,i}. \tag{1.69}$$

With the help of Figure 1.12 and assuming that every unlabeled resistor in this figure has a resistance R_0, the power consumed by each OpAmp can be assessed. Since all the voltages in this circuit are known from the operating conditions, the currents can be evaluated with Ohm's and Kirchhoff's laws. Thus, the power consumption of the OpAmps is

$$P_1(t) = 2I_{Q,1}V_{CC,1} + \left|\frac{\alpha V(t) - \Delta V_{in}}{2R_0}\right| V_{CC,1}, \tag{1.70}$$

$$P_2(t) = 2I_{Q,2}V_{CC,2} + \left|\frac{\alpha V(t) - \Delta V_{in}}{2R_0}\right| V_{CC,2}, \tag{1.71}$$

$$P_3(t) = 2I_{Q,3}V_{CC,3} + \left|\frac{\alpha V(t) + \Delta V_{in}}{2R_0}\right| V_{CC,3}, \tag{1.72}$$

$$P_4(t) = 2I_{Q,4}V_{CC,4} + \left|\frac{V_{out}(t) + 2\Delta V_{out}}{2R_0}\right| V_{CC,4}, \tag{1.73}$$

$$P_5(t) = 2I_{Q,5}V_{CC,5} + \left|\frac{V_{out}(t) + 2\Delta V_{out}}{2R_0}\right| V_{CC,5}, \tag{1.74}$$

$$P_6(t) = 2I_{Q,6}V_{CC,6} + \left|\frac{V_{out}(t)}{R_i} + \frac{V_{out}(t)}{2R_0}\right| V_{CC,6}, \tag{1.75}$$

and

$$P_7(t) = 2I_{Q,7}V_{CC,7} + \left|\frac{V_{out}(t)}{R_i} - \frac{V(t)}{R_1 + R_2}\right| V_{CC,7}. \tag{1.76}$$

In addition, the voltage references quiescently dissipate power due to the current flowing through the resistors

$$P_{V_{in}} = \left(\frac{\Delta V_{in}}{R_{in,2}}\right)^2 (R_{in,1} + R_{in,2}), \tag{1.77}$$

and

$$P_{V_{out}} = \left(\frac{\Delta V_{out}}{R_{out,2}}\right)^2 (R_{out,1} + R_{out,2}). \tag{1.78}$$

The overall power consumption can be assessed in terms of average power. If the signals are harmonic with period T, the average power is given by

$$P_{avg,i} = \frac{1}{T}\int_0^T P_i(t)dt. \tag{1.79}$$

Finally, the total power consumption of the DVA P_{DA} is computed as

$$P_{DA} = \sum_{i=1}^{7} P_{avg,i} + P_{V_{in}} + P_{V_{out}} + P_{MCU}. \tag{1.80}$$

1.5.3 A practical example

As a practical example, the power consumption of the DVA presented in Section 1.3.3 is assessed, and the predicted power consumption is compared to the experimentally measured one. In this study, only the power consumption of the PCB was considered, while that of the MCU was not measured (in the experimental setup, the MCU is powered via USB, not via the external power supply). If available, this contribution can be used in the assessment of the total power consumption of the DVA by simple addition.

All the OpAmps on the PCB are identical OPA454 from Texas Instruments. They are assumed to all have the same quiescent current, $I_{Q,i} = I_Q$, $\forall i$. The typical value for this quiescent current is given in the datasheet of the OpAmp and is 3.136mA at that supply voltage [105]. The power supply provides identical voltages to every electronic component, so that $V_{CC,i} = V_{CC}$, $\forall i$. The voltages and currents of the PCB are given in Table 1.2, and its resistances are listed in Table 1.3.

Parameter	V_{CC}	I_Q	ΔV_{in}	ΔV_{out}
Value	10V	3.136mA	1.65V	1.65V

Table 1.2: Voltages and currents of the PCB.

The characteristics of the experimental setup were obtained by fitting the FRFs measured when the patches were in short-circuit and open-circuit. A series RL

Parameter	R_0	R_1	R_2	$R_{in,1}$	$R_{in,2}$	$R_{out,1}$	$R_{out,2}$	R_i
Value	1kΩ	13.66kΩ	2.7kΩ	2.83kΩ	560Ω	2.83kΩ	560Ω	269Ω

Table 1.3: Resistances of the PCB.

Parameter	m	k_{sc}	k_{oc}	θ_p	C_p^ε	R	L
Value	3.88kg	148.27kN/m	150.49kN/m	95kV/m	244.7nF	3 025Ω	105.44H

Table 1.4: Characteristics of the beam and the shunt circuit.

shunt circuit with optimal characteristics was then emulated by the DVA. All the characteristics of this setup are reported in Table 1.4.

Since the emulated shunt circuit is a series RL one, the output and piezoelectric voltages are related through their Laplace transform as

$$V_{out}(s) = \alpha g Y_s(s) V(s) = \frac{\alpha g}{Ls + R} V(s). \tag{1.81}$$

The last specification to estimate the power consumption of the PCB is V. To ease the comparison with experiments, it is assumed that the system is excited by a constant forcing amplitude f. This forcing was set such that the maximum piezoelectric voltage does not exceed V_{CC} ; in this case, $f = 0.15$. When the shunt circuit is connected to the electrodes of the transducer, the force-to-voltage transfer function is related to the force-to-displacement one by

$$\frac{V}{f} = \theta_p \frac{x}{f} - \frac{1}{C_p^\varepsilon} \frac{q}{f} = \theta_p \frac{x}{f} - \frac{1}{sC_p^\varepsilon} Y_s(s) \frac{V}{f}. \tag{1.82}$$

Thus,

$$\frac{V}{f} = \left(1 + \frac{Y_s(s)}{sC_p^\varepsilon}\right)^{-1} \theta_p \frac{x}{f}, \tag{1.83}$$

where x/f is given by Equation (1.34).

In order to experimentally measure the power delivered to the PCB, it is necessary to measure the current sourced or sinked by the supply. With this in mind, two series resistors with small resistances of 10Ω were connected to the leads at positive and negative voltages. The sensing terminals of the power supply were connected to the other terminals of the resistors in order to compensate for the voltage drop incurred by the resistors, i.e., to ensure that $V_{CC} = 10V$. The currents were monitored by measuring the voltage drops across the series resistors with a dSPACE MicroLabBox. Figure 1.22 displays the circuit that was used.

Figure 1.23 compares the power computed with the method outlined in the previous section with that actually measured on the experimental setup. Because the DVA used in this work has twice the circuits depicted in Figure 1.12, the computation had to account for twice this circuit, one of them being at rest (but still being supplied quiescent power). It can be seen that the two graphs feature a good qualitative agreement. The quiescent power

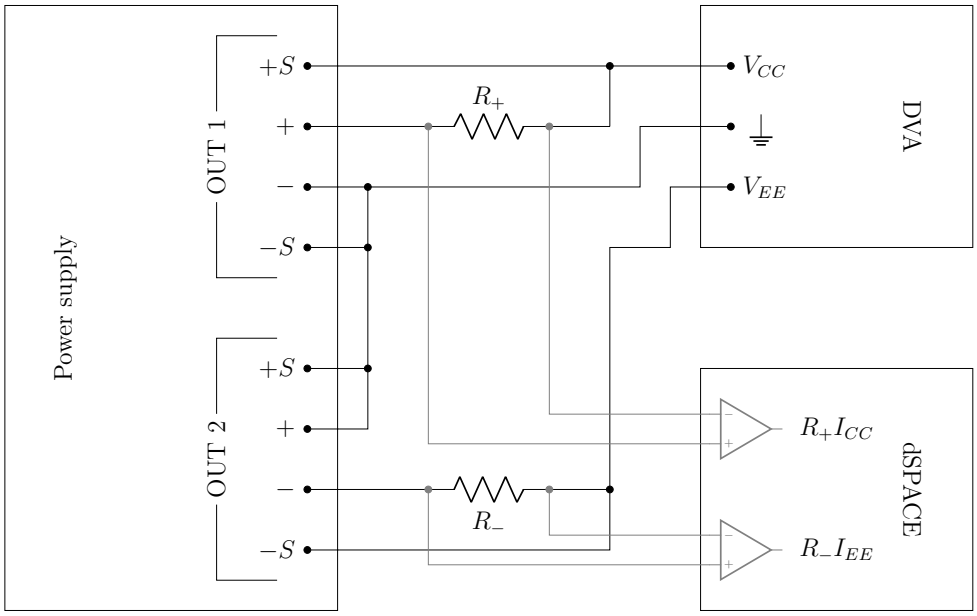

Figure 1.22: Schematic of the circuit used to monitor the power consumption of the PCB. In the power supply, $S+$ and $S-$ are the sensing terminals for the positive and negative supplied voltages, respectively.

consumption of the PCB (0.978W) is lower than predicted (1.112W). This discrepancy could be explained by uncertain experimental parameters, such as the quiescent currents of the OpAmps. The maximum power amplitude increase compared to the quiescent case is 6.6mW, which is in fair agreement with the predicted one (5.7mW). The maximum predicted power exceeds by 13% the measured power. Therefore, the proposed model can be used to give a relatively accurate idea of the actual power consumption of the DVA.

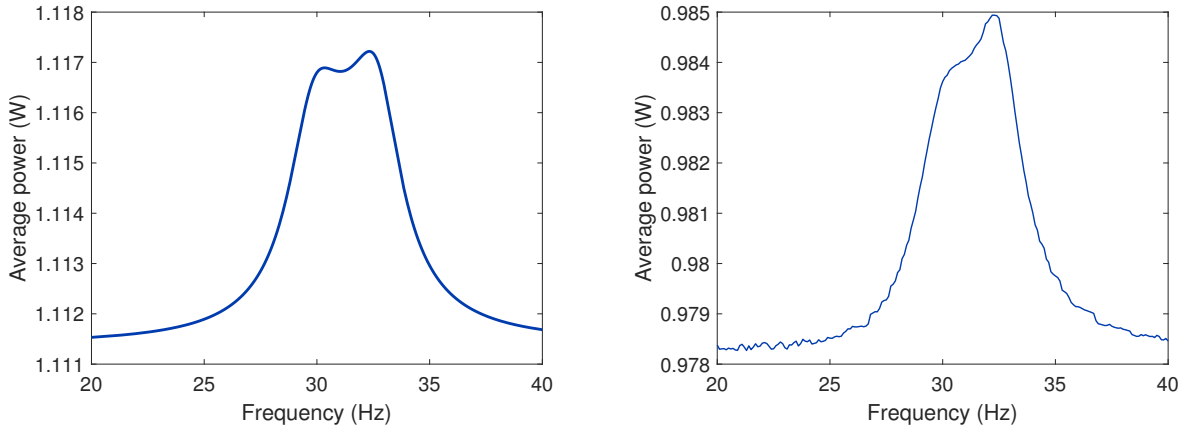

(a) (b)

Figure 1.23: Predicted (a) and experimentally measured (b) power consumption of the PCB when the DVA is used to control a beam forced at 0.15N.

The power consumption of the DVA is of the order of the Watt. It mainly comes from quiescent consumption, whereas a small fraction of its total power is actually used for the practical realization of shunt damping. It should be noted that the DVA presented here is more of a prototype, and could be optimized to minimize its power consumption. There are several paths that can be explored to reach this goal:

- OA1 to OA6 can be powered with low-voltage power supplies, which would lower their power consumption. OA7 is the only OpAmp requiring high-voltage power supplies because of its connections to the piezoelectric transducer. This feature was implemented in the DVA presented in Chapter 5.
- If $\Delta V_{in} = \Delta V_{out}$, the signals to and from the MCU must be shifted by the same amount. Instead of connecting the ground of the MCU to that of the PCB, it could be connected to a voltage reference of $-\Delta V_{in}$. This way, the MCU voltage signals would naturally be shifted by the correct amount. This would only require a voltage reference, and suppress the need for OA2, OA3, OA5 and OA6.
- Ultra-low-power OpAmps could be used in the PCB. Unfortunately, this kind of OpAmp usually also has very reduced bandwidths.
- Some OpAmps could be replaced by switched electronics, as in [56]. This is probably one of the best ways to reduce power consumption, but a quantization of this statement, as well as a characterization of the newly introduced parameters (such as the PWM period), remain to be done.

1.6 Stability

From a theoretical standpoint, a passive control system guarantees the stability of the controlled system [108]. If the problem is cast into a feedback control one, the system exhibits an infinite gain margin but a finite phase margin. Because a digital unit needs to sample the signals it is working with, unavoidable delays occur in the control loop. These delays introduce a phase lag which may destabilize the controlled system if they are too large.

Necasek et al [62] and Sugino et al [66] pinpointed the fact that in some cases a DVA needs to have a sampling frequency much higher than the typical frequencies of interest. It is the purpose of this section to understand why such a high sampling frequency may be needed, how delay-induced instabilities may arise and how to counteract them. After reviewing the basics of digital signal processing, the problem is cast as a feedback control one, and a relation between the EEMCF and the phase margin is highlighted. Values of the maximum sampling period under which the system remains stable are then derived. Finally, a stabilization procedure is proposed.

1.6.1 Basics of digital signal processing

Figure 1.24 depicts a schematic representation of the process undergone by an input signal $u(t)$ (typically, the piezoelectric voltage) to be transformed to an output signal $y(t)$ (typically, the piezoelectric current) by a digital unit [33].

A sample-and-hold circuit (SHC) holds the input signal $u(t)$ constant at specific times, multiples of the sampling period τ. The resulting sampled signal, called *discrete signal* can be seen in Figure 1.25(a). The ADC then quantizes the signal in order to code it on discrete words of finite length. The quantized discrete signal, called *digital signal*, can thus only take discrete values (multiples of the quantum y_q) at discrete instants in time, as shown in Figure 1.25(b).

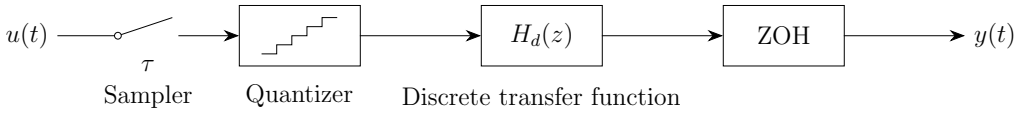

Figure 1.24: Block diagram representation of the input/output relation in a digital system.

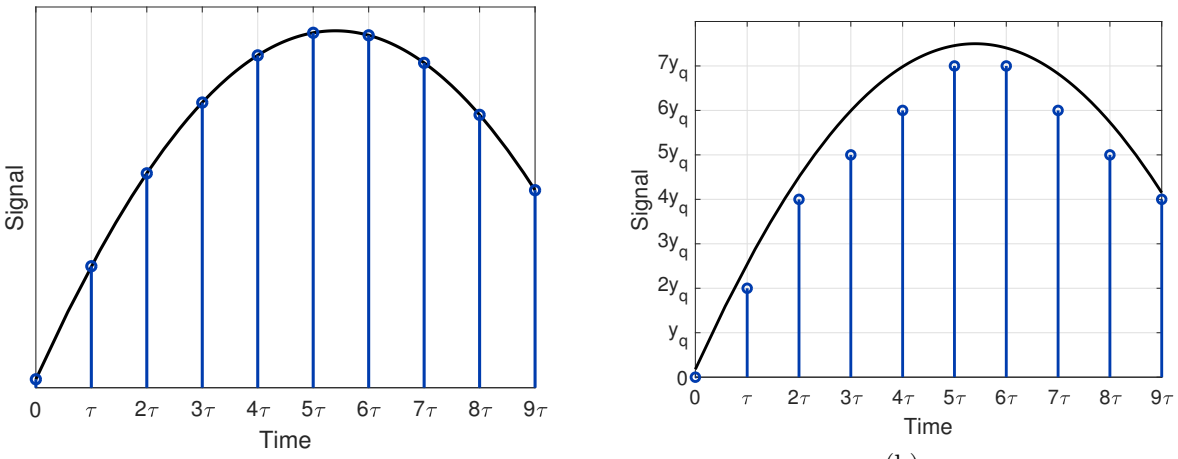

Figure 1.25: Sampling effect on a signal (a): continuous-time signal (—) and discrete signal (-∘); sampling and quantization effect on a signal (b): continuous-time signal (—) and digital signal (-∘).

To emulate the desired admittance, the MCU operates on the input signal coming from the ADC. This signal being discrete, a discrete I/O transfer function must thus be employed. Tustin's method [113] is used to discretize the continuous transfer function. If the continuous transfer function to be emulated is given by $Y_s(s)$, a discrete z-transform $Y_{s,d}(z)$ is obtained by substituting the s variable by a bilinear function of z as

$$Y_{s,d}(z) = Y_s(s)\big|_{s=\frac{2}{\tau}\frac{z-1}{z+1}}. \tag{1.84}$$

The resulting discrete transfer function is a rational function of the z variable. Rearranging it as

$$Y_{s,d}(z) = \frac{\sum_{m=0}^{M} b_m z^{-m}}{\sum_{n=0}^{N} a_n z^{-n}} \tag{1.85}$$

defines a difference equation linking the input and output:

$$\sum_{n=0}^{N} a_n y(k\tau - n\tau) = \sum_{m=0}^{M} b_m u(k\tau - m\tau), \qquad k \in \mathbb{Z}. \tag{1.86}$$

The resulting output signal is also a discrete signal. It is applied to the continuous system with the DAC by holding its value constant for the sample interval by a zero-order hold (ZOH). Figure 1.26 illustrates such a signal. When compared to the original continuous signal that the output is supposed to follow, it is seen that the average output of the ZOH is a delayed version of the former by a time $\tau/2$.

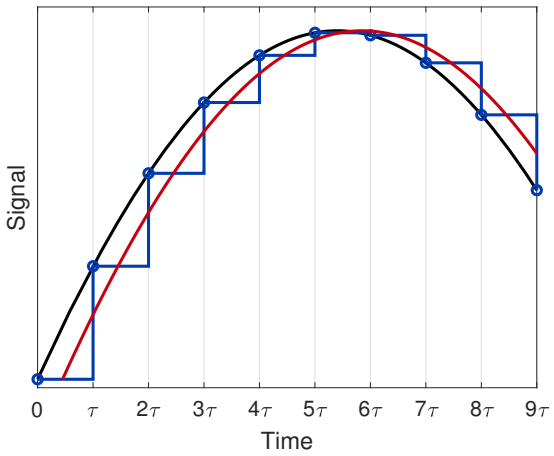

Figure 1.26: Effect of a ZOH: continuous-time signal (—), ZOH output signal (-○-) and continuous average of the discrete signal (—).

If the MCU operates at a high enough clock frequency, it may be considered that the digitization of the input signal and computation of the output signal occur instantaneously at each sampling time. The differences between the continuous transfer function and the digital one then principally comes from the delay brought by the ZOH, as well as the frequency warping stemming from the discretization of the transfer function.

Both sampling and quantization have a detrimental effect on passivity [114], which may eventually have consequences on the stability of the controlled system. If the voltage ranges are properly set as explained in Section 1.3, quantization will in general have negligible effects. A high enough sampling frequency can also be chosen, so as to avoid any issue related to time delays. However, quantifying what "high enough" means requires careful inspection, as shall be shown in this section.

1.6.2 Open-loop analysis

The stability of the controlled system can be assessed using the analysis tools from feedback control theory [115]. The action of the shunt circuit is first represented as a feedback. It is then shown that for systems with small electromechanical coupling, the phase margin can be very small, which makes the system prone to delay-induced instabilities. Before moving on to a closed-loop analysis, a physical explanation on why the system is sensitive to phase lags is provided, showing that delays can make the digital admittance non-passive.

1.6.2.1 Open-loop transfer function

If an unforced system is considered, the piezoelectric voltage and charge are linked by the dynamic capacitance given in Equation (1.23). Moreover, connecting an admittance $Y_s(s)$ to the electrodes of the transducer further imposes the relation Equation (1.32) in the case of a series RL shunt. This suggests that the dynamics of the unforced controlled system may be represented with the feedback diagram depicted in Figure 1.27.

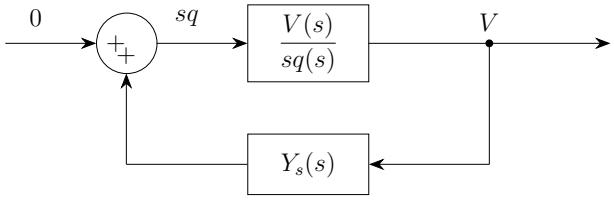

Figure 1.27: Block diagram representation of the controlled system.

Using Equations (1.23) and (1.32), one may form the open-loop transfer function

$$H(s) = -\frac{V(s)}{sq(s)}Y_s(s) = \frac{1}{C_p^\varepsilon}\frac{s^2+\omega_{sc}^2}{s^2+\omega_{oc}^2}\frac{1}{Ls^2+Rs} \tag{1.87}$$

such that the poles of the closed-loop system may be found by solving the characteristic equation

$$1 + H(s) = 0 \tag{1.88}$$

Neutral stability is reached when a pole of the closed-loop system lies on the imaginary axis, i.e., if there is a value $s = j\omega$ (where j is the unit imaginary number ($j^2 = -1$)) such that

$$1 + H(j\omega) = 0. \tag{1.89}$$

In feedback control theory, the stability of a closed-loop system is often quantified by measuring how far $H(j\omega)$ is from -1, i.e. from $|H(j\omega)| = 1$ and $\angle H(j\omega) = \pm 180°$ (where the operators $|\cdot|$ and $\angle$ give the magnitude and argument of a complex number, respectively) for all values of ω. This leads to the definition of a gain margin GM

$$GM = 20\log_{10}\left(\frac{1}{|H(j\omega)|}\right) = -20\log_{10}\left(|H(j\omega)|\right), \qquad \text{when } \angle H(j\omega) = \pm 180°, \tag{1.90}$$

which quantifies by which amount the open-loop transfer function can be multiplied by a gain inside the loop before the closed-loop system reaches neutral stability. For most systems, the closed-loop system is stable if GM is positive and unstable otherwise (i.e., increasing the gain causes instabilities). A phase margin PM can also be defined by

$$PM = \min\left\{\angle H(j\omega) + 180°, 180° - \angle H(j\omega)\right\}, \qquad \text{when } |H(j\omega)| = 1, \tag{1.91}$$

which quantifies the distance from $\pm 180°$ at the crossover frequency, i.e. when $|H(j\omega)| = 1$. Phenomena bringing phase modification such as delays in the loop can affect the phase of this open-loop transfer function and lead to instabilities of the closed-loop system. These margins are therefore important quantities to monitor when dealing with a control loop, and are easily read from a Bode plot [115].

Note that by normalizing the Laplace variable with the short-circuit resonance frequency

$$\overline{s} = \frac{s}{\omega_{sc}} \tag{1.92}$$

and using Equations (1.20), (1.37), (1.38) and (1.87),

$$H(s) = H\left(\omega_{sc}\overline{s}\right) = \frac{\overline{s}^2+1}{\overline{s}^2+1+K_c^2}\frac{1}{\dfrac{1}{\left(1+K_c^2\right)\delta^2(K_c)}\overline{s}^2 + \dfrac{2\zeta(K_c)}{\delta(K_c)\sqrt{1+K_c^2}}\overline{s}}, \tag{1.93}$$

the coefficients of the open-loop transfer function depend only on the EEMCF. This parameter is thus expected to play an important role in stability.

The transfer function given in Equation (1.87) has a simple pole at $s = 0$, a simple pole at $s = R/L = 2\omega_{oc}\zeta(Kc)/\delta^3(Kc) \overset{K_c \ll 1}{\ll} \omega_{oc}$, a double zero at $s = \omega_{sc}$ and a double pole at ω_{oc}. The phase of this transfer function is thus bounded between -180° and 180°, and the system has an infinite gain margin. The two low-frequency poles make the phase approach -180° early on; the 180° phase gain at ω_{oc} is quickly compensated for by the 180° phase drop at ω_{oc}. Thus, before ω_{sc} and after ω_{oc}, the phase of the transfer function is expected to be close to -180°.

Figure 1.28(a) features Bode plots of the open-loop transfer function given in Equation (1.93) for various values of K_c around the short- and open-circuit resonance frequencies. As expected, the system has an infinite gain margin. There are two crossover frequencies, and the phase margin is calculated at the highest one (which also corresponds to the lowest phase margin). The phase margin decreases with K_c. This trend is also highlighted in Figure 1.28(b).

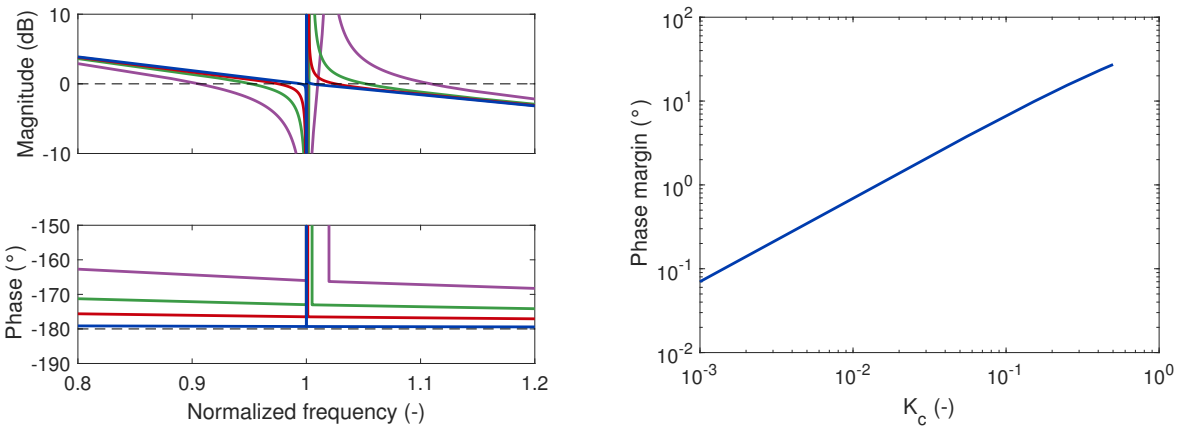

(a) (b)

Figure 1.28: Bode plot of the open-loop transfer function (a): $K_c = 0.01$ (—), $K_c = 0.05$ (—), $K_c = 0.1$ (—) and $K_c = 0.2$ (—) ; phase margin as a function of K_c (b).

As stated earlier, the EEMCF is typically small, and thus the system may have a small phase margin. This in turn makes it very sensitive to time delays in the loop.

1.6.2.2 Destabilization mechanism

In order to have an intuitive understanding of the effect of delays, a simple model is introduced in the first instance. Considering the case of a series RL shunt circuit, the delays imparted by the sampling procedure are modeled as a pure time delay $\tau/2$:

$$L\ddot{q}(t) + R\dot{q}(t) = V\left(t - \frac{\tau}{2}\right). \tag{1.94}$$

Taking the Laplace transform of this equation yields

$$q = \frac{e^{-\frac{s\tau}{2}}}{Ls^2 + Rs}V = \frac{e^{-\frac{s\tau}{2}}}{s}Y_s(s) = \frac{1}{s}Y_d(s), \tag{1.95}$$

where Y_s is the nominal shunt admittance and Y_d is an equivalent delayed admittance. In order to see how these two quantities differ with a simple exposition, the formulas from Thomas et al [75] (which are incidentally identical to a linearization of Equations (1.37) and (1.38) with respect to K_c) are used to tune the inductance and the resistance.

$$L = \frac{1}{C_p^\varepsilon \omega_{oc}^2}, \qquad R = \sqrt{\frac{3}{2}} \frac{K_c}{\omega_{oc} C_p^\varepsilon}. \tag{1.96}$$

The admittance of the shunt circuit evaluated at ω_{oc} is thus

$$Y_s(j\omega_{oc}) = \frac{1}{j\omega_{oc}L + R} = \frac{C_p^\varepsilon \omega_{oc}}{j + \sqrt{\frac{3}{2}} K_c} = \frac{C_p^\varepsilon \omega_{oc}}{1 + \frac{3}{2}K_c^2} \left(\sqrt{\frac{3}{2}} K_c - j \right). \tag{1.97}$$

An important feature of this admittance is that it has a positive real part. In fact, it must be so for any passive circuit, because the average power dissipated across an admittance Y is

$$P = \frac{1}{2} \Re \{V^* I\} = \frac{1}{2} \Re \{V^* Y V\} = \frac{1}{2} \Re \{Y\} |V|^2 \tag{1.98}$$

and must be positive, because the circuit dissipates true power ($\Re$ denotes the operator that gives the real part of a complex number and superscript $*$ denotes complex conjugate). Another important feature is that since $K_c \ll 1$, this real part is much lower than the absolute value of the imaginary part.

The nominal admittance $Y_s(j\omega_{oc})$ given by Equation (1.97) is plotted in Figure 1.29 (where $\Im$ represents the operator that gives the imaginary part of a complex number). Using Equation (1.95), the delayed admittance $Y_d(j\omega_{oc})$ can be obtained through a clockwise rotation of angle $\omega_{oc}\tau/2$ of the complex vector $Y_s(j\omega_{oc})$. If this angle (i.e., the delay τ) is large enough, this rotation may result in a delayed admittance with a negative real part. Because the nominal admittance is almost aligned with the imaginary axis, this can happen for relatively small delays. Hence, they entail a possible generation of true power within the delayed admittance, which may be transmitted to the structure and potentially cause the instability of the closed-loop system.

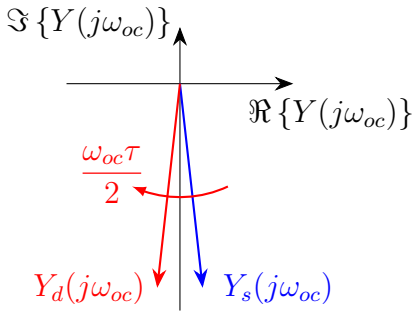

Figure 1.29: Representation of the admittance in the complex plane.

More quantitatively, the delayed admittance is given by

$$Y_d(j\omega_{oc}) = \frac{C_p^{\varepsilon}\omega_{oc}}{1+\frac{3}{2}K_c^2}\left[\sqrt{\frac{3}{2}}K_c\cos\left(\frac{\omega_{oc}\tau}{2}\right) - \sin\left(\frac{\omega_{oc}\tau}{2}\right) \right. \\ \left. -j\left(\cos\left(\frac{\omega_{oc}\tau}{2}\right) + \sqrt{\frac{3}{2}}K_c\sin\left(\frac{\omega_{oc}\tau}{2}\right)\right)\right], \quad (1.99)$$

whose real part becomes negative when

$$\tau = \frac{2}{\omega_{oc}}\arctan\left(\sqrt{\frac{3}{2}}K_c\right) = \frac{1}{\omega_{oc}}\sqrt{6}K_c + O(K_c^3) = \frac{1}{\omega_{sc}}\sqrt{6}K_c + O(K_c^3). \quad (1.100)$$

It should however be noted that passivity is a sufficient but non-necessary condition for stability. This is fortunate, because for any non-zero delay τ, the admittance becomes non-passive at high frequencies, but if these frequencies are far enough from the mechanical resonance the closed-loop system is stable. A more refined model is therefore needed to assess the stability of the closed-loop system.

1.6.3 Closed-loop analysis

The poles of the closed-loop system can be computed with a model accounting for the delays of the ZOH. Root loci given by the variation of the time delay τ are traced, and the destabilizing effect of the delays can clearly be observed. In order to quantify their importance, approximations of the model are made in order to determine the value of the sampling period τ_c above which the closed-loop system becomes unstable.

1.6.3.1 Characteristic equation

The closed-loop system is represented in Figure 1.30. Delays are introduced in the system by the ZOH.

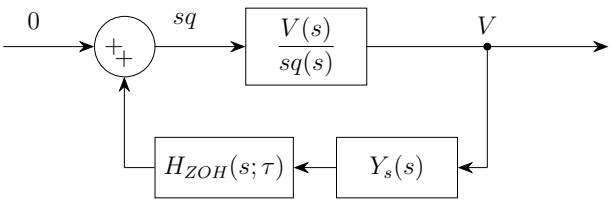

Figure 1.30: Block diagram representation of the controlled system with a ZOH.

Sampling makes the system time variant. However, if the signals are band-limited (i.e., their frequency content beyond the frequency π/τ is zero so as to respect the conditions for the Nyquist-Shannon sampling theorem), this time varying character may be neglected. Assuming the output of the ZOH is dominated by the fundamental harmonic of the frequency it is subject to, an equivalent continuous transfer function can be shown to be [33]

$$H_{ZOH}(s;\tau) = \frac{1-e^{-s\tau}}{s\tau}. \quad (1.101)$$

Based on Figure 1.30, the characteristic equation is then

$$1 - \frac{V(s)}{sq(s)} Y_s(s) H_{ZOH}(s;\tau) = 1 + H(s)\frac{1 - e^{-s\tau}}{s\tau} = 0. \tag{1.102}$$

where H is given by Equation (1.87) and is the open-loop transfer function of the system without delays, i.e., for $\tau = 0$. The characteristic roots of Equation (1.102) are the poles of the closed-loop system. A condition for stability of this system is that all the poles must have a negative real part [116]. An inherent difficulty introduced by the presence of delays is that this characteristic equation is now transcendental because of the complex exponential. For nonzero τ, the system possesses an infinity of poles, and they cannot be found in closed-form.

1.6.3.2 Root loci

Equation (1.102) is transcendental and thus not easy to solve, even numerically. One must resort to numerical solvers such as MATLAB's routine `fsolve` to find the roots of this equation. These solvers usually require an initial guess, close enough to the actual roots of the equation to ensure convergence. In the case of Equation (1.102), the roots are known when $\tau = 0$, because they are the roots of a polynomial. The idea is thus to use homotopy: at each step, starting from a known solution for a given τ, τ is incremented by $\Delta\tau$ and Equation (1.102) is solved with `fsolve` using as initial guess the solution for τ. If the increment is small enough, `fsolve` is generally able to find the solution. The procedure is then repeated until τ reaches a prescribed final value.

Figure 1.31 shows root loci (parametrized by τ) of the controlled system with delays for various values of K_c. The maximum value for τ is the maximum sampling period satisfying the Nyquist-Shannon sampling theorem if the system was forced at its resonant frequency ω_{sc}, π/ω_{sc}. Only the poles with positive imaginary part are shown, but they complex conjugate counterpart also satisfy the characteristic equation.

In all cases, the poles of the original system initially move to the right of the complex plane with increasing delays, and for large enough τ the highest-frequency poles cross the imaginary axis, which makes the closed-loop system unstable. As expected, the value of τ for which this instability occurs grows with K_c. Intuitively, a controlled system with a higher K_c will have poles which are further in the left half of the complex plane; a larger delay effect will thus be required to bring them to the right half.

Figure 1.31 does not feature all the poles of the delayed system, except for $\tau = 0$. As soon as $\tau > 0$ a countable infinite set of poles emanate from $-\infty$. Figure 1.32 shows some of these poles, starting from $\tau = 0.01/\omega_{sc}$, for the lowest ($K_c = 0.01$) and highest ($K_c = 0.3$) EEMCFs considered in Figure 1.31 (the procedure to find an initial guess for these poles is detailed in Section B.1). As Figures 1.32(a) and 1.32(c) show, the poles start off with a very high frequency and progressively move in toward the right of the complex plane. Even for large τ, their damping ratios and frequencies nonetheless remain rather high compared to the poles that originate from the poles of the original system, as testified by the zoom on low frequencies featured in Figures 1.32(b) and 1.32(d), and this feature is pretty insensitive to the EEMCF. Thus, these poles are not causing stability issues and will not be considered hereinafter.

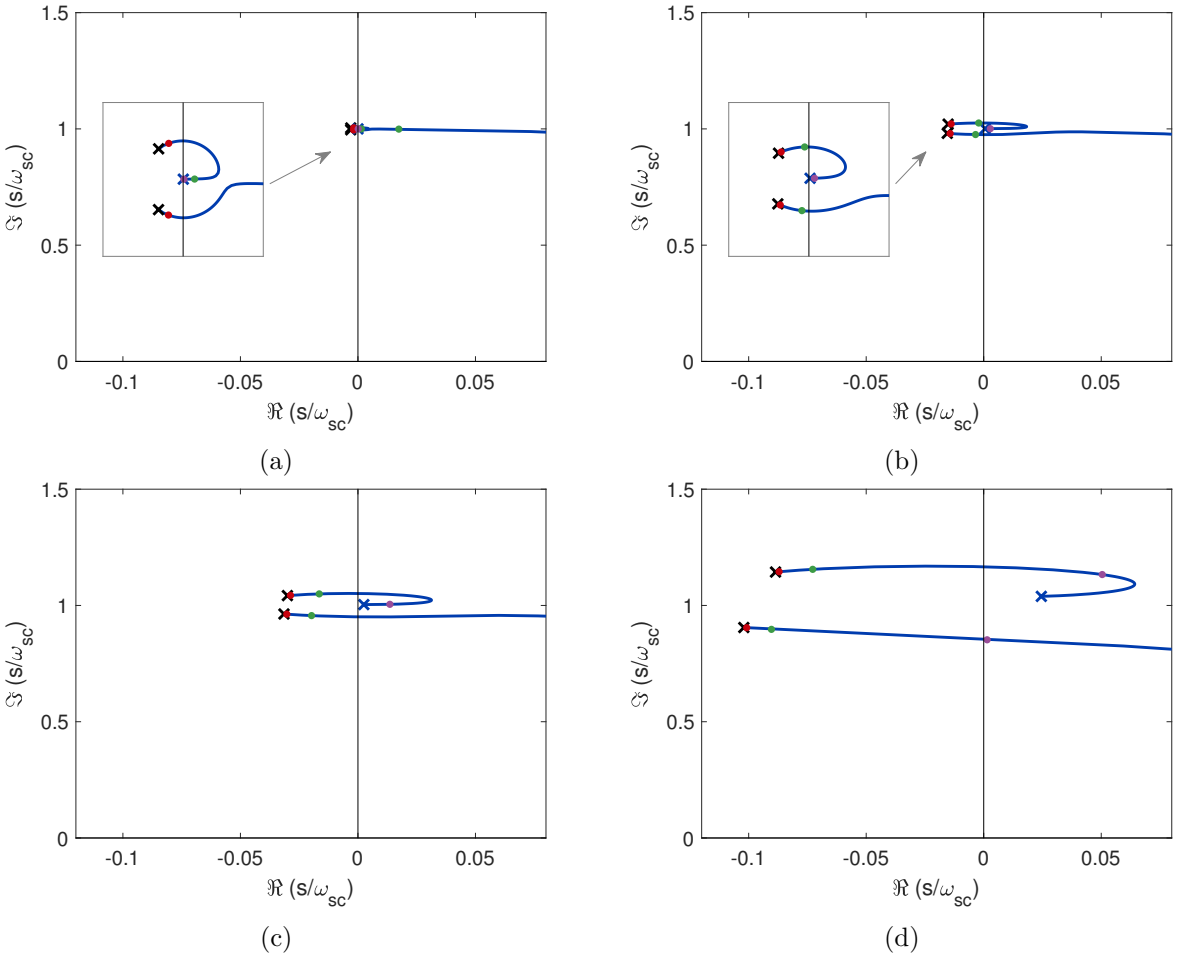

Figure 1.31: Root loci (parametrized by τ) of the closed-loop system with delays ($\times$: poles for $\tau = 0$, $\bullet$: $\tau = 0.01/\omega_{sc}$, $\bullet$: $\tau = 0.1/\omega_{sc}$, $\bullet$: $\tau = 1/\omega_{sc}$, $\times$: $\tau = \pi/\omega_{sc}$): $K_c = 0.01$ (a), $K_c = 0.05$ (b), $K_c = 0.1$ (c) and $K_c = 0.3$ (d).

1.6.3.3 Critical delays

Of particular interest is the value of τ for which the system becomes marginally stable, i.e., at which the poles of the closed-loop system cross the imaginary axis, signalling the onset of instability. An inconvenient feature of Equation (1.102) is that this value can only be obtained by solving a transcendental equation. However, the following approximation can be made at frequencies comparatively low to the sampling frequency:

$$H_{ZOH}(s;\tau) = \frac{1-e^{-s\tau}}{s\tau} = e^{-\frac{s\tau}{2}}\frac{e^{\frac{s\tau}{2}}-e^{-\frac{s\tau}{2}}}{s\tau} = e^{-\frac{s\tau}{2}}\frac{\sum_{k=0}^{+\infty}\left(\frac{s\tau}{2}\right)^k - \sum_{k=0}^{+\infty}\left(-\frac{s\tau}{2}\right)^k}{s\tau}$$
$$= e^{-\frac{s\tau}{2}}\sum_{k=0}^{+\infty}\left(\frac{s\tau}{2}\right)^{2k} \approx e^{-\frac{s\tau}{2}}, \quad (1.103)$$

which justifies the near-equivalence between a ZOH and a pure delay of $\tau/2$ observed in the beginning of this section. With a pure delay model, the method of Walton et al [116] can be used to compute the characteristics roots of interest. Equation (1.102) is rewritten as

$$1 + H(s)e^{-\frac{s\tau}{2}} = 0, \quad (1.104)$$

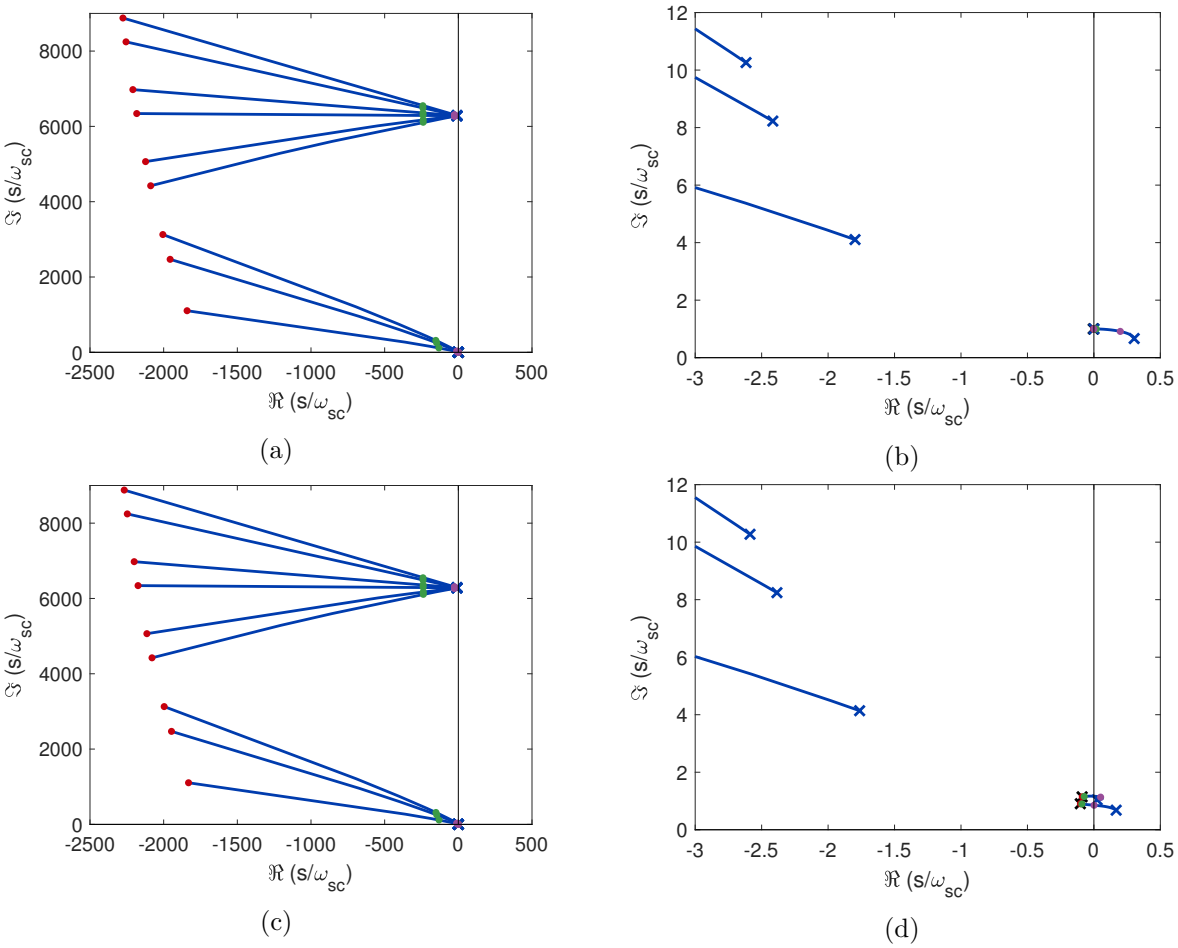

Figure 1.32: Root loci (parametrized by τ) of the closed-loop system with delays ($\times$: poles for $\tau = 0$, $\bullet$: $\tau = 0.01/\omega_{sc}$, $\bullet$: $\tau = 0.1/\omega_{sc}$, $\bullet$: $\tau = 1/\omega_{sc}$, $\times$: $\tau = \pi/\omega_{sc}$): $K_c = 0.01$(a) and (b), $K_c = 0.3$ (c) and (d).

The time delay resulting in purely imaginary characteristic roots is noted τ_c. At this delay, a pair of complex conjugate poles or a single real pole cross the imaginary axis, possibly changing the stability of the system. Thus, $s = j\omega_c$ and $s = -j\omega_c$ satisfy the characteristic equation

$$\begin{cases} 1 + H(j\omega_c)e^{-\frac{j\omega_c\tau_c}{2}} = 0 \\ 1 + H(-j\omega_c)e^{\frac{j\omega_c\tau_c}{2}} = 0 \end{cases}. \tag{1.105}$$

Multiplication of these two equations yield

$$H(j\omega_c)H(-j\omega_c) = 1. \tag{1.106}$$

This equation is a polynomial; hence, there is a finite set of frequencies at which the poles of the closed-loop system cross the imaginary axis [116]. The corresponding time delay τ_c can then be found using either line of Equation (1.105) as

$$\tau_c = \frac{2}{\omega_c}\left[\angle - H(j\omega_c) + 2k\pi\right], \qquad k \in \mathbb{Z}. \tag{1.107}$$

1.6.3.4 Series approximations

Using Equation (1.87), it can be seen that Equation (1.106) is a quartic polynomial of ω_c^2. In theory, it can thus be solved in closed form. However, due to the complexity of the expression, the complete solution is not reported here. A more convenient form is obtained through Maclaurin series expansion in powers of K_c of the analytical solution, which is easily performed with a symbolic calculation software such as Wolfram Mathematica. This provides an approximation of the three frequencies (the fourth root being such that $\omega_c^2 < 0$ is meaningless)

$$\begin{cases} \omega_{c,1} = \omega_{sc}\left(1 - K_c + \frac{5}{8}K_c^2 - \frac{73}{128}K_c^3 + O(K_c^4)\right) \\ \omega_{c,2} = \omega_{sc}\left(1 + \frac{1}{2}K_c^2 + O(K_c^4)\right) \\ \omega_{c,3} = \omega_{sc}\left(1 + K_c + \frac{5}{8}K_c^2 + \frac{73}{128}K_c^3 + O(K_c^4)\right) \end{cases} . \tag{1.108}$$

Inserting these critical frequencies into Equation (1.107) and expanding the result in power series of K_c gives the corresponding delays

$$\begin{cases} \tau_{c,1} = \frac{1}{\omega_{sc}}\left(\sqrt{6}\left(K_c + K_c^2\right) + \frac{19}{32}\sqrt{\frac{3}{2}}K_c^3 + O(K_c^4)\right) \\ \tau_{c,2} = \frac{1}{\omega_{sc}}\left(2\pi + \sqrt{6}K_c - \frac{\pi}{2}K_c^2 - \frac{37}{32}\sqrt{\frac{3}{2}}K_c^3 + O(K_c^4)\right) \\ \tau_{c,3} = \frac{1}{\omega_{sc}}\left(\sqrt{6}\left(K_c - K_c^2\right) + \frac{19}{32}\sqrt{\frac{3}{2}}K_c^3 + O(K_c^4)\right) \end{cases} . \tag{1.109}$$

Among these values, $\tau_c = \tau_{c,3}$ is the smallest and is thus called *critical delay* herein, because it corresponds to the largest admissible value of sampling time for a marginally stable closed-loop system. It also corresponds to the highest critical frequency, which is coherent with the root loci analysis. The leading order of K_c is one, which means that electromechanical systems exhibiting a small EEMCF are subject to these instabilities. It may also be noted that the first-order coefficient in K_c obtained in Equation (1.109) for $\tau_{c,3}$ corresponds to that of the linearized value of τ leading to a non-passive delayed admittance (Equation (1.100)).

To assess the accuracy of these series, they were compared with a direct numerical resolution of Equations (1.102) and (1.104) with $s = j\omega_c(K_c)$. As with the root loci, these equations were solved with the `fsolve` routine from MATLAB, using a homotopy on K_c. Figure 1.33 compares the obtained results for $\tau_{c,1}$ and $\tau_{c,3}$ ($\tau_{c,2}$ being significantly larger, it was omitted).

For small EEMCF, the three models agree almost perfectly. Incidentally, this is also the range where the instabilities can be a critical problem. For large EEMCF ($K_c \gtrsim 0.3$), the critical sampling frequency becomes a fraction of the minimum sampling frequency to comply with the Nyquist-Shannon theorem ($\tau = \pi/\omega_{sc}$), and thus delay-induced instabilities may not be the driving factor to set the sampling frequency.

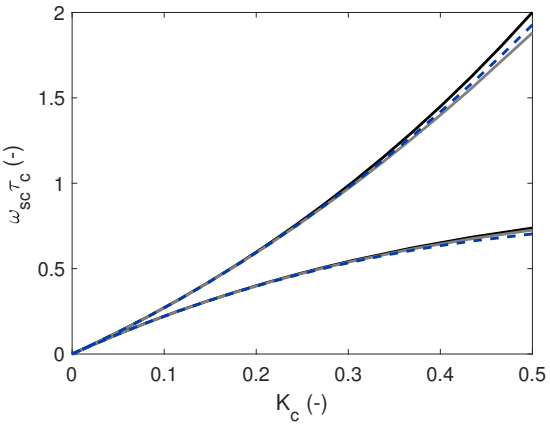

Figure 1.33: Critical delays $\tau_{c,1}$ (upper curves) and $\tau_{c,3}$ (lower curves): ZOH model (—), pure delay model (—) and series approximation (- -).

1.6.3.5 FRF of the controlled system

Considering vibration mitigation goals, stability is a necessity but not the only concern; performance in terms of vibration reduction must also be assessed. It is known that a small phase margin can lead to amplifications in the closed-loop transfer function near the crossover frequency [4]. Figure 1.34 shows representative FRFs of the controlled system including the ZOH (using Equation (1.101)). Small delays ($\tau \leq 0.1\tau_c$) have an imperceptible effect on the FRF compared to the continuous case. Conversely, a strong effect can be observed for large delays, especially on the rightmost peak whose amplitude grows with the delay. At $\tau = \tau_c$, the poles that lie on the imaginary axis create an undamped resonance in the FRF. Figure 1.34(a) shows a similarity with Figure 1.9(b), and delays are somewhat equivalent to a diminution of the resistance. When the EEMCF is higher, delays also cause a slight detuning of the frequency of the absorber, as shown in Figure 1.34(b).

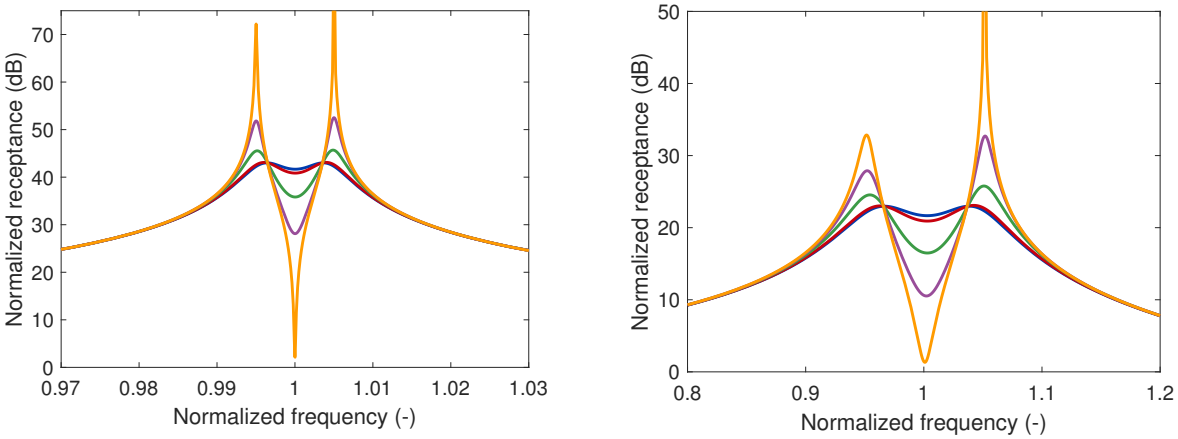

Figure 1.34: FRF of the controlled system with a delayed admittance, $K_c = 0.01$ (a) and $K_c = 0.1$ (b): $\tau = 0.01\tau_c$ (—), $\tau = 0.1\tau_c$ (—), $\tau = 0.5\tau_c$ (—), $\tau = 0.8\tau_c$ (—) and $\tau = \tau_c$ (—).

The foregoing approximations were also verified by time simulations of the systems' responses to a unit-amplitude swept sine forcing under various sampling frequencies.

The simulation of the system represented as a block diagram in Figure 1.35 was carried out with Simulink. In addition to the sampling delay, this simulation accounts for the time-varying character of the system caused by sampling, as well as the effect of the discretization of the transfer function with Tustin's method.

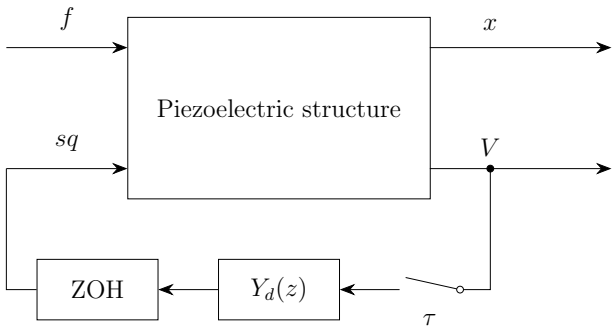

Figure 1.35: Block diagram representation of the controlled system used for time simulations.

Figure 1.36 shows the envelopes of the systems' responses. The fact that the FRF is nearly not affected for $\tau \leq 0.1\tau_c$ is verified, and so is the progressive degradation, up to the onset of instability for $\tau \approx \tau_c$.

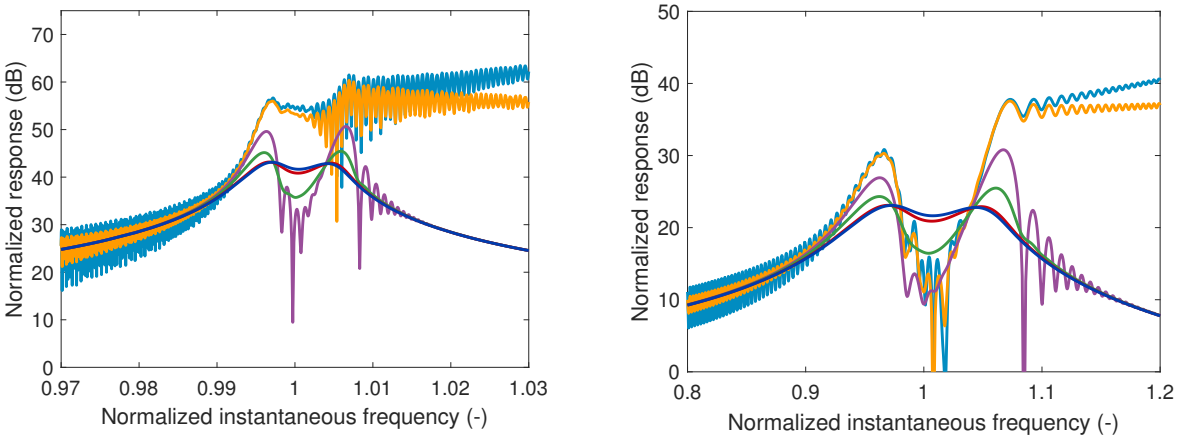

(a) (b)

Figure 1.36: Simulated envelope of the response of the controlled system with a delayed admittance to a unit-amplitude swept sine, $K_c = 0.01$ (a) and $K_c = 0.1$ (b): $\tau = 0.01\tau_c$ (—), $\tau = 0.1\tau_c$ (—), $\tau = 0.5\tau_c$ (—), $\tau = 0.8\tau_c$ (—), $\tau = \tau_c$ (—) and $\tau = 1.01\tau_c$ (—).

A rule of thumb to choose the delay is thus to use a sampling time which is at most one tenth of the critical delay. Besides, the sampling time must also be small enough so as to respect the Nyquist condition. Typical sampling frequencies of ten to thirty times the highest frequency of interest are often recommended, the factor thirty being recommended for the accuracy of the emulation used here [33]. The sampling time should therefore satisfy

$$\tau \leq \frac{1}{\omega_{sc}} \min\left\{\frac{2\pi}{10}, \frac{\sqrt{6}}{10}\left(K_c - K_c^2\right) + \frac{19}{320}\sqrt{\frac{3}{2}}K_c^3\right\}. \tag{1.110}$$

1.6.4 Discussion

The delay-induced instabilities are clearly defeating the purpose of the DVA and should therefore be avoided. If the closed-loop system is prone to these instabilities, there are two possible options:

1. Choose a high enough sampling frequency.
2. Modify the implemented admittance in anticipation of the delays.

The first option is the most obvious and straightforward, but not always most desirable one for two main reasons.

The first reason is that a given digital unit's power consumption is a growing function of its clock frequency (see Equation (1.63)), which must be high enough to handle data at a given sampling frequency. Increasing the sampling frequency will increase β_{MCU} and/or f_{CPU}, leading to a higher power consumption. Moreover, if f_{CPU} is increased, $V_{CC,MCU}$ will also have to be increased, which leads to an actual power consumption proportional to f_{CPU}^3 [110].

The second reason is that the required sampling frequency to make the delays effect negligible or let alone to have a stable closed-loop system may be very large. This would require high-frequency specialized equipments, whose financial cost may become prohibitively large.

Therefore, when the consequences of a sufficient increase in the sampling frequency are unacceptable, the other solution may be preferable. In this case, it is sought to modify the programmed admittance in order to anticipate the effects of the sampling delays.

1.6.5 Stabilization procedure

The stabilization procedure reported herein was proposed in [117], but the results have been reviewed and expanded. The principles of this approach are very similar to a pole placement approach: it is sought to place the poles of a modified delayed system as close as possible to those of the nominal system. To do so, the parameters of the shunt admittance are modified.

1.6.5.1 Pole placement via transfer function modification

The admittance of a shunt circuit can be expressed as a rational transfer function

$$Y_s(s) = \frac{\sum_{m=0}^{M} b_m s^m}{\sum_{n=0}^{N} a_n s^n} \tag{1.111}$$

According to Equation (1.88), the poles of the nominal closed-loop system p_k ($k = 1, \cdots, K$) satisfy the equation

$$1 - \frac{V(p_k)}{p_k q(p_k)} Y_s(p_k) = 0. \tag{1.112}$$

In order to anticipate the delays, a modified admittance is introduced as

$$\widetilde{Y}_s(s) = \frac{\sum_{m=0}^{M} b_m(1+\delta_{b_m})s^m}{\sum_{n=0}^{N} a_n(1+\delta_{a_n})s^n}, \tag{1.113}$$

where δ_{a_n} and δ_{b_m} are modification factors and are unknown for now. The poles of the modified delayed closed-loop system would be the solutions of Equation (1.102):

$$1 - \frac{V(s)}{sq(s)}\frac{1-e^{-\tau s}}{\tau s}\widetilde{Y}_s(s) = 0. \tag{1.114}$$

By comparing Equations (1.112) and (1.114), in order for p_k to be a pole of the modified delayed system, the modified delayed admittance must be equal to the nominal one at $s = p_k$:

$$\frac{1-e^{-\tau p_k}}{\tau p_k}\widetilde{Y}_s(p_k) = \frac{1-e^{-\tau p_k}}{\tau p_k}\frac{\sum_{m=0}^{M} b_m(1+\delta_{b_m})p_k^m}{\sum_{n=0}^{N} a_n(1+\delta_{a_n})p_k^n} = \frac{\sum_{m=0}^{M} b_m p_k^m}{\sum_{n=1}^{N} a_n p_k^n} = Y_s(p_k). \tag{1.115}$$

Rearranging this equation, the following relation is obtained

$$\frac{1-e^{-\tau p_k}}{\tau p_k}\frac{\sum_{m=0}^{M} b_m\delta_{b_m}p_k^m}{\sum_{m=0}^{M} b_m p_k^m} - \frac{\sum_{n=0}^{N} a_n\delta_{a_n}p_k^n}{\sum_{n=0}^{N} a_n p_k^n} = 1 - \frac{1-e^{-\tau p_k}}{\tau p_k}, \tag{1.116}$$

which, when imposed for $k = 1, \cdots, K$, defines a linear system that can be put in a matrix form as

$$\begin{bmatrix} \frac{1-e^{-\tau p_1}}{\tau p_1}\frac{b_0}{\sum_{m=0}^{M} b_m p_1^m} & \cdots & \frac{1-e^{-\tau p_1}}{\tau p_1}\frac{b_M p_1^M}{\sum_{m=0}^{M} b_m p_1^m} & -\frac{a_0}{\sum_{n=0}^{N} a_n p_1^n} & \cdots & -\frac{a_N p_1^N}{\sum_{n=0}^{N} a_n p_1^n} \\ \vdots & & \vdots & \vdots & & \vdots \\ \frac{1-e^{-\tau p_K}}{\tau p_K}\frac{b_0}{\sum_{m=0}^{M} b_m p_K^m} & \cdots & \frac{1-e^{-\tau p_K}}{\tau p_K}\frac{b_M p_K^M}{\sum_{m=0}^{M} b_m p_K^m} & -\frac{a_0}{\sum_{n=0}^{N} a_n p_K^n} & \cdots & -\frac{a_N p_K^N}{\sum_{n=0}^{N} a_n p_K^n} \end{bmatrix} \begin{bmatrix} \delta_{b_0} \\ \vdots \\ \delta_{b_M} \\ \delta_{a_0} \\ \vdots \\ \delta_{a_N} \end{bmatrix}$$
$$= \begin{bmatrix} 1 - \frac{1-e^{-\tau p_1}}{\tau p_1} \\ \vdots \\ 1 - \frac{1-e^{-\tau p_K}}{\tau p_K} \end{bmatrix}, \tag{1.117}$$

or, in short,

$$\mathbf{P}\boldsymbol{\delta} = \mathbf{d}. \tag{1.118}$$

This system has a trivial solution $\boldsymbol{\delta} = [-1, \cdots, -1]^T$. This makes all the coefficients of the modified admittance equal to zero, which clearly is not an acceptable solution. To resolve this, one of the modification factor can be imposed to an arbitrary value, for instance 0. For this particular choice, the column associated with this modification coefficient may simply be removed from $\mathbf{P}$. Thus, the number of unknowns is reduced to

$M + N + 1$. Since this number may not be equal to K, the system may not be square. To solve it, the pseudoinverse (denoted by a superscript †) is used.

$$\boldsymbol{\delta} = \mathbf{P}^{\dagger}\mathbf{d}. \tag{1.119}$$

By doing so, if $\mathbf{d}$ is in the range of $\mathbf{P}$,

- If $M + N + 1 < K$, the system is overdetermined, and Equation (1.118) is approximated with the least squares error.
- If $M + N + 1 = K$, the system is well-posed, and the pseudoinverse is equal to the inverse of a square matrix, providing the latter is non-singular.
- If $M + N + 1 > K$, the system is underdetermined, and $\boldsymbol{\delta}$ obtained with Equation (1.119) is the least-squares solution to Equation (1.118).

The formulation presented herein differs slightly from that presented in [117], in that the unknowns are modification factors rather than the coefficients of the modified transfer function. The latter generally have widely different scales, which can make the problem badly conditioned, and in case of an underdetermined system, some coefficient may undergo a very large relative modification. By contrast, the formulation used in this thesis allows to obtain a somewhat balanced relative modification of the coefficients. It should also be noted that the procedure only requires the knowledge of the sampling period τ in addition to what is already known for tuning the shunt circuit. This parameter is set by the user and is thus well-known and well-controlled.

1.6.5.2 Numerical verification

Figure 1.37 shows the results of the stabilization procedure on the FRF of the controlled system. The maximum sampling period π/ω_{sc}, is about 130 and 14 times greater than τ_c for $K_c = 0.01$ and $K_c = 0.1$, respectively. A remarkable feature is that two FRFs for a different EEMCF but with an identical sampling frequency look similar, unlike the unmodified case. Therefore, with this modification, the EEMCF no longer appears to play a role in the delay-induced degradation of the vibration reduction. The FRFs for $\tau > 0.1/\omega_{sc}$ do not exhibit as good performance as the others, but it is not advised to choose such a low sampling frequency anyway [33].

A second check was made with the time simulation of the system featured in Figure 1.35 using the modified admittance parameters. By comparing Figures 1.37 and 1.38, it can be observed that both models agree well for $\tau \leq 0.1/\omega_{sc}$. However, discrepancies appear above this limit. In particular, the system is unstable for sampling periods equal to and above $\tau = 1/\omega_{sc}$ and $\tau = \pi/\omega_{sc}$ for $K_c = 0.01$ and $K_c = 0.1$, respectively. This can be attributed to the time-variant characteristics of sampling which were neglected in the analysis, as well as the frequency warping due to Tustin's transform. In practice, it is not advised to choose a sampling frequency smaller than thirty times the highest frequency of interest [33]. Equation (1.110) therefore becomes

$$\tau \leq \frac{2\pi}{30\omega_{sc}} \tag{1.120}$$

to ensure the stability of the closed-loop system with a modified admittance with some margin.

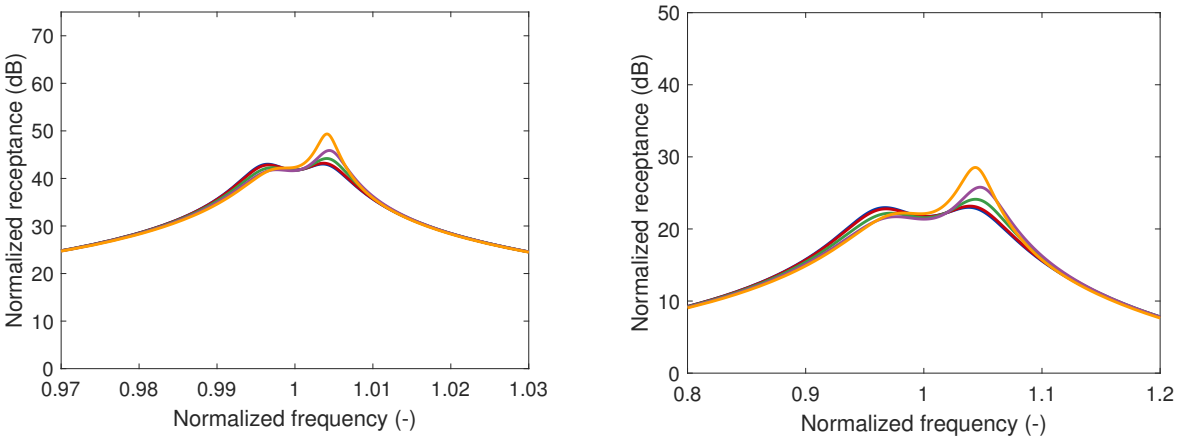

(a) (b)

Figure 1.37: FRF of the controlled system with a modified delayed admittance, $K_c = 0.01$ (a) and $K_c = 0.1$ (b): $\tau = 0.01/\omega_{sc}$ (—), $\tau = 0.1/\omega_{sc}$ (—), $\tau = 0.5/\omega_{sc}$ (—), $\tau = 1/\omega_{sc}$ (—) and $\tau = \pi/\omega_{sc}$ (—).

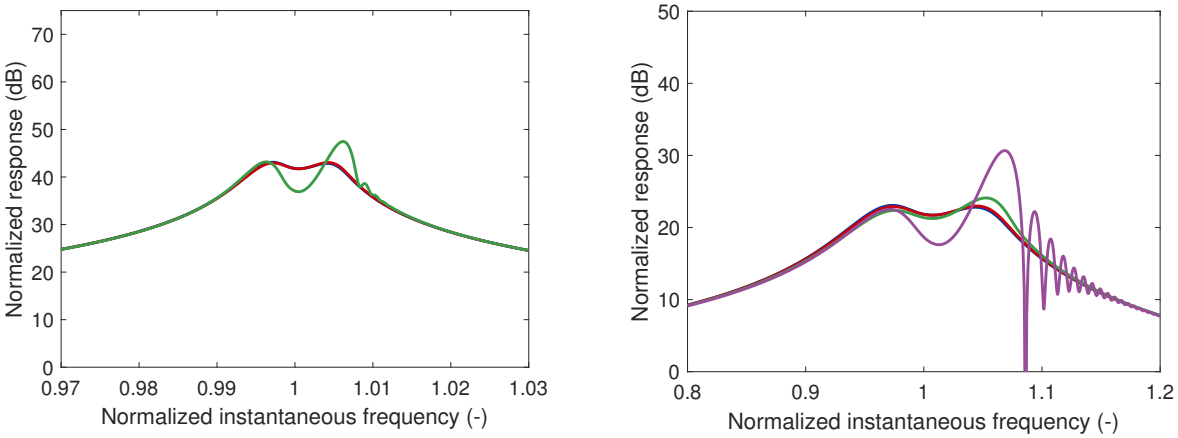

(a) (b)

Figure 1.38: Simulated envelope of the response of the controlled system with a delayed, modified admittance to a unit-amplitude swept sine, $K_c = 0.01$ (a) and $K_c = 0.1$ (b): $\tau = 0.01/\omega_{sc}$ (—), $\tau = 0.1/\omega_{sc}$ (—), $\tau = 0.5/\omega_{sc}$ (—) and $\tau = 1/\omega_{sc}$ (—).

1.6.6 Experimental validation

To experimentally validate the developments about delay-induced instabilities and the proposed stabilization procedure, the experimental setup of Section 1.3.3 is considered again. FRFs were measured under progressively decreasing sampling frequencies. As testified by Figure 1.39(a), the destabilization effect of the sampling frequency is clearly observable. The results featured in this figure are close to those of Figure 1.34(b) (the coupling factor of the experimental setup is 0.116, which is close to the EEMCF of 0.1 used therein), which validates the model used to describe sampling delays. From Equation (1.109), the stability limit of the unmodified system should theoretically be reached at $\tau = 1.3 \times 10^{-3}$s. The experimental system is still stable but very lightly damped. This small discrepancy can be explained by the presence of structural damping in the host, as well as by experimental uncertainties.

The stabilization procedure recovers the performance of a case without delays,

as shown in Figure 1.39(b). Namely, all the curves are virtually superimposed up to $\tau = \tau_c$, which validates the proposed developments. Fourfold a sampling period leads to a system with modified admittance where the effect of sampling are observable, more than in the numerical model featured in Figure 1.37(b), but similarly to the time simulation in Figure 1.38(b). Nevertheless, a case with such a high sampling period when the admittance is unmodified is not disclosed here, as it leads to an unstable closed-loop system.

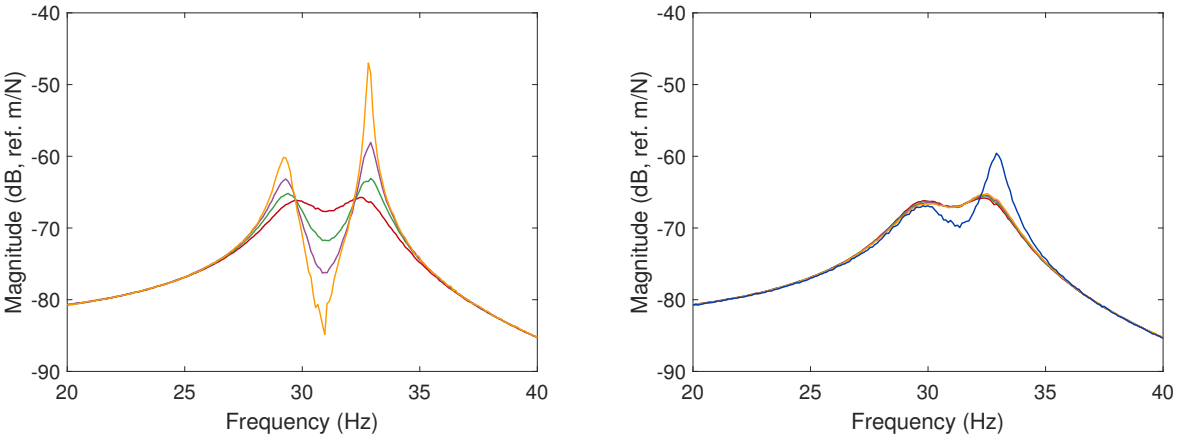

Figure 1.39: Experimental FRF of the beam ($K_c = 0.116$) with an unmodified (a) and a modified (b) admittance: $\tau = 10^{-4}$s$\approx 0.1\tau_c$ (—), $\tau = 6.5 \times 10^{-4}s= 0.5\tau_c$ (—), $\tau = 10^{-3}$s$\approx 0.8\tau_c$ (—), $\tau = 1.3 \times 10^{-3}s= \tau_c$ (—) and $\tau = 5 \times 10^{-3}$s$\approx 1/\omega_{sc}$ (—) .

1.7 Conclusion

This first chapter introduced the DVA used for piezoelectric shunt damping and reviewed its strengths and weaknesses. In Section 1.2, important notions associated with piezoelectric structures and piezoelectric shunt damping were reviewed. The importance of the EEMCF was highlighted. The general working principles of a DVA and its practical realization were presented in Section 1.3. The central role of the digital processing unit and the advantages it brings were underlined. The equivalence of the action of a DVA to that of a piezoelectric shunt was then experimentally validated on a beam. Section 1.4 defined notions of passivity, and discussed the interest of implementing a passive control law with a non-passive control system. The implications of the non-passive character of the control system were discussed afterwards. Section 1.5 described a method to evaluate the power consumption of a DVA. Calculations and experimental measurements showed that the power consumed by the absorber is of the order of the Watt, and that most of it comes from quiescent power consumption. Finally, Section 1.6 investigated the effects of sampling delays in the controlled system. Instabilities were shown to arise, especially quickly for systems with low electromechanical coupling, whose open-loop transfer function exhibits a small phase margin. A stabilization procedure was proposed, wherein the delays effect is anticipated and the poles of the modified delayed closed-loop system were placed as close as possible to their nominal position through modifications of the shunt admittance. The theoretical developments were eventually experimentally validated.

The DVA is a viable approach to implement piezoelectric shunt damping. Table 1.5 compares the different approaches mentioned in the introduction of Section 1.3 in terms of advantages and drawbacks. From this thesis' standpoint, the main advantage provided by the DVA, i.e., its flexibility, is central, as this will allow to implement more complex shunt circuits in the next chapters. Among the two drawbacks of the DVA, the possibility for instability was mitigated by a method presented in Section 1.6. Power consumption remains a potential issue. Embedded systems have become more and more ubiquitous in our society [110], and smart way to power them have been proposed. This is a point in favor of the possible industrial deployment of DVAs in smart structures. However, the PCB of the DVA presented in Section 1.3 appears to consume a large amount of power, and possible ideas to reduce it were listed in Section 1.5.

Implementation	Advantages	Drawbacks
Passive circuit	Passivity	Hardware modifications Resistance/nonlinearity/size tradeoff [23, 97, 98]
Synthetic inductor	High inductance	Hardware modifications Power consumption Frequency-dependent resistance [24]
Digital absorber	High inductance Flexibility	Power consumption Possibility of instabilities

Table 1.5: Summary of the advantages and drawbacks of the different approaches implementing shunt damping.

2 Multimodal vibration damping with a single transducer

Abstract

This chapter presents a technique to control multiple resonances of a structure with a shunt circuit possessing multiple branches connected to a single transducer. After a brief review of the dynamics of multiple-degree-of-freedom structures, a three-step tuning procedure is proposed. The first step is the identification of the piezoelectric structure. The second step consists in specifying the characteristics of the shunt circuit impedance or admittance. With a few simplifying assumptions, the problem becomes similar to the control of a single mode, and well-established tuning formulas can be used. From these characteristics, the third step derives the actual parameters of the electrical elements making up the shunt circuit. The approach is numerically verified and experimentally validated on piezoelectric beams.

2.1 Introduction

Structures exhibit multiple modes, and several of them may be excited during operation, e.g. by broadband, transient or multi-harmonic forcing. If they impart an unacceptably large motion amplitude, they should be controlled. The shunt circuits reviewed in Section 1.2.2 are typically used to target a single mode. Various approaches have been proposed in the literature to extend the control ability of piezoelectric shunt damping to multiple modes.

The tuning procedure for shunt circuits becomes more complicated when there are multiple modes than when considering a SDoF structure. Berardengo et al [77] showed that the frequency-dependent character of the piezoelectric capacitance due to the electromechanical interaction (see, e.g., de Marneffe [118]) is to be taken into account during tuning for improved accuracy. The significant impact on performance of non-resonant modes was illustrated by Hogsberg and Krenk [119], and an explicit correction for background flexibility and inertia was proposed. Gardonio et al [120] showed that simple lumped-parameter models yield inaccurate tuning of the shunt parameters for a simply-supported plate. The near-equivalence of using the effective electromechanical coupling coefficient and a residual-mode corrected electromechanical coupling coefficient when tuning shunt circuit parameters was demonstrated by Toftekær et al [121].

An advantage of piezoelectric absorbers is their conceptually simple extension to the control of multiple resonances. A first approach is to use as many shunted transducers as resonances to be controlled [122]. A second approach for multimodal piezoelectric shunt damping is based on multiple patches interconnected through an electrical network. The network is designed to be the electrical analog of the mechanical structure to which it is coupled [123, 124].

A third approach uses a single transducer, as multiple transducers cannot always be accommodated for practical reasons [14]. Since the classical RL shunt resonates with the transducer at a specific frequency, one can devise a more complex electrical circuit that resonates at multiple frequencies. Edberg et al [125] tested this concept experimentally for two modes; the circuit topology was later generalized by Hollkamp [126] to control an arbitrary number of resonances. In view of the difficulty to tune the circuit, Wu [127] introduced the so-called current blocking shunt circuit, which, however, requires a large number of electrical components. Behrens et al [128] proposed a current flowing shunt circuit and Fleming et al [129] developed a series-parallel impedance structure requiring a lower number of components. The downside of these latter topologies is that they may provide a rather low vibration reduction on the controlled modes. The aforementioned shunt circuits are discussed in more details in [14]. More recently, ladder topologies were proposed by Agneni et al [130] and Goldstein [131].

The two first approaches require multiple transducers and will be studied in Chapter 3. The focus of the present chapter is on multiple-branch shunt circuits connected to a single transducer.

After reviewing important aspects of the dynamics of multiple-degree-of-freedom (MDoF) piezoelectric structures, this chapter will focus on tuning a shunt circuit connected to a single transducer whose goal is to mitigate multiple resonances. For this aim, the circuit should contain a certain number of electrical elements in order to have multiple resonances itself. The dynamics of a MDoF structure and those of the circuit are governed by high-order transfer functions. In the SDoF case, tuning the shunt circuit involved equations of the same order as these transfer functions [83], but closed-form solutions are beyond reach for the MDoF case. Hence, if tackled directly, mitigating multiple resonances simultaneously is a substantially more complex problem. The purpose of this chapter is to propose a method which under mild approximations simplifies the problem and offers a tuning approach based on the SDoF case.

In the proposed approach, tuning a multi-branch shunt circuit requires three distinct steps (also schematically represented in Figure 2.1):

1. Identification of the host system's characteristics
2. Specification of the circuit's immittance characteristics
3. Tuning of the circuit's electrical components

The first step consists in determining the resonance frequencies and capacitance at constant strain of the transducer. As in the SDoF case, knowing the information conveyed in the dynamic capacitance (or the dynamic elastance) is sufficient to complete this step. All the essential aspects are covered in Section 2.2.

The second step is based on an analysis of the electromechanical coupling existing between the resonances of the structure and those of the electrical circuit. After a few simplifying assumptions, it is possible to show that the problem reduces to a problem similar to the SDoF case, and the formulas given in Chapter 1 can be used. Namely, a *baseline case* can be chosen either as the series RL shunt or parallel RL shunt, depending on the topology of the shunt circuit. This step is explained in Section 2.3. Its output specifies a set of frequencies and associated damping ratios for the shunt circuit. When a DVA is used, these characteristics are sufficient to synthesize a passive shunt circuit,

as explained in Section 2.4. The developments are numerically verified in Section 2.5 and experimentally validated in Section 2.6.

The last step uses the specifications to find the values of the electrical elements making up the shunt circuit. The procedure varies depending on the circuit topology, and is applied to shunt circuits proposed in the literature. Namely, Hollkamp's shunt circuit [126] and the current flowing shunt circuit [128] are tuned in Section 2.7, the series-parallel impedance structure [129] and a similar circuit are tuned in Section 2.8, and the current blocking shunt circuit [127] is tuned in Section 2.9. The tuning procedure is numerically verified in Section 2.10 and experimentally validated in Section 2.11. It is also compared to the method proposed in [132, 133].

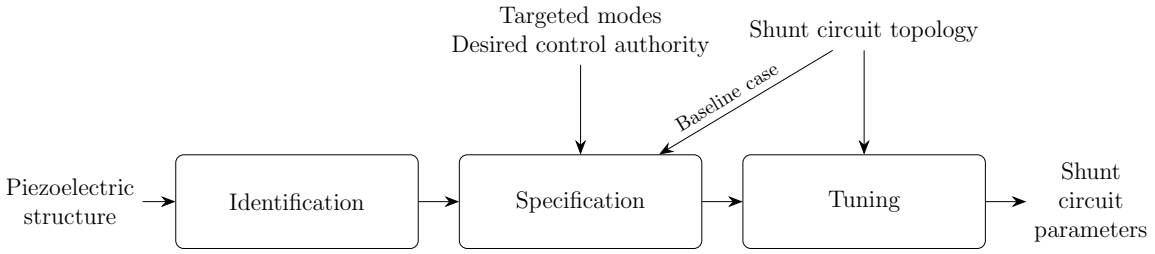

Figure 2.1: Conceptual flowchart of the proposed shunt circuit tuning approach.

2.2 Modeling piezoelectric structures with a single piezoelectric transducer

Models of piezoelectric structures can be obtained analytically [4, 14], via a Rayleigh-Ritz approach [78, 134] or the finite element method (FEM) [135–138]. Introducing the vector of generalized mechanical degrees of freedom (DoFs) $\mathbf{x}$ and the vector of generalized mechanical loading $\mathbf{f}$, the governing equations of the structure with a single piezoelectric transducer are obtained as

$$\begin{cases} \mathbf{M}\ddot{\mathbf{x}} + \mathbf{K}_{sc}\mathbf{x} + \boldsymbol{\gamma}_p V = \mathbf{f} \\ \boldsymbol{\gamma}_p^T \mathbf{x} - C_p^{\varepsilon} V = q \end{cases}, \tag{2.1}$$

which can be seen as a MDoF version of Equation (1.6). In these equations, $\mathbf{M}$ is the structural mass matrix, $\mathbf{K}_{sc}$ is the structural stiffness matrix when the transducer is short-circuited, $\boldsymbol{\gamma}_p$ is a piezoelectric coupling vector and C_p^{ε} is the piezoelectric capacitance at constant strain. Alternatively, the piezoelectric voltage may be used as independent variable. After inversion of the electrical equation, the governing equations become

$$\begin{cases} \mathbf{M}\ddot{\mathbf{x}} + \mathbf{K}_{oc}\mathbf{x} - \boldsymbol{\theta}_p q = \mathbf{f} \\ \boldsymbol{\theta}_p^T \mathbf{x} - \dfrac{1}{C_p^{\varepsilon}} q = V \end{cases}, \tag{2.2}$$

where

$$\mathbf{K}_{oc} = \mathbf{K}_{sc} + \frac{1}{C_p^{\varepsilon}} \boldsymbol{\gamma}_p \boldsymbol{\gamma}_p^T, \qquad \boldsymbol{\theta}_p = \frac{1}{C_p^{\varepsilon}} \boldsymbol{\gamma}_p \tag{2.3}$$

are the open-circuit stiffness matrix and a piezoelectric coupling vector, respectively. Equation (2.2) can be seen as a MDoF version of Equation (1.11).

2.2.1 Short-circuit and open-circuit modes

The short-circuit modes are the resonant modes of the structures when the transducer is short-circuited ($V = 0$). They satisfy the following generalized eigenvalue problem

$$\mathbf{K}_{sc}\mathbf{\Phi}_{sc} = \mathbf{M}\mathbf{\Phi}_{sc}\mathbf{\Omega}_{sc}^2, \qquad \mathbf{\Omega}_{sc} = \begin{bmatrix} \omega_{sc,1} & & \\ & \ddots & \\ & & \omega_{sc,N} \end{bmatrix} \tag{2.4}$$

where $\mathbf{\Phi}_{sc}$ is the matrix of short-circuit mode shapes, $\mathbf{\Omega}_{sc}$ is a diagonal matrix containing the short-circuit resonance frequencies $\omega_{sc,n}$ and N is the number of mechanical DoFs. The mode shapes are usually mass-normalized, i.e.,

$$\mathbf{\Phi}_{sc}^T\mathbf{M}\mathbf{\Phi}_{sc} = \mathbf{I}, \qquad \mathbf{\Phi}_{sc}^T\mathbf{K}_{sc}\mathbf{\Phi}_{sc} = \mathbf{\Omega}_{sc}^2, \tag{2.5}$$

where $\mathbf{I}$ is the identity matrix. If the generalized DoFs are expressed in terms of short-circuit modal amplitudes $\boldsymbol{\eta}_{sc}$ as

$$\mathbf{x}(t) = \mathbf{\Phi}_{sc}\boldsymbol{\eta}_{sc}(t), \tag{2.6}$$

then, Equation (2.1) can be rewritten, after premultiplication of the mechanical equation by $\mathbf{\Phi}_{sc}^T$, as

$$\begin{cases} \ddot{\boldsymbol{\eta}}_{sc} + \mathbf{\Omega}_{sc}^2\boldsymbol{\eta}_{sc} + \mathbf{\Phi}_{sc}^T\boldsymbol{\gamma}_p V = \mathbf{\Phi}_{sc}^T\mathbf{f} \\ \boldsymbol{\gamma}_p^T\mathbf{\Phi}_{sc}\boldsymbol{\eta}_{sc} - C_p^{\varepsilon}V = q \end{cases}. \tag{2.7}$$

Similar developments can be made with the open-circuit modes, which are the resonant modes of the structures with the transducer open-circuited ($q = 0$). They satisfy the following generalized eigenvalue problem

$$\mathbf{K}_{oc}\mathbf{\Phi}_{oc} = \mathbf{M}\mathbf{\Phi}_{oc}\mathbf{\Omega}_{oc}^2, \qquad \mathbf{\Omega}_{oc} = \begin{bmatrix} \omega_{oc,1} & & \\ & \ddots & \\ & & \omega_{oc,N} \end{bmatrix} \tag{2.8}$$

where $\mathbf{\Phi}_{oc}$ is the matrix of open-circuit mode shapes and $\mathbf{\Omega}_{oc}$ is a diagonal matrix containing the open-circuit resonance frequencies $\omega_{oc,n}$. The generalized DoFs can be expressed in terms of open-circuit modal amplitudes $\boldsymbol{\eta}_{oc}$ as

$$\mathbf{x}(t) = \mathbf{\Phi}_{oc}\boldsymbol{\eta}_{oc}(t), \tag{2.9}$$

and Equation (2.2) can be rewritten, after premultiplication of the mechanical equation by $\boldsymbol{\Phi}_{oc}^T$, as

$$\begin{cases} \ddot{\boldsymbol{\eta}}_{oc} + \boldsymbol{\Omega}_{oc}^2 \boldsymbol{\eta}_{oc} - \boldsymbol{\Phi}_{oc}^T \boldsymbol{\theta}_p q = \boldsymbol{\Phi}_{oc}^T \mathbf{f} \\ \boldsymbol{\theta}_p^T \boldsymbol{\Phi}_{oc} \boldsymbol{\eta}_{oc} - \dfrac{1}{C_p^\varepsilon} q = V \end{cases} . \tag{2.10}$$

2.2.2 Dynamic capacitance

Assuming that the structure is unforced ($\mathbf{f} = \mathbf{0}$), taking the Laplace transform of the mechanical equation in Equation (2.7) and inserting it into the electrical equation gives a dynamic relation between V and q, the *dynamic capacitance* $C_p(s)$:

$$-\left[C_p^\varepsilon + \boldsymbol{\gamma}_p^T \boldsymbol{\Phi}_{sc} \left(s^2 \mathbf{I} + \boldsymbol{\Omega}_{sc}^2\right)^{-1} \boldsymbol{\Phi}_{sc}^T \boldsymbol{\gamma}_p\right] V = -C_p^\varepsilon \left[1 + \sum_{n=1}^{N} \frac{\gamma_{\phi,n}^2}{C_p^\varepsilon} \frac{1}{s^2 + \omega_{sc,n}^2}\right] V = C_p(s) V = q, \tag{2.11}$$

where the modal coupling coefficients $\gamma_{\phi,n}$ are given by

$$\boldsymbol{\gamma}_p^T \boldsymbol{\Phi}_{sc} = \begin{bmatrix} \gamma_{\phi,1} & \cdots & \gamma_{\phi,N} \end{bmatrix}. \tag{2.12}$$

Applying an identical procedure starting from the open-circuit configuration (Equation (2.10)) yields the inverse transfer function, the *dynamic elastance* $E_p(s)$, as

$$-\left[\frac{1}{C_p^\varepsilon} - \boldsymbol{\theta}_p^T \boldsymbol{\Phi}_{oc} \left(s^2 \mathbf{I} + \boldsymbol{\Omega}_{oc}^2\right)^{-1} \boldsymbol{\Phi}_{oc}^T \boldsymbol{\theta}_p\right] q = -\frac{1}{C_p^\varepsilon} \left[1 - \sum_{n=1}^{N} \frac{C_p^\varepsilon \theta_{\phi,n}^2}{s^2 + \omega_{oc,n}^2}\right] q = E_p(s) q = V, \tag{2.13}$$

where the modal coupling coefficients $\theta_{\phi,n}$ are given by

$$\boldsymbol{\theta}_p^T \boldsymbol{\Phi}_{oc} = \begin{bmatrix} \theta_{\phi,1} & \cdots & \theta_{\phi,N} \end{bmatrix}. \tag{2.14}$$

Equations (2.11) and (2.13) show that the poles of the dynamic capacitance (elastance) are the short-circuit (open-circuit) resonance frequencies. Furthermore, since the dynamic capacitance (elastance) is the inverse of the dynamic elastance (capacitance), the zeros of the former are the poles of the latter, i.e., the open-circuit (short-circuit) resonance frequencies, as in Section 1.2.1.2. Therefore, an alternate expression for the dynamic capacitance is

$$C_p(s) = -C_p^\varepsilon \frac{\prod_{n=1}^{N} \left(s^2 + \omega_{oc,n}^2\right)}{\prod_{n=1}^{N} \left(s^2 + \omega_{sc,n}^2\right)} = \frac{1}{E_p(s)}. \tag{2.15}$$

Figure 2.2 plots the magnitude of a typical Bode plot of a hypothetical structure with three resonance frequencies. The advantage of knowing the dynamic capacitance (or

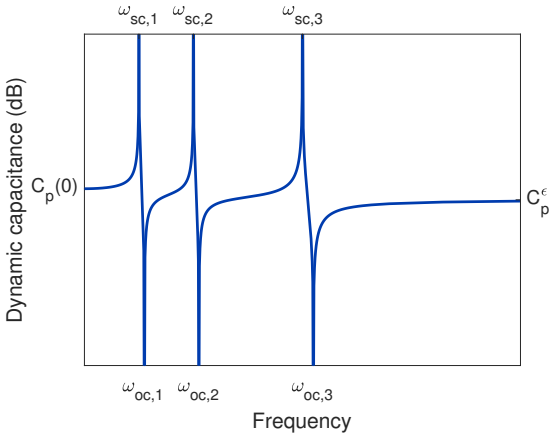

Figure 2.2: Dynamic capacitance magnitude of a piezoelectric transducer bonded to an MDoF structure.

elastance) is obvious, as it directly gives the short- and open-circuit resonance frequencies, as well as the capacitance at constant strain.

Equation (2.11) indicates that the coefficients $\gamma_{\phi,n}^2/C_p^\varepsilon$ can be thought of as residues associated with the poles $\pm j\omega_{sc,n}$. The cover-up method [115] can be used to deduce them from the short- and open-circuit resonance frequencies and the piezoelectric capacitance C_p^ε with Equation (2.15). Indeed, from Equations (2.11) and (2.15),

$$C_p(s) = -C_p^\varepsilon \left[1 + \sum_{n=1}^{N} \frac{\gamma_{\phi,n}^2}{C_p^\varepsilon} \frac{1}{s^2 + \omega_{sc,n}^2}\right] = -C_p^\varepsilon \frac{\prod_{n=1}^{N} \left(s^2 + \omega_{oc,n}^2\right)}{\prod_{n=1}^{N} \left(s^2 + \omega_{sc,n}^2\right)}. \tag{2.16}$$

Multiplying these equations by $s^2 + \omega_{sc,r}^2$ yields

$$-C_p^\varepsilon \left(s^2 + \omega_{sc,r}^2\right) \left[1 + \sum_{n=1}^{N} \frac{\gamma_{\phi,n}^2}{C_p^\varepsilon} \frac{1}{s^2 + \omega_{sc,n}^2}\right] - \gamma_{\phi,r}^2 = -C_p^\varepsilon \frac{\prod_{n=1}^{N} \left(s^2 + \omega_{oc,n}^2\right)}{\prod_{n=1,n\neq r}^{N} \left(s^2 + \omega_{sc,n}^2\right)}. \tag{2.17}$$

Taking the limit of this equation as $s \to j\omega_{sc,r}$,

$$\gamma_{\phi,r}^2 = C_p^\varepsilon \frac{\prod_{n=1}^{N} \left(\omega_{oc,n}^2 - \omega_{sc,r}^2\right)}{\prod_{n=1,n\neq r}^{N} \left(\omega_{sc,n}^2 - \omega_{sc,r}^2\right)}. \tag{2.18}$$

Similar developments from Equation (2.13) would have yielded

$$\theta_{\phi,r}^2 = -\frac{1}{C_p^\varepsilon} \frac{\prod_{n=1}^{N} \left(\omega_{sc,n}^2 - \omega_{oc,r}^2\right)}{\prod_{n=1,n\neq r}^{N} \left(\omega_{oc,n}^2 - \omega_{oc,r}^2\right)}. \tag{2.19}$$

Equations (2.18) and (2.19) give a practical way to evaluate the modal coupling coefficients experimentally from simple measurements of the resonance frequencies and the piezoelectric capacitance C_p^ε. As shall be shown in this chapter, this is sufficient to tune a shunt circuit with multiple resonance frequencies.

2.2.3 Electromechanical coupling factors

An EEMCF can be defined for each mode analogously to Equation (1.20) as

$$K_{c,n}^2 = \frac{\omega_{oc,n}^2 - \omega_{sc,n}^2}{\omega_{sc,n}^2}. \tag{2.20}$$

This EEMCF quantifies the electromechanical coupling existing between mode n and the piezoelectric transducer. Similarly to the SDoF case, it is an important quantity to know when tuning shunt circuits [121].

2.3 Specifications for the shunt circuit

Traditionally, dissipative shunt circuits were first tuned by considering their lossless counterparts [13, 19, 74, 75] because of the simplicity and effectiveness of Den Hartog's fixed points-based tuning approach [8]. The same approach shall be used herein, but for a different reason: it leads to a simple evaluation of the electromechanical coupling. The most general form of immittance is assumed for the lossless shunt circuit. It will then be demonstrated that the immittance of an equivalent circuit resulting from the connection of the piezoelectric transducer with a lossless circuit takes a specific form. This immittance can be expanded in partial fractions, where the resonance frequencies of the circuit are directly identifiable. Associated with these frequencies are residues (that can be seen as resonance amplitudes squared) which characterize the electromechanical coupling existing between the mechanical and electrical resonances. Specifically, *effective* short- and open-circuit resonance frequencies can be evaluated to compute an EEMCF. These effective frequencies may differ from those of the structure because the circuit itself influences them.

With this partial fraction expansion and a few simplifying assumptions, it is possible to show that the problem can be put into a simpler form similar to the SDoF case. From there on, a specification procedure can be devised. The procedure takes as input the identified piezoelectric structures, a set of modes to be controlled and a set of associated residues, which characterize the control authority on these modes. For each targeted mode, the tuning formulas presented in Chapter 1 are used to fully specify the characteristics of the

immittance in terms of zeros frequencies and damping ratios. The type of single-mode RL shunt to which these formulas are associated (series RL or parallel RL) constitutes the baseline case. The simplifying assumptions make this procedure sequential, i.e., the characteristics of the immittance can be determined one by one without iterations.

The models used in this section are generic, but Sections 2.7-2.9 will show how to use the obtained specifications in order to tune multi-branch shunt circuits which were proposed in the literature.

2.3.1 Admittance-based model

This section uses the Norton-type model (Equation (2.1)). It is shown that when the piezoelectric transducer is connected to a passive lossless circuit, Norton's equivalent admittance takes a specific form. The problem is then simplified by considering a pair of resonant mechanical and electrical modes, whereas the contribution from other non-resonant modes is seen as a background contribution, similarly to [119, 139]. This allows for the extraction of *effective* short- and open-circuit resonance frequencies, which can be used to specify the characteristics of Norton's equivalent admittance. Sections 2.3.1.1 to 2.3.1.6 describe the dynamics of the structure coupled to the shunt circuit, and Section 2.3.1.7 uses these developments to derive specifications on the shunt circuit.

2.3.1.1 Norton's equivalent admittance

The connection of a shunt circuit of admittance Y_s to the electrodes of the piezoelectric transducer imposes the following relation between the charge and voltage

$$q = \frac{Y_s(s)}{s} V. \tag{2.21}$$

Inserting this relation into Equation (2.1), the governing equations for the coupled system are obtained as

$$\begin{cases} \mathbf{M}\ddot{\mathbf{x}} + \mathbf{K}_{sc}\mathbf{x} + \boldsymbol{\gamma}_p V = \mathbf{f} \\ \dfrac{Y_N(s)}{s} V - \boldsymbol{\gamma}_p^T \mathbf{x} = 0 \end{cases}, \tag{2.22}$$

in which

$$Y_N(s) = sC_p^\varepsilon + Y_s(s) \tag{2.23}$$

is Norton's equivalent admittance of the parallel connection of the shunt circuit with a capacitor of capacitance C_p^ε, as schematized in Figure 2.3.

Condensing the electrical equation into the mechanical one in Equation (2.22) yields

$$\left(\mathbf{M}s^2 + \mathbf{K}_{sc} + \frac{s}{Y_N(s)} \boldsymbol{\gamma}_p \boldsymbol{\gamma}_p^T \right) \mathbf{x} = \mathbf{f}. \tag{2.24}$$

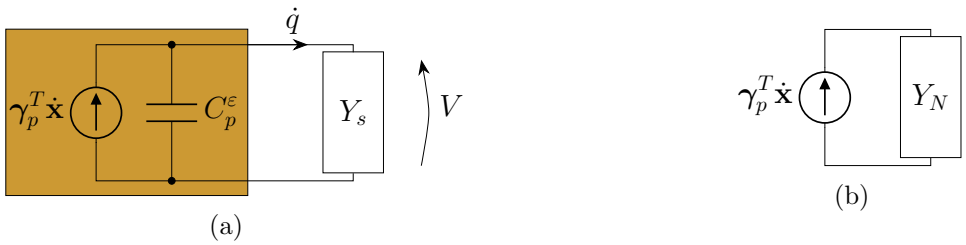

Figure 2.3: Shunt circuit connected to a piezoelectric transducer (a) and Norton's equivalent model (b).

When connecting an inductance to the electrodes of the transducers, $Y_s(s) = 1/(Ls)$, Norton's admittance takes the form

$$Y_N(s) = sC_p^\varepsilon + \frac{1}{Ls} = C_p^\varepsilon \frac{s^2 + \dfrac{1}{LC_p^\varepsilon}}{s}. \tag{2.25}$$

Thus,

$$\frac{s}{Y_N(s)} = \frac{1}{C_p^\varepsilon} \frac{s^2}{s^2 + \dfrac{1}{LC_p^\varepsilon}}. \tag{2.26}$$

As discussed in Section 1.2, the zero of this admittance (which is a pole of $s/Y_N(s)$) can be set equal to a short-circuit resonance frequency of the structure, in order to suppress completely this resonance. The purpose of this section is to set specifications on passive shunt circuits having such electrical resonances used to damp multiple structural resonances.

2.3.1.2 Implications of Foster's reactance theorem

Because the shunt circuit is made up of passive reactive lossless elements, Foster's reactance theorem[1] [141, 142] stipulates that its admittance must be of the form

$$Y_s(s) = K_s \frac{s\displaystyle\prod_{i=1}^{N_z}(s^2 + z_{s,i}^2)}{\displaystyle\prod_{i=1}^{N_p}(s^2 + p_{s,i}^2)} \tag{2.27}$$

with $K_s > 0$,

$$0 \leq p_{s,1} < z_{s,1} < p_{s,2} < z_{s,2} < \cdots \tag{2.28}$$

and either $N_z = N_p - 1$ or $N_z = N_p$. Inserting Equation (2.27) into Equation (2.23) gives

$$\frac{s}{Y_N(s)} = \frac{s}{sC_p^\varepsilon + Y_s(s)} = \frac{\displaystyle\prod_{i=1}^{N_p}(s^2 + p_{s,i}^2)}{C_p^\varepsilon \displaystyle\prod_{i=1}^{N_p}(s^2 + p_{s,i}^2) + K_s \displaystyle\prod_{i=1}^{N_z}(s^2 + z_{s,i}^2)}. \tag{2.29}$$

[1] The mechanical counterpart of this theorem is the alternation of resonances and antiresonances in a driving-point receptance [140].

The degree of the numerator and that of the denominator are equal given that $N_z \leq N_p$, and thus this transfer function is always biproper. Moreover, it cannot possess a pole at $s = 0$ but may have a double zero at $s = 0$ (if $p_{s,1} = 0$). Therefore, it takes the general form

$$\frac{s}{Y_N(s)} = \frac{1}{C_p^\varepsilon}\left(r_0 + \sum_{i=1}^{N_s} \frac{r_i s^2}{s^2 + z_i^2}\right), \tag{2.30}$$

where z_i is a zero of Norton's admittance, and r_i is its associated residue. It can be noted that the terms in the sum featured in Equation (2.30) have the same form as in the case of Equation (2.26). These terms correspond to electrical resonances imparted by the connection of the piezoelectric transducer to the shunt circuit. It can be anticipated that

- the zeros z_i of Y_N must be close to the structural resonance frequencies targeted for shunt damping.
- the residues r_i, which can be seen as (squared) modal amplitudes associated with the electrical resonances, should be maximized in order to maximize performance.

These two points shall be developed further hereafter.

2.3.1.3 Passivity constraints

Foster's reactance theorem [141] can also be used to set limitations on the values that the residues can take. First of all, because the parallel connection of a passive circuit with a capacitor makes up a circuit which is itself passive, every residue r_i must be positive. Second, by equating Equations (2.29) and (2.30) for $s \to \infty$, it is remarked that

$$\lim_{s\to\infty} \frac{s}{Y_N(s)} = \lim_{s\to\infty} \frac{\prod_{i=1}^{N_p}(s^2 + p_{s,i}^2)}{C_p^\varepsilon \prod_{i=1}^{N_p}(s^2 + p_{s,i}^2) + K_s \prod_{i=1}^{N_z}(s^2 + z_{s,i}^2)} = \frac{1}{C_p^\varepsilon}\sum_{i=0}^{N_s} r_i. \tag{2.31}$$

If $N_z = N_p - 1$,

$$\frac{1}{C_p^\varepsilon}\sum_{i=0}^{N_s} r_i = \frac{1}{C_p^\varepsilon}, \tag{2.32}$$

and if $N_z = N_p$,

$$\frac{1}{C_p^\varepsilon}\sum_{i=0}^{N_s} r_i = \frac{1}{C_p^\varepsilon + K_s} \in \left[0, \frac{1}{C_p^\varepsilon}\right[. \tag{2.33}$$

The foregoing developments show that the residues must satisfy the passivity constraints

$$r_i \geq 0 \ \forall i \in [0, N_s], \qquad 0 \leq \sum_{i=0}^{N_s} r_i \leq 1. \tag{2.34}$$

It shall be shown that the last constraint places fundamental limits on the performance of multimodal shunt circuits.

2.3.1.4 Background contributions

In the remainder of this section, it is assumed that mode k of Norton's admittance targets resonance r of the structure. Non-resonant mechanical modes are identified by a subscript n ($n = 1, \cdots, r-1, r+1, \cdots, N$). The external forcing is also assumed to be zero in order to characterize the poles of the system. Equation (2.22) can be rewritten using short-circuit modal coordinates as

$$\begin{cases} \left(s^2\mathbf{I} + \mathbf{\Omega}_{sc}^2\right)\boldsymbol{\eta}_{sc} + \mathbf{\Phi}_{sc}^T\boldsymbol{\gamma}_p V = \mathbf{0} \\ \dfrac{Y_N(s)}{s}V - \boldsymbol{\gamma}_p^T\mathbf{\Phi}_{sc}\boldsymbol{\eta}_{sc} = 0 \end{cases} \tag{2.35}$$

Since the structural matrices are diagonal, the non-resonant modal coordinates may be expressed as a sole function of V

$$\eta_{sc,n} = -\frac{\gamma_{\phi,n}}{s^2 + \omega_{sc,n}^2}V, \tag{2.36}$$

which, inserted back into the electrical equation, yields

$$\begin{cases} \left(s^2 + \omega_{sc,r}^2\right)\eta_{sc,r} + \gamma_{\phi,r}V = 0 \\ \left(\dfrac{Y_N(s)}{s} + \displaystyle\sum_{n=1,n\neq r}^{N}\frac{\gamma_{\phi,n}^2}{s^2+\omega_{sc,n}^2}\right)V - \gamma_{\phi,r}\eta_{sc,r} = 0 \end{cases}. \tag{2.37}$$

Finally, expressing V as a function of $\eta_{sc,r}$ and substituting the resulting expression into the mechanical equation, one gets

$$\left(s^2 + \omega_{sc,r}^2 + \frac{\gamma_{\phi,r}^2}{C_p^\varepsilon}\frac{C_p^\varepsilon\dfrac{s}{Y_N(s)}}{1 + C_p^\varepsilon\dfrac{s}{Y_N(s)}\displaystyle\sum_{n=1,n\neq r}^{N}\frac{\gamma_{\phi,n}^2}{C_p^\varepsilon}\frac{1}{s^2+\omega_{sc,n}^2}}\right)\eta_{sc,r} = 0. \tag{2.38}$$

So far, no approximation was made. However, Equation (2.38) is potentially of high order in s and thus complicated to work with. Moreover, it also requires the knowledge of every characteristic from Norton's admittance (r_i and z_i for each electrical mode), which would not ease its use within a specification procedure. Approximations shall thus be made to simplify the problem. The first approximation is a classical one and regards the non-resonant mechanical modes [119]. From their contribution given in Equation (2.38), only the static contribution from modes with frequency higher than $\omega_{sc,r}$ is retained (the other contribution decaying in s^{-2}). In other words,

$$\sum_{n=1,n\neq r}^{N}\frac{\gamma_{\phi,n}^2}{C_p^\varepsilon}\frac{1}{s^2+\omega_{sc,n}^2} \approx \sum_{n=r+1}^{N}\frac{\gamma_{\phi,n}^2}{\omega_{sc,n}^2 C_p^\varepsilon}. \tag{2.39}$$

The second approximation consists in similarly simplifying the dynamics of non-resonant electrical modes. Electrical modes whose frequency is lower than z_k are assumed to be capacitively-dominated, i.e.,

$$\frac{r_i s^2}{s^2 + z_i^2} \approx r_i, \qquad i < k, \tag{2.40}$$

and electrical modes whose frequency is higher than z_k are assumed to be inductively-dominated

$$\frac{r_i s^2}{s^2 + z_i^2} \approx \frac{r_i s^2}{z_i^2}, \qquad i > k. \tag{2.41}$$

For conciseness, the following dimensionless quantities are introduced

$$\kappa_{\bar{r}} = \sum_{n=r+1}^{N} \frac{\gamma_{\phi,n}^2}{\omega_{sc,n}^2 C_p^{\varepsilon}}, \qquad \kappa_r = \sum_{n=r}^{N} \frac{\gamma_{\phi,n}^2}{\omega_{sc,n}^2 C_p^{\varepsilon}}, \tag{2.42}$$

representing the static influence from higher-frequency modes without and with mode r, respectively, and

$$y_l = \sum_{i=0}^{k-1} r_i, \qquad y_h = \sum_{i=k+1}^{N_s} \frac{r_i \omega_{sc,r}^2}{z_i^2}, \tag{2.43}$$

representing the influence of capacitively-dominated and inductively-dominated electrical modes, respectively. It can be remarked that computing y_l and y_h requires the knowledge of all the residues but only the zeros from higher-frequency modes. Using the simplifying assumptions (Equations (2.39)-(2.41)) into Equation (2.38), a dynamic equation of lower order including the background contribution of non-resonant mechanical and electrical modes is obtained as

$$\left(s^2 + \omega_{sc,r}^2 + \omega_{sc,r}^2 \left(\kappa_r - \kappa_{\bar{r}} \right) \frac{y_l + \dfrac{r_k s^2}{s^2 + z_k^2} + y_h \dfrac{s^2}{\omega_{sc,r}^2}}{1 + \kappa_{\bar{r}} \left(y_l + \dfrac{r_k s^2}{s^2 + z_k^2} + y_h \dfrac{s^2}{\omega_{sc,r}^2} \right)} \right) \eta_{sc,r} = 0. \tag{2.44}$$

2.3.1.5 Effective short-circuit and open-circuit resonance frequencies

Going back to the single-mode case, Section 1.2 highlighted the relevance of short- and open-circuit resonance frequencies for tuning. In these cases, associated Norton's equivalent admittances are, using Equation (2.23),

$$\frac{s}{Y_{N,sc}} = \frac{s}{Y_N}\bigg|_{Y_s=\infty} = 0, \qquad \frac{s}{Y_{N,oc}} = \frac{s}{Y_N}\bigg|_{Y_s=0} = \frac{1}{C_p^{\varepsilon}}. \tag{2.45}$$

By analogy, we define modal short circuit and modal open circuit Norton's admittances by replacing the resonant term by its asymptotic values for $s \to 0$ and $s \to \infty$, respectively. In other words, the resonant electrical term can be replaced by

$$\lim_{s \to 0} \frac{r_k s^2}{s^2 + z_k^2} = 0 \tag{2.46}$$

and

$$\lim_{s \to \infty} \frac{r_k s^2}{s^2 + z_k^2} = r_k, \tag{2.47}$$

in the case of a modal short circuit and modal open circuit, respectively. Substituting these expressions into Equation (2.44) defines effective resonance frequencies. Based

on their value, it is possible to assess an EEMCF which will eventually be used to specify the characteristics of the shunt circuit.

Substituting the electrical resonant term by its expression in Equation (2.46) into Equation (2.44) gives a quadratic equation in s^2. The effective short-circuit resonance frequency $\widehat{\omega}_{sc,r}$ can be found by solving this equation for $s = j\widehat{\omega}_{sc,r}$ as

$$\widehat{\omega}_{sc,r} = \frac{\omega_{sc,r}}{\sqrt{\dfrac{1+y_l\kappa_{\overline{r}}+y_h\kappa_r}{2+2y_l\kappa_r} + \sqrt{\left(\dfrac{1+y_l\kappa_{\overline{r}}+y_h\kappa_r}{2+2y_l\kappa_r}\right)^2 - \dfrac{y_h\kappa_{\overline{r}}}{1+y_l\kappa_r}}}}. \tag{2.48}$$

Proceeding in an analogous way with Equation (2.47), the effective open-circuit resonance frequency $\widehat{\omega}_{oc,r}$ can be estimated by

$$\widehat{\omega}_{oc,r} = \frac{\omega_{sc,r}}{\sqrt{\dfrac{1+(y_l+r_k)\kappa_{\overline{r}}+y_h\kappa_r}{2+2(y_l+r_k)\kappa_r} + \sqrt{\left(\dfrac{1+(y_l+r_k)\kappa_{\overline{r}}+y_h\kappa_r}{2+2(y_l+r_k)\kappa_r}\right)^2 - \dfrac{y_h\kappa_{\overline{r}}}{1+(y_l+r_k)\kappa_r}}}}. \tag{2.49}$$

2.3.1.6 Coupling assessment

Equation (2.20) can be replaced by an EEMCF based on the effective short- and open-circuit resonance frequencies

$$\widehat{K}^2_{c,r} = \frac{\widehat{\omega}^2_{oc,r} - \widehat{\omega}^2_{sc,r}}{\widehat{\omega}^2_{sc,r}}. \tag{2.50}$$

We note the following particular cases

$$\widehat{K}^2_{c,r}\Big|_{r_k=0} = 0, \qquad \widehat{K}^2_{c,r}\Big|_{r_k=1} = K^2_{c,r} \tag{2.51}$$

and it is possible to show that $\widehat{\omega}_{oc,r}$ is a growing function of r_k, and thus so is $\widehat{K}_{c,r}$.

A more explicit expression of $\widehat{K}_{c,r}$ as a function of r_k can be obtained if one neglects the influence of non-resonant terms ($y_l = y_h = \kappa_{\overline{r}} = 0$). The effective short- and open-circuit resonance frequencies are then estimated by

$$\widehat{\omega}^2_{sc,r} \approx \omega^2_{sc,r}, \qquad \widehat{\omega}^2_{oc,r} \approx \left(1 + r_k\frac{\gamma^2_{\phi,r}}{\omega^2_{sc,r}C^{\varepsilon}_p}\right)\omega^2_{sc,r}. \tag{2.52}$$

The EEMCF is

$$\widehat{K}^2_{c,r} \approx r_k\frac{\gamma^2_{\phi,r}}{\omega^2_{sc,r}C^{\varepsilon}_p} \approx r_k K^2_{c,r}, \tag{2.53}$$

where $K^2_{c,r}$ is approximated under the same assumptions (i.e., starting from Equation (2.7) and neglecting the contribution from non-resonant mechanical modes [137]). The expressions given in Equation (2.52) are generally not accurate enough to be used to tune a shunt circuit but Equation (2.53) gives a remarkably concise expression of the

EEMCF as a function of the residue. It can be used as an approximate quantitative guide to select a set of residues based on the performance desired for specific modes.

In any case, the larger the residue associated to one mode, the larger the EEMCF, as anticipated. From Equation (2.34), it is noted that a residue cannot be greater than unity, and in case it is unitary all the other residues are zero. Thus, regarding a specific mode, a passive multimodal shunt circuit can at best perform as well as a single-mode shunt circuit. When multiple modes are targeted, performance on one mode has to be traded for performance on the other modes. This highlights a fundamental limitation in performance that can be expected from passive multimodal shunt circuits.

It can also be noted that the residue r_0 in Equation (2.30) is not associated to any mode, but still intervenes in the passivity constraint (Equation (2.34)). Hence, in terms of vibration reduction, $r_0 = 0$ is desirable to maximize the value of the other residues. Some topologies of shunt circuits however force this residue to be non-zero, as shall be seen.

2.3.1.7 Specifications for the shunt circuit

The previous developments can be assembled into a tuning procedure, which goes as follows. The user first selects the modes to be controlled and their associated residues, knowing that the latter will quantify the electromechanical coupling with the former. Typically, Equation (2.53) can be used at this stage to predict the EEMCF. The tuning procedure then consists in defining the zeros of Norton's equivalent admittance z_i and to add dissipation to the circuit through specification of associated damping ratios ζ_i in order to provide nearly-optimal vibration reduction.

From the tuning formulas of the SDoF case, the zeros can be computed from the EEMCF and the effective resonance frequencies as

$$\omega_{e,k} = \delta\left(\widehat{K}_{c,r}\right)\widehat{\omega}_{oc,r} \tag{2.54}$$

or

$$\omega_{e,k} = \nu\left(\widehat{K}_{c,r}\right)\widehat{\omega}_{sc,r}, \tag{2.55}$$

depending on whether the circuit has to be tuned based on the series RL (Equation (1.37)) or parallel RL (Equation (1.45)) SDoF case, respectively[2]. In general, the best-suited baseline case will depend on the topology of the dissipative shunt circuit. The damping ratios can also be determined as

$$\zeta_k = \zeta\left(\widehat{K}_{c,r}\right) \tag{2.56}$$

or

$$\zeta_k = \varsigma\left(\widehat{K}_{c,r}\right), \tag{2.57}$$

depending on the baseline case: series RL (Equation (1.37)) or parallel RL (Equation (1.45)) SDoF, respectively.

From Equation (2.44), the electrical resonance frequency $\omega_{e,k}$ of the lossless circuit creates a zero in the mechanical receptance if

$$1 + \kappa_{\bar{r}}\left(y_l + \frac{r_k s^2}{s^2 + z_k^2} + y_h\frac{s^2}{\omega_{sc,r}^2}\right) = 0 \tag{2.58}$$

[2]Other tuning formulas for the series or parallel RL shunt circuits [13, 19, 74, 75, 82] can also be used.

for $s = j\omega_{e,k}$. Solving for z_k eventually yields

$$z_k = \omega_{e,k} \sqrt{1 + \frac{r_k}{\dfrac{1}{\kappa_{\overline{r}}} + y_l - y_h \dfrac{\omega_{e,k}^2}{\omega_{sc,r}^2}}}. \tag{2.59}$$

From Equation (2.40), it is seen that when tuning z_k, z_{k+1} to z_{N_s} have to be known. In order to have a sequential specification procedure where everything is known when considering resonance k, this suggests that the electrical resonances have to be specified in descending order of frequency. Figure 2.4 summarizes the proposed approach.

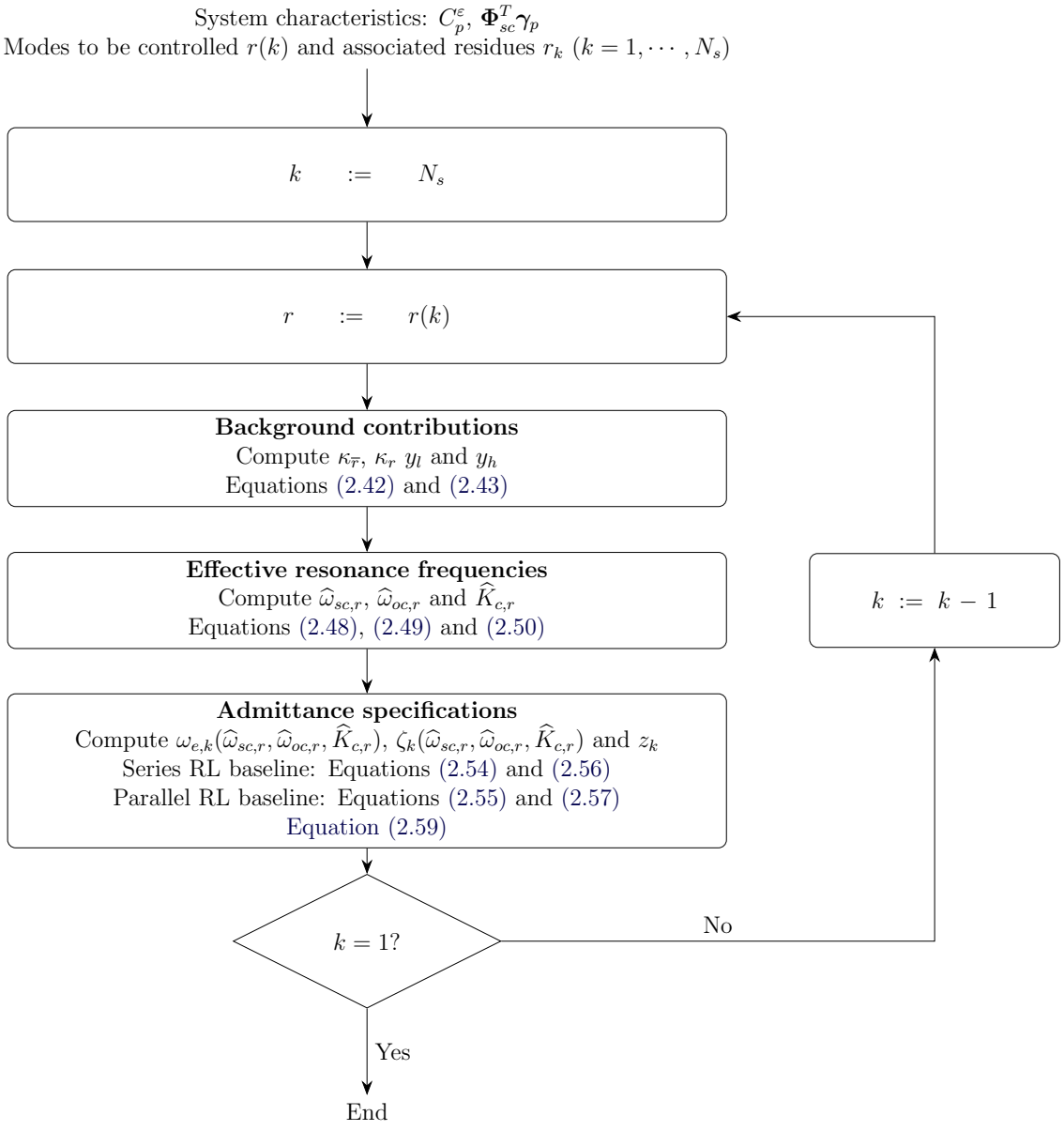

Figure 2.4: Flowchart of the proposed admittance specification approach.

Ideally, the shunt circuit admittance Y_s should be chosen such that Norton's dissipative admittance is of the form

$$Y_N(s) = sC_p^\varepsilon + Y_s(s) = sC_p^\varepsilon \left(r_0 + \sum_{i=1}^{N_s} \frac{r_i s^2}{s^2 + 2\zeta_i z_i s + z_i^2} \right)^{-1}. \tag{2.60}$$

The values of the electrical components that make the shunt circuit up can then be derived, but they depend specifically on the shunt circuit topology.

2.3.2 Impedance-based model

This section uses the Thévenin-type model (Equation (2.2)). In this case, Thévenin's equivalent impedance plays a similar role here to Norton's admittance in Section 2.3.1. An approach essentially similar to that exposed therein can be followed to specify the characteristics of Thévenin's equivalent impedance. Sections 2.3.2.1 to 2.3.2.6 describe the dynamics of the structure coupled to the shunt circuit, and Section 2.3.2.7 uses these developments to derive specifications on the shunt circuit.

2.3.2.1 Thévenin's equivalent impedance

If the shunt circuit impedance Z_s is considered, the charge-voltage relation reads

$$V = sZ_s(s)q, \tag{2.61}$$

which, inserted into Equation (2.2), yields

$$\begin{cases} \mathbf{M}\ddot{\mathbf{x}} + \mathbf{K}_{oc}\mathbf{x} - \boldsymbol{\theta}_p q = \mathbf{f} \\ sZ_T(s)q - \boldsymbol{\theta}_p^T \mathbf{x} = 0 \end{cases}, \tag{2.62}$$

in which

$$Z_T(s) = \frac{1}{sC_p^\varepsilon} + Z_s(s) \tag{2.63}$$

is Thévenin's equivalent impedance of the series connection of the shunt circuit with a capacitor of capacitance C_p^ε, as depicted in Figure 2.5.

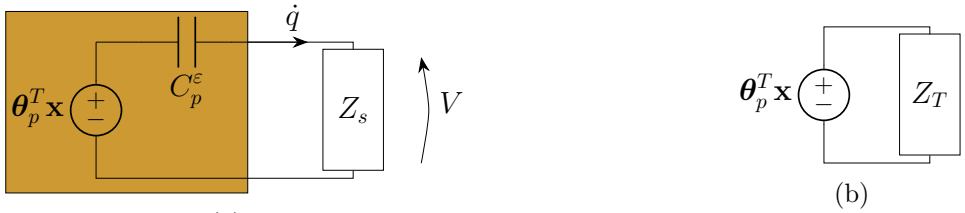

Figure 2.5: Shunt circuit connected to a piezoelectric transducer (a) and Thévenin's equivalent model (b).

The receptance of the controlled structure then satisfies

$$\left(\mathbf{M}s^2 + \mathbf{K}_{oc} - \frac{1}{sZ_T(s)}\boldsymbol{\theta}_p\boldsymbol{\theta}_p^T\right)\mathbf{x} = \mathbf{f}. \tag{2.64}$$

When connecting an inductance to the electrodes of the transducers, $Z_s(s) = Ls$, and Thévenin's impedance takes the form

$$Z_T(s) = \frac{1}{sC_p^\varepsilon} + Ls = \frac{1}{C_p^\varepsilon}\frac{LC_p^\varepsilon s^2 + 1}{s}. \tag{2.65}$$

Thus,

$$\frac{1}{sZ_T(s)} = C_p^\varepsilon \frac{1}{LC_p^\varepsilon s^2 + 1}. \tag{2.66}$$

As discussed in Section 1.2, the zero of this impedance (which is a pole of $1/(sZ_T(s))$) can be set equal to that of the structure, in order to suppress completely a single resonance.

2.3.2.2 Implications of Foster's reactance theorem

Foster's reactance theorem [141, 142] can be used to deduce several properties of $Z_T(s)$. If the shunt impedance is made of passive reactive lossless elements, it must be of the form

$$Z_s(s) = K_s \frac{\prod_{i=1}^{N_z}(s^2 + z_{s,i}^2)}{s\prod_{i=1}^{N_p}(s^2 + p_{s,i}^2)} \tag{2.67}$$

with $K_s > 0$,

$$0 \leq z_{s,1} < p_{s,1} < z_{s,2} < p_{s,2} < \cdots \tag{2.68}$$

and either $N_p = N_z - 1$ or $N_p = N_z$. Inserting Equation (2.67) into Equation (2.63) gives

$$\frac{1}{sZ_T(s)} = \frac{1}{\frac{1}{C_p^\varepsilon} + sZ_s(s)} = \frac{\prod_{i=1}^{N_p}(s^2 + p_{s,i}^2)}{\frac{1}{C_p^\varepsilon}\prod_{i=1}^{N_p}(s^2 + p_{s,i}^2) + K_s\prod_{i=1}^{N_z}(s^2 + z_{s,i}^2)}. \tag{2.69}$$

In this case, the degree of the numerator is equal to or lower than that of the denominator given that $N_p \leq N_z$, and thus this transfer function is proper. Moreover, it can neither possess a pole at $s = 0$ nor a zero at $s = 0$. Therefore, it takes the general form

$$\frac{1}{sZ_T(s)} = C_p^\varepsilon \left(r_0 + \sum_{i=1}^{N_s} \frac{r_i}{\frac{s^2}{z_i^2} + 1} \right), \tag{2.70}$$

where z_i is a zero of Thévenin's impedance, and r_i is its associated residue. It can be noted that the terms in the sum featured in Equation (2.70) have the same form as in the case of Equation (2.66). These terms correspond to electrical resonances imparted by the connection of the piezoelectric transducer to the shunt circuit. Again, it can be anticipated that

- the zeros z_i of Z_T must be close to the structural resonance frequencies targeted for shunt damping.
- the residues r_i should be maximized in order to maximize performance.

2.3.2.3 Passivity constraints

Because the series connection of a passive circuit with a capacitor makes up a circuit which is itself passive, every residue r_i must be positive. By equating Equations (2.63) and (2.70) for $s \to 0$, it is remarked that

$$\lim_{s\to 0} \frac{1}{sZ_T(s)} = \lim_{s\to 0} \frac{\prod_{i=1}^{N_p}(s^2+p_{s,i}^2)}{\frac{1}{C_p^\varepsilon}\prod_{i=1}^{N_p}(s^2+p_{s,i}^2) + K_s\prod_{i=1}^{N_z}(s^2+z_{s,i}^2)} = C_p^\varepsilon \sum_{i=0}^{N_s} r_i. \tag{2.71}$$

Thus

$$C_p^\varepsilon \sum_{i=0}^{N_s} r_i = \frac{1}{\frac{1}{C_p^\varepsilon} + K_s \frac{\prod_{i=1}^{N_z} z_{s,i}^2}{\prod_{i=1}^{N_p} p_{s,i}^2}} \in \left[0, C_p^\varepsilon\right], \tag{2.72}$$

the upper bound C_p^ε being reached if $z_{s,1} = 0$.

The foregoing developments show that the residues must satisfy the passivity constraints

$$r_i \geq 0 \ \forall i \in [0, N_s], \qquad 0 \leq \sum_{i=0}^{N_s} r_i \leq 1. \tag{2.73}$$

Again, the last constraint places fundamental limits on the performance of multimodal shunt circuits.

2.3.2.4 Background contributions

In the remainder of this section, it is assumed that mode k of Thévenin's impedance targets resonance r of the structure. As in Section 2.3.1.5, an unforced system is considered, and it is possible to isolate a resonant frequency from Equation (2.10) and to obtain

$$\left(s^2 + \omega_{oc,r}^2 - \theta_{\phi,r}^2 C_p^\varepsilon \frac{\frac{1}{C_p^\varepsilon}\frac{1}{sZ_T(s)}}{1 - \frac{1}{C_p^\varepsilon}\frac{1}{sZ_T(s)} \sum_{n=1,n\neq r}^{N} \frac{\theta_{\phi,n}^2 C_p^\varepsilon}{s^2+\omega_{oc,n}^2}} \right) \eta_{oc,r} = 0. \tag{2.74}$$

Assuming that the lower-frequency electrical modes ($z_i < z_k$) are inductively-dominated, i.e.,

$$\frac{r_i}{\frac{s^2}{z_i^2}+1} \approx \frac{r_i z_i^2}{s^2}, \qquad i < k, \tag{2.75}$$

that the higher-frequency electrical modes ($z_k < z_i$) are capacitively-dominated,

$$\frac{r_i}{\frac{s^2}{z_i^2}+1} \approx r_i, \qquad i > k \tag{2.76}$$

and that the non-resonant mechanical modes contribute only through static response of the higher-frequency modes,

$$\sum_{n=1,n\neq r}^{N} \frac{\theta_{\phi,n}^2 C_p^{\varepsilon}}{s^2+\omega_{oc,n}^2} \approx \sum_{n=r+1}^{N} \frac{\theta_{\phi,n}^2 C_p^{\varepsilon}}{\omega_{oc,n}^2}, \tag{2.77}$$

a quadratic equation for the effective short- and open-circuit resonance frequencies can be obtained. The following quantities are introduced

$$\kappa_{\bar{r}} = \sum_{n=r+1}^{N} \frac{\theta_{\phi,n}^2 C_p^{\varepsilon}}{\omega_{oc,n}^2}, \qquad \kappa_r = \sum_{n=r}^{N} \frac{\theta_{\phi,n}^2 C_p^{\varepsilon}}{\omega_{oc,n}^2}. \tag{2.78}$$

and

$$z_l = \sum_{i=1}^{k-1} \frac{r_i z_i^2}{\omega_{oc,r}^2}, \qquad z_h = r_0 + \sum_{i=k+1}^{N_s} r_i. \tag{2.79}$$

With the aforementioned approximations, Equation (2.74) simplifies to

$$\left(s^2+\omega_{oc,r}^2 - \omega_{oc,r}^2(\kappa_r-\kappa_{\bar{r}}) \frac{z_l \dfrac{\omega_{oc,r}^2}{s^2} + \dfrac{r_k}{\dfrac{s^2}{z_k^2}+1} + z_h}{1-\kappa_{\bar{r}}\left(z_l \dfrac{\omega_{oc,r}^2}{s^2} + \dfrac{r_k}{\dfrac{s^2}{z_k^2}+1} + z_h \right)} \right) \eta_{oc,r} = 0. \tag{2.80}$$

2.3.2.5 Effective short-circuit and open-circuit resonance frequencies

Thévenin's equivalent impedances with short- and open-circuited transducer are

$$\frac{1}{sZ_{N,sc}} = C_p^{\varepsilon}, \qquad \frac{1}{sZ_{N,oc}} = 0. \tag{2.81}$$

By analogy, we define modal-short-circuit and modal-open-circuit impedances given respectively by replacing the resonant term by its asymptotic values for $s \to 0$ and $s \to \infty$, respectively, that is,

$$\lim_{s\to 0} \frac{r_k}{\dfrac{s^2}{z_k^2}+1} = r_k, \tag{2.82}$$

and

$$\lim_{s\to \infty} \frac{r_k}{\dfrac{s^2}{z_k^2}+1} = 0, \tag{2.83}$$

respectively.

Substituting Equation (2.82) into Equation (2.80), the effective short-circuit resonance frequency is the solution for $s = j\widehat{\omega}_{sc,r}$, and is thus given by

$$\widehat{\omega}_{sc,r} = \omega_{oc,r}\sqrt{\frac{1 - z_l\kappa_{\overline{r}} - (z_h + r_k)\kappa_r}{2 - 2(z_h + r_k)\kappa_{\overline{r}}} + \sqrt{\left(\frac{1 - z_l\kappa_{\overline{r}} - (z_h + r_k)\kappa_r}{2 - 2(z_h + r_k)\kappa_{\overline{r}}}\right)^2 + \frac{z_l\kappa_r}{1 - (z_h + r_k)\kappa_{\overline{r}}}}}, \tag{2.84}$$

And with Equation (2.83) substituted into Equation (2.80), the effective open-circuit resonance frequency can be estimated as

$$\widehat{\omega}_{oc,r} = \omega_{oc,r}\sqrt{\frac{1 - z_l\kappa_{\overline{r}} - z_h\kappa_r}{2 - 2z_h\kappa_{\overline{r}}} + \sqrt{\left(\frac{1 - z_l\kappa_{\overline{r}} - z_h\kappa_r}{2 - 2z_h\kappa_{\overline{r}}}\right)^2 + \frac{z_l\kappa_r}{1 - z_h\kappa_{\overline{r}}}}}. \tag{2.85}$$

2.3.2.6 Coupling assessment

The EEMCF given in Equation (2.50) is recalled here

$$\widehat{K}^2_{c,r} = \frac{\widehat{\omega}^2_{oc,r} - \widehat{\omega}^2_{sc,r}}{\widehat{\omega}^2_{sc,r}} \tag{2.86}$$

We note the following particular cases

$$\widehat{K}^2_{c,r}\Big|_{r_k=0} = 0, \qquad \widehat{K}^2_{c,r}\Big|_{r_k=1} = K^2_{c,r} \tag{2.87}$$

and it is possible to show that $\widehat{\omega}_{sc,r}$ is a decreasing function of r_k, and thus $\widehat{K}_{c,r}$ is a growing function of r_k.

A more explicit expression of $\widehat{K}_{c,r}$ as a function of r_k can be obtained if one neglects the influence of non-resonant terms ($z_l = z_h = \kappa_{\overline{r}} = 0$). The effective short- and open-circuit resonance frequencies are then estimated by

$$\widehat{\omega}^2_{sc,r} \approx \omega^2_{oc,r}\left(1 - r_k\theta^2_{\phi,r}C^{\varepsilon}_p\right), \qquad \widehat{\omega}^2_{oc,r} \approx \omega^2_{oc,r}. \tag{2.88}$$

The EEMCF is

$$\widehat{K}^2_{c,r} \approx \frac{r_k K^2_{c,r}}{1 + K^2_{c,r} - r_k K^2_{c,r}} \overset{K^2_{c,r} \ll 1}{\approx} r_k K^2_{c,r}. \tag{2.89}$$

Again, it can be observed that the EEMCF can be predicted from the residue with a rather simple formula. This highlights the same performance trade-off as in the admittance-based models.

2.3.2.7 Specifications for the shunt circuit

As in the admittance-based model case, it is possible to set an electrical resonance frequency and associated damping ratio based on the effective modal characteristics of the electromechanical system. The formulas from the SDoF baseline case can be used to

specify the electrical resonance frequency $\omega_{e,k}$ and damping ratio $\zeta_{e,k}$, as in Section 2.3.1.7. To obtain a zero of the mechanical receptance in Equation (2.80), z_k should satisfy

$$1 - \kappa_{\overline{r}} \left(z_l \frac{\omega_{oc,r}^2}{s^2} + \frac{r_k}{\frac{s^2}{z_k^2} + 1} + z_h \right) = 0, \tag{2.90}$$

for $s = j\omega_{e,k}$, i.e.,

$$z_k = \frac{\omega_{e,k}}{\sqrt{1 - \frac{r_k}{\frac{1}{\kappa_{\overline{r}}} + z_l \frac{\omega_{oc,r}^2}{\omega_{e,k}^2} - z_h}}}. \tag{2.91}$$

It is now possible to devise a specification procedure for the shunt circuit's characteristics. From a set of modes to be controlled and associated residues, the zeros of Thévenin's impedance and the desired damping for optimal vibration reduction can be computed. Equation (2.75) shows that in order to tune z_k, z_1 to z_{k-1} have to be known, which suggests that the tuning must be done in ascending order of frequency. Figure 2.6 summarizes the proposed approach.

With these specifications, the shunt circuit impedance Z_s should ideally be such that Thévenin's dissipative impedance is

$$Z_T(s) = \frac{1}{sC_p^\varepsilon} + Z_s(s) = \frac{1}{sC_p^\varepsilon} \left(r_0 + \sum_{i=1}^{N_s} \frac{r_i}{\frac{s^2}{z_i^2} + 2\zeta_i \frac{s}{z_i} + 1} \right)^{-1} \tag{2.92}$$

2.3.3 Equivalence between the models

Two types of specification procedures were developed in the previous sections. They both yield a set of frequencies z_i and a set of associated damping ratios ζ_i. Whether the admittance-based or impedance-based specification is used, these parameters will be very close provided they use the same baseline case, but not rigorously identical. The small discrepancies come from the difference in the frequencies around which the approximations are made (either short- or open-circuit resonance frequencies), and are generally negligible in front of the other approximations.

It is now shown that the two approaches are equivalent in the lossless case (assuming identical frequencies z_i), but not in the dissipative case (assuming identical frequencies z_i and damping rations ζ_i). The shunt admittance is the inverse of the shunt impedance, i.e.,

$$Y_s(s) = \frac{1}{Z_s(s)}. \tag{2.93}$$

Thus, a relation between Norton's admittance defined in Equation (2.23) and Thévenin's impedance defined in Equation (2.63) can be derived as

$$Y_N(s) = \frac{sC_p^\varepsilon Z_T(s)}{Z_T(s) - \frac{1}{sC_p^\varepsilon}}, \tag{2.94}$$

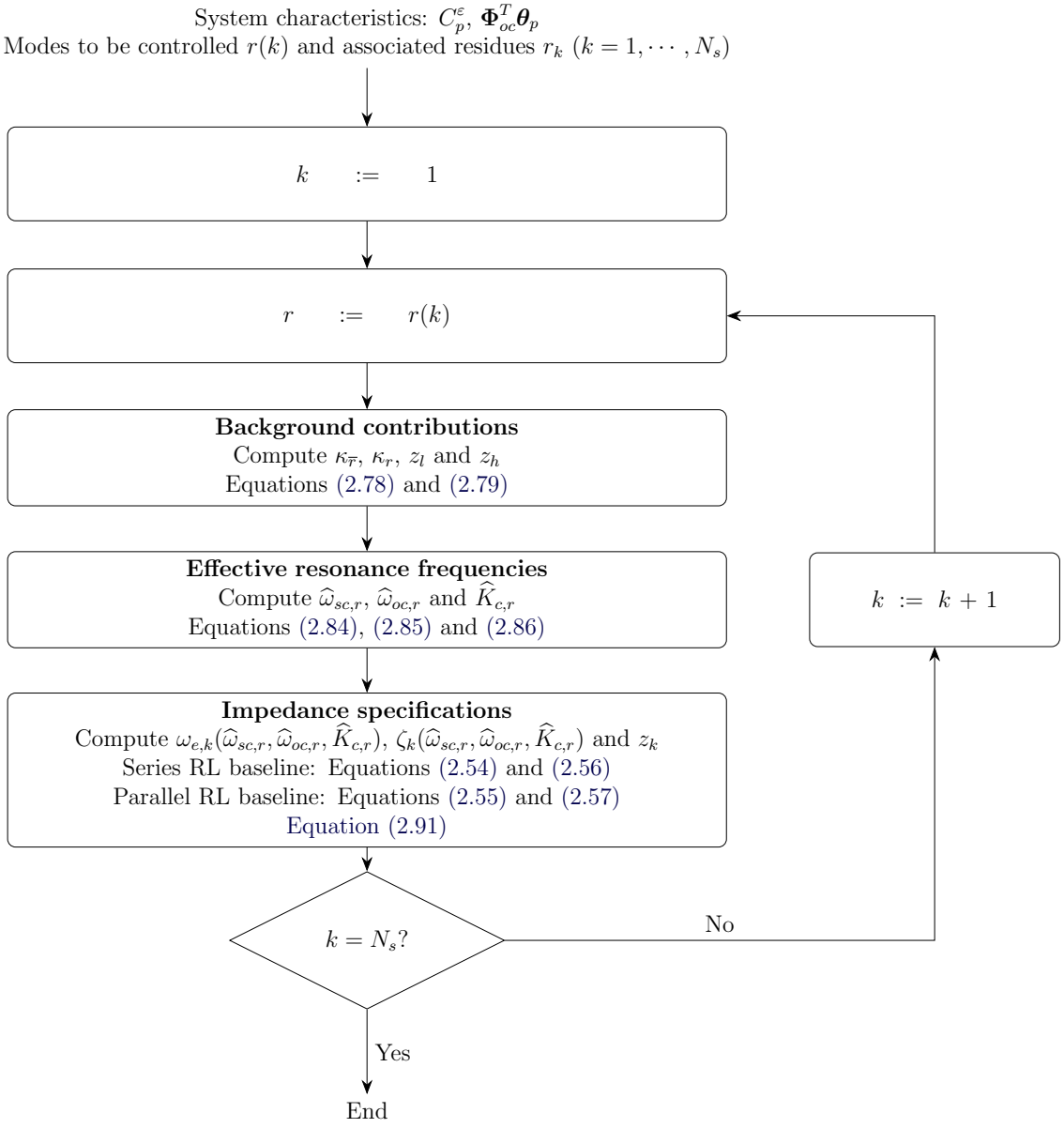

Figure 2.6: Flowchart of the proposed impedance specification approach.

and the inverse relation is

$$Z_T(s) = \frac{Y_N(s)}{sC_p^\varepsilon(Y_N(s) - sC_p^\varepsilon)}. \tag{2.95}$$

2.3.3.1 Lossless case

In the lossless case, if Norton's admittance is given by Equation (2.23), then, by Equation (2.95), one obtains

$$\frac{1}{sZ_T(s)} = C_p^\varepsilon \left(1 - \sum_{i=0}^{N_s} r_i + \sum_{i=1}^{N_s} \frac{r_i}{\dfrac{s^2}{z_i^2} + 1}\right), \tag{2.96}$$

which is of the same form as Equation (2.63) (the only difference being the expression of r_0). Specifically, the zeros of Z_T are identical to those of Y_N, and their associated residues are also identical. Thus, the two approaches are equivalent in the lossless case. While passing from one model to the other, it should be kept in mind that all the residues stay identical except for r_0, which becomes

$$r_0 := 1 - \sum_{i=0}^{N_s} r_i. \tag{2.97}$$

2.3.3.2 Dissipative case

If dissipative circuits are considered, Norton's dissipative admittance would ideally be given by Equation (2.60), while Thévenin's dissipative impedance would ideally be given by Equation (2.92). Inserting Equation (2.60) into Equation (2.95), the following expression is obtained after transforming Norton's admittance to Thévenin's impedance:

$$\frac{1}{sZ_T(s)} = C_p^{\varepsilon} \left(1 - r_0 - \sum_{i=1}^{N_s} \frac{r_i \left(2\zeta_i \dfrac{s}{z_i} + 1 \right)}{\dfrac{s^2}{z_i^2} + 2\zeta_i \dfrac{s}{z_i} + 1} \right). \tag{2.98}$$

This shows that if dissipative circuits are considered ($\zeta_i \neq 0$), the two approaches are no longer completely equivalent, because Equations (2.92) and (2.98) do not have the same form. The damping ratios are generally moderately small, so the discrepancy is moderate as well.

2.3.3.3 Choosing a model type

As stated in the beginning of this subsection, the specifications of the shunt circuit are almost identical using either model. Thus, when specifying the characteristics, either model can be used, and the choice can be based on convenience.

By contrast, when tuning the shunt circuit, the baseline model type is important. Circuits containing series RL branches are generally best tuned with the series RL shunt baseline case, whereas circuits with parallel RL branches are best tuned with parallel RL shunt baseline case. The sequel of this chapter will illustrate these concepts on the DVA and various shunt circuits, most of which have been proposed previously in the literature (see, e.g., [14] for a review).

2.4 Multimodal damping with a digital vibration absorber

When using a DVA, there is no need to explicitly set electrical parameters; the characteristics of the admittance as a transfer function are sufficient to program the digital unit and to make the DVA act as a passive shunt circuit. Hence, step 3 as depicted in Figure 2.1 is not necessary in this case.

If the shunt circuit specifications come from an admittance-based approach (Section 2.3.1), the shunt admittance can then be determined from Equation (2.23),

$$Y_s(s) = Y_N(s) - sC_p^\varepsilon. \tag{2.99}$$

In other terms, using Equation (2.60),

$$Y_s(s) = sC_p^\varepsilon \frac{1 - r_0 - \sum_{i=1}^{N_s} \frac{r_i s^2}{s^2 + 2\zeta_i z_i s + z_i^2}}{r_0 + \sum_{i=1}^{N_s} \frac{r_i s^2}{s^2 + 2\zeta_i z_i s + z_i^2}}. \tag{2.100}$$

This model works best if the admittance is tuned with the parallel RL baseline.

If the shunt circuit specifications come from an impedance-based approach (Section 2.3.2), the shunt admittance can then be determined from Equation (2.63) as

$$Y_s(s) = \frac{1}{Z_s(s)} = \frac{1}{Z_T(s) - \frac{1}{sC_p^\varepsilon}}, \tag{2.101}$$

that is, using Equation (2.92),

$$Y_s(s) = sC_p^\varepsilon \frac{r_0 + \sum_{i=1}^{N_s} \frac{r_i}{\frac{s^2}{z_i^2} + 2\zeta_i \frac{s}{z_i} + 1}}{1 - r_0 - \sum_{i=1}^{N_s} \frac{r_i}{\frac{s^2}{z_i^2} + 2\zeta_i \frac{s}{z_i} + 1}}. \tag{2.102}$$

This model works best if the admittance is tuned with the series RL baseline.

Similar forms to Equations (2.100) and (2.102) were proposed by Moheimani et al [14, 108, 143] by casting the passive control problem into a feedback one and using Youla's parametrization of all stabilizing controllers. However, the role of the residues was not as thoroughly discussed as here, and the tuning procedure was different for z_i (set equal to the corresponding open-circuit resonance frequency therein) and ζ_i (tuned by an optimization algorithm therein).

2.5 Numerical verification of the specification procedure

The cantilever beam that first appeared in Thomas et al [137] and was later studied in several works [75, 76, 121, 133] is used as a first example to numerically demonstrate the proposed approach. It is a clamped-free aluminum beam on which two PIC 151 piezoelectric patches are symmetrically bonded, as depicted in Figure 2.7. The geometrical and material properties of the system were taken

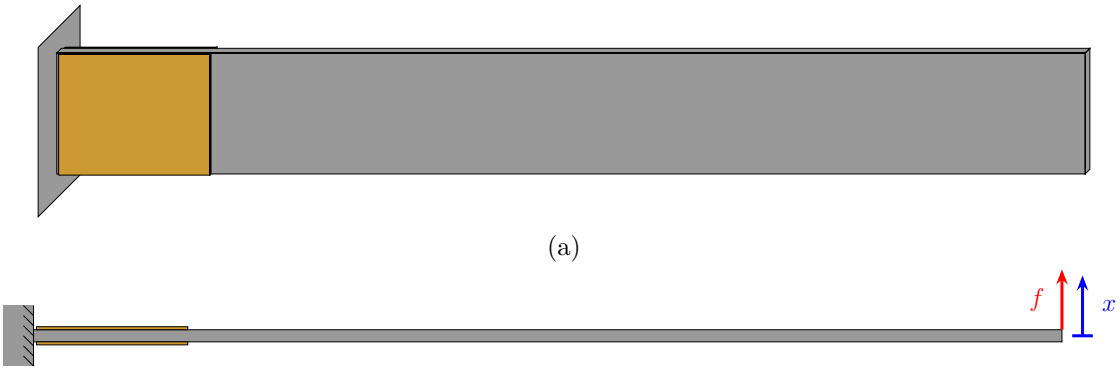

(a)

(b)

Figure 2.7: Schematic representation of the cantilever piezoelectric beam from [137]: perspective view (a) and top view (b).

from [137]. The patches have opposite polarization, and they are connected in series to form one equivalent piezoelectric transducer. A finite element (FE) model was built following the procedure described in [137].

The beam is transversely excited on its free end. Modal damping was set to 0.1% on all the modes. The driving-point FRF therefore exhibits lightly-damped resonances which can be targeted by the above-mentioned shunt circuits in order to reduce the vibratory amplitude.

The ideal shunt circuits presented in Section 2.4 are considered. The first two bending modes of the beam are targeted at first to keep the exposition simple.

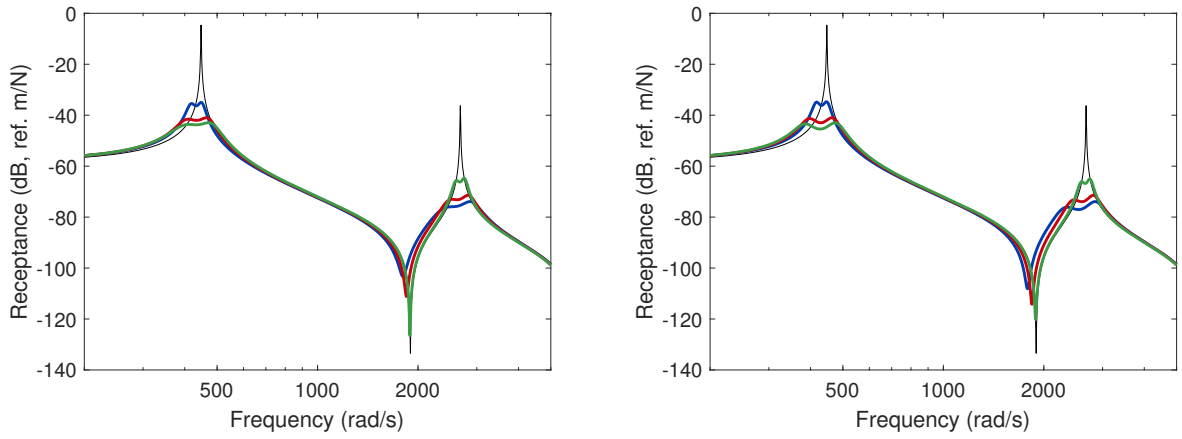

(a) (b)

Figure 2.8: FRF of the beam with open-circuited patches (—) and controlled with a circuit with ideal Thévenin's impedance (a) and ideal Norton's admittance (b): $r_1 = 0.1$, $r_2 = 0.9$ (—), $r_1 = 0.5$, $r_2 = 0.5$ (—) and $r_1 = 0.9$, $r_2 = 0.1$ (—).

Figure 2.8 presents the FRFs of the controlled beam with both approaches (yielding ideal Norton's admittance and Thévenin's impedance), using various values of the residues associated with modes 1 (r_1) and 2 (r_2), while respecting the passivity constraint $r_1 + r_2 = 1$. Both techniques yield similar performance in terms of vibration reduction, given identical residues. As expected, the greater r_1 the greater the vibration attenuation on mode 1, but the smaller the vibration attenuation on mode 2. The residues can thus be set to balance the control authority on specific modes, at the expense of that on other modes.

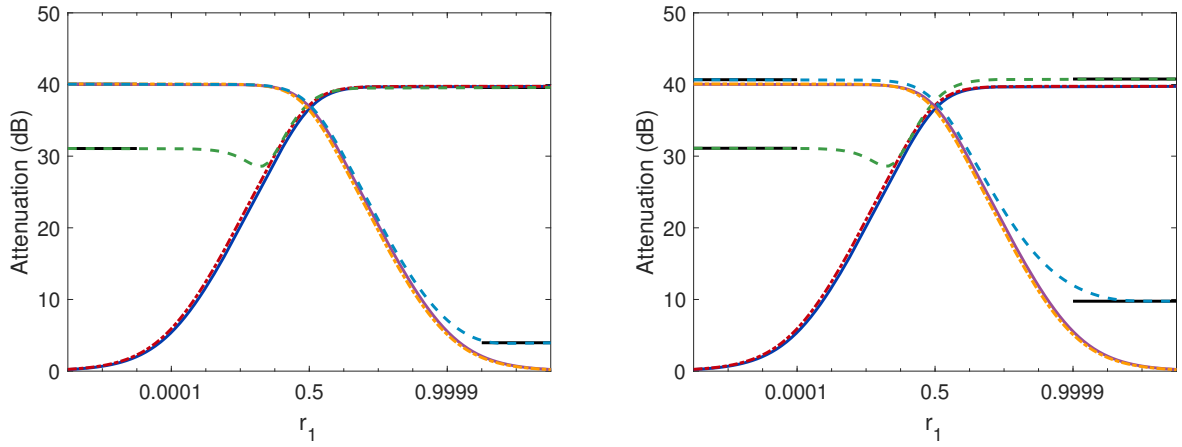

Figure 2.9: Attenuation of the modes as a function of the first residue for a circuit with ideal Thévenin's impedance (a) and ideal Norton's admittance (b): attenuation predicted with [75] using the EEMCF computed from effective short- and open-circuit resonance frequencies (— : mode 1, — : mode 2), with [75] using a linearized EEMCF (-·- : mode 1, -·- : mode 2) and (as defined in [75]) computed from the FRFs of the controlled systems (- - : mode 1, - - : mode 2). Black lines on the left and right indicate the attenuation of a single-mode (series (a) and parallel (b)) RL shunt tuned to mode 1 and 2, respectively.

The impact of the residues on the vibration reduction of the modes is also confirmed in Figure 2.9, where the attenuation on each mode is plotted against the value of the residue r_1 (while $r_2 = 1 - r_1$)[3]. This figure compares the attenuation (as defined in [75], i.e., the amplitude of the uncontrolled case at $\omega_{sc,r}$ over that of the controlled case at $\omega_{oc,r}$) computed in different ways. The first way is to use the prediction formula in [75] (Equation (35) therein). This formula relates the EEMCF and modal damping ratio to the attenuation. The EEMCF used can either be computed from Equation (2.50) using the effective short- and open-circuit resonance frequencies, or predicted from the linearized version given in Equation (2.53) (or Equation (2.89)). These two ways are shown in full and dash-dotted lines in Figure 2.10, respectively, and agree quite closely. This proves that the simple prediction of the EEMCF from the residues is conveniently accurate. The other way to compute the attenuation is to estimate it directly from the FRF, and is shown in dashed lines in Figure 2.10. An excellent agreement is obtained between the methods in Figure 2.10(a) when the considered modes are not associated with a very low residue. In Figure 2.10(b), that agreement is slightly worse, but this is because the formula in [75] is based on the series RL shunt. Nevertheless, the prediction formulas remain acceptable to predict the performance of this circuit.

The apparent disagreement between the prediction and the computed attenuation when the residue associated to a specific mode is low can be explained. The attenuation computed from the FRFs featured in Figure 2.9 is actually misleading, because it indicates (for instance) that a single-mode RL shunt on mode 2 could bring nearly 30dB of attenuation on mode 1, which is not the case if the peak amplitudes are compared. This is merely due to the way the attenuation is defined in [75], where the FRFs that

[3]The unusual scale for the abscissa in these figures is given by $\log_{10}(r_1/(1-r_1))$ in order to enlarge the regions where $r_1 \approx 0$ and $r_1 \approx 1$.

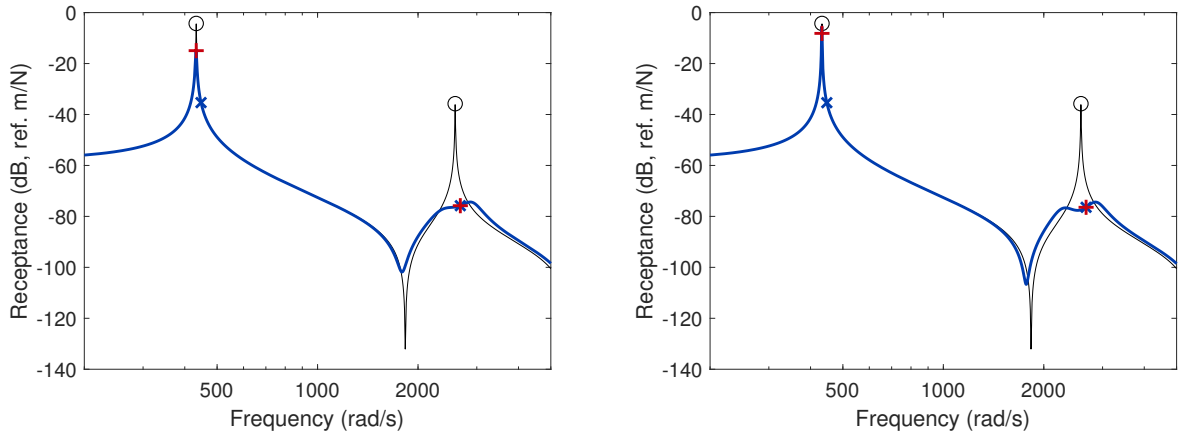

Figure 2.10: FRF of the beam with short-circuited patches (—) and controlled by a series (a) and parallel (b) RL shunt tuned to the second mode (—). The points (∘ and ×) indicate the frequencies at which these FRFs are evaluated to compute the attenuation according to [75], while the points (∘ and +) indicate the frequencies to compute the attenuation in this work.

are to be compared are computed at fixed frequencies. This works for a single-mode shunt but not for a case with multiple modes, as testified by Figure 2.10. Indeed, if the controlled FRF is evaluated at $\omega_{oc,1}$, it is far from indicating the true peak amplitude.

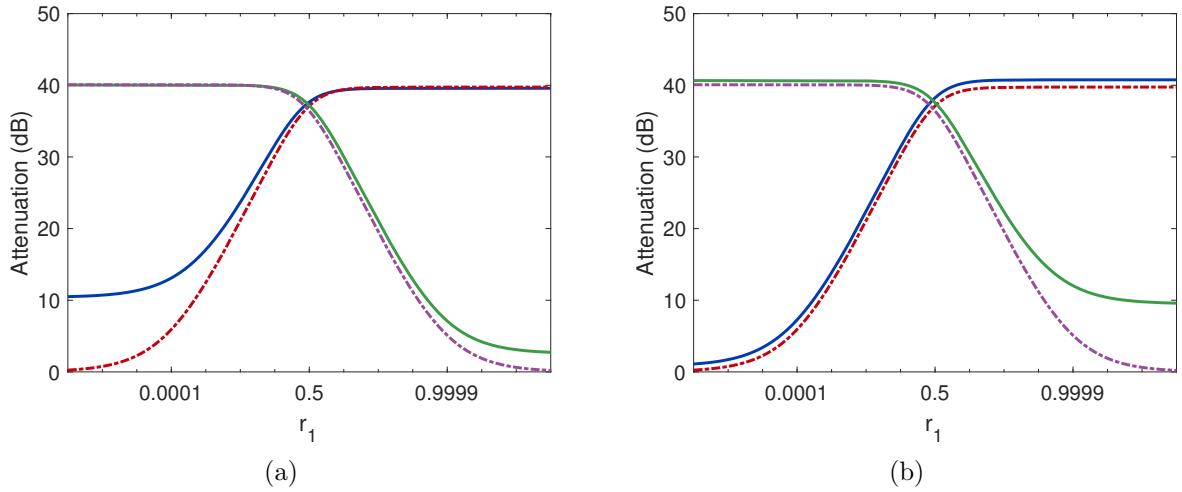

Figure 2.11: Attenuation of the modes as a function of the first residue for a circuit with ideal Thévenin's impedance (a) and ideal Norton's admittance (b): attenuation computed from the FRF (— : mode 1, — : mode 2) and attenuation predicted with [75] using a linearized EEMCF (-·- : mode 1, -·- : mode 2).

A more sensible choice for the attenuation in this case would be to compute the controlled FRF at the effective open-circuit resonance frequency ($\widehat{\omega}_{oc,r}$). Figure 2.11 features the attenuation defined this way. A better agreement is observed. The prediction formula still underestimates the attenuation, but this is simply because it overlooks the action of the shunts on other modes. For instance, it can be seen in Figure 2.11 that a series RL shunt on mode 2 can have a non-negligible attenuation effect on mode 1 and the converse is also true for a parallel RL shunt. Although not directly aimed at resonant shunts, this aspect is discussed more in depth in [144]. In any case, the observed trends verify

the relevance of using an EEMCF such as defined in Equation (2.50), and its predicted approximation Equation (2.53) (or Equation (2.89)) to guide the choice of the residues.

2.6 Experimental validation of the specification procedure

The piezoelectric beam studied in Section 1.3.3 is considered again to experimentally validate the developments in this chapter. The two first transversal bending modes of the beam were targeted for shunt damping. This time, two cells (as depicted in Figure 1.15(b)) were connected in parallel to form one equivalent piezoelectric transducer in order to simultaneously maximize the EEMCFs of these modes, as indicated in Figure 2.12.

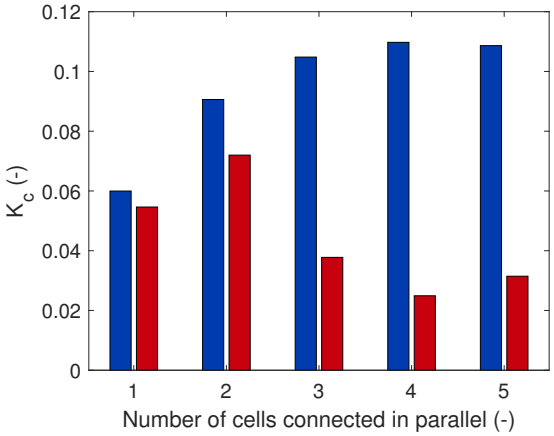

Figure 2.12: EEMCFs of the parallel connection of various numbers of cells closest to the clamped edge with the first (■) and second (■) bending modes of the beam.

The approach to implement a multimodal shunt circuit is fairly straightforward, as in Section 1.3.3. The peaks of the FRFs of the structure with short- and open-circuited patches can be used to estimate the short- and open-circuit resonance frequencies, and the capacitance of the patches can be measured with a multimeter. All these parameters are reported in Table 2.1. From there on, the modal coupling coefficients could be evaluated from Equation (2.18) or (2.19), thereby completing the identification step without the need to build a model of the structure. The specification procedure was then performed, and the obtained admittance was emulated by a DVA following the procedure outlined in Section 1.3. Delay-induced instabilities were also suppressed using the method described in Section 1.6.

Parameter	$f_{sc,1}$	$f_{oc,1}$	$K_{c,1}$	$f_{sc,2}$	$f_{oc,2}$	$K_{c,2}$	C_p^ε
Value	31.36Hz	31.49Hz	0.091	144.55Hz	144.92Hz	0.072	99nF

Table 2.1: Parameters of the experimental setup.

The ideal impedance and admittance described in Section 2.4 were used to obtain the FRFs featured in Figure 2.13. These experimental results validate the analysis presented

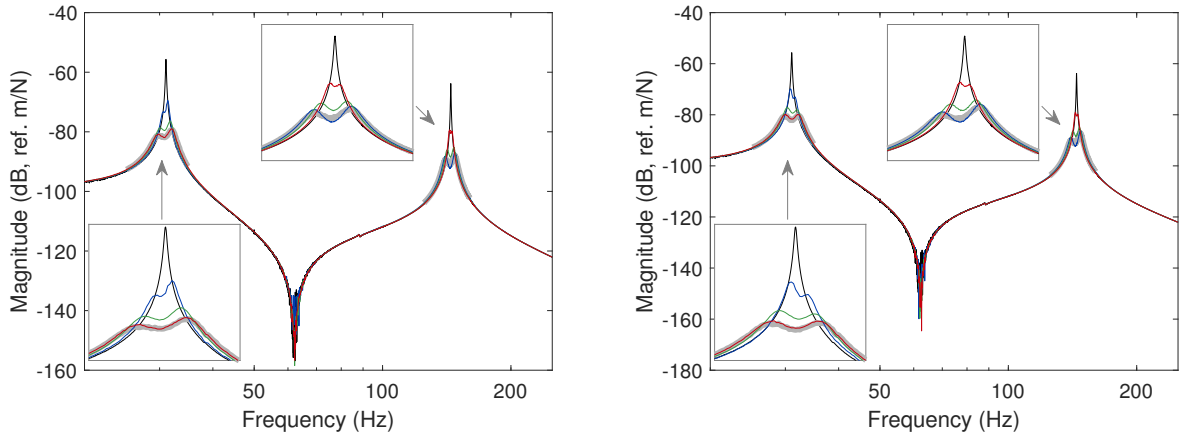

Figure 2.13: Experimental FRF of the beam with open-circuited patches (—) and controlled with a shunt circuit with ideal Thévenin's impedance (a) and ideal Norton's admittance (b): $r_1 = 0.1$ (—), $r_1 = 0.5$ (—) and $r_1 = 0.9$ (—). Thick gray lines indicate the FRF of the beam controlled with single-mode series (a) or parallel (b) RL shunts.

in this chapter: the DVA is able to control the two modes, and the control authority over the modes can be traded off with the residues. Moreover, the performance of the two shunt circuit types is similar, and tends to a single-mode shunt of associated type on a specific mode when the residue associated to that mode tends to one.

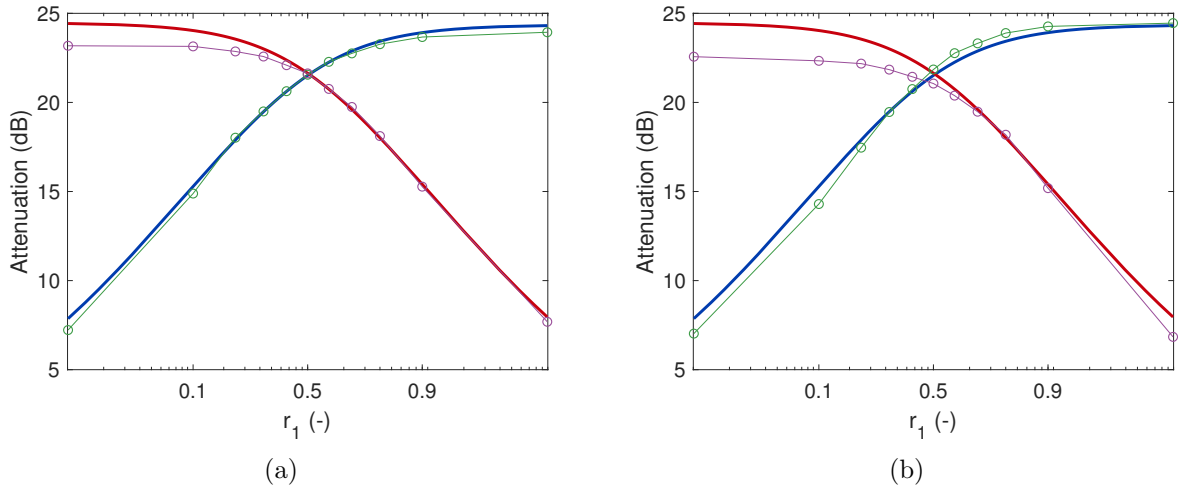

Figure 2.14: Experimental attenuation of the two first modes of the beam with a shunt circuit with ideal Thévenin's impedance (a) and ideal Norton's admittance (b): mode 1 (— : prediction [75], -○-: measurement) and mode 2 (— : prediction [75], -○-: measurement).

A more thorough analysis was pursued by measuring the FRFs for more values of the residues. All these FRFs are not shown for brevity but Figure 2.14 summarizes their information, by providing the attenuation as a function of r_1. The experimental results were compared to the theoretical formula from [75]. To use this formula, the damping ratio on both modes was estimated from the short-circuit FRF using the half-power method. Again, an excellent agreement with theory is obtained, except for small r_1. The attenuation in mode 2 is somewhat overestimated by the

prediction, which could be explained by the slightly underdamped appearance of the peaks associated with mode 2 in Figure 2.13.

2.7 Hollkamp's and current flowing shunt circuits tuning

Now that the theoretical developments on the specification procedure are numerically verified and experimentally validated, the remainder of this chapter is devoted to the third step of the tuning procedure given in Figure 2.1, i.e., tuning the electrical parameters of a passive shunt circuit.

Two multimodal shunt circuits are featured in Figure 2.15: Hollkamp's shunt circuit [126] and a current flowing (CF) shunt circuit proposed by Behrens et al [128]. These circuits can be tuned using the series RL baseline case with either approach proposed herein. The lossless circuits ($R_i = 0$) connected in parallel to a capacitor are shown in Figure 2.16 and are used to build Norton's equivalent admittance Y_N. It can be recognized that the resulting circuits are equivalent to Foster's first canonical form [142].

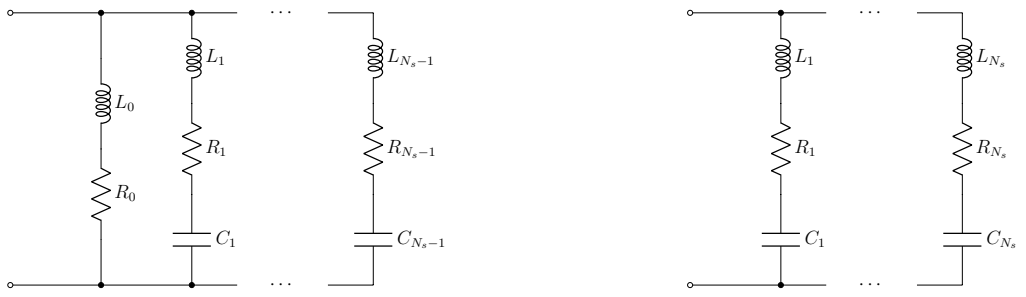

Figure 2.15: Hollkamp's shunt circuit (a) and current flowing shunt circuit (b).

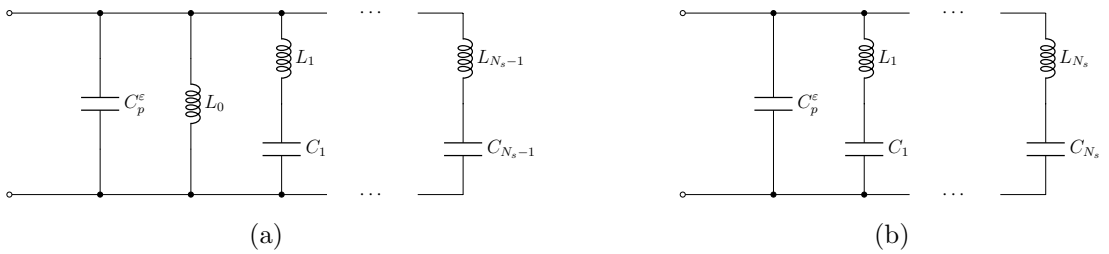

Figure 2.16: Norton's admittance model of a piezoelectric transducer connected to Hollkamp's lossless shunt circuit (a) and a lossless current flowing shunt circuit (b).

Tuning either type of circuit requires to compute the zero-pole-gain (ZPK) representation of Y_N. From Equation (2.30),

$$Y_N(s) = sC_p^\varepsilon \left(r_0 + \sum_{i=1}^{N_s} \frac{r_i s^2}{s^2 + z_i^2} \right)^{-1} = Ks \frac{\prod_{i=1}^{N_s} (s^2 + z_i^2)}{\prod_{i=1}^{N_s} (s^2 + p_i^2)}. \tag{2.103}$$

The poles of Norton's equivalent admittance can be found as the solution of the polynomial equation

$$r_0 \prod_{i=1}^{N_s}(s^2+z_i^2) + \sum_{i=1}^{N_s} r_i s^2 \prod_{j=1,j\neq i}^{N_s}(s^2+z_j^2) = 0. \tag{2.104}$$

Realistically, this polynomial is of moderate order. Moreover, its coefficients are known. Thus, the poles can readily be found with a computer. We note that when $r_0 = 0$, $p_1 = 0$ is a solution and thus Y_N has a simple pole at $s = 0$, whereas it has a simple zero at $s = 0$ if $r_0 \neq 0$. The gain K can be determined later.

2.7.1 Hollkamp's shunt circuit

The admittance of the lossless circuit featured in Figure 2.16(a) reads

$$Y_N(s) = sC_p^\varepsilon + \frac{1}{sL_0} + \sum_{n=1}^{N_s-1} \frac{\frac{1}{L_n}s}{s^2+\frac{1}{L_nC_n}} = \frac{K}{s}\frac{\prod_{i=1}^{N_s}(s^2+z_i^2)}{\prod_{i=1}^{N_s-1}(s^2+p_i^2)} \tag{2.105}$$

In this equation, the admittance computed as the parallel connection of a capacitor, an inductor and $N_s - 1$ branches of series LC circuits is represented in its partial fraction expansion. The fact that there are $N_s - 1$ complex conjugate poles indicates that this circuit can only be used if $r_0 = 0$. Equating the admittance to its ZPK representation and taking the limit for $s \to \infty$ in Equation (2.105), the gain K is found to be

$$K = C_p^\varepsilon, \tag{2.106}$$

which completely specifies the ZPK representation. The electrical parameters may then be derived from it. The admittance possesses several poles to which are associated residues which can directly be related to the electrical parameters. To evaluate these residues, the cover-up method [115] can be used. This gives the single inductance L_0 as

$$L_0 = \frac{1}{C_p^\varepsilon}\frac{\prod_{i=1}^{N_s-1} p_i^2}{\prod_{i=1}^{N_s} z_i^2} \tag{2.107}$$

whereas the inductances in the LC branches are identified as

$$L_k = -\frac{p_k^2}{C_p^\varepsilon}\frac{\prod_{i=1,i\neq k}^{N_s-1}(p_i^2-p_k^2)}{\prod_{i=1}^{N_s}(z_i^2-p_k^2)}. \tag{2.108}$$

Finally, the capacitances are computed from the poles of the admittance as

$$C_k = \frac{1}{L_k p_k^2}. \tag{2.109}$$

2.7.2 Current flowing shunt circuit

The admittance of the undamped CF shunt circuit shown in Figure 2.16(b) reads

$$Y_N(s) = sC_p^\varepsilon + \sum_{n=1}^{N_s} \frac{\frac{1}{L_n}s}{s^2+\frac{1}{L_nC_n}} = Ks\frac{\prod_{i=1}^{N_s}(s^2+z_i^2)}{\prod_{i=1}^{N_s}(s^2+p_i^2)}. \tag{2.110}$$

This time, the N_s complex conjugate poles impose $r_0 \neq 0$. In a similar way to Hollkamp's shunt circuit, the gain K is found to be

$$K = C_p^\varepsilon, \tag{2.111}$$

whereas the inductances are given by

$$L_k = \frac{1}{C_p^\varepsilon} \frac{\prod_{i=1, i\neq k}^{N_s} (p_i^2 - p_k^2)}{\prod_{i=1}^{N_s} (z_i^2 - p_k^2)}, \tag{2.112}$$

and the capacitances by

$$C_k = \frac{1}{L_k p_k^2}. \tag{2.113}$$

It can be noted that when $r_0 \to 0$, one of the double roots of Equation (2.104), say, p_1, tends to zero. Then, Equation (2.113) shows that $C_1 \to \infty$, i.e., the capacitance becomes nearly equivalent to a short-circuit. By replacing C_1 in Figure 2.15(b) by a short-circuit, the same circuit topology as that of Hollkamp's shunt circuit is obtained. Therefore, the CF shunt circuit tends to Hollkamp's shunt circuit as $r_0 \to 0$.

2.7.3 Resistances tuning

As discussed in Section 2.3.3, either the admittance or the impedance model can be chosen to tune the lossless circuit, but the dissipative case exhibits dissimilarities. In the case of Hollkamp's and the CF shunt circuits, the best baseline case is the series RL shunt, because the resistors are placed in series with the inductors in these circuits (and in particular when $N_s = 1$, Hollkamp's shunt circuit reduces to a series RL shunt). Tuning based on the parallel RL circuit can also be used but gives less optimal results.

The purpose of the following procedure is to impose approximately the desired modal damping on the zeros of Thévenin's impedance. From Equation (2.63), its inverse is

$$\frac{1}{Z_T(s)} = \frac{1}{\frac{1}{sC_p^\varepsilon} + \frac{1}{Y_s(s)}} = \frac{Y_s(s)\left(1 + \frac{Y_s(s)}{sC_p^\varepsilon}\right) - \frac{Y_s^2(s)}{sC_p^\varepsilon}}{1 + \frac{Y_s(s)}{sC_p^\varepsilon}} = Y_s(s) - \frac{1}{sC_p^\varepsilon} \frac{Y_s^2(s)}{1 + \frac{Y_s(s)}{sC_p^\varepsilon}}, \tag{2.114}$$

where Hollkamp's dissipative shunt circuit admittance is given by

$$Y_s(s) = \frac{1}{sL_0 + R_0} + \sum_{n=1}^{N_s - 1} \frac{s}{L_n s^2 + R_n s + \frac{1}{C_n}} \tag{2.115}$$

and can also be expressed by

$$Y_s(s) = s\begin{bmatrix}1 & \cdots & 1\end{bmatrix}\left(\begin{bmatrix}0 & & & \\ & \frac{1}{C_1} & & \\ & & \ddots & \\ & & & \frac{1}{C_{N_s-1}}\end{bmatrix} + s\begin{bmatrix}R_0 & & & \\ & R_1 & & \\ & & \ddots & \\ & & & R_{N_s-1}\end{bmatrix} + s^2\begin{bmatrix}L_0 & & & \\ & L_1 & & \\ & & \ddots & \\ & & & L_{N_s-1}\end{bmatrix}\right)^{-1}\begin{bmatrix}1\\ \vdots \\ 1\end{bmatrix} \tag{2.116}$$

Using this matrix-based model and by comparing Equation (2.114) with the Sherman-Morrison formula (Equation (A.1)), we can see that the inverse of Thévenin's impedance given in Equation (2.114) can be obtained if the inverted matrix is rank-one updated, i.e.,

$$\frac{1}{Z_T(s)} = s\begin{bmatrix}1 & \cdots & 1\end{bmatrix}\left(\begin{bmatrix}0 & & & \\ & \frac{1}{C_1} & & \\ & & \ddots & \\ & & & \frac{1}{C_{N_s-1}}\end{bmatrix} + \begin{bmatrix}1\\ \vdots \\ 1\end{bmatrix}\begin{bmatrix}1 & \cdots & 1\end{bmatrix}\frac{1}{C_p^{\varepsilon}} + s\begin{bmatrix}R_0 & & & \\ & R_1 & & \\ & & \ddots & \\ & & & R_{N_s-1}\end{bmatrix} + s^2\begin{bmatrix}L_0 & & & \\ & L_1 & & \\ & & \ddots & \\ & & & L_{N_s-1}\end{bmatrix}\right)^{-1}\begin{bmatrix}1\\ \vdots \\ 1\end{bmatrix} \tag{2.117}$$

This type of model can also be derived using KCL and Kirchhoff's voltage law (KVL) [145]. In the lossless case, the zeros of Thévenin's impedance are the generalized eigenvalues

of the generalized eigenvalue problem

$$\left(\begin{bmatrix} 0 & & & \\ & \frac{1}{C_1} & & \\ & & \ddots & \\ & & & \frac{1}{C_{N_s-1}} \end{bmatrix} + \begin{bmatrix} 1 \\ \vdots \\ 1 \end{bmatrix} \begin{bmatrix} 1 & \cdots & 1 \end{bmatrix} \frac{1}{C_p^{\varepsilon}} \right) \boldsymbol{\Phi}_e = \begin{bmatrix} L_0 & & & \\ & L_1 & & \\ & & \ddots & \\ & & & L_{N_s-1} \end{bmatrix} \boldsymbol{\Phi}_e \boldsymbol{\Omega}_e^2, \tag{2.118}$$

where

$$\boldsymbol{\Omega}_e^2 = \begin{bmatrix} z_1^2 & & \\ & \ddots & \\ & & z_{N_s}^2 \end{bmatrix}, \tag{2.119}$$

and $\boldsymbol{\Phi}_e$ can be seen as an electrical mode shape matrix. In order to impose the desired damping on the zeros of Thévenin's impedance, the mode shape matrix should ideally diagonalize the resistance matrix. However, this is not the case in general, and the following relation is only approximate

$$\boldsymbol{\Phi}_e^T \begin{bmatrix} R_0 & & & \\ & R_1 & & \\ & & \ddots & \\ & & & R_{N_s-1} \end{bmatrix} \boldsymbol{\Phi}_e \approx \begin{bmatrix} 2\zeta_1 z_1 & & & \\ & 2\zeta_2 z_2 & & \\ & & \ddots & \\ & & & 2\zeta_{N_s} z_{N_s} \end{bmatrix} \tag{2.120}$$

By enforcing this relation on the diagonal of this resulting matrix (regardless of its off-diagonal elements), the following set of resistances can be obtained:

$$\begin{bmatrix} R_0 \\ \vdots \\ R_{N_s-1} \end{bmatrix} = \begin{bmatrix} \phi_{e,0,1}^2 & \cdots & \phi_{e,(N_s-1),1}^2 \\ \vdots & \ddots & \vdots \\ \phi_{e,0,N_s}^2 & \cdots & \phi_{e,(N_s-1),N_s}^2 \end{bmatrix}^{-1} \begin{bmatrix} 2\zeta_1 z_1 \\ \vdots \\ 2\zeta_{N_s} z_{N_s} \end{bmatrix}. \tag{2.121}$$

The same procedure can be followed for the CF shunt circuit by simple adaptation of the involved matrices, since its dissipative admittance is given by

$$Y_s(s) = \sum_{n=1}^{N_s} \frac{s}{L_n s^2 + R_n s + \frac{1}{C_n}}, \tag{2.122}$$

or, equivalently,

$$Y_s(s) = s\begin{bmatrix}1 & \cdots & 1\end{bmatrix}\left(\begin{bmatrix}\frac{1}{C_1} & & \\ & \ddots & \\ & & \frac{1}{C_{N_s}}\end{bmatrix} + s\begin{bmatrix}R_1 & & \\ & \ddots & \\ & & R_{N_s}\end{bmatrix} + s^2\begin{bmatrix}L_1 & & \\ & \ddots & \\ & & L_{N_s}\end{bmatrix}\right)^{-1}\begin{bmatrix}1\\ \vdots \\ 1\end{bmatrix}. \quad (2.123)$$

2.8 Series-parallel impedance and second Foster form tuning

The series-parallel impedance structure (SPIS) shunt circuit proposed by Fleming et al [129] is shown in Figure 2.17(b). Figure 2.17(a) features a shunt circuit which is to the SPIS what Hollkamp's circuit is to the CF circuit. This circuit is based on the second Foster canonical form (SFCF) and can be seen as the dual of Hollkamp's circuit. These circuits can be tuned with either specification approach using the parallel RL baseline case. The lossless circuits ($R_i = \infty$) connected in series to a capacitor are shown in Figure 2.18 and are used to build Thévenin's equivalent impedance Z_T. It can be recognized that the resulting circuits are equivalent to Foster's second canonical form [142].

Tuning either type of circuit requires to compute the ZPK representation of Z_T. From Equation (2.70),

$$Z_T(s) = \frac{1}{sC_p^{\varepsilon}}\left(r_0 + \sum_{i=1}^{N_s}\frac{r_i}{\frac{s^2}{z_i^2}+1}\right)^{-1} = \frac{K}{s}\frac{\prod_{i=1}^{N_s}\left(\frac{s^2}{z_i^2}+1\right)}{\prod_{i=1}^{N_s}\left(\frac{s^2}{p_i^2}+1\right)}. \quad (2.124)$$

The poles of Thévenin's equivalent impedance can be found as the solution of the polynomial equation

$$r_0\prod_{i=1}^{N_s}\left(\frac{s^2}{z_i^2}+1\right) + \sum_{i=1}^{N_s} r_i \prod_{j=1, j\neq i}^{N_s}\left(\frac{s^2}{z_j^2}+1\right) = 0, \quad (2.125)$$

which can be solved with a computer. We note that when $r_0 \neq 0$, there are N_s poles, whereas when $r_0 = 0$ there are $N_s - 1$ poles. The gain K can be determined later.

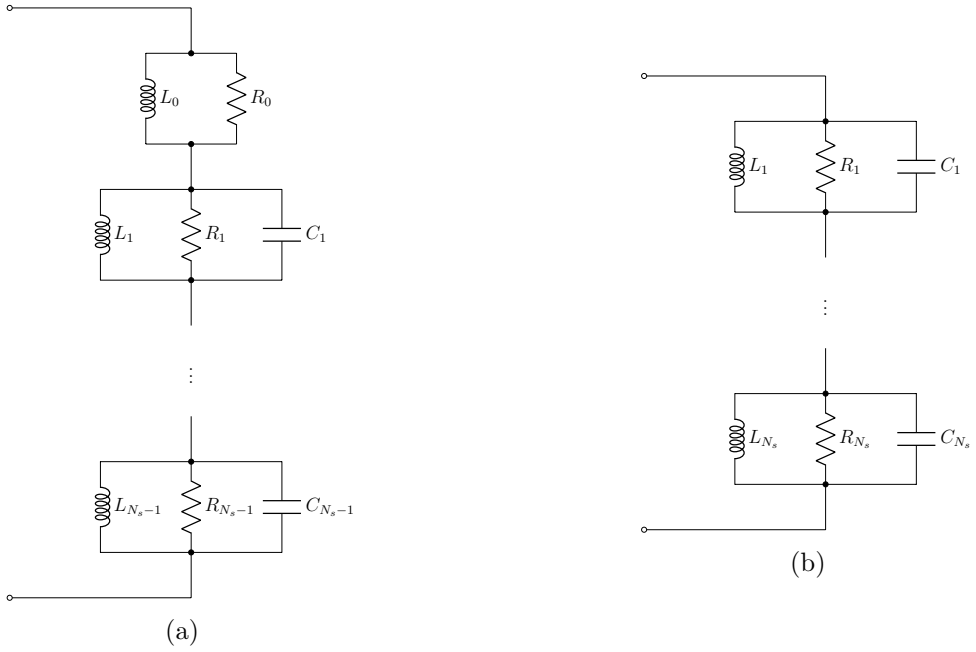

Figure 2.17: Shunt circuit based on the second Foster canonical form (a) and a series-parallel impedance structure (b).

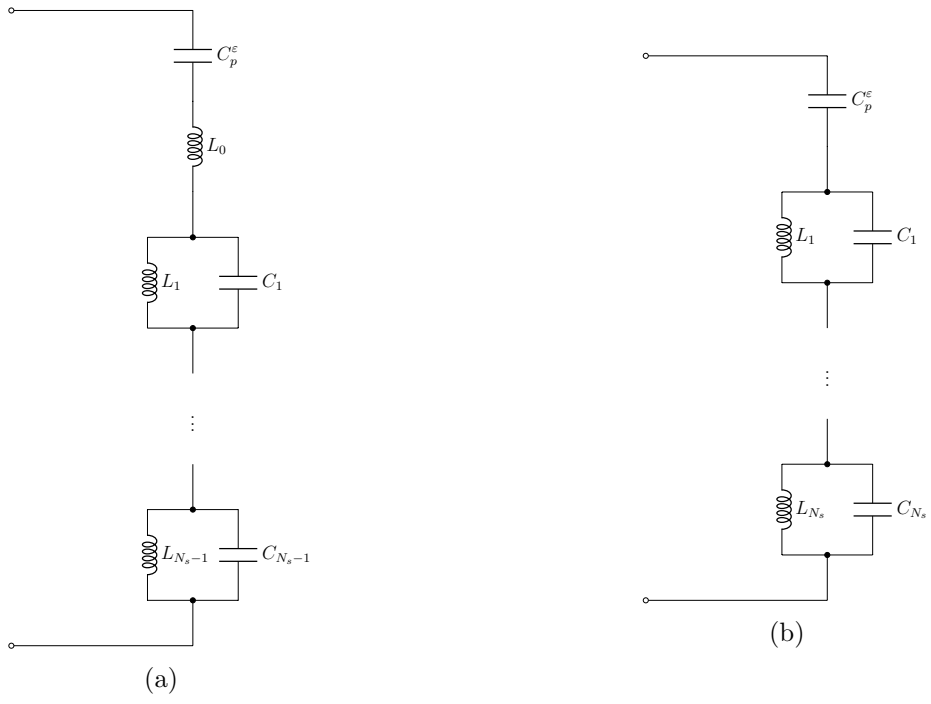

Figure 2.18: Thévenin's impedance model of a piezoelectric transducer connected to a lossless shunt circuit based on the second Foster canonical form (a) and a lossless series-parallel impedance structure (b).

2.8.1 Second Foster canonical form

The impedance of the undamped SFCF circuit is computed as the series connection of a capacitor, an inductor and $N_s - 1$ branches of parallel LC circuits as

$$Z_T(s) = sL_0 + \frac{1}{sC_p^\varepsilon} + \sum_{n=1}^{N_s-1} \frac{L_n s}{L_n C_n s^2 + 1} = \frac{K}{s} \frac{\prod_{i=1}^{N_s} \left(\frac{s^2}{z_i^2} + 1 \right)}{\prod_{i=1}^{N_s-1} \left(\frac{s^2}{p_i^2} + 1 \right)} \tag{2.126}$$

Since there are $N_s - 1$ complex conjugate poles, this circuit requires $r_0 = 0$. Evaluating the residue associated with the simple pole at $s = 0$, K is found as

$$K = \frac{1}{C_p^\varepsilon}, \tag{2.127}$$

and the limit for $s \to \infty$ then gives

$$L_0 = \frac{1}{C_p^\varepsilon} \frac{\prod_{i=1}^{N_s-1} p_i^2}{\prod_{i=1}^{N_s} z_i^2}. \tag{2.128}$$

The cover-up method enables the identification of the inductances of the LC circuits as

$$L_k = -\frac{1}{C_p^\varepsilon p_k^2} \frac{\prod_{i=1}^{N_s} \left(1 - \frac{p_k^2}{z_i^2} \right)}{\prod_{i=1, i\neq k}^{N_s-1} \left(1 - \frac{p_k^2}{p_i^2} \right)} \tag{2.129}$$

while the capacitances are found from the poles of the impedance as

$$C_k = \frac{1}{L_k p_k^2}. \tag{2.130}$$

2.8.2 Series-parallel impedance structure

The undamped impedance of the SPIS reads

$$Z_T(s) = \frac{1}{sC_p^\varepsilon} + \sum_{n=1}^{N_s} \frac{L_n s}{L_n C_n s^2 + 1} = \frac{K}{s} \frac{\prod_{i=1}^{N_s} \left(\frac{s^2}{z_i^2} + 1 \right)}{\prod_{i=1}^{N_s} \left(\frac{s^2}{p_i^2} + 1 \right)}, \tag{2.131}$$

where, using the same techniques as previously,

$$K = \frac{1}{C_p^\varepsilon}, \tag{2.132}$$

$$L_k = -\frac{1}{C_p^\varepsilon p_k^2} \frac{\prod_{i=1}^{N_s} \left(1 - \frac{p_k^2}{z_i^2} \right)}{\prod_{i=1, i\neq k}^{N_s} \left(1 - \frac{p_k^2}{p_i^2} \right)}, \tag{2.133}$$

and

$$C_k = \frac{1}{L_k p_k^2}. \tag{2.134}$$

It can be noted that when $r_0 \to 0$, one of the double roots of Equation (2.125), say, p_1, tends to infinity. Hence, Equation (2.134) shows that $C_1 \to 0$, i.e., the capacitance tends to an open-circuit, which in Figure 2.17(b) would correspond to a topology similar to that of the SFCF shunt circuit. Thus, as r_0 tends to zero, the SPIS shunt circuit tends to the SFCF shunt circuit.

2.8.3 Resistances tuning

A procedure completely analogous that exposed in Section 2.7.3 can be followed. In this case, the parallel RL baseline case should be chosen, because the resistors are in parallel with the inductors in the SFCF and SPIS shunt circuits (and when $N_s = 1$, the SFCF circuit reduces to a parallel RL shunt circuit).

Using Equation (2.67), the inverse of Norton's admittance is given by

$$\frac{1}{Y_N(s)} = \frac{1}{sC_p^\varepsilon + \dfrac{1}{Z_s(s)}} = Z_s(s) - sC_p^\varepsilon \frac{Z_s^2(s)}{1 + sC_p^\varepsilon Z_s(s)}, \tag{2.135}$$

where the dissipative impedance of the SFCF circuit is given by

$$Z_s(s) = \frac{1}{\dfrac{1}{sL_0} + \dfrac{1}{R_0}} + \sum_{n=1}^{N_s-1} \frac{s}{C_n s^2 + \dfrac{1}{R_n} s + \dfrac{1}{L_n}}, \tag{2.136}$$

or equivalently by

$$Z_s(s) = s \begin{bmatrix} 1 & \cdots & 1 \end{bmatrix} \left(\begin{bmatrix} \frac{1}{L_0} & & & \\ & \frac{1}{L_1} & & \\ & & \ddots & \\ & & & \frac{1}{L_{N_s-1}} \end{bmatrix} + s \begin{bmatrix} \frac{1}{R_0} & & & \\ & \frac{1}{R_1} & & \\ & & \ddots & \\ & & & \frac{1}{R_{N_s-1}} \end{bmatrix} + s^2 \begin{bmatrix} 0 & & & \\ & C_1 & & \\ & & \ddots & \\ & & & C_{N_s-1} \end{bmatrix} \right)^{-1} \begin{bmatrix} 1 \\ \vdots \\ 1 \end{bmatrix}. \tag{2.137}$$

Once again, by comparison of Equation (2.135) to the Sherman-Morrison formula (Equation (A.1)), the inverse of Norton's admittance can be obtained after a

rank-one update of the inverted matrix

$$\frac{1}{Y_N(s)} = s\begin{bmatrix}1 & \cdots & 1\end{bmatrix}\left(\begin{bmatrix}\frac{1}{L_0} & & & \\ & \frac{1}{L_1} & & \\ & & \ddots & \\ & & & \frac{1}{L_{N_s-1}}\end{bmatrix} + s\begin{bmatrix}\frac{1}{R_0} & & & \\ & \frac{1}{R_1} & & \\ & & \ddots & \\ & & & \frac{1}{R_{N_s-1}}\end{bmatrix} + s^2\begin{bmatrix}0 & & & \\ & C_1 & & \\ & & \ddots & \\ & & & C_{N_s-1}\end{bmatrix} + s^2\begin{bmatrix}1\\ \vdots \\ 1\end{bmatrix}\begin{bmatrix}1 & \cdots & 1\end{bmatrix}C_p^{\varepsilon}\right)^{-1}\begin{bmatrix}1\\ \vdots \\ 1\end{bmatrix}. \quad (2.138)$$

In the lossless case, the zeros of Norton's admittance are the generalized eigenvalues of the generalized eigenvalue problem

$$\begin{bmatrix}\frac{1}{L_0} & & & \\ & \frac{1}{L_1} & & \\ & & \ddots & \\ & & & \frac{1}{L_{N_s-1}}\end{bmatrix}\mathbf{\Phi}_e = \left(\begin{bmatrix}0 & & & \\ & C_1 & & \\ & & \ddots & \\ & & & C_{N_s-1}\end{bmatrix} + \begin{bmatrix}1\\ \vdots \\ 1\end{bmatrix}\begin{bmatrix}1 & \cdots & 1\end{bmatrix}C_p^{\varepsilon}\right)\mathbf{\Phi}_e\mathbf{\Omega}_e^2. \quad (2.139)$$

By enforcing the diagonal of the transformed matrix containing the resistances (regardless of its off-diagonal elements), the following set of resistances can be obtained:

$$\begin{bmatrix}\frac{1}{R_0}\\ \vdots \\ \frac{1}{R_{N_s-1}}\end{bmatrix} = \begin{bmatrix}\phi_{e,0,1}^2 & \cdots & \phi_{e,(N_s-1),1}^2 \\ \vdots & \ddots & \vdots \\ \phi_{e,0,N_s}^2 & \cdots & \phi_{e,(N_s-1),N_s}^2\end{bmatrix}^{-1}\begin{bmatrix}2\zeta_1 z_1\\ \vdots \\ 2\zeta_{N_s} z_{N_s}\end{bmatrix}. \quad (2.140)$$

A similar procedure can be followed for the SPIS circuit, because its dissipative impedance

$$Z_s(s) = \sum_{n=1}^{N_s}\frac{s}{C_n s^2 + \frac{1}{R_n}s + \frac{1}{L_n}}, \quad (2.141)$$

is equivalently given by

$$Z_s(s) = s\begin{bmatrix}1 & \cdots & 1\end{bmatrix}\left(\begin{bmatrix}\frac{1}{L_1} & & \\ & \ddots & \\ & & \frac{1}{L_{N_s}}\end{bmatrix} + s\begin{bmatrix}\frac{1}{R_1} & & \\ & \ddots & \\ & & \frac{1}{R_{N_s}}\end{bmatrix} + s^2\begin{bmatrix}C_1 & & \\ & \ddots & \\ & & C_{N_s}\end{bmatrix}\right)^{-1}\begin{bmatrix}1 \\ \vdots \\ 1\end{bmatrix}. \quad (2.142)$$

2.9 Current blocking shunt circuit tuning

The current blocking (CB) shunt circuit was originally proposed by Wu [127], and later simplified by Agneni et al [130]. A different tuning methodology was proposed in [133], and will be compared to that proposed herein in Section 2.10.4. Once again, the dynamics of the lossless circuit are first analyzed to assess the electromechanical coupling, and the actual tuning of the circuits featured in Figure 2.19(a,b) is tackled in Sections 2.9.3 and 2.9.4, respectively.

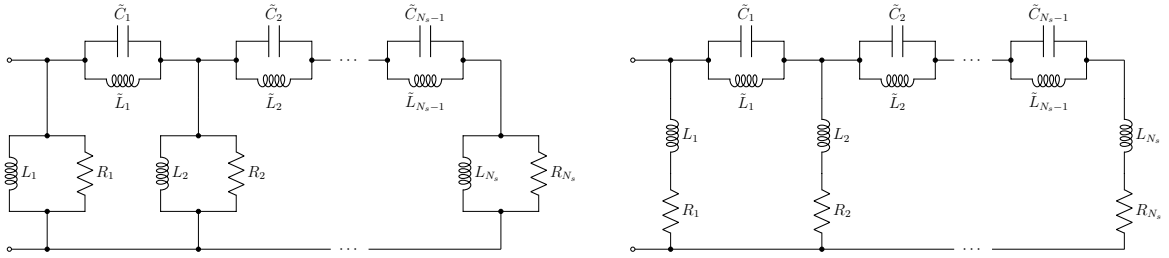

(a) (b)

Figure 2.19: Simplified current blocking shunt circuit with parallel RL shunts (a) and series RL shunts (b).

2.9.1 Lossless circuit tuning

Figure 2.20 features Norton's admittance model using a lossless CB shunt circuit. The resulting circuit is composed of a parallel capacitor, followed by a repetition of $N_s - 1$ stages with identical topology (a shunt with an inductor and a branch with a parallel LC circuit) and finally terminated by an inductor. The parallel LC circuits are so-called current-blocking filters, because they act as band-stop filters. Indeed, their impedance is given by

$$\tilde{Z}_i = \frac{1}{\frac{1}{\tilde{L}_i s} + s\tilde{C}_i} \quad (2.143)$$

and becomes infinite at $s = j\sqrt{1/(\tilde{L}_i\tilde{C}_i)}$. Hence, by properly setting the blocking frequency of these filters, it is possible to decouple some parts of the circuits at specific frequencies.

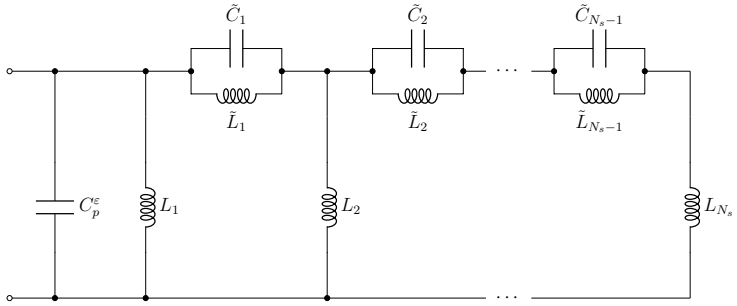

Figure 2.20: Norton's admittance model of a piezoelectric transducer connected to a lossless current blocking shunt circuit.

The tuning approach traditionally chosen for the CB shunt circuit thus consists in considering sequentially each stage in ascending order [127, 130, 133]. By tuning the filter of the considered stage to the frequency of the targeted resonance, the influence of the following stages of unknown characteristics can be neglected close to that frequency, and the shunt can be tuned taking into account the rest of the circuit (the piezoelectric capacitance and previous stages of known characteristics). The procedure can be repeated until all the stages have been tuned.

Figure 2.21 shows a representation of the tuning considerations for stage k. The shunt impedances and current blocking filters are represented up to stage k, whereas the remainder of the CB circuit is represented altogether with the impedance Z_{k+1}. The voltage across the shunt inductance k is noted V_k and the current entering stage k is noted I_k.

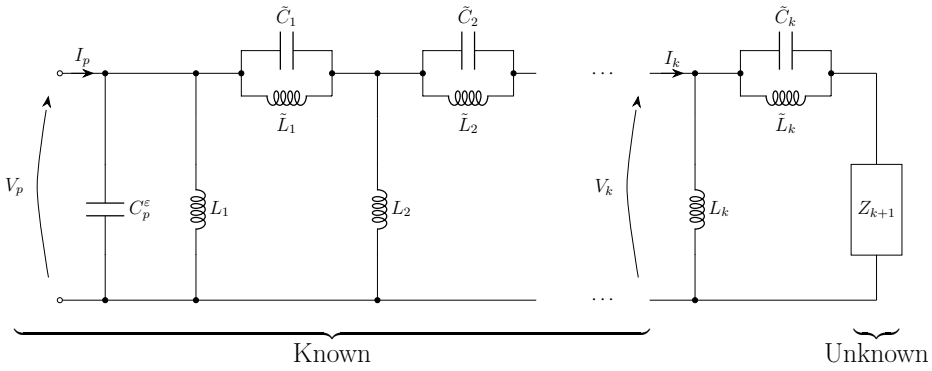

Figure 2.21: Norton's admittance model of a piezoelectric transducer connected to a lossless current blocking shunt circuit: tuning considerations at stage k.

The relations between V_p, I_p, V_k and I_k can be obtained using the two-port network theory [69]. These relations are expressed with a transfer matrix $\mathbf{H}_{CB}^{(k)}$

$$\begin{bmatrix} V_p \\ I_p \end{bmatrix} = \mathbf{H}_{CB}^{(k)}(s) \begin{bmatrix} V_k \\ I_k \end{bmatrix} = \begin{bmatrix} h_{11}^{(k)}(s) & h_{12}^{(k)}(s) \\ h_{21}^{(k)}(s) & h_{22}^{(k)}(s) \end{bmatrix} \begin{bmatrix} V_k \\ I_k \end{bmatrix}. \tag{2.144}$$

The expression of the transfer matrix results from the cascade connection of the parallel capacitor, and stages 1 to $k-1$ [133][4]

$$\mathbf{H}_{CB}^{(k)}(s) = \begin{bmatrix} 1 & 0 \\ sC_p^{\varepsilon} & 1 \end{bmatrix} \prod_{i=1}^{k-1} \begin{bmatrix} 1 & \dfrac{\frac{1}{\tilde{C}_i}s}{s^2 + \frac{1}{\tilde{L}_i\tilde{C}_i}} \\ \dfrac{1}{L_i s} & 1 + \dfrac{\frac{1}{\tilde{C}_i}s}{s^2 + \frac{1}{\tilde{L}_i\tilde{C}_i}} \dfrac{1}{L_i s} \end{bmatrix}. \tag{2.145}$$

The relation between I_k and V_k can be deduced from Figure 2.21 as

$$\frac{I_k}{V_k} = Y_k(s) = \frac{1}{L_k s} + \frac{1}{\dfrac{\frac{1}{\tilde{C}_k}s}{s^2 + \frac{1}{\tilde{L}_k\tilde{C}_k}} + Z_{k+1}(s)}. \tag{2.146}$$

The relation between I_p and V_p, i.e. Norton's equivalent admittance, is then deduced from Equations (2.144) and (2.146) as

$$Y_N(s) = \frac{I_p}{V_p} = \frac{h_{22}^{(k)}(s)Y_k(s) + h_{21}^{(k)}(s)}{h_{12}^{(k)}(s)Y_k(s) + h_{11}^{(k)}(s)}. \tag{2.147}$$

A zero of Norton's admittance occurs if

$$Y_N(jz_k) = 0. \tag{2.148}$$

The problem can be made independent of Z_{k+1} if the current blocking filter has an infinite impedance at z_k. This is the case if

$$z_k^2 = \frac{1}{\tilde{L}_k\tilde{C}_k}. \tag{2.149}$$

Equation (2.146) then becomes at $s = jz_k$

$$Y_k(jz_k) = \frac{1}{jz_k L_k} \tag{2.150}$$

Solving Equation (2.148) with Equations (2.147) and (2.150) yields

$$L_k = -\frac{1}{jz_k}\frac{h_{22}^{(k)}(jz_k)}{h_{21}^{(k)}(jz_k)}. \tag{2.151}$$

This tuning approach guarantees that Norton's admittance will have a zero at the desired frequency regardless of Z_{k+1}. A free parameter yet remains for the lossless case, as the two parameters of the current blocking filter are only constrained by one relation given in Equation (2.149). It shall be shown next that the filter capacitance is actually set by the value of the residue r_k.

[4]What is termed transfer matrix in this thesis is the inverse of what is termed transfer matrix in [133].

2.9.2 Coupling assessment

Norton's equivalent admittance is such that

$$\frac{s}{Y_N(s)} = \frac{1}{C_p^\varepsilon} \sum_{i=1}^{N_s} \frac{s^2 r_i}{s^2 + z_i^2}. \tag{2.152}$$

Thus, the residue r_k may be evaluated as

$$\begin{aligned} r_k = \lim_{s \to j z_k} C_p^\varepsilon (s^2 + z_k^2) \frac{1}{sY(s)} &= \lim_{s \to j z_k} C_p^\varepsilon (s^2 + z_k^2) \frac{h_{12}^{(k)}(s) Y_k(s) + h_{11}^{(k)}(s)}{s h_{22}^{(k)}(s) Y_k(s) + s h_{21}^{(k)}(s)} \\ &= \lim_{s \to j z_k} C_p^\varepsilon \frac{\dfrac{h_{12}^{(k)}(s)}{L_k s} + h_{11}^{(k)}(s)}{\dfrac{\dfrac{h_{22}^{(k)}(s)}{L_k} + s h_{21}^{(k)}(s)}{s^2 + z_k^2} + h_{22}^{(k)}(s) \tilde{C}_k}. \end{aligned} \tag{2.153}$$

Hence, the impedance of the higher-frequency stages $Z_{k+1}(s)$ has no influence on the residue (provided that Equation (2.149) holds). This is a more formal justification of the physically-motivated assumption made in [133]. However, the residue remains rather uneasy to compute in that way, because no further simplification can be made in general when considering the full CB circuit.

Equation (2.153) shows that the residue computed considering the whole CB circuit would be identical to that computed when considering $Z_{k+1} = 0$, i.e., by replacing the next stages by a short circuit, as pictured in Figure 2.22.

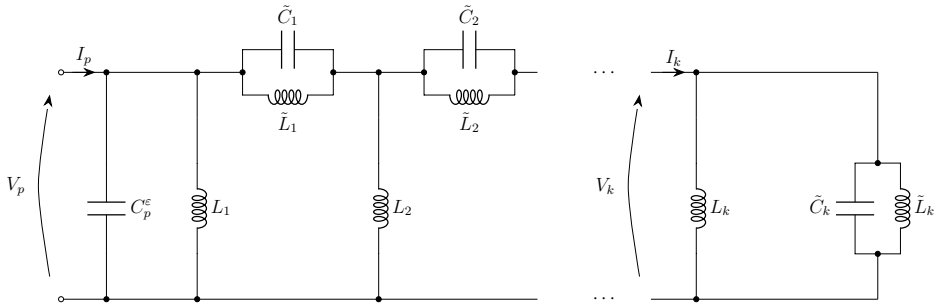

Figure 2.22: Norton's admittance model of a piezoelectric transducer connected to a lossless current blocking shunt circuit: simplified tuning considerations at stage k.

The fact that $Z_{k+1}(s)$ can be short-circuited and the fact that Norton's equivalent admittance has as zeros $z_1, \cdots, z_k$ leads to the following expression

$$\frac{1}{C_p^\varepsilon} \sum_{i=1}^{k} \frac{r_i s^2}{s^2 + z_i^2} = s \frac{h_{12}^{(k)}(s) \left(\dfrac{1}{L_k s} + \tilde{C}_k \dfrac{s^2 + z_k^2}{s} \right) + h_{11}^{(k)}(s)}{h_{22}^{(k)}(s) \left(\dfrac{1}{L_k s} + \tilde{C}_k \dfrac{s^2 + z_k^2}{s} \right) + h_{21}^{(k)}(s)} \tag{2.154}$$

Taking the limit as $s \to \infty$, the sum of residues can be evaluated

$$\sum_{i=1}^{k} r_i = \lim_{s\to\infty} sC_p^{\varepsilon} \frac{h_{12}^{(k)}(s)\left(\frac{1}{L_k s} + \tilde{C}_k \frac{s^2+z_k^2}{s}\right) + h_{11}^{(k)}(s)}{h_{22}^{(k)}(s)\left(\frac{1}{L_k s} + \tilde{C}_k \frac{s^2+z_k^2}{s}\right) + h_{21}^{(k)}(s)} \tag{2.155}$$

To evaluate this limit, the asymptotic behavior of the two-port network must be determined. Taking the limit as $s \to \infty$, the following asymptotic behaviors (indicated by the symbol $\sim$) can be derived from Equation (2.145)

$$\mathbf{H}_{CB}^{(k)}(s) = \begin{bmatrix} h_{11}^{(k)}(s) & h_{12}^{(k)}(s) \\ h_{21}^{(k)}(s) & h_{22}^{(k)}(s) \end{bmatrix} \underset{\sim}{s\to\infty} \begin{bmatrix} 1 & \sum_{i=1}^{k-1} \frac{1}{s\tilde{C}_i} \\ sC_p^{\varepsilon} & 1 + \sum_{i=1}^{k-1} \frac{C_p^{\varepsilon}}{\tilde{C}_i} \end{bmatrix} \tag{2.156}$$

The network associated with such a transfer matrix is depicted in Figure 2.23. Intuitively, the components governing this asymptotic behavior are the capacitances, because the inductances tend to have a much higher impedance at high frequency. In fact, Figure 2.23 can be obtained from Figure 2.22 after replacing the inductances by open circuits.

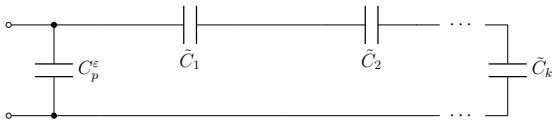

Figure 2.23: Asymptotic behavior of the current blocking shunt circuit simplified at stage k for $s \to \infty$.

Inserting Equation (2.156) into Equation (2.155), the sum of residues can then be evaluated as

$$\sum_{i=1}^{k} r_i = \lim_{s\to\infty} sC_p^{\varepsilon} \frac{\sum_{i=1}^{k-1} \frac{1}{s\tilde{C}_i}\left(\frac{1}{L_k s} + \tilde{C}_k \frac{s^2+z_k^2}{s}\right) + 1}{\left(1 + \sum_{i=1}^{k-1} \frac{C_p^{\varepsilon}}{\tilde{C}_i}\right)\left(\frac{1}{L_k s} + \tilde{C}_k \frac{s^2+z_k^2}{s}\right) + sC_p^{\varepsilon}} = \frac{1 + \sum_{i=1}^{k-1} \frac{\tilde{C}_k}{\tilde{C}_i}}{1 + \frac{\tilde{C}_k}{C_p^{\varepsilon}} + \sum_{i=1}^{k-1} \frac{\tilde{C}_k}{\tilde{C}_i}} \tag{2.157}$$

A remarkable feature of this equation is that the residues depend only on the filter and piezoelectric capacitances. By extracting $\tilde{C}_k$, it is expressed as

$$\tilde{C}_k = \frac{1 - \sum_{i=1}^{k} r_i}{\sum_{i=1}^{k} r_i \left(\frac{1}{C_p^{\varepsilon}} + \sum_{i=1}^{k-1} \frac{1}{\tilde{C}_i}\right) - \sum_{i=1}^{k-1} \frac{1}{\tilde{C}_i}}, \tag{2.158}$$

or as a sole function of the residues and the piezoelectric capacitance

$$\tilde{C}_k = \frac{C_p^\varepsilon}{\dfrac{\sum_{i=1}^{k} r_i}{1-\sum_{i=1}^{k} r_i} + \sum_{j=1}^{k-1}(-1)^{k-j}\dfrac{\sum_{i=1}^{j} r_i}{1-\sum_{i=1}^{j} r_i}}. \tag{2.159}$$

2.9.3 Dissipative circuit tuning with parallel RL shunts

The case of a dissipative CB shunt circuit is now considered. In case parallel RL shunts are used as in Figure 2.19(a), the parallel RL baseline should be used. The transfer matrix resulting in a cascade connection of a parallel capacitance C_p^ε and the $k-1$ first stages of the current blocking circuit read

$$\mathbf{H}_{CB}^{(k)} = \begin{bmatrix} 1 & 0 \\ sC_p^\varepsilon & 1 \end{bmatrix} \prod_{i=1}^{k-1} \begin{bmatrix} 1 & \dfrac{\frac{1}{\tilde{C}_i}s}{s^2+\frac{1}{\tilde{L}_i\tilde{C}_i}} \\ \dfrac{1}{L_i s}+\dfrac{1}{R_i} & 1+\dfrac{\frac{1}{\tilde{C}_i}s}{s^2+\frac{1}{\tilde{L}_i\tilde{C}_i}}\left(\dfrac{1}{L_i s}+\dfrac{1}{R_i}\right) \end{bmatrix}. \tag{2.160}$$

Using Equation (2.146), Norton's admittance can be equated to its nominal value

$$Y_N(jz_k) = -\sum_{i=1}^{N_s} \frac{r_i z_k^2}{z_i^2 + 2j\zeta_i z_i z_k - z_k^2} = \frac{h_{22}^{(k)}(jz_k)Y_k(jz_k) + h_{21}^{(k)}(jz_k)}{h_{12}^{(k)}(jz_k)Y_k(jz_k) + h_{11}^{(k)}(jz_k)}. \tag{2.161}$$

Extracting $Y_k(jz_k)$ from this relation yields

$$Y_k(jz_k) = \frac{h_{11}^{(k)}(jz_k)Y_N(jz_k) - h_{21}^{(k)}(jz_k)}{h_{22}^{(k)}(jz_k) - h_{12}^{(k)}(jz_k)Y_N(jz_k)}, \tag{2.162}$$

which sets the ideal value of $Y_k(jz_k)$. If the filter capacitance and inductance are properly tuned (Equations (2.159) and (2.149), respectively), the admittance Y_k evaluated at the frequency z_k is then only determined by the k^{th} shunt

$$Y_k(jz_k) = \frac{1}{jL_k z_k} + \frac{1}{R_k} + \frac{1}{\dfrac{\frac{1}{j\tilde{C}_k z_k}}{\frac{1}{\tilde{L}_k\tilde{C}_k} - z_k^2} + Z_{k+1}(jz_k)} = \frac{1}{jL_k z_k} + \frac{1}{R_k}, \tag{2.163}$$

so that the inductances and resistances can be set as

$$L_k = -\frac{1}{z_k \Im\{Y_k(jz_k)\}} \tag{2.164}$$

and

$$R_k = \frac{1}{\Re\{Y_k(jz_k)\}}, \tag{2.165}$$

respectively.

2.9.4 Dissipative circuit tuning with series RL shunts

When series RL shunts are used as in Figure 2.19(b), the series RL baseline should be used. The transfer matrix resulting in a cascade connection of a series capacitance C_p^ε and the $k-1$ first stages of the current blocking circuit read

$$\mathbf{H}_{CB}^{(k)} = \begin{bmatrix} 1 & \dfrac{1}{sC_p^\varepsilon} \\ 0 & 1 \end{bmatrix} \prod_{i=1}^{k-1} \begin{bmatrix} 1 & \dfrac{\frac{1}{\tilde{C}_i}s}{s^2 + \frac{1}{\tilde{L}_i\tilde{C}_i}} \\ \dfrac{1}{L_is + R_i} & 1 + \dfrac{\frac{1}{\tilde{C}_i}s}{s^2 + \frac{1}{\tilde{L}_i\tilde{C}_i}} \dfrac{1}{L_is + R_i} \end{bmatrix}. \tag{2.166}$$

Taking the inverse of Equation (2.146), Thévenin's impedance can be equated to its nominal value

$$Z_T(jz_k) = \sum_{i=1}^{N_s} \frac{r_i}{1 + 2j\zeta_i \dfrac{z_k}{z_i} - \dfrac{z_k^2}{z_i^2}} = \frac{h_{12}^{(k)}(jz_k)Y_k(jz_k) + h_{11}^{(k)}(jz_k)}{h_{22}^{(k)}(jz_k)Y_k(jz_k) + h_{21}^{(k)}(jz_k)}, \tag{2.167}$$

and thus, Y_k at $s = jz_k$ should be given by

$$Y_k(jz_k) = \frac{h_{11}^{(k)}(jz_k) - h_{21}^{(k)}(jz_k)Z_T(jz_k)}{h_{22}^{(k)}(jz_k)Z_T(jz_k) - h_{12}^{(k)}(jz_k)}, \tag{2.168}$$

which sets the ideal value of $Y_k(jz_k)$. If the filter capacitance and inductance are properly tuned (Equations (2.159) and (2.149), respectively), the admittance Y_k evaluated at the frequency z_k is once again only determined by the k^{th} shunt

$$Y_k(jz_k) = \frac{1}{jL_kz_k + R_k} + \frac{1}{\dfrac{1}{\dfrac{j\tilde{C}_kz_k}{\frac{1}{\tilde{L}_k\tilde{C}_k} - z_k^2}} + Z_{k+1}(jz_k)} = \frac{1}{jL_kz_k + R_k}, \tag{2.169}$$

so that the inductances and resistances can be set as

$$L_k = \frac{1}{z_k}\Im\left\{\frac{1}{Y_k(jz_k)}\right\} \tag{2.170}$$

and

$$R_k = \Re\left\{\frac{1}{Y_k(jz_k)}\right\}, \tag{2.171}$$

respectively.

2.10 Numerical verification of the tuning procedure

The beam used in Section 2.5 is considered again in this section, in order to demonstrate the tuning procedure and to show that the passive shunt circuits discussed above are nearly equivalent to the ideal ones discussed in Section 2.4. The first two modes are targeted to start with. To give an idea of the orders of magnitudes, Table 2.2 lists the resistances and inductances of series and parallel RL shunt circuits that target mode one or two.

Mode	R	L
1	65.24kΩ	405.74H
2	11.7kΩ	12.17H

(a)

Mode	R	L
1	654.1kΩ	449.9H
2	109.61kΩ	13.6H

(b)

Table 2.2: Parameters of series (a) and parallel (b) single-mode RL shunts.

2.10.1 Hollkamp's shunt circuit

To check the tuning approach for Hollkamp's shunt circuit, a similar set of residues to that used in Figure 2.8 was considered. Figure 2.24 features the resulting FRFs and Table 2.3 gathers the associated electrical parameters. Similar trends between Hollkamp's shunt circuit and those in Figure 2.8 are observed, except for the case where $r_1 = 0.1$. It can also be observed in Table 2.3 that R_0 is negative for this problematic case.

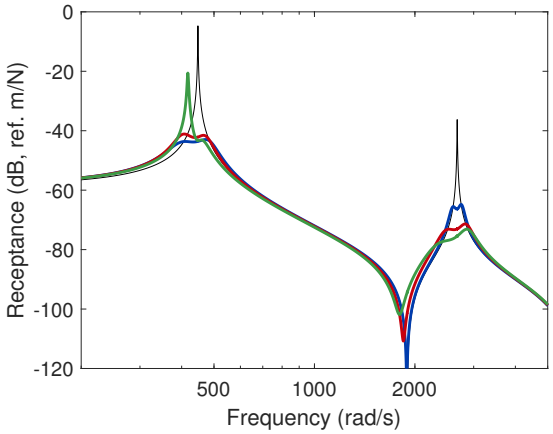

Figure 2.24: FRF of the beam with open-circuited patches (—) and controlled with Hollkamp's shunt circuit: $r_1 = 0.9$, $r_2 = 0.1$ (—), $r_1 = 0.5$, $r_2 = 0.5$ (—) and $r_1 = 0.1$, $r_2 = 0.9$ (—).

	R_0	L_0	C_1	R_1	L_1
$r_1 = 0.9$, $r_2 = 0.1$	56.95kΩ	376H	1.01nF	38.1kΩ	150H
$r_1 = 0.5$, $r_2 = 0.5$	23.3kΩ	239H	8.76nF	17.91kΩ	28.7H
$r_1 = 0.1$, $r_2 = 0.9$	-11.13kΩ	63.73H	57.4nF	19.36kΩ	17.46H

Table 2.3: Parameters of Hollkamp's shunt circuit.

The apparent issue with $r_1 = 0.1$ and $r_2 = 0.9$ is due to the physical behavior of the circuit in this configuration. This behavior is illustrated in Figure 2.25, where the resistance in either branch is varied while the other one is maintained at zero. On the one hand, from Figure 2.25(a), it can be seen that R_0 barely affects mode 2, but can be tuned to

optimally damp mode one. On the other hand Figure 2.25(b) indicates that R_1 has a significant effect on mode 2. However, its effect is even more pronounced on mode 1, and when mode 2 is optimally damped mode 1 is overdamped. From this setting, the tuning method seeks to retrieve a correct damping on mode 1 (and barely affect that on mode 2) by setting R_0 to a negative value. Hence, there does not seem to exist a set of positive resistances that optimally damp modes 1 and 2 simultaneously. This rules out this circuit for practical implementation in this case. Indeed, a passive resistor with negative resistance does not exist. Even with a DVA, the implementation is strongly inadvisable, as the equivalent controller would be unstable. In general, it was observed by the author that Hollkamp's shunt circuit is suited for emphasis on lower-frequency modes, but may perform poorly if emphasis is put on higher-frequency modes, and a rule of thumb should be to use this circuit with residues satisfying $r_{k+1} \leq r_k$ $(k = 1, \cdots, N_s - 1)$, but a verification of the electrical parameters is also advisable.

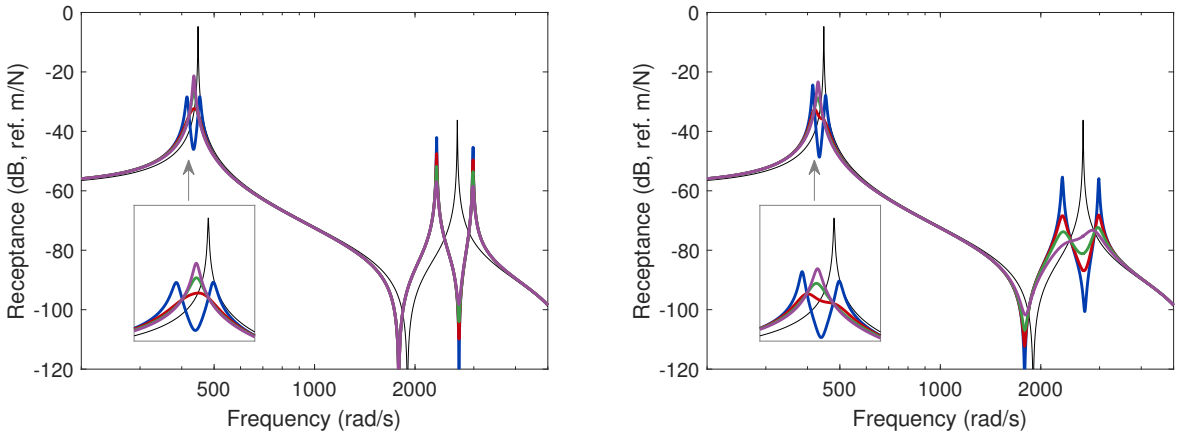

(a) (b)

Figure 2.25: FRF of the beam with open-circuited patches (—) and controlled with Hollkamp's shunt circuit ($r_1 = 0.1$, $r_2 = 0.9$): $R_1 = 0$ and $R_0 = 1\text{k}\Omega$ (—), $R_0 = 5\text{k}\Omega$ (—), $R_0 = 10\text{k}\Omega$ (—) and $R_0 = 20\text{k}\Omega$ (—) (a); $R_0 = 0$ and $R_1 = 1\text{k}\Omega$ (—), $R_1 = 5\text{k}\Omega$ (—), $R_1 = 10\text{k}\Omega$ (—) and $R_1 = 20\text{k}\Omega$ (—) (b).

2.10.2 Second Foster form

Figure 2.26 depicts the FRFs of the beam controlled with an SFCF shunt circuit, and Table 2.4 gathers the associated electrical parameters.

	R_0	L_0	C_1	R_1	L_1
$r_1 = 0.9$, $r_2 = 0.1$	-536kΩ	110H	1.89nF	335.1kΩ	303H
$r_1 = 0.5$, $r_2 = 0.5$	393kΩ	26.9H	10.98nF	415kΩ	226H
$r_1 = 0.1$, $r_2 = 0.9$	132kΩ	15.1H	93.5nF	196kΩ	50.4H

Table 2.4: Parameters of the SFCF shunt circuit.

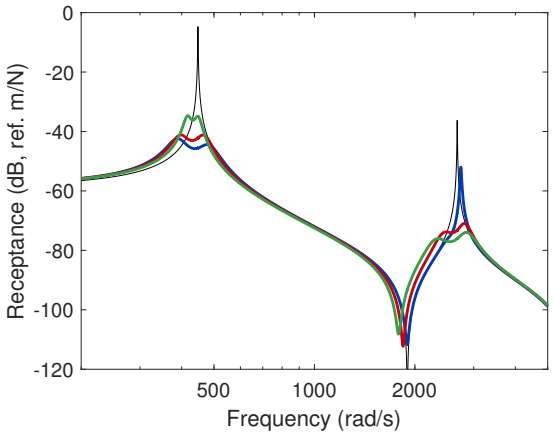

Figure 2.26: FRF of the beam with open-circuited patches (—) and controlled with an SFCF shunt circuit: $r_1 = 0.9$, $r_2 = 0.1$ (—), $r_1 = 0.5$, $r_2 = 0.5$ (—) and $r_1 = 0.1$, $r_2 = 0.9$ (—).

An issue with $r_1 = 0.9$ is observable in Figure 2.26. As can be seen in Table 2.4, this is due to a negative resistance. This issue is similar to the one occuring with Hollkamp's shunt circuit, and it can be shown that it comes from the physical behavior of the circuit in this configuration as well. The difference of this case with Hollkamp's shunt circuit is that is appears when emphasis is put on the lower-frequency mode. It was observed by the author that, conversely to Hollkamp's shunt circuit, the SFCF circuit is suited for emphasis on higher-frequency modes, but may perform poorly if emphasis is put on lower-frequency modes, and a rule of thumb should be to use this circuit with residues satisfying $r_{k+1} \geq r_k$ $(k = 1, \cdots, N_s - 1)$, but a verification of the electrical parameters is also advisable.

2.10.3 Current flowing and series-parallel impedance structure

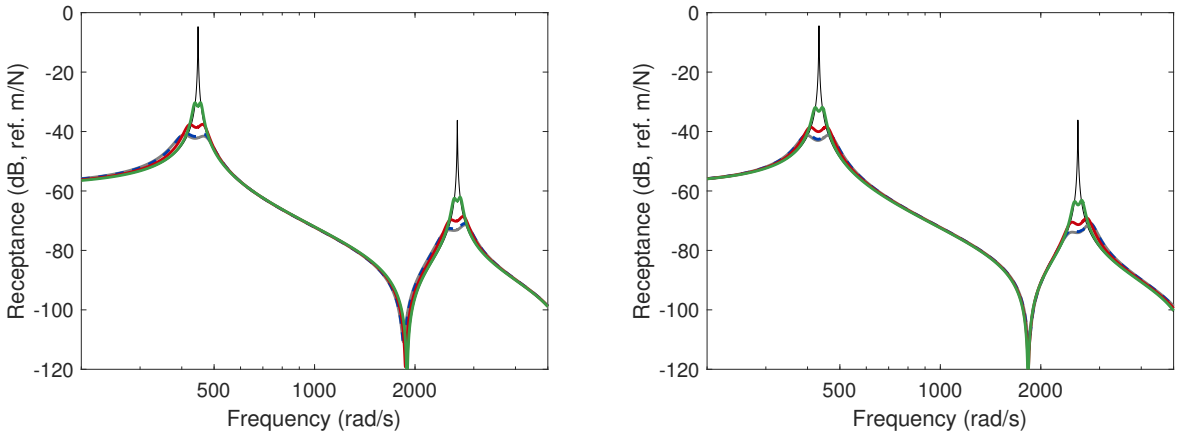

(a) (b)

Figure 2.27: (a): FRF of the beam with open-circuited patches (—) and controlled with Hollkamp's shunt circuit (—) and a CF shunt circuit with $r_0 = 0.1$ (- -), $r_0 = 0.5$ (—) and $r_0 = 0.9$ (—). (b): FRF of the beam with short-circuited patches (—) and controlled with an SFCF shunt circuit (—) and an SPIS shunt circuit with $r_0 = 0.1$ (- -), $r_0 = 0.5$ (—) and $r_0 = 0.9$ (—).

The performance of the CF and SPIS shunt circuits is investigated in Figure 2.27 for various values of r_0 and by setting $r_1 = r_2 = (1 - r_0)/2$. For reference, Hollkamp's and a SFCF shunt circuits are also used with $r_1 = r_2 = 0.5$. As expected from the theoretical analysis, the CF and SPIS circuits performance tends to approach that of Hollkamp's and an SFCF circuits when $r_0 \to 0$, respectively. When $r_0 \to 1$, the passivity constraint (Equation (2.34) or (2.73)) imposes that $r_1 \to 0$ and $r_2 \to 0$, i.e., the control authority over the first and second modes gradually vanishes.

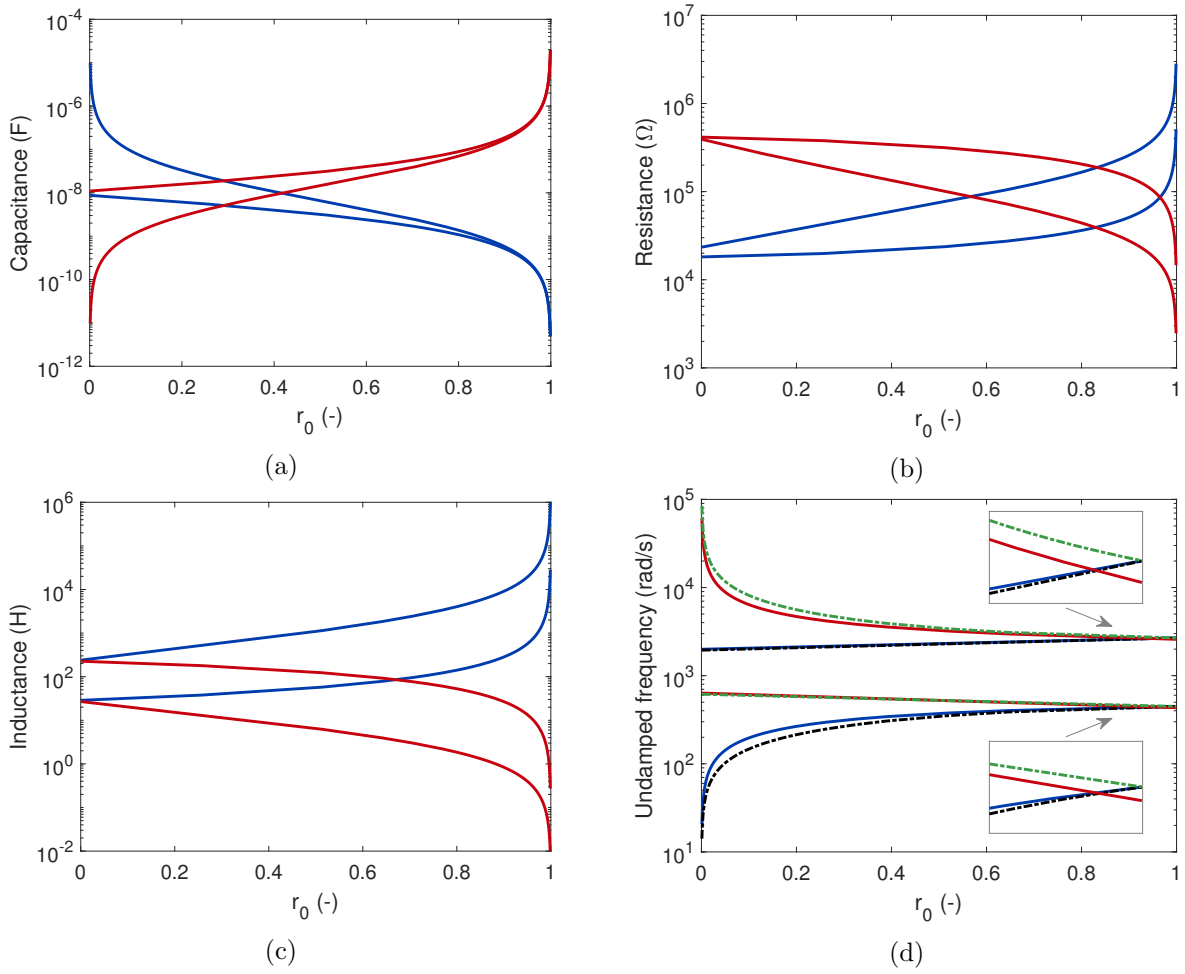

Figure 2.28: Capacitances (a), resistances (b), inductances (c) and resonance frequencies of branches of the lossless circuits (d) of the CF circuit branches (—) and SPIS circuit branches (—). In (d), the tuning rules from [128] (- - -) and from [129] (- - -) are also plotted.

The electrical parameters as functions of r_0 (keeping $r_1 = r_2 = (1 - r_0)/2$) are plotted in Figure 2.28. Two asymptotic states for the CF can be identified. As $r_0 \to 0$, the capacitance in the first branch tends to infinity, i.e., to a short-circuit, and the CF circuit becomes equivalent to Hollkamp's circuit. When $r_0 \to 1$, the capacitances tend to zero while the resistances and inductances tend to infinity, i.e., the CF globally tends to an open-circuit. Similarly, two asymptotic states for the SPIS can be identified: the SFCF circuit when $r_0 \to 0$, and a short-circuit when $r_0 \to 1$. This latter state has the practical advantage that the inductances are quite small when $r_0 \lesssim 1$, and it was what motivated its introduction in [129]. However, this comes at the expense of reduced performance on the controlled modes.

Figure 2.28(d) also features the resonance frequencies of the branches of the lossless circuits, i.e., $\sqrt{1/(C_n L_n)}$. These resonance frequencies are compared to the tuning rules proposed in the works first proposing the CF [128] and SPIS [129] shunt circuits, considering that the capacitances are equal to those given by the proposed tuning approach, and that the inductances are computed with the methods therein. For the CF circuit, the tuning rules agree well for large r_0, but a substantial error is made using the rules in [128] for small r_0. According to Figure 2.28(a), small r_0 correspond to high capacitances, which is desirable from a vibration reduction point of view in this case, as discussed in [146]. It was also identified therein that the issue comes from a strong interaction between the branches, whereas in [128] they are tuned independently. A similar observation can be made for the SPIS circuit, but the discrepancy is larger for large r_0 in this case. This is simply due to the fact that the circuit is tuned to the open-circuit resonance frequencies in [129], whereas it is tuned to the short-circuit ones herein. To conclude the comparison, it should also be pointed out that no quantitative selection method for the capacitances in the circuit was proposed in [128, 129], while in this chapter they are deduced from the residues. Furthermore, the resistances tuning was carried out using numerical optimization [147].

2.10.4 Current blocking shunt circuit

The last circuits are the CB circuits with series and parallel RL shunts. For these circuits, a comparison with the tuning approach proposed in [133] is performed.

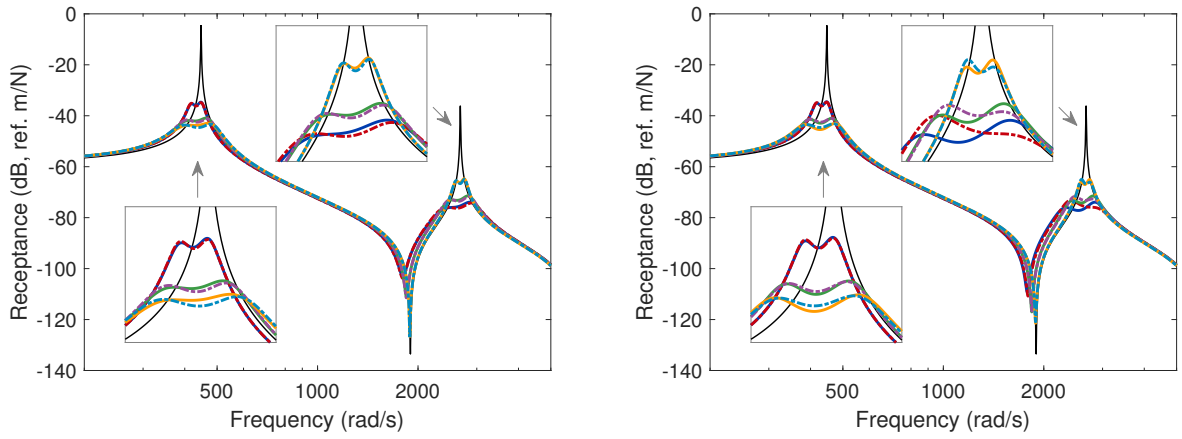

Figure 2.29: FRF of the beam with open-circuited patches (—), controlled with a CB circuit with series RL shunts (a) and a CB circuit with parallel RL shunts (b), with $r_1 = 0.1$, $r_2 = 0.9$ (— : this chapter, - - - : [133]), $r_1 = 0.5$, $r_2 = 0.5$ (— : this chapter, - - - : [133]) and $r_1 = 0.9$, $r_2 = 0.1$ (— : this chapter, - - - : [133]).

Figure 2.29 shows the FRFs of the beam controlled with CB shunt circuits of both types (with series and parallel RL shunts) tuned with both approaches. The filter capacitances were determined with the approach in this chapter, and were used as an input for the method in [133]. There exist slight differences (which are larger for parallel RL shunts on the second mode), but the performance and trends in terms of vibration mitigation are essentially the same.

	R_1	L_1	R_2	L_2	$\tilde{C}_1$	$\tilde{L}_1$
$r_1 = 0.9$, $r_2 = 0.1$	128.7kΩ	229H	13.32kΩ	14.5H	88.32nF	58.55H
$r_1 = 0.5$, $r_2 = 0.5$	98.98kΩ	414H	17.27kΩ	27.2H	9.81nF	465H
$r_1 = 0.1$, $r_2 = 0.9$	70.35kΩ	411.5H	38.51kΩ	144.9H	1.09nF	3 747H

Table 2.5: Parameters of the CB circuit with series RL shunts.

	R_1	L_1	R_2	L_2	$\tilde{C}_1$	$\tilde{L}_1$
$r_1 = 0.9$, $r_2 = 0.1$	205.4kΩ	533.8H	269.2kΩ	15.7H	88.32nF	59.31H
$r_1 = 0.5$, $r_2 = 0.5$	460.67kΩ	492.8H	412.21kΩ	29H	9.81nF	492.9H
$r_1 = 0.1$, $r_2 = 0.9$	620kΩ	457.9H	4.288MΩ	147.4H	1.09nF	4 121H

Table 2.6: Parameters of the CB circuit with parallel RL shunts.

The approach proposed in this chapter has several advantages over the one proposed in [133]. It is more generic, as it can be extended to other shunt circuits. It is easier to implement and provides more insight. Namely, it requires as input the residues whose connection with the EEMCF has been established, whereas the approach in [133] requires the filter capacitance values, whose impact on coupling is less straightforward to assess (Equation (2.159)). Finally, it decouples the identification procedure from the tuning procedure, which permits to use more robust identification approaches than that proposed in [133].

2.10.5 Comparison between the circuits

The near-equivalence of every shunt circuit presented in this work is demonstrated in Figure 2.30. As expected, the performance of the CF and SPIS circuits is slightly worse than that of the other circuits because the residue $r_0 \neq 0$, leading to lower residues for the other modes.

The proposed approach also works with more than two modes. Figure 2.31 displays the mobility (the transfer function between force and velocity) of the beam when its five first bending modes are targeted. The residues were set to $r_i = 1/5$ for $i = 1, \cdots, 5$ and $r_i = 1/6$ for $i = 0, \cdots, 5$. Clearly, all circuit types exhibit similar performance, with a slight worsening for the CF and SPIS circuits.

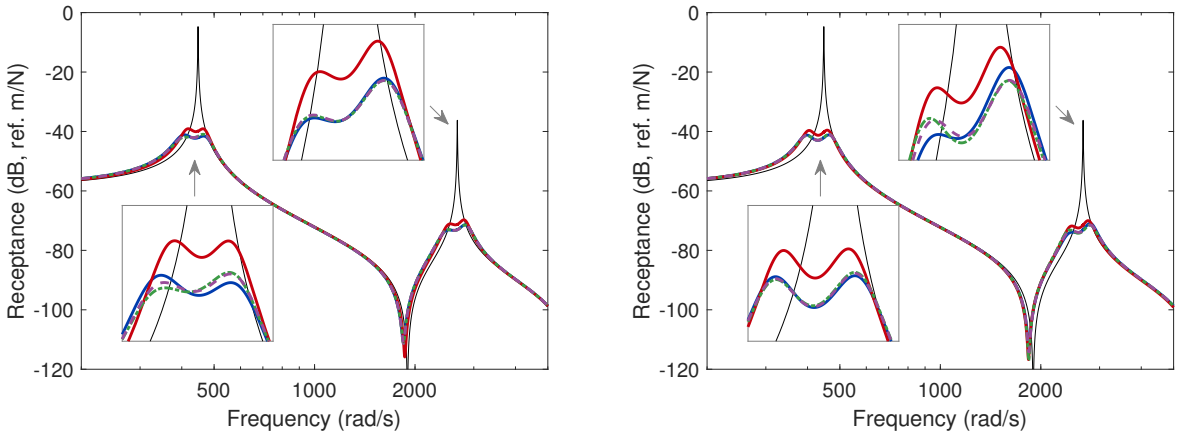

(a) (b)

Figure 2.30: FRFs of the beam with open-circuited patches (—) and various shunt circuits targeting the two first modes. Circuits based on the series RL shunt (a): Hollkamp's shunt circuit (—), CF shunt circuit (—), CB circuit with series RL shunts (- - -) and shunt circuit with ideal Thévenin's impedance (- -). Circuits based on the parallel RL shunt (b): SFCF shunt circuit (—), SPIS shunt circuit (—), CB circuit with parallel RL shunts (- - -) and shunt circuit with ideal Norton's admittance (- -).

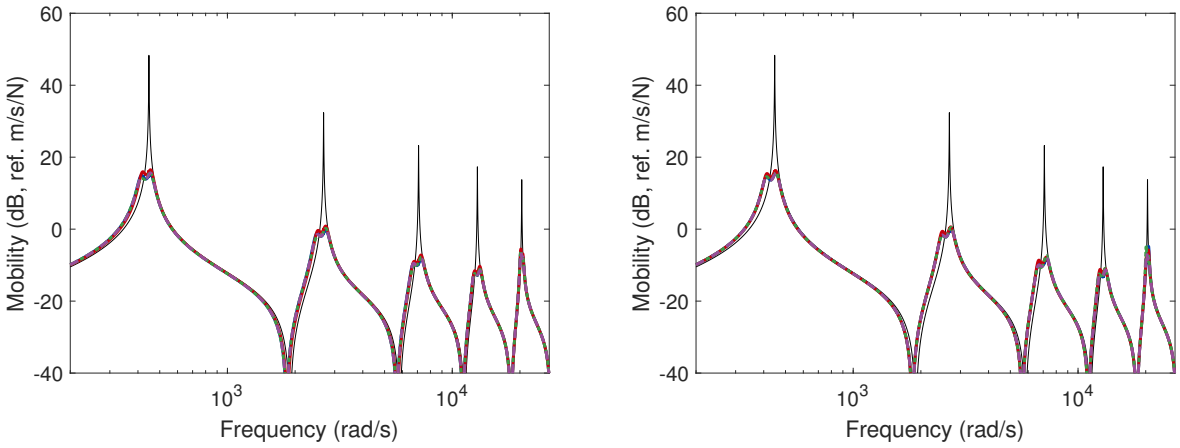

(a) (b)

Figure 2.31: FRFs of the beam with open-circuited patches (—) and various shunt circuits targeting the five first modes. Circuits based on the series RL shunt (a): Hollkamp's shunt circuit (—), CF shunt circuit (—), CB circuit with series RL shunts (- - -) and shunt circuit with ideal Thévenin's impedance (- -). Circuits based on the parallel RL shunt (b): SFCF shunt circuit (—), SPIS shunt circuit (—), CB circuit with parallel RL shunts (- - -) and shunt circuit with ideal Norton's admittance (- -).

2.11 Experimental validation of the tuning procedure

A last example is featured in this section to show the equivalence between the ideal impedance and admittance with a shunt circuit with known electrical components on the experimental setup considered in Section 1.3.3. CB shunt circuits with series and parallel RL shunts were emulated and compared to the ideal ones in

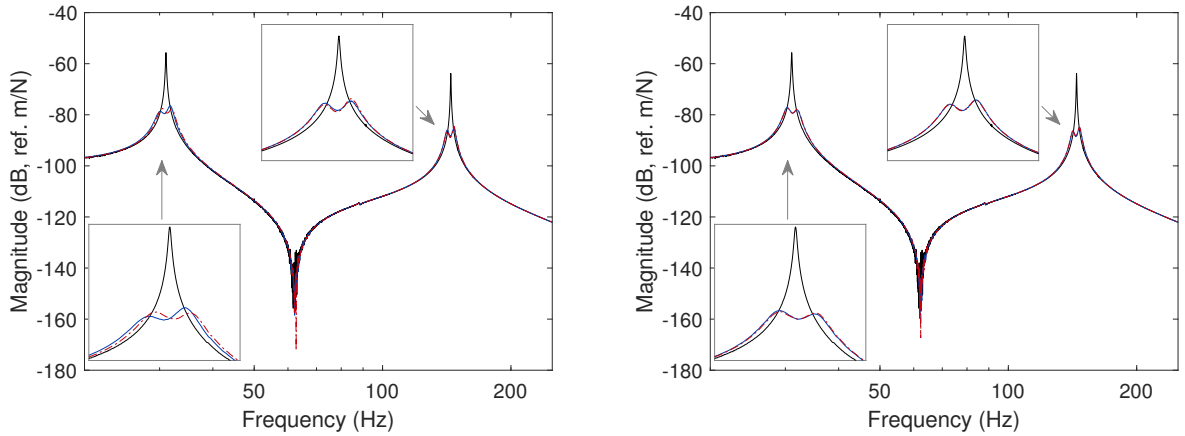

Figure 2.32: Experimental FRF of the beam with open-circuited patches (—) and controlled with various shunt circuits. Circuits based on series RL shunts (a): shunt circuit with ideal Thévenin's impedance (—) and CB circuit with series RL shunts (- - -). Circuits based on parallel RL shunts (b): shunt circuit with ideal Norton's admittance (—) and CB circuit with parallel RL shunts (- - -).

Section 2.6. As shown in Figure 2.32, when provided with equal residues, these circuits are almost perfectly equivalent to the ideal ones.

2.12 Conclusion

Structures can exhibit multiple problematic modes, and this chapter proposed a tuning procedure for shunt circuits connected to a single piezoelectric transducer that resonates at multiple frequencies to mitigate the structural resonances. The procedure consists in three sequential steps.

The first step is to identify the piezoelectric structure through its piezoelectric capacitance, and short- and open-circuit resonance frequencies. From this information, it is possible to compute the modal coupling coefficients which are then used in the following steps.

The second step specifies a number of characteristics for the resonances of the shunt circuit. This specification is made by sequentially considering pairs of resonant mechanical and electrical modes. Upon simplifying the contribution of non-resonant modes to background contributions, it was shown that the problem essentially reduces to a problem similar to that of a single-mode series or parallel RL shunt. It was thus possible to use the well-established tuning formulas for these cases. This step takes as input the residues associated with the targeted modes. These residues are closely related to the EEMCF, and can be used to balance the control authority between the targeted modes, but are constrained by the passivity requirement on the shunt circuit.

The last step consists in deriving the actual parameters of the shunt circuit. Several circuit topologies presented in the literature were reviewed. The proposed tuning approach was successfully applied to them. We note that this last step can be bypassed when using digital absorbers.

The approach was numerically verified and experimentally validated on piezoelectric

beams. Numerous simulations were used to illustrate the properties of the various shunt circuits. The main conclusions on the advantages and drawbacks of these circuits are summarized in Table 2.7.

Circuit type	Advantages	Drawbacks
Hollkamp	Requires the least electrical components	Not suited for $r_{k+1} > r_k$
CF	/	Suboptimal ($r_0 \neq 0$)
SFCF	Requires the least electrical components	Not suited for $r_{k+1} < r_k$
SPIS	Low inductance	Suboptimal ($r_0 \neq 0$)
CB	Versatile	Requires the most electrical components
Ideal	Versatile	Unknown topology and electrical components (but realizable with a DVA)

Table 2.7: Comparison of the different shunt circuits studied in this chapter.

3 Multimodal vibration damping with multiple transducers

Abstract

This chapter presents a method that provides multimodal damping with multiple piezoelectric transducers using an electrical network interconnecting them. The characteristics of the network are specified in terms of modal properties. On the one hand, the electrical resonance frequencies are chosen to be close to those of the targeted set of structural modes. On the other hand, the electrical mode shapes are selected to maximize the electromechanical coupling between the mechanical and electrical modes while guaranteeing the passivity of the network. The effectiveness of this modal-based synthesis is demonstrated using a free-free beam and a fully clamped plate. Because the resulting network may require a large number of interconnections, a decentralization approach breaking down the network into multiple disconnected networks is proposed, and the modal-based synthesis is adapted to such a situation. This simplification comes at the expense of performance and/or number of controlled modes.

3.1 Introduction

Using a single transducer for multimodal vibration mitigation as in Chapter 2 makes up for a potentially compact solution, but the transducer placement on the structure may limit the performance in terms of vibration reduction of some modes. From this standpoint, it is desirable to use multiple transducers distributed over the structure to ensure sufficient electromechanical coupling with all targeted modes.

A first approach consists in using at least as many individually-shunted transducers as resonances to be controlled. Examples where this approach was considered include beams [122, 148] and truss-cored sandwich panels [149]. The recent work of Toftekær and Høgsberg [139] proposed explicit corrections to account for non-resonant modes and cross-interaction between the different shunt circuits.

A second approach for multimodal piezoelectric shunt damping is based on multiple patches interconnected through an electrical network. Dell'Isola and Vidoli [150] used piezoelectric actuators uniformly distributed over a truss beam and designed an electrical transmission line with similar wavespeed as a target mechanical wave speed, opening the possibility for efficient electrical dissipation of the mechanical energy. Vidoli and Dell'Isola [151] then studied the spectral properties of the operators governing the dynamics of a beam and characterized the coupling existing between mechanical and electrical modes. An important conclusion of their work was that the mechanical and electrical modal characteristics should coincide in order to obtain strong coupling. This led Alessandroni et al [123] to find electrical circuits analog to beams and plates, i.e., having identical resonance frequencies and mode shapes. They also derived optimal

resistances to efficiently damp one targeted mode. Maurini et al [152] studied different circuit topologies and showed that one of them could provide multimodal damping of a beam. Porfiri et al [153] synthesized a passive circuit analog to a vibrating beam made only of inductors, capacitors and ideal transformers. The theoretical concepts presented in these works were experimentally validated on rods [154], beams [155] and plates [156, 157]. Reviews on this approach can be found in [97, 98, 124].

The aforementioned works used a homogenized model of a simple structure, later discretized with finite differences in order to derive a circuit with lumped elements being analog to the structure. Real-life structures may be more complex. This is what motivated Darleux et al [98, 157] to develop a library of elemental electrical cells analog to various elemental structures. By assembling these cells into a network similarly to the way their mechanical counterparts are assembled in a complex structure, it is possible to create a network analog to that structure. This approach potentially requires a large number of cells and transducers.

In a slightly different spirit, Giorgio et al [158] proposed a generic approach, where an electrical network was tuned based on the finite element model of a structure. The idea developed therein was to find a transformation of the electrical DoFs of the network that makes the piezoelectric coupling matrix nearly diagonal in order to consider mechanical and electrical modes by pairs, thereby allowing a tuning based on the classical resistive-inductive shunt formulas [19]. This method was numerically verified and experimentally validated. However, it has two potential drawbacks. The first one is that it requires to solve a quadratic system of N_s^2 equations, where N_s is the number of modes to be controlled. For such systems, an iterative numerical solver is needed which may not always converge to a satisfactory solution. The second issue is that the number of piezoelectric transducers needs to be equal to the number of targeted mechanical modes, which somewhat limits the flexibility of this approach.

The goal of the present chapter is to propose a procedure for synthesizing an electrical network to be used for multimodal piezoelectric damping based on the modal properties of the host structure. The proposed approach specifies the characteristics of the resonant electrical modes of the network while requiring that the network is realizable using passive electrical elements. Specifically, by matching the electrical resonance frequencies to those of a set of targeted mechanical modes, and by analytically optimizing the electrical mode shapes, it is possible to derive the nodal admittance matrix of the network allowing to efficiently mitigate the targeted mechanical resonances. The proposed method, termed *modal-based synthesis*, is non-iterative and can accommodate a different number of transducers and targeted modes.

Sections 3.2 and 3.3 review the aspects about modeling piezoelectric structures and electrical networks, respectively. An electrical network aiming to provide multimodal vibration damping is introduced in Section 3.4, and the dynamics of the coupled system are analyzed. The electromechanical interaction between a mechanical mode and its electrical counterpart is described in terms of coupling factors. The actual design of the electrical network is undertaken in Section 3.5. Limitations on the electrical modal characteristics are imposed by the passivity requirement on the network. Under these constraints, the electrical modal characteristics are optimized and the network is synthesized. The approach is numerically demonstrated on a SDoF piezoelectric system, a free-free beam and a fully clamped plate in Section 3.6. The networks yielded by the proposed approach could be complicated and require a lot of electrical connections. With the aim to simplify

them, Section 3.7 analyzes the impact of imposing a disconnection between different parts of the network. This decentralization procedure can be brought up to the point where the network is broken down into multiple shunt circuits, bridging the concepts seen in this chapter with those seen in Chapter 2. This decentralization approach is finally illustrated with a piezoelectric beam in Section 3.8.

3.2 Modeling piezoelectric structures with multiple piezoelectric transducers

This section extends what was presented in Section 2.2 to multiple transducers. Introducing the vectors of electrical voltages $\mathbf{V}$ and electrical charges $\mathbf{q}$, the governing equations of the piezoelectric structure are obtained as

$$\begin{cases} \mathbf{M}\ddot{\mathbf{x}} + \mathbf{K}_{sc}\mathbf{x} + \boldsymbol{\Gamma}_p\mathbf{V} = \mathbf{f} \\ \boldsymbol{\Gamma}_p^T\mathbf{x} - \mathbf{C}_p^{\varepsilon}\mathbf{V} = \mathbf{q} \end{cases}. \tag{3.1}$$

In these equations, $\mathbf{K}_{sc}$ is the structural stiffness matrix with *every* piezoelectric transducer short-circuited, $\boldsymbol{\Gamma}_p$ is a piezoelectric coupling matrix and $\mathbf{C}_p^{\varepsilon}$ is the piezoelectric capacitance matrix at constant strain. Alternatively, the piezoelectric voltages may be used as independent variables:

$$\begin{cases} \mathbf{M}\ddot{\mathbf{x}} + \mathbf{K}_{oc}\mathbf{x} - \boldsymbol{\Theta}_p\mathbf{q} = \mathbf{f} \\ \boldsymbol{\Theta}_p^T\mathbf{x} - \mathbf{E}_p^{\varepsilon}\mathbf{q} = \mathbf{V} \end{cases}, \tag{3.2}$$

where

$$\mathbf{K}_{oc} = \mathbf{K}_{sc} + \boldsymbol{\Gamma}_p\left(\mathbf{C}_p^{\varepsilon}\right)^{-1}\boldsymbol{\Gamma}_p^T, \qquad \boldsymbol{\Theta}_p = \left(\mathbf{C}_p^{\varepsilon}\right)^{-1}\boldsymbol{\Gamma}_p, \qquad \mathbf{E}_p^{\varepsilon} = \left(\mathbf{C}_p^{\varepsilon}\right)^{-1} \tag{3.3}$$

are the open-circuit stiffness matrix, a piezoelectric coupling matrix and the matrix of elastance at constant strain, respectively.

3.2.1 Short-circuit and open-circuit modes

The short-circuit and open-circuit modes are the resonant modes of the structure with every transducer short-circuited ($\mathbf{V} = \mathbf{0}$) and open-circuited ($\mathbf{q} = \mathbf{0}$), respectively. Following the same methodology as in Section 2.2.1, one obtains

$$\begin{cases} \ddot{\boldsymbol{\eta}}_{sc} + \boldsymbol{\Omega}_{sc}^2\boldsymbol{\eta}_{sc} + \boldsymbol{\Phi}_{sc}^T\boldsymbol{\Gamma}_p\mathbf{V} = \boldsymbol{\Phi}_{sc}^T\mathbf{f} \\ \boldsymbol{\Gamma}_p^T\boldsymbol{\Phi}_{sc}\boldsymbol{\eta}_{sc} - \mathbf{C}_p^{\varepsilon}\mathbf{V} = \mathbf{q} \end{cases} \tag{3.4}$$

and

$$\begin{cases} \ddot{\boldsymbol{\eta}}_{oc} + \boldsymbol{\Omega}_{oc}^2\boldsymbol{\eta}_{oc} - \boldsymbol{\Phi}_{oc}^T\boldsymbol{\Theta}_p\mathbf{q} = \boldsymbol{\Phi}_{oc}^T\mathbf{f} \\ \boldsymbol{\Theta}_p^T\boldsymbol{\Phi}_{oc}\boldsymbol{\eta}_{oc} - \mathbf{E}_p^{\varepsilon}\mathbf{q} = \mathbf{V} \end{cases}. \tag{3.5}$$

The generalized DoFs can also be expanded in modes with hybrid electrical boundary conditions (some patches in short circuit and some patches in open circuit).

3.2.2 Dynamic capacitance

Assuming that the structure is unforced ($\mathbf{f} = \mathbf{0}$), taking the Laplace transform of the mechanical equation in Equation (3.4) and inserting it into the electrical equation gives a dynamic relation between $\mathbf{V}$ and $\mathbf{q}$:

$$-\left[\mathbf{C}_p^{\varepsilon} + \boldsymbol{\Gamma}_p^T \boldsymbol{\Phi}_{sc} \left(s^2\mathbf{I} + \boldsymbol{\Omega}_{sc}^2\right)^{-1} \boldsymbol{\Phi}_{sc}^T \boldsymbol{\Gamma}_p\right] \mathbf{V} = \mathbf{C}_p(s)\mathbf{V} = \mathbf{q}. \tag{3.6}$$

$\mathbf{C}_p(s)$ is the dynamic capacitance matrix. Similarly, the dynamic elastance matrix $\mathbf{E}_p(s)$ is obtained from Equation (3.5)

$$-\left[\mathbf{E}_p^{\varepsilon} - \boldsymbol{\Theta}_p^T \boldsymbol{\Phi}_{oc} \left(s^2\mathbf{I} + \boldsymbol{\Omega}_{oc}^2\right)^{-1} \boldsymbol{\Phi}_{oc}^T \boldsymbol{\Theta}_p\right] \mathbf{q} = \mathbf{E}_p(s)\mathbf{q} = \mathbf{V}. \tag{3.7}$$

Equations (3.6) and (3.7) show that the poles of the dynamic capacitance (elastance) are the short-circuit (open-circuit) resonance frequencies. However, unlike in Section 2.2.2, the open-circuit (short-circuit) resonance frequencies cannot be deduced directly from the dynamic capacitance (elastance) when there is more than one transducer. The only information that can be deduced from the zeros is that those of the diagonal entries of the dynamic capacitance (elastance) matrix are the resonance frequencies of the structure when the corresponding transducer is open-circuited (short-circuited) while all the other transducers are short-circuited (open-circuited). In some sense, these zeros allow to quantify the coupling of the transducer *alone* with the structure.

Nevertheless, the identification of the dynamic capacitance (elastance) matrices yields an estimate of the piezoelectric capacitance (elastance) at constant strain, short-circuit (open-circuit) resonance frequencies and projection of the piezoelectric coupling matrices on the short-circuit (open-circuit) modal basis. The tuning method discussed in this chapter will require this information only. Thus, as long as multiple-input multiple-output (MIMO) electrical measurements on all the transducers are available to obtain the dynamic capacitance or elastance matrix, no mathematical model of the structure will be required.

3.2.3 Electromechanical coupling factors

An EEMCF can be defined for mode r as

$$K_{c,r}^2 = \frac{\omega_{oc,r}^2 - \omega_{sc,r}^2}{\omega_{sc,r}^2}, \tag{3.8}$$

This EEMCF quantifies the electromechanical coupling existing between mode r and *all* the piezoelectric transducers. If only one type of resonance frequency (short-circuit or open-circuit) is known, Section D.1 discusses ways to estimate this EEMCF.

3.3 Modeling electrical networks

An electrical network contains a series of nodes. One of them, called ground, is taken as a reference to express the voltage levels. The voltage difference between a node and ground is simply called the voltage of that node. These nodes can also be fed with a current. The nodes are interconnected by branches, and connected to the ground by shunts. Each of these branches and shunts is assumed to have a given admittance.

A part of an electrical network containing N_e nodes (excluding ground) is shown in Figure 3.1, where node n and the nodes to which it is linked are represented. Electrical nodes other than n may have other electrical connections which are not displayed therein.

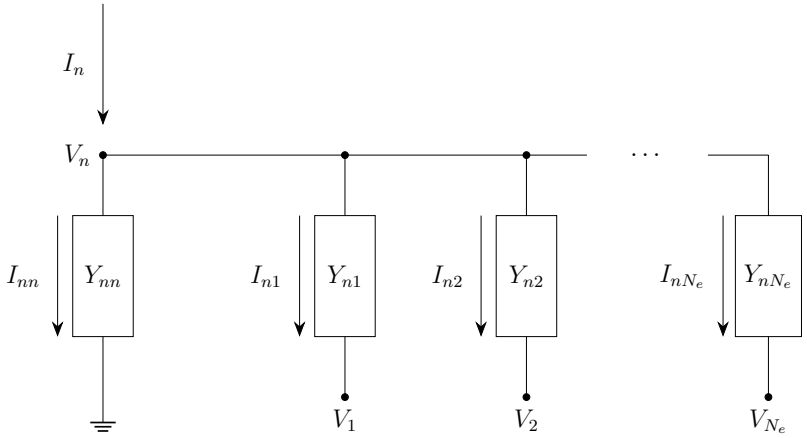

Figure 3.1: Partial representation of an electrical network with node n and its connected nodes.

The current flowing in the shunt is given by

$$I_{nn} = Y_{nn}(s)V_n, \tag{3.9}$$

while that flowing from node n to node m is

$$I_{nm} = Y_{nm}(s)(V_n - V_m). \tag{3.10}$$

Applying KCL to node n, the externally-supplied current I_n must be equal to the current flowing out of this node through the branches and shunt:

$$I_n = \sum_{j=1}^{N_e} I_{nm} = Y_{nn}(s)V_n + \sum_{n=1, m\neq n}^{N_e} Y_{nm}(s)(V_n - V_m) = \sum_{m=1}^{N_e} Y_{nm}(s)V_n - \sum_{m=1, m\neq n}^{N_e} Y_{nm}(s)V_m. \tag{3.11}$$

Writing out this equation for every node gives the linear system of equations

$$\begin{bmatrix} \sum_{n=1}^{N_e} Y_{1n}(s) & -Y_{12}(s) & \cdots & -Y_{1N_e}(s) \\ -Y_{21}(s) & \sum_{n=1}^{N_e} Y_{2n}(s) & \cdots & \vdots \\ \vdots & \vdots & \ddots & \vdots \\ -Y_{N_e1}(s) & \cdots & \cdots & \sum_{n=1}^{N_e} Y_{N_en}(s) \end{bmatrix} \begin{bmatrix} V_1 \\ V_2 \\ \vdots \\ V_{N_e} \end{bmatrix} = \begin{bmatrix} I_1 \\ I_2 \\ \vdots \\ I_{N_e} \end{bmatrix}, \tag{3.12}$$

or, in short,

$$\mathbf{Y}(s)\mathbf{V} = \mathbf{I}, \tag{3.13}$$

where $\mathbf{V}$ and $\mathbf{I}$ are the nodal voltage and current vectors, respectively, and $\mathbf{Y}(s)$ is the (symmetric) nodal admittance matrix [159].

In the particular case where each branch and shunt is a parallel connection of a capacitor (of capacitance C_{nm}), a resistor (of conductance G_{nm}) and an inductor (of reluctance B_{nm}), every admittance has the form

$$Y_{nm}(s) = sC_{nm} + G_{nm} + \frac{B_{nm}}{s} \tag{3.14}$$

and the admittance matrix takes the form

$$\mathbf{Y}(s) = s\mathbf{C} + \mathbf{G} + \frac{1}{s}\mathbf{B}, \tag{3.15}$$

where $\mathbf{C}$, $\mathbf{G}$ and $\mathbf{B}$ are the (symmetric) capacitance, conductance and reluctance matrices of the network, respectively.

3.4 Dynamics of the electromechanical system

In order to achieve multimodal damping with multiple piezoelectric transducers, a properly tuned *interconnecting network* can be electrically connected to these transducers, as shown in Figure 3.2. In this section, it is assumed that the network has known electrical characteristics, and an analysis of its coupling with the resonant modes of the structure is carried out. This will highlight the importance of the modal characteristics of the *overall network* obtained by combining the electrical properties of the interconnecting network together with those of the transducers. These modal characteristics will then be used as design variables in the next section in order to synthesize the network.

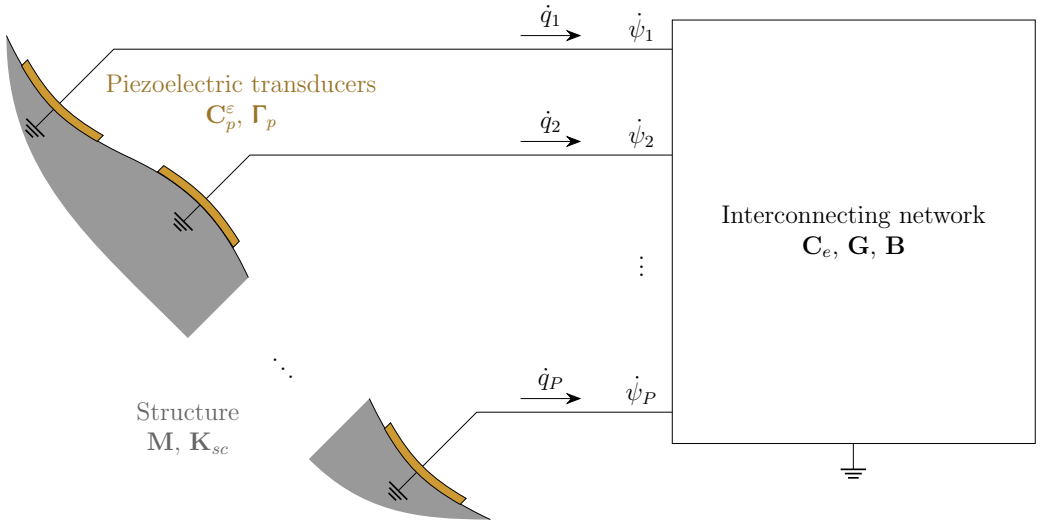

Figure 3.2: Schematic of a structure (in gray) with multiple piezoelectric transducers (in orange) connected to an electrical network.

3.4.1 Governing equations

The interconnecting network is governed by the following equations

$$\mathbf{C}_e\ddot{\boldsymbol{\psi}} + \mathbf{G}\dot{\boldsymbol{\psi}} + \mathbf{B}\boldsymbol{\psi} = \dot{\mathbf{q}}, \tag{3.16}$$

where $\mathbf{C}_e$ is the capacitance matrix of the interconnecting network. The vector

$$\boldsymbol{\psi}^T = \begin{bmatrix} \boldsymbol{\psi}_p^T & \boldsymbol{\psi}_i^T \end{bmatrix} \tag{3.17}$$

describes the flux linkages of the P ports to be connected to the piezoelectric transducers $\boldsymbol{\psi}_p$ and I possible internal electrical DoFs $\boldsymbol{\psi}_i$. In total, the number of electrical DoFs is noted $N_e = P + I$. Equation (3.16) is obtained as the inverse Laplace transform of Equations (3.13) and (3.15) by replacing $\mathbf{C}$ by $\mathbf{C}_e$ and recalling that $s\boldsymbol{\psi} = \mathbf{V}$ (Equation (1.40)).

Connecting the network to the transducers imposes the charges flowing in the ports of the interconnecting network to be equal to those flowing out of the transducers, as shown in Figure 3.2, leading to the relation

$$\dot{\mathbf{q}} = \mathbf{E}_p\dot{\mathbf{q}}_p, \tag{3.18}$$

where $\mathbf{E}_p$ is a localization matrix given by

$$\mathbf{E}_p^T = \begin{bmatrix} \mathbf{I}_{P\times P} & \mathbf{0}_{P\times I} \end{bmatrix}. \tag{3.19}$$

The ports associated to internal DoFs are not fed with an external current ($\dot{\mathbf{q}}_i = \mathbf{0}$). According to Equation (3.17), the flux linkages of the ports connected to the piezoelectric transducers are also given by

$$\boldsymbol{\psi}_p = \mathbf{E}_p^T\boldsymbol{\psi}. \tag{3.20}$$

Upon connecting the network to the transducers of the piezoelectric structure and differentiating the second relation, Equation (3.1) becomes,

$$\begin{cases} \mathbf{M}\ddot{\mathbf{x}} + \mathbf{K}_{sc}\mathbf{x} + \boldsymbol{\Gamma}_p\mathbf{E}_p^T\dot{\boldsymbol{\psi}} = \mathbf{f} \\ \left(\mathbf{C}_e + \mathbf{E}_p\mathbf{C}_p^{\varepsilon}\mathbf{E}_p^T\right)\ddot{\boldsymbol{\psi}} + \mathbf{G}\dot{\boldsymbol{\psi}} + \mathbf{B}\boldsymbol{\psi} - \mathbf{E}_p\boldsymbol{\Gamma}_p^T\dot{\mathbf{x}} = \mathbf{0} \end{cases}. \tag{3.21}$$

In the sequel, the capacitance matrix of the overall network is noted

$$\mathbf{C} = \mathbf{C}_e + \mathbf{E}_p\mathbf{C}_p^{\varepsilon}\mathbf{E}_p^T. \tag{3.22}$$

3.4.2 Electrical modes and modal equations

The mechanical modes with short-circuited transducers are defined by the generalized eigenvalue problem in Equation (2.4), and they verify a series of orthogonality relationships such as Equation (2.5). In a similar way, the electrical modes $\boldsymbol{\Phi}_e$

of the lossless network decoupled from the structure ($\mathbf{G} = \mathbf{0}$ and $\mathbf{\Gamma}_p = \mathbf{0}$) can be defined by the following equation:

$$\mathbf{B\Phi}_e = \mathbf{C\Phi}_e\mathbf{\Omega}_e^2, \qquad \mathbf{\Omega}_e^2 = \begin{bmatrix} \omega_{e,1}^2 & & \\ & \ddots & \\ & & \omega_{e,N_e}^2 \end{bmatrix}, \tag{3.23}$$

where $\omega_{e,i}$ is the i^{th} natural frequency of the network. The mode shapes also verify orthogonality properties and can be capacitance-normalized

$$\mathbf{\Phi}_e^T\mathbf{C\Phi}_e = \mathbf{I}, \qquad \mathbf{\Phi}_e^T\mathbf{B\Phi}_e = \mathbf{\Omega}_e^2. \tag{3.24}$$

It is assumed that the electrical conductance matrix is such that the mode shapes also respect the same kind of orthogonality relations

$$\mathbf{\Phi}_e^T\mathbf{G\Phi}_e = 2\mathbf{Z}_e\mathbf{\Omega}_e, \qquad \mathbf{Z}_e = \begin{bmatrix} \zeta_{e,1} & & \\ & \ddots & \\ & & \zeta_{e,N_e} \end{bmatrix}, \tag{3.25}$$

where $\mathbf{Z}_e$ is a diagonal matrix containing the electrical modal damping ratios.

The governing equations can be projected on the mechanical and electrical modal bases. For the electrical DoFs, $\boldsymbol{\psi} = \mathbf{\Phi}_e\boldsymbol{\eta}_e$ is inserted into the second line of Equation (3.21), which is then premultiplied by $\mathbf{\Phi}_e^T$ and simplified using the modal orthogonality relationships. Eventually, one obtains the governing equations of the electromechanical system in modal form

$$\begin{cases} \left(s^2\mathbf{I} + \mathbf{\Omega}_{sc}^2\right)\boldsymbol{\eta}_{sc} + s\mathbf{\Gamma}_{\mathbf{\Phi}}\boldsymbol{\eta}_e = \mathbf{\Phi}_{sc}^T\mathbf{f} \\ \left(s^2\mathbf{I} + 2s\mathbf{Z}_e\mathbf{\Omega}_e + \mathbf{\Omega}_e^2\right)\boldsymbol{\eta}_e - s\mathbf{\Gamma}_{\mathbf{\Phi}}^T\boldsymbol{\eta}_{sc} = \mathbf{0} \end{cases}, \tag{3.26}$$

where

$$\mathbf{\Gamma}_{\mathbf{\Phi}} = \mathbf{\Phi}_{sc}^T\mathbf{\Gamma}_p\mathbf{E}_p^T\mathbf{\Phi}_e. \tag{3.27}$$

3.4.3 Effective characteristics

As in Sections 2.3.1.4 and 2.3.2.4, this section simplifies the dynamics of the electromechanical system by considering only a pair of mechanical and electrical resonant modes. Different approximations are made to account for the non-resonant modes in what follows.

3.4.3.1 Modal characteristics

Around the frequency $\omega_{sc,r}$, it is assumed at first that only mechanical mode r and electrical mode k are responding, i.e., $\eta_{sc,i} = 0$, $\forall i \neq r$ and $\eta_{e,i} = 0$, $\forall i \neq k$. Furthermore, an unforced structure is considered ($\mathbf{f} = \mathbf{0}$) in order to characterize only the poles of the electromechanical system. Equation (3.26) then becomes

$$\begin{cases} \left(s^2 + \omega_{sc,r}^2\right) \eta_{sc,r} + s\gamma_{\mathbf{\Phi},rk}\eta_{e,k} = 0 \\ \left(s^2 + 2\zeta_{e,k}\omega_{e,k}s + \omega_{e,k}^2\right) \eta_{e,k} - s\gamma_{\mathbf{\Phi},rk}\eta_{sc,r} = 0 \end{cases}, \tag{3.28}$$

where

$$\gamma_{\mathbf{\Phi},rk} = \boldsymbol{\phi}_{sc,r}^T \mathbf{\Gamma}_p \mathbf{E}_p^T \boldsymbol{\phi}_{e,k}. \tag{3.29}$$

This system has the same form as the Laplace transform of Equation (1.42). An EEMCF can then be deduced by analogy to Equation (1.19) as

$$\widehat{K}_{c,rk}^2 = \frac{\gamma_{\mathbf{\Phi},rk}^2}{\omega_{sc,r}^2} = \frac{\left(\boldsymbol{\phi}_{sc,r}^T \mathbf{\Gamma}_p \mathbf{E}_p^T \boldsymbol{\phi}_{e,k}\right)^2}{\omega_{sc,r}^2}. \tag{3.30}$$

3.4.3.2 Background contributions from the mechanical modes

The higher-frequency mechanical modes are now supposed to respond statically, whereas the lower-frequency modes are assumed to be negligible, i.e., $\boldsymbol{\eta}_{sc,<r} = 0$. Subscripts $< r$ and $> r$ refers to mechanical modes of frequencies lower and greater than that of mode r, respectively. Neglecting the inertia forces in the mechanical equations for higher-frequency modes, their static response is then given by

$$\boldsymbol{\eta}_{sc,>r} = -s\mathbf{\Omega}_{sc,>r}^{-2} \mathbf{\Phi}_{sc,>r}^T \mathbf{\Gamma}_p \mathbf{E}_p^T \boldsymbol{\psi} = -s\mathbf{\Omega}_{sc,>r}^{-2} \mathbf{\Gamma}_{\mathbf{\Phi}} \boldsymbol{\eta}_e. \tag{3.31}$$

Inserting this relation back into the electrical equation in Equation (3.26) while still assuming $\eta_{e,i} = 0$, $\forall i \neq k$ yields the following system of equations

$$\begin{cases} \left(s^2 + \omega_{sc,r}^2\right) \eta_{sc,r} + s\gamma_{\mathbf{\Phi},rk}\eta_{e,k} = 0 \\ \left(\left(1 + \widehat{\kappa}_k\right) s^2 + 2\zeta_{e,k}\omega_{e,k}s + \omega_{e,k}^2\right) \eta_{e,k} - s\gamma_{\mathbf{\Phi},rk}\eta_{sc,r} = 0 \end{cases}, \tag{3.32}$$

where

$$\widehat{\kappa}_k = \boldsymbol{\phi}_{e,k}^T \mathbf{E}_p \mathbf{\Gamma}_p^T \mathbf{\Phi}_{sc,>r} \mathbf{\Omega}_{sc,>r}^{-2} \mathbf{\Phi}_{sc,>r}^T \mathbf{\Gamma}_p \mathbf{E}_p^T \boldsymbol{\phi}_{e,k}. \tag{3.33}$$

$\widehat{\kappa}_k$ represents the background contribution of the non-resonant mechanical modes on the dynamics of electrical mode k, and is positive or zero since the matrix of mechanical resonance frequencies is positive definite. It is the electrical modal counterpart of the modal blocked capacitance [77, 160]. Noting once again the similarity between the Laplace transform of Equation (1.42) and Equation (3.32), an EEMCF can be defined as

$$\widehat{K}_{c,rk}^2 = \frac{\gamma_{\mathbf{\Phi},rk}^2}{(1 + \widehat{\kappa}_k)\omega_{sc,r}^2}. \tag{3.34}$$

3.4.3.3 Background contributions from the mechanical and electrical modes

A contribution from non-resonant electrical modes is now added, but it comes only from lower-frequency modes ($i < k$). These modes are assumed to be capacitively-dominated. Under these assumptions, Equation (3.26) becomes

$$\begin{cases} \left(s^2 + \omega_{sc,r}^2\right) \eta_{sc,r} + s\gamma_{\mathbf{\Phi},rk}\eta_{e,k} + s\boldsymbol{\gamma}_{\mathbf{\Phi},r<k}\boldsymbol{\eta}_{e,<k} = 0 \\ \left(s^2 + 2\zeta_{e,k}\omega_{e,k}s + \omega_{e,k}^2\right) \eta_{e,k} - s\gamma_{\mathbf{\Phi},rk}\eta_{sc,r} - s\boldsymbol{\gamma}_{\mathbf{\Phi},>rk}^T\boldsymbol{\eta}_{sc,>r} = 0 \\ \boldsymbol{\Omega}_{sc,>r}^2\boldsymbol{\eta}_{sc,>r} + s\boldsymbol{\gamma}_{\mathbf{\Phi},>rk}\eta_{e,k} + s\boldsymbol{\Gamma}_{\mathbf{\Phi},>r<k}\boldsymbol{\eta}_{e,<k} = \mathbf{0} \\ s^2\boldsymbol{\eta}_{e,<k} - s\boldsymbol{\gamma}_{\mathbf{\Phi},r<k}^T\eta_{sc,r} - s\boldsymbol{\Gamma}_{\mathbf{\Phi},>r<k}^T\boldsymbol{\eta}_{sc,>r} = \mathbf{0} \end{cases}, \tag{3.35}$$

where the subscript $< k$ indicates electrical modes with index $i < k$, and the modal piezoelectric coupling matrix is partitioned as

$$\boldsymbol{\Gamma}_{\mathbf{\Phi}} = \begin{bmatrix} \boldsymbol{\phi}_{sc,r}^T \\ \mathbf{\Phi}_{sc,>r}^T \end{bmatrix} \boldsymbol{\Gamma}_p \mathbf{E}_p^T \begin{bmatrix} \boldsymbol{\phi}_{e,k} & \mathbf{\Phi}_{e<k} \end{bmatrix} = \begin{bmatrix} \gamma_{\mathbf{\Phi},rk} & \boldsymbol{\gamma}_{\mathbf{\Phi},r<k} \\ \boldsymbol{\gamma}_{\mathbf{\Phi},>rk} & \boldsymbol{\Gamma}_{\mathbf{\Phi},>r<k} \end{bmatrix}. \tag{3.36}$$

The last two lines of Equation (3.35) govern the dynamics of non-resonant modes, and can be put in the form

$$\begin{bmatrix} \boldsymbol{\Omega}_{sc,>r}^2 & \boldsymbol{\Gamma}_{\mathbf{\Phi},>r<k} \\ -\boldsymbol{\Gamma}_{\mathbf{\Phi},>r<k}^T & \mathbf{I} \end{bmatrix} \begin{bmatrix} \boldsymbol{\eta}_{sc,>r} \\ s\boldsymbol{\eta}_{e,<k} \end{bmatrix} = \begin{bmatrix} -s\boldsymbol{\gamma}_{\mathbf{\Phi},>rk}\eta_{e,k} \\ \boldsymbol{\gamma}_{\mathbf{\Phi},r<k}^T\eta_{sc,r} \end{bmatrix}. \tag{3.37}$$

This system can be solved for the non-resonant modal amplitudes. It should be noted that despite the potentially large size of the featured matrix imparted by the potential large size of $\boldsymbol{\Omega}_{sc,r}$, inverting it is not expensive because block inversion formulas (Equation (A.5)) can be used. In doing so, the only inversions that need to be performed are those of $\boldsymbol{\Omega}_{sc,r}^2$, which is immediate since it is diagonal, and that of its Schur complement

$$\mathbf{S} = \mathbf{I} + \boldsymbol{\Gamma}_{\mathbf{\Phi},>r<k}^T\boldsymbol{\Omega}_{sc,>r}^{-2}\boldsymbol{\Gamma}_{\mathbf{\Phi},>r<k} \tag{3.38}$$

of maximum size $(N_e - 1) \times (N_e - 1)$, hence realistically moderate. The non-resonant modal amplitudes can be found as

$$\begin{bmatrix} \boldsymbol{\eta}_{sc,>r} \\ s\boldsymbol{\eta}_{e,<k} \end{bmatrix} = \begin{bmatrix} \boldsymbol{\Omega}_{sc,>r}^{-2} - \boldsymbol{\Omega}_{sc,>r}^{-2}\boldsymbol{\Gamma}_{\mathbf{\Phi},>r<k}\mathbf{S}^{-1}\boldsymbol{\Gamma}_{\mathbf{\Phi},>r<k}^T\boldsymbol{\Omega}_{sc,>r}^{-2} & -\boldsymbol{\Omega}_{sc,>r}^{-2}\boldsymbol{\Gamma}_{\mathbf{\Phi},>r<k}\mathbf{S}^{-1} \\ \mathbf{S}^{-1}\boldsymbol{\Gamma}_{\mathbf{\Phi},>r<k}^T\boldsymbol{\Omega}_{sc,>r}^{-2} & \mathbf{S}^{-1} \end{bmatrix} \begin{bmatrix} -s\boldsymbol{\gamma}_{\mathbf{\Phi},>rk}\eta_{e,k} \\ \boldsymbol{\gamma}_{\mathbf{\Phi},r<k}^T\eta_{sc,r} \end{bmatrix} \tag{3.39}$$

Inserting these relations back into the first two lines of Equation (3.35) yields the system

$$\begin{cases} \left(s^2 + \widehat{\omega}_{sc,r}^2\right) \eta_{sc,r} + s\widehat{\gamma}_{\mathbf{\Phi},rk}\eta_{e,k} = 0 \\ \left(\left(1 + \widehat{\kappa}_{e,k}\right) s^2 + 2\zeta_{e,k}\omega_{e,k}s + \omega_{e,k}^2\right) \eta_{e,k} - s\widehat{\gamma}_{\mathbf{\Phi},rk}\eta_{sc,r} = 0 \end{cases}, \tag{3.40}$$

were the effective modal characteristics accounting for the background contributions of non-resonant mechanical and electrical modes are given by

$$\widehat{\omega}_{sc,r}^2 = \omega_{sc,r}^2 + \boldsymbol{\gamma}_{\boldsymbol{\Phi},r<k}\mathbf{S}^{-1}\boldsymbol{\gamma}_{\boldsymbol{\Phi},r<k}^T, \tag{3.41}$$

$$\widehat{\gamma}_{\boldsymbol{\Phi},rk} = \gamma_{\boldsymbol{\Phi},rk} - \boldsymbol{\gamma}_{\boldsymbol{\Phi},r<k}\mathbf{S}^{-1}\boldsymbol{\Gamma}_{\boldsymbol{\Phi},>r<k}^T\boldsymbol{\Omega}_{sc,>r}^{-2}\boldsymbol{\gamma}_{\boldsymbol{\Phi},>rk}, \tag{3.42}$$

and

$$\widehat{\kappa}_{e,k} = \boldsymbol{\gamma}_{\boldsymbol{\Phi},>rk}^T\left(\boldsymbol{\Omega}_{sc,>r}^{-2} - \boldsymbol{\Omega}_{sc,>r}^{-2}\boldsymbol{\Gamma}_{\boldsymbol{\Phi},>r<k}\mathbf{S}^{-1}\boldsymbol{\Gamma}_{\boldsymbol{\Phi},>r<k}^T\boldsymbol{\Omega}_{sc,>r}^{-2}\right)\boldsymbol{\gamma}_{\boldsymbol{\Phi},>rk}. \tag{3.43}$$

Since $\mathbf{S}$ is positive definite, so is its inverse, and $\widehat{\omega}_{sc,r} \geq \omega_{sc,r}$. It can be noted with the Sherman-Morrison-Woodbury (SMW) formula (Equation (A.2)) that

$$\boldsymbol{\Omega}_{sc,>r}^{-2} - \boldsymbol{\Omega}_{sc,>r}^{-2}\boldsymbol{\Gamma}_{\boldsymbol{\Phi},>r<k}\mathbf{S}^{-1}\boldsymbol{\Gamma}_{\boldsymbol{\Phi},>r<k}^T\boldsymbol{\Omega}_{sc,>r}^{-2} = \left(\boldsymbol{\Omega}_{sc,>r}^2 + \boldsymbol{\Gamma}_{\boldsymbol{\Phi},>r<k}\boldsymbol{\Gamma}_{\boldsymbol{\Phi},>r<k}^T\right)^{-1} \tag{3.44}$$

The right-hand side of this latter equation does not offer a computationally advantageous way of computing this matrix in general, but it shows that the matrix is positive definite. Hence, $\widehat{\kappa}_{e,k} \geq 0$.

From Equation (3.40), an EEMCF can be defined as

$$\widehat{K}_{c,rk}^2 = \frac{\widehat{\gamma}_{\boldsymbol{\Phi},rk}^2}{\left(1 + \widehat{\kappa}_{e,k}\right)\widehat{\omega}_{sc,r}^2}. \tag{3.45}$$

3.5 Design of an electrical network

The goal of this section is to find optimal electrical modal parameters for the network and to deduce its electrical capacitance, conductance and reluctance matrices from Equations (3.24) and (3.25). Similarly to what has been explained in Section 1.2 and Chapter 2, the natural frequencies of the network should be close to those of a targeted set of structural modes [151]. The choice of the electrical mode shapes is less straightforward. As explained in Section 1.2, it is desirable from a vibration reduction performance perspective to maximize the EEMCF. Any of its estimates (Equations (3.30), (3.34) and (3.45)) is maximized if the amplitude of the electrical mode shapes at the piezoelectric transducers are maximized themselves. Their amplitude is however limited by passivity constraints, as shall be seen.

3.5.1 Passivity

The passivity of the network is set as a design requirement in this work. Passive control has the advantage of guaranteeing the stability of the controlled system (because a passive system can only store or dissipate energy), and theoretically does not need external power sources for operation. It will be shown that this requirement places limits on the attainable modal characteristics, which in turn limits the performance of the passive control system. The electrical modal characteristics can be optimized under the passivity constraints, and these optimal characteristics can finally be used to synthesize the electrical network.

According to Gannett and Chua [107], the nodal admittance matrix given in Equation (3.15) must fulfill the conditions

(i) $\mathbf{Y}(s)$ has no poles in $\{s \in \mathbb{C} | \Re(s) > 0\}$ ($\Re$ denotes the real part operator),

(ii) $\mathbf{Y}(\sigma)$ is a real matrix for $\sigma \in \mathbb{R}^+$,

(iii) $\mathbf{Y}(s) + \mathbf{Y}^H(s)$ is positive semidefinite in $\{s \in \mathbb{C} | \Re(s) > 0\}$ (superscript H denotes Hermitian transposition),

(iv) The network associated to $\mathbf{Y}$ is controllable

in order to be the admittance matrix of a passive network (i.e., realizable using passive capacitors, resistors, inductors and ideal transformers). According to Equation (3.15), $\mathbf{Y}(s)$ has one simple pole at $s = 0$ (for a nonzero reluctance matrix), so Condition (i) is satisfied. Condition (ii) is satisfied since $\mathbf{C}$, $\mathbf{G}$ and $\mathbf{B}$ are real matrices. Condition (iv) is also verified, because all the electrical states are controllable and observable for an admittance matrix of the form of Equation (3.15). Now, since $\mathbf{C}$, $\mathbf{G}$ and $\mathbf{B}$ are also symmetric matrices, using Equation (3.15), Condition (iii) becomes

$$\mathbf{Y}(\sigma + j\omega) + \mathbf{Y}^H(\sigma + j\omega) = 2\sigma\mathbf{C} + 2\mathbf{G} + \frac{2\sigma}{\sigma^2 + \omega^2}\mathbf{B} \succeq 0, \tag{3.46}$$

where $\succeq 0$ indicates that the matrix is positive semidefinite. For $\sigma > 0$ and $\omega \in \mathbb{R}$, this matrix is positive semidefinite if $\mathbf{C}$, $\mathbf{G}$ and $\mathbf{B}$ are positive semidefinite themselves, which gives the criteria to satisfy Condition (iii). Because of Equations (3.24) and (3.25), the matrices $\mathbf{C}$, $\mathbf{G}$ and $\mathbf{B}$ are guaranteed to be positive semidefinite, which eventually ensures the passivity of the overall network.

Now, one must consider that the piezoelectric transducers are integrated into the overall network associated with the matrix $\mathbf{C}$. The capacitance matrix $\mathbf{C}_e$ of the interconnecting network is obtained by removing the contribution of the piezoelectric capacitance from $\mathbf{C}$, as indicated by Equation (3.22). Thus, if $\mathbf{C}_e$ is the capacitance matrix of a passive interconnecting network, it must satisfy

$$\mathbf{C}_e = \mathbf{C} - \mathbf{E}_p \mathbf{C}_p^\varepsilon \mathbf{E}_p^T \succeq 0. \tag{3.47}$$

A positive semidefinite matrix has positive eigenvalues, and a necessary (but not sufficient) condition for this is that the determinant of this matrix (being equal to the product of the eigenvalues) must be positive. This determinant is given by

$$\det\left(\mathbf{C} - \mathbf{E}_p \mathbf{C}_p^\varepsilon \mathbf{E}_p^T\right) = \det\left(\left(\mathbf{C}_p^\varepsilon\right)^{-1} - \mathbf{E}_p^T \mathbf{C}^{-1} \mathbf{E}_p\right) \det\left(\mathbf{C}\right) \det\left(\mathbf{C}_p^\varepsilon\right), \tag{3.48}$$

where Equation (A.4) has been used. Since both $\mathbf{C}$ and $\mathbf{C}_p^\varepsilon$ are positive definite, a necessary condition for the positive semidefiniteness of $\mathbf{C}_e$ is thus

$$\left(\mathbf{C}_p^\varepsilon\right)^{-1} - \mathbf{E}_p^T \mathbf{\Phi}_e \mathbf{\Phi}_e^T \mathbf{E}_p \succeq 0, \tag{3.49}$$

in which the identity $\mathbf{C}^{-1} = \mathbf{\Phi}_e \mathbf{\Phi}_e^T$ (inferred from Equation (3.24)) has been used. If the modal amplitudes $\mathbf{\Phi}_e^T \mathbf{E}_p$ are initially zero, this condition will be satisfied because $\mathbf{C}_p^\varepsilon$ is itself positive definite. Increasing gradually these modal amplitudes will affect continuously the eigenvalues of the matrix in Equation (3.49), up to the point where one of them reaches zero. Increasing the amplitudes beyond this point, the matrix will no longer be positive semidefinite, and the interconnecting network will no longer be passive.

3.5.2 Optimal electrical mode shapes

Equation (3.49) constrains the amplitude of the electrical mode shapes but leaves freedom on their actual shape. However, some choices yield better electromechanical coupling factors than others. The purpose of this subsection is to provide an expression for the set of electrical mode shapes maximizing the modal electromechanical coupling coefficients. Since at this stage the mode shapes are unknown, the dynamics are approximated considering only the background contribution from non-resonant mechanical modes (Section 3.4.3.2).

3.5.2.1 Optimization for a single mode

It is first considered that the network targets a single mode of the structure. To simplify the exposition, the electrical mode shape at the piezoelectric transducers is made dimensionless by the transformation

$$\boldsymbol{\varphi}_p = \left(\mathbf{C}_p^{\varepsilon}\right)^{1/2} \mathbf{E}_p^T \boldsymbol{\phi}_e = \left(\mathbf{C}_p^{\varepsilon}\right)^{1/2} \boldsymbol{\phi}_p. \tag{3.50}$$

Inserting this relation into Equation (3.49) yields

$$\left(\mathbf{C}_p^{\varepsilon}\right)^{-1} - \left(\mathbf{C}_p^{\varepsilon}\right)^{-1/2} \boldsymbol{\varphi}_p \boldsymbol{\varphi}_p^T \left(\mathbf{C}_p^{\varepsilon}\right)^{-1/2} \succeq 0. \tag{3.51}$$

Since this constitutes a rank-one update of the piezoelectric elastance matrix, Equation (A.3) can be used to compute its determinant.

$$\det\left(\left(\mathbf{C}_p^{\varepsilon}\right)^{-1} - \left(\mathbf{C}_p^{\varepsilon}\right)^{-1/2} \boldsymbol{\varphi}_p \boldsymbol{\varphi}_p^T \left(\mathbf{C}_p^{\varepsilon}\right)^{-1/2}\right) = \left(1 - \boldsymbol{\varphi}_p^T \boldsymbol{\varphi}_p\right) \det\left(\left(\mathbf{C}_p^{\varepsilon}\right)^{-1}\right). \tag{3.52}$$

A necessary condition for passivity requires this determinant to be positive. Equation (3.51) is therefore satisfied if the dimensionless mode shape satisfies

$$|\boldsymbol{\varphi}_p| \leq 1. \tag{3.53}$$

The contribution from non-resonant mechanical modes is first neglected, and the EEMCF defined in Equation (3.30) is used. The EEMCF is maximized if the quantity squared in the numerator is itself maximized, leading to the following constrained optimization problem

$$\begin{aligned} &\underset{\boldsymbol{\varphi}_p}{\text{Maximize}} \quad \boldsymbol{\phi}_{sc,r}^T \boldsymbol{\Gamma}_p \left(\mathbf{C}_p^{\varepsilon}\right)^{-1/2} \boldsymbol{\varphi}_p \\ &\text{Subject to} \quad \boldsymbol{\varphi}_p^T \boldsymbol{\varphi}_p \leq 1 \end{aligned}. \tag{3.54}$$

Since the objective function is a linear function of $\boldsymbol{\varphi}_p$, its gradient is constant. A solution which maximizes this objective function should thus be aligned with this gradient, yielding

$$\boldsymbol{\varphi}_p^{\star} = \alpha_p \left(\mathbf{C}_p^{\varepsilon}\right)^{-1/2} \boldsymbol{\Gamma}_p^T \boldsymbol{\phi}_{sc,r}, \tag{3.55}$$

where α_p should be set so as to respect the constraint. The admissible solution to this optimization problem can be found as

$$\boldsymbol{\varphi}_p^{\star} = \frac{1}{\sqrt{\boldsymbol{\phi}_{sc,r}^T \boldsymbol{\Gamma}_p \left(\mathbf{C}_p^{\varepsilon}\right)^{-1} \boldsymbol{\Gamma}_p^T \boldsymbol{\phi}_{sc,r}}} \left(\mathbf{C}_p^{\varepsilon}\right)^{-1/2} \boldsymbol{\Gamma}_p^T \boldsymbol{\phi}_{sc,r}, \tag{3.56}$$

and the associated optimal capacitance-normalized mode shape at the piezoelectric transducers is retrieved with Equation (3.50) as

$$\boldsymbol{\Phi}_p^\star = \frac{1}{\sqrt{\boldsymbol{\Phi}_{sc,r}^T \boldsymbol{\Gamma}_p \left(\mathbf{C}_p^\varepsilon\right)^{-1} \boldsymbol{\Gamma}_p^T \boldsymbol{\Phi}_{sc,r}}} \left(\mathbf{C}_p^\varepsilon\right)^{-1} \boldsymbol{\Gamma}_p^T \boldsymbol{\Phi}_{sc,r}. \tag{3.57}$$

It is possible to account for the background contribution of non-resonant mechanical modes to further optimize the mode shapes by considering Equation (3.34) instead of Equation (3.30). The problem is much more complex and an approximate solution is developed in Section D.2.

3.5.2.2 Optimization for multiple modes

In order for the network to mitigate N_s structural resonances, it is assumed that the dimensionless electrical mode shapes are simply scaled versions of their optimal counterparts in the single-mode case, i.e.,

$$\overline{\boldsymbol{\Phi}}_p = \begin{bmatrix} \boldsymbol{\varphi}_{p,1} & \cdots & \boldsymbol{\varphi}_{p,N_s} \end{bmatrix} = \overline{\boldsymbol{\Phi}}_p^\star \mathbf{D}_p = \begin{bmatrix} \boldsymbol{\varphi}_{p,1}^\star & \cdots & \boldsymbol{\varphi}_{p,N_s}^\star \end{bmatrix} \begin{bmatrix} d_{p,1} & & \\ & \ddots & \\ & & d_{p,N_s} \end{bmatrix}, \tag{3.58}$$

where $d_{p,k}$ is the positive scaling factor associated to electrical mode k. In order to satisfy the passivity constraints (Equation (3.49)), these scaling factors must be chosen such that

$$\mathbf{I} - \overline{\boldsymbol{\Phi}}_p^\star \mathbf{D}_p^2 \left(\overline{\boldsymbol{\Phi}}_p^\star\right)^T \succeq 0. \tag{3.59}$$

To determine them, a set of positive relative scaling factors $\overline{d}_{p,k}$ can be chosen arbitrarily. Their magnitude does not matter, but their relative magnitude can be set so as to put more control authority on specific modes at the expense of control authority on other modes. The actual scaling factors are obtained by multiplication by a scalar factor α_p

$$\mathbf{D}_p = \alpha_p \begin{bmatrix} \overline{d}_{p,1} & & \\ & \ddots & \\ & & \overline{d}_{p,N_s} \end{bmatrix} = \alpha_p \overline{\mathbf{D}}_p, \tag{3.60}$$

which can be determined to enforce the passivity constraints. From Equation (3.59), it should satisfy

$$\alpha_p \leq \frac{1}{\sqrt{\lambda_{Max}\left(\overline{\boldsymbol{\Phi}}_p^\star \overline{\mathbf{D}}_p^2 \left(\overline{\boldsymbol{\Phi}}_p^\star\right)^T\right)}}, \tag{3.61}$$

where $\lambda_{Max}(\cdot)$ is the maximum eigenvalue of the matrix at hand. The capacitance-normalized mode shapes at the piezoelectric transducers can finally be retrieved as

$$\boldsymbol{\Phi}_p = \left(\mathbf{C}_p^{\varepsilon}\right)^{-1/2} \overline{\boldsymbol{\Phi}}_p = \alpha_p \left(\mathbf{C}_p^{\varepsilon}\right)^{-1/2} \overline{\boldsymbol{\Phi}}_p^{\star} \overline{\mathbf{D}}_p. \tag{3.62}$$

The mode shapes obtained this way are proportional to α_p. Equation (3.34) shows that the EEMCF is a growing function of α_p. Hence, the inequality in Equation (3.61) should ideally be an equality to maximize the amplitude of the electrical modes at the piezoelectric transducers and thus the coupling.

It should be pointed out that if the piezoelectric patches are all identical, $\mathbf{C}_p^{\varepsilon}$ is proportional to the identity matrix. $\boldsymbol{\Gamma}_p^T \boldsymbol{\Phi}_{sc}$ can be seen as modal strains in the transducers, and the electrical mode shapes $\boldsymbol{\Phi}_p$ are proportional to them, according to Equation (3.57) in this case. Hence, the network is an analog of the structure, because it features identical resonance frequencies and mode shapes, as in [123] (but the scaling factors make the electrical mode shapes in Equation (3.62) a scaled version of their mechanical counterparts).

3.5.3 Optimal electrical frequencies and damping ratios

In order to fully specify the characteristics of the network, its natural frequencies and associated damping ratios should also be prescribed. The electrical mode shapes are now known, and the model in Section 3.4.3.3 can be used. The modal characteristics can simply be tuned by using Equations (1.45) and (1.46) with the characteristics of the system in Equation (3.40), i.e., by replacing C_p^{ε} by $1 + \widehat{\kappa}_{e,k}$, ω_{sc} by $\widehat{\omega}_{sc,r}$, K_c by $\widehat{K}_{c,rk}$, B by $\omega_{e,k}^2$ and G by $2\zeta_{e,k}\omega_{e,k}$. The optimal effective frequency and damping ratio for electrical mode k are thus given by

$$\omega_{e,k}^2 = \nu^2\left(\widehat{K}_{c,rk}\right)\widehat{\omega}_{sc,r}^2\left(1+\widehat{\kappa}_{e,k}\right), \qquad \zeta_{e,k} = \varsigma\left(\widehat{K}_{c,rk}\right)\left(1+\widehat{\kappa}_{e,k}\right), \tag{3.63}$$

respectively.

3.5.4 Network synthesis

Now that all the modal characteristics are specified, the capacitance, conductance and reluctance matrices of the network can be computed so as to satisfy Equations (3.24) and (3.25). Depending on the number of transducers P compared to the number of targeted modes N_s, different cases must be considered. More rigorously and generally, these cases can be discriminated by comparing the rank of $\boldsymbol{\Phi}_p$ to N_s and P.

3.5.4.1 Full-rank Φ_p

The case $P = N_s$ with full-rank $\boldsymbol{\Phi}_p$ is the simplest, because the matrix $\boldsymbol{\Phi}_e = \boldsymbol{\Phi}_p$ is square and non-singular. The electrical matrices can then be obtained from the inversion of Equations (3.24) and (3.25)

$$\mathbf{C} = \boldsymbol{\Phi}_e^{-T}\boldsymbol{\Phi}_e^{-1}, \qquad \mathbf{G} = 2\boldsymbol{\Phi}_e^{-T}\mathbf{Z}_e\boldsymbol{\Omega}_e\boldsymbol{\Phi}_e^{-1}, \qquad \mathbf{B} = \boldsymbol{\Phi}_e^{-T}\boldsymbol{\Omega}_e^2\boldsymbol{\Phi}_e^{-1}. \tag{3.64}$$

3.5.4.2 $\mathbf{rank}\,(\boldsymbol{\Phi}_p) < N_s$

If $P < N_s$, there are less transducers than targeted structural modes, and the matrix $\boldsymbol{\Phi}_p$ has more columns than rows. It could also be that $P \geq N_s$ but $\boldsymbol{\Phi}_p$ is rank-deficient. In both cases, this mathematically translates to $\text{rank}\,(\boldsymbol{\Phi}_p) < N_s$, and internal DoFs $\boldsymbol{\psi}_i$ should be introduced. The minimal number of internal DoFs required to make the problem well-posed is $I = N_s - \text{rank}\,(\boldsymbol{\Phi}_p)$. The mode shapes on these DoFs $\boldsymbol{\Phi}_i$ should be specified in order to obtain a mode shape matrix of rank N_s

$$\boldsymbol{\Phi}_e = \begin{bmatrix} \boldsymbol{\Phi}_p \\ \boldsymbol{\Phi}_i \end{bmatrix}, \tag{3.65}$$

and the electrical matrices can then be obtained with Equation (3.64). As long as the electrical mode shape matrix is non-singular, the mode shapes on the internal DoFs can be chosen arbitrarily without affecting the performance of the network. A practical choice to ensure the non-singularity of the mode shape matrix could be to chose $\boldsymbol{\Phi}_i = \mathbf{W}^T$, where $\mathbf{W}$ contains the orthogonal basis of the kernel of $\boldsymbol{\Phi}_p$, i.e.,

$$\boldsymbol{\Phi}_p \mathbf{W} = \mathbf{0}, \qquad \mathbf{W}^T \mathbf{W} = \mathbf{I}. \tag{3.66}$$

If $\text{rank}\,(\boldsymbol{\Phi}_p) = P$, Equation (3.64) can be used to synthesize the electrical matrices.

3.5.4.3 $\mathbf{rank}\,(\boldsymbol{\Phi}_p) < P$

If $P > N_s$, there are more transducers than targeted structural modes, and the matrix $\boldsymbol{\Phi}_e = \boldsymbol{\Phi}_p$ has more rows than columns. More generally, the rank of $\boldsymbol{\Phi}_e$ may be smaller than P. Compliance with Equations (3.24) and (3.25) leads to an underconstrained problem. This leaves some freedom on the choice of the other electrical mode shapes of the network, but the passivity constraint (Equation (3.49)) still has to be satisfied. A simple way to enforce Equations (3.24) and (3.25) is to choose

$$\mathbf{C} = \boldsymbol{\Phi}_e \left(\boldsymbol{\Phi}_e^T \boldsymbol{\Phi}_e\right)^{-2} \boldsymbol{\Phi}_e^T + \mathbf{V}\mathbf{D}_V\mathbf{V}^T, \qquad \mathbf{G} = \boldsymbol{\Phi}_e \left(\boldsymbol{\Phi}_e^T \boldsymbol{\Phi}_e\right)^{-1} 2\mathbf{Z}_e\boldsymbol{\Omega}_e \left(\boldsymbol{\Phi}_e^T \boldsymbol{\Phi}_e\right)^{-1} \boldsymbol{\Phi}_e^T,$$
$$\mathbf{B} = \boldsymbol{\Phi}_e \left(\boldsymbol{\Phi}_e^T \boldsymbol{\Phi}_e\right)^{-1} \boldsymbol{\Omega}_e^2 \left(\boldsymbol{\Phi}_e^T \boldsymbol{\Phi}_e\right)^{-1} \boldsymbol{\Phi}_e^T, \tag{3.67}$$

having ensured $\text{rank}\,(\boldsymbol{\Phi}_e) = N_s$ for $\boldsymbol{\Phi}_e^T\boldsymbol{\Phi}_e$ to be regular (see Section 3.5.4.2). $\mathbf{D}_V$ is symmetric positive definite matrix, and $\mathbf{V}$ contains the orthogonal basis of the kernel of $\boldsymbol{\Phi}_e^T$, i.e.,

$$\boldsymbol{\Phi}_e^T \mathbf{V} = \mathbf{0}, \qquad \mathbf{V}^T\mathbf{V} = \mathbf{I}. \tag{3.68}$$

$\mathbf{D}_V$ does not affect the electromechanical coupling with the targeted modes, but has to be chosen such that Equation (3.47) is satisfied. The projection of this equation on the subspace spanned by $\boldsymbol{\Phi}_e$ satisfies the equation, and that on $\mathbf{V}$ yields the condition

$$\mathbf{D}_V - \mathbf{V}^T\mathbf{E}_p\mathbf{C}_p^{\varepsilon}\mathbf{E}_p^T\mathbf{V} \succeq 0. \tag{3.69}$$

The choice of $\mathbf{D}_V$ to satisfy this condition is not unique. In an attempt to reduce the number of electrical components needed for the network, one can try to make the

capacitance matrix $\mathbf{C}$ as close as possible to the piezoelectric capacitance matrix $\mathbf{E}_p\mathbf{C}_p^{\varepsilon}\mathbf{E}_p^T$. Imposing an equality of these matrices in the subspace spanned by $\mathbf{V}$ yields

$$\mathbf{V}^T\mathbf{E}_p\mathbf{C}_p^{\varepsilon}\mathbf{E}_p^T\mathbf{V} = \mathbf{V}^T\mathbf{C}\mathbf{V} = \mathbf{V}^T\mathbf{V}\mathbf{D}_V\mathbf{V}^T\mathbf{V} = \mathbf{D}_V, \tag{3.70}$$

on account of Equations (3.67) and (3.68). This choice of $\mathbf{D}_V$ satisfies Equation (3.69), since the involved matrix is $\mathbf{0}$.

In this case, the network has N_s resonant electrical modes, and $P - N_s$ purely capacitively-dominated modes, given by

$$\mathbf{V}\mathbf{D}_V^{1/2}, \tag{3.71}$$

which satisfy the generalized eigenvalue problem in Equation (3.23) (accounting for Equations (3.67) and (3.68)), with zero electrical resonance frequencies.

3.5.5 Summary of the modal-based synthesis

The proposed design procedure is summarized in Figure 3.3: from a set of targeted modes and associated scaling factors reflecting the desired control authority on these modes, the electrical matrices of the network can be obtained. Given the central role played by modal properties in this approach, it is named modal-based synthesis.

It is noted that unlike in Chapter 2, the order in which the resonant frequencies of the network are assigned is not important, because the influence of inductively-dominated modes has been neglected in this chapter.

3.5.6 Implications of passivity on performance

To close this section, guidelines on choosing the relative scaling factors are given, and the impact of passivity on performance is discussed.

3.5.6.1 Scaling factors and modes orthogonality

Using Equation (A.4), Equation (3.59) can also be put in the form

$$\mathbf{D}_p^{-2} - \left(\overline{\mathbf{\Phi}}_p^{\star}\right)^T \overline{\mathbf{\Phi}}_p^{\star} \succeq 0. \tag{3.72}$$

Since the optimal dimensionless mode shapes are unit vectors, the elements on the diagonal of the matrix $\left(\overline{\mathbf{\Phi}}_p^{\star}\right)^T \overline{\mathbf{\Phi}}_p^{\star}$ are equal to one. If these vectors are mutually orthogonal, this matrix is equal to the identity, and in this case

$$\mathbf{D}_p^{-2} - \mathbf{I} \succeq 0. \tag{3.73}$$

The elements on the diagonal of $\mathbf{D}_p$ can be chosen independently and should be smaller than or equal to one. The optimal case is when $\mathbf{D}_p$ is set equal to the identity to comply with Equation (3.72). As soon as the dimensionless mode shapes are not mutually orthogonal, the elements on the diagonal of $\mathbf{D}_p$ have to be smaller than one. Indeed, if $\mathbf{D}_p = \mathbf{I}$, the matrix in Equation (3.72) would have zero elements on its diagonal but

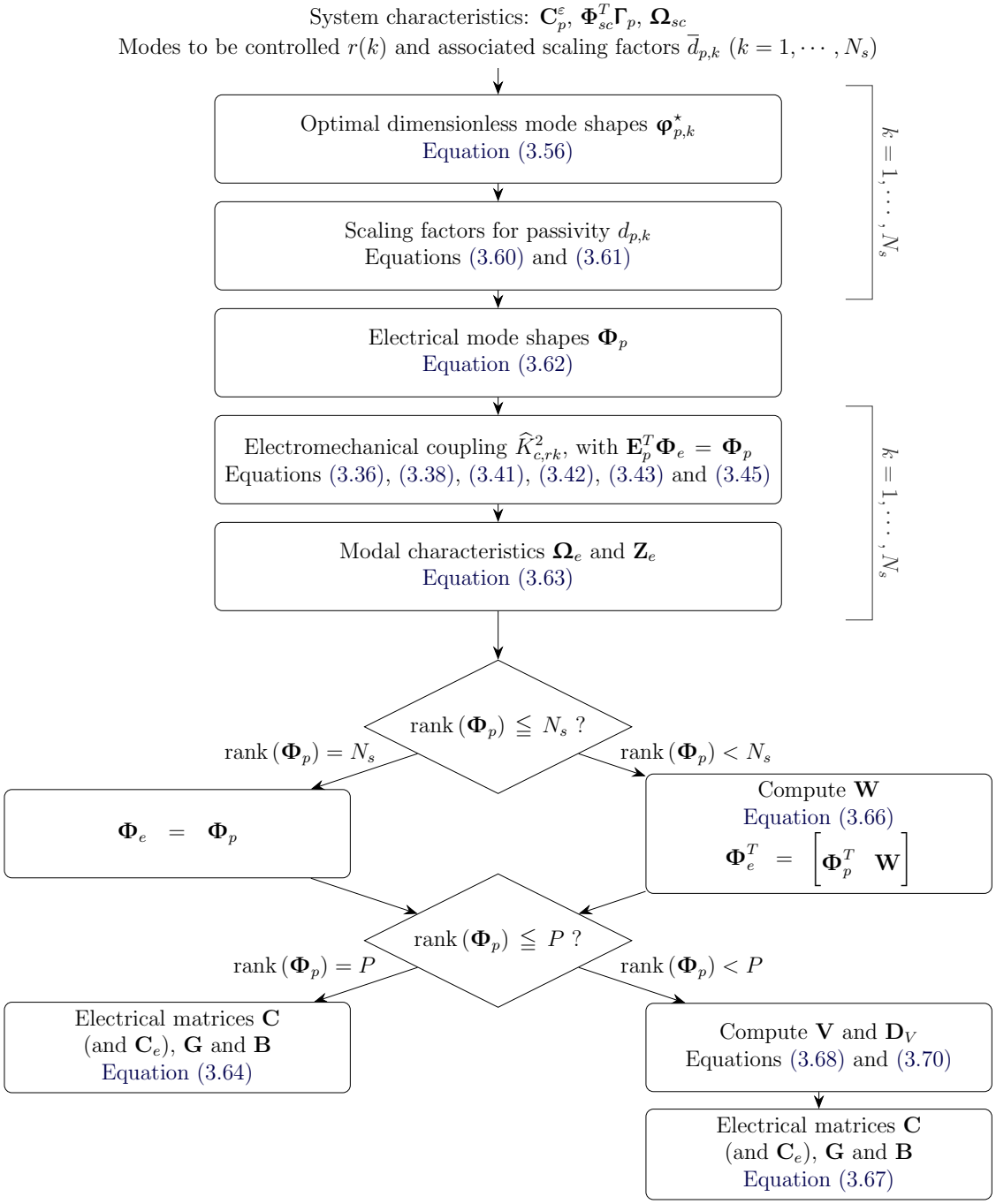

Figure 3.3: Flowchart of the proposed modal-based synthesis.

non-zero off-diagonal elements. Hence, some of its principal minors would be negative, which means that the matrix is not positive semidefinite [161].

The other limit case is when the mode shapes are all aligned. In this case, Equation (3.72) becomes[1]

$$\mathbf{D}_p^{-2} - \mathbf{1}_{N_s \times N_s} = \mathbf{D}_p^{-2} - \mathbf{1}_{N_s \times 1}\mathbf{1}_{1 \times N_s} \succeq 0. \tag{3.74}$$

[1]If some mode shapes are antiparallel, their opposite can be considered without loss of generality, such that the scalar product between all of them is equal to one.

Using once again Equation (A.3), this condition is satisfied if

$$1 - \mathbf{1}_{1\times N_s}\mathbf{D}_p^2\mathbf{1}_{N_s\times 1} = 1 - \sum_{k=1}^{N_s} d_{p,k}^2 \geq 0, \tag{3.75}$$

i.e.

$$\sum_{k=1}^{N_s} d_{p,k}^2 \leq 1 \tag{3.76}$$

This time, the *sum* of the scaling coefficients squared is constrained to be smaller than one. We note the similarity between this equation and Equation (2.34). Indeed, the squared scaling coefficients $d_{p,k}^2$ in this chapter play the same role as the residues r_k in Chapter 2, i.e., they determine the EEMCF that the circuit or network has with the target mode. One notable difference can nonetheless be observed between networks and shunt circuits. Passivity constrains the *sum* of the residues to be at most equal to one for shunt circuits in all cases (Equation (2.34)), whereas for networks each of the scaling factor can reach one *simultaneously*, provided the dimensionless optimal mode shapes are mutually orthogonal, but this constraint can become identical to that on shunt circuits if the modes shapes are aligned. Therefore, networks are expected to be able to exhibit better (and in the worst case identical) performance than shunt circuits. This nonetheless comes at the expense of more complex electrical interconnections.

Selecting relative scaling factors as proposed in Section 3.5.2.2 is not a trivial task, and the optimality of a given choice depends on the orthogonality between the modes. A safe choice is to pick equal relative scaling factors in general, i.e., $\overline{d}_{p,k} = 1$, $k = 1, \cdots, N_s$. The relation between modes orthogonality and scaling factors optimality is discussed more in depth in Section D.3 with a simple example.

3.5.6.2 Coupling limit for passive networks

Performance limits in terms of attainable EEMCF with the network are demonstrated in Section D.4. To summarize the results in this appendix, an electrical network can perform at best equally to a case where all the patches are shunted to target a specific mode, when the scaling factor associated to that mode is equal to one. This feature is similar to what was derived for the shunt circuits (Sections 2.3.1.6 and 2.3.2.6). Furthermore, when the best case of orthogonal optimal electrical mode shapes occurs, this performance can be reached simultaneously on every targeted mode.

The patches location could be designed to enhance performance of passive networks through the tailoring of $\mathbf{\Phi}_p^\star$. However, this problem would not be simple, because these electrical modes have a non-trivial dependency on $\mathbf{\Phi}_{sc}$, $\mathbf{\Gamma}_p$ and $\mathbf{C}_p^\varepsilon$. Among these characteristics, $\mathbf{\Phi}_{sc}$ itself has a rather intricate dependency on the size and placement of the piezoelectric patches. To find out the solution of such problem, the optimization approach proposed in [158] could be a good candidate.

3.6 Examples

The modal-based synthesis is illustrated with three examples: a SDoF structure, a free-free beam and a fully clamped plate. The SDoF example is used to gain

intuition about the method. The free-free beam outlines the main aspects of the method concerning multimodal vibration mitigation and discusses the influence of the scaling factors. A comparison with an assembled analog network [153, 155] is also made. Finally, the fully clamped plate example illustrates the method with a structure featuring rather closely-spaced resonance frequencies, and reveals the importance of accounting for background contributions of non-resonant modes. The modal-based synthesis is also compared to the method in [158].

3.6.1 Single-degree-of-freedom structure

This illustrates simply the connection between the electrical mode amplitude, performance and passivity. The system is governed by Equation (1.6). The mass-normalized mechanical mode shape for this system is

$$\phi_{sc} = \frac{1}{\sqrt{m}}. \tag{3.77}$$

Since there is only a pair of mechanical and electrical modes, there is no background contribution to be accounted for. The direct application of Equation (3.57) yields the optimal electrical mode shape

$$\phi_p^\star = \frac{1}{\sqrt{\phi_{sc}\gamma_p \dfrac{1}{C_p^\varepsilon}\gamma_p\phi_{sc}}} \frac{1}{C_p^\varepsilon}\gamma_p\phi_{sc} = \frac{1}{\sqrt{C_p^\varepsilon}}. \tag{3.78}$$

The actual electrical mode shape can be set with a given amplitude α_p

$$\phi_p = \alpha_p \phi_p^\star \tag{3.79}$$

The passivity condition (Equation (3.49)) becomes

$$\frac{1}{C_p^\varepsilon} - \alpha_p^2 \left(\phi_p^\star\right)^2 = \frac{1}{C_p^\varepsilon}\left(1 - \alpha_p^2\right) \geq 0, \tag{3.80}$$

i.e., $\alpha_p \leq 1$ guarantees passivity. The EEMCF can be computed using Equation (3.45)

$$\widehat{K}_c^2 = \frac{\alpha_p^2\gamma_p^2 m}{C_p^\varepsilon \omega_{sc}^2} = \alpha_p^2 K_c^2. \tag{3.81}$$

Combining Equations (3.63) and (3.64), the electrical parameters (which are equal to the electrical matrices) are given by

$$C = \frac{C_p^\varepsilon}{\alpha_p^2}, \qquad G = 2\varsigma\left(\widehat{K}_c\right)\nu\left(\widehat{K}_c\right)\omega_{sc}\frac{C_p^\varepsilon}{\alpha_p^2}, \qquad B = \nu^2\left(\widehat{K}_c\right)\omega_{sc}^2\frac{C_p^\varepsilon}{\alpha_p^2}. \tag{3.82}$$

The capacitance matrix of the interconnecting network, which simply gives the capacitance of a capacitor placed in parallel with the shunt, is given by

$$C_e = C - C_p^\varepsilon = \frac{1-\alpha_p^2}{\alpha_p^2} C_p^\varepsilon. \tag{3.83}$$

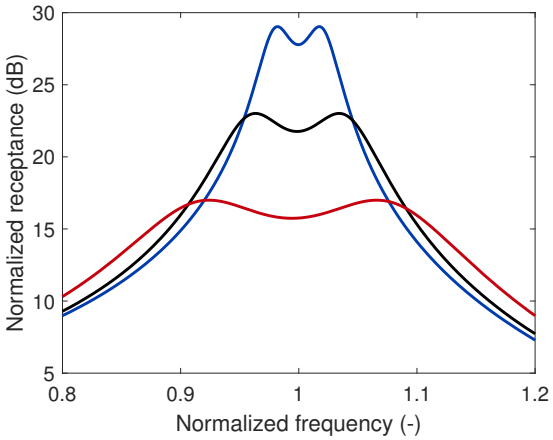

Figure 3.4: Application of the method to a SDoF case ($K_c = 0.1$) with a parallel RLC circuit: $\alpha_p = 0.5$ (—), $\alpha_p = 1$/parallel RL shunt (—) and $\alpha_p = 2$ (—). The receptance is normalized by k_{sc}, and the frequency is normalized by ω_{sc}.

Several cases can be discriminated depending on the value of α_p, and examples of the receptance for each case are featured in Figure 3.4. Because the method does not make any approximation in this case, two peaks of exact equal amplitude are observed in each case.

When $\alpha_p < 1$, the passivity condition is fulfilled, the capacitance C_e is positive and thus the circuit is realizable with passive electrical components. The amplitude of the electrical mode shape is suboptimal, the EEMCF is decreased and so is the vibration reduction. This is in accordance with common knowledge about the detrimental effect of a parallel capacitor on performance [85, 129, 133].

For $\alpha_p = 1$, the passivity condition is at its boundary, and C_e vanishes. The circuit is still realizable with passive elements; this is actually the classical parallel RL shunt case discussed in Section 1.2.

Cases with $\alpha_p > 1$ violate the passivity condition, and indeed a negative capacitance C_e is needed. The EEMCF is boosted by this negative capacitance, which is one of the driving motivation for using such active electrical elements [77, 89, 118].

3.6.2 Free-free beam

The free-free beam in [155] is used to demonstrate other features of the modal-based approach and to compare it to methods based on electrical analogs. The beam is composed of 20 identical cells where a pair of thin piezoelectric patches symmetrically bonded to the structure and electrically connected in parallel, as shown in Figure 3.5, can be used to damp the vibrations of the beam. The beam was modeled using the finite element method [137] with ten elements per cell. This yielded the matrices $\mathbf{M}$, $\mathbf{K}_{sc}$ and $\mathbf{\Gamma}_p$.

3.6.2.1 Damping of the first four modes

A network targeting the first four flexible modes of the beam was synthesized with the modal-based method described in Figure 3.3, choosing unit scaling factors for each mode ($\overline{d}_{p,k} = 1$, $k = 1, 2, 3, 4$). The FRF of the beam transversely excited at one end and whose transverse displacement is measured at the other end is shown

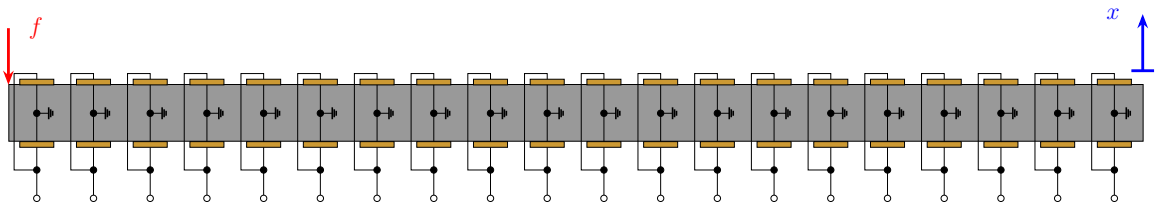

Figure 3.5: Schematic representation of a free-free beam (in gray) with twenty piezoelectric patches (in orange) connected in parallel by pairs.

in Figure 3.6. It is observed that the electrical network can very effectively damp out the resonant vibrations of the four targeted modes.

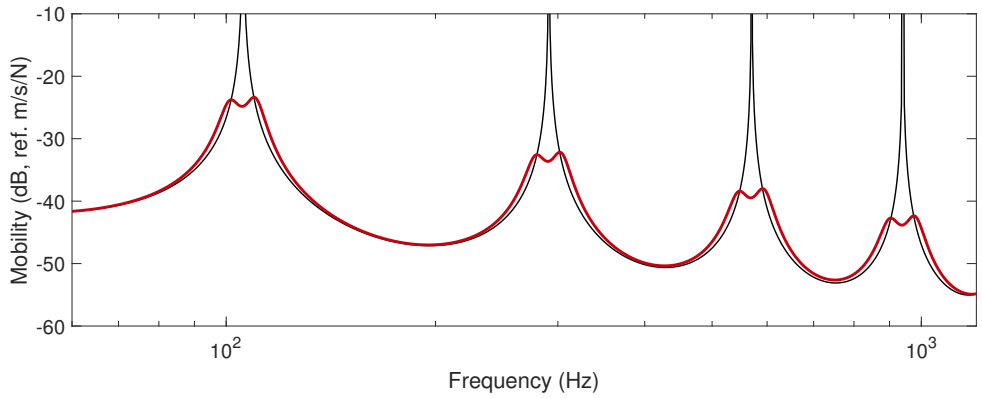

Figure 3.6: Velocity FRF of the beam with short-circuited patches (—), with the network synthesized with the modal-based approach (—).

3.6.2.2 Relative scaling factors

The influence of the relative scaling factors can also be studied. To make things easier to understand, the piezoelectric structure is simplified by grouping the 20 patches into two groups of ten adjacent patches and connecting the groups in parallel. A first network can be synthesized with unit relative scaling factors ($\overline{d}_{p,k} = 1,\ k = 1,2,3,4$). The resulting FRF is shown in Figure 3.7. Compared to Figure 3.6, the parallel connection of the patches has reduced the control authority of the network, especially on mode 4. This can be understood by the fact that the parallel connection of the patches makes this mode almost unobservable and uncontrollable because of charge cancellation. This baseline case is compared in Figure 3.8 to every other investigated case studied hereafter in terms of attenuation on each mode.

In an attempt to improve the control authority over mode 1, one may set $\overline{d}_{p,1} = 2$ while leaving the other relative scaling factors unchanged. In doing so, Figure 3.7 shows that the vibration reduction on mode 1 can be improved by 2dB, but this is done at the expense of vibration reduction on the other modes (by approximately 4dB for all of them). Thus, the relative scaling factors can be used to favor vibration mitigation over some modes, as expected. The vibration reduction improvement on mode 1 can be maximized if mode 3 is left uncontrolled. In this case, a further 1dB can be obtained on mode 1.

In addition to improving performance on mode 1, mode 2 can also be emphasized by choosing $\overline{d}_{p,1} = \overline{d}_{p,2} = 2$ while leaving the other relative scaling factors equal to one. In

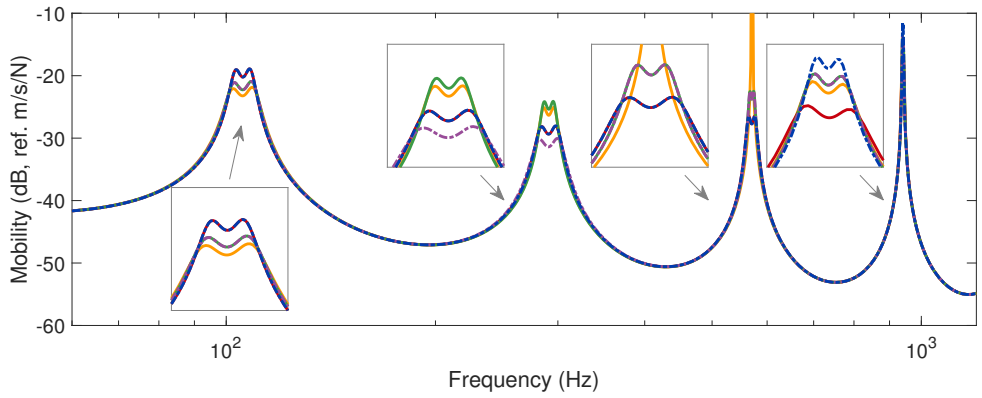

Figure 3.7: Velocity FRF of the beam with grouped patches connected to a network synthesized with the modal-based approach: $[\overline{d}_{p,1}, \overline{d}_{p,2}, \overline{d}_{p,3}, \overline{d}_{p,4}] = [1,1,1,1]$ (—), $[\overline{d}_{p,1}, \overline{d}_{p,2}, \overline{d}_{p,3}, \overline{d}_{p,4}] = [2,1,1,1]$ (—), $[\overline{d}_{p,1}, \overline{d}_{p,2}, \overline{d}_{p,3}, \overline{d}_{p,4}] = [2,1,0,1]$ (—), $[\overline{d}_{p,1}, \overline{d}_{p,2}, \overline{d}_{p,3}, \overline{d}_{p,4}] = [2,2,1,1]$ (- - -) and $[\overline{d}_{p,1}, \overline{d}_{p,2}, \overline{d}_{p,3}, \overline{d}_{p,4}] = [2,2,2,1]$ (- - -).

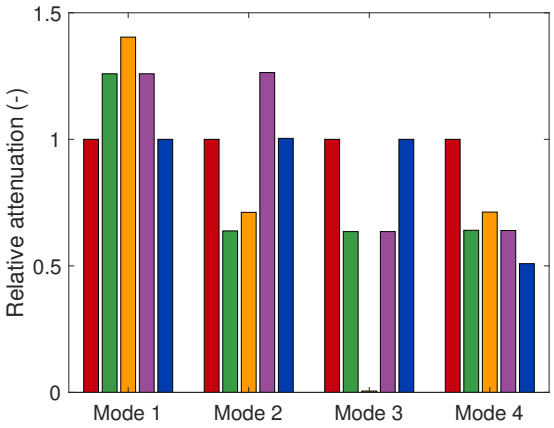

Figure 3.8: Relative attenuation (compared to the baseline case) on each mode: $[\overline{d}_{p,1}, \overline{d}_{p,2}, \overline{d}_{p,3}, \overline{d}_{p,4}] = [1,1,1,1]$ (■), $[\overline{d}_{p,1}, \overline{d}_{p,2}, \overline{d}_{p,3}, \overline{d}_{p,4}] = [2,1,1,1]$ (■), $[\overline{d}_{p,1}, \overline{d}_{p,2}, \overline{d}_{p,3}, \overline{d}_{p,4}] = [2,1,0,1]$ (■), $[\overline{d}_{p,1}, \overline{d}_{p,2}, \overline{d}_{p,3}, \overline{d}_{p,4}] = [2,2,1,1]$ (■) and $[\overline{d}_{p,1}, \overline{d}_{p,2}, \overline{d}_{p,3}, \overline{d}_{p,4}] = [2,2,2,1]$ (■).

this case, Figure 3.7 indicates that the vibration reduction on mode 2 can be improved without affecting the performance on other modes. While this might seem in contradiction with the previous observation, this result can be understood by looking at the modal assurance criterion of the optimal dimensionless electrical mode shapes $\left|\left(\overline{\boldsymbol{\Phi}}_p^{\star}\right)^T \overline{\boldsymbol{\Phi}}_p^{\star}\right|^2$ (auto MAC), indicating how correlated these modes are [157]. The dimensionless mode shapes and auto MAC matrix are featured in Figure 3.9, which clearly shows that modes are similar by pairs, as viewed by the connected patches: mode 1 is similar to mode 3 and mode 2 is similar to mode 4. These mode pairs are also orthogonal to each other. Thus, the scaling factors $\overline{d}_{p,1}$ and $\overline{d}_{p,2}$ affect orthogonal directions and thus different eigenvalues of $\overline{\boldsymbol{\Phi}}_p^{\star}\overline{\mathbf{D}}_p^2\left(\overline{\boldsymbol{\Phi}}_p^{\star}\right)^T$. When $\overline{d}_{p,2}$ was equal to one, the largest eigenvalue was the one associated to $\overline{d}_{p,1}$. Increasing $\overline{d}_{p,2}$ up to two does not change this fact, and according to Equation (3.61) α_p stays identical, and so do $d_{p,1}$, $d_{p,3}$ and $d_{p,4}$, while $d_{p,2}$ increases (because $\overline{d}_{p,2}$ increases). Thus, performance on mode 2 (or mode 4) can be improved without affecting mode 1, 3 and 4 (or mode 2) up to some point.

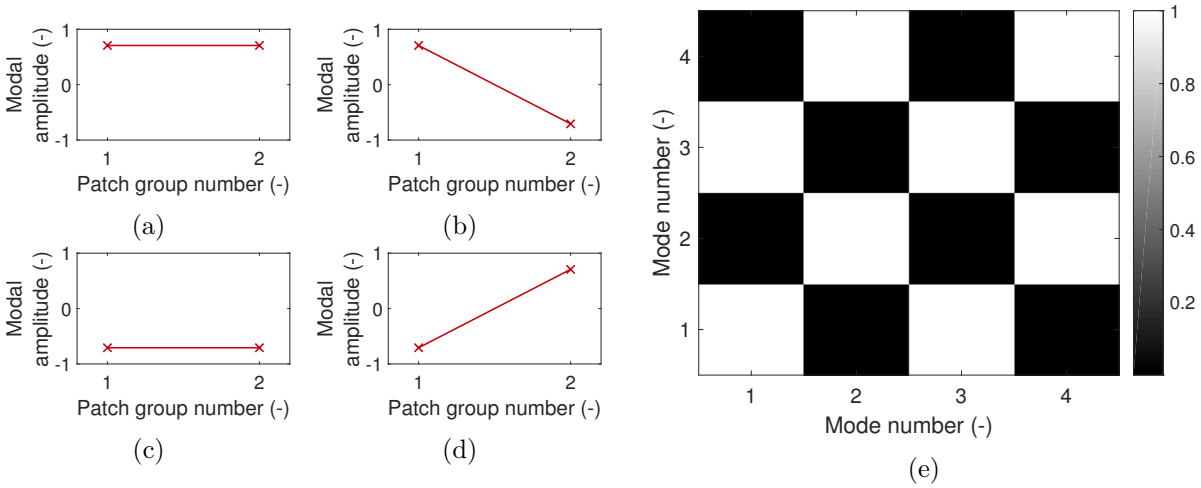

Figure 3.9: Optimal dimensionless mode shape 1 (a), 2 (b), 3 (c), 4 (d) and auto MAC of the optimal dimensionless electrical mode shapes (e).

A final example where mode 3 is also emphasized is shown in Figure 3.7, where $\overline{d}_{p,1} = \overline{d}_{p,2} = \overline{d}_{p,3} = 2$ and $\overline{d}_{p,4} = 1$. In this case, performance of mode 1 is affected as expected, because the dimensionless electrical modes 1 and 3 are not orthogonal. Performance on modes 2 and 4 is also affected because the maximum eigenvalue of $\overline{\mathbf{\Phi}}_p^{\star}\overline{\mathbf{D}}_p^2\left(\overline{\mathbf{\Phi}}_p^{\star}\right)^T$ has increased and thus α_p has decreased. Finally, setting all the relative scaling factors equal to 2 would be identical to setting them to 1.

This analysis showed that the relative scaling factors can indeed be used to balance the control authority over the modes, but they have to be assigned with care. The most significant scaling factor is the one which affects the largest eigenvalue of $\overline{\mathbf{\Phi}}_p^{\star}\overline{\mathbf{D}}_p^2\left(\overline{\mathbf{\Phi}}_p^{\star}\right)^T$. Orthogonality of the dimensionless electrical mode shapes can be assessed with the auto MAC in order to guide the choice of these scaling factors and to understand the trends in the resulting FRFs. In general, starting by setting them all equal to one would be advisable, and fine-tuning of these factors is possible if the analysis is made cautiously.

3.6.2.3 Comparison with an analog electrical network

An electrical cell having dynamics analog to those of the mechanical cell was proposed by Porfiri et al [153]; it is shown in Figure 3.10(b). The electrical matrices of this cell can be built as

$$\mathbf{C}_c = \begin{bmatrix} 0 \\ 0 \\ 1 \\ 0 \\ 0 \end{bmatrix} 2C_p^{\varepsilon} \begin{bmatrix} 0 \\ 0 \\ 1 \\ 0 \\ 0 \end{bmatrix}^T, \quad \mathbf{G}_c = \begin{bmatrix} -a \\ 1 \\ -1 \\ 0 \\ 0 \end{bmatrix} \frac{1}{R} \begin{bmatrix} -a \\ 1 \\ -1 \\ 0 \\ 0 \end{bmatrix}^T + \begin{bmatrix} 0 \\ 0 \\ -1 \\ a \\ 1 \end{bmatrix} \frac{1}{R} \begin{bmatrix} 0 \\ 0 \\ -1 \\ a \\ 1 \end{bmatrix}^T, \quad \mathbf{B}_c = \begin{bmatrix} 1 \\ 0 \\ 0 \\ -1 \\ 0 \end{bmatrix} \frac{1}{L} \begin{bmatrix} 1 \\ 0 \\ 0 \\ -1 \\ 0 \end{bmatrix}^T, \tag{3.84}$$

using the same ordering in the DoFs as in Figure 3.10(b) [159]. The localization matrix in this cell is $\mathbf{E}_{p,c}^T = \begin{bmatrix} 0 & 0 & 1 & 0 & 0 \end{bmatrix}$ in this case. The characteristics of the electrical cell are reported in Table 3.1, where the resistance was optimally tuned to the first mode. The matrices of the overall network $\mathbf{C}$, $\mathbf{G}$, $\mathbf{B}$ and $\mathbf{E}_p$ can then be built by standard finite element assembly procedures [140]. The analog network features the same resonance frequencies and mode shapes as the beam. When the two systems are coupled via the piezoelectric patches, as shown in Figure 3.10(a), broadband damping in the structure is achieved.

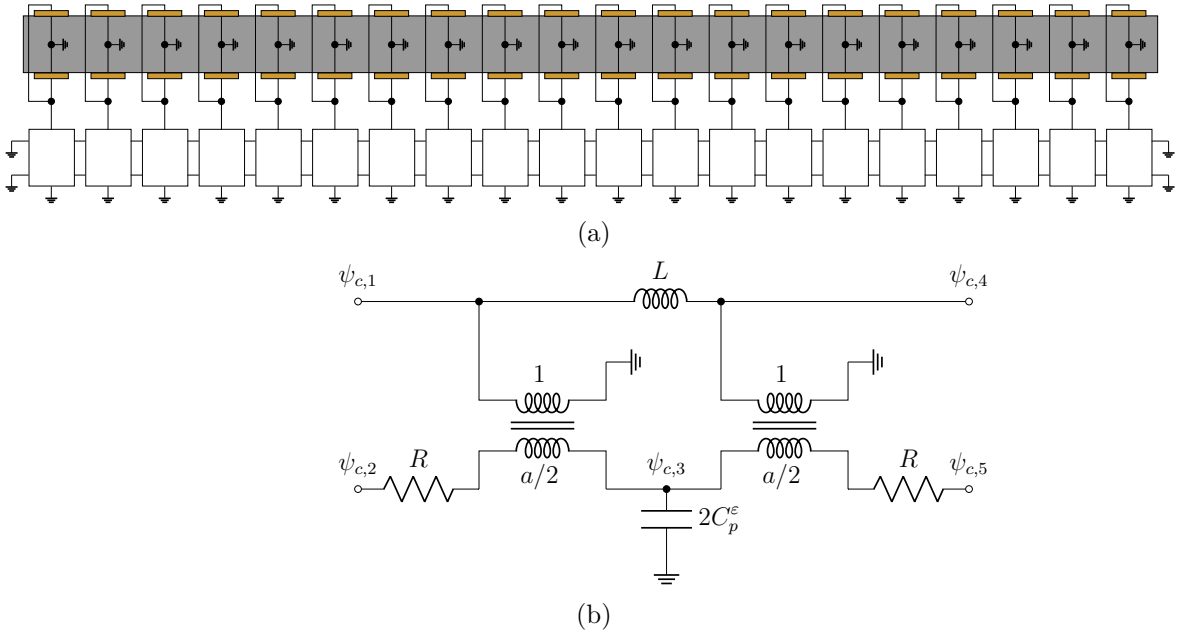

Figure 3.10: Schematic representation of a free-free beam (in gray) coupled to an electrical network (in white) through piezoelectric patches (in orange) (a) and electrical cell analog to the mechanical cell (b).

Parameter	C_p^ε	R	L	a
Value	21.96nF	57.5Ω	161.1mH	1

Table 3.1: Characteristics of the electrical cell.

Figure 3.11 indicates that the modal-based approach yields a more accurate tuning of the electrical network with respect to the H_∞ norm. However, unlike the analog network based on elementary cells, the electrical matrices do not have a band structure, which means that there may exist a large number of interconnections in the network. Thus, the network obtained with the proposed approach may potentially be more difficult to realize practically.

It should be pointed out that since the piezoelectric patches are all identical, the network synthesized with the modal-based approach is also an analog of the structure in a prescribed frequency band, because it features identical resonance frequencies and

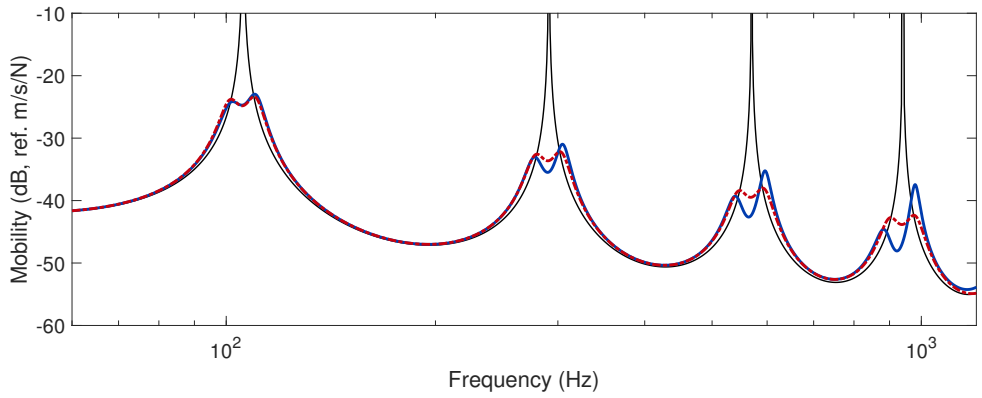

Figure 3.11: Velocity FRF of the beam with short-circuited patches (—), with a network assembled from analog electrical cells [155] (—) and with a network synthesized with the modal-based approach (-·-).

mode shapes as the targeted ones. This is confirmed in Figure 3.12, where the first four piezoelectric modal strain shapes and the first four electrical mode shapes obtained with either method are displayed (the patches are numbered according to their position, from one end of the beam to the other). The differences between the two methods come from the differences in electrical resonance frequencies and damping ratios.

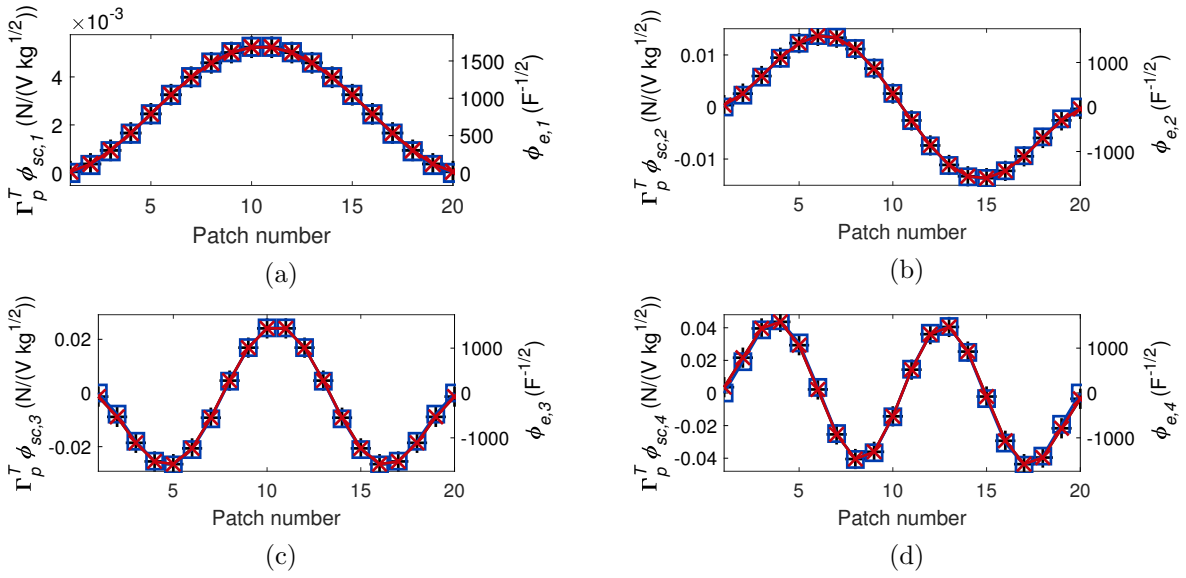

Figure 3.12: Modal strain in the piezoelectric transducers (-+-), electrical mode shapes of a network assembled from analog electrical cells [155] (-□-) and electrical mode shapes of a network synthesized with the modal-based approach (-×-): mode 1 (a), 2 (b), 3 (c) and 4 (d).

3.6.3 Fully clamped plate

The second example is the fully clamped plate depicted in Figure 3.13(a) [158]. Five pairs of piezoelectric patches are bonded symmetrically on either side of the plate, each pair being electrically connected in parallel. The finite element model of the piezoelectric structure in Figure 3.13(b) was developed in SAMCEF (see [136] for implementation

details) and a reduced-order model was imported in MATLAB. The Craig-Bampton technique was used with 20 retained modes [140]. The plate is subjected to a pointwise force located on a node of the finite element mesh at 41% of the plate length and 30% of the plate width from the lower left corner in Figure 3.13, in order to make it as close as possible to what was used in [158]. Besides that, the characteristics of the system were identical to those reported therein.

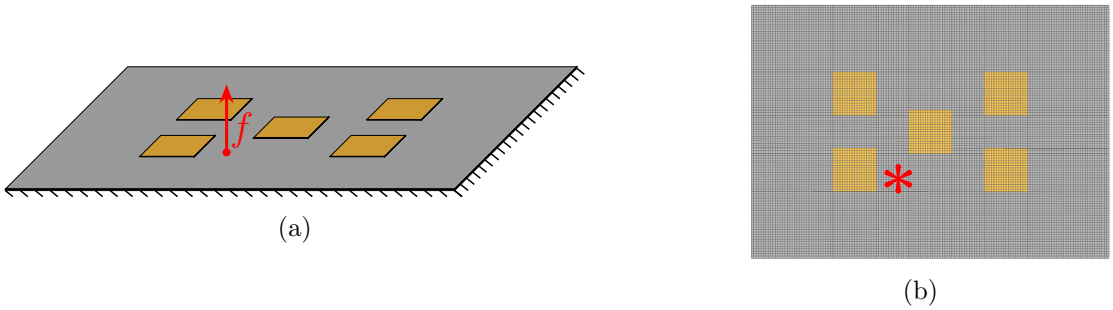

(a) (b)

Figure 3.13: Schematic representation of a fully clamped plate (in gray) excited by a point force (in red) to which are bonded piezoelectric patches (in orange) (a) and finite element mesh of the plate (b).

3.6.3.1 Control of the first five modes

The driving-point FRF of the plate coupled to the electrical network obtained with a modal-based synthesis targeting the first five modes of the plate is shown in Figure 3.14. Identical scaling factors for the five modes were used. As for the beam, the electrical network can very effectively damp out the resonant vibrations of the targeted modes.

The method in [158] was also used to synthesize an electrical network. The cornerstone of that method is to find an orthogonal transformation matrix $\mathbf{U}$ for the $P = N_s$ electrical DoFs such that $\boldsymbol{\psi} = \mathbf{U}\boldsymbol{\chi}$ (where $\boldsymbol{\chi}$ are the transformed electrical DoFs). The matrix $\mathbf{U}$ is aimed to make the transformed piezoelectric coupling matrix as close as possible from a diagonal matrix. The unknowns of this problem are the N_s^2 entries of $\mathbf{U}$. A system of N_s^2 quadratic equations is built to impose the orthogonality of $\mathbf{U}$ and the optimal closeness of the transformed coupling matrix to a diagonal matrix. It can be solved numerically to find the unknowns. Similarly to that method, the present paper uses a transformation of the electrical DoFs with the electrical modes, $\boldsymbol{\psi} = \boldsymbol{\Phi}_e \boldsymbol{\eta}_e$, but the matrix $\boldsymbol{\Phi}_e$ needs not be orthogonal. It is not explicitly set to diagonalize the piezoelectric coupling matrix, and it can be computed directly. Moreover, the modal-based method does not require the number of controlled modes N_s to be equal to the number of transducers P. Figure 3.14 reveals that the performance of the resulting network is found to be close to that of the modal-based synthesis. Despite the marked implementation differences between the methods, they both aim at optimally using the control capability offered by the transducers, which makes this result quite expectable in the end. The difference in performance mainly comes from the account for the contribution of non-resonant modes, as shall be shown in Section 3.6.3.2.

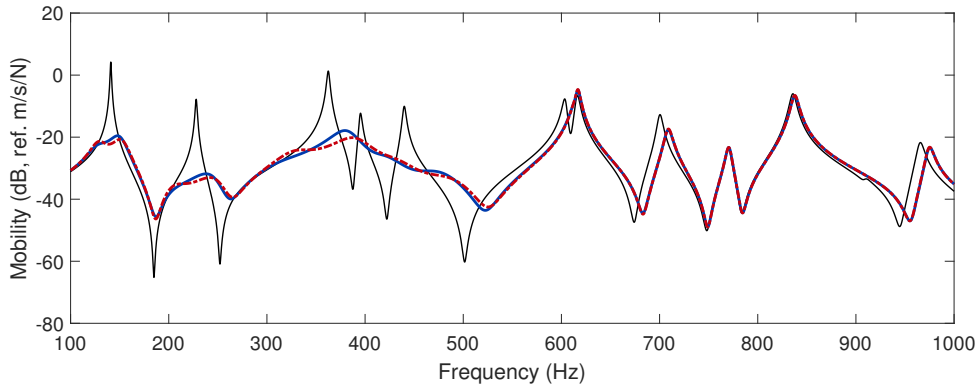

Figure 3.14: Velocity FRF of the plate with short-circuited patches (—), with a network synthesized with the method in [158] (—) and with a network synthesized with the modal-based approach (- - -).

3.6.3.2 Influence of background contributions

The example of the plate features rather closely-spaced resonance frequencies, and illustrates the relevance of accounting for non-resonant modes influence, and to make the additional effort of developing models including effective characteristics as in Section 3.4.3.

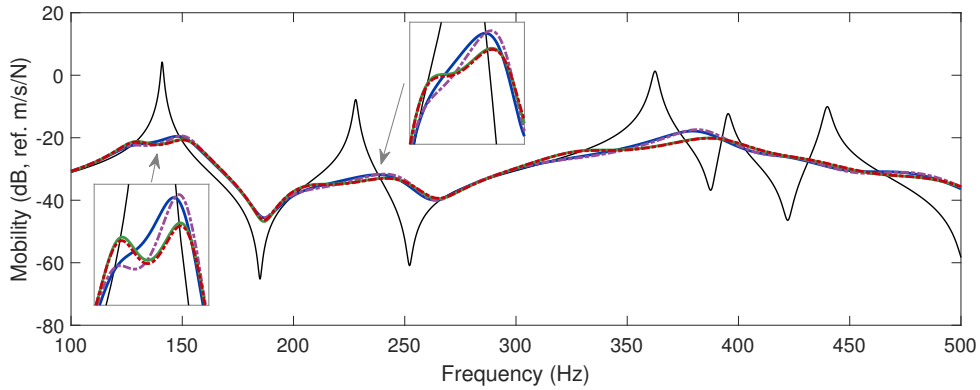

Figure 3.15: Velocity FRF of the plate with short-circuited patches (—), with a network synthesized with the method in [158] (—) and with a network synthesized with the modal-based approach neglecting background contributions (- - -), accounting for background contributions when tuning the frequencies and damping ratios, without (- - -) and with (—) corrections for the electrical mode shapes.

Figure 3.15 features the FRFs of the plate with networks accounting for background contributions of non-resonant modes in different ways. When the influence of non-resonant modes is overlooked (setting $\widehat{\omega}_{sc,r} = \omega_{sc,r}$, $\widehat{\gamma}_{\boldsymbol{\Phi},rk} = \gamma_{\boldsymbol{\Phi},rk}$ and $\widehat{\kappa}_{e,k} = 0$), the performance of a network synthesized with a modal-based approach becomes nearly identical to that synthesized with the method in [158]. Accounting for the background contributions when tuning the resonance frequencies and damping ratios (Section 3.5.3) allows for a better balance between the two peaks, and thus a better vibration reduction. Further accounting for their influence when specifying the electrical mode shapes (following the method described in Section D.2) leads to a nearly identical performance, although slightly worse. This result may seem surprising at first, but can be explained. While the performance index (Equation (D.12)) is slightly better using residual-corrected mode shapes, these corrected mode shapes are less mutually orthogonal than the uncorrected ones, leading

to smaller scaling factors (Equation (3.60)). The overall effect results in a slightly smaller EEMCF, leading to a slightly worse performance in the end.

These results show that accounting for background contributions of non-resonant modes is beneficial when tuning the frequencies and damping ratios of the overall network. However, the electrical mode shapes did not appear to benefit from this correction in this example. It is hard to generalize this last conclusion to any structure, and the problem can be intricate due to the scaling factors being automatically set to satisfy the passivity constraints. However, it can be conjectured that the improvement brought by the correction will be rather marginal in general. The method proposed in Section 3.5.2.1 being simpler than that proposed in Section D.2, the former would thus be recommended for practicality.

3.6.3.3 Control of the first twelve modes

A network targeting more modes than the number of piezoelectric patches was also designed. In order mitigate the vibration between 0 and 1000Hz, the first twelve modes with identical scaling factors were considered. The network performance is compared against that of the network targeting five modes in Figure 3.16. While vibration mitigation is less effective for the first few modes, the higher-frequency modes are now damped with the exception the 9^{th} mode. This is explained by the fact that the electromechanical coupling that the patches have with this mode is rather low, as shown in Figure 3.17. In this plot, the EEMCFs were obtained by considering the resonance frequencies of the plate when all the patches are shorted, and when all the patches are in open-circuit. Better mitigation results could be obtained with more patches or with optimally-located patches.

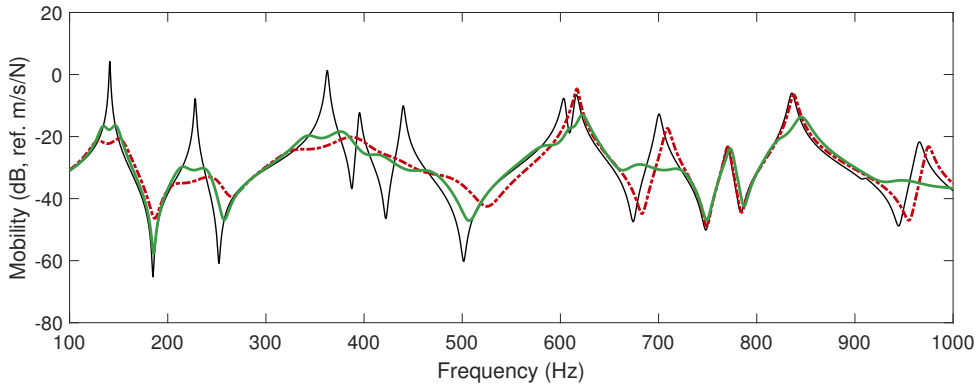

Figure 3.16: Velocity FRF of the plate with short-circuited patches (—) and with a network synthesized with the modal-based approach targeting the first five (-·-) and twelve (—) modes.

3.7 Centralized and decentralized networks

The approach proposed in this chapter consists in a centralized control approach, because all the piezoelectric transducers are interconnected through the same overall network. By contrast, the approach proposed in Chapter 2 could also be used with each transducer individually connected to its own shunt circuit, and not to other transducers. It would then be a decentralized control approach.

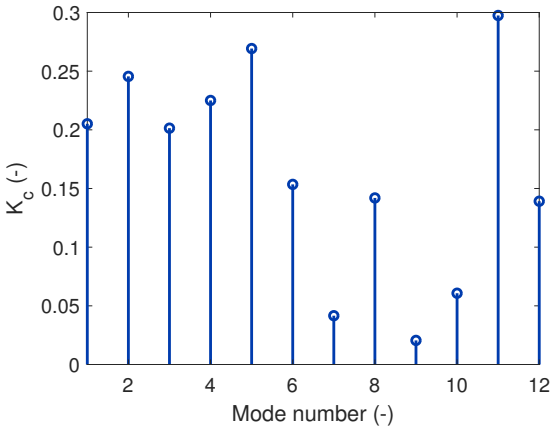

Figure 3.17: EEMCF of the first fifteen modes of the plate obtained by short- and open-circuiting all the patches.

The purpose of this section is to show that the theory presented in this chapter encompasses that presented in Chapter 2 (up to some approximations on the non-resonant modes). By imposing a certain topology of the electrical matrices, it is possible to decentralize partially the network by separating it into smaller networks, or totally by breaking it down to individual shunt circuits. The advantage of doing so is that the obtained electrical networks or circuits would require less interconnections, making their practical realization easier. The procedure to achieve this goal and its impact are discussed, and the tuning approach is extended to cases where the network is decentralized.

3.7.1 Decentralized networks

The electrical DoFs can be separated into N_g groups in order to obtain N_g unconnected networks of smaller size. From Section 3.3, the elements of the admittance matrix (Equation (3.15)) associated to two DoFs of different networks should be zero. Then, there exists an ordering that makes the electrical matrices of the interconnecting network block diagonal (each block being associated to a network), i.e.,

$$\mathbf{C}_e = \begin{bmatrix} \mathbf{C}_{e,11} & \mathbf{0} & \cdots & \mathbf{0} \\ \mathbf{0} & \mathbf{C}_{e,22} & \ddots & \mathbf{0} \\ \vdots & \ddots & \ddots & \vdots \\ \mathbf{0} & \mathbf{0} & \cdots & \mathbf{C}_{e,N_gN_g} \end{bmatrix}, \quad \mathbf{G} = \begin{bmatrix} \mathbf{G}_{11} & \mathbf{0} & \cdots & \mathbf{0} \\ \mathbf{0} & \mathbf{G}_{22} & \ddots & \mathbf{0} \\ \vdots & \ddots & \ddots & \vdots \\ \mathbf{0} & \mathbf{0} & \cdots & \mathbf{G}_{N_gN_g} \end{bmatrix},$$

$$\mathbf{B} = \begin{bmatrix} \mathbf{B}_{11} & \mathbf{0} & \cdots & \mathbf{0} \\ \mathbf{0} & \mathbf{B}_{22} & \ddots & \mathbf{0} \\ \vdots & \ddots & \ddots & \vdots \\ \mathbf{0} & \mathbf{0} & \cdots & \mathbf{B}_{N_gN_g} \end{bmatrix}. \quad (3.85)$$

With this ordering, the piezoelectric localization matrix also exhibits a block diagonal structure

$$\mathbf{E}_p = \begin{bmatrix} \mathbf{E}_{p,1} & \mathbf{0} & \cdots & \mathbf{0} \\ \mathbf{0} & \mathbf{E}_{p,2} & \ddots & \mathbf{0} \\ \vdots & \ddots & \ddots & \vdots \\ \mathbf{0} & \mathbf{0} & \cdots & \mathbf{E}_{p,N_g} \end{bmatrix}. \tag{3.86}$$

The capacitance matrix of the overall network is still given by Equation (3.22) but it should be noted that since $\mathbf{C}_p^\varepsilon$ is diagonal, $\mathbf{E}_p\mathbf{C}_p^\varepsilon\mathbf{E}_p^T$ is diagonal as well. Thus, the matrix $\mathbf{C}$ also has a block diagonal character.

Localization matrices to each group of DoFs are also introduced

$$\mathbf{E}_g = \begin{bmatrix} \mathbf{E}_{g,1} & \mathbf{E}_{g,2} & \cdots & \mathbf{E}_{g,N_g} \end{bmatrix} = \begin{bmatrix} \mathbf{I} & \mathbf{0} & \cdots & \mathbf{0} \\ \mathbf{0} & \mathbf{I} & \ddots & \mathbf{0} \\ \vdots & \ddots & \ddots & \vdots \\ \mathbf{0} & \mathbf{0} & \cdots & \mathbf{I} \end{bmatrix}, \tag{3.87}$$

and localization matrices relating the piezoelectric DoFs of a specific group to those of the whole piezoelectric structure are introduced as

$$\mathbf{E}_p\mathbf{E}_p^T = \begin{bmatrix} \mathbf{E}_{pg,1} & \mathbf{E}_{pg,2} & \cdots & \mathbf{E}_{pg,N_g} \end{bmatrix}. \tag{3.88}$$

3.7.2 Electrical modes of the decentralized networks

Owing to the block diagonal structure of the electrical matrices, the generalized eigenvalue problems on each block are decoupled. Assuming that group g is used to resonate at $N_{s,g}$ frequencies indexed by a set $\mathbf{k}(g)$, this problem then reads

$$\mathbf{C}_{gg}\boldsymbol{\Phi}_{e,g\mathbf{k}(g)}\boldsymbol{\Omega}^2_{e,\mathbf{k}(g)} = \mathbf{B}_{gg}\boldsymbol{\Phi}_{e,g\mathbf{k}(g)}, \tag{3.89}$$

where $\boldsymbol{\Phi}_{e,g\mathbf{k}(g)}$ contains the mode shapes of modes $\mathbf{k}(g)$ restricted to the DoFs of group g. The group can then be assigned to a maximum number of modes equal to its number of electrical DoFs. The generalized eigenvectors matrix of the overall network then also has a block diagonal topology

$$\boldsymbol{\Phi}_e = \begin{bmatrix} \boldsymbol{\Phi}_{e,1\mathbf{k}(1)} & \mathbf{0} & \cdots & \mathbf{0} \\ \mathbf{0} & \boldsymbol{\Phi}_{e,2\mathbf{k}(2)} & \ddots & \mathbf{0} \\ \vdots & \ddots & \ddots & \vdots \\ \mathbf{0} & \mathbf{0} & \cdots & \boldsymbol{\Phi}_{e,N_g\mathbf{k}(N_g)} \end{bmatrix}. \tag{3.90}$$

The number of DoFs of the network is equal to the sum of the number of DoFs of each group. This means that the decentralized networks are still able to control the same number of modes as the centralized one. In this case, each group would have to be assigned to a distinct set of modes. However, by constraining the topology of the electrical matrices in Equation (3.85), the maximum coupling reachable with these modes is also constrained, since the mode shapes have to be zero on groups to which they are not assigned.

3.7.2.1 Modal characteristics

It is now considered that a specific set of $N_{g,k}$ networks indexed by $\mathbf{g}(k) = \begin{bmatrix} g_1(k) & \cdots & g_{N_{g,k}}(k) \end{bmatrix}$ is associated with the k^{th} electrical resonance that targets the mechanical mode $r(k)$. The resonant mode shapes at the piezoelectric transducers are gathered in a mode shape matrix

$$\boldsymbol{\Phi}_{p,\mathbf{g}(k)k} = \mathbf{E}_p^T \begin{bmatrix} \mathbf{E}_{g,g_1(k)} \boldsymbol{\phi}_{e,g_1(k)k} & \cdots & \mathbf{E}_{e,g_{N_{g,k}}(k)} \boldsymbol{\phi}_{e,g_{N_{g,k}}(k)k} \end{bmatrix} = \begin{bmatrix} \mathbf{E}_{pg,g_1(k)} \boldsymbol{\phi}_{p,g_1(k)k} & \cdots & \mathbf{E}_{pg,g_{N_{g,k}}(k)} \boldsymbol{\phi}_{p,g_{N_{g,k}}(k)k} \end{bmatrix}, \tag{3.91}$$

where $\boldsymbol{\phi}_{e,g_i(k)k}$ is the mode shape of group $g_i(k)$ on all its electrical DoFs, and $\boldsymbol{\phi}_{p,g_i(k)k}$ is that mode shape on the electrical DoFs associated to the piezoelectric transducers in that group. Figure 3.18 schematically represents an example of these mode shapes.

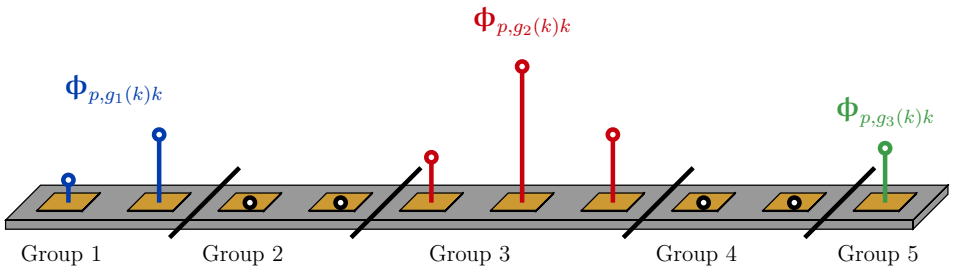

Figure 3.18: Example of a structure with $P = 10$ transducers grouped into $N_g = 5$ groups (separated by thick black lines): modes associated to electrical resonance k, with $\mathbf{g}(k) = \begin{bmatrix} 1 & 3 & 5 \end{bmatrix}$.

The electrical resonance frequencies (gathered in a diagonal matrix $\boldsymbol{\Omega}_{e,\mathbf{g}(k)k}$) and damping ratios (gathered in a diagonal matrix $\mathbf{Z}_{e,\mathbf{g}(k)k}$) associated to these mode shapes in the resonant networks are generally close. Making the assumption that they are identical,

$$\boldsymbol{\Omega}_{e,\mathbf{g}(k)k} \approx \omega_{e,k}\mathbf{I}, \qquad \mathbf{Z}_{e,\mathbf{g}(k)k} \approx \zeta_{e,k}\mathbf{I}. \tag{3.92}$$

Considering only the resonant modes, Equation (3.26) becomes

$$\begin{cases} \left(s^2 + \omega_{sc,r}^2\right) \eta_{sc,r} + s\boldsymbol{\phi}_{sc,r}^T \boldsymbol{\Gamma}_p \boldsymbol{\Phi}_{p,\mathbf{g}(k)k} \boldsymbol{\eta}_{e,\mathbf{g}(k)} = 0 \\ \left(s^2 + 2\zeta_{e,k}\omega_{e,k}s + \omega_{e,k}^2\right) \boldsymbol{\eta}_{e,\mathbf{g}(k)} - s\boldsymbol{\Phi}_{p,\mathbf{g}(k)k}^T \boldsymbol{\Gamma}_p^T \boldsymbol{\phi}_{sc,r} \eta_{sc,r} = \mathbf{0} \end{cases}. \tag{3.93}$$

Expressing the resonant electrical modal amplitude as a function of the mechanical one and inserting them into the mechanical equation yields

$$\left(s^2+\omega_{sc,r}^2+\frac{s^2}{s^2+2\zeta_{e,k}\omega_{e,k}s+\omega_{e,k}^2}\boldsymbol{\phi}_{sc,r}^T\boldsymbol{\Gamma}_p\boldsymbol{\Phi}_{p,\mathbf{g}(k)k}\boldsymbol{\Phi}_{p,\mathbf{g}(k)k}^T\boldsymbol{\Gamma}_p^T\boldsymbol{\phi}_{sc,r}\right)\eta_{sc,r}=0. \tag{3.94}$$

The effective open-circuit resonance frequency for this system is obtained by setting $\omega_{e,k}=0$, i.e.,

$$\widehat{\omega}_{oc,r}^2=\omega_{sc,r}^2+\boldsymbol{\phi}_{sc,r}^T\boldsymbol{\Gamma}_p\boldsymbol{\Phi}_{p,\mathbf{g}(k)k}\boldsymbol{\Phi}_{p,\mathbf{g}(k)k}^T\boldsymbol{\Gamma}_p^T\boldsymbol{\phi}_{sc,r}. \tag{3.95}$$

An EEMCF for this system would thus be given by Equation (3.8) using the effective open-circuit resonance frequency

$$\widehat{K}_{c,rk}^2=\frac{\widehat{\omega}_{oc,r}^2-\omega_{sc,r}^2}{\omega_{sc,r}^2}=\frac{1}{\omega_{sc,r}^2}\boldsymbol{\phi}_{sc,r}^T\boldsymbol{\Gamma}_p\boldsymbol{\Phi}_{p,\mathbf{g}(k)k}\boldsymbol{\Phi}_{p,\mathbf{g}(k)k}^T\boldsymbol{\Gamma}_p^T\boldsymbol{\phi}_{sc,r}. \tag{3.96}$$

3.7.2.2 Global and local electrical mode shapes

If there were only one electrical resonant mode targeting mode r, Equation (3.94) would be

$$\left(s^2+\omega_{sc,r}^2+\frac{s^2}{s^2+2\zeta_{e,k}\omega_{e,k}s+\omega_{e,k}^2}\boldsymbol{\phi}_{sc,r}^T\boldsymbol{\Gamma}_p\widehat{\boldsymbol{\phi}}_{p,k}\widehat{\boldsymbol{\phi}}_{p,k}^T\boldsymbol{\Gamma}_p^T\boldsymbol{\phi}_{sc,r}\right)\eta_{sc,r}=0, \tag{3.97}$$

which has the same form as Equation (3.94). A unique equivalent global electrical mode shape $\widehat{\boldsymbol{\phi}}_{p,k}$ can be found which satisfies

$$\boldsymbol{\phi}_{sc,r}^T\boldsymbol{\Gamma}_p\boldsymbol{\Phi}_{p,\mathbf{g}(k)k}\boldsymbol{\Phi}_{p,\mathbf{g}(k)k}^T\boldsymbol{\Gamma}_p^T\boldsymbol{\phi}_{sc,r}=\boldsymbol{\phi}_{sc,r}^T\boldsymbol{\Gamma}_p\widehat{\boldsymbol{\phi}}_{p,k}\widehat{\boldsymbol{\phi}}_{p,k}^T\boldsymbol{\Gamma}_p^T\boldsymbol{\phi}_{sc,r}=\left(\boldsymbol{\phi}_{sc,r}^T\boldsymbol{\Gamma}_p\widehat{\boldsymbol{\phi}}_{p,k}\right)^2. \tag{3.98}$$

This global mode shape is a combination of the local mode shapes

$$\widehat{\boldsymbol{\phi}}_{p,k}=\boldsymbol{\Phi}_{p,\mathbf{g}(k)k}\mathbf{c}_k. \tag{3.99}$$

Inserting this expression into Equation (3.98), the coefficients of this global mode shape can be found as

$$\mathbf{c}_k=\frac{1}{\sqrt{\boldsymbol{\phi}_{sc,r}^T\boldsymbol{\Gamma}_p\boldsymbol{\Phi}_{p,\mathbf{g}(k)k}\boldsymbol{\Phi}_{p,\mathbf{g}(k)k}^T\boldsymbol{\Gamma}_p^T\boldsymbol{\phi}_{sc,r}}}\boldsymbol{\Phi}_{p,\mathbf{g}(k)k}^T\boldsymbol{\Gamma}_p^T\boldsymbol{\phi}_{sc,r} \tag{3.100}$$

and the global mode shape itself is thus given by

$$\widehat{\boldsymbol{\phi}}_{p,k}=\frac{1}{\sqrt{\boldsymbol{\phi}_{sc,r}^T\boldsymbol{\Gamma}_p\boldsymbol{\Phi}_{p,\mathbf{g}(k)k}\boldsymbol{\Phi}_{p,\mathbf{g}(k)k}^T\boldsymbol{\Gamma}_p^T\boldsymbol{\phi}_{sc,r}}}\boldsymbol{\Phi}_{p,\mathbf{g}(k)k}\boldsymbol{\Phi}_{p,\mathbf{g}(k)k}^T\boldsymbol{\Gamma}_p^T\boldsymbol{\phi}_{sc,r}. \tag{3.101}$$

This global mode shape spans the same subspace as $\boldsymbol{\Phi}_{p,\mathbf{g}(k)k}$ since it is a linear combination of these local modes.

3.7.2.3 Effective characteristics with background contributions from the mechanical and electrical modes

Following the exact same procedure as described in Section 3.4.3.3, the system in Equation (3.26) simplifies to

$$\begin{cases} \left(s^2 + \widehat{\omega}_{sc,r}^2\right) \eta_{sc,r} + s\widehat{\boldsymbol{\gamma}}_{\boldsymbol{\Phi},rk}\boldsymbol{\eta}_{e,\mathbf{g}(k)k} = 0 \\ \left(\left(\mathbf{I} + \widehat{\boldsymbol{\kappa}}_{e,k}\right) s^2 + 2\mathbf{Z}_{e,\mathbf{g}(k)k}\boldsymbol{\Omega}_{e,\mathbf{g}(k)k} s + \boldsymbol{\Omega}_{e,\mathbf{g}(k)k}^2\right) \boldsymbol{\eta}_{e,\mathbf{g}(k)k} - s\widehat{\boldsymbol{\gamma}}_{\boldsymbol{\Phi},rk}^T \eta_{sc,r} = 0 \end{cases}, \tag{3.102}$$

were $\boldsymbol{\eta}_{e,\mathbf{g}(k)k}$ are the modal amplitudes associated with the mode shapes given in Equation (3.91), and the effective modal characteristics accounting for the background contributions of non-resonant mechanical and electrical modes are given by

$$\widehat{\omega}_{sc,r}^2 = \omega_{sc,r}^2 + \boldsymbol{\gamma}_{\boldsymbol{\Phi},r<k}\mathbf{S}^{-1}\boldsymbol{\gamma}_{\boldsymbol{\Phi},r<k}^T, \tag{3.103}$$

$$\widehat{\boldsymbol{\gamma}}_{\boldsymbol{\Phi},rk} = \boldsymbol{\gamma}_{\boldsymbol{\Phi},rk} - \boldsymbol{\gamma}_{\boldsymbol{\Phi},r<k}\mathbf{S}^{-1}\boldsymbol{\Gamma}_{\boldsymbol{\Phi},>r<k}^T\boldsymbol{\Omega}_{sc,>r}^{-2}\boldsymbol{\Gamma}_{\boldsymbol{\Phi},>rk}, \tag{3.104}$$

and

$$\widehat{\boldsymbol{\kappa}}_{e,k} = \boldsymbol{\Gamma}_{\boldsymbol{\Phi},>rk}^T\left(\boldsymbol{\Omega}_{sc,>r}^{-2} - \boldsymbol{\Omega}_{sc,>r}^{-2}\boldsymbol{\Gamma}_{\boldsymbol{\Phi},>r<k}\mathbf{S}^{-1}\boldsymbol{\Gamma}_{\boldsymbol{\Phi},>r<k}^T\boldsymbol{\Omega}_{sc,>r}^{-2}\right)\boldsymbol{\Gamma}_{\boldsymbol{\Phi},>rk}, \tag{3.105}$$

using the following notation for the modal piezoelectric coupling matrix

$$\boldsymbol{\Gamma}_{\boldsymbol{\Phi}} = \begin{bmatrix} \boldsymbol{\Phi}_{sc,r}^T \\ \boldsymbol{\Phi}_{sc,>r}^T \end{bmatrix} \boldsymbol{\Gamma}_p \begin{bmatrix} \boldsymbol{\Phi}_{p,\mathbf{g}(k)} & \boldsymbol{\Phi}_{p,<k} \end{bmatrix} = \begin{bmatrix} \boldsymbol{\gamma}_{\boldsymbol{\Phi},rk} & \boldsymbol{\gamma}_{\boldsymbol{\Phi},r<k} \\ \boldsymbol{\Gamma}_{\boldsymbol{\Phi},>rk} & \boldsymbol{\Gamma}_{\boldsymbol{\Phi},>r<k} \end{bmatrix}. \tag{3.106}$$

Similarly to Equation (3.96), an EEMCF can be defined from the characteristics of the system in Equation (3.102) as

$$\widehat{K}_{c,rk}^2 = \frac{1}{\widehat{\omega}_{sc,r}^2}\widehat{\boldsymbol{\gamma}}_{\boldsymbol{\Phi},rk}\left(\mathbf{I} + \widehat{\boldsymbol{\kappa}}_{e,k}\right)^{-1}\widehat{\boldsymbol{\gamma}}_{\boldsymbol{\Phi},rk}^T. \tag{3.107}$$

3.7.3 Design of the decentralized networks

3.7.3.1 Passivity

Passivity constrains the electrical mode shapes amplitudes in a similar way to Section 3.5.1, but each network has to be considered separately owing to the local nature of the electrical modes. The network associated to that group is passive if

$$\left(\mathbf{E}_{g,g}^T\mathbf{C}_p^{\varepsilon}\mathbf{E}_{g,g}\right)^{-1} - \mathbf{E}_{p,g}^T\boldsymbol{\Phi}_{e,g\mathbf{k}(g)}\boldsymbol{\Phi}_{e,g\mathbf{k}(g)}^T\mathbf{E}_{p,g} = \left(\mathbf{C}_{p,gg}^{\varepsilon}\right)^{-1} - \boldsymbol{\Phi}_{p,g\mathbf{k}(g)}\boldsymbol{\Phi}_{p,g\mathbf{k}(g)}^T \succeq 0, \tag{3.108}$$

where $\mathbf{C}_{p,gg}^{\varepsilon} = \mathbf{E}_{g,g}^T\mathbf{C}_p^{\varepsilon}\mathbf{E}_{g,g}$ is the capacitance matrix at constant strain of the P_g piezoelectric transducers connected to group g, and $\boldsymbol{\Phi}_{p,g\mathbf{k}(g)}$ is the electrical mode shapes matrix on these transducers.

3.7.3.2 Optimal electrical mode shapes

Similarly to Section 3.5.2.1, it is sought to maximize the EEMCF defined in Equation (3.96) by maximizing the objective function

$$\left(\boldsymbol{\phi}_{sc,r}^T \boldsymbol{\Gamma}_p \widehat{\boldsymbol{\phi}}_{p,k}\right)^2 = \boldsymbol{\phi}_{sc,r}^T \boldsymbol{\Gamma}_p \boldsymbol{\Phi}_{p,\mathbf{g}(k)k} \boldsymbol{\Phi}_{p,\mathbf{g}(k)k}^T \boldsymbol{\Gamma}_p^T \boldsymbol{\phi}_{sc,r} = \sum_{i=1}^{N_{g,k}} \left(\boldsymbol{\phi}_{sc,r}^T \boldsymbol{\Gamma}_p \mathbf{E}_{pg,g_i(k)} \boldsymbol{\phi}_{p,g_i(k)k}\right)^2. \tag{3.109}$$

This objective function features a sum of squared terms, and is maximized if these terms are themselves maximized. Each of these terms is related to a specific group, and can thus be optimized considering only that group. Moreover, the passivity constraints given in Equation (3.108) also pertain to a single group at a time. Thus, the global constrained optimization problem can be broken down into smaller local constrained optimization problems

$$\begin{aligned} \underset{\boldsymbol{\Phi}_{p,g_i(k)k}}{\text{Maximize}} \quad & \boldsymbol{\phi}_{sc,r}^T \boldsymbol{\Gamma}_p \mathbf{E}_{pg,g_i(k)} \boldsymbol{\phi}_{p,g_i(k)k} \\ \text{Subject to} \quad & \boldsymbol{\phi}_{p,g_i(k)k}^T \left(\mathbf{C}_{p,g_i(k)g_i(k)}^{\varepsilon}\right)^{-1} \boldsymbol{\phi}_{p,g_i(k)k} \leq 1 \end{aligned}, \tag{3.110}$$

for each group targeting mode $r(k)$, i.e., $\forall i = 1, \cdots, N_{g,k}$. This problem was solved in Section 3.5.2.1 and the optimal solution is given by

$$\boldsymbol{\phi}_{p,g_i(k)k}^{\star} = \frac{1}{\sqrt{\boldsymbol{\phi}_{sc,r}^T \boldsymbol{\Gamma}_p \mathbf{E}_{pg,g_i(k)} \left(\mathbf{C}_{p,g_i(k)g_i(k)}^{\varepsilon}\right)^{-1} \mathbf{E}_{pg,g_i(k)}^T \boldsymbol{\Gamma}_p^T \boldsymbol{\phi}_{sc,r}}} \left(\mathbf{C}_{p,g_i(k)g_i(k)}^{\varepsilon}\right)^{-1} \mathbf{E}_{pg,g_i(k)}^T \boldsymbol{\Gamma}_p^T \boldsymbol{\phi}_{sc,r}. \tag{3.111}$$

This optimal mode shape is a scaled version of the optimal mode shape in Section 3.5.2.1, restricted to the piezoelectric DoFs of the considered group.

Once all the optimal electrical mode shapes of a group are determined, the actual mode shapes can be computed so as to respect passivity. Assuming relative scaling factors are given for each modes and each group, the set related to a group g is gathered in a diagonal scaling matrix

$$\overline{\mathbf{D}}_{p,g} = \begin{bmatrix} \overline{d}_{p,gk_1(g)} & & \\ & \ddots & \\ & & \overline{d}_{p,gk_{N_{s,g}}(g)}, \end{bmatrix} \tag{3.112}$$

and the electrical mode shape matrix is given by

$$\boldsymbol{\Phi}_{p,g\mathbf{k}(g)} = \frac{1}{\lambda_{Max}\left(\left(\mathbf{C}_{p,gg}^{\varepsilon}\right)^{1/2} \boldsymbol{\Phi}_{p,g\mathbf{k}(g)}^{\star} \overline{\mathbf{D}}_{p,g}^2 \left(\boldsymbol{\Phi}_{p,g\mathbf{k}(g)}^{\star}\right)^T \left(\mathbf{C}_{p,gg}^{\varepsilon}\right)^{1/2}\right)} \boldsymbol{\Phi}_{p,g\mathbf{k}(g)}^{\star} \overline{\mathbf{D}}_{p,g}. \tag{3.113}$$

3.7.3.3 Automatic selection of the local scaling factors

Setting the scaling factors for each group and each mode can be a tedious task, and may result in a poor choice that undermines the performance of

the decentralized networks. This section presents a procedure to choose them automatically, based on global scaling factors.

According to Equations (3.96) and (3.109), the EEMCF of the network, which is a scaled-down version of the EEMCF of the structure by a global factor $d_{p,k}$, can be expressed as

$$\widehat{K}^2_{c,rk} = d^2_{p,k} K^2_{c,r} = \frac{1}{\omega^2_{sc,r}} \sum_{i=1}^{N_{g,k}} \left(\boldsymbol{\Phi}^T_{sc,r} \boldsymbol{\Gamma}_p \mathbf{E}_{pg,g_i(k)} \boldsymbol{\Phi}^\star_{p,g_i(k)k} \right)^2 d^2_{p,g_i(k)k}. \tag{3.114}$$

It is seen that every group involved with mode k has a positive participation to the EEMCF, and the amount of increase is controlled by the local relative scaling factor. Thus, a global scaling factor $d_{p,k}$ on mode k can be enforced if the local scaling factors $d_{p,g_i(k)k}$ verify

$$d^2_{p,k} = \frac{1}{K^2_{c,r} \omega^2_{sc,r}} \sum_{i=1}^{N_{g,k}} \left(\boldsymbol{\Phi}^T_{sc,r} \boldsymbol{\Gamma}_p \mathbf{E}_{pg,g_i(k)} \boldsymbol{\Phi}^\star_{p,g_i(k)k} \right)^2 d^2_{p,g_i(k)k}. \tag{3.115}$$

This is in general an underconstrained system, and several combinations of the local scaling factors can give the same global scaling factor. However, because the maximum value of the scaling factors is one (see Section 3.5.6.1), the maximum global scaling factor that can be enforced with the considered configuration of decentralized networks is thus

$$\max\left(d^2_{p,k}\right) = \frac{1}{K^2_{c,r} \omega^2_{sc,r}} \sum_{i=1}^{N_{g,k}} \left(\boldsymbol{\Phi}^T_{sc,r} \boldsymbol{\Gamma}_p \mathbf{E}_{pg,g_i(k)} \boldsymbol{\Phi}^\star_{p,g_i(k)k} \right)^2. \tag{3.116}$$

Now, this limit is reached if there is only one targeted mode. When multiple modes are considered, the local scaling factors should be optimally distributed so as to maximize the attainable global scaling factors. In terms of relative scaling factors, Equation (3.115) can be written

$$\overline{d}^2_{p,k} = \mathbf{k}^T_{p,k} \overline{\mathbf{d}}^2_{pg,k}. \tag{3.117}$$

where

$$\mathbf{k}^T_{p,k} = \frac{1}{K^2_{c,r} \omega^2_{sc,r}} \left[\left(\boldsymbol{\Phi}^T_{sc,r} \boldsymbol{\Gamma}_p \mathbf{E}_{pg,g_1(k)} \boldsymbol{\Phi}^\star_{p,g_1(k)k} \right)^2 \quad \cdots \quad \left(\boldsymbol{\Phi}^T_{sc,r} \boldsymbol{\Gamma}_p \mathbf{E}_{pg,g_{N_{g,k}}(k)k} \boldsymbol{\Phi}^\star_{p,g_{N_{g,k}}(k)k} \right)^2 \right] \tag{3.118}$$

and

$$\overline{\mathbf{d}}^2_{pg,k} = \left[\overline{d}^2_{p,g_1(k)k} \quad \cdots \quad \overline{d}^2_{p,g_{N_{g,k}}(k)k} \right] \tag{3.119}$$

The k^{th} global relative scaling factor in Equation (3.117) grows the fastest if the local relative scaling factors are aligned with its gradient, i.e.,

$$\overline{\mathbf{d}}^2_{pg,k} = \alpha_{p,k} \mathbf{k}_{p,k}. \tag{3.120}$$

Using this distribution for every local relative scaling factor and writing Equation (3.117) for each controlled mode yields

$$\left[\overline{d}^2_{p,1} \quad \cdots \quad \overline{d}^2_{p,N_s} \right] = \left[\alpha_{p,1} \mathbf{k}^T_{p,1} \mathbf{k}_{p,1} \quad \cdots \quad \alpha_{p,N_s} \mathbf{k}^T_{p,N_s} \mathbf{k}_{p,N_s} \right]. \tag{3.121}$$

In an attempt to set the desired relative magnitude between the global scaling factors, the local ones can thus be chosen by

$$\overline{\mathbf{d}}_{pg,k}^2 = \frac{\overline{d}_{p,k}^2}{\mathbf{k}_{p,k}^T \mathbf{k}_{p,k}} \mathbf{k}_{p,k}. \tag{3.122}$$

It should be underlined that, because the scaling factors of different groups are constrained by different passivity constraints, the local scaling factors may not be proportional to the local ones given in Equation (3.122), and will not guarantee that the global scaling factors will have the desired relative magnitudes. Solving this problem exactly would probably require some iterations.

3.7.3.4 Electrical frequencies and damping ratios

Once the electrical mode shapes are determined over all groups, the electrical frequencies and damping ratios can be specified. They are tuned so as to enforce the global mode shape given in Equation (3.101), accounting for the background contributions of non-resonant modes. In the basis of the resonant modes, this global mode shape is expressed by its coefficients (Equation (3.100)). Using the system with the effective characteristics in Equation (3.102), the global mode shape is a resonant mode shape of the overall network at a frequency $\omega_{e,k}$ if it satisfies

$$\left(\mathbf{\Omega}_{e,\mathbf{g}(k)k}^2 - \omega_{e,k}^2 \left(\mathbf{I} + \widehat{\boldsymbol{\kappa}}_{e,k}\right)\right) \mathbf{c}_k = \mathbf{0} \tag{3.123}$$

With the effective short-circuit resonance frequency in Equation (3.103) and the EEMCF in Equation (3.107), the optimal global electrical resonance frequency $\omega_{e,k}$ and damping ratio $\zeta_{e,k}$ can be computed from Equations (1.45) and (1.46) as

$$\omega_{e,k}^2 = \nu^2 \left(\widehat{K}_{c,rk}\right) \widehat{\omega}_{sc,r}^2, \qquad \zeta_{e,k} = \varsigma \left(\widehat{K}_{c,rk}\right). \tag{3.124}$$

By contrast with Equation (3.63), the background-corrected capacitance has not yet been accounted for here. $\mathbf{\Omega}_{e,\mathbf{g}(k)k}$ should be set in order to enforce Equation (3.123). Because it is a diagonal matrix,

$$\omega_{e,k}^2 \left(\mathbf{I} + \widehat{\boldsymbol{\kappa}}_{e,k}\right) \mathbf{c}_k = \mathbf{\Omega}_{e,\mathbf{g}(k)k}^2 \mathbf{c}_k = \mathrm{diag}\left(\mathbf{c}_k\right) \boldsymbol{\omega}_{e,\mathbf{g}(k)k}^2 \tag{3.125}$$

where diag$(\cdot)$ is an operator that turns a vector into a diagonal matrix (whose diagonal is that vector) and $\boldsymbol{\omega}_{e,\mathbf{g}(k)k}^2$ is a vector containing the squared electrical resonance frequencies on the diagonal of $\mathbf{\Omega}_{e,\mathbf{g}(k)k}^2$. This vector is determined as

$$\boldsymbol{\omega}_{e,\mathbf{g}(k)k}^2 = \omega_{e,k}^2 \mathrm{diag}^{-1}\left(\mathbf{c}_k\right) \left(\mathbf{I} + \widehat{\boldsymbol{\kappa}}_{e,k}\right) \mathbf{c}_k, \tag{3.126}$$

which now accounts for the background-corrected capacitance, and finally

$$\mathbf{\Omega}_{e,\mathbf{g}(k)k}^2 = \mathrm{diag}\left(\boldsymbol{\omega}_{e,\mathbf{g}(k)k}^2\right). \tag{3.127}$$

As for the damping ratio matrix, it is simply set by

$$\mathbf{Z}_{e,\mathbf{g}(k)k} = \frac{\zeta_{e,k}}{\omega_{e,k}} \mathbf{\Omega}_{e,\mathbf{g}(k)k}. \tag{3.128}$$

It can be noted that, since $\mathbf{c}_k \sim O\left(1\right)$ and $\widehat{\boldsymbol{\kappa}}_{e,k} \sim O\left(K_{c,r}^2\right)$ (by comparison of Equations (3.30) and (3.105)), Equation (3.126) indicates that each element in $\boldsymbol{\omega}_{e,\mathbf{g}(k)k}^2$ is proportional to $\omega_{e,k}^2$ with a factor of order $O\left(1 + K_{c,r}^2\right)$. Together with Equation (3.128), this justifies the approximation made in Equation (3.92).

3.7.3.5 Modal-based synthesis for decentralized networks

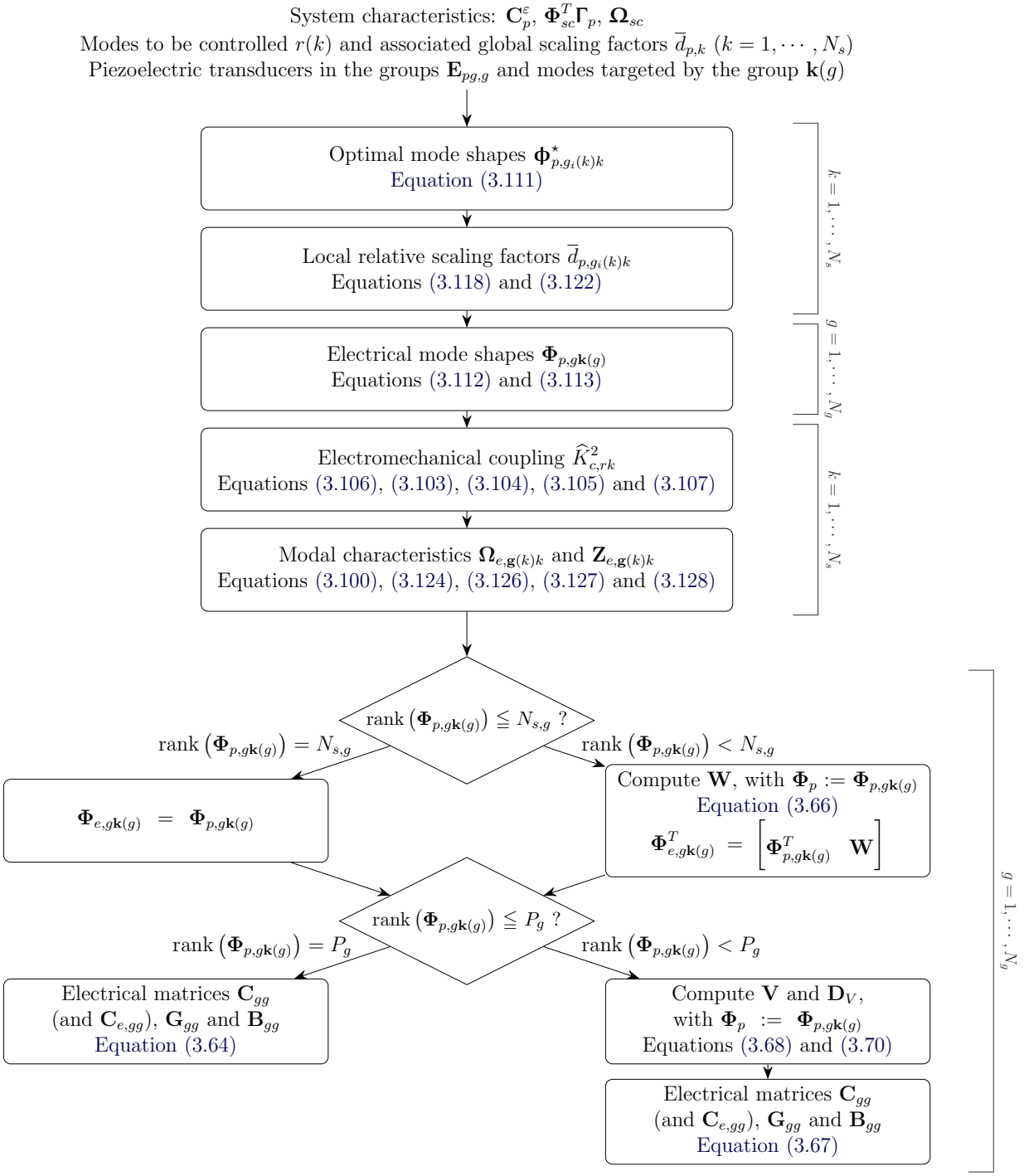

Figure 3.19: Flowchart of the proposed modal-based synthesis for decentralized networks.

The modal-based synthesis for decentralized networks is summarized in Figure 3.19. Compared to the centralized case, the user must also specify how the piezoelectric transducers are allocated to each group, and which modes are targeted by each group. The second step (determination of the local relative scaling factors) can be bypassed if the user submits them as an input to the algorithm.

3.8 Examples

The control of a piezoelectric structure with multiple decentralized networks is illustrated with the free-free beam example of Section 3.6.2.

3.8.1 Multiple RL shunts targeting one mode

The first example illustrates the decentralized control approach by shunting each pair of patches of the beam with simple parallel RL shunts. In this case, the matrices featured in Equation (3.85) are diagonal, and each entry on the diagonal corresponds to a capacitance, a conductance or a reluctance depending on the matrix at hand. All shunts are first assumed to target the same mode, and four cases are considered in which the first four modes are targeted.

Tuning multiple RL shunts targeting the same modes is not an easy task: the frequency to which they should be tuned is not clear, and neither is the method to compute their EEMCF to use Equations (1.45) and (1.46). By contrast, the proposed decentralized modal-based approach automatically tunes these shunts without ambiguity about these parameters, and accounts for the interaction between the shunts.

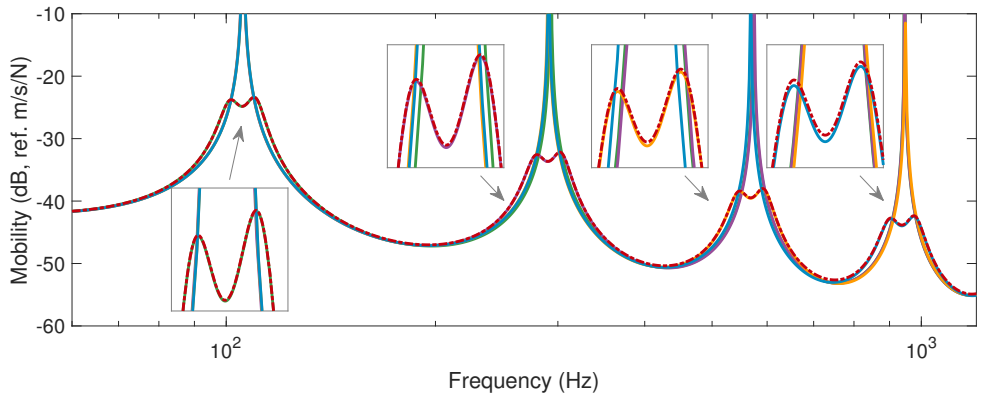

Figure 3.20: Velocity FRF of the beam with parallel RL shunts targeting mode 1 (—), 2 (—), 3 (—) and 4 (—), and with the centralized network synthesized with the modal-based approach (- - -).

Figure 3.20 features the FRFs obtained with the parallel RL shunts and compares it to the centralized network analyzed in Section 3.6.2.1. When all patches are assigned to a given frequency, the associated resonance is mitigated in the same fashion as the single-mode resonant RL shunt discussed in Section 1.2.2. The other modes remain largely undamped. With the centralized network, nearly the same performance is obtained on all the targeted modes simultaneously. This is possible because the optimal electrical mode shapes in this network are orthogonal, as discussed in Section 3.5.6. Looking closely at the FRFs, the RL shunts slightly outperform the centralized network on their targeted mode, especially for higher-frequency modes. This comes from the detrimental capacitive influence of non-resonant modes in the centralized network (see Section D.4.1).

3.8.2 Multiple RL shunts targeting several modes

The patches are now individually shunted with a single parallel RL shunt, but the shunts now target different modes. Figure 3.21 depicts two considered distributions of the first four modes among the shunts: adjacent (Figure 3.21(a)) and alternate (Figure 3.21(b)) distributions. In general, choosing to assign specific modes to specific patches is not a trivial task and could constitute an interesting extension to the proposed method, but is beyond the scope of the present chapter.

The tuning problem for multiple RL shunts targeting several modes is not trivial either, because the shunts may interact either resonantly or through quasi-static responses. A calibration procedure was proposed by Toftekær and Høgsberg [139], where the electrical boundary conditions on the patches associated with non-resonant shunts were considered either as a short- or open-circuit, depending on whether the shunt targets a higher- or lower-frequency mode, respectively. This method proved efficient, but has the downside that a potentially large eigenvalue problem has to be solved with the considered electrical boundary conditions for each resonant mode. The proposed modal-based approach implicitly applies this procedure in the case of multiple RL shunts, because a patch associated with only capacitively-dominated mode is effectively in open circuit. However, the approach does not require the solution of an eigenvalue problem because this solution is accurately approximated accounting for the background contributions of non-resonant modes.

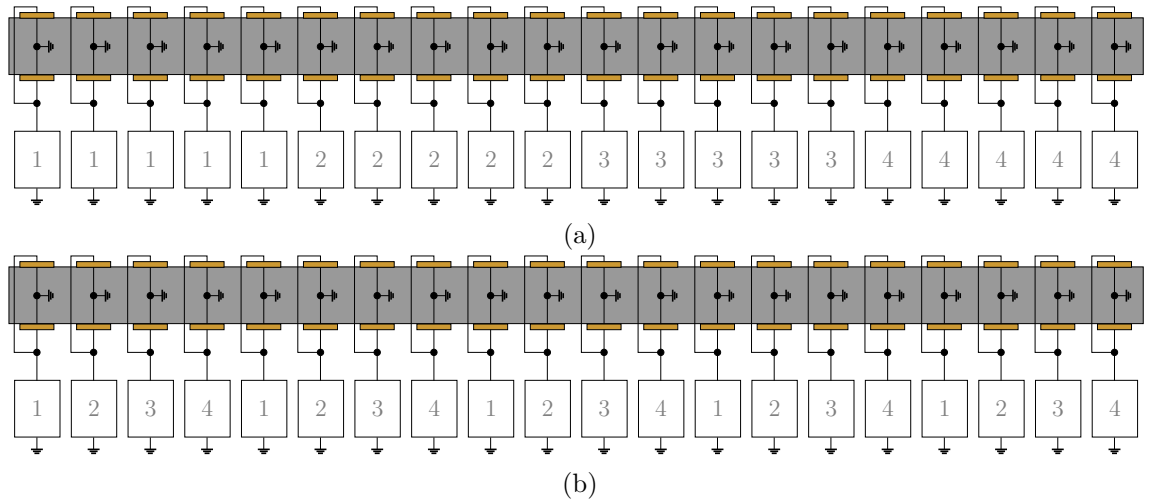

Figure 3.21: Schematic representation of a free-free beam (in gray) coupled to multiple RL shunts (in white) through piezoelectric patches (in orange) with adjacent (a) or alternate (b) distribution. The number inside the boxes representing RL shunts indicates the mode that the shunt targets.

Figure 3.22 compares the performance of the RL shunts to that of the centralized network. This time, both control strategies mitigate simultaneously the targeted modes. However, the price to pay for the simplifications in electrical interconnections in the RL shunts compared to the centralized network is a global decrease in performance. The distribution of patches among the modes also has a strong impact on performance. The adjacent distribution's performance is particularly poor on mode 1. This is due to the relatively small modal strain incurred by the first mode shapes on the patches close to the edge that are assigned to mode 1 (see Figure 3.21(a)).

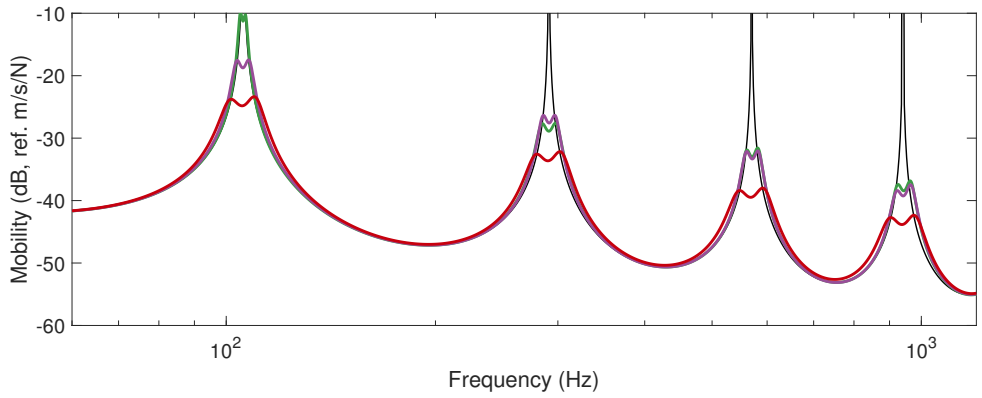

Figure 3.22: Velocity FRF of the beam with parallel RL shunts targeting mode 1 to 4 with adjacent (—) and alternate (—) distributions, and with the centralized network synthesized with the modal-based approach (—).

3.8.3 Multiple multimodal shunt circuits

The last example featuring individually-shunted patches is the case of multiple shunt circuits having themselves multiple resonance frequencies. The extra feature brought by the method proposed in this chapter compared to that of Chapter 2 is the account for the interaction between the different shunt circuits.

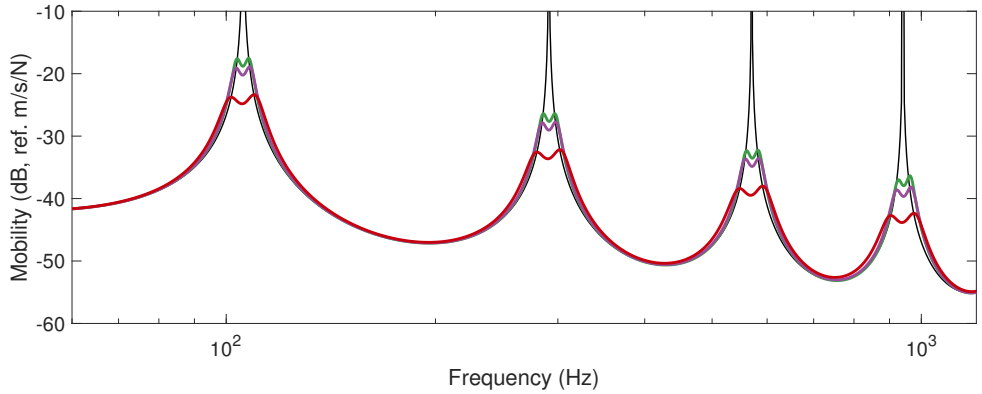

Figure 3.23: Velocity FRF of the beam with shunt circuits targeting mode 1 to 4 and with local relative scaling factors all equal to one (—) or optimized (—), and with the centralized network synthesized with the modal-based approach (—).

Figure 3.23 compares the FRFs of the multiple shunt circuits to that of the network. We note that such comparison was made in [58, 59]. It was not completely fair, because in these two references the CF shunt circuit was used with rather small capacitances, which means on the account of the example in Section 2.10.3 that the performance of this circuit was substantially worse than what can be expected from multi-branch shunt circuits.

In Figure 3.23, two strategies were used to set the local relative scaling factors for each shunt circuit. The first one arbitrarily set them all to one, whereas the second one used the optimization approach outlined in Section 3.7.3.3. The latter strategy offers a globally better performance than the former, which stresses the importance of adequately choosing the distribution of control authority over the modes among the transducers. The decentralized approach nonetheless exhibits a lower performance than its centralized counterpart.

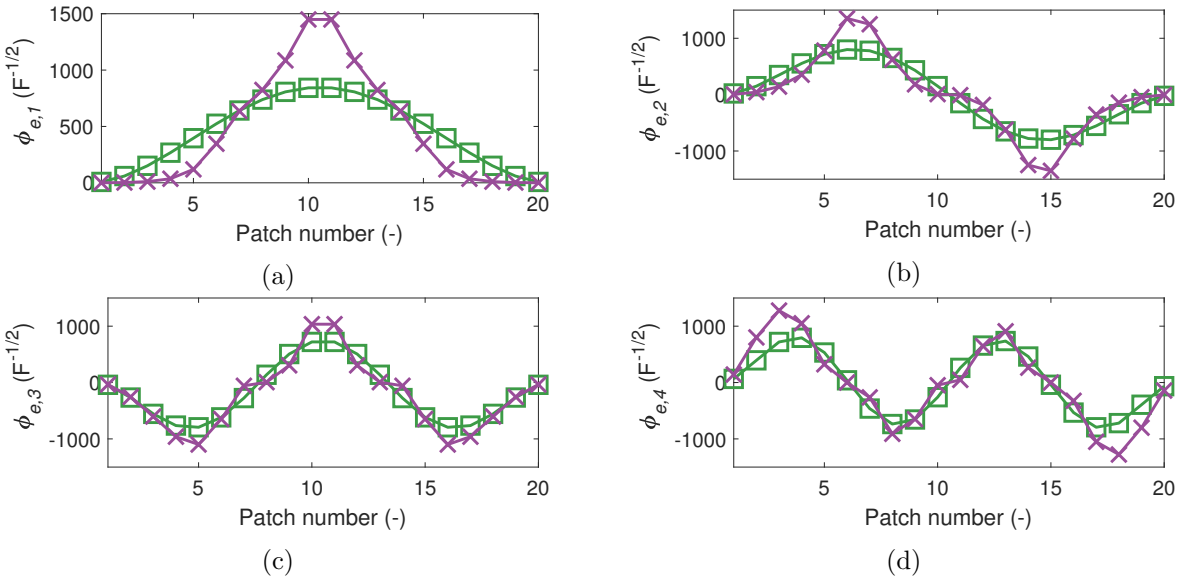

Figure 3.24: Equivalent global electrical mode shapes of the shunt circuits with local relative scaling factors all equal to one (-□-) or optimized (-×-): mode 1 (a), 2 (b), 3 (c) and 4 (d).

In order to better understand why the procedure presented in Section 3.7.3.3 exhibits a better performance than choosing the local relative scaling factors all equal to ones, the equivalent global electrical mode shapes can be analyzed in Figure 3.24. It can be observed that the procedure amplifies the mode shapes associated to a specific mode in regions where the other mode shapes are small in amplitude, thereby exploiting the mode shape at hand to its maximum. The global scaling factors are thus higher, as exhibited in Figure 3.25. However, because the passivity constraints on each group affect the local scaling factors non-uniformly, the relative magnitude between the global scaling factors cannot be exactly enforced with this method.

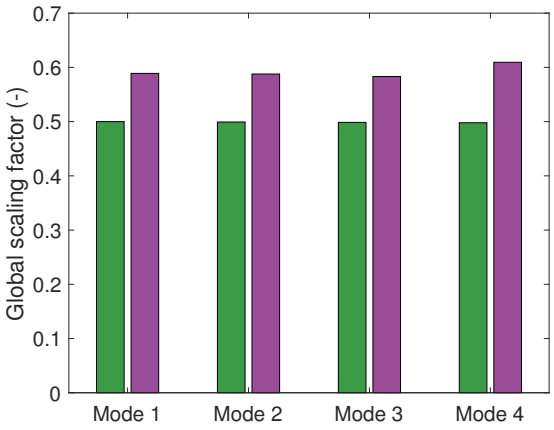

Figure 3.25: Global scaling factors attained by the shunt circuits with local relative scaling factors all equal to one (■) or optimized (■).

3.8.4 Multiple decentralized networks

The last example briefly investigates the impact of partial or total decentralization, by considering decentralized networks interconnecting a decreasing number of transducers. The case where there is only one transducer per group of electrical DoFs boils down to the above example of the multiple shunt circuits.

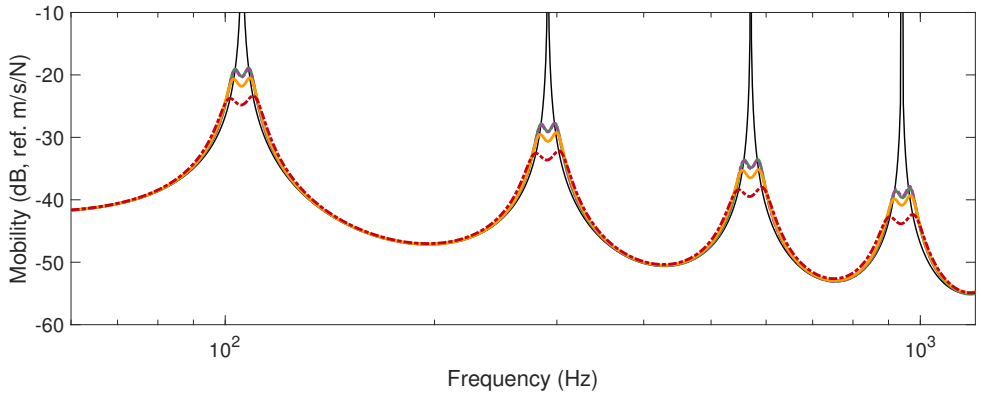

Figure 3.26: Velocity FRF of the beam shunt circuits targeting mode 1 to 4 (—) and with networks targeting mode 1 to 4 and interconnecting five (-·-), ten (—) and twenty (-·-) pairs of adjacent patches.

Figure 3.26 shows the FRFs obtained by creating groups of various sizes of adjacent piezoelectric patches that target the first four modes. The patches numbers used in the networks are given in Table 3.2. It can again be seen that decentralization plays a detrimental role on performance. In this case, this is due to the fact that the mode shapes are far from being orthogonal, which undermines performance and makes it close to that of shunt circuits, as discussed in Section 3.5.6.1.

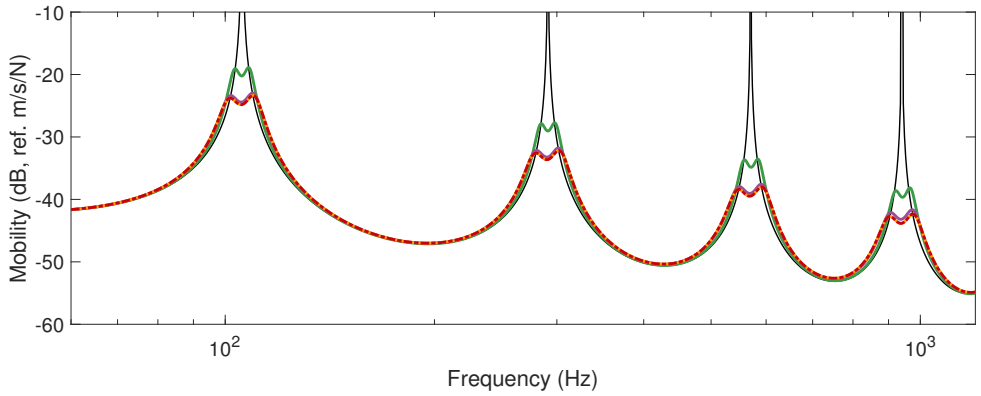

Figure 3.27: Velocity FRF of the beam shunt circuits targeting mode 1 to 4 (—) and with networks targeting mode 1 to 4 and interconnecting five (—), ten (-·-) and twenty (-·-) pairs of alternated patches.

Using another arrangement where the patches are alternately connected to the networks (as given in Table 3.2), Figure 3.27 shows that decentralization now has a much weaker impact on performance. This is due to the near-orthogonality that the mode shapes now exhibit under this alternate distribution. Once again, this highlights the importance of adequately distributing the transducers among the networks.

	Group 1	Group 2	Group 3	Group 4
4 groups, adjacent	1,2,3,4,5	6,7,8,9,10	11,12,13,14,15	16,17,18,19,20
4 groups, alternate	1,5,9,13,17	2,6,10,14,18	3,7,11,15,19	4,8,12,16,20
2 groups, adjacent	1,2,3,4,5, 6,7,8,9,10	11,12,13,14,15, 16,17,18,19,20	/	/
2 groups, alternate	1,3,5,7,9, 11,13,15,17,19	2,4,6,8,10, 12,14,16,20	/	/

Table 3.2: Patches distribution among the decentralized networks for different cases.

3.9 Conclusion

Aiming to provide a simple and systematic design strategy to mitigate multiple resonances of complex structures, this chapter leveraged the concept of passive electrical networks interconnecting piezoelectric transducers. By tailoring the electrical modal properties, effective multimodal damping can be obtained. Specifically, the electrical mode shapes were optimized in order to maximize performance while guaranteeing the passivity of the network. Passivity was formally interpreted as a performance limiter which restricts the maximal amplitude attainable by the mode shapes. The resonance frequencies and damping ratios of the electrical modes were then tuned to make the action of the network equivalent to that of a resonant shunt at multiple frequencies. The electrical matrices of the network could eventually be retrieved from these modal properties. The proposed modal-based synthesis was applied in various numerical example and demonstrated its ability to provide broadband damping.

In order to reduce the potentially numerous interconnections in the electrical network, partially or totally decentralized electrical networks were investigated. The modal-based synthesis was adapted to these cases, and it was demonstrated that this would either lead to a lower performance or a lower number of controlled modes than the centralized network. This decentralization procedure also allowed to bridge the three commonly used approaches for multimodal piezoelectric shunt damping, namely multiple piezoelectric shunts, multimodal circuits, and electrical networks. These strategies were compared with a piezoelectric free-free beam, and the superior performance of a centralized electrical network was demonstrated. However, practical operational considerations may lead to favor the other solutions because of their simplicity.

The examples developed in this chapter highlighted several possible areas to explore as a continuation of this work. A first aspect would be the impact of patches distributions among the networks. It was shown that the mutual orthogonality of the optimal mode shapes played a prominent role in the performance of the networks. However, the transducers selection was made on an empirical basis, and it could be interesting to develop an automatic selection procedure. Specifying other mode shapes than those optimal for the case where the network controls a single mode could also be beneficial.

Another question to be addressed concerns the practical realization of the networks. This was partially answered in the second part of this chapter, where decentralization

was brought up to the point where the networks boil down to mere shunt circuits. In case of RL shunts, the electrical parameters are directly given by the diagonal elements of the electrical matrices. For multimodal shunt circuits, the characteristics obtained in this chapter are the scaling factors (whose squares are in this case identical to the residues in Chapter 2), the resonance frequencies and damping ratios. This gives all the specifications necessary to tune passive shunt circuits, as in the second part of Chapter 2. The realization of a network interconnecting multiple transducers remains nevertheless unsolved for now, and a procedure should be designed in order to deduce the topology and electrical constituents of the network. If this problem is solved, the impact of some variables that are underconstrained (such as when the electrical mode shape matrix is rank-deficient) on topology and on the parameters could also be investigated.

Finally, this theoretical work should be experimentally validated. If the network is to be realized with passive elements, the previous perspective is a prerequisite. DVAs could constitute a potentially simple and efficient solution to implement these networks, and the correspondence of the network with an assembly of passive components would no longer be an issue. Special precautions would however have to be taken with respect to what was presented in Chapter 1. The first one is that the circuits would have to be adapted to multiple piezoelectric transducers. The DVA would also have to act as an impedance, because the admittance matrix (Equation (3.15)) is improper.

4 Numerical optimization of piezoelectric vibration absorbers

Abstract

This chapter presents a computational method for the purpose of multimodal vibration mitigation with piezoelectric vibration absorbers. The goal of the proposed algorithm is to simultaneously minimize the maximum amplitude of the problematic resonances. To circumvent the issues associated with direct H_∞ optimization, a norm-homotopy optimization approach is developed. The algorithm aims to minimize norms of increasing order of a transfer function. Starting from a low order for which the cost function is smooth, the norm order is gradually increased, which numerically stiffens the problem but makes it closer to the H_∞ one. The outcome of the algorithm is termed all-equal-peak design because all controlled peaks are equal in amplitude. This all-equal-peak design is illustrated on a two-degree-of-freedom structure, two beams and a plate.

4.1 Introduction

Chapters 2 and 3 presented techniques to control multiple modes of a structure. The tuning approaches proposed therein approximated the dynamics of the electromechanical system at hand by considering pairs of resonant modes, and the non-resonant modes were cast as background contributions, as proposed by Høgsberg and Krenk [119]. However, this approximation can be challenged for structures with closely-spaced modes, or when these non-resonant modes substantially contribute to the response in comparison with the resonant ones. This is generally observable by the presence of unbalanced peaks.

When the performance associated with the initial tuning is unsatisfactory, it may be complex and time-consuming to manually adapt the parameters of the shunt circuit. This can nonetheless be done automatically through numerical optimization, wherein the characteristics of the shunt circuit are adapted in order to minimize a given quantity, e.g., the H_∞ norm of a particular transfer function.

Numerical optimization for vibration mitigation was largely used with TMDs (see [162] for a short review). Its use with piezoelectric damping is less widespread. Steffen and Inman [163] used a genetic algorithm to optimize the parameters of multiple piezoelectric shunt circuits. Fleming et al [147] resorted to gradient-based optimization to minimize the H_2 norm of a transfer function in order to determine the resistances of multiple-branch shunt circuits. Jeon [164] used particle swarm optimization to tune a series-parallel impedance-type circuit whereas Cigada et al [146] also exploited gradient-based algorithms to tune a current flowing shunt circuit. Beradengo et al [165] obtained the optimal impedance of a passive circuit through optimization based on linear matrix inequalities. An interesting feature of this work is that the circuit topology is not assumed beforehand, but it is rather an outcome of the optimization process. Gardonio et al [166] proposed a

tuning strategy for the parameters of a CF shunt circuit using Newton's method based on the maximization of the power dissipated in the shunt. This approach holds promises, as it is potentially implementable for real-time tuning of the absorbers.

Numerical optimization can also be used to place the transducers on a structure in an effort to maximize the EEMCF with specific modes. For instance, Ducarne et al [76] used an extensive parameter space exploration to optimize the characteristics of piezoelectric patches placed on a cantilever beam. Giorgio et al [58, 158] optimized the placement of multiple piezoelectric patches on a plate in order to maximize the norm of the coupling matrix. The placement of the transducers is an important and challenging aspect of piezoelectric damping, but is not addressed in this work.

Despite its versatility, numerical optimization suffers from important drawbacks. First, it generally requires an accurate model of the structure to be controlled, which is not often available in practice. Second, the cost function may be nonsmooth and non-convex, and the global minimum can be difficult to reach.

To address these issues, a new kind of optimization algorithm is proposed in this chapter. The developed algorithm attempts to minimize the norms of different orders of a transfer function. It starts with a low-order norm, which is smooth and can easily be numerically optimized. Based on the optimal solution with lower-order norms, it then progressively increases the order, which makes the problem numerically stiffer[1], but closer to the H_∞ optimization problem. The outcome of the algorithm generally is a so-called *all-equal-peak design*, i.e., all the peaks of the controlled resonances are equal in amplitude. The algorithm can directly work with experimental FRFs, thereby bypassing the need to build a model of the structure.

Section 4.2 highlights the challenges associated with a direct optimization of the H_∞ norm. The norm-homotopy (NH) approach is introduced to address these issues in Section 4.3, and an optimization algorithm for piezoelectric vibration absorbers is presented. It is then illustrated with several examples in Section 4.4.

4.2 Challenges associated to H_∞ optimization

The parameters of vibration absorbers are usually optimized with respect to a specific metric. Figure 4.1 features contours of typical metrics, the H_2 and H_∞ norms of the receptance, for various resistances and inductances of a series RL shunt in the case of a SDoF structure (see Section 1.2.2.2). The parameters minimizing these norms are close but not identical. A notable difference can be observed, i.e., the H_2 norm is smooth whereas the H_∞ norm is not. In particular, a sharp corner in the contour lines of the H_∞ norm can be observed around $L \approx L_{opt}^{RLS}$ for $R \lesssim R_{opt}^{RLS}$.

This nonsmooth character can be understood by looking at the receptance for a fixed resistance and a varying inductance, as illustrated in Figure 4.2. When L is too small, the leftmost peak has the highest amplitude and determines the H_∞ norm. As L is increased, this peak decreases while the rightmost peak increases, up to the point where this latter becomes more prominent. The point where they are equal is where the H_∞ norm is nonsmooth.

[1] Numerical stiffness refers to the tendency of a problem to exhibit a solution largely sensitive to the parameters of this problem, and is not to be confused with mechanical stiffness.

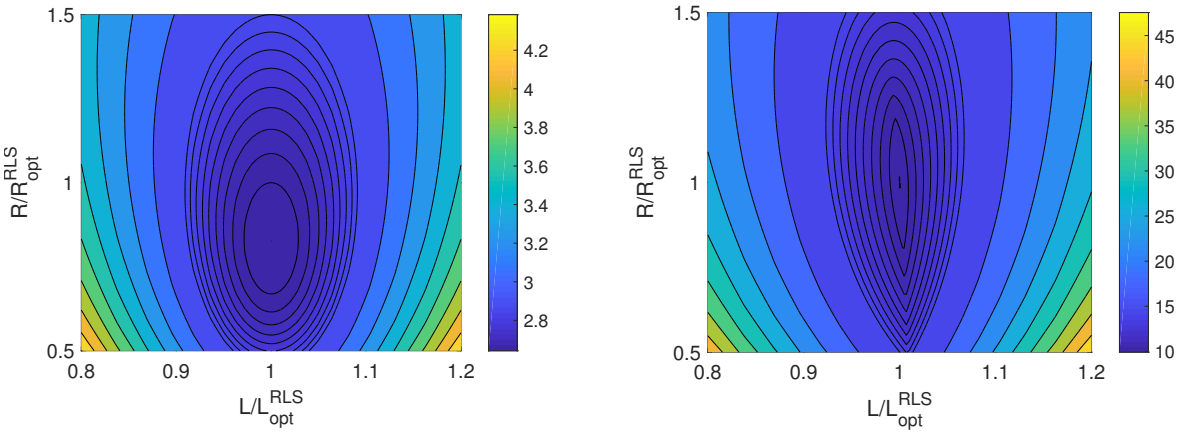

(a) (b)

Figure 4.1: Contours of the H_2 (a) and H_∞ (b) norms of the receptance of a SDoF oscillator with a series RL piezoelectric shunt (contour levels are not evenly spaced).

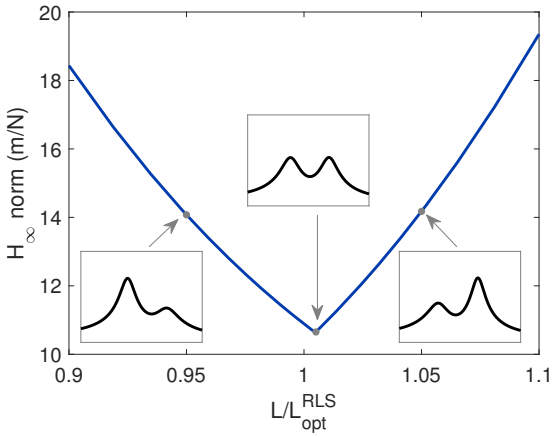

Figure 4.2: H_∞ norm of the receptance of a SDoF oscillator with a series RL piezoelectric shunt, with $R = 0.75R_{opt}^{RLS}$. Plots of the receptance for $L = 0.95L_{opt}^{RLS}$,$L = 1.005L_{opt}^{RLS}$ (corresponding to the minimum H_∞ norm) and $L = 1.05L_{opt}^{RLS}$ are inset.

To illustrate the difficult convergence of a gradient-based method applied to a nonsmooth cost function [167], the parameters of the series RL shunt were numerically optimized for various initial guesses of resistance and inductance. Two types of cost functions were considered, namely the H_2 and H_∞ norms of the receptance. The parameters were optimized with MATLAB's `fmincon` routine. In this simple case, the numerical solutions can be compared to the analytical ones [81]. The numerical optimizations are assessed through their number of iterations and the relative error of their optimal cost functions with respect to the analytical one. The resulting maps are presented in Figure 4.3.

The H_2-norm optimization consistently finds the optimal solution (the maximum relative error being 3×10^{-14}) and takes at most 11 iterations. By contrast, the output of the H_∞ optimization can reach a relative error as high as 17.7% at the cost of up to 80 iterations.

Looking at an example where $R_0 = 0.5R_{opt}^{RLS}$ and $L_0 = L_{opt}^{RLS}$ in Figure 4.4 shows that the optimizer struggles at the discontinuity of the cost function surface and zigzags around this region, taking smaller and smaller steps up to the point where it terminates prematurely.

An alternate approach is to use `fminimax`, specialized for optimization problems aiming

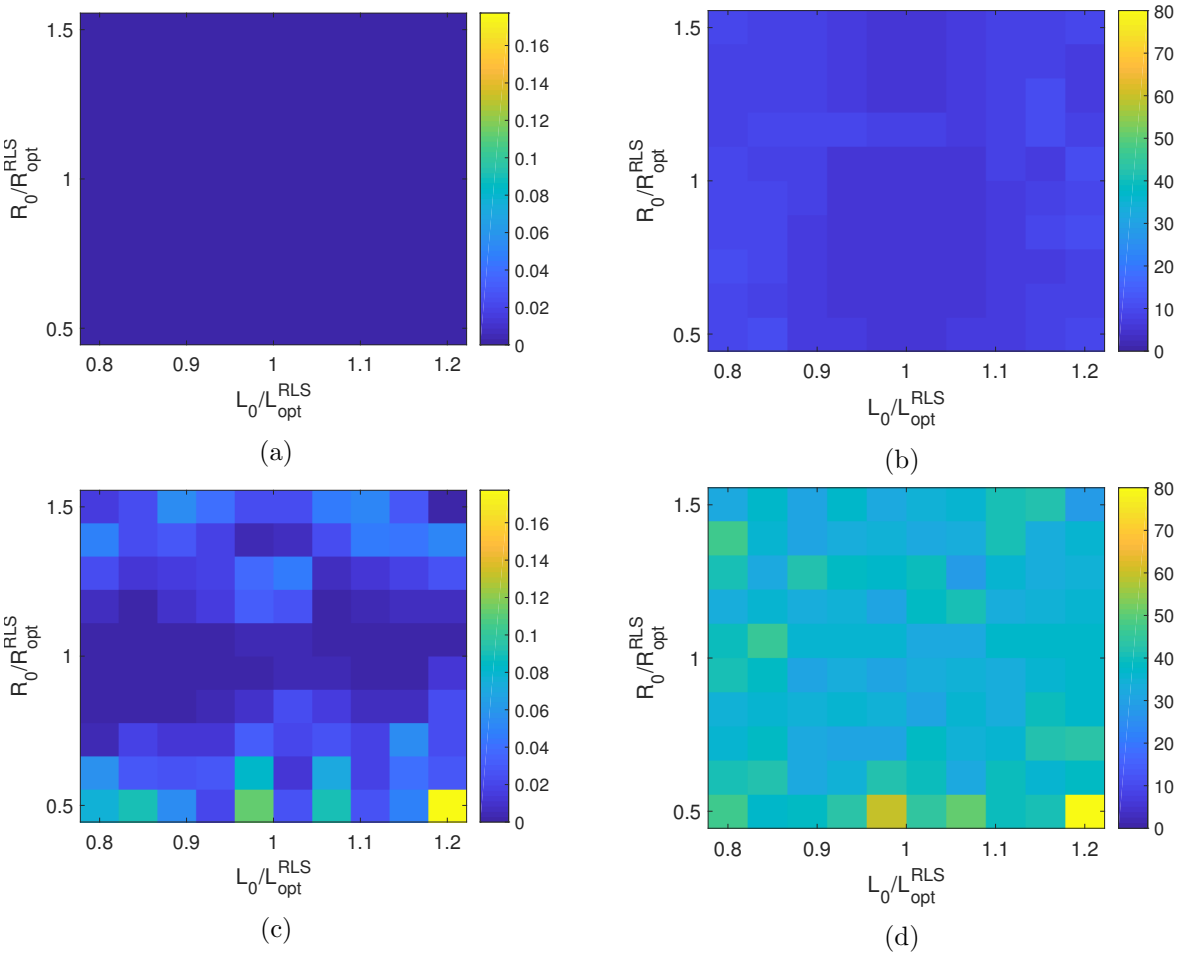

Figure 4.3: Relative error of the H_2 (a) and H_∞ (c) optimizations, and number of iterations of the H_2 (b) and H_∞ (d) optimizations of the receptance of a SDoF oscillator with a series RL piezoelectric shunt, with initial resistance R_0 and inductance L_0.

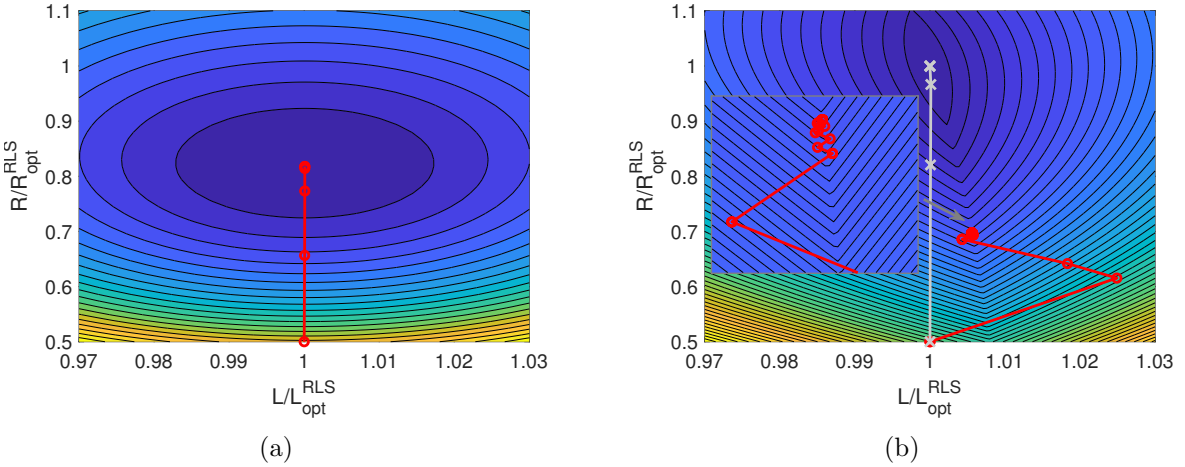

Figure 4.4: Optimization variables history of the H_2 (a) and H_∞ (b) ($-\circ-$: `fmincon`, $-\times-$: `fminimax`) optimizations of the receptance of a SDoF oscillator with a series RL piezoelectric shunt with initial guess $R_0 = 0.5R_{opt}^{RLS}$ and $L_0 = L_{opt}^{RLS}$.

to minimize the maximum value of a given set of functions. In this case, the set of functions is the set of values of the FRF sampled at different frequencies. As testified

by Figure 4.4(b), the output of this optimizer is much closer to the optimal solution than that of `fmincon`. However, examples in Section 4.4 will show that it is not as robust when multiple resonances are targeted.

4.3 A norm-homotopy approach for H_∞ optimization

4.3.1 General principles

The strategy proposed herein relies on a NH optimization during which problems of increasing complexity are solved sequentially using the previously-obtained parameters as an initial guess for the next problem. Specifically, the p-norm of the receptance is minimized, and p is sequentially increased so as to approach the H_∞ norm, as schematically presented in Fig. 4.5. A low value of p puts more weight on the parts of the transfer function with lower amplitudes and makes the optimization problem less stiff, whereas the subsequent increase in p ensures that resonances with high amplitudes are penalized enough.

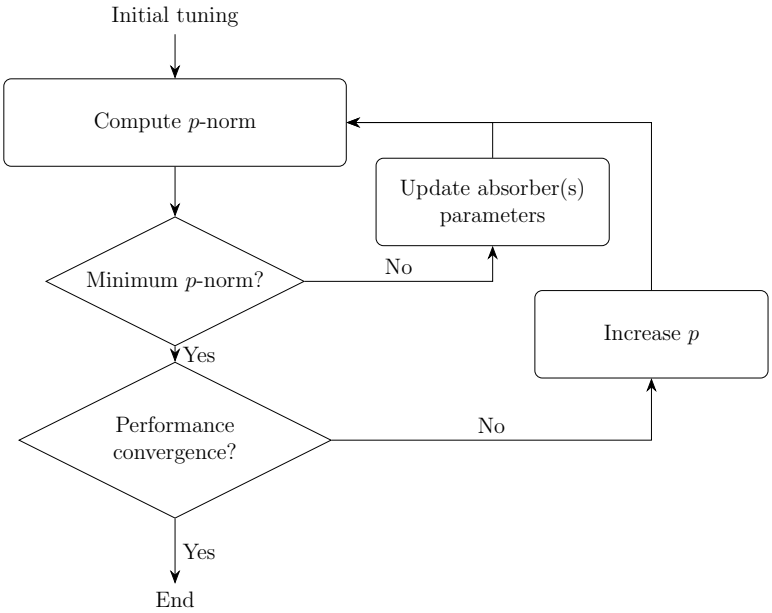

Figure 4.5: Conceptual flowchart of the proposed norm-homotopy optimization algorithm.

4.3.2 p-norm of a transfer function

The p-norm of a function f is given by

$$H_p\{f\} = \left(\int_0^\infty |f(\omega)|^p d\omega \right)^{1/p}. \tag{4.1}$$

In practice, the p-norm can be estimated with a quadrature formula using a finite set of samples at frequencies ω_n $(n = 1, \cdots, N_\omega)$ as

$$H_p\{f\} \approx \chi \left(\sum_{n=1}^{N_\omega} \left| \frac{f(\omega_n)}{\chi} \right|^p w_n \right)^{1/p}, \tag{4.2}$$

where w_n are quadrature weights and χ is a strictly positive scaling factor that does not affect the p-norm. χ improves numerical conditioning for high values of p, and a typical choice would be

$$\chi = \max_{n \in [1, N_\omega]} |f(\omega_n)|. \tag{4.3}$$

In [162], it was proposed to use the p-norm of the vector containing the peaks amplitudes of the receptance. This requires to locate them using numerical search algorithms. In this thesis, it is rather proposed to approximate directly the p-norm of the transfer function with quadrature formulas. This has two main advantages. The first is that the algorithm is often more robust. The sampling points are set in the beginning of the algorithm, which allows to define precisely the frequency bands of interest. By contrast, a peak-finding algorithm may converge to a peak which is not of interest. The second advantage is the ability of the proposed approach to work directly with experimental measurements without the need to fit any model. As shall be shown hereafter, the only required information comes from the frequency responses of the host system.

4.3.3 Frequency response of the controlled structure

Starting either from Equation (3.1) or Equation (3.2), the dynamics of the controlled electromechanical system can be put into the generic form

$$\begin{cases} \mathbf{M}_0 s^2 \mathbf{x} + \mathbf{C}_0 s \mathbf{x} + \mathbf{K}_0 \mathbf{x} + \mathbf{B}_0 \mathbf{x}_e = \mathbf{f} \\ \left(\mathbf{H}_A(s) + \mathbf{H}_{A0} \right) \mathbf{x}_e - \mathbf{B}_0^T \mathbf{x} = \mathbf{0} \end{cases}, \tag{4.4}$$

where $\mathbf{x}_e$ is a vector of electrical DoFs (charge or voltage), $\mathbf{H}_A(s)$ is a matrix characterizing the dynamics of the absorbers, $\mathbf{H}_{A0}$ is the piezoelectric capacitance or elastance matrix at constant strain, and $\mathbf{B}_0$ is a piezoelectric coupling matrix. Subscript 0 is used to refer to the host system. If a Norton-type model is used, by comparison with Equation (3.1),

$$\mathbf{K}_0 := \mathbf{K}_{sc}, \qquad \mathbf{B}_0 := \mathbf{\Gamma}_p, \qquad \mathbf{x}_e := \mathbf{V}, \qquad \mathbf{H}_{A0} := \mathbf{C}_p^\varepsilon, \qquad \mathbf{H}_A(s) := \frac{1}{s} \mathbf{Y}_s(s), \tag{4.5}$$

where $\mathbf{Y}_s(s)$ is the admittance matrix of the circuits/networks connected to the piezoelectric transducers, and if a Thévenin-type model is used, by comparison with Equation (3.2),

$$\mathbf{K}_0 := \mathbf{K}_{oc}, \qquad \mathbf{B}_0 := -\mathbf{\Theta}_p, \qquad \mathbf{x}_e := \mathbf{q}, \qquad \mathbf{H}_{A0} := -\mathbf{E}_p^\varepsilon, \qquad \mathbf{H}_A(s) := -s \mathbf{Z}_s(s), \tag{4.6}$$

where $\mathbf{Z}_s(s)$ is the impedance matrix of the circuits/networks connected to the piezoelectric transducers. Going back to the generic model in Equation (4.4), the electrical DoFs can be deduced from the second line of this equation as

$$\mathbf{x}_e = \left(\mathbf{H}_A(s) + \mathbf{H}_{A0} \right)^{-1} \mathbf{B}_0^T \mathbf{x}. \tag{4.7}$$

Inserting this relation into the first line of Equation (4.4) gives

$$\begin{aligned}\left(\mathbf{M}_0 s^2 + \mathbf{C}_0 s + \mathbf{K}_0 + \mathbf{B}_0 \left(\mathbf{H}_A(s) + \mathbf{H}_{A0}\right)^{-1} \mathbf{B}_0^T\right) \mathbf{x} \\ = \left(\mathbf{H}_0(s) + \mathbf{B}_0 \left(\mathbf{H}_A(s) + \mathbf{H}_{A0}\right)^{-1} \mathbf{B}_0^T\right) \mathbf{x} = \mathbf{H}_c(s)\mathbf{x} = \mathbf{f},\end{aligned} \tag{4.8}$$

where $\mathbf{H}_0(s)$ and $\mathbf{H}_c(s)$ are the dynamic stiffness matrices of the uncontrolled and controlled structures, respectively. The latter is thus obtained from the former with a low-rank update representing the feedback action of the absorbers. Using the SMW formula (Equation (A.2)), the inverse of $\mathbf{H}_c$ can be expressed as

$$\mathbf{H}_c^{-1}(s) = \mathbf{H}_0^{-1}(s) - \mathbf{H}_0^{-1}(s)\mathbf{B}_0 \left(\mathbf{H}_A(s) + \mathbf{H}_{A0} + \mathbf{B}_0^T \mathbf{H}_0^{-1}(s)\mathbf{B}_0\right)^{-1} \mathbf{B}_0^T \mathbf{H}_0^{-1}(s). \tag{4.9}$$

In practice, one is often interested in a particular transfer function. If the forcing can be described by a spatial distribution $\mathbf{w}_f$ and amplitude f such that $\mathbf{f} = \mathbf{w}_f f$, and if the output is a combination of the generalized DoFs of the structure given by $\mathbf{w}_u$, the uncontrolled and controlled receptances are respectively given by

$$h_0(s) = \mathbf{w}_u^T \mathbf{H}_0^{-1}(s)\mathbf{w}_f, \qquad h_c(s) = \mathbf{w}_u^T \mathbf{H}_c^{-1}(s)\mathbf{w}_f. \tag{4.10}$$

Hence, using Equation (4.9), the controlled receptance can also be expressed as

$$h_c(s) = h_0(s) - \mathbf{w}_u^T \mathbf{H}_0^{-1}(s)\mathbf{B}_0 \left(\mathbf{H}_A(s) + \mathbf{H}_{A0} + \mathbf{B}_0^T \mathbf{H}_0^{-1}(s)\mathbf{B}_0\right)^{-1} \mathbf{B}_0^T \mathbf{H}_0^{-1}(s)\mathbf{w}_f. \tag{4.11}$$

We note that the only FRFs of the host system that need to be known to use Equation (4.11) are contained in the matrix

$$\begin{bmatrix} \mathbf{0} & \mathbf{0} \\ \mathbf{0} & \mathbf{H}_{A0} \end{bmatrix} + \begin{bmatrix} \mathbf{w}_u & \mathbf{B}_0 \end{bmatrix}^T \mathbf{H}_0^{-1}(s) \begin{bmatrix} \mathbf{w}_f & \mathbf{B}_0 \end{bmatrix} = \begin{bmatrix} h_0(s) & \mathbf{w}_u^T \mathbf{H}_0^{-1}(s)\mathbf{B}_0 \\ \mathbf{B}_0^T \mathbf{H}_0^{-1}(s)\mathbf{w}_f & \mathbf{H}_{A0} + \mathbf{B}_0^T \mathbf{H}_0^{-1}(s)\mathbf{B}_0 \end{bmatrix}, \tag{4.12}$$

which can either be computed from a model, or directly measured from an experimental setup. This is an incentive for using the SMW formula [168] in addition to the advantage it brings in terms of computational cost when evaluating the controlled receptance. Indeed, a direct resolution of Equation (4.8) would require the resolution of a large-size linear system, whereas Equation (4.11) only requires the factorization of a matrix whose size is equal to the number of piezoelectric transducers, i.e., of small size.

4.3.4 p-norm optimization

The goal of the optimization algorithm is to find the optimal electrical parameters of the absorbers through the nonlinear programming problem

$$\begin{aligned} \underset{\boldsymbol{\xi}}{\text{Minimize}} \quad & H_p\left\{|h_c|^2\right\} \\ \text{Subject to} \quad & \mathbf{c}\left(\boldsymbol{\xi}\right) \leq 0 \end{aligned} \tag{4.13}$$

where $\boldsymbol{\xi}$ is the vector containing the absorber parameters. The squared amplitude of the transfer function at hand $|h_c|^2$ is used rather than the transfer function itself to make

the optimization problem smooth. Constraints $\mathbf{c}$ can be added to guarantee the passivity of the absorber, usually through the positivity of some parameters. This problem can be solved numerically with standard optimization routines.

The gradients of the p-norm are computed analytically to increase the speed and accuracy of the proposed algorithm. From Equation (4.2), the l^{th} element of the gradient of the p-norm with respect to the absorbers parameter ξ_l is given by

$$\frac{\partial H_p\left\{|h_c|^2\right\}}{\partial \xi_l} = \left(\sum_{i=1}^{N_\omega}\left(\frac{1}{\chi}\left|h_c(j\omega_i,\boldsymbol{\xi})\right|^2\right)^{p-1}\frac{\partial\left|h_c(j\omega_i,\boldsymbol{\xi})\right|^2}{\partial\xi_l}\right)\left(\sum_{i=1}^{N_\omega}\left(\frac{1}{\chi}\left|h_c(j\omega_i,\boldsymbol{\xi})\right|^2\right)^{p}\right)^{\frac{1}{p}-1}. \tag{4.14}$$

The derivative of the squared receptance is simply

$$\frac{\partial\left|h_c(j\omega_i,\boldsymbol{\xi})\right|^2}{\partial\xi_l} = \frac{\partial}{\partial\xi_l}\left(h_c^*(j\omega_i,\boldsymbol{\xi})h_c(j\omega_i,\boldsymbol{\xi})\right) = 2\Re\left\{h_c^*(j\omega_i,\boldsymbol{\xi})\frac{\partial h_c(j\omega_i,\boldsymbol{\xi})}{\partial\xi_l}\right\}. \tag{4.15}$$

The derivative of the receptance with respect to ξ_l is computed thanks to Equation (4.11) as

$$\frac{\partial h_c(j\omega_i,\boldsymbol{\xi})}{\partial\xi_l} = \mathbf{w}_u^T\mathbf{G}(j\omega_i)\frac{\partial\mathbf{H}_A(j\omega_i)}{\partial\xi_l}\mathbf{G}^T(j\omega_i)\mathbf{w}_f \tag{4.16}$$

where

$$\mathbf{G}(j\omega_i) = \mathbf{H}_0^{-1}(j\omega_i)\mathbf{B}_0\left(\mathbf{H}_A(j\omega_i)+\mathbf{H}_{A0}+\mathbf{B}_0^T\mathbf{H}_0^{-1}(j\omega_i)\mathbf{B}_0\right)^{-1}. \tag{4.17}$$

Despite the rather complicated structure of Equations (4.16) and (4.17), computing the gradient of the cost function is not cumbersome for two reasons. First, each element in Equation (4.17) is known from the computation of $h_c(j\omega_i,\boldsymbol{\xi})$. Second, the derivative of $\mathbf{H}_A$ with respect to ξ_l can be computed analytically. The procedure to compute them depends on the type of absorber at hand (circuits or networks), and is detailed hereafter.

4.3.4.1 Derivatives for shunt circuits

Multi-branch shunt circuits can be modeled using their transfer functions (with Equations (2.115), (2.122), (2.136) and (2.141) for Hollkamp's, the CF, SFCF and SPIS shunt circuits, respectively), and their derivative with respect to the electrical parameters can readily be computed. It is the same for the circuits with ideal Norton's admittance and ideal Thévenin's impedance (Equations (2.60) and (2.92), respectively) when using the residues, frequencies and damping ratios. For the CB shunt circuit, working with transfer matrices can be somewhat impractical, and a convenient alternative is to work with its state-space model, as developed in Section C.1. In this case, the immittance of the circuit has the form

$$\mathbf{C}_A\left(s\mathbf{I}-\mathbf{A}_A\right)^{-1}\mathbf{B}_A+\mathbf{D}_A. \tag{4.18}$$

The derivative of this immittance with respect to a given parameter ξ_l can then be computed by

$$\frac{\partial\mathbf{C}_A}{\partial\xi_l}\left(s\mathbf{I}-\mathbf{A}_A\right)^{-1}\mathbf{B}_A+\mathbf{C}_A\left(s\mathbf{I}-\mathbf{A}_A\right)^{-1}\frac{\partial\mathbf{A}_A}{\partial\xi_l}\left(s\mathbf{I}-\mathbf{A}_A\right)^{-1}\mathbf{B}_A + \mathbf{C}_A\left(s\mathbf{I}-\mathbf{A}_A\right)^{-1}\frac{\partial\mathbf{B}_A}{\partial\xi_l}+\frac{\partial\mathbf{D}_A}{\partial\xi_l}. \tag{4.19}$$

If the shunt admittance is modeled, the electrical DoFs should be the voltages, and the absorber's transfer matrix is

$$\mathbf{H}_A(s) = \frac{Y_s(s)}{s}, \tag{4.20}$$

whereas if the shunt impedance is modeled, the electrical DoFs should be the charges, and the absorber's transfer matrix is

$$\mathbf{H}_A(s) = -sZ_s(s). \tag{4.21}$$

4.3.4.2 Derivatives for networks

The electrical DoFs for a network are the nodal voltages, and the transfer matrix for a network is given by (using Equation (3.15))

$$\mathbf{H}_A(s) = \frac{1}{s}\mathbf{Y}(s) = \mathbf{C}_e + \frac{1}{s}\mathbf{G} + \frac{1}{s^2}\mathbf{B}. \tag{4.22}$$

According to Section 3.5.1, the matrices $\mathbf{C}_e$, $\mathbf{G}$ and $\mathbf{B}$ need to be symmetric positive semidefinite in order for the network to be realizable with passive elements. It is possible to parametrize these matrices based on their eigenstructure and Givens parametrization in such a way that this condition is enforced. This rather technical aspect is discussed in Section E.1. The derivative of the transfer matrix is given by

$$\frac{\partial \mathbf{H}_A(s)}{\partial \xi_l} = \frac{\partial \mathbf{C}_e}{\partial \xi_l} + \frac{1}{s}\frac{\partial \mathbf{G}}{\partial \xi_l} + \frac{1}{s^2}\frac{\partial \mathbf{B}}{\partial \xi_l}. \tag{4.23}$$

4.3.5 Norm-homotopy optimization procedure

Once the optimization has converged for a given value of p, p is then increased in order to penalize high-amplitude peaks more strongly and approach the H_∞ optimum. The optimization problem in Equation (4.13) is solved starting from the previously-obtained optimal solution. A heuristic scheme for p given by the double exponential progression

$$p = 2^{2^k}, \qquad k \in \mathbb{N} \tag{4.24}$$

is considered. The value of k starts from zero and is incremented by one after convergence. This NH algorithm may be terminated when no significant change is observed in the absorbers parameters and/or in the value of the p-norm.

Figure 4.6 summarizes schematically the proposed NH optimization algorithm.

4.4 Examples

This section presents several examples to illustrate typical outputs of the NH optimization algorithm. The p-norm is evaluated using a trapezoidal quadrature with sampling frequencies uniformly distributed in frequency bands around the targeted resonances. These bands and the number of samples within them were chosen empirically. A small number of sampling points makes the optimization faster but less accurate.

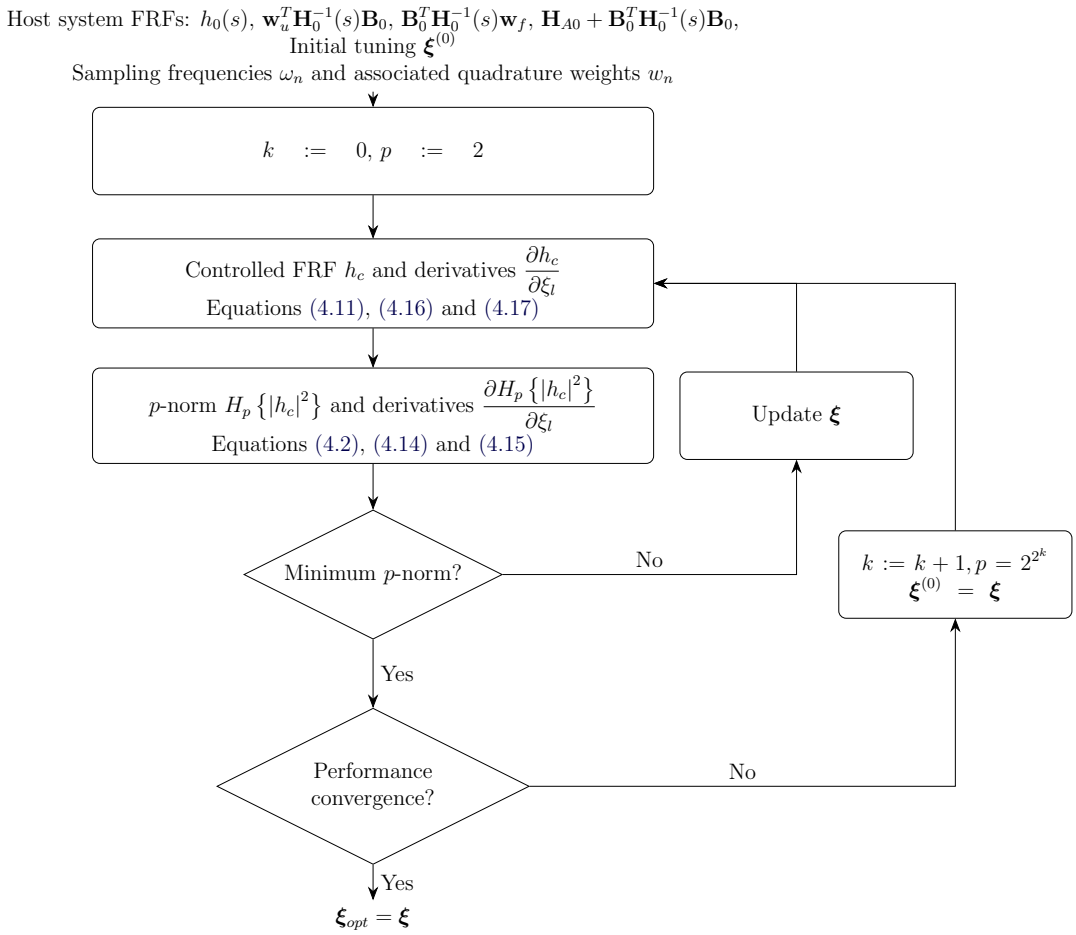

Figure 4.6: Flowchart of the proposed norm-homotopy optimization algorithm.

While a finite number of samples does not guarantee to capture the maximum of a FRF exactly, it can be well-approximated with a sufficient resolution because the FRF varies slowly in the vicinity of its maximum. In general, 50 points were chosen per frequency band encompassing the two peaks associated to a controlled resonance. A more automatic selection procedure could be devised based e.g. on the EEMCF (because it governs the bandwidth of RL shunts).

The optimization problem (4.13) is solved in MATLAB thanks to the `fmincon` routine. This routine is called for each p-norm optimization step with an initial guess given by the optimal solution computed by the previous p-norm optimization (except for the first optimization, where the initial guess is formed using the methods in Chapters 2 and 3 for circuits and networks, respectively).

Some results were compared to the output of `fminimax`. To make the approaches comparable, `fminimax` was given FRFs of the controlled structure computed in the same way as in the NH algorithm, namely with the SMW formula at the sampling frequencies used in the NH algorithm.

4.4.1 Two-degree-of-freedom structure

The first example used to demonstrate the NH optimization algorithm is the two-degree-of-freedom structure depicted in Figure 4.7 with the characteristics given

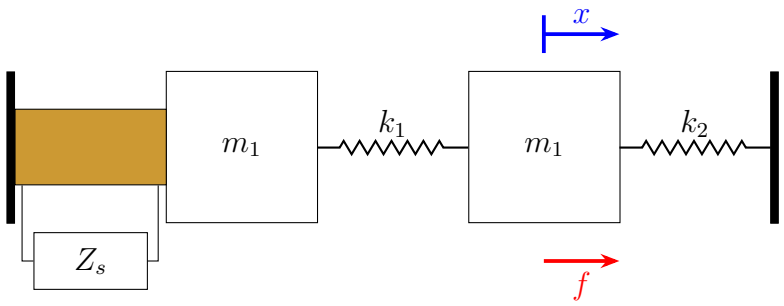

Figure 4.7: Two-degree-of-freedom structure with a piezoelectric stack shunted with a circuit of impedance Z_s.

in Table 4.1. Modal damping of 0.1% was added to the structure.

Parameter	m_1	m_2	k_1	k_2	$k_{p,sc}$	γ_p	C_p^ε
Value	1kg	1kg	1N/m	1N/m	0.96N/m	0.2N/V	1F

Table 4.1: Characteristics of the two-degree-of-freedom structure.

Hollkamp's shunt circuit [126] and the CB circuit with series RL shunts [127] were considered to demonstrate the approach. Their initial tuning was performed with the method outlined in Chapter 2 (Sections 2.7 and 2.9, respectively), using a balanced control authority over the two modes (i.e., $r_1 = r_2 = 0.5$). Figure 4.8 depicts the driving-point receptance at the second mass. It can be observed that the initial tuning results in FRFs with slightly unbalanced peaks.

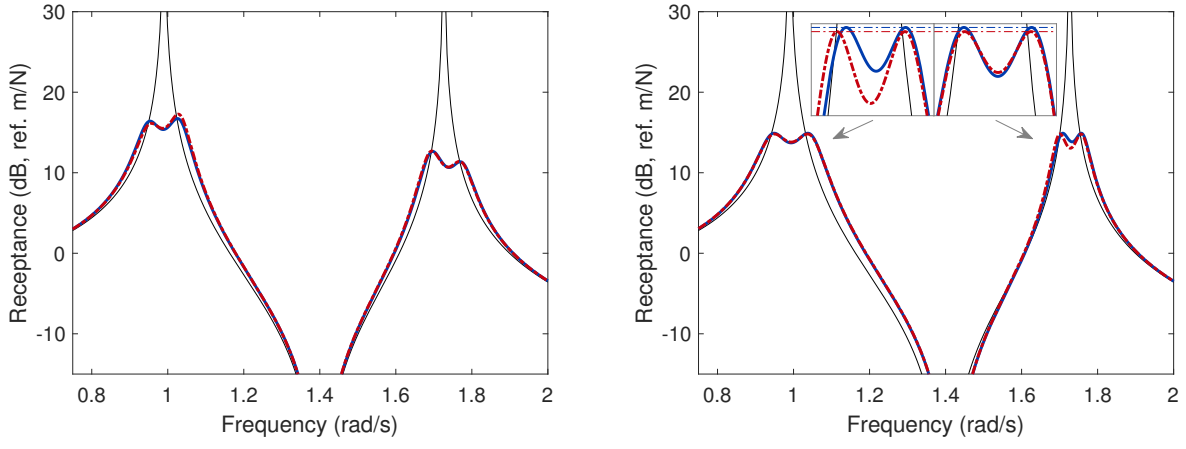

(a) (b)

Figure 4.8: FRF of the two-degree-of-freedom system: short-circuited patches (—) and controlled with Hollkamp's circuit (—) and a current blocking circuit with series RL shunts (- - -): initial tuning (a) and optimal tuning (b).

Upon optimizing the circuits' characteristics with the NH algorithm, FRFs where all peaks have the same amplitude are obtained in both cases. Because of this salient feature, this design is called *all-equal-peak design*. It appears to be a generalization of the equal-peak design for the SDoF case [83]. The optimal H_∞ norms obtained with

both shunt circuits are almost identical, although it can be observed in the insets of Figure 4.8 that the CB circuit slightly outperforms Hollkamp's circuit. This difference is nonetheless quite insignificant, which supports the statement made in Chapter 2 that passive shunts can exhibit at their best similar performance.

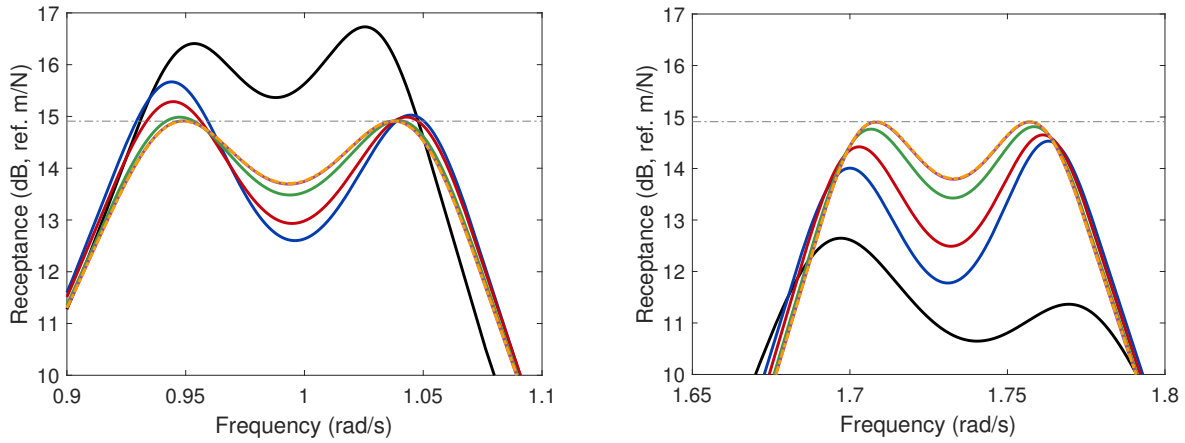

(a) (b)

Figure 4.9: Different steps of the NH optimization on the FRF of the two-degree-of-freedom system with Hollkamp's shunt circuit near the first (a) and second (b) resonance: initial tuning (—), $k = 1$ (—), $k = 2$ (—), $k = 3$ (—), $k = 4$ (—) and $k = 5$ (- - -).

Figure 4.9 analyzes the different steps of the NH optimization. For low-order p-norms, the algorithm reduces the global imbalance existing between the peaks. As p is increased, the higher-amplitude peaks are more and more penalized, and the design converges to an all-equal-peak one when $p = 4.29 \times 10^9$ ($k = 5$).

In spite of the rather marginal change in vibration attenuation between the initial and optimal tunings in Figure 4.8, the electrical parameters of both circuits underwent significant changes during the optimization, as testified in Tables 4.2 and 4.3.

	R_0	L_0	C_1	R_1	L_1
Initial value	0.0843Ω	0.6718H	0.2538F	0.2371Ω	1.9752H
Optimal value	0.1354Ω	0.8373H	0.1113F	0.2775Ω	3.5598H

Table 4.2: Initial and NH optimal parameters of Hollkamp's shunt circuit for the two-degree-of-freedom structure.

Lastly, the results of the NH optimization were compared to those obtained with `fminimax`. The comparison is presented in Figure 4.10. With Hollkamp's shunt circuit, both optimizers converged to the same optimal solution. However, this is not the case for the CB circuit. The optimal solution of `fminimax` is also an all-equal-peak design, but is slightly worse than that of the NH algorithm. Comparing Tables 4.3 and 4.4, the optimal parameters obtained with the two approaches are markedly different. This advocates for the presence of multiple local minima in the H_∞ norm even for this simple example, and shows that the all-equal-peak property is not sufficient to guarantee a global optimum.

	R_1	L_1	R_2	L_2	$\tilde{C}_1$	$\tilde{L}_1$
Initial value	0.247Ω	0.9792H	0.1193Ω	1.0066H	1F	1.0102H
Optimal value	5.5596Ω	3.7073H	0.0929Ω	0.7321H	2.6971F	0.1865H

Table 4.3: Initial and NH optimal parameters of the current blocking circuit with series RL shunts for the two-degree-of-freedom structure.

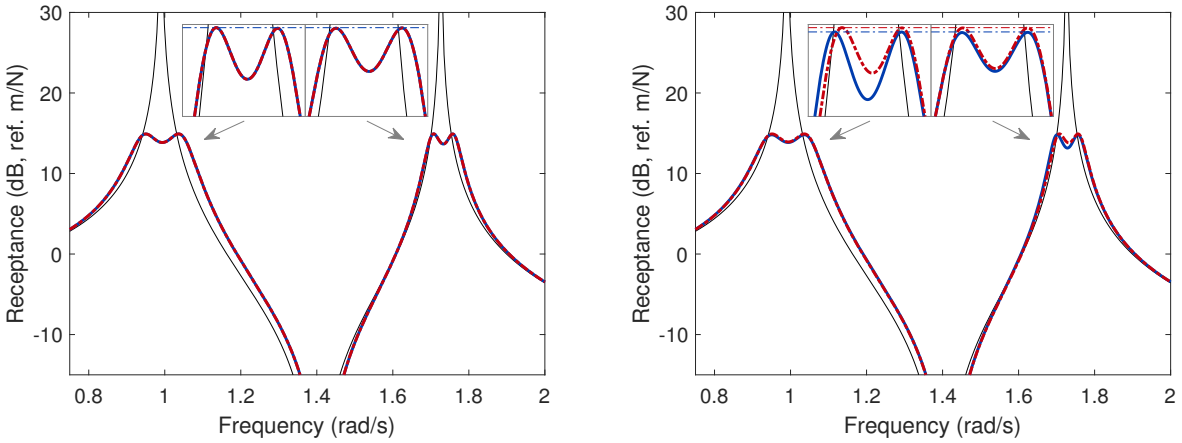

(a) (b)

Figure 4.10: FRF of the two-degree-of-freedom system: short-circuited patches (—) and controlled with Hollkamp's circuit (a) and a CB circuit with series RL shunts (b): NH optimal solution (—) and `fminimax`'s optimal solution (- - -).

	R_1	L_1	R_2	L_2	$\tilde{C}_1$	$\tilde{L}_1$
Optimal value	0.1769Ω	0.921H	0.2405Ω	2.5296H	0.2215F	6.1282H

Table 4.4: `fminimax`'s optimal parameters of the current blocking circuit with series RL shunts for the two-degree-of-freedom structure.

4.4.2 Cantilever piezoelectric beam

The piezoelectric cantilever beam introduced in [137] and studied in Section 2.5 is considered again to illustrate peculiar features of the algorithm. A shunt circuit yielding ideal Norton's admittance (see Section 2.4) is used.

The NH optimization is first used to mitigate the first two resonances of the beam's tip driving-point receptance. Despite the similarity with the two-degree-of-freedom example, the optimal result in Figure 4.11(a) is not an all-equal-peak design, yet it exhibits a lower H_∞ norm than the initial design. The reason for the absence of the all-equal-peak feature can be understood by looking at the FRF obtained with a parallel RL shunt circuit tuned to the first mode in Figure 4.11(b). In this case, the mere single-mode shunt yields a significant reduction of the second mode, whose controlled amplitude is lower than that of the first mode. This stems from both the ability of parallel RL shunts to damp higher-frequency modes, and the comparatively low modal amplitude of the

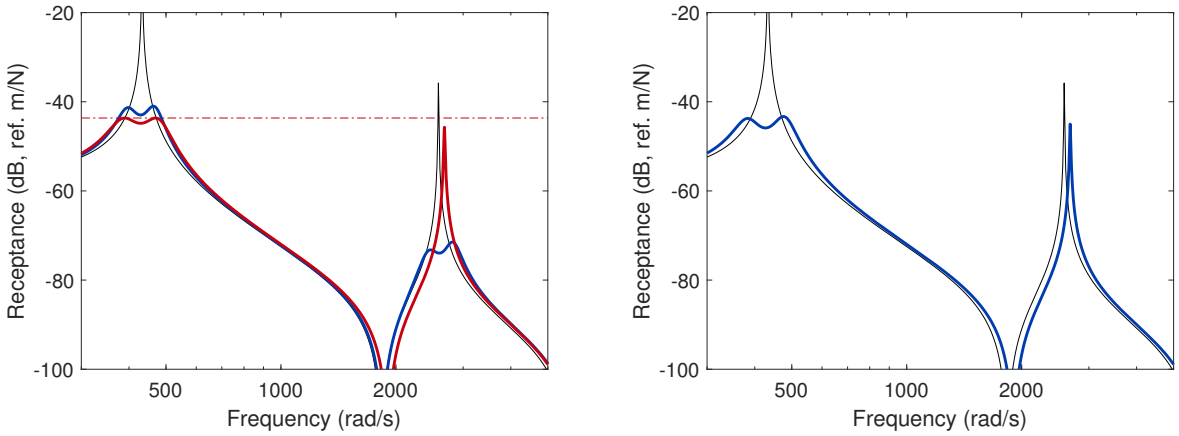

Figure 4.11: FRF of the cantilever beam with short-circuited patches (—) and controlled with an ideal Norton's admittance circuit (— : initial tuning, — : NH optimal tuning) (a) and a parallel RL shunt circuit targeting the first mode (—) (b).

second mode at the beam tip. The two-mode circuit can thus perform at best like an single parallel RL shunt targeting the first mode.

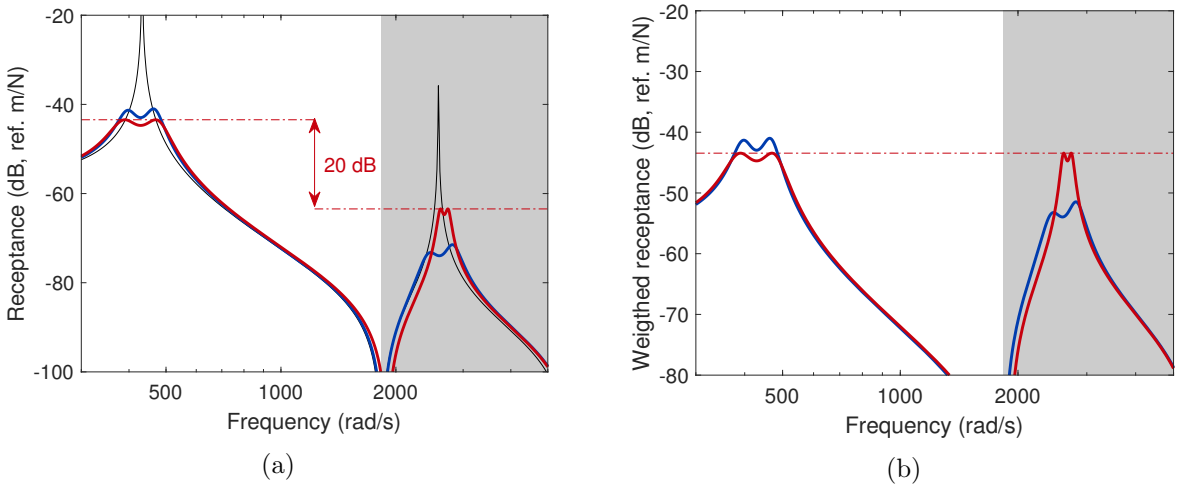

Figure 4.12: FRF of the cantilever beam with short-circuited patches (—) and controlled with an ideal Norton's admittance circuit (— : initial tuning, — : NH optimal tuning with scaled FRF): true FRF (a) and scaled FRF (b). The gray area indicates the frequency region where the FRF is multiplied by 10 in the NH optimization.

In a similar spirit to the use of residues in Chapter 2 and relative scaling factors in Chapter 3, the FRF can be scaled differently at different frequencies to put more emphasis on certain modes. Figure 4.12(a) displays a result obtained by multiplying the receptance of the beam by 10 at frequencies near that of the second mode. In this case, peaks associated to the same modes have the same amplitude, but peaks associated to different modes have an amplitude difference of 20dB. The NH algorithm retrieves the all-equal-peak design, as shown in Figure 4.12(b).

The algorithm can work with other transfer functions than receptances. Figure 4.13 presents the accelerance of the beam, for which an all-equal-peak design is also obtained.

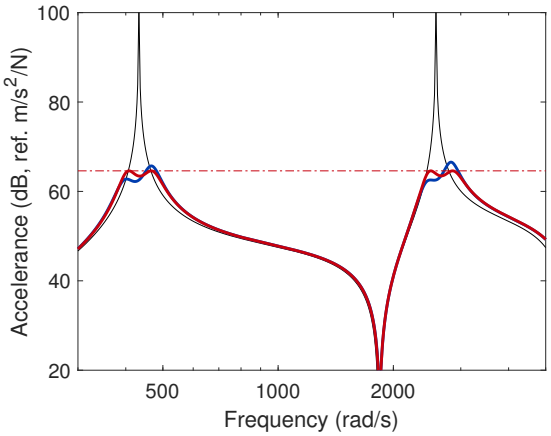

Figure 4.13: Accelerance of the cantilever beam with short-circuited patches (—) and controlled with an ideal Norton's admittance circuit (— : initial tuning, — : NH optimal tuning with scaled FRF).

4.4.3 Free-free piezoelectric beam

The free-free beam in [155] and studied in Section 3.6.2 is used to assess the ability of the NH algorithm to tune networks.

A fully centralized network is considered first, as in Section 3.6.2.1. Applying the NH algorithm to the mobility of the beam yields an all-equal-peak design (Figure 4.14). The control performance on the first mode is slightly improved but largely at the expense of the vibration reduction of higher-frequency modes. The arguable inability of the NH algorithm to improve performance is not surprising, because the network is in giving near-optimal control on all modes simultaneously.

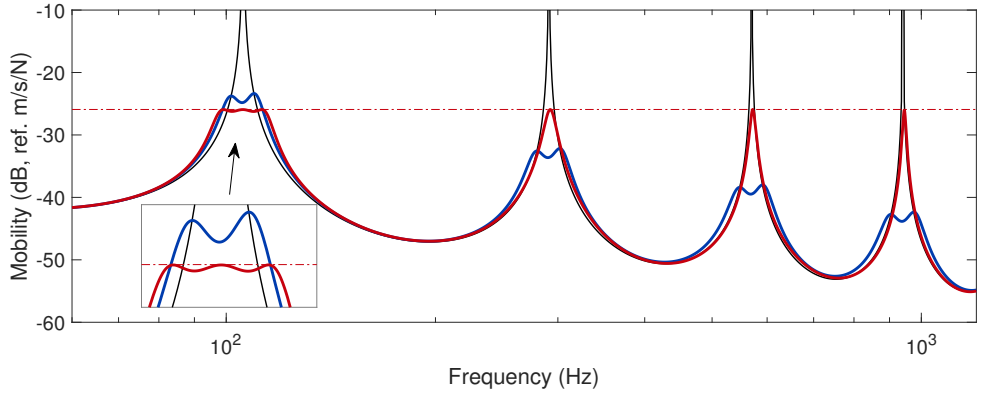

Figure 4.14: Velocity FRF of the beam with short-circuited patches (—), with a network synthesized with the modal-based approach (—) and tuned with the NH optimization (—).

A peculiar outcome obtained around the first mode is shown in the inset of Figure 4.14. The optimization algorithm splits and distributes the electrical resonance frequencies around that of the structure with the result that the controlled FRF exhibits three peaks instead of a traditional pair of peaks. This strategy was recently shown to provide better vibration reduction than a mere single-resonance-frequency shunt [169].

The control of higher-frequency modes could be improved by e.g. weighting the mobility. A sensible choice to scale the FRF around a specific mode is to evaluate it when all patches

are shunted targeting a single mode, as it would represent a near best-case reduction. The inverse of this transfer function's amplitude evaluated at the (short-circuit) resonance frequency of the uncontrolled structure could then be used as a scaling factor near this resonance. Doing so for every resonance would yield a more "natural" way of scaling the transfer function for a network (a FRF scaled this way is hereafter referred to as naturally-scaled FRF). Figure 4.15 presents the results obtained with such a scaling on the first four modes. The performance is hardly affected, and the NH optimization simply fine-tunes the electrical parameters to obtain perfectly balanced peaks (as indicated in the inset). This marginal improvement seems to indicate that the network is already performing nearly-optimally, which supports the theory developed in Chapter 3.

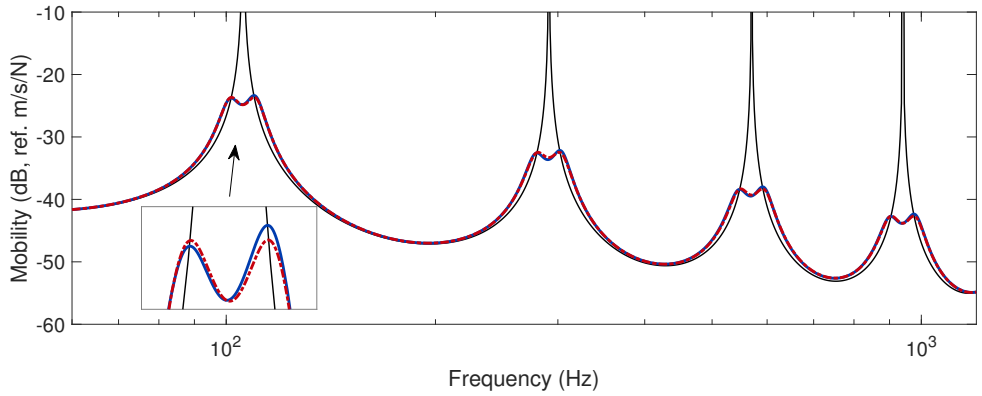

Figure 4.15: Velocity FRF of the beam with short-circuited patches (—), with a network synthesized with the modal-based approach (—) and tuned with the NH optimization using a naturally-scaled FRF (- - -).

Decentralized networks are now considered. In Section 3.8.4, it was shown that the distribution of patches among the networks has a strong impact on performance. This result may seem surprising, because the same number of piezoelectric transducers is used, which should intuitively lead to the same control authority on the modes of the structure. The four networks interconnecting five patches in adjacent and alternate ways (see Table 3.2) are thus reconsidered. Their characteristics are optimized with the NH algorithm using a naturally-scaled FRF.

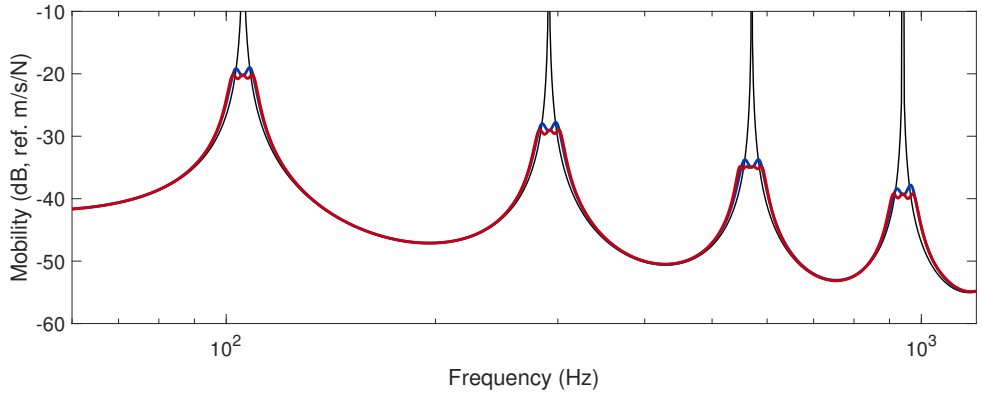

Figure 4.16: Velocity FRF of the beam with short-circuited patches (—), with a network synthesized with the modal-based approach (—) and tuned with the NH optimization using a naturally-scaled FRF (—).

Starting off with the adjacent patch distribution, Figure 4.16 shows that the algorithm is able to slightly improve the vibration attenuation by distributing the electrical frequencies of the networks around the targeted structural frequency, similarly to [169]. The third resonance of the host even exhibits four peaks.

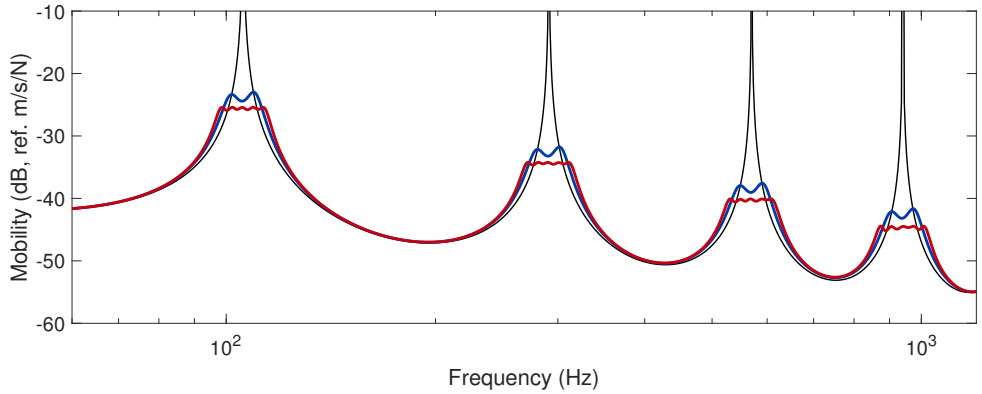

Figure 4.17: Velocity FRF of the beam with short-circuited patches (—), with a network synthesized with the modal-based approach (—) and tuned with the NH optimization using a naturally-scaled FRF (—).

Figure 4.17 features the FRF of the beam using the same strategy with an alternate patch distribution; the electrical resonance frequencies are even more distributed around the host resonance, which leads to five peaks per controlled mode. It would thus appear that more distributed electrical resonances provide better vibration reduction, in the limits of the number of possible resonances (i.e., the number of electrical DoFs of the networks). The relative improvement brought by the optimization is similar to that with adjacent patch distribution. By comparison of Figures 4.16 and 4.17, it can be seen that the performance is still better with the alternate distribution. A further insight into the dynamics and coupling of networks may be needed to understand why the distribution is so impactful. The possibility that the optimizer reached a local minimum should also be investigated.

4.4.4 Simply-supported plate

The simply-supported piezoelectric plate in Figure 4.18(a) is the last example to demonstrate the algorithm in a more challenging case. The geometrical and material properties of the setup are reported in Tables 4.5 and 4.6, respectively. A near-square plate was chosen to feature closely-spaced resonance frequencies [140]. A pair of symmetrically-bonded patches are placed on the structure to ensure good coupling with the lowest-frequency modes, and the forcing point $(x_f, y_f) = (155mm, 335mm)$ was chosen to excite those modes. The patches are connected in parallel and used as an equivalent transducer to be connected to a shunt cicuit. They are made of PIC 255, and the material characteristics were taken from [138]. The FE model of the plate in Figure 4.18(b) was built with SAMCEF [136]. Modal damping of 0.1% was assigned to all modes of the model.

A CB circuit with series shunts was considered to mitigate the first four modes of the plate. The initial tuning was performed using a balanced control authority over the modes ($r_1 = r_2 = r_3 = r_4 = 0.25$). The parameters are reported in Table 4.7(a). The frequencies of the second and third modes are quite close, and

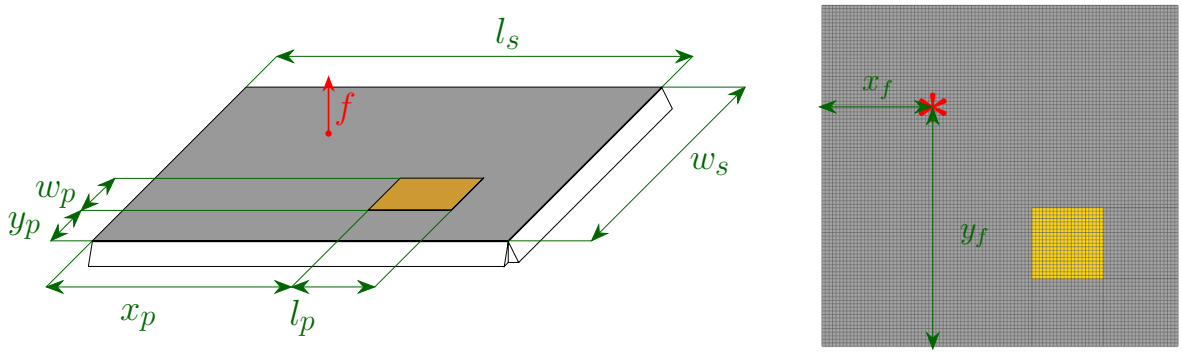

(a) (b)

Figure 4.18: Schematic representation of a simply-supported plate (in gray) excited by a point force (in red) to which are bonded piezoelectric patches (in orange) (a) and finite element mesh of the plate (b).

Parameter	l_s	w_s	t_s	x_p	y_p	l_p	w_p	t_p
Value	500mm	480mm	1mm	295mm	95mm	100mm	100mm	0.25mm

Table 4.5: Geometrical characteristics of the simply-supported piezoelectric plate as indicated in Figure 4.18(a) (t_s and t_p are the thickness of the plate and one patch, respectively).

Parameter	E_s	ν_s	ρ_s
Value	68GPa	0.36	2.7×10^3kg/m^3

(a)

Parameter	E_p^E	$E_{p,z}^E$	ν_p	$\nu_{p,z}$	$\nu_{z,p}$	ρ_p	d_{31}	ϵ_{33}^σ
Value	62.1GPa	48.3GPa	0.32	0.3	0.39	7.8×10^3kg/m^3	-180pC/V	15.4nF/m

(b)

Table 4.6: Material characteristics of the simply-supported piezoelectric plate (aluminum (a) and PIC 255 (b)).

this results in an initial tuning with unbalanced peaks but nonetheless able to reduce the amplitudes of the four targeted resonances. Another issue is that this initial tuning yields a negative resistance in the third shunt.

The NH algorithm is again able to output an all-equal-peak design; the performance on the first mode is improved at the expense on performance on the three other modes. The parameters of this configuration are given in Table 4.7(b). The same optimization performed with `fminimax` is shown in Figure 4.20. This tuning is substantially worse than the initial one. This surprising outcome was explained by a detailed look at the optimization process: `fminimax` takes a large step early on in the optimization process which seriously detunes the absorber. The optimizer does not seem to be able to recover from this inadequate step afterwards, and terminates

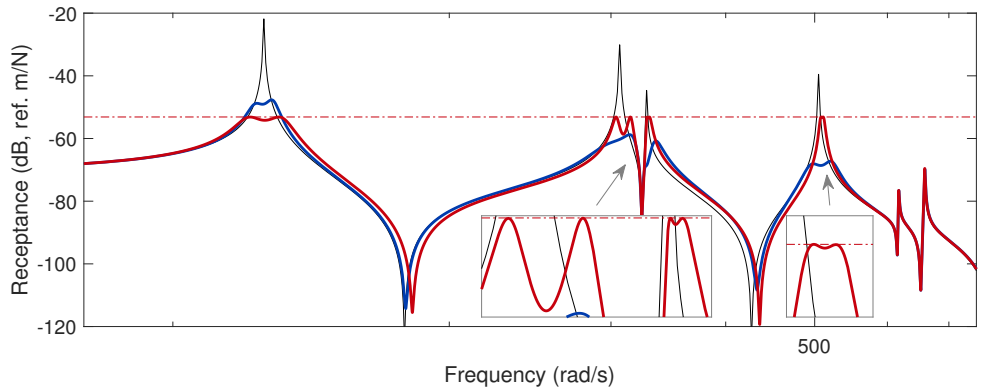

Figure 4.19: FRF of the simply-supported plate with short-circuited patches (—) and controlled with a CB circuit with series RL shunts (— : initial tuning, — : NH optimal tuning).

early when only two peaks are equated in amplitude.

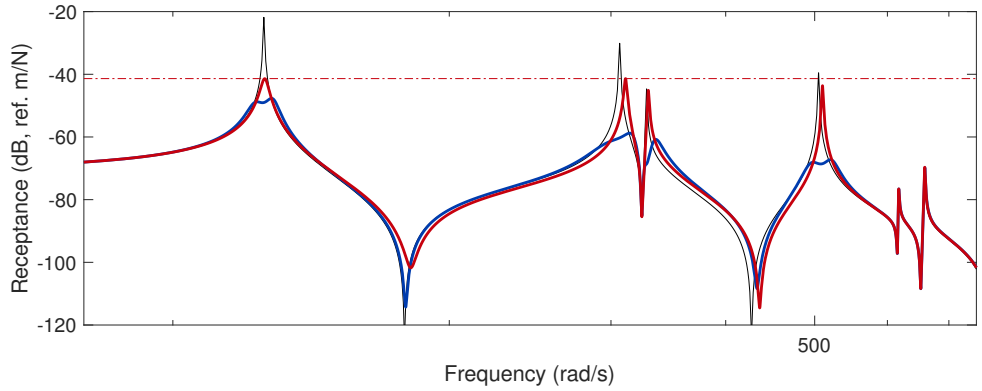

Figure 4.20: FRF of the simply-supported plate with short-circuited patches (—) and controlled with a CB circuit with series RL shunts (— : initial tuning, — : `fminimax`'s optimal tuning).

The performance degradation on modes 3 and 4 in Figure 4.19 is rather large when comparing the initial and optimized cases. Figure 4.21 displays the receptance when a naturally-scaled FRF is considered, and Table 4.7(c) lists the associated parameters. While the H_∞ norm is worse than in Figure 4.19, the overall reduction of the resonances is better in this case, which makes it a practical alternative to pure H_∞ optimization. We note that the optimized circuit controls modes 2 and 3 with a single electrical resonance, whereas another resonance has been assigned to the first mode, featuring a triple peak in the controlled FRF. Finally, the improvement in the controlled FRF comparing the initial tuning to the optimized one in Figure 4.21 appears quite marginal. However, it should be noted that the initial tuning requires a negative resistance, whereas the optimal one does not and is thus realizable with passive electrical elements.

4.5 Conclusion

Fine-tuning of the parameters of a piezoelectric vibration absorber for optimal performance can be a tedious task if performed manually. For this purpose, numerical

Parameter	R_i	L_i	$\tilde{C}_i$	$\tilde{L}_i$
$i=1$	2.36kΩ	64.77H	2.66μF	22.88H
$i=2$	1.95kΩ	17.21H	1.33μF	7.71H
$i=3$	-19.47kΩ	101.83H	443.7μF	20.31H
$i=4$	2kΩ	30.31H	/	/

(a)

Parameter	R_i	L_i	$\tilde{C}_i$	$\tilde{L}_i$
$i=1$	0.9GΩ	789.32H	1.14μF	12.46H
$i=2$	89.7mΩ	70.03H	8.47μF	1.11H
$i=3$	225.6kΩ	5.69mH	424.5nF	10.13H
$i=4$	6.554kΩ	97.55H	/	/

(b)

Parameter	R_i	L_i	$\tilde{C}_i$	$\tilde{L}_i$
$i=1$	632.9mΩ	36.43H	6.52μF	11.24H
$i=2$	3.08kΩ	22.79H	8.23μF	8.75H
$i=3$	453.6MΩ	38.83H	1.07μF	5.44H
$i=4$	1.28kΩ	17.91H	/	/

(c)

Table 4.7: Parameters of a CB shunt controlling the simply-supported plate: initial tuning (a), NH optimal tuning (b) and NH optimal tuning with naturally-scaled FRF (c).

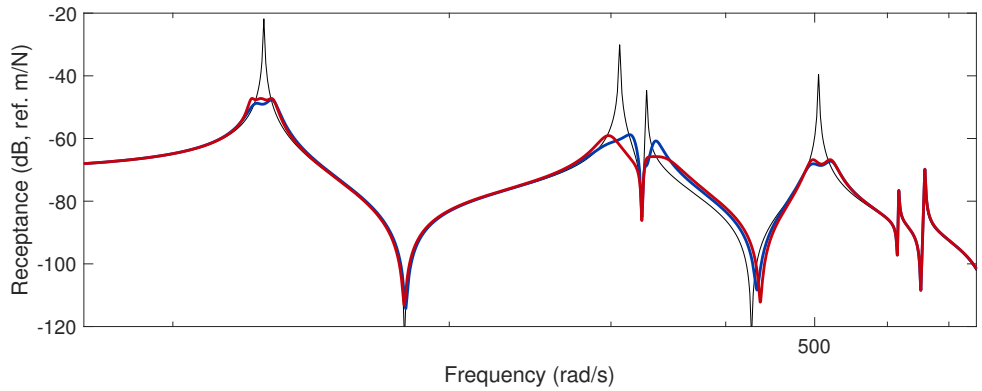

Figure 4.21: FRF of the simply-supported plate with short-circuited patches (—) and controlled with a CB circuit with series RL shunts (— : initial tuning, — : NH optimal tuning with naturally-scaled FRF).

optimization can be used. However, when the cost function is the H_∞ norm of a transfer function, gradient-based numerical optimizers can struggle to find an optimal tuning. The encountered issues mainly stem from the presence of multiple local minima, and the nonsmooth character of the cost function.

To partly remedy these problems, a NH optimization procedure was proposed in this chapter. In this approach, a sequence of optimization problems is solved. Starting with the optimization of low-order norms of transfer functions, the problem becomes less numerically stiff and each peak in the FRF influences the cost function. As the order of the norm increases, the problem becomes closer to a H_∞ optimization problem, and the high-amplitude peaks of the transfer function are more penalized. Most of the time, the outcome of the algorithm is an all-equal-peak design, in which all controlled peaks feature the same amplitude. This approach appears to provide a numerically robust way to perform H_∞ optimization. It should however be emphasized that there is no theoretical guarantee that it reaches the global minimum.

The approach was formulated using the SMW formula to allow for a reduction in the computational burden, and the possibility to work directly with experimental measurements. The algorithm is also quite versatile. Indeed, it is possible to work with classical transfer functions such as the receptance, mobility or accelerance, and to weight some frequency bands to put more emphasis on specific modes.

The proposed optimization method was applied to various piezoelectric structures and demonstrated its ability to efficiently minimize the H_∞ norm of transfer functions with passive vibration absorbers. Furthermore, the findings it provided further support the general statements made in the previous chapters. For structures with closely-spaced resonance frequencies, the algorithm can bring real enhancement in the initial tuning. Hence, it constitutes an additional tuning tool for electrical circuits or networks, but its outcome should be verified and assessed with the engineering judgment of the designer.

The algorithm in its present form is focused toward the optimization of single-input single-output (SISO) transfer functions but it could be generalized to MIMO transfer functions by simple concatenation of the different transfer functions in the NH optimization. More efficient quadrature formulas than the trapezoidal rule used in the examples herein could be exploited. This would probably allow for a reduction of the number of sampling frequencies, thereby speeding up the

algorithm. An interesting extension would be to concurrently optimize the size and position of piezoelectric transducers; this would however probably require a lot more information from the host structure. The outcome of the proposed optimization approach could also be experimentally validated.

5 Mitigation of nonlinear vibrations

Abstract

Nonlinear structural behaviors can be particularly detrimental to tuned vibration absorbers, owing mainly to the dependency of the resonance frequency of the host on the amplitude of vibration. Properly-tuned nonlinear absorbers can overcome this difficulty. Specifically, if they are tuned according to a nonlinear principle of similarity, i.e., the functional form of their nonlinearity is identical to that of their host, they can outperform their linear counterparts by working efficiently in a broader forcing amplitude range. This chapter illustrates this fact experimentally using a digital vibration absorber. The approach is also theoretically extended to the control of multiple nonlinear resonances, building upon the developments in the previous chapters.

5.1 Introduction

Resonant piezoelectric vibration absorbers can be used to mitigate structural vibrations, but they rely on a precise *tuning* of the electrical resonance frequency according to that of the host structure. The latter may be variable due to, e.g., time-varying characteristics or structural nonlinearities. Hence, resonant piezoelectric vibration damping is often considered as lacking robustness. Vibration absorbers purposely including nonlinear elements were thought of as a possible solution against this lack of robustness, because the presence of nonlinearities can broaden the bandwidth of the absorber [170]. Reviews on these techniques with mechanical absorbers can be found in [171, 172].

Focusing on applications with smart materials, Agnes [173] and Agnes and Inman [174] investigated the effect of adding nonlinear elements in the shunt circuit of a piezoelectric absorber. They found that its bandwidth could be increased; however, undesirable nonlinear phenomena such as quasiperiodic (QP) and chaotic motions could also be observed. Along the same lines, Richard et al utilized continuous switching of a piezoelectric shunt to realize a nonlinear absorber [92]. In [175], Zhou et al explored a piezoelectric NES comprising an essential nonlinearity made of a ferroelectric capacitor and a negative capacitance circuit. Because this absorber has no preferential resonance frequency, it can pump the energy from the host structure in an irreversible fashion [28]. This energy transfer is, however, conditioned upon an energy threshold. In other words, the transfer does not occur if the vibrational energy of the host structure is not large enough [176].

In order to provide effective vibration mitigation in a wide range of forcing amplitudes, Viguié and Kerschen [177] derived a qualitative tuning rule for a nonlinear tuned vibration absorber (NLTVA), i.e., the frequency-energy dependence of the absorber should be identical to that of the host structure. More recently, Habib et al [178] introduced a *nonlinear principle of similarity* to develop NLTVAs whose performance is much less sensitive to forcing amplitude. This principle states that the functional

form of the NLTVA's nonlinearity should be identical to that of the host structure. If the nonlinear coefficient of the absorber is tuned adequately, the equal-peak method can be generalized to nonlinear regimes of motion, at least up to the merging of an isolated resonance [179]. Detroux et al. [180] studied the associated adverse dynamics and how the NLTVA parameters can be adapted to prevent such undesirable phenomena. Soltani and Kerschen [181] extended this concept to a nonlinear piezoelectric tuned vibration absorber (NPTVA). The absorber contains a nonlinear electrical element whose nonlinearity is similar to that present in the host structure. The principle of similarity also proved efficient to modify multiple nonlinear resonances in [182] and to design nonlinear active control schemes in [36, 183]. Techniques going beyond this principle of similarity to tailor the behavior of systems in strongly nonlinear regimes of motion were recently proposed in [184, 185].

Focusing now on experimental demonstrations, a nonlinear absorber relying on the saturation phenomenon was realized through digital control in [186] and [187]. The first practical implementation of a NPTVA was achieved in [104] whereas Silva et al [188] realized a piezoelectric NES using analog electronics. An interesting feature of [104] is that the use of synthetic inductors (and, thus, of a power supply) was avoided, leading to a fully passive piezoelectric absorber. Different nonlinear absorbers, including an NES and an NLTVA were realized experimentally using a tunable magnetic vibration absorber [189]. Zhao et al [36] also experimentally demonstrated the efficiency of an active nonlinear positive position feedback (NPPF) to mitigate nonlinear vibrations.

A more challenging scenario is when multiple resonances are to be mitigated. The design methods presented in Chapters 2, 3 and 4 rely on a precise frequency tuning, and nonlinear resonances can deteriorate performance as well. Several studies addressed the case where an NES is used for mitigating sequentially several linear resonances, see, e.g., [190, 191]. An example of a multimodal NLTVA is given in [192], where an analog electrical network augmented with a nonlinear capacitor (being analog itself to the structural nonlinearity) was used to maintain performance of the network in nonlinear regimes of motion. Besides this work, there are very few studies dealing with multimodal nonlinear absorbers attached to a nonlinear host.

The practical realization of a passive nonlinear absorber is not easily achievable, be it with mechanical or electrical elements. By contrast, the full flexibility of the DVA can be exploited to implement arbitrarily complex nonlinear laws, hence, paving the way for a more widespread use of nonlinear absorbers in real-world applications. This is what is pursued in the first part of this chapter and in [193–195]. The second part of this chapter introduces a tuning methodology for NPTVAs that mitigate several nonlinear resonances simultaneously. Specifically, the objective is to maintain equal peaks in the frequency response for all controlled resonances in both linear and nonlinear regimes of motion. The problem is similar to that in [196, 197] but is extended to piezoelectric absorbers [145].

This chapter first reviews a series of important concepts associated with nonlinear vibrations in Section 5.2. Section 5.3 explains the working principles of the NPTVA. Section 5.4 then presents a DVA used to experimentally mitigate a nonlinear resonance of a clamped-free beam. It demonstrates how a linear absorber loses its efficiency after being detuned, whereas a NPTVA is able to maintain performance over a broader range of forcing amplitudes. Section 5.5 discusses how this concept can be extended to the simultaneous control of multiple nonlinear resonances, using nonlinear versions of the shunt circuits studied in Chapter 2. This approach is

numerically demonstrated in Section 5.6.

5.2 Important features of nonlinear vibrations

Nonlinearity is the rule rather than the exception, and nonlinear systems can exhibit a rich and complex dynamical behavior [198]. In structural dynamics, nonlinearities are categorized based on their origin: material or constitutive, geometric, inertia, body forces and friction [199]. Geometric nonlinearities occur because of the nonlinear strain-displacement relation. In piezoelectric structures, geometric nonlinearities may have a significant impact on coupling [200]. Material nonlinearities due to the nonlinearity of a given material's constitutive equations are also common. Piezoelectric materials are often subject to hysteresis [101, 201, 202] coming from the reorientation of the polarization of ferroelectric domains due to extreme events, such as large strains or strong electric fields. In this thesis, the focus is placed on geometric nonlinearities, although material nonlinearities are also encountered in Section 5.4.

5.2.1 The Duffing oscillator

A celebrated example in nonlinear vibrations is the Duffing oscillator [203], governed by

$$m\ddot{x} + c\dot{x} + kx + k_3x^3 = f, \tag{5.1}$$

where k_3 is the nonlinear stiffness coefficient. As an illustrative example, the Duffing oscillator with parameters given in Table 5.1 is briefly studied in this section.

Parameter	m (kg)	c (kg/s)	k (N/m)	k_3 (N/m^3)
Value	1	0.05	1	0.1

Table 5.1: Parameters of the Duffing oscillator.

Figure 5.1 features the nonlinear frequency responses (NFRs) of the system for two excitation amplitudes. The method to compute these NFRs will be explained in Section 5.2.2. The first forcing amplitude is 0.01N, and is low enough so as to make the nonlinear forces in the system negligible. Hence, the NFR is virtually identical to the FRF of a SDoF oscillator governed by Equation (5.1) with $k_3 = 0$.

For a forcing amplitude of 1N, the regime is strongly nonlinear. A first striking feature is the change in the resonance frequency of the system. This illustrates the salient *frequency-energy* dependence in nonlinear systems, i.e., the resonance frequency of a nonlinear structure depends on the forcing amplitude.

Another peculiar feature is the existence of multiple solutions for some frequencies, which is why an NFR is not a function. Some of them are unstable, meaning in this context that they cannot be observed because an infinitesimal perturbation to the equilibrium of these unstable solutions would drive the system toward another stable solution. Stability changes occur through *bifurcations* (in this case, fold bifurcations), which indicate a qualitative change in the dynamics of the system as a parameter (in this case, the forcing

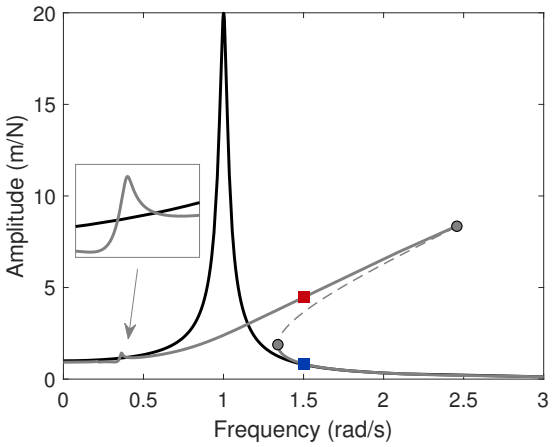

Figure 5.1: NFR of the Duffing oscillator excited by a forcing amplitude of 0.01N (—) and 1N (—). —: stable solution, - - : unstable solution, •: fold bifurcation, ■: stable attractors at 1N and ω=1.5rad/s.

frequency) is varied [204]. Whether the system is on the high- or low-amplitude branch (as depicted in Figure 5.1) depends on its initial state. This can be assessed with basins of attraction (BoAs), as in Figure 5.2. These BoAs were obtained by the time integration of Equation (5.1) starting from different initial conditions. They represent the attractor to which the system converges with these initial conditions. This confirms the coexistence of two attractors when the Duffing oscillator is forced at ω=1.5rad/s at an amplitude of 1N.

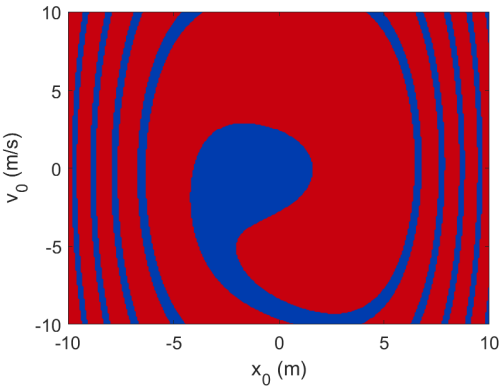

Figure 5.2: BoAs (represented with the steady-state motion amplitude) of the Duffing oscillator harmonically-forced at 1N and ω=1.5rad/s for various initial positions (x_0) and velocities (v_0). The corresponding attractors in the NFR are given in Figure 5.1: ■: $|x/f| = 0.83$m/N, ■:$|x/f| = 4.49$m/N.

Finally, another resonance can be observed at ω=0.33rad/s in the inset of Figure 5.1. This resonance is due to the third harmonic of the displacement generated by the cubic stiffness. This harmonic component coincides with the resonance frequency of the underlying linear system, which thus resonates in a so-called 3:1 *superharmonic resonance*.

5.2.2 The harmonic balance

In this thesis, the harmonic balance method (HBM) is used to solve the governing equations in the frequency domain. This method has gained wide acceptance in structural

dynamics, see, e.g., [205–207]. It has also be extended to piezoelectric structures [208].

The governing equations of a piezoelectric system can generically be cast into the set of nonlinear first-order ordinary differential equations (see, e.g., Section F.1)

$$\dot{\mathbf{x}}_s = \mathbf{A}_s \mathbf{x}_s + \mathbf{B}_s \mathbf{f} + \mathbf{f}_{nl}(\mathbf{x}_s), \tag{5.2}$$

where $\mathbf{A}_s$ is the state-evolution matrix, $\mathbf{B}_s$ is the state-input matrix, $\mathbf{f}$ is the external forcing and $\mathbf{f}_{nl}(\mathbf{x}_s)$ gathers the nonlinearities of the system. A classical HBM formalism is used to express the vector of N_x state variables $\mathbf{x}_s$ with a truncated Fourier series with N_h harmonics. In the frequency domain, the vector of generalized DoFs can be characterized by a column vector of length $N_z = (2N_h + 1)N_x$ gathering the harmonic coefficients $\mathbf{z}$

$$\mathbf{x}_s(t) = (\mathbf{Q}(\omega t) \otimes \mathbf{I}_{N_x})\, \mathbf{z} \tag{5.3}$$

where $\mathbf{Q}(\omega t)$ is a vector of $2N_h + 1$ harmonic functions

$$\mathbf{Q}(\omega t) = \left[\frac{1}{\sqrt{2}} \quad \sin(\omega t) \quad \cos(\omega t) \quad \cdots \quad \sin(N_h \omega t) \quad \cos(N_h \omega t) \right], \tag{5.4}$$

and $\otimes$ denotes the Kronecker tensor product. Using a Galerkin procedure, Equation (5.2) may be expressed in the frequency domain as

$$[(\mathbf{I}_{2N_h+1} \otimes \mathbf{A}_s) - (\boldsymbol{\nabla}(\omega) \otimes \mathbf{I}_{N_x})]\, \mathbf{z} + \mathbf{b}(\mathbf{z}) = \mathbf{A}_L(\omega)\mathbf{z} + \mathbf{b}(\mathbf{z}) = \mathbf{b}_{ext}, \tag{5.5}$$

where $\mathbf{A}_L(\omega)\mathbf{z}$, $\mathbf{b}(\mathbf{z})$ and $\mathbf{b}_{ext}$ are the frequency-domain expressions of the generalized loads in the underlying linear system, the nonlinear loads $\mathbf{f}_{nl}(\mathbf{x}_s)$ and the external loads $-\mathbf{B}_s\mathbf{f}$, respectively. The frequency-domain differential operator $\boldsymbol{\nabla}(\omega)$ is given by

$$\boldsymbol{\nabla}(\omega) = \begin{bmatrix} 0 & & \mathbf{0} \\ & \begin{bmatrix} 1 & & \\ & \ddots & \\ & & N_h \end{bmatrix} \otimes \begin{bmatrix} 0 & -\omega \\ \omega & 0 \end{bmatrix} & \\ \mathbf{0} & & \end{bmatrix}. \tag{5.6}$$

Expressing the nonlinear forces in the frequency domain can be achieved using the alternating frequency–time domain (AFT) method [205, 209]. With this method, the harmonic coefficients are used to compute the state variables in the time domain using Equation (5.3). The nonlinear forces can then easily be computed in the time domain. Finally, the frequency-domain expression of the nonlinear forces is derived with an inverse Fourier transform of the obtained time series.

For a given set of parameters, Equation (5.5) can be solved for the harmonic coefficients $\mathbf{z}$ using, e.g., a Newton-Raphson procedure. A branch of solutions can then be computed through numerical continuation [204], thereby giving the NFRs.

Stability changes and bifurcations can be characterized by monitoring the Floquet exponents of the system [206]. They are estimated by the eigenvalues (with the smallest absolute imaginary parts) of the frequency-domain Jacobian matrix, namely

$$\mathbf{J}(\omega, \mathbf{z}) = [(\mathbf{I}_{2N_h+1} \otimes \mathbf{A}_s) - (\boldsymbol{\nabla}(\omega) \otimes \mathbf{I}_{N_x})] + \frac{\partial \mathbf{b}}{\partial \mathbf{z}}. \tag{5.7}$$

The solution is unstable if any of these eigenvalues has a positive real part, and is stable otherwise.

5.3 The nonlinear piezoelectric vibration absorber

The performance of piezoelectric vibration absorbers controlling nonlinear structures is now investigated.

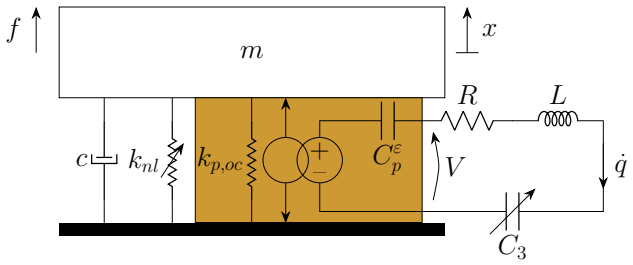

Figure 5.3: Nonlinear SDoF piezoelectric structure controlled by a series RL and nonlinear capacitor shunt.

Figure 5.3 features a NPTVA, where a nonlinear capacitor is connected in series to the RL shunt in order to counteract the detuning effect of the structural nonlinearity. The functional form of this nonlinear electrical element is chosen according to a principle of similarity [178, 181], i.e., it should be identical to that of the host structure. The governing equations thus read

$$\begin{cases} m\ddot{x} + c\dot{x} + k_{oc}x + k_3x^3 - \theta_p q = f \\ L\ddot{q} + R\dot{q} + \dfrac{1}{C_p^\varepsilon}q + C_3q^3 - \theta_p x = 0 \end{cases}. \tag{5.8}$$

where C_3 is the cubic elastance coefficient ($C_3 = 0$ for a linear shunt circuit). This coefficient can be determined from the parameters of the system using the simplified formula in [104]:

$$C_3 = \frac{2L^2}{m^2}k_3, \tag{5.9}$$

Figure 5.4 shows the NFRs of the Duffing oscillator controlled by either a linear absorber (Figure 5.4(a)) or a NPTVA (Figure 5.4(b)). The parameters of these systems are those of the experimental setup studied in Section 5.4 and are given in Tables 5.2 and 5.3. As the forcing amplitude increases, the linear absorber becomes severely detuned, which generates detrimental vibrations. The apparition of Neimark-Sacker bifurcations indicate the presence of QP oscillations in the response of the structure [206]. QP oscillations feature the presence of frequency components in the structural response which are not integer multiples of the forcing frequency [210]. By contrast with damped linear systems, QP oscillations can persist in the steady-state response of harmonically-forced nonlinear systems. An example of such a response is given in the inset of Figure 5.4(a), where the second frequency component acts as a slow modulation of the motion amplitude. Conversely to its linear counterpart, the NPTVA performance remains practically unchanged for the different forcing amplitudes.

The working range of the NPTVA is not endless. Figure 5.5(a) depicts the NFR of the system controlled by the NPTVA for higher forcing amplitudes. Together

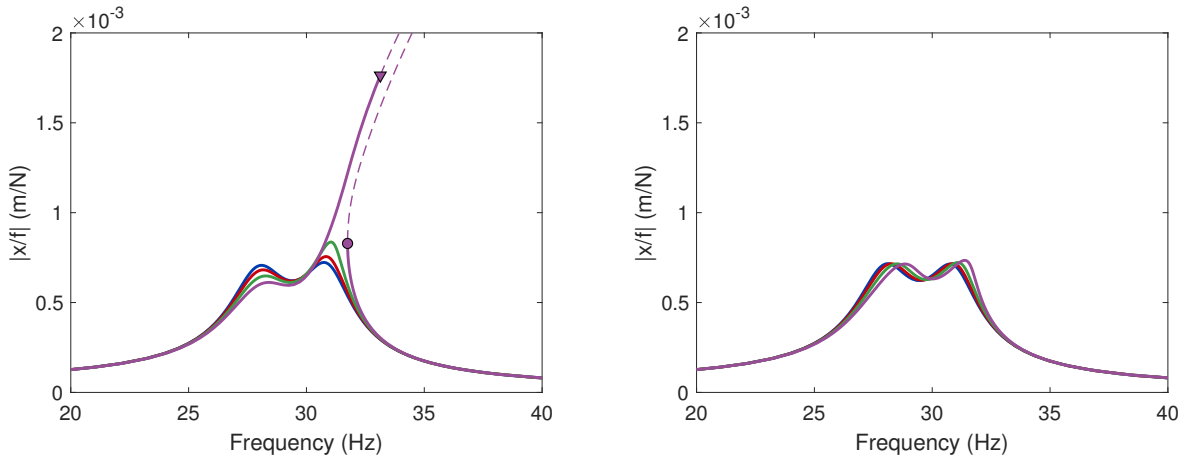

Figure 5.4: NFRs of a Duffing oscillator controlled by a linear absorber (a) and a NPTVA (b): 0.2N (—), 0.4N (—), 0.6N (—), 0.8N (—). —: stable periodic solution, - - : unstable periodic solution, - · -: QP solution, •: fold bifurcation, ▼: Neimark-Sacker bifurcation. In (a), the inset depicts the time series of the displacement in the controlled structure at the marked point of the QP branch (○).

with the main response appears a high-amplitude isolated response called a detached resonance curve (DRC). DRCs are another peculiarity of nonlinear systems. Their presence is clearly undesirable in vibration mitigation applications, because they are not detected by classical continuation procedures, being detached from the main NFR. Unsuspected stable, high-amplitude attractors may thus exist for some combinations of forcing frequencies and amplitudes. When the forcing amplitude reaches 1.2N, this DRC coalesces with the main NFR at the rightmost peak, dramatically increasing its amplitude and marking the end of the working range of the NPTVA.

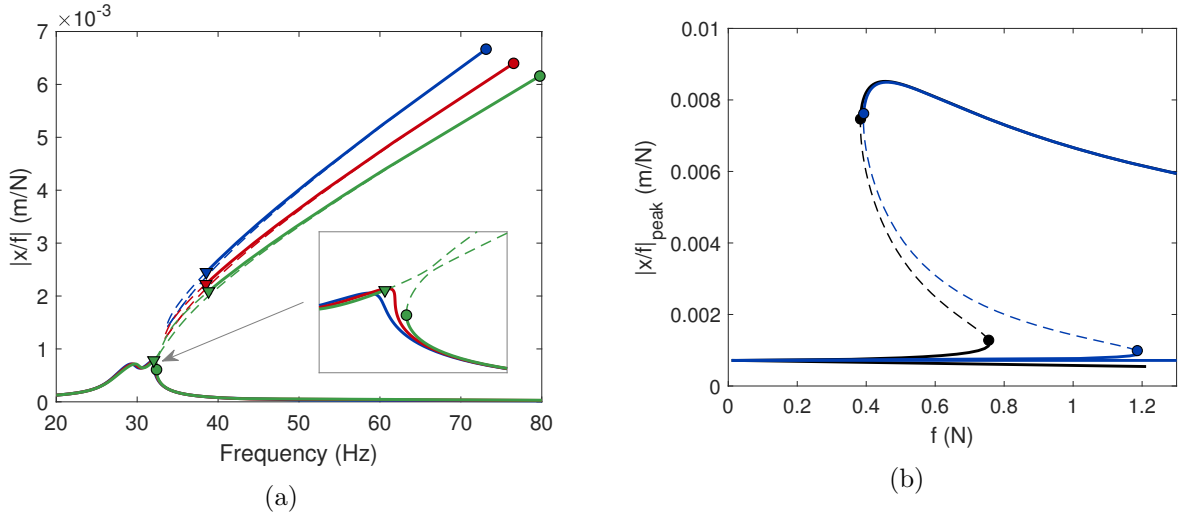

Figure 5.5: NFRs of a Duffing oscillator controlled by a NPTVA (a): 1N (—), 1.1N (—) and 1.2N (—), and loci of resonant peaks (b) for the linear absorber (—) and the NPTVA (—). —: stable solution, - - : unstable solution, •: fold bifurcation, ▼: Neimark-Sacker bifurcation.

Figure 5.5(b) summarizes the performance of the linear and nonlinear absorbers, by

tracing the locus of resonant peaks (computed with the method proposed in [211]) in the forcing amplitude - response amplitude plane. In both cases, the peak amplitudes are equal for low forcing. The rightmost peak amplitude grows and eventually turns back when the DRC merges with the main NFR, at 0.75N and 1.18N for the linear and nonlinear absorbers, respectively. At this point, the unstable response tracked by the numerical method corresponds to the local minimum of the DRC. A second turn-back occurs at a lower forcing amplitude but at a higher response amplitude, and beyond this point the numerical method tracks the local maximum of the DRC. This turn-back where the local minimum and maximum join signals the birth of the DRC. The NPTVA does not appear to substantially modify the DRC onset compared to the linear absorber, but outperforms it before 1.18N by maintaining peaks of near-equal amplitude, and by delaying the DRC coalescence with the main NFR. Beyond that point, the worst-case amplitudes are similar for the linear and nonlinear absorbers.

5.4 Digital nonlinear piezoelectric vibration absorber

5.4.1 A digital piezoelectric vibration absorber

A challenge pertaining to the implementation of a NPTVA is the tailoring of the nonlinear behavior of the electrical components so as to obey the principle of similarity. Even if this problem was addressed for cubic nonlinearities through the use of saturable inductors [104], there is not much variety in the functional forms that can be realized with electrical components. The DVA solves this issue, since the realization of an arbitrary impedance possible.

5.4.1.1 Hardware

The DVA used in this chapter is similar to that used in Chapter 1 and mostly follows what was described in Section 1.3.1. The schematic of the digital absorber is depicted in Figure 5.6. The voltage references ΔV_{in} and ΔV_{out} are generated by shunt voltage regulators. OA4 now implements a differential amplifier with unity gain. OpAmps 1 to 4 are powered with low voltages, whereas OA5, a PA78 power operational amplifier from APEX Microtechnology [212], is separately powered with high voltages. This makes it able to cope with the high voltages generated by the piezoelectric transducer, which went up to $\pm$ 150V.

5.4.1.2 Software

As in Section 1.3.2, the MCU (Arduino Due) can easily be programmed to implement an arbitrary I/O relation with MATLAB Simulink. This section explains how a simple nonlinear feedback can be used to emulate a NPTVA.

The nonlinear voltage can be computed if the charge flowing through the piezoelectric transducer is known. It can be retrieved from the output voltage since

$$V_{out} = R_i \dot{q} \tag{5.10}$$

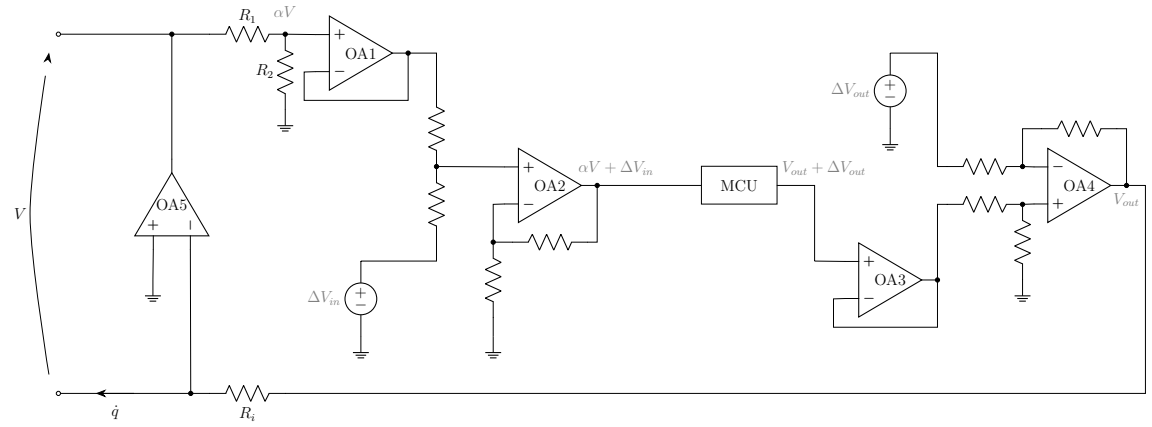

Figure 5.6: Layout of the digital absorber used to emulate a NPTVA.

Moreover, from the second line of Equation (5.8),

$$\alpha V = \alpha V_L + \alpha V_{NL}, \tag{5.11}$$

where $V_L = L\ddot{q} + R\dot{q}$ is the voltage across the RL circuit, $V_{NL} = C_3 q^3$ is the voltage across the nonlinear capacitor, and V is the voltage across the electrodes of the piezoelectric transducer (Equation (1.11)). Then, Equations (5.10) and (5.11) suggest that the nonlinear shunt circuit may be implemented by adding a nonlinear feedback to the block diagram in Figure 1.13, as depicted in Figure 5.7.

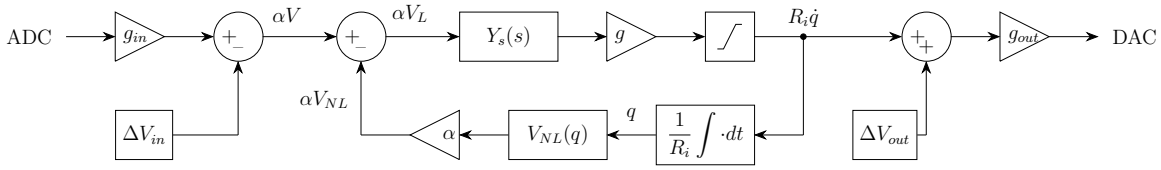

Figure 5.7: Block diagram of the synthesized NPTVA.

Small signal offsets are unavoidable in practice. This causes a drift of the integrator and an eventual clipping of the signals. As a remedy, a lossy integrator (i.e., a first-order lowpass filter) or a bandpass filter can replace the integrator. The passband of such filters should be in a low frequency range, such that the filter behaves as an integrator in the frequency range of interest. The advantage of using a bandpass filter over a lossy integrator is its ability to completely reject DC offsets, preventing asymmetric AC signal distortion due to the nonlinearity.

5.4.1.3 Stability

Similarly to Section 1.6, delay-induced instabilities must be suppressed before using a DVA to control nonlinear structures. For a digital NPTVA, the underlying linear system must be stabilized by modification of its linear characteristics such as proposed in Section 1.6.5. Its nonlinear characteristics can be left unchanged, and this is sufficient to guarantee the stability of the controlled nonlinear system for low enough

forcing amplitudes[1]. Indeed, the action of the nonlinearities would just be equivalent to small perturbations applied to a stable system.

For the experimental validation treated in this chapter, delay-induced instabilities were not an issue because the sampling frequency of 10kHz was large enough to avoid instabilities, and the adverse dynamical phenomena described in Section 5.3 were encountered before any potential issue with sampling. For other cases, a more thorough closed-loop stability analysis could be carried out based on power considerations, by analogy to Section 1.6.2.2. This is the basic idea of Lyapunov's analysis [213]. A challenge associated with this method would be to find a suitable Lyapunov function. Alternatively, describing functions could be used to approximately assess the stability of the controlled system by analyzing an open-loop transfer function formed with these describing functions for multiple values of the external forcing amplitude [213].

5.4.2 Linear absorber controlling a nonlinear structure

5.4.2.1 Experimental setup

The structure under investigation is identical to that presented in Section 1.3.3. A picture of the experimental setup is featured in Figure 5.8. This time, the electrodynamic shaker is placed near the free end of the beam attached to the thin lamina, where the structure is the most compliant in order to trigger its nonlinear behavior.

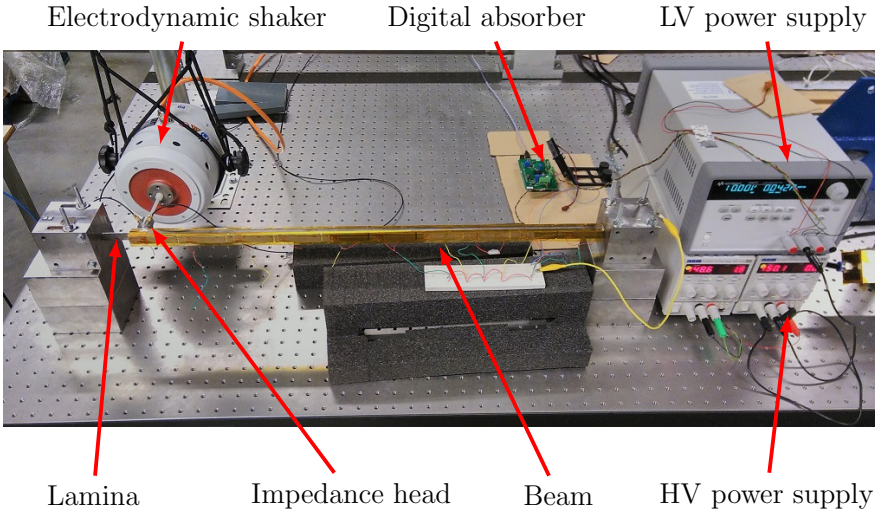

Figure 5.8: Picture of the experimental setup.

The digital absorber connected to the patches is powered by a high-voltage (HV) power supply with ±150V (to power the operational amplifier OA5 in Figure 5.6) and with a low-voltage (LV) power supply with ±10V (to power the interface with the microcontroller unit). The MCU is programmed and powered via USB.

The voltage division ratio $\alpha = 0.0109$ was set so that a maximum input voltage at the MCU (± 1.65V) corresponds nearly to a maximum output voltage of OA5 (±

[1]In this section, stability is understood as the ability of the DVA to reproduce stable equilibria similar to those of a purely passive nonlinear shunt circuit. In case of instability, the system would undergo limit cycle oscillations whose amplitudes are solely limited by the saturation of the OpAmp.

150V). The current injector resistance R_i=152.9Ω was measured with a multimeter (FLUKE 177), and the gain $g = 14,021$ was deduced from Equation (1.56). The voltage offsets ΔV_{in} and ΔV_{out} were both set to 1.65V, so that the full ADC and DAC ranges of the MCU could be used.

5.4.2.2 System identification

The first step to tune the shunt circuit is to identify the parameters of the host system. The piezoelectric capacitance was measured with a multimeter. The linear mechanical parameters were determined from a low-level broadband excitation. A first test was performed with open-circuited patches ($q = 0$). The obtained FRF was fitted to obtain a minimum least-squares error between the model and the measurements, giving an estimate of the parameters m, c and k_{oc}. The process was repeated with short-circuited patches, giving an estimation of k_{sc}, the structural stiffness when the piezoelectric patches are short-circuited ($V = 0$). From Equations (1.10) and (1.12), the following relation holds:

$$k_{sc} = k_{oc} - \theta_p^2 C_p^\epsilon \tag{5.12}$$

so that θ_p can be deduced from the estimated quantities. The system has a generalized electromechanical coupling factor K_c=12.43%. Table 5.2 contains the identified parameters. Figure 5.9(a) shows an excellent agreement between the experimental and predicted FRFs.

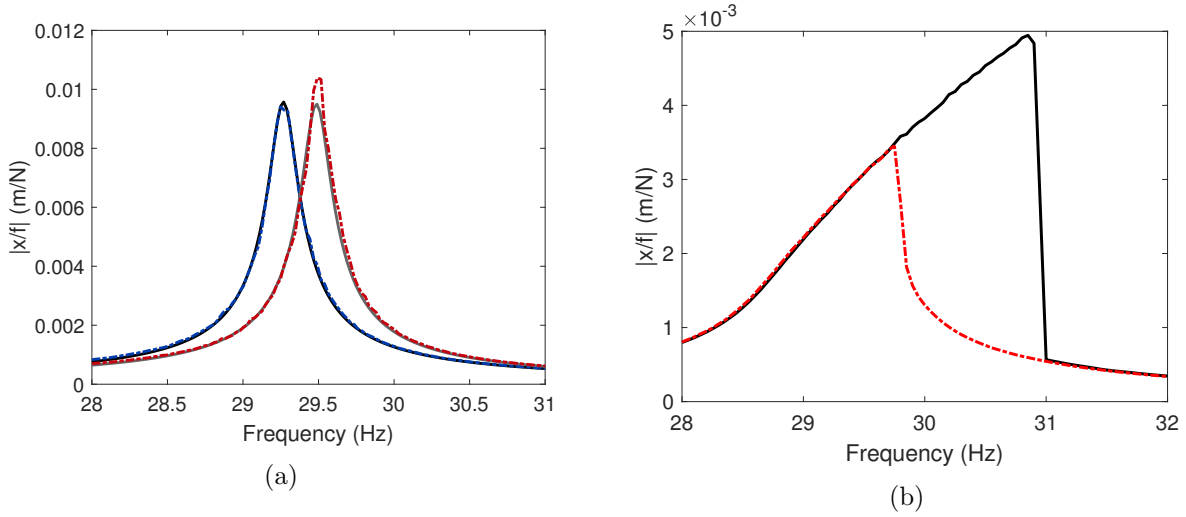

Figure 5.9: Frequency responses of the experimental setup: (a) experimental and predicted FRFs: model (sc: —, oc: —) and measurements (sc: -·-, oc: -·-), (b) nonlinear frequency response at 0.2N: step up (—) and step down (-·-).

The nonlinear stiffness of the thin lamina was estimated by exciting the system with short-circuited patches at higher forcing amplitudes. The excitation was a stepped sine with a controlled amplitude of 0.2N between 28 and 32Hz. Figure 5.9(b) shows the frequency response of the structure, when the frequency is stepped up or down. The uncontrolled structure exhibits multistability at this forcing amplitude, which is a signature of its nonlinear behavior. Following [104], the recorded force and acceleration signals were digitally bandpass filtered and gathered in vectors $\mathbf{f}$ and $\ddot{\mathbf{x}}$, respectively.

The velocity and displacement vectors were estimated by time integration. Rewriting the first line of Equation (5.8) (under short-circuit conditions)

$$\mathbf{x}^3 k_3 = \mathbf{f} - [\ddot{\mathbf{x}}, \dot{\mathbf{x}}, \mathbf{x}] \begin{bmatrix} m \\ c \\ k_{sc} \end{bmatrix} \tag{5.13}$$

shows that the nonlinear force vector $\mathbf{x}^3 k_3$ can be calculated from the knowledge of the linear parameters at each time instant. It is represented by the black dots in Figure 5.10. Eventually, the nonlinear coefficient k_3 in Table 5.2 was identified through simple least-squares fitting of the nonlinear force with a cubic law.

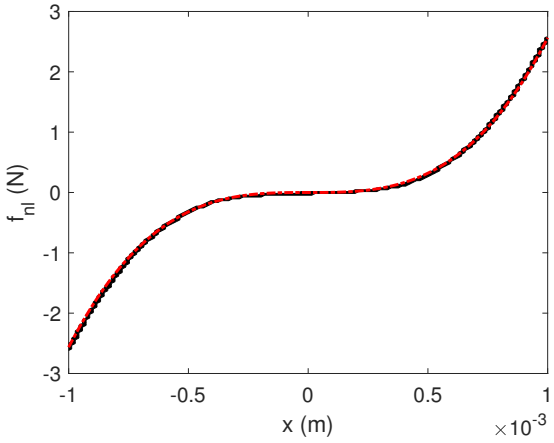

Figure 5.10: Nonlinear stiffness curve: measurement (•) and fitted cubic law (---).

Parameter	m	c	k_{oc}	k_3	C_p^ε	θ_p
Value	0.446kg	0.569Ns/m	1.521×10^4N/m	2.505×10^9N/m^3	250nF	3.042×10^4N/C

Table 5.2: Identified parameters of the experimental setup.

5.4.2.3 Synthesized admittance

Based on the previous system identification, the parameters of the digital linear shunt in Table 5.3 were computed using Equations (1.37) and (1.38). The slight variability of the results from one test to another led to adaptations of the inductance L of the order of 1% of the theoretical value. This adaptation was carried out to obtain equal peaks at the lowest forcing amplitude, namely f=0.2N. The shunt circuit admittance was synthesized in the MCU after transforming the continuous admittance (Equation (1.32)) into a discrete transfer function using Tustin's method with a sampling frequency of the MCU set to 10kHz.

The input and output signals were measured by the MCU and recorded by a computer. The piezoelectric charge and current time derivative were estimated by time integration

Parameter	L	R	C_3
Value	117.42H	3 295Ω	3.4022×10^{14}V/C^3

Table 5.3: Parameters of the linear and nonlinear piezoelectric tuned vibration absorbers.

and time derivation of the output signal, respectively. Figures 5.11(a) and 5.11(b), which compare the theoretical and post-processed voltages across the resistor and inductor, respectively, confirm that the MCU implements the desired input-output transfer function.

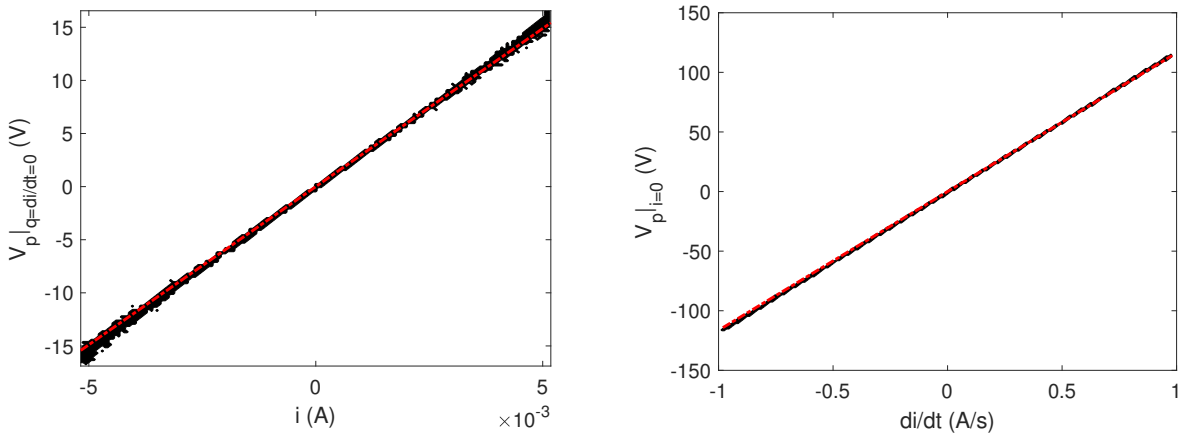

(a) (b)

Figure 5.11: Voltage across the resistor (a) and the inductor (b): theoretical law (---) and measurements (•).

5.4.2.4 Performance of the linear absorber

The experimental NFRs for forcing levels ranging from 0.2N to 0.8N are presented in Figure 5.12(a). At 0.2N, the nonlinearity of the thin lamina is not activated; the linear absorber gives rise to two equal peaks in the response. As the forcing level is increased, a clear detuning of the linear absorber is observed. The comparison with the theoretical NFRs in Figure 5.4(a) reveals that the detuning is in fact more important than predicted. After detailed investigations, this detuning was attributed to the nonlinear behavior of the piezoelectric patches, as in [104]. The model in Equation (5.8) was thus upgraded using a negative cubic elastance $C_{p,3}$ and a positive cubic resistance $R_{p,3}$, so that

$$V = \theta_p x - \frac{1}{C_p^\varepsilon} q - C_{p,3} q^3 - R_{p,3} \dot{q}^3, \tag{5.14}$$

with values given in Table 5.4. The NFRs predicted through this updated model in Figure 5.12(b) are now in close agreement with the experimental NFRs in Figure 5.12(a).

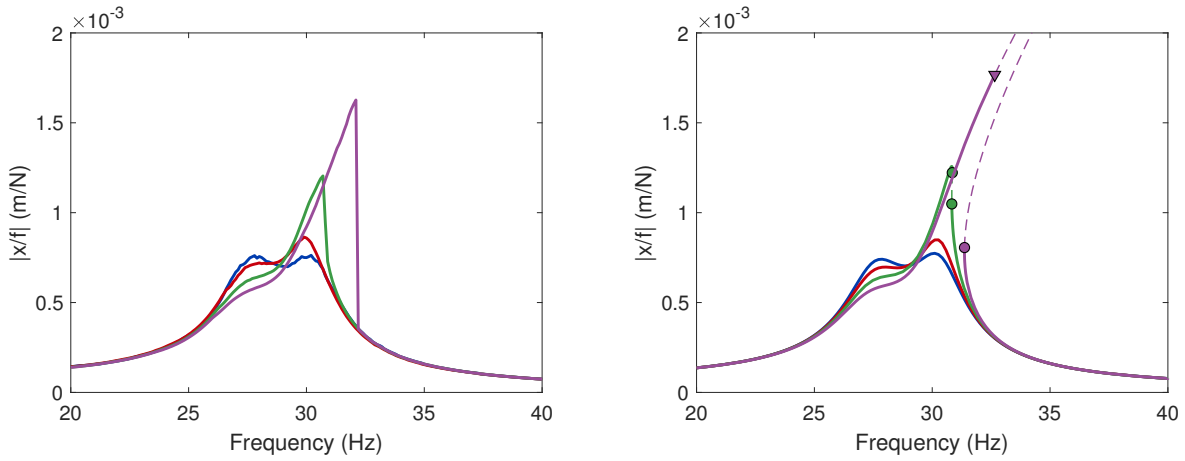

Figure 5.12: Experimental (a) and theoretical (updated) NFRs (b) of the nonlinear beam with a linear DVA: 0.2N (—), 0.4N (—), 0.6N (—), 0.8N (—). —: stable solution, - - : unstable solution, • : fold bifurcation, ▼: Neimark-Sacker bifurcation.

Parameter	$C_{p,3}$	$R_{p,3}$
Value	-2.3629×10^{14}V/C^3	1.5352×10^{7}V/A^3

Table 5.4: Identified nonlinear parameters of the piezoelectric transducer.

5.4.3 Experimental demonstration of a digital NPTVA

5.4.3.1 Synthesized nonlinear admittance

To address the detuning of the linear absorber, a cubic elastance was introduced in the synthetic admittance (αV_{NL} in Figure 5.7). Accounting for the nonlinear behavior of the piezoelectric transducer, the value of the nonlinear elastance was calculated to be $C_3 - C_{p,3} \approx 1.7C_3$. The measured voltage of the nonlinear capacitor in Figure 5.13 was found to closely follow the law prescribed by the design.

We note that, to fully comply with the theoretical work of [181], a negative cubic resistance should also have been added to the synthesized shunt circuit to compensate for the positive cubic resistance in Equation (5.14), but this was avoided to prevent any risk of instability caused by such an active component. The linear resistance was nevertheless diminished by 10% in an attempt to limit the dissipation in the circuit at high forcing amplitudes. As shall be shown in Section 5.4.3.4, this has a limited impact on the performance of the digital NPTVA.

5.4.3.2 Performance of the NPTVA

Figure 5.14(a) displays the experimental NFRs for forcing levels ranging from 0.2N to 0.8N. Clearly, the NPTVA is able to maintain equal peaks in the frequency response for all forcing levels considered, confirming its superior performance over its linear counterpart. Furthermore, these experimental curves are in excellent

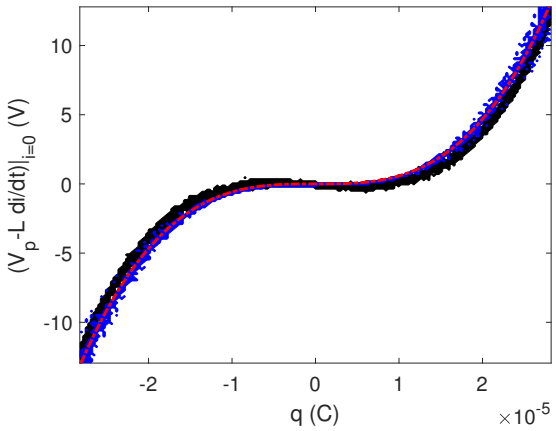

Figure 5.13: Voltage across the nonlinear capacitor: theoretical law (---), direct measurements of V_{nl} (•) and post-processed measurements from the input and output signals (•).

agreement with the theoretical NFRs in Figure 5.14(b).

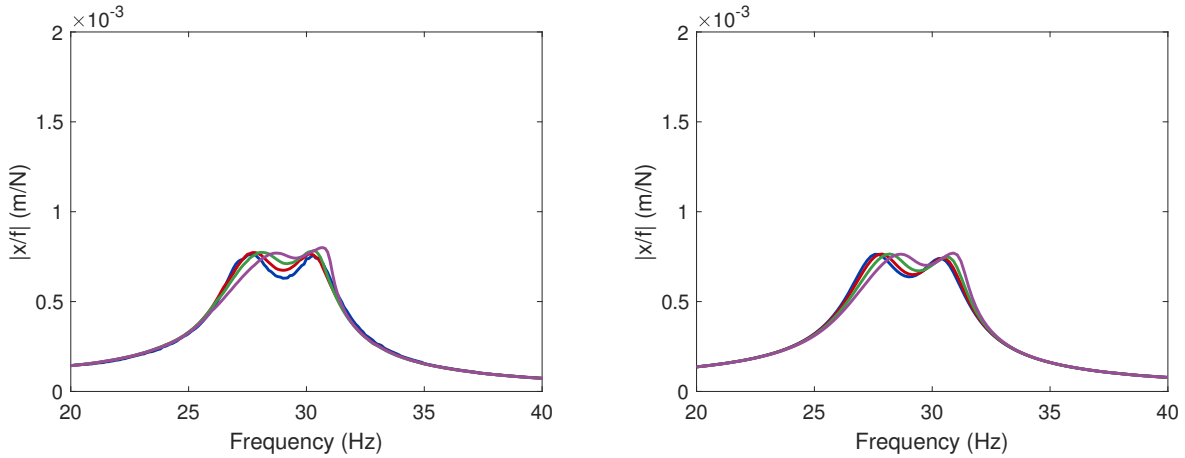

Figure 5.14: Experimental (a) and theoretical (updated) NFRs (b) of the nonlinear beam with a digital NPTVA: 0.2N (—), 0.4N (—), 0.6N (—), 0.8N (—).

A series of tests at higher forcing amplitudes were performed to investigate the potentially adverse dynamics brought by the NPTVA. Because of the detuning of the linear absorber, these tests were not performed with this latter absorber in order to avoid the rupture of the thin lamina. Figure 5.15(a) depicts that the NPTVA starts to be slightly detuned at 1N, with a more pronounced detuning at 1.2N. The theoretical response in Figure 5.15(b) indicates that a detached resonance curve merges with the main response, marking the end of the working range of the NPTVA [181].

The digital NPTVA suffers from another limitation depicted in Figure 5.16. At 1.2N, the input signal of the MCU reaches its saturation limits, meaning that the operational amplifier OA5 in Figure 5.6 saturates correspondingly. The output signal saturates as well. This issue can be resolved by decreasing R_i, thereby decreasing g by virtue of Equation (1.56), and thus the magnitude of the output signal, but this was not attempted in this work since the input voltage saturates anyway.

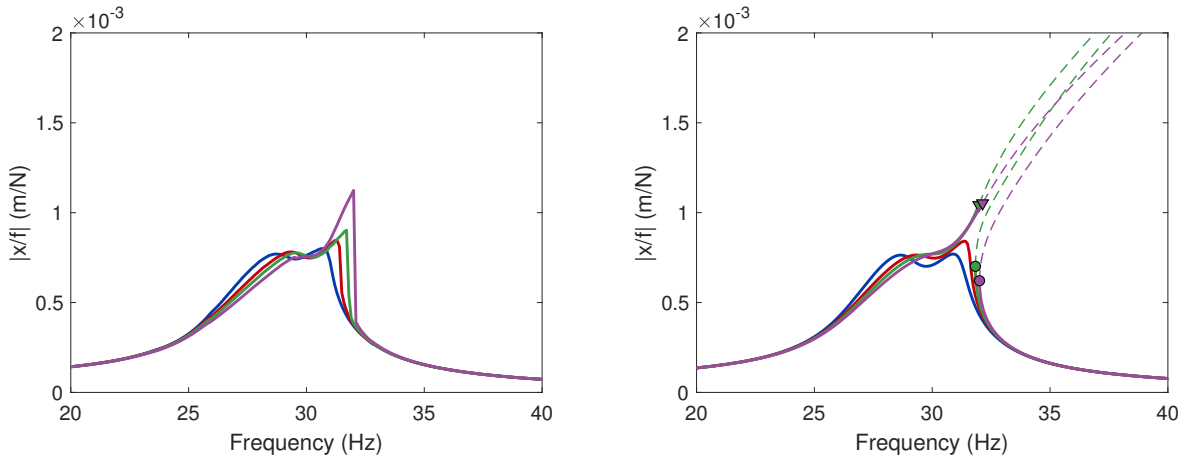

Figure 5.15: Experimental NFRs (a) and theoretical (updated) NFRs (b) of the nonlinear beam with a digital NPTVA: 0.8N (—), 1.0N (—), 1.1N (—), 1.2N (—). —: stable solution, - - : unstable solution, ● : fold bifurcation, ▼: Neimark-Sacker bifurcation.

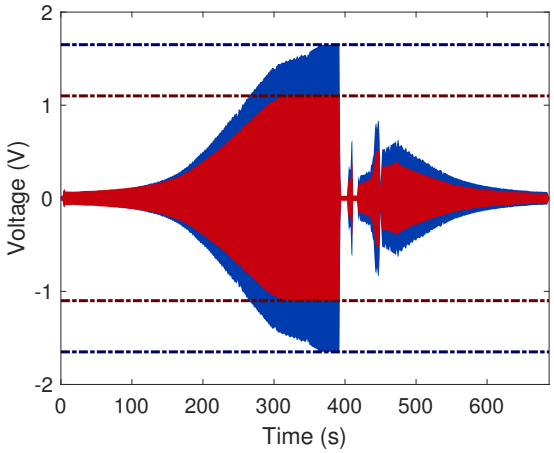

Figure 5.16: Signals recorded in the MCU for a NPTVA at f=1.2N: input voltage (—) and its saturation limits at ±1.65V (-·-), output voltage (—) and its saturation limits at ±1.1V (-·-).

5.4.3.3 Validation of the principle of similarity

Quadratic, $C_2\text{sign}(q)q^2$, and quintic, C_5q^5, nonlinear elastances were also considered separately in the MCU. After fitting the cubic nonlinear restoring force of the thin lamina with quadratic and quintic laws, as shown in Figure 5.17, the coefficient of the nonlinear elastance was computed based on this assumed restoring force using the formulas from [178].

Figure 5.18 displays the corresponding NFRs. In both cases, a clear detuning is observed compared to Figure 5.14, which confirms the fact that a cubic elastance is the optimal choice for a cubic nonlinearity in the host structure, which, in turn, validates the adopted principle of similarity. The detuning can be understood from Figure 5.17, where the stiffness is first overestimated (resp. underestimated) and then underestimated (resp. overestimated) for a quadratic (resp. quintic) nonlinearity,

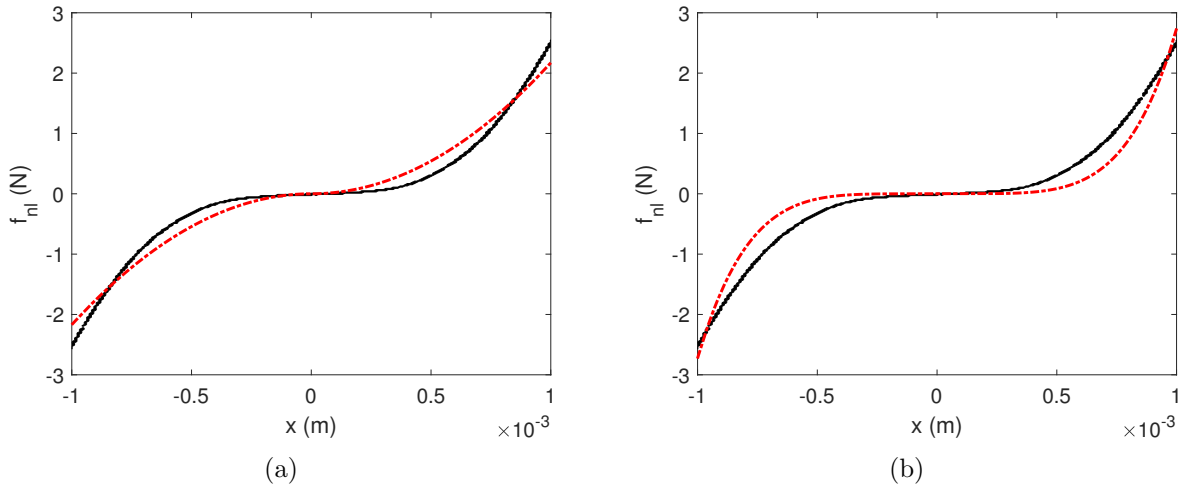

Figure 5.17: Fitting the cubic nonlinearity of the thin lamina with a quadratic (a) or a quintic (b) nonlinearity: measurements (•) and fitted model (- - -).

leading to the same trend for the absorber frequency.

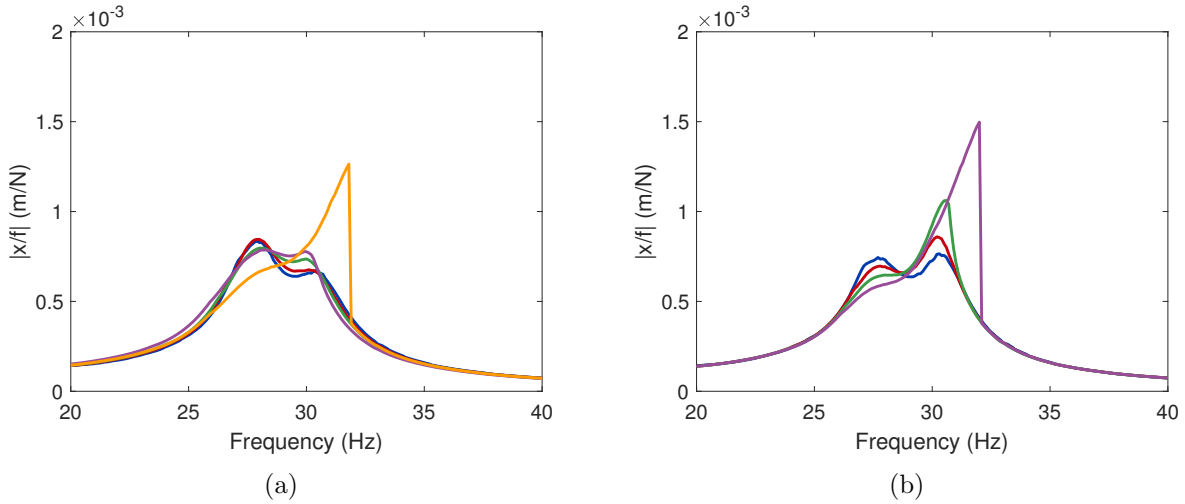

Figure 5.18: Experimental NFRs of the nonlinear beam with a digital NPTVA with quadratic (a) or quintic (b) elastance: 0.2N (—), 0.4N (—), 0.6N (—), 0.8N (—), and 1.0N (—).

5.4.3.4 Parametric study

Given the ease with which the parameters of a digital absorber can be modified, performing a parametric study was relatively straightforward. At 0.6N, Figure 5.19(a) shows that the nominal nonlinear elastance (i.e., without the correction for the nonlinearity of the piezoelectric transducer) cannot enforce equal peaks. It is only when the nominal value is multiplied by 2 that equal peaks are obtained. A too large nonlinear elastance is also detrimental to performance. Finally, Figure 5.19(b) shows what happens when the resistance is varied in a nonlinear regime of motion. As announced in Section 5.4.3.2, decreasing the resistance by 10% has almost no effect on the maximum amplitude

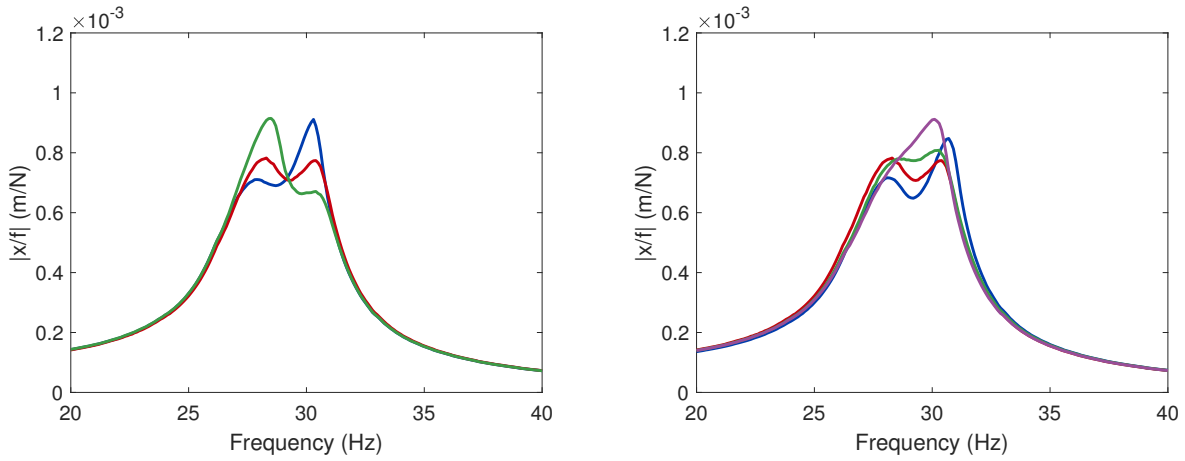

Figure 5.19: Experimental NFRs of the nonlinear beam with a NPTVA at f=0.6N: (a) nominal nonlinear elastance multiplied by 1.0 (—), 2.0 (—) and 3.0 (—), and (b) nominal resistance multiplied by 0.8 (—), 0.9 (—), 1.0 (—) and 1.1 (—).

5.5 Multimodal nonlinear piezoelectric vibration absorber

The principle of similarity can be used to tailor multiple nonlinear resonances [182]. This aspect is exploited herein to design multimodal NPTVAs. This section presents the adaptation of what was proposed in [197] to piezoelectric vibration absorbers, in a more general way than exposed in [145].

It is assumed that the design of the linear absorbers has been carried out (Chapters 2, 3 and 4) and that the controlled FRF exhibits pairs of peaks of (nearly) equal amplitude in place of the targeted resonances. These linear absorbers can be augmented with nonlinear elements in order to counteract the detuning effect of the nonlinearities in the host structure. In what follows, the nonlinearities are assumed to be odd polynomials of order $p > 1$, and a nonlinear principle of similarity is used to ensure that the nonlinear absorbers are effective in a larger range of forcing amplitudes.

The nonlinear forces are separated into contributions from the nonlinearities in the host system $\mathbf{b}_0$ and those in the absorber. Each of the latter N_{nl} nonlinerities is characterized by a coefficient $b_{a,n}$ and a vector function $\mathbf{b}_{a,n}$ depending both on its spatial distribution and its functional form. In the frequency domain, the nonlinear forces thus read

$$\mathbf{b}_{nl}(\mathbf{z}) = \mathbf{b}_0(\mathbf{z}) + \sum_{n=1}^{N_{nl}} b_{a,n}\mathbf{b}_{a,n}(\mathbf{z}). \tag{5.15}$$

The external forcing can be scaled with an amplitude parameter f such that $\mathbf{b}_{ext} = f\overline{\mathbf{b}}_{ext}$ (where $\bar{\cdot}$ denotes in the sequel a parameter normalized by the external forcing). Normalizing the harmonic coefficients in the same way, $\mathbf{z} = f\overline{\mathbf{z}}$, the governing equations in Equation (5.5) become upon division by f

$$\mathbf{A}_L(\omega)\overline{\mathbf{z}} + \epsilon\left(\mathbf{b}_0(\overline{\mathbf{z}}) + \sum_{n=1}^{N_{nl}} b_{a,n}\mathbf{b}_{a,n}(\overline{\mathbf{z}})\right) = \overline{\mathbf{b}}_{ext}, \tag{5.16}$$

where $\epsilon = f^{p-1}$ is a parameter that quantifies the strength of the nonlinearities. When $\epsilon \to 0$, the nonlinear forces vanish and the system tends to its underlying linear counterpart.

Equation (5.16) can be solved numerically. The amplitude of the nonlinear motion can then be inferred, and optimization algorithms can be used to tune the nonlinear coefficients of the absorbers according to the objectives at hand, following, e.g., an approach similar to [185]. Owing to the nonlinear nature of these equations, this process may be time-consuming and end up in a local minimum.

5.5.1 Nonlinear frequency response approximation

Following the approach in [178], an approximate solution to Equation (5.16) can be derived. It is first assumed that the Fourier series expansion used in the HBM only contains fundamental harmonics of the forcing frequency. In this case, the vector of harmonic coefficients only contains sine ($\overline{\mathbf{z}}_s$) and cosine ($\overline{\mathbf{z}}_c$) harmonic coefficients

$$\overline{\mathbf{z}}^T = \begin{bmatrix} \overline{\mathbf{z}}_s^T & \overline{\mathbf{z}}_c^T \end{bmatrix} \tag{5.17}$$

and Equation (5.3) becomes

$$\frac{\mathbf{x}_s(t)}{f} = \left(\begin{bmatrix} \sin(\omega t) & \cos(\omega t) \end{bmatrix} \otimes \mathbf{I}_{N_x} \right) \overline{\mathbf{z}} = \sin(\omega t)\, \overline{\mathbf{z}}_s + \cos(\omega t)\, \overline{\mathbf{z}}_c. \tag{5.18}$$

The normalized harmonic coefficients are then expanded in powers of ϵ

$$\overline{\mathbf{z}} = \sum_{i=0}^{+\infty} \epsilon^i \overline{\mathbf{z}}^{(i)} \tag{5.19}$$

Inserting this ansatz into Equation (5.16), expanding this equation in powers of ϵ and equating like powers of ϵ leads to a hierarchy of linear equations

$$\overline{\mathbf{z}}^{(0)} = \mathbf{A}_L^{-1} \overline{\mathbf{b}}_{ext}, \tag{5.20}$$

and

$$\overline{\mathbf{z}}^{(1)} = -\mathbf{A}_L^{-1} \left(\mathbf{b}_0(\overline{\mathbf{z}}^{(0)}) + \sum_{n=1}^{N_{nl}} b_{a,n} \mathbf{b}_{a,n}(\overline{\mathbf{z}}^{(0)}) \right) = \overline{\mathbf{z}}_0^{(1)} + \sum_{n=1}^{N_{nl}} b_{a,n} \overline{\mathbf{z}}_{a,n}^{(1)}, \tag{5.21}$$

to zeroth- and first-order of ϵ, respectively. Equation (5.20) is the exact solution of Equation (5.16) when $\epsilon = 0$; it expresses that the zeroth-order motion is the response of the underlying linear system. The proposed method may thus be seen as a perturbation method around the equilibrium of the underlying linear structure. Equation (5.21) shows that the first-order nonlinear motion is due to the nonlinear forces triggered by the zeroth-order motion. Moreover, the contribution from each nonlinearity on this first-order motion can be separated explicitly. Because these two equations are linear, they can readily be solved with standard linear algebra methods.

If the response at a particular dof localized by $\mathbf{w}_u$ is to be computed, the sine and cosine coefficients associated with it are given by

$$\overline{q}_s^{(i)} = [\mathbf{w}_u^T, \mathbf{0}] \overline{\mathbf{z}}^{(i)}, \qquad \overline{q}_c^{(i)} = [\mathbf{0}, \mathbf{w}_u^T] \overline{\mathbf{z}}^{(i)}, \tag{5.22}$$

The squared motion amplitude to first order in ϵ is given by

$$\begin{aligned}\overline{H} &= \left(\overline{q}_s^{(0)}\right)^2 + \left(\overline{q}_c^{(0)}\right)^2 + 2\epsilon\left(\overline{q}_s^{(0)}\overline{q}_{s,0}^{(1)} + \overline{q}_c^{(0)}\overline{q}_{c,0}^{(1)}\right) + 2\epsilon\sum_{n=1}^{N_{nl}} b_{a,n}\left(\overline{q}_s^{(0)}\overline{q}_{s,a,n}^{(1)} + \overline{q}_c^{(0)}\overline{q}_{c,a,n}^{(1)}\right) \\ &= \overline{H}^{(0)} + \epsilon\overline{H}_0^{(1)} + \epsilon\sum_{n=1}^{N_{nl}} b_{a,n}\overline{H}_{a,n}^{(1)}\end{aligned}, \tag{5.23}$$

where the subscripts in the sine and cosine coefficients correspond to those of the harmonic coefficiens (Equation (5.21)). Equation (5.23) shows that the effects of the different nonlinearities can once again be separated. In some sense, the nonlinear coefficients of the absorbers can be used to shape the first-order effects of all nonlinearities on the NFR.

5.5.2 Peaks of the nonlinear frequency response

In this section, it is demonstrated that the frequency-energy dependence is not relevant to first order in ϵ. Properties imposed on the peaks of the NFR can thus be imposed considering the linear resonance frequency ω_i and not its nonlinear counterpart $\omega_{nl,i}$

In order to locate a resonance, the necessary condition [178]

$$\left.\frac{\partial\overline{H}}{\partial\omega}\right|_{\omega=\omega_{nl,i}} = 0 \tag{5.24}$$

is considered. The deviation of the nonlinear resonance frequency from its linear counterpart is defined as

$$\Delta\omega_i = \omega_{nl,i} - \omega_i. \tag{5.25}$$

Equation (5.24) can be doubly expanded as a Maclaurin series in $\Delta\omega_i$ and a power series in ϵ as

$$\left.\frac{\partial\overline{H}}{\partial\omega}\right|_{\omega=\omega_{nl,i}} = \sum_{k=0}^{+\infty}\frac{(\Delta\omega_i)^k}{k!}\left.\frac{\partial^{k+1}\overline{H}}{\partial\omega^{k+1}}\right|_{\omega=\omega_i} = \sum_{k=0}^{+\infty}\frac{(\Delta\omega_i)^k}{k!}\left(\sum_{l=0}^{+\infty}\epsilon^l\frac{\partial^{k+1}\overline{H}^{(l)}}{\partial\omega^{k+1}}\right)\Bigg|_{\omega=\omega_i} = 0. \tag{5.26}$$

By definition of the linear resonance frequencies and by interpreting $\overline{H}^{(0)}$ as the linear (squared) FRF amplitude, the term corresponding to $(k,l) = (0,0)$ vanishes. The terms corresponding to $(k,l) = (1,0)$ and $(k,l) = (0,1)$ then indicate that $\Delta\omega_i \sim O(\epsilon)$.

The squared amplitude evaluated at the nonlinear resonance frequency is then itself doubly expanded as

$$\left.\overline{H}\right|_{\omega=\omega_{nl,i}} = \sum_{k=0}^{+\infty}\frac{(\Delta\omega_i)^k}{k!}\left(\sum_{l=0}^{+\infty}\epsilon^l\frac{\partial^k\overline{H}^{(l)}}{\partial\omega^k}\right)\Bigg|_{\omega=\omega_i} \tag{5.27}$$

which becomes, if only terms up to first order in ϵ are considered,

$$\left.\overline{H}\right|_{\omega=\omega_{nl,i}} = \left.\overline{H}^{(0)}\right|_{\omega_i} + \Delta\omega_i\left.\frac{\partial\overline{H}^{(0)}}{\partial\omega}\right|_{\omega_i} + \epsilon\left.\overline{H}^{(1)}\right|_{\omega_i} + O\left(\epsilon^2\right) \tag{5.28}$$

Because the second term in the right hand side of Equation (5.28) vanishes by definition of the linear resonance frequencies, there is no remaining term depending on $\Delta\omega_i$. Equation (5.28) thus indicates that, to first order in ϵ, the nonlinear shift of the resonance frequencies has no effect.

5.5.3 Enforcing equal peaks in nonlinear regimes of motion

The condition to maintain equal peaks around a specific nonlinear resonance i is

$$\overline{H}(\omega_{nl,i,1}) - \overline{H}(\omega_{nl,i,2}) = 0, \tag{5.29}$$

where $\omega_{nl,i,1}$ and $\omega_{nl,i,2}$ are the frequencies of the two peaks in the NFR of the controlled structure near the i^{th} host resonance frequency. Because of the results in Section 5.5.2, this equation can equivalently be expressed using $\omega_{i,1}$ and $\omega_{i,2}$, the linear counterparts of $\omega_{nl,i,1}$ and $\omega_{nl,i,2}$, respectively, as

$$\overline{H}(\omega_{i,1}) - \overline{H}(\omega_{i,2}) = 0. \tag{5.30}$$

Combining this result with Equations (5.23) and (5.30) yields

$$\overline{H}^{(0)}(\omega_{i,1}) - \overline{H}^{(0)}(\omega_{i,2}) + \epsilon \left(\overline{H}_0^{(1)}(\omega_{i,1}) - \overline{H}_0^{(1)}(\omega_{i,2}) + \sum_{n=1}^{N_{nl}} b_{a,n} \left(\overline{H}_{a,n}^{(1)}(\omega_{i,1}) - \overline{H}_{a,n}^{(1)}(\omega_{i,2}) \right) \right) = 0 \tag{5.31}$$

Since the linear FRF is assumed to already exhibit equal peaks, the first two terms in Equation (5.31) cancel out. Equation (5.31) then becomes independent of ϵ, which sets one condition on the nonlinear coefficients. Enforcing Equation (5.31) for each controlled resonance $i = 1, ..., N_s$, one eventually obtains the linear system of equations

$$\begin{bmatrix} \Delta_1 \overline{H}_{a,1}^{(1)} & \Delta_1 \overline{H}_{a,2}^{(1)} & \cdots & \Delta_1 \overline{H}_{a,N_{nl}}^{(1)} \\ \Delta_2 \overline{H}_{a,1}^{(1)} & \Delta_2 \overline{H}_{a,2}^{(1)} & \cdots & \Delta_2 \overline{H}_{a,N_{nl}}^{(1)} \\ \vdots & \vdots & \ddots & \vdots \\ \Delta_{N_s} \overline{H}_{a,1}^{(1)} & \Delta_{N_s} \overline{H}_{a,2}^{(1)} & \cdots & \Delta_{N_s} \overline{H}_{a,N_{nl}}^{(1)} \end{bmatrix} \begin{bmatrix} b_{a,1} \\ \vdots \\ b_{a,N_{nl}} \end{bmatrix} = - \begin{bmatrix} \Delta_1 \overline{H}_0^{(1)} \\ \vdots \\ \Delta_{N_s} \overline{H}_0^{(1)} \end{bmatrix} \tag{5.32}$$

with the shorthand notation

$$\Delta_i \overline{H}_l^{(1)} = \overline{H}_l^{(1)}(\omega_{i,1}) - \overline{H}_l^{(1)}(\omega_{i,2}). \tag{5.33}$$

The system (5.32) can be solved to find the nonlinear coefficients that impose equal peaks for all controlled nonlinear resonances. If the number of nonlinearities in the absorber is equal to the number of controlled resonances ($N_{nl} = N_s$) and assuming the system is non-singular, these coefficients are uniquely determined. A graphical interpretation of the counterbalancing action of the absorbers' nonlinearities is displayed in Figure 5.20.

The assumption of equality of the peaks amplitude in the linear FRF can be relaxed. Indeed, Equation (5.32) can be interpreted as requiring a cancelling nonlinear action of the absorbers on the imbalance brought by the nonlinearities of the host structure, to first order. Approximately equal peaks in the linear regime will therefore remain approximately equal in nonlinear regimes.

5.5.4 Enforcing the all-equal-peak property in nonlinear regimes of motion

The all-equal-peak design introduced in Chapter 4 can also be extended to nonlinear regimes of motion. The same amplitude is imposed on every peak, i.e.,

$$\overline{H}(\omega_{1,1}) - \overline{H}(\omega_{i,l}) = 0, \qquad \forall i \in [1, N_s], \forall l \in [1, 2]. \tag{5.34}$$

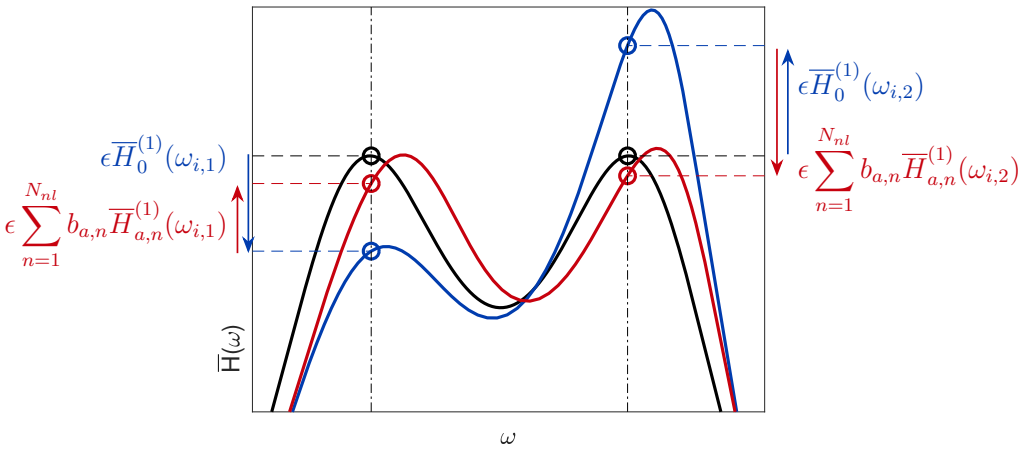

Figure 5.20: Action of the nonlinearities on the frequency response: underlying linear structure $\overline{H}^{(0)}$ (—), nonlinear structure with linear absorbers (—) and nonlinear structure with nonlinear absorbers (—).

If the FRF of the underlying linear structure exhibits an all-equal-peak property, then, following the same developments as in Section 5.5.3, Equation (5.34) translates to the linear system

$$\begin{bmatrix} \Delta_{1,2}\overline{H}_{a,1}^{(1)} & \Delta_{1,2}\overline{H}_{a,2}^{(1)} & \cdots & \Delta_{1,2}\overline{H}_{a,N_{nl}}^{(1)} \\ \Delta_{2,1}\overline{H}_{a,1}^{(1)} & \Delta_{2,1}\overline{H}_{a,2}^{(1)} & \cdots & \Delta_{2,1}\overline{H}_{a,N_{nl}}^{(1)} \\ \vdots & \vdots & \ddots & \vdots \\ \Delta_{N_s,2}\overline{H}_{a,1}^{(1)} & \Delta_{N_s,2}\overline{H}_{a,2}^{(1)} & \cdots & \Delta_{N_s,2}\overline{H}_{a,N_{nl}}^{(1)} \end{bmatrix} \begin{bmatrix} b_{a,1} \\ \vdots \\ b_{a,N_{nl}} \end{bmatrix} = - \begin{bmatrix} \Delta_{1,2}\overline{H}_0^{(1)} \\ \vdots \\ \Delta_{N_s,2}\overline{H}_0^{(1)} \end{bmatrix} \tag{5.35}$$

with the shorthand notation

$$\Delta_{i,k}\overline{H}_l^{(1)} = \overline{H}_l^{(1)}(\omega_{1,1}) - \overline{H}_l^{(1)}(\omega_{i,k}). \tag{5.36}$$

This time, the nonlinear coefficients can be exactly determined if the number of nonlinearities in the absorber is equal to the number of peaks minus one, i.e. $N_{nl} = 2N_s - 1$ (assuming there are two peaks per controlled resonance).

5.5.5 Nonlinear shunt circuits

In order to create tunable nonlinear circuits for nonlinear multimodal piezoelectric damping, the multi-branch shunt circuits seen in Chapter 2 can be endowed with nonlinear electrical elements. By extension of [181], nonlinear capacitors can be placed in series with every series RL shunt. For instance, Figure 5.21 depicts a nonlinear version of Hollkamp's shunt circuit, and Figure 5.22(a) features a nonlinear current blocking (NCB) shunt circuit. These two circuits provide N_s additional design DoFs, that can be tuned to secure pairs of equal peaks in the NFR of a controlled structure.

Figure 5.22(b) displays an augmented nonlinear current blocking (ANCB), where nonlinear capacitors are placed in series with the filter capacitors. These $N_s - 1$ additional design DoFs yield a total of $2N_s - 1$ design DoFs for the ANCB circuit, allowing it to enforce the all-equal-peak property in the NFR of the controlled structure.

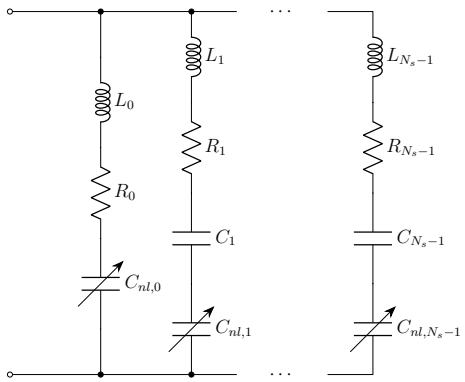

Figure 5.21: Nonlinear Hollkamp's shunt circuit.

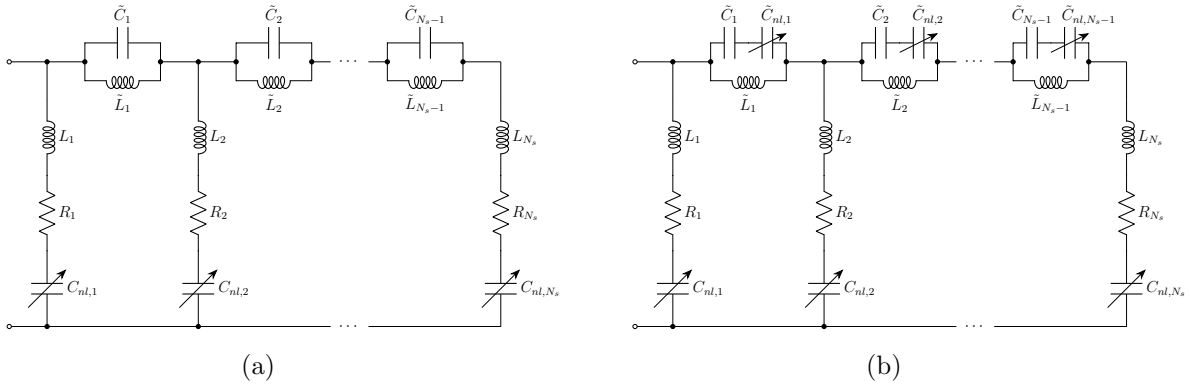

Figure 5.22: Nonlinear CB (a) and augmented nonlinear CB (b) shunt circuits.

The models of these nonlinear shunt circuits are developed in Section F.2. Other arrangements could be envisioned. For instance, nonlinear inductors could be used instead of nonlinear capacitors [104]. Circuits with parallel RL shunts could also be made nonlinear. Finally, the ideal Norton's admittance and Thévenin's impedance circuits, as well as the networks studied in Chapters 2 and 3, respectively, could also be augmented with nonlinear elements. However, it is not yet completely clear how passivity would be enforced in these nonlinear circuits/networks.

5.6 Examples of multimodal nonlinear vibration mitigation

5.6.1 Two-degree-of-freedom structure

The structure studied in Section 4.4.1 with the adjunction of a cubic spring (with coefficient $k_{nl} = 1 \times 10^{-3}\text{N/m}^3$) between the second mass and ground, as depicted in Figure 5.23, is considered as a first example. The performance of Hollkamp's, an NCB and an ANCB shunt circuits are compared with this host structure.

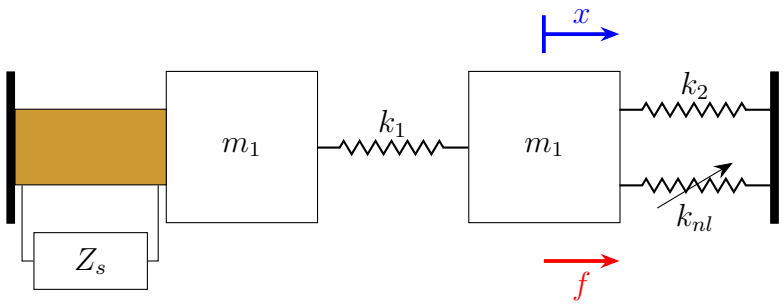

Figure 5.23: Nonlinear two-degree-of-freedom structure with a piezoelectric stack shunted with a circuit of impedance Z_s.

5.6.1.1 Nonlinear Hollkamp's shunt circuit

Starting off with Hollkamp's shunt circuit, Equation (5.32) was solved using the optimal parameters in Table 4.2, yielding the coefficients listed in Table 5.5. Figure 5.24 compares the NFR of the structure controlled by the linear and nonlinear Hollkamp's shunt circuits in weakly to moderately nonlinear regimes of motion. The imbalance in the peaks signals the quick detuning of the linear absorber due to the hardening nonlinearity in the structure. By contrast, the nonlinear absorber is able to track the changes in resonance frequencies and maintain balanced peaks, similarly to a NPTVA.

Parameter	$C_{nl,0}$	$C_{nl,1}$
Value	4.17×10^{-4}V/C^3	7.83×10^{-3}V/C^3

Table 5.5: Values of the nonlinear elastances in the nonlinear version of Hollkamp's shunt circuit controlling the two-degree-of-freedom structure.

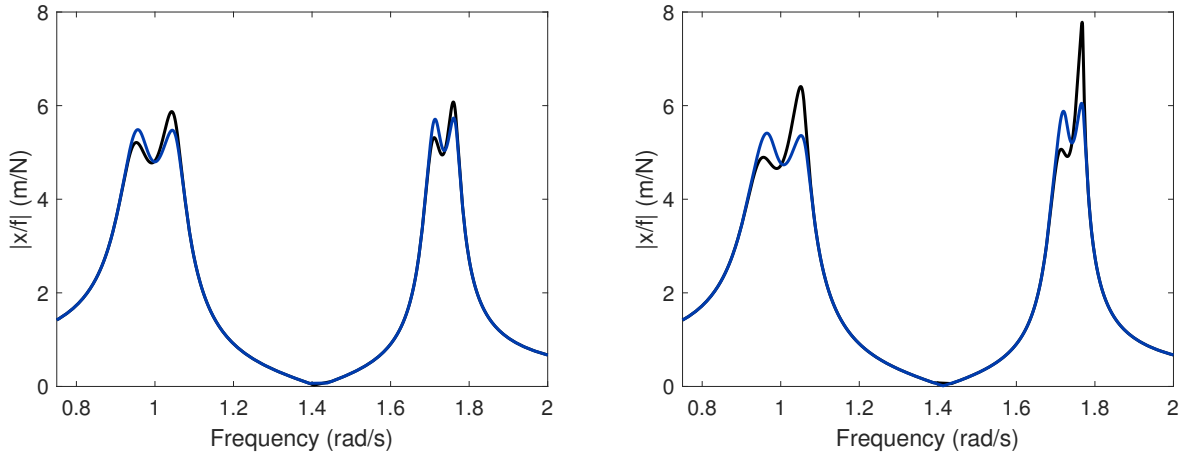

Figure 5.24: NFRs of the two-degree-of-freedom structure with linear (—) and nonlinear (—) Hollkamp's shunt circuits: f=1N (a) and f=1.5N (b).

The dynamics in strongly nonlinear regimes of motion are illustrated in Figure 5.25. The nonlinear absorber is able to maintain performance at f=1.7N, whereas a DRC has merged

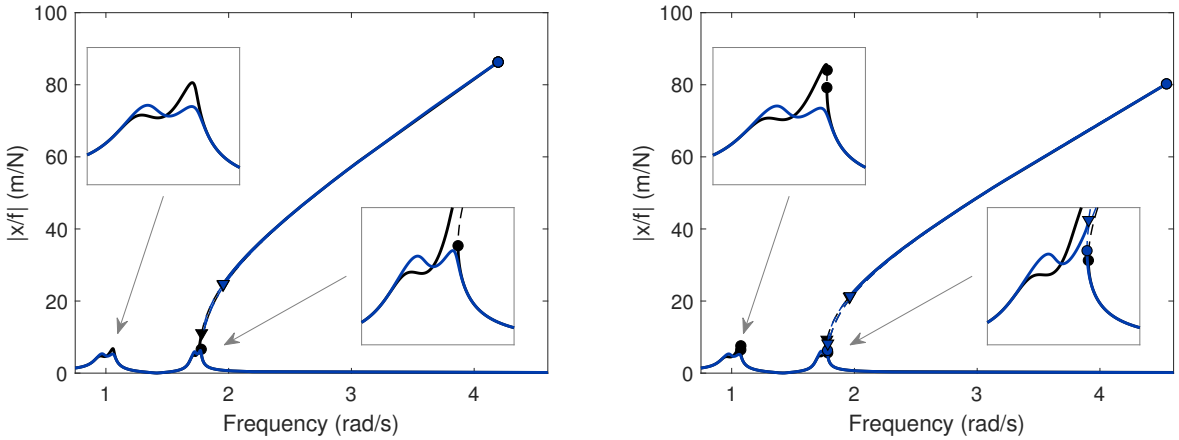

Figure 5.25: NFRs of the two-degree-of-freedom structure with linear (—) and nonlinear (—) Hollkamp's shunt circuits: f=1.7N (a) and f=2N (b). —: stable solution, - - : unstable solution, •: fold bifurcation, ▼: Neimark-Sacker bifurcation.

with the main NFR with linear absorbers. However, a DRC can also be encountered with the nonlinear absorber at f=2N. The reason for the failure of the nonlinear absorber in these strongly nonlinear regimes of motion stems from the approximations made by truncating Equation (5.19) to a first order in ϵ, which makes the method only able to accurately represent the dynamics of the structure in weakly nonlinear regimes of motion.

The performance of both absorbers is summarized in Figure 5.26, which shows the peaks loci in the forcing amplitude-response amplitude plane. Noting the similarity between Figures 5.5(b) and 5.26(d), the performance of both multimodal absorbers on mode 2 is qualitatively similar to that of their respective counterparts in the single-mode case. No DRC seems to be present near the first mode, where the vibration levels remain comparatively low. Geometrically, the action of the absorbers nonlinearities in Equation (5.32) imposes the tangency between the two peaks loci around ϵ=0 (i.e., f=0), which can be observed in Figures 5.26(a) and 5.26(b).

The apparent inability of Hollkamp's shunt circuit to mitigate the DRC can be understood in terms of its action on the structure through the amplitude of the charge at the piezoelectric transducer in Figure 5.27. For the rightmost peak associated with the first host resonance, Figure 5.27(a) shows that both linear and nonlinear absorbers are activated in all forcing ranges but the nonlinear one is the most efficient. Paradoxically, the structure controlled with nonlinear absorbers exhibits a behavior which appears more linear, owing to the canceling action of the absorber's nonlinearities. As for the rightmost peak associated with the second host resonance, Figure 5.27(b) outlines the behavior of the absorber on the DRC. Slightly after the DRC coalescence with the main NFR (indicated by the first fold bifurcation), linearity between the motion and piezoelectric charge amplitudes no longer holds, and the piezoelectric charge amplitude decreases with the motion amplitude. On the maximum amplitude of the DRC (attained after the second fold bifurcation), the absorber is essentially inactivated, as its charge amplitude is low. Because of this low amplitude, the nonlinearities in the nonlinear version of Hollkamp's circuit have a small effect compared to the linear electrical components, and the nonlinear circuit behaves similarly to its linear counterpart.

Finally, Figure 5.25(b) features Neimark-Sacker bifurcations which are at the onset of QP

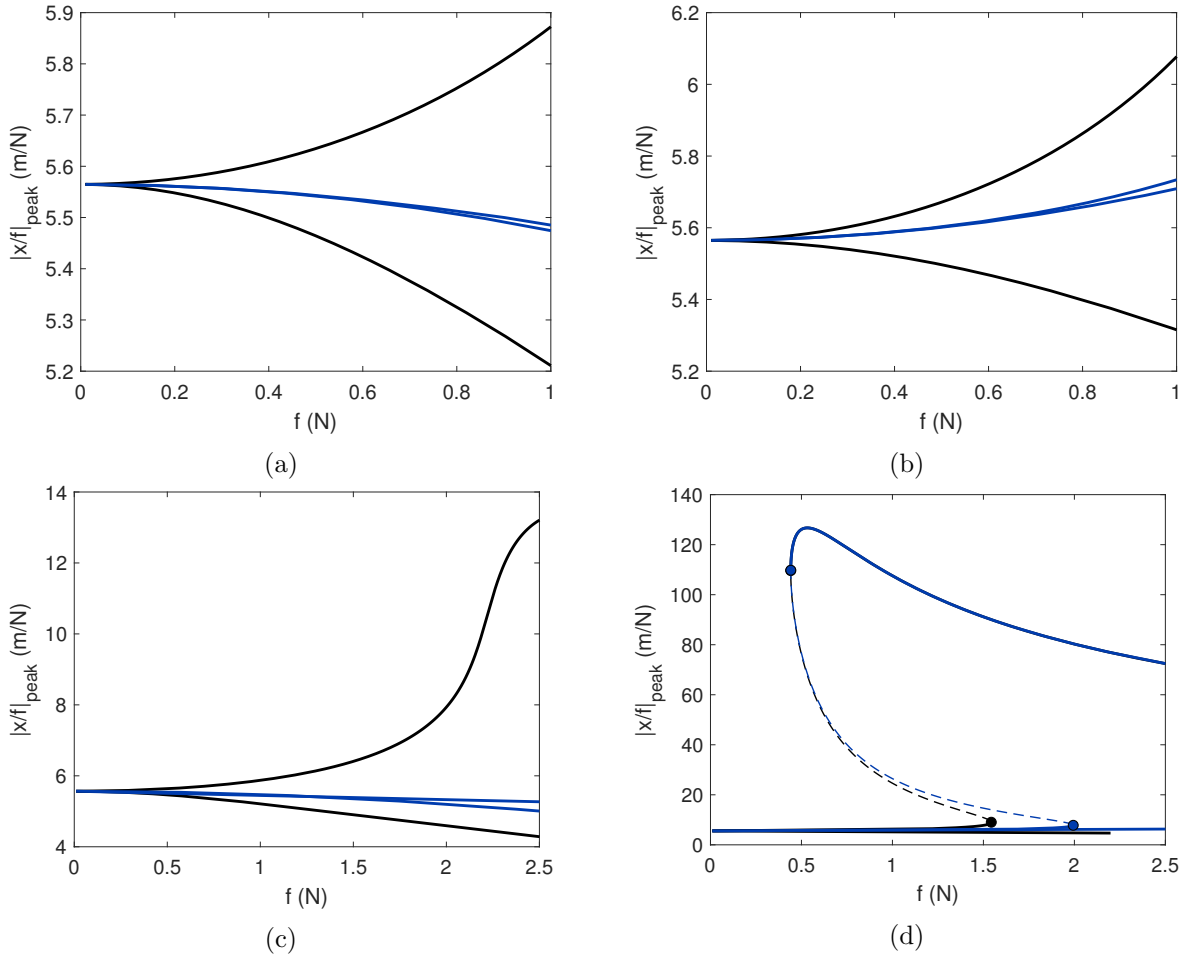

Figure 5.26: Peaks loci of the two-degree-of-freedom structure with linear (—) and nonlinear (—) Hollkamp's shunt circuits: peaks associated with the first and second host resonances at low (a,b) and high (c,d) forcing amplitudes. —: stable solution, - - : unstable solution, •: fold bifurcation.

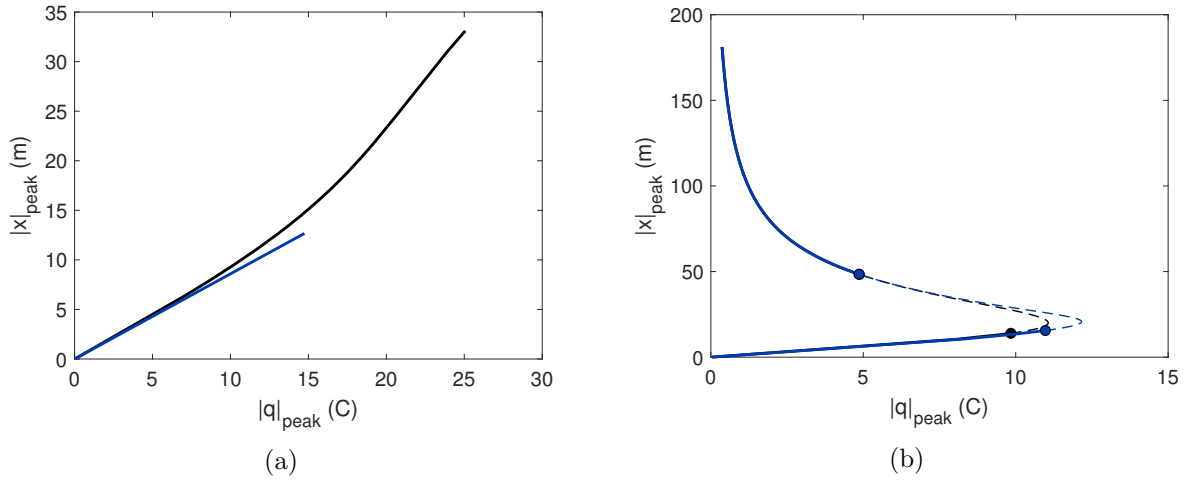

Figure 5.27: Charge amplitude in the transducer vs motion amplitude at the peaks of the NFR of the two-degree-of-freedom structure with linear (—) and nonlinear (—) Hollkamp's shunt circuits: rightmost peaks associated with the first (a) and second (b) host resonance. —: stable solution, - - : unstable solution, •: fold bifurcation.

oscillations. QP responses cannot be assessed with classical HBM because the motion is no longer periodic, but it is possible to compute them using the method proposed in [210]. The stability of the solution was assessed with the method in [214].

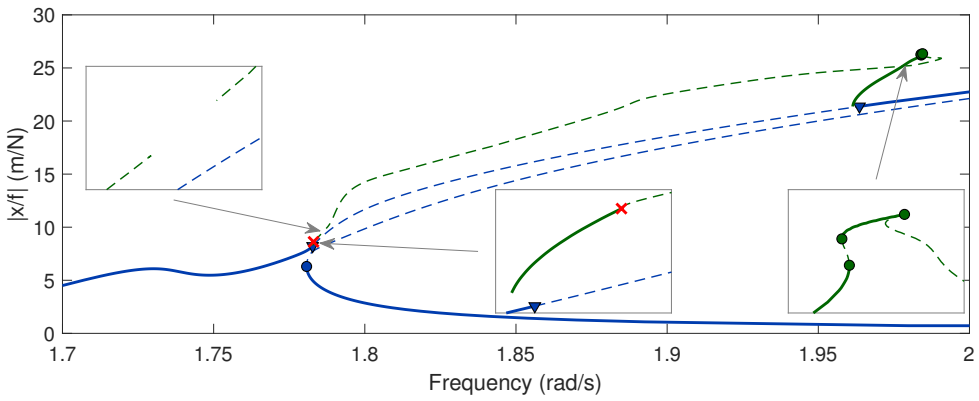

Figure 5.28: NFR of the two-degree-of-freedom structure with nonlinear Hollkamp's shunt circuit at f=2N: periodic solutions (—) and QP solutions (—). —: stable solution, - - : unstable solution, •: fold bifurcation, ▼: Neimark-Sacker bifurcation, ×: unclassified bifurcation.

The QP regime exhibits a more complicated frequency response than the harmonic one, as displayed in Figure 5.28. A forcing amplitude f=2N was considered, i.e., slightly after the DRC coalescence with the main NFR. Two branches emanate from the Neimark-Sacker bifurcations but do not join. They are only partially stable, and the lowest- and highest-amplitude branches lose stability through fold bifurcations and an unclassified bifurcation, respectively. Thus, the DRC does not seem to be connected to the main NFR by any fully stable branch.

5.6.1.2 Nonlinear current blocking shunt circuit

Considering now an NCB, Equation (5.32) was solved using the optimal parameters in Table 4.3, yielding the coefficients listed in Table 5.6. We note that the first nonlinear elastance features a relatively large, negative parameter.

Parameter	$C_{nl,1}$	$C_{nl,2}$
Value	-0.62V/C^3	1.13×10^{-3}V/C^3

Table 5.6: Values of the nonlinear elastances in the NCB controlling the two-degree-of-freedom structure, with the linear characteristics of Table 4.3.

Figure 5.29(a) shows a NFR at f=1N of the controlled systems. The NCB is able to maintain equal peaks in the NFR, but the latter is unstable in most of the frequency range. This issue stems from the negative nonlinear elastance, which makes the first branch unstable. For large enough amplitudes, this instability propagates to the whole system. Thus, the proposed method is mathematically successful, but this NCB is useless in this case.

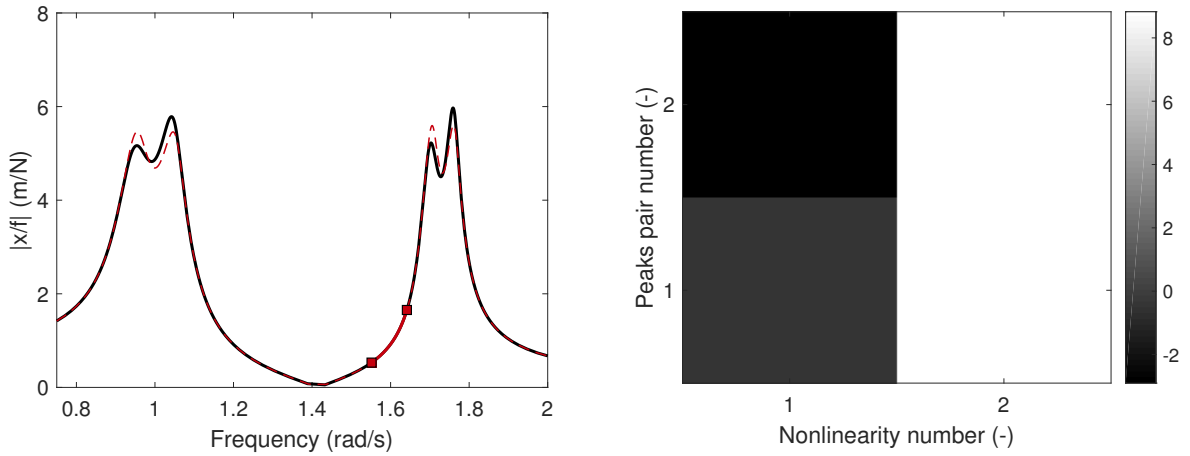

(a) (b)

Figure 5.29: NFRs of the two-degree-of-freedom structure with linear (—) and nonlinear (—) CB shunt circuits at f=1N (a) and influence matrix of the nonlinearities on the peaks imbalance (in logarithmic scale of absolute values) (b). —: stable solution, - - : unstable solution, ■: bifurcation point.

The origin of the negative nonlinear elastance can be explained by looking at the matrix in Equation (5.32), as depicted in Figure 5.29(b). It can be observed that the second nonlinear coefficient has a strong impact on the balance of the peaks pairs associated to both modes. By contrast, the first nonlinear coefficient has only limited influence near pair 1 and almost no influence on pair 2. In a similar manner to what has been seen in Section 2.10.1 with the resistances of Hollkamp's shunt circuit, the numerical resolution sets the second nonlinear coefficient to satisfy the requirements on pair 2, and then adjusts first nonlinear coefficient to satisfy those on pair 1. In this case, this unfortunately results in a large, negative value.

The issue thus mainly comes from the influence of the second shunt branch on the first pair. The original purpose of the current blocking filters of the CB shunt circuit was precisely to solve this issue [127]. However, the filter was detuned from the frequency of the first mode during the NH optimization process: it can be seen in Table 4.3 that the frequency of the current blocking filter is 1.41rad/s, i.e., rather far from the frequency of the first mode. To retrieve the desirable independence between the shunt branches, the NH optimization was run again but this time the filter was forced to remain tuned at its original frequency. The parameters of this new optimal CB are gathered in Table 5.7, and the associated receptance is similar to that of Hollkamp's shunt circuit.

Parameter	R_1	L_1	R_2	L_2	$\tilde{C}_1$	$\tilde{L}_1$
Optimal value	0.1964Ω	0.9777H	0.2243Ω	2.1666H	0.3019F	3.3462H

Table 5.7: NH optimal parameters of the current blocking circuit with series RL shunts for the two-degree-of-freedom structure (forcing the resonance frequency of the current blocking filter to its initial value).

Solving Equation (5.32) with the parameters in Table 5.7 yields the coefficients listed in Table 5.8. This time, all nonlinear coefficients are positive.

Parameter	$C_{nl,1}$	$C_{nl,2}$
Value	8.13×10^{-4}V/C^3	5.36×10^{-3}V/C^3

Table 5.8: Values of the nonlinear elastances in the NCB controlling the two-degree-of-freedom structure, with the linear characteristics of Table 5.7.

Examples of NFRs of the structure controlled by this NCB are given in Figure 5.30. The dynamics of the controlled system are quite similar to those with Hollkamp's shunt circuit. It may be noted in Figure 5.30(b) that the DRC is not merged with the main NFR at f=2N, but is close to be. This is confirmed by the peaks loci in Figure 5.31.

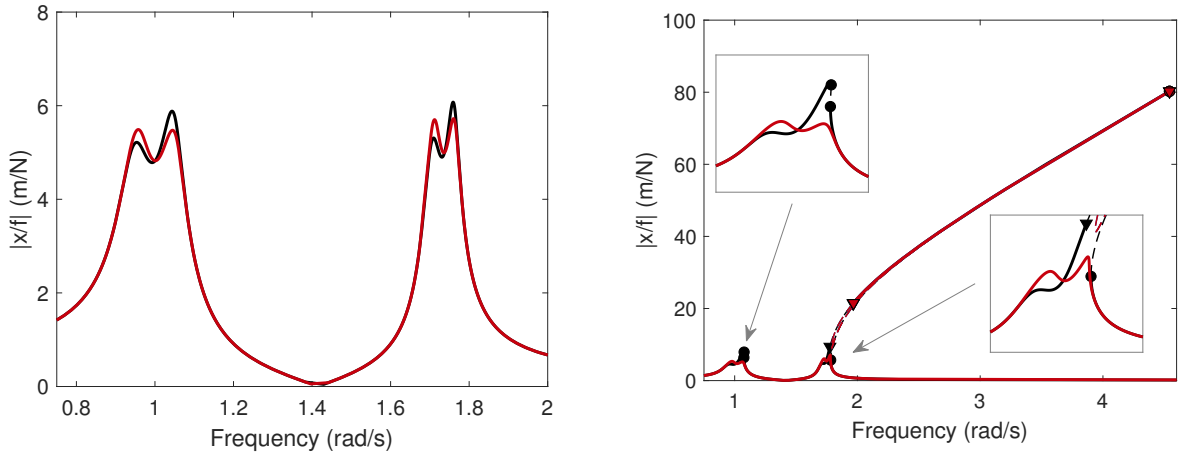

(a) (b)

Figure 5.30: NFRs of the two-degree-of-freedom structure with linear (—) and nonlinear (—) CB shunt circuits: f=1N (a) and f=2N (b). —: stable solution, - - : unstable solution, •: fold bifurcation, ▼: Neimark-Sacker bifurcation.

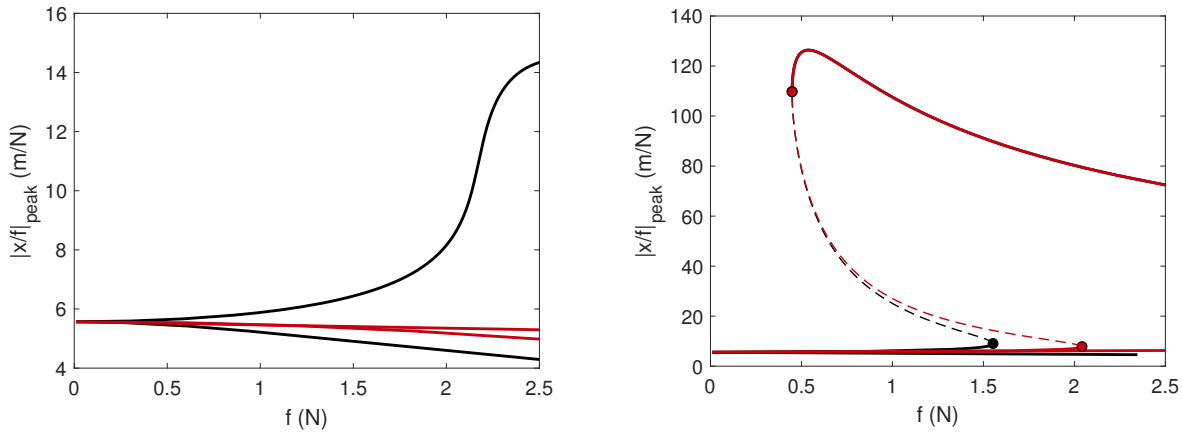

(a) (b)

Figure 5.31: Peaks loci of the two-degree-of-freedom structure with linear (—) and nonlinear (—) CB shunt circuits: peaks associated with the first (a) and second (b) host resonances. —: stable solution, - - : unstable solution, •: fold bifurcation.

5.6.1.3 Augmented nonlinear current blocking shunt circuit

To maintain the all-equal-peak property in nonlinear regimes of motion, a ANCB circuit is now considered. Using the optimal CB with parameters in Table 5.7, the nonlinear elastances obtained by solving Equation (5.35) are reported in Table 5.9. The nonlinear elastance coefficient in the filter is moderately negative, which does not provoke any instability.

Parameter	$C_{nl,1}$	$C_{nl,2}$	$\tilde{C}_{nl,1}$
Value	9.23×10^{-4}V/C^3	6.65×10^{-2}V/C^3	-1.21×10^{-2}V/C^3

Table 5.9: Values of the nonlinear elastances in the NCB controlling the two-degree-of-freedom structure, with the linear characteristics of Table 5.7.

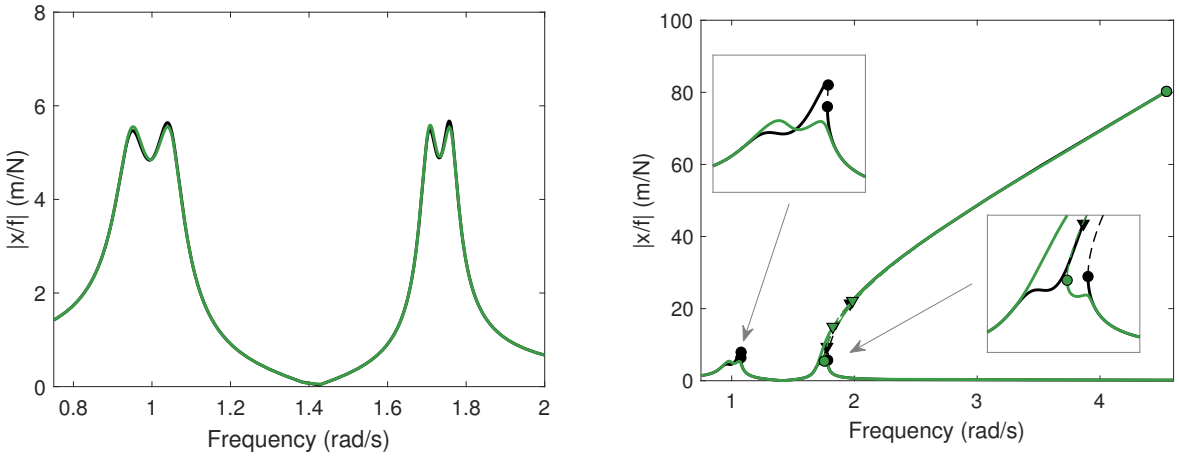

Figure 5.32: NFRs of the two-degree-of-freedom structure with linear (—) and augmented nonlinear (—) CB shunt circuits: f=1N (a) and f=2N (b). —: stable solution, - - : unstable solution, •: fold bifurcation, ▼: Neimark-Sacker bifurcation.

The NFR of the controlled system at f=1N is depicted in Figure 5.32(a). Unlike the two other circuits, the ANCB causes the leftmost peak associated with the second resonance to be detuned. This is due to the adverse effect of the nonlinear filter capacitor. The leftmost peak eventually merges with a DRC and at f=2N, and the system controlled by a ANCB exhibits a NFR with maximum amplitude similar to those of the other cases. The DRC merged with the NFR has a complex structure whose detailed description is beyond the scope of the present example. Figure 5.33 features the peaks loci of the structure controlled by a ANCB.

The early advantage of the ANCB compared to an NCB can be observed in Figure 5.34. While the solution of Equation (5.32) forces a pair-by-pair tangency at the origin, Equation (5.35) enforce a tangency between all pairs, thereby exhibiting a lower maximum amplitude for weakly nonlinear regimes of motion.

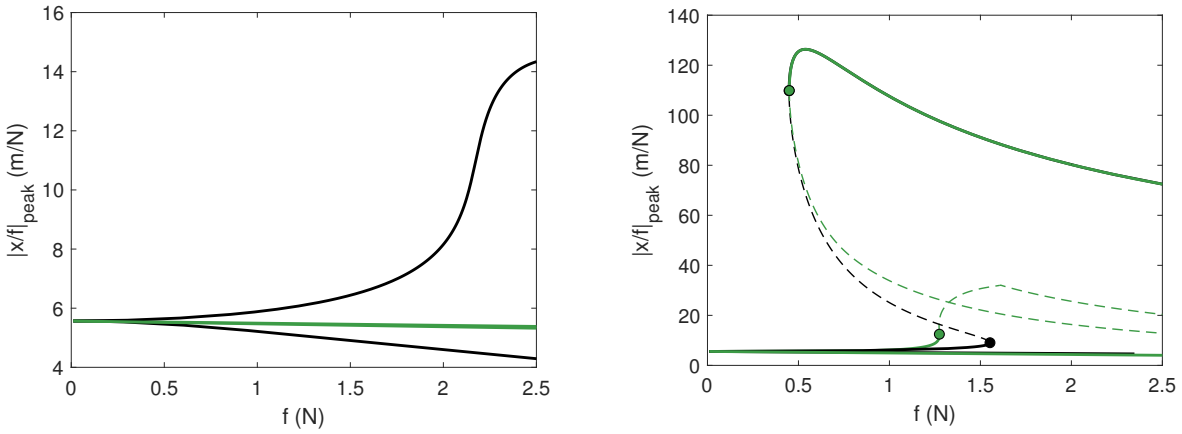

(a) (b)

Figure 5.33: Peaks loci of the two-degree-of-freedom structure with linear (—) and augmented nonlinear (—) CB shunt circuits: peaks associated with the first (a) and second (b) host resonances. —: stable solution, - - : unstable solution, •: fold bifurcation.

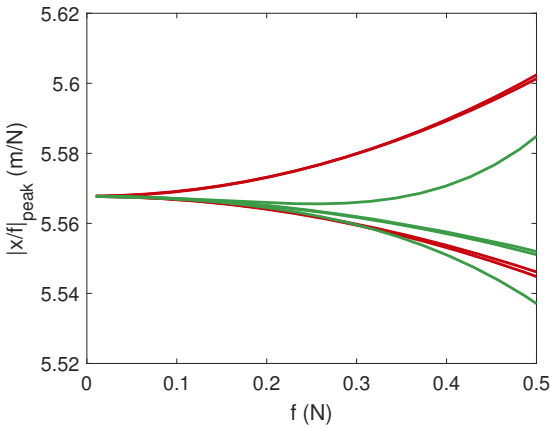

Figure 5.34: Peaks loci of the two-degree-of-freedom structure with NCB (—) and ANCB (—) shunt circuits.

5.6.1.4 Comparison between the circuits

Figure 5.35 summarizes the results obtained with the different nonlinear shunt circuits controlling the two-degree-of-freedom structure by featuring the highest-amplitude peak in each case. In weakly nonlinear regimes of motions, the ANCB exhibits the best performance, since it balances the peaks amplitude. However, the nonlinearity in the filter induces adverse dynamics on the system, and makes this solution less efficient in strongly nonlinear regimes of motions, where the nonlinear version of Hollkamp's circuit and the NCB exhibit the best performance. All nonlinear shunt circuits are however subject to the apparition of a DRC which appears similar in each case.

5.6.2 Simply-supported plate

The simply-supported plate studied in Section 4.4.4 is used as a second example. A cubic spring of coefficient $k_{nl} = 91.26 \times 10^4 \mathrm{N/m}^3$ is connected to the plate at the forcing point

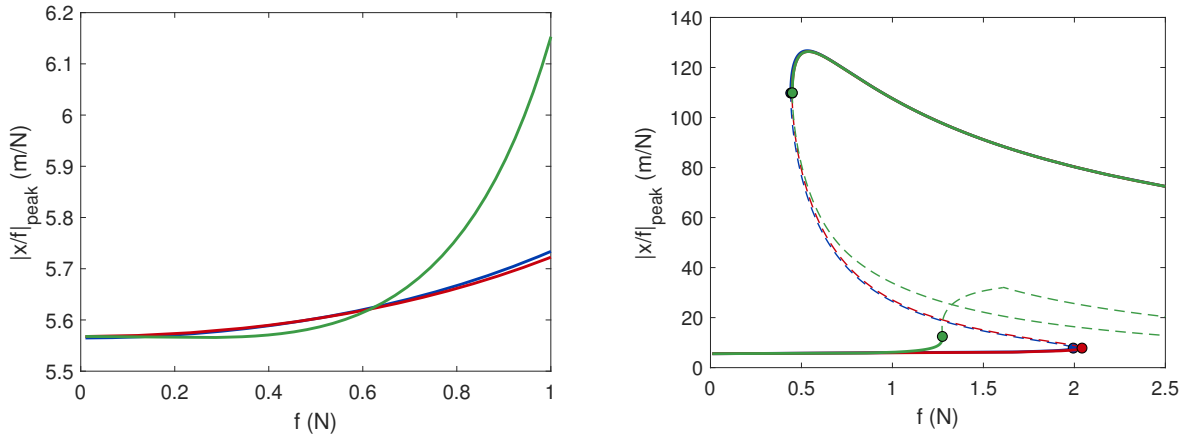

Figure 5.35: Peaks loci of the highest-amplitude peak of the two-degree-of-freedom structure with a nonlinear version of Hollkamp's circuit (—), an NCB (—) and a ANCB (—): weakly to moderately (a) and strongly (b) nonlinear regimes of motion. —: stable solution, - - : unstable solution, •: fold bifurcation.

location. To counteract the effects of this nonlinearity, an NCB circuit is used.

The nonlinear coefficients obtained using the CB parameters in Table 4.7(b) are listed in Table 5.10. A large, negative nonlinear elastance is obtained in the third branch. This stems from the same reasons as in the two-degree-of-freedom example. An extremely large nonlinear elastance is also obtained in the first branch, because it has to compensate for the large series resistance which has the tendency to hinder any nonlinear behavior by limiting the charge flow. These issues are solved by running the NH algorithm with forced current blocking filters frequencies, yielding the linear parameters reported in Table 5.11. The nonlinear elastances obtained with this setup are shown in Table 5.10; they are all positive and more homogeneous in terms of orders of magnitude.

Parameter	$C_{nl,1}$	$C_{nl,2}$	$C_{nl,3}$	$C_{nl,4}$
CB in Table 4.7(b)	1.36×10^{31}V/C^3	2.1×10^{10}V/C^3	-3.82×10^{15}V/C^3	4.35×10^{12}V/C^3
CB in Table 5.11	5.37×10^{9}V/C^3	4.9×10^{11}V/C^3	3.62×10^{15}V/C^3	2.04×10^{13}V/C^3

Table 5.10: Values of the nonlinear elastances in the NCB controlling the simply-supported plate.

Figure 5.36 displays several NFRs of the plate controlled with CB and NCB shunt circuits. Similar trends to the two-degree-of-freedom example can be observed. The hardening nonlinearity first detunes the linear absorber resulting in high-amplitude resonances, whereas the nonlinear absorber is able to maintain equal peaks in a broader range of forcing amplitudes. For high enough forcing amplitudes, it eventually becomes detuned as well.

The performance of a ANCB was also investigated, but it essentially features the same issues as in the two-degree-of-freedom case, i.e., it is efficient for weakly nonlinear regimes of motion, but the adverse dynamics induced by the nonlinearities in the current blocking filters result in the appearance of DRC that quickly merge with the main NFR.

Parameter	R_i	L_i	$\tilde{C}_i$	$\tilde{L}_i$
$i = 1$	1.04kΩ	60.69H	70.13nF	868.76H
$i = 2$	3.75kΩ	190.99H	24.83nF	413.38H
$i = 3$	127.71kΩ	5.33kH	8.2nF	1.1kH
$i = 4$	10.517kΩ	1.18kH	/	/

Table 5.11: NH optimal parameters of the CB circuit with series RL shunts for the simply-supported plate (forcing the resonance frequency of the current blocking filters to their initial values).

5.7 Conclusion

Linear tuned vibration absorbers generally exhibit good performance when their frequency matches that of their host. Nonlinear structural behaviors can change the resonance frequencies of structures with increasing forcing amplitudes, which eventually leads to inefficient vibration mitigation. Hopefully, it is possible to augment linear absorbers with nonlinear elements so as to extend their forcing amplitude working range. Specifically, by choosing the absorbers' nonlinearities according to a principle of similarity, they are able to track the frequency changes in the host structure and stay efficient over a broader range of forcing amplitudes than their linear counterpart.

After briefly reviewing some aspects associated with nonlinear vibrations and NLTVAs, this chapter presented the experimental realization of a digital NPTVA. Due to its inherent flexibility, this absorber can synthesize linear and nonlinear shunt circuits (with arbitrary mathematical forms for the nonlinearity). The experimental demonstration on a structure with hardening nonlinear behavior showed the superiority of the digital nonlinear absorber over its linear counterpart. It also served to validate the adopted principle of similarity.

A tuning methodology for nonlinear vibration absorbers that mitigate several nonlinear resonances simultaneously was then proposed. The nonlinear absorbers were shown to be able to maintain equal peaks in the frequency response over a broader range of forcing amplitudes than their linear counterparts.

Adverse attractors, including detached resonance curves and QP responses were studied, highlighting that the coupled system can exhibit complex and potentially detrimental dynamics. However, these attractors were observed whether or not nonlinearities were used in the absorbers. The all-equal-peak property was also extended to nonlinear absorbers, but was only effective for weakly nonlinear regimes of motion.

The approach proposed to control multiple nonlinear resonances should also be experimentally validated. It could be extended to ideal immittance circuits and networks as well.

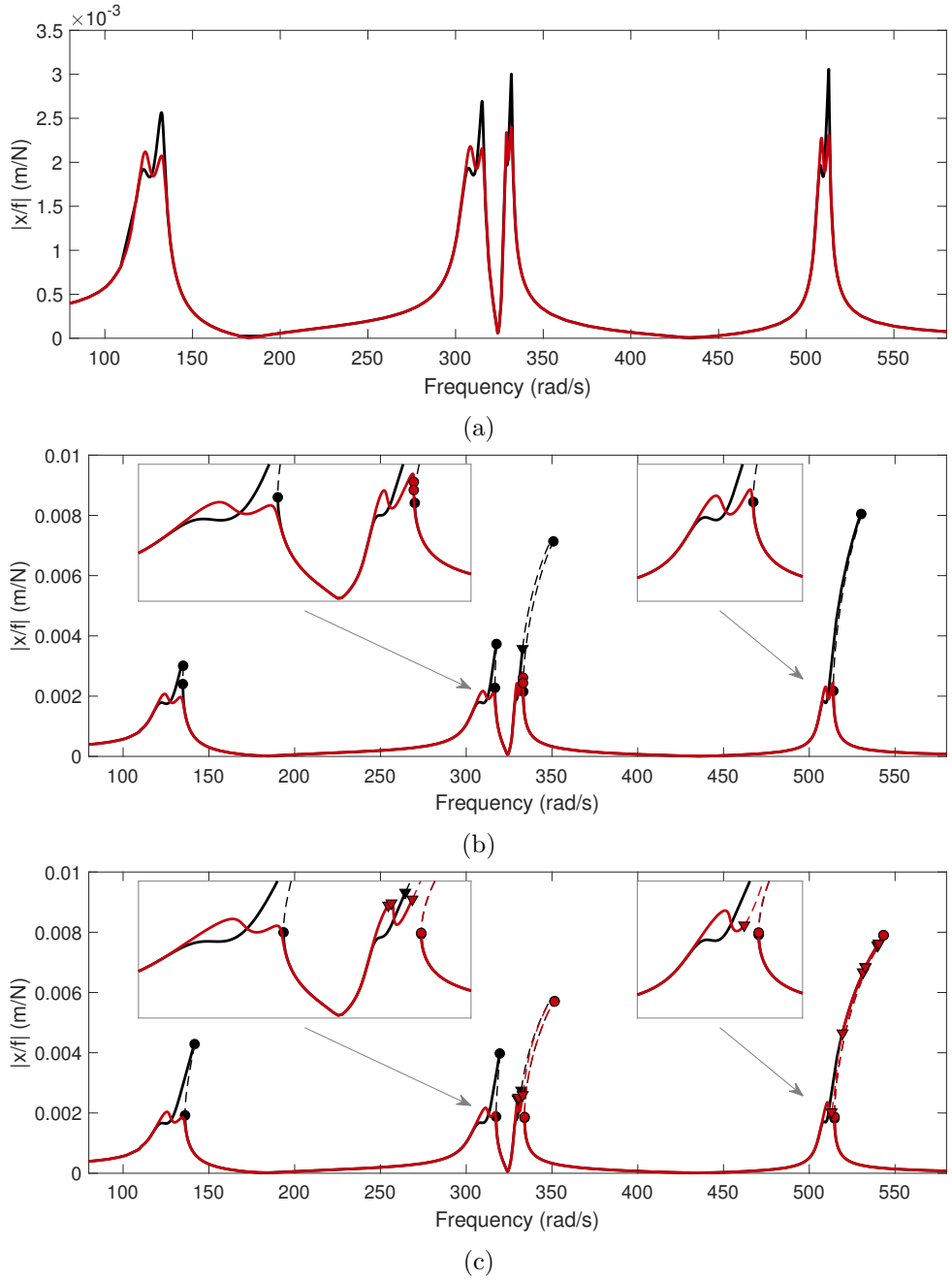

Figure 5.36: NFRs of the simply-supported plate controlled by linear (—) and nonlinear (—) CB shunt circuits: f=1.5N (a), f=2N (b) and f=2.5N (c). —: stable solution, - - : unstable solution, •: fold bifurcation, ▼: Neimark-Sacker bifurcation.

6 Damping of bladed structures

Abstract

The purpose of this chapter is to apply and adapt the control strategies proposed in the previous chapters to integrally bladed structures. They possess a large number of degrees of freedom, and exhibit complex dynamics with frequency regions with high modal density. A model-order reduction technique is thus first proposed to reduce the burden associated with the computation of frequency responses. A hybrid strategy is developed to allow for the control of multiple families of modes with closely-spaced resonance frequencies. Effective vibration mitigation of a bladed rail and a bladed drum is then demonstrated using various shunt damping techniques.

6.1 Introduction

6.1.1 Vibration mitigation of turbomachines

Bladed structures of turbomachines are submitted to harsh loading conditions, and the advent of integrally bladed structures, mainly motivated by weight reduction, raised new issues linked to their low inherent damping. For this reason, vibration mitigation means are used to ensure safety and durability.

The most popular approach by far is friction damping. By incorporating a contact surface between vibrating parts, energy can be dissipated through friction [51, 215]. There exist multiple ways to create such contact surfaces: either at the root of the blades, between the blades themselves, or at the shrouds. Figure 6.1(a) schematically depicts an example, where damping is provided through friction at the blades roots, as well as by underplatform dampers. For BLISKs and BluMs, the absence of interfaces limits the possibilities, but friction may be introduced by placing the contact surface at the underside of the blades support, using friction rings [52] (as depicted in Figure 6.1(b)) or friction fingers [216]. An approach combining the concept of friction damper and TMD was recently proposed in Lupini et al [217]. Friction damping has the merit of being a very simple solution to implement. However, friction is an inherently nonlinear phenomenon, and the damper's performance thus depends on the vibration level. There exist mature techniques to model it on a macro-scale level [51, 52, 218, 219], but these are significantly involved. Moreover, some parameters of the dampers, such as the friction coefficient, are not easily controllable and may exhibit a strong time-varying character owing to e.g. normal load, temperature [220] and wear [221, 222]. These variations are complex to control and their effects remain challenging to characterize experimentally [223].

Another approach to mitigate the vibrations of bladed structures consists in using viscoelastic materials having greater damping than the bladed part's constituent. In classical assemblies, a viscoelastic material can be placed at the interface between the blade root and the disk [53]. This simple solution has the advantage of being easily integrable in bladed assemblies and does not disrupt the aerodynamic flow. This is no

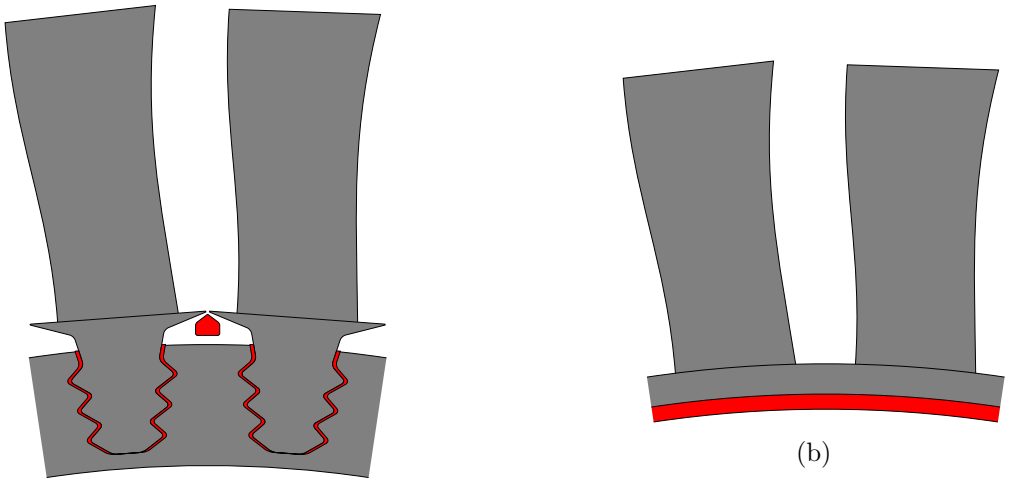

(a) (b)

Figure 6.1: Friction damping of bladed structures: bladed assembly with friction damping at the blade roots and with underplatform dampers (a) and integrally bladed structure with a friction ring (b). Friction surfaces/devices are indicated in red.

longer an option for BLISKs and BluMs, but other approaches were proposed, such as polymeric, metallic or ceramic oxide coating [224, 225]. Coatings are sensitive to erosion and foreign object damage, and put limits on the finish on the aerodynamic surfaces of the blades, which is why coating on the internal sides of a hollow blade was proposed in [226]. This approach however substantially complexifies the manufacturing process of the blades.

Piezoelectric damping was also considered for passive damping of bladed structures, but in contrast to the two previous solutions, this technology is not mature enough to be considered industrial state of the art. Tang and Wang [227] proposed to bond a piezoelectric patch to each blade (as in Figure 6.2(a)) and to shunt each of them with a series RL shunt. They augmented this passive system with charge and current feedback to optimally control multiple spatial harmonics. A passive realization of this concept, wherein capacitors were used instead of the charge feedback, was proposed by Yu and Wang [228] and later experimentally validated on a bladed disk mock-up [229]. This control strategy was also shown to be robust with respect to mistuning and non-engine-order excitation [230]. Interestingly, the concept proposed in these studies appears to be very similar to the analog network concept reported in the introduction of Chapter 3, although they were both independently proposed. Networks implemented only with capacitive and resistive elements were studied in [231] to avoid using inductors with impractically large inductance. Bladed structures with multiple individually-shunted piezoelectric patches were studied in [232, 233]. Kauffman and Lesieutre [234] proposed a frequency-detuning scheme switching a piezoelectric transducer between its short- and open-circuit state in order to set the structural resonance frequency away from that of a harmonic excitation.

An issue with the aforementioned works is that they require to place piezoelectric patches on the surface of the blade. This is unacceptable for the engine manufacturer, because such protrusion would lead to important perturbation in the aerodynamic flow. Schwarzendahl et al [235] proposed to incorporate a piezoelectric transducer on the inside of each blade. In this way, any vibration straining the blade would also strain the piezoelectric material and hence be controllable without disrupting the airflow. While this ambitious solution

holds promises, it may not be suitable for industrial application for the time being given its involved manufacturing difficulty [236]. Alternatively, Zhou et al [237], Viguié et al [238] and Mokrani et al [239] placed piezoelectric patches under the blades root on the underside of the wheel of the disk, as shown in Figure 6.2(b). This placement exhibits the maximum strain energy on the wheel when the blades vibrate. Because the patch is not directly on the blade, electromechanical coupling is sacrificed to some extent in order to satisfy the integration constraints. With this setup, Mokrani [54] proposed to use modal filters to target specific modes by an ingenious parallel connection of piezoelectric patches. In addition, the parallel connection had the advantage of having a larger equivalent capacitance, thereby requiring a smaller shunt inductance. Unfortunately, this approach is not very robust to mistuning [240]. Piezoelectric NES were also proposed in [175] as a robust control solution, but the added complexity of this essentially nonlinear control approach makes it uneasy to tune.

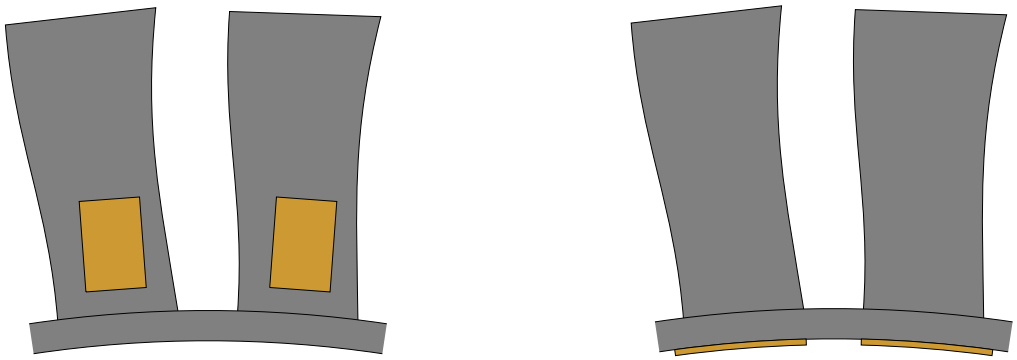

(a) (b)

Figure 6.2: Piezoelectric damping of integrally bladed structures: piezoelectric patches on the blades (a) and on the underside of the support, under the blades (b).

The performance of friction rings was compared to that obtained using synchronized switch damping on negative capacitor (SSDNC) in [241] with a simplified spring-mass model of a BLISK. The SSDNC approach showed comparable performance to friction damping on a single mode, while exhibiting a globally less nonlinear behavior, and outperformed friction rings when multiple modes were excited. Dampers combining both friction and piezoelectric damping were recently proposed in [242], where piezoelectric patches were distributed on a friction ring placed in the wheel of the disk. This hybrid damper was numerically demonstrated to always exhibit better performance, up to 30% more vibration reduction than a mere friction ring. Piezoelectric damping allowed to outperform pure friction damping at low excitation levels. At higher forcing amplitudes, friction was able to provide a substantial increase in damping. Finally, for high enough levels, the piezoelectric friction ring was in a full-sliding state, losing its efficiency and preventing the piezoelectric transducers from acting on the structure, thereby showing similar performance to the mere friction ring.

Among other possible solutions, eddy current dampers were investigated in [243] and showed performance comparable to that of a TMD but the device integration within the bladed part was not discussed in this preliminary study. Impact dampers were proposed in [244], wherein a rolling ball placed inside a cavity within a blade dissipates energy through impacts on the cavity walls. The ABH concept was used in [245] with blade trailing edges tapered with a power-law profile. These two latter solutions are promising, but would again require substantial manufacturing efforts.

6.1.2 Motivation and chapter outline

The goal of this chapter is to assess the previously proposed control strategies on an industrial bladed structure. This structure is a BluM produced by Safran Aero Boosters and is used in low-pressure compressors of aircraft engines. It is shown in Figure 6.3(a). As in [54], it comprises 76 (nominally) identical blades, and 28 piezoelectric patches are distributed circumferentially inside the rim, under the blades root as shown in Figure 6.3(b) in order to provide the possibility for piezoelectric damping.

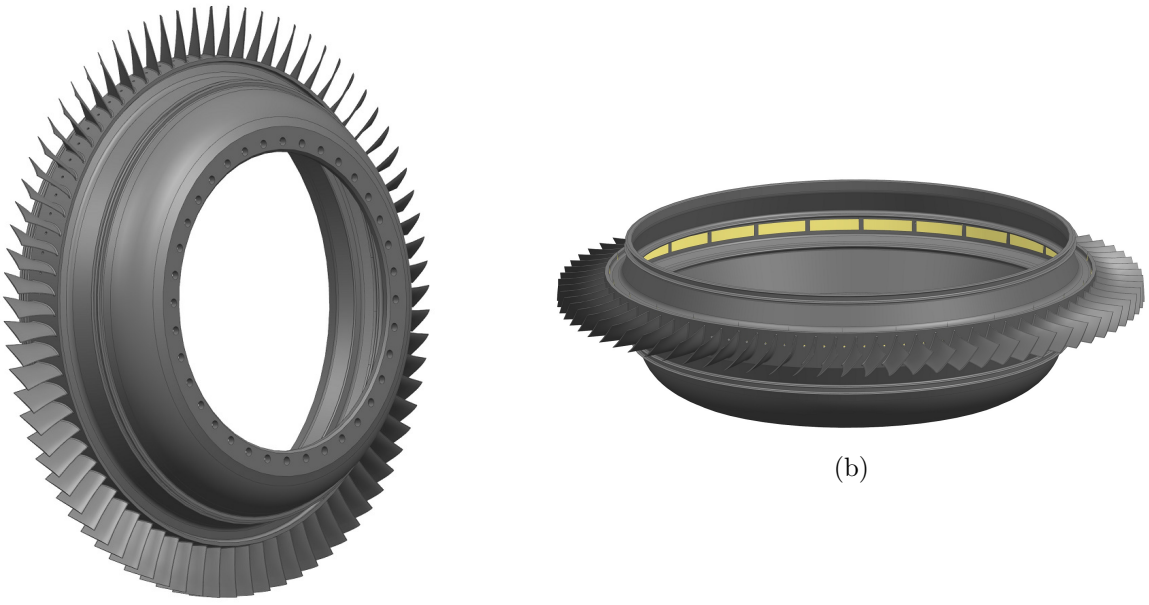

(a) (b)

Figure 6.3: BluM of a low-pressure compressor: general view (a) and view of the piezoelectric patches (b).

This chapter starts by briefly reviewing the main dynamical feature of bladed structures in Section 6.2. They generally have complex geometries and numerous fine details, which results in FE models with a large number of DoFs. To make the analysis of the controlled systems tractable, a model-order reduction procedure for piezoelectric structures is presented in Section 6.3. A hybrid control strategy for structures with closely-spaced resonance frequencies is proposed in Section 6.4. The techniques presented in this thesis are then illustrated on two bladed structures. The first one, a bladed rail, is studied in Section 6.5. This bladed rail exhibits dynamical features of bladed structures, such as frequency bands with high modal density, while being simpler than a typical turbomachine part. The second structure, the industrial BluM, is studied in Section 6.6.

6.2 Dynamics of bladed structures

The description made in this section is rather qualitative and the interested reader can find more details in, e.g., [49, 50, 54, 246, 247].

The bladed structures studied in this thesis consist of flexible blades attached to a comparatively stiff support. In a nominal structure, blades are identical and are weakly coupled via the support, which leads to natural structural frequencies close to those of the cantilevered blade. The more blades, the more modes of this type. Consequently, structures with numerous blades can exhibit high modal density in frequency regions near the natural frequencies of the cantilevered blade.

6.2.1 Cyclic symmetric bladed structures

6.2.1.1 Mode shapes

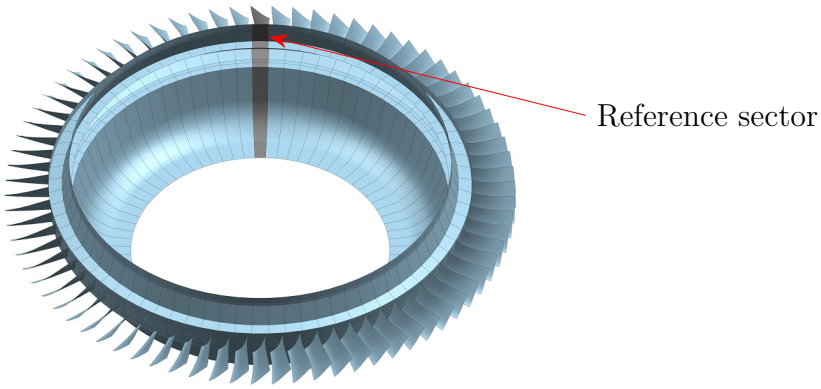

Figure 6.4: Cyclic symmetry of the BluM.

BLISKs and BluMs are nominally cyclic symmetric, i.e., they can be generated as the repetition of a *reference sector*, as illustrated in Figure 6.4 (the BluM without piezoelectric patches is considered in this section). As a consequence, the mode shapes of the structure are identical on each sector, up to a phase difference [50, 246]. These modes are thus modulated by a *spatial harmonic* in the circumferential direction. The relative phase of a sector is governed by its relative position on the structure and by N_{ND}, the number of *nodal diameters* exhibited by a mode. In a cyclic symmetric structure with N_{Sec} sectors, N_{ND} takes integer values ranging from 0 to $N_{ND,max} = N_{Sec}/2$ ($N_{ND,max} = (N_{Sec} - 1)/2$) for even (odd) values of N_{Sec}. When N_{ND} does not assume its minimum or maximum value, there are two orthogonal modes associated to the same frequency (usually called the sine and cosine modes).

Modes with different number of nodal diameters but involving a similar deformation of the blades form a *mode family*. A common way to represent the numerous natural frequencies of a bladed structure is via the nodal diameter vs. frequency diagram, as featured in Figure 6.5. Every frequency given in this chapter is normalized with the first natural frequency of the cantilevered blade, and this normalization is indicated with an overline ($\bar{\cdot}$).

Modes with a low number of nodal diameters involve the participation of the drum and the blades. It can also be noted that there are numerous frequency veerings in these regions. Eventually, at high numbers of nodal diameters, the support participation becomes negligible and the mode family features blade-alone modes, recognizable by the horizontal lines in the nodal diameter vs. frequency diagram. The structure thus has a large number of modes around these frequency regions. Lines are drawn in Figure 6.5 to help the visualization of drum-dominated and blade-dominated modes.

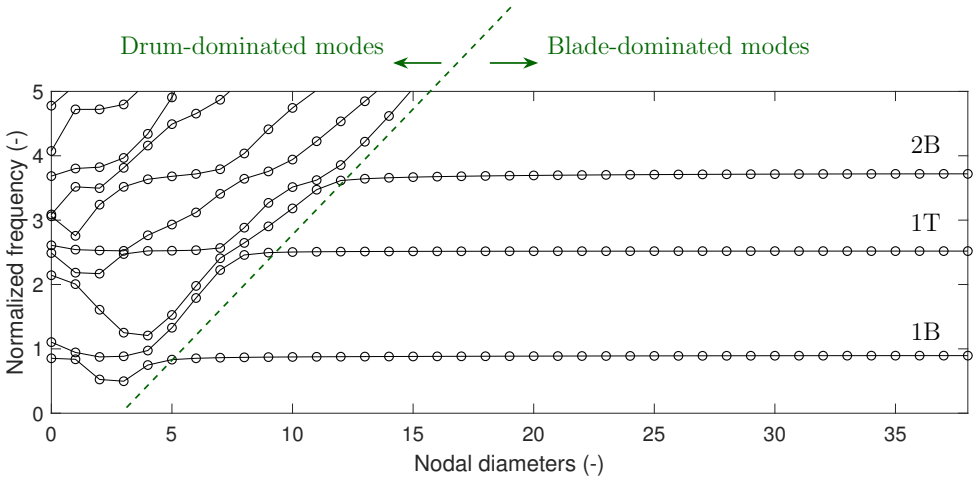

Figure 6.5: Nodal diameters vs frequencies diagram of the BluM.

For illustration, the lowest-frequency mode shapes of a cantilevered blade of the BluM, comprising the first (1B) and second (2B) bending modes and the first torsion mode (1T), are shown in Figure 6.6.

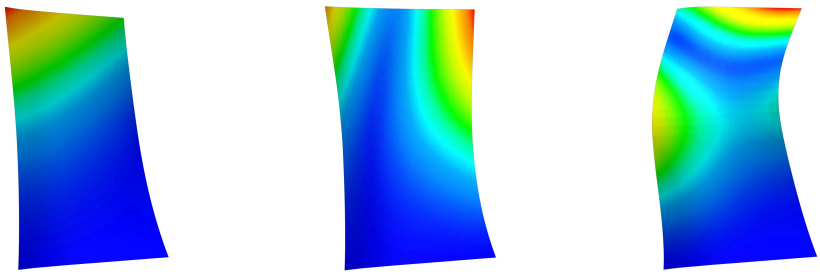

(a) (b) (c)

Figure 6.6: First (1B, $\overline{\omega} = 1$) (a), second (1T, $\overline{\omega} = 2.59$) (b) and third (2B, $\overline{\omega} = 4.05$) (c) cantilevered blade modes.

Figure 6.7 features various mode shapes of the full BluM. The qualitative correspondence between a mode family and its associated cantilevered blade mode, as well as the sector-to-sector phase difference can clearly be observed. In the extreme cases $N_{ND} = 0$ and $N_{ND} = 38$ the sectors are all vibrating in-phase and out-of-phase, respectively.

Figure 6.8 shows the three lowest-frequency modes of the BluM. The drum participation in the two first mode shapes is clearly visible, and it becomes smaller (yet still visible) for the third one which has a higher number of nodal diameters.

We note that, regarding vibration mitigation with piezoelectric patches placed under the rim, the modal participation of the drum is an important element. Indeed, if a mode is almost exclusively located on the blades without straining the drum, the piezoelectric patches are not strained, which eventually results in low electromechanical coupling with that mode.

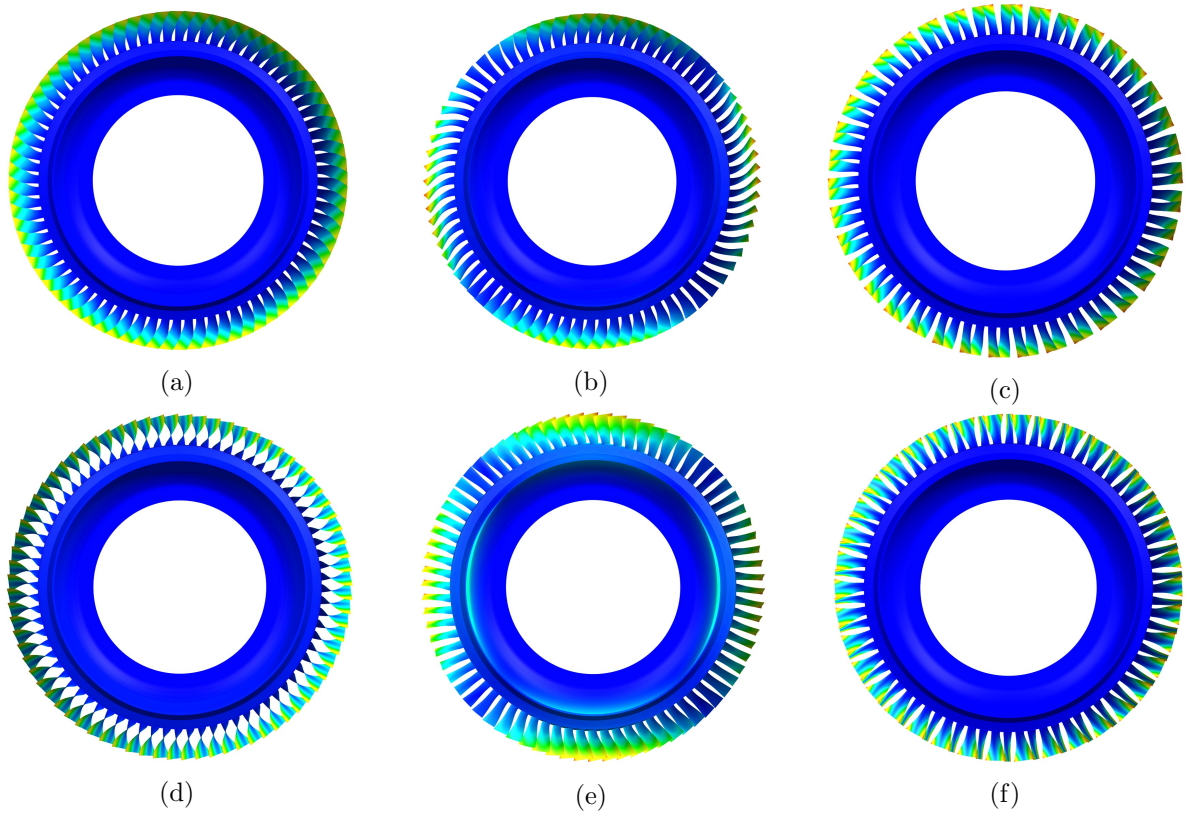

Figure 6.7: Mode shapes of the BluM: 1B-type modes ($N_{ND} = 0$ (a), $N_{ND} = 2$ (b), $N_{ND} = 38$ (c)), 1T-type modes ($N_{ND} = 0$ (d), $N_{ND} = 2$ (e), $N_{ND} = 38$ (f)).

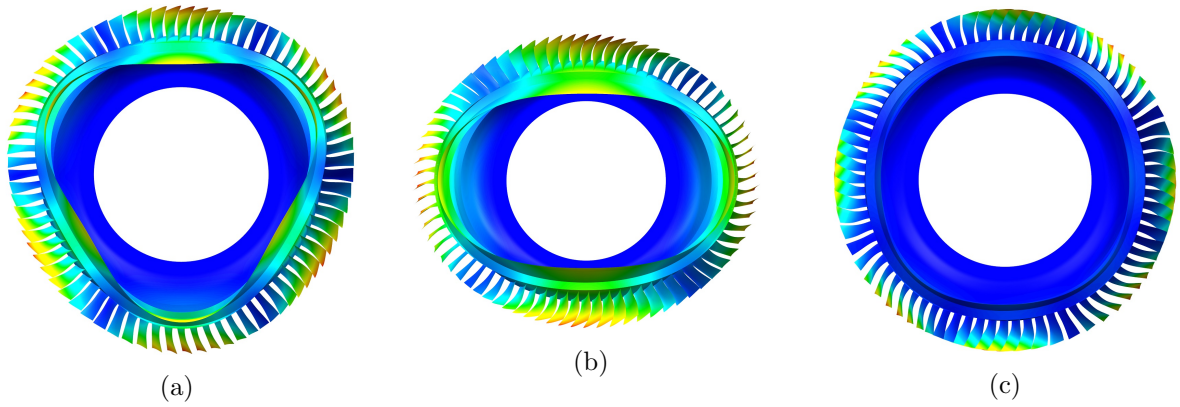

Figure 6.8: Lowest-frequency mode shapes of the BluM with 3 (a), 2 (b) and 4 (c) nodal diameters.

6.2.1.2 Engine-order excitation

One of the main sources of excitation for bladed structures comes from the aerodynamic forces. Typically, the stator blades in front of the rotor creates stationary circumferential pressure fluctuations, as schematized in Figure 6.9. In the rotating frame, these fluctuations are perceived as a periodic rotating excitation.

The pressure distribution can be described by circumferential harmonics using Fourier decomposition. In the frame linked to the rotor rotating at an angular speed Ω_{rot}, a harmonic N_{EO} provokes N_{EO} full cycles of excitation in a complete

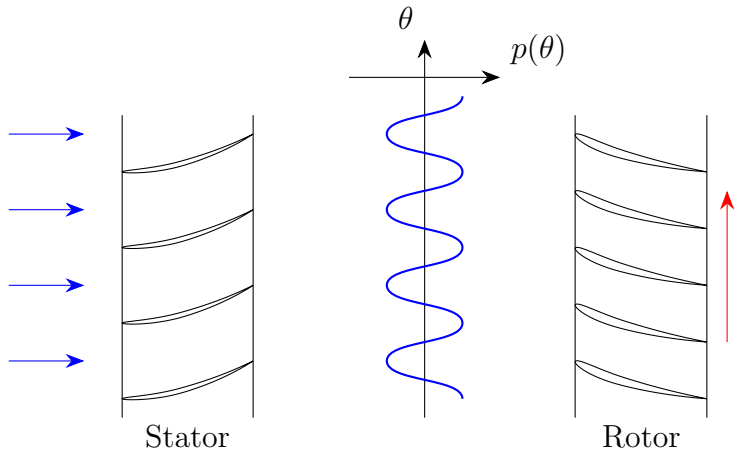

Figure 6.9: Schematic representation of the aerodynamic excitation on a rotor from a stator.

rotation, and thus induces an excitation frequency of

$$\omega(N_{EO}) = N_{EO}\Omega_{rot}. \tag{6.1}$$

The excitation frequency is a multiple of the engine rotation speed. This type of excitation is thus called an *engine-order excitation*, and N_{EO} is called the *engine order*. A mode can resonate if this excitation frequency is equal to its resonant frequency, which gives a *frequency matching* condition. The engine order should also be able to spatially excite the considered mode. It should thus satisfy the relation

$$N_{EO} = \begin{cases} N_{ND} + kN_{Sec}, & k \in \mathbb{Z} \\ -N_{ND} + kN_{Sec}, & k \in \mathbb{Z} \end{cases}. \tag{6.2}$$

The appearance of a term with an integer k is due to the aliasing of the spatial harmonic N_{EO} on the N_{Sec} sectors [247]. Alternatively, the modes with nodal diameters excited by a given engine order can be expressed in a compact way as

$$N_{ND}(N_{EO}) = \frac{N_{Sec}}{\pi}\left|\arcsin\left(\sin\left(\pi\frac{N_{EO}}{N_{Sec}}\right)\right)\right|. \tag{6.3}$$

The nodal diameter-engine order correspondence yields a *shape matching* condition. Computing the frequencies in Equation (6.1) and the nodal diameters in Equation (6.3) shows the effect of the engine order N_{EO} at the rotation speed Ω_{rot}. If for any value of N_{EO} a pair matches one of the points of the frequency vs nodal diameters diagram, resonance may occur. Figure 6.10 shows an example where the rotation speed is such that the mode with $N_{ND} = 17$ of the 1B family is resonant under the action of the 17^{th} engine order. It can also be noted that other resonances are potentially excited by higher engine orders at this rotation speed.

The natural frequencies of a bladed disk change in operation due to, e.g., temperature and rotation. This latter effect is generally assessed with a Campbell diagram, and the conditions for resonant excitation are predicted with a nodal diameter vs fequency diagram that depends on the rotation speed [247]. In this thesis, these effects were not considered.

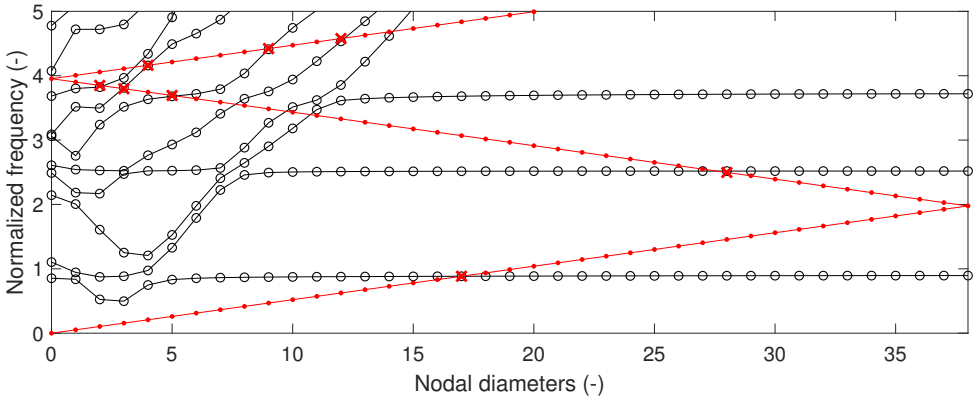

Figure 6.10: Nodal diameters vs frequencies diagram of the BluM: resonance of the 1B-type mode with $N_{ND} = 17$. $-\bullet-$: engine-order excitation, $\times$: resonant modes.

6.2.2 Mistuned bladed structures

Real bladed structures depart from their idealized cyclic-symmetric counterparts due to unavoidable sector-to-sector differences. These differences may occur because of manufacturing tolerances, or in-operation wear, for instance. Even when small, mistuning can have a drastic effect on the dynamics of a bladed disk. In particular, a mistuned structure exhibits modes which are no longer spatial harmonics but a combination of them.

An undesirable consequence of mistuning is the localization of a mode to a few blades. Modes in the veering regions are particularly sensitive to this because they allow for interblade coupling via the support. Localization concentrates the vibratory energy on a few blades which can accelerate their failure due to high-cycle fatigue.

Another issue with mistuning is the excitation of unexpected modes: because the mistuned modes are composed of multiple spatial harmonics, an engine order may excite several of them [248]. This can be critical, because modes which were not expected to be excited during the design phase can be excited during tests or operation.

The case of a BluM where all blades but one are identical is used to illustrate the localization phenomenon. Young's modulus of the marginal blade was decreased by 5% from its nominal value. Such a mistuning pattern could represent a damaged blade. Figure 6.11 shows that some modes tend to localize to that blade, which in this case could accelerate its failure even more. In practice, mistuning also occurs randomly throughout the bladed structure's circumference.

6.3 Reduced-order modeling of piezoelectric structures

Bladed structures require a fine discretization of the structure to accurately represent its dynamics. In order to use models of tractable size that nonetheless reproduce the dynamics of the structure faithfully, a reduced-order model (ROM) can be built. Two types of model-order reduction techniques are often used with bladed structures

1. Classical model-order reduction techniques, such as Craig-Bampton reduction [249].

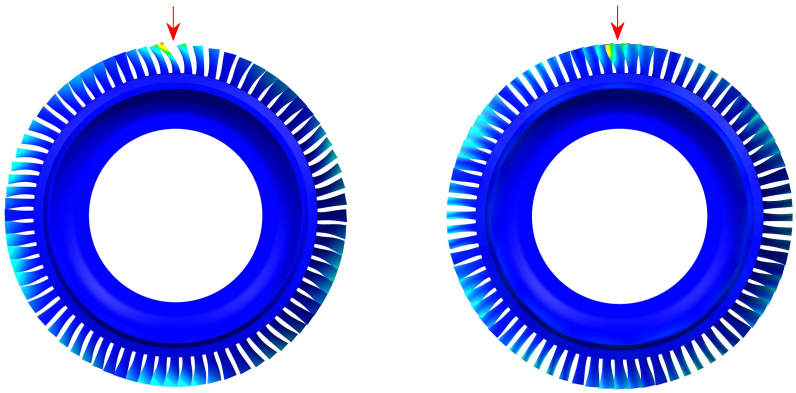

(a) (b)

Figure 6.11: Mode shapes localization to a blade due to mistuning: 1B-type mode (a) and 1T-type mode (b). The marginal blade is indicated by a red arrow.

2. Exact model-order reduction techniques exploiting the cyclic symmetry of bladed structures [246].

In this section, the focus will be put on the first approach, but it could also be used in conjunction with the other approach, such as in [250].

A structure with bonded piezoelectric transducers is considered. The vector of generalized mechanical DoFs is partitioned into boundary and internal DoFs indicated by subscripts b and i, respectively. With this partition, Equation (3.1) reads

$$\begin{bmatrix} \mathbf{M}_{bb} & \mathbf{M}_{bi} & \mathbf{0} \\ \mathbf{M}_{ib} & \mathbf{M}_{ii} & \mathbf{0} \\ \mathbf{0} & \mathbf{0} & \mathbf{0} \end{bmatrix} \begin{bmatrix} \ddot{\mathbf{x}}_b \\ \ddot{\mathbf{x}}_i \\ \ddot{\mathbf{V}} \end{bmatrix} + \begin{bmatrix} \mathbf{K}_{bb} & \mathbf{K}_{bi} & \boldsymbol{\Gamma}_b \\ \mathbf{K}_{ib} & \mathbf{K}_{ii} & \boldsymbol{\Gamma}_i \\ \boldsymbol{\Gamma}_b^T & \boldsymbol{\Gamma}_i^T & -\mathbf{C}_p^\varepsilon \end{bmatrix} \begin{bmatrix} \mathbf{x}_b \\ \mathbf{x}_i \\ \mathbf{V} \end{bmatrix} = \begin{bmatrix} \mathbf{f}_b \\ \mathbf{f}_i \\ \mathbf{q} \end{bmatrix}. \tag{6.4}$$

Following the classical Craig-Bampton reduction procedure [140, 249], the boundary and electrical DoFs are retained, while the internal DoFs are assumed unforced ($\mathbf{f}_i = \mathbf{0}$) and are approximated by

$$\mathbf{x}_i \approx \boldsymbol{\Phi}_c \mathbf{x}_b + \boldsymbol{\Phi}_{c,p} \mathbf{V} + \boldsymbol{\Phi}_i \boldsymbol{\eta}_i, \tag{6.5}$$

where the constraint modes are given by

$$\boldsymbol{\Phi}_c = -\mathbf{K}_{ii}^{-1} \mathbf{K}_{ib}, \tag{6.6}$$

the piezoelectric constraint modes are given by

$$\boldsymbol{\Phi}_{c,p} = -\mathbf{K}_{ii}^{-1} \boldsymbol{\Gamma}_i, \tag{6.7}$$

and the retained mass-normalized component normal modes (CNMs) are defined as the modes of the structures when the boundary DoFs are blocked

$$\mathbf{K}_{ii} \boldsymbol{\Phi}_i = \mathbf{M}_{ii} \boldsymbol{\Phi}_i \boldsymbol{\Omega}_i^2, \qquad \boldsymbol{\Phi}_i^T \mathbf{M}_{ii} \boldsymbol{\Phi}_i = \mathbf{I}, \qquad \boldsymbol{\Phi}_i^T \mathbf{K}_{ii} \boldsymbol{\Phi}_i = \boldsymbol{\Omega}_i^2, \tag{6.8}$$

where $\mathbf{\Omega}_i$ is a diagonal matrix containing the CNM angular frequencies and $\boldsymbol{\eta}_i$ is the vector of associated modal coordinates. Equation (6.5) defines a reduction matrix by

$$\begin{bmatrix} \mathbf{x}_b \\ \mathbf{x}_i \\ \mathbf{V} \end{bmatrix} = \begin{bmatrix} \mathbf{I} & \mathbf{0} & \mathbf{0} \\ \mathbf{\Phi}_c & \mathbf{\Phi}_i & \mathbf{\Phi}_{c,p} \\ \mathbf{0} & \mathbf{0} & \mathbf{I} \end{bmatrix} \begin{bmatrix} \mathbf{x}_b \\ \boldsymbol{\eta}_i \\ \mathbf{V} \end{bmatrix} = \mathbf{R}_{CB} \begin{bmatrix} \mathbf{x}_b \\ \boldsymbol{\eta}_i \\ \mathbf{V} \end{bmatrix}. \tag{6.9}$$

The reduced mass matrix is

$$\mathbf{M}_{CB} = \mathbf{R}_{CB}^T \mathbf{M} \mathbf{R}_{CB} = \begin{bmatrix} \widetilde{\mathbf{M}}_{bb} & \widetilde{\mathbf{M}}_{bi} & \widetilde{\mathbf{M}}_{be} \\ \widetilde{\mathbf{M}}_{ib} & \mathbf{I} & \widetilde{\mathbf{M}}_{ie} \\ \widetilde{\mathbf{M}}_{eb} & \widetilde{\mathbf{M}}_{ei} & \widetilde{\mathbf{M}}_{ee} \end{bmatrix}, \tag{6.10}$$

where

$$\widetilde{\mathbf{M}}_{bb} = \mathbf{M}_{bb} - \mathbf{M}_{bi}\mathbf{K}_{ii}^{-1}\mathbf{K}_{ib} - \mathbf{K}_{bi}\mathbf{K}_{ii}^{-1}\mathbf{M}_{ib} + \mathbf{K}_{bi}\mathbf{K}_{ii}^{-1}\mathbf{M}_{ii}\mathbf{K}_{ii}^{-1}\mathbf{K}_{ib}, \tag{6.11}$$

$$\widetilde{\mathbf{M}}_{ib} = \widetilde{\mathbf{M}}_{bi}^T = \mathbf{\Phi}_i^T \left(\mathbf{M}_{ib} - \mathbf{M}_{ii}\mathbf{K}_{ii}^{-1}\mathbf{K}_{ib} \right), \tag{6.12}$$

$$\widetilde{\mathbf{M}}_{ee} = \mathbf{\Gamma}_i^T \mathbf{K}_{ii}^{-1} \mathbf{M}_{ii} \mathbf{K}_{ii}^{-1} \mathbf{\Gamma}_i \tag{6.13}$$

and

$$\widetilde{\mathbf{M}}_{ie} = \widetilde{\mathbf{M}}_{ei}^T = \mathbf{\Phi}_i^T \mathbf{M}_{ii} \mathbf{K}_{ii}^{-1} \mathbf{\Gamma}_i. \tag{6.14}$$

The reduced stiffness matrix is

$$\mathbf{K}_{CB} = \mathbf{R}_{CB}^T \mathbf{K}_{sc} \mathbf{R}_{CB} = \begin{bmatrix} \widetilde{\mathbf{K}}_{bb} & \mathbf{0} & \widetilde{\mathbf{K}}_{be} \\ \mathbf{0} & \mathbf{\Omega}_i^2 & \mathbf{0} \\ \widetilde{\mathbf{K}}_{eb} & \mathbf{0} & \widetilde{\mathbf{K}}_{ee} \end{bmatrix}, \tag{6.15}$$

where

$$\widetilde{\mathbf{K}}_{bb} = \mathbf{K}_{bb} - \mathbf{K}_{bi}\mathbf{K}_{ii}^{-1}\mathbf{K}_{ib}, \tag{6.16}$$

$$\widetilde{\mathbf{K}}_{be} = \widetilde{\mathbf{K}}_{eb}^T = \mathbf{\Gamma}_b - \mathbf{K}_{bi}\mathbf{K}_{ii}^{-1}\mathbf{\Gamma}_i \tag{6.17}$$

and

$$\widetilde{\mathbf{K}}_{ee} = -\mathbf{C}_p^{\varepsilon} - \mathbf{\Gamma}_i^T \mathbf{K}_{ii}^{-1} \mathbf{\Gamma}_i. \tag{6.18}$$

Equation (6.10) indicates that piezoelectric coupling is no longer represented with static coupling terms (as in Equation (3.1)), but also features non-trivial inertial coupling terms in the reduced model. To retrieve a static coupling, the following transformation matrix that modifies the CNM coordinates $\boldsymbol{\eta}_i$ to $\boldsymbol{\upsilon}_i$ is introduced

$$\mathbf{R}_{MCB} = \begin{bmatrix} \mathbf{I} & \mathbf{0} & \mathbf{0} \\ \mathbf{0} & \mathbf{I} & -\widetilde{\mathbf{M}}_{ie} \\ \mathbf{0} & \mathbf{0} & \mathbf{I} \end{bmatrix}, \qquad \begin{bmatrix} \mathbf{x}_b \\ \boldsymbol{\eta}_i \\ \mathbf{V} \end{bmatrix} = \mathbf{R}_{MCB} \begin{bmatrix} \mathbf{x}_b \\ \boldsymbol{\upsilon}_i \\ \mathbf{V} \end{bmatrix} \tag{6.19}$$

and the modified Craig-Bampton (MCB) reduced mass and stiffness matrices are obtained as

$$\mathbf{M}_{MCB} = \mathbf{R}_{MCB}^T \mathbf{M}_{CB} \mathbf{R}_{MCB}, \qquad \mathbf{K}_{MCB} = \mathbf{R}_{MCB}^T \mathbf{K}_{CB} \mathbf{R}_{MCB}. \tag{6.20}$$

It can be shown that these matrices contain the following entries

$$\mathbf{M}_{MCB} = \begin{bmatrix} \widetilde{\mathbf{M}}_{bb} & \widetilde{\mathbf{M}}_{bi} & \left(\boldsymbol{\Phi}_c^T \mathbf{M}_{ii} - \mathbf{M}_{bi}\right)\left(\mathbf{M}_{ii}^{-1} - \boldsymbol{\Phi}_i \boldsymbol{\Phi}_i^T\right) \mathbf{M}_{ii} \boldsymbol{\Phi}_{c,p} \\ \widetilde{\mathbf{M}}_{ib} & \mathbf{I} & \mathbf{0} \\ \boldsymbol{\Phi}_{c,p}^T \mathbf{M}_{ii}\left(\mathbf{M}_{ii}^{-1} - \boldsymbol{\Phi}_i \boldsymbol{\Phi}_i^T\right)\left(\mathbf{M}_{ii} \boldsymbol{\Phi}_c - \mathbf{M}_{ib}\right) & \mathbf{0} & \boldsymbol{\Phi}_{c,p}^T \mathbf{M}_{ii}\left(\mathbf{M}_{ii}^{-1} - \boldsymbol{\Phi}_i \boldsymbol{\Phi}_i^T\right) \mathbf{M}_{ii} \boldsymbol{\Phi}_{c,p} \end{bmatrix} \tag{6.21}$$

and

$$\mathbf{K}_{MCB} = \begin{bmatrix} \widetilde{\mathbf{K}}_{bb} & \mathbf{0} & \boldsymbol{\Gamma}_b + \boldsymbol{\Phi}_c^T \boldsymbol{\Gamma}_i \\ \mathbf{0} & \boldsymbol{\Omega}_i^2 & \boldsymbol{\Phi}_i^T \boldsymbol{\Gamma}_i \\ \boldsymbol{\Gamma}_b^T + \boldsymbol{\Gamma}_i^T \boldsymbol{\Phi}_c & \boldsymbol{\Gamma}_i^T \boldsymbol{\Phi}_i & -\mathbf{C}_p^{\varepsilon} - \boldsymbol{\Gamma}_i^T \left(\mathbf{K}_{ii}^{-1} - \boldsymbol{\Phi}_i \boldsymbol{\Omega}_i^{-2} \boldsymbol{\Phi}_i^T\right) \boldsymbol{\Gamma}_i \end{bmatrix}. \tag{6.22}$$

Upon performing the transformation given by Equation (6.20), part of the inertial coupling terms have been transformed back to static coupling terms. As shown by the mass matrix in Equation (6.21), there remains non-zero entries associated with the electrical DoFs. To remove these terms, the following assumption is made

$$\mathbf{M}_{ii}^{-1} - \boldsymbol{\Phi}_i \boldsymbol{\Phi}_i^T \approx 0. \tag{6.23}$$

Equation (6.8) shows that this equation consists in the mass matrix associated to the internal DoFs minus its spectral expansion trucated to the set of retained CNMs [140], which justifies the approximation in the framework of a ROM. Hence, the approximation made on the MCB reduced mass matrix reads

$$\mathbf{M}_{MCB} \approx \begin{bmatrix} \widetilde{\mathbf{M}}_{bb} & \widetilde{\mathbf{M}}_{bi} & \mathbf{0} \\ \widetilde{\mathbf{M}}_{ib} & \mathbf{I} & \mathbf{0} \\ \mathbf{0} & \mathbf{0} & \mathbf{0} \end{bmatrix} \tag{6.24}$$

so that no generalized inertia load acts on the electrical DoFs. A ROM with the same form as Equation (3.1) can thus be obtained.

It was assumed that all electrical DoFs are retained. This is generally the case if these DoFs are associated with electrodes. Piezoelectric FEs may also have internal electrical DoFs that may not be retained. Upon applying a Craig-Bampton reduction retaining the desired boundary mechanical DoFs and the electrodes DoFs, the same MCB transformation can nonetheless be applied (see Section G.1).

In this thesis, geometrical and meshing operations of the bladed structures were carried out using Siemens NX. To make computations tractable on a personal computer, these structures were modeled using shell-type (Mindlin) FEs. The inclusion of piezoelectric patches and the modal analysis were carried out with SAMCEF [136]. A Craig-Bampton reduction was performed to yield the reduced matrices (Equations (6.10) and (6.15)). These matrices were imported in MATLAB and the MCB transformation (Equations (6.19), (6.20) and (6.24)) could then be executed.

6.4 Hybrid strategy for piezoelectric structures with closely-spaced resonance frequencies

6.4.1 Mean shunt with series RL shunts

To tackle the complexity associated with the control of multiple modes with closely-spaced resonance frequencies, Mokrani [54] proposed to use a *mean shunt* strategy. In this approach, it is considered that R mechanical modes indexed by $\mathbf{r}$ have closely-spaced resonance frequencies. They are targeted by an array of transducers shunted with series RL shunts tuned to a *single* frequency. This frequency is the average of the targeted resonant short-circuit frequencies

$$\widehat{\omega}_{sc,\mathbf{r}} = \frac{1}{R}\sum_{r\in\mathbf{r}} \omega_{sc,r}. \tag{6.25}$$

The overall EEMCF of all transducers over all targeted modes is evaluated by

$$\widehat{K}^2_{c,\mathbf{r}} = \sum_{p=1}^{P} \frac{1}{R}\sum_{r\in\mathbf{r}} \frac{\omega^2_{oc,rp} - \omega^2_{sc,r}}{\omega^2_{oc,rp}}, \tag{6.26}$$

where $\omega_{oc,rp}$ is the r^{th} resonance frequency of the structure when transducer p is in open-circuit and every other transducer is in short-circuit (i.e., the frequency of a zero of the p^{th} diagonal entry of the dynamic capacitance matrix). We note that this frequency squared is used at the denominator to normalize the EEMCF, because a different convention is used in [54]. Finally, the static capacitance of transducer p is given by the p^{th} diagonal entry of the dynamic capacitance matrix at $s = 0$ (Equation (3.6))

$$C_{p,static} = \left(\mathbf{C}_p(0)\right)_{pp}. \tag{6.27}$$

With these quantities, the mean shunt tuning rules read [54]

$$L_p = \frac{1}{\widehat{\omega}^2_{sc,\mathbf{r}} C_{p,static}}, \qquad R_p = \frac{2\widehat{K}_{c,\mathbf{r}}}{\widehat{\omega}_{sc,\mathbf{r}} C_{p,static}}, \qquad p \in \begin{bmatrix} 1 & \dots & P \end{bmatrix}. \tag{6.28}$$

6.4.2 Hybrid strategy

Given its simplicity and its robustness, the mean shunt strategy is an attractive option for bladed structures. However, this approach is ineffective if the targeted modes do not all have closely-spaced frequencies. To take the best out of this approach while also enabling the control of widely-spaced modes, the mean shunt and multimodal absorber strategies developed in Chapter 3 can be combined. Namely, a multimodal circuit/network can be devised, with a part of electrical resonances that single-handedly control a set of closely-spaced resonant mechanical modes exploiting the mean shunt strategy, and another part of electrical resonances that control isolated mechanical modes. Such a tuning strategy is called *hybrid strategy* in the sequel. By contrast, the strategy where all the targeted mechanical modes are considered independently when applying the method of Chapter 3 is called *isolated-mode strategy*.

Starting from Equation (3.26) with R resonant mechanical modes,

$$\begin{cases} \left(s^2\mathbf{I} + \boldsymbol{\Omega}_{sc,\mathbf{r}}^2\right)\boldsymbol{\eta}_{sc,\mathbf{r}} + s\boldsymbol{\Gamma}_{\boldsymbol{\Phi},\mathbf{rk}}\boldsymbol{\eta}_{e,\mathbf{k}} = \mathbf{0} \\ \left(s^2\mathbf{I} + 2s\mathbf{Z}_{e,\mathbf{k}}\boldsymbol{\Omega}_{e,\mathbf{k}} + \boldsymbol{\Omega}_{e,\mathbf{k}}^2\right)\boldsymbol{\eta}_{e,\mathbf{k}} - s\boldsymbol{\Gamma}_{\boldsymbol{\Phi},\mathbf{rk}}^T\boldsymbol{\eta}_{sc,\mathbf{r}} = \mathbf{0} \end{cases}, \tag{6.29}$$

where the background contribution from non-resonant modes has been neglected for now, since Chapter 3 showed that they are not relevant when tuning the electrical mode shapes. Assuming a modal open-circuit ($\boldsymbol{\Omega}_{e,\mathbf{k}} = \mathbf{0}$) and substituting the electrical equations into the mechanical ones, the open-circuit modal stiffness matrix reads

$$\widehat{\boldsymbol{\Omega}}_{oc,\mathbf{r}}^2 = \boldsymbol{\Omega}_{sc,\mathbf{r}}^2 + \boldsymbol{\Gamma}_{\boldsymbol{\Phi},\mathbf{rk}}\boldsymbol{\Gamma}_{\boldsymbol{\Phi},\mathbf{rk}}^T. \tag{6.30}$$

The eigenvalues of this matrix are the squared open-circuit resonance frequencies, but its non-diagonal character makes their direct evaluation uneasy. However, its trace, which is equal to the sum of the eigenvalues, reads

$$\sum_{r=1}^{R}\widehat{\omega}_{oc,r}^2 = \sum_{r=1}^{R}\left(\omega_{sc,r}^2 + \boldsymbol{\phi}_{sc,r}^T\boldsymbol{\Gamma}_p\boldsymbol{\Phi}_{p,\mathbf{k}}\boldsymbol{\Phi}_{p,\mathbf{k}}^T\boldsymbol{\Gamma}_p^T\boldsymbol{\phi}_{sc,r}\right) = \sum_{r=1}^{R}\left(\omega_{sc,r}^2 + \sum_{k=1}^{K}\left(\boldsymbol{\phi}_{sc,r}^T\boldsymbol{\Gamma}_p\boldsymbol{\Phi}_{p,k}\right)^2\right). \tag{6.31}$$

The aim is to maximize the overall EEMCF, given as the sum of the EEMCFs with every resonant mode, given by

$$\begin{aligned}\widehat{K}_{c,\mathbf{rk}}^2 = \sum_{r=1}^{R}\frac{\widehat{\omega}_{oc,r}^2 - \omega_{sc,r}^2}{\omega_{sc,r}^2} &= \sum_{r=1}^{R}\sum_{k=1}^{K}\frac{1}{\omega_{sc,r}^2}\left(\boldsymbol{\phi}_{sc,r}^T\boldsymbol{\Gamma}_p\boldsymbol{\Phi}_{p,k}\right)^2 \\ &= \sum_{k=1}^{K}\boldsymbol{\phi}_{p,k}^T\boldsymbol{\Gamma}_p^T\boldsymbol{\Phi}_{sc,\mathbf{r}}\boldsymbol{\Omega}_{sc,\mathbf{r}}^{-2}\boldsymbol{\Phi}_{sc,\mathbf{r}}^T\boldsymbol{\Gamma}_p\boldsymbol{\phi}_{p,k}.\end{aligned} \tag{6.32}$$

The optimal electrical mode shapes of a passive network are thus the solution of the optimization problem

$$\begin{aligned}\underset{\boldsymbol{\Phi}_{p,\mathbf{k}}}{\text{Maximize}} \quad & \sum_{k=1}^{K}\boldsymbol{\phi}_{p,k}^T\boldsymbol{\Gamma}_p^T\boldsymbol{\Phi}_{sc,\mathbf{r}}\boldsymbol{\Omega}_{sc,\mathbf{r}}^{-2}\boldsymbol{\Phi}_{sc,\mathbf{r}}^T\boldsymbol{\Gamma}_p\boldsymbol{\phi}_{p,k} \\ \text{Subject to} \quad & \left(\mathbf{C}_p^{\varepsilon}\right)^{-1} - \boldsymbol{\Phi}_{p,\mathbf{k}}\boldsymbol{\Phi}_{p,\mathbf{k}}^T \succeq 0\end{aligned}. \tag{6.33}$$

Using the dimensionless electrical mode shapes (Equation (3.50)), this problem is rewritten

$$\begin{aligned}\underset{\overline{\boldsymbol{\Phi}}_{p,\mathbf{k}}}{\text{Maximize}} \quad & \sum_{k=1}^{K}\boldsymbol{\varphi}_{p,k}^T\left(\mathbf{C}_p^{\varepsilon}\right)^{-1/2}\boldsymbol{\Gamma}_p^T\boldsymbol{\Phi}_{sc,\mathbf{r}}\boldsymbol{\Omega}_{sc,\mathbf{r}}^{-2}\boldsymbol{\Phi}_{sc,\mathbf{r}}^T\boldsymbol{\Gamma}_p\left(\mathbf{C}_p^{\varepsilon}\right)^{-1/2}\boldsymbol{\varphi}_{p,k} \\ \text{Subject to} \quad & \mathbf{I} - \overline{\boldsymbol{\Phi}}_{p,\mathbf{k}}\overline{\boldsymbol{\Phi}}_{p,\mathbf{k}}^T \succeq 0\end{aligned}. \tag{6.34}$$

The passivity constraint indicates that there can be at most $K = P$ orthogonal unit dimensionless electrical mode shapes. Hence, the solution to this optimization problem is to select the dimensionless electrical mode shapes as the eigenvectors of

$$\left(\mathbf{C}_p^{\varepsilon}\right)^{-1/2}\boldsymbol{\Gamma}_p^T\boldsymbol{\Phi}_{sc,\mathbf{r}}\boldsymbol{\Omega}_{sc,\mathbf{r}}^{-2}\boldsymbol{\Phi}_{sc,\mathbf{r}}^T\boldsymbol{\Gamma}_p\left(\mathbf{C}_p^{\varepsilon}\right)^{-1/2}.$$

If the rank of this matrix is smaller than P (which is the case when $R < P$), this matrix has less than P strictly positive eigenvalues. The other eigenvalues are zero and would not increase the overall EEMCF if set as an electrical mode shape. Hence, only the eigenvectors associated to strictly positive eigenvalues should be assigned as electrical dimensionless mode shapes. When the rank of this matrix is equal to P, the whole set of eigenvectors should be retained, leading to P electrical modes controlling R mechanical resonances. In this case, the set of dimensionless electrical mode shapes spans $\mathbb{R}^P$, and can equivalently be chosen as $\overline{\mathbf{\Phi}}_p = \mathbf{I}$ for simplicity.

Once the mode shapes are determined, the global EEMCF can be computed (Equation (6.32)). The optimal effective frequency and damping ratio for electrical mode k are thus given by

$$\omega_{e,k}^2 = \nu^2\left(\widehat{K}_{c,\mathbf{rk}}\right)\widehat{\omega}_{sc,avg}^2, \qquad \zeta_{e,k} = \varsigma\left(\widehat{K}_{c,\mathbf{rk}}\right), \tag{6.35}$$

where $\widehat{\omega}_{sc,avg}^2$ is the average of the squared resonant short-circuit frequencies accounting for the background contribution of non-resonant modes, i.e.,

$$\widehat{\omega}_{sc,avg}^2 = \frac{1}{R}\text{trace}\left(\mathbf{\Omega}_{sc,\mathbf{r}}^2 + \mathbf{\Gamma}_{\mathbf{\Phi},\mathbf{r}<k}\mathbf{S}^{-1}\mathbf{\Gamma}_{\mathbf{\Phi},\mathbf{r}<k}^T\right), \tag{6.36}$$

where $\mathbf{S}$ is given by Equation (3.38).

Finally, to account for the effect of background contributions when tuning the electrical frequencies and damping ratios, a procedure similar to Section 3.7.3.4 is followed. If the number of resonant electrical mode shapes is less than P, the modal coordinates of equivalent global mode shapes are computed using

$$\mathbf{C_k} = \mathbf{\Phi}_{p,\mathbf{k}}^T\mathbf{\Gamma}_p^T\mathbf{\Phi}_{sc,\mathbf{r}} \tag{6.37}$$

and normalizing each column of this matrix to have unit vectors. When the number of resonant electrical mode shapes is equal to P, $\mathbf{C_k} = \mathbf{I}$ can be chosen without loss of generality. Similarly to Equation (3.123), it is sought to impose the global electrical mode shapes

$$\left(\mathbf{\Omega}_{e,\mathbf{k}}^2 - \omega_{e,k}^2\left(\mathbf{I} + \widehat{\boldsymbol{\kappa}}_{e,\mathbf{k}}\right)\right)\mathbf{C_k} = \mathbf{0}. \tag{6.38}$$

This equation cannot be solved exactly if there are more than one resonant electrical mode, but can be solved in the least-squares sense, yielding

$$\boldsymbol{\omega}_{e,\mathbf{k}}^2 = \mathbf{mdiag}\left(\mathbf{C_k}\mathbf{C_k}^T\right)\text{mdiag}\left(\widehat{\omega}_{e,k}\left(\mathbf{I} + \widehat{\boldsymbol{\kappa}}_{e,k}\right)\mathbf{C_k}\right), \tag{6.39}$$

where mdiag is an operator giving a vector equal to the diagonal of its argument and $\mathbf{mdiag}\left(\cdot\right) = \text{diag}\left(\text{mdiag}\left(\cdot\right)\right)$. Finally, the electrical resonance frequencies are

$$\mathbf{\Omega}_{e,\mathbf{k}}^2 = \text{diag}\left(\boldsymbol{\omega}_{e,\mathbf{k}}^2\right) \tag{6.40}$$

and the electrical damping ratios are

$$\mathbf{Z}_{e,\mathbf{k}} = \frac{\zeta_{e,k}}{\omega_{e,k}}\mathbf{\Omega}_{e,\mathbf{k}}. \tag{6.41}$$

6.5 Damping of a bladed rail

The bladed rail with five blades depicted in Figure 6.12 was used as a transition between academic structures and the BluM, similarly to [54]. This simpler structure exhibits several dynamical features similar to those of a BluM, and in particular, closely-spaced resonant modes grouped as families. To approach the same control strategy as that of the BluM, five patches are placed on the underside of the rail, under the blades root, as depicted in Figure 6.12(b). A superelement was created with the method described in Section 6.3, retaining mechanical DoFs on the blades tip at the leading edge, the piezoelectric voltages of the patches, and 50 CNMs. Modal damping of 0.01% was added to each mode of this ROM.

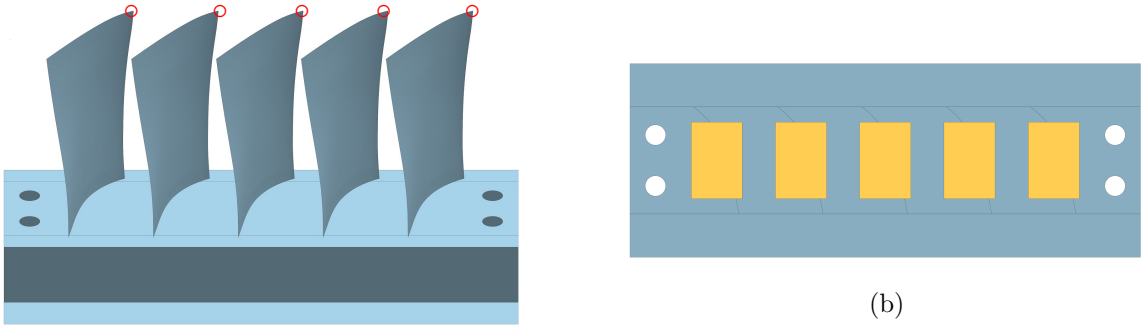

(a) (b)

Figure 6.12: Overall (a) and bottom (b) views of the bladed rail with piezoelectric patches. The red circles indicate the position of the retained DoFs.

6.5.1 Dynamics of the bladed rail

Figure 6.13 shows the natural frequencies of the bladed rail with short-circuited patches. Three plateaus are observable among the first twenty frequencies, and they correspond to a mode family. Modes with frequencies in between these plateaus involve the participation of the support. For illustration, Figure 6.14 depicts modes in the 1B (Figure 6.14(a)), 1T (Figure 6.14(b)) and 2B (Figure 6.14(d)) families, as well as a support-dominated mode (Figure 6.14(c)).

6.5.2 Control of the first family of modes

Four control strategies are considered to mitigate the vibrations of the first family of modes:

1. Individual series RL shunts tuned according to the mean shunt strategy proposed in [54].
2. Individual parallel RL shunts tuned with the isolated-mode strategy.
3. Individual multimodal shunt circuits with ideal Norton's admittance targeting all modes tuned with the isolated-mode strategy.

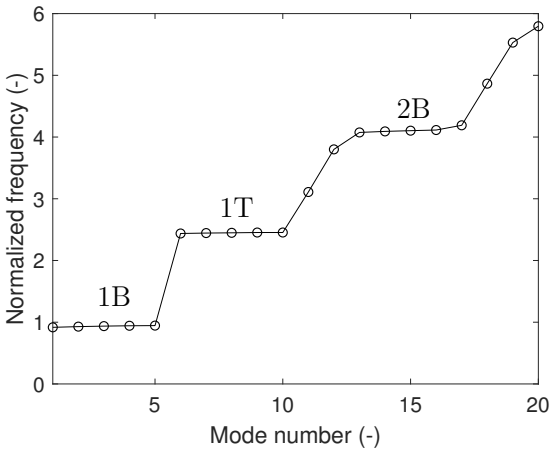

Figure 6.13: Natural frequencies of the bladed rail with short-circuited patches.

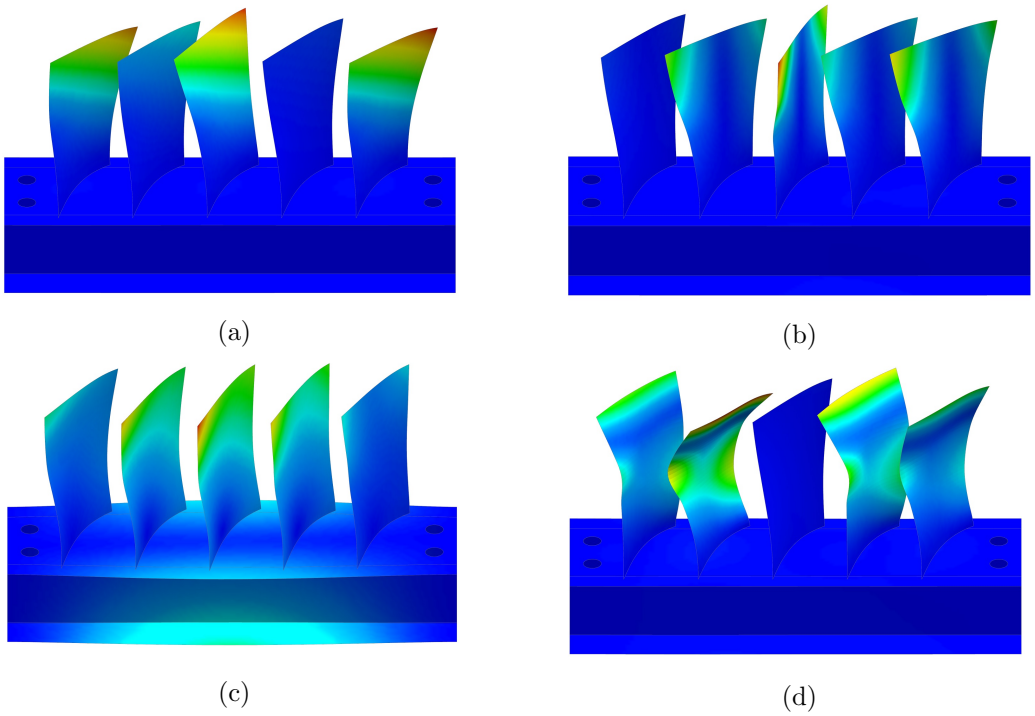

Figure 6.14: Mode shapes of the third (a), eighth (b), eleventh (c) and fifteenth (d) modes of the bladed rail.

4. A network interconnecting the patches targeting all modes tuned with the isolated-mode strategy.

In strategies 2 to 4, the relative control authority on each mode is balanced, i.e., unit (global) relative scaling factors were assigned to each mode.

Figure 6.15(a) features FRFs of the first blade tip controlled by these strategies. Globally, they are equally effective. The mean shunt and network exhibit similar performance with a rather flat FRF, whereas the optimal circuits (RL shunts or multimodal circuits) tend to attenuate the vibrations near the center of the controlled bandwidth more, at the expense of vibration amplitude near its boundaries.

The robustness of the four control strategies is now investigated. The circuits and

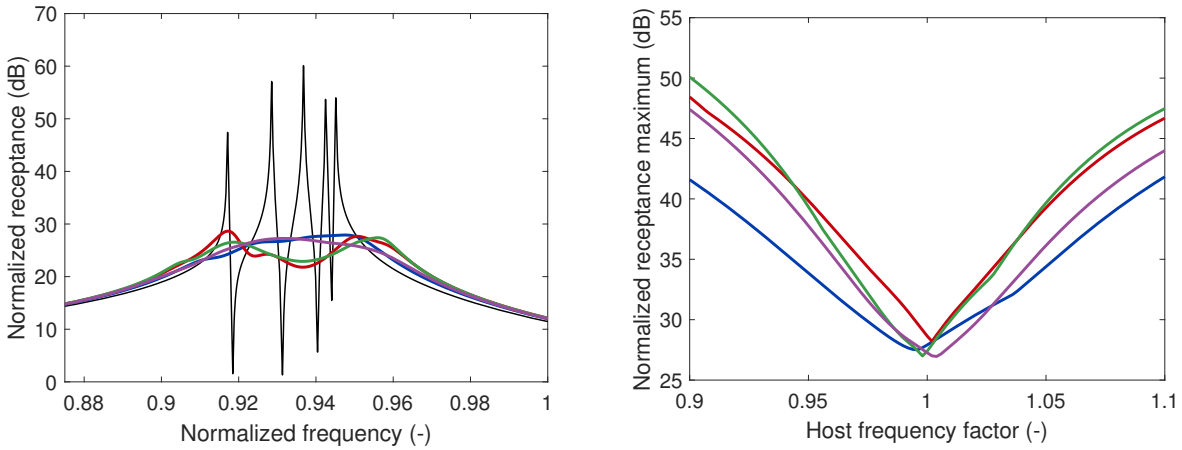

(a) (b)

Figure 6.15: Driving-point receptance (a) and maximum receptance magnitude (b) of the first blade tip with patches in short circuit (—), connected to individual RL shunts tuned with the mean shunt strategy [54] (—), optimal RL shunts (—), multimodal shunts (—) and network (—).

network are tuned based on the characteristics of the nominal host structure, and the frequencies of the actual host are modified by multiplication with a scalar factor. Figure 6.15(b) displays the maximum receptance as a function of the frequency factor. All strategies are close to being optimal near the nominal case, which confirms the effectiveness of the proposed tuning rules. However, because they all are resonant absorbers, performance is deteriorated as the frequencies move away from their nominal values. It can however be noted that the mean shunt offers better robustness than the other approaches, whose robustness is somewhat similar.

The better robustness of the mean shunt strategy can be explained by the fact that it is the approach with the highest electrical damping (hence the highest bandwidth) because it adds up the electromechanical coupling with all targeted modes. By contrast, the other strategies only exploit the electromechanical coupling of a single mode at a time, yielding an electrical circuit or network with distributed frequencies but with less electrical damping, resulting overall in a narrower bandwidth.

6.5.3 Control of the three first families of modes

More than one family of modes could be problematic. In this case, Figure 6.16 features the FRFs of the first blade tip when the bladed rail is controlled by multimodal circuits or a network targeting the three first families of modes as well as the two isolated modes between family two and three with an isolated-mode strategy. Individual RL shunts were not considered owing to the difficulty of attributing them to a specific modes. With both strategies, effective vibration reduction on all target modes is observable.

We note that the multimodal shunt circuits require seventeen electrical resonances per shunt. This number can however be brought down if the hybrid strategy is adopted. Figure 6.17 shows FRFs with multimodal circuits or a network targeting the same set of modes, but using mean shunts targeting each of the three families of modes. Performance is slightly degraded, but all targeted resonances are again mitigated. The order of the

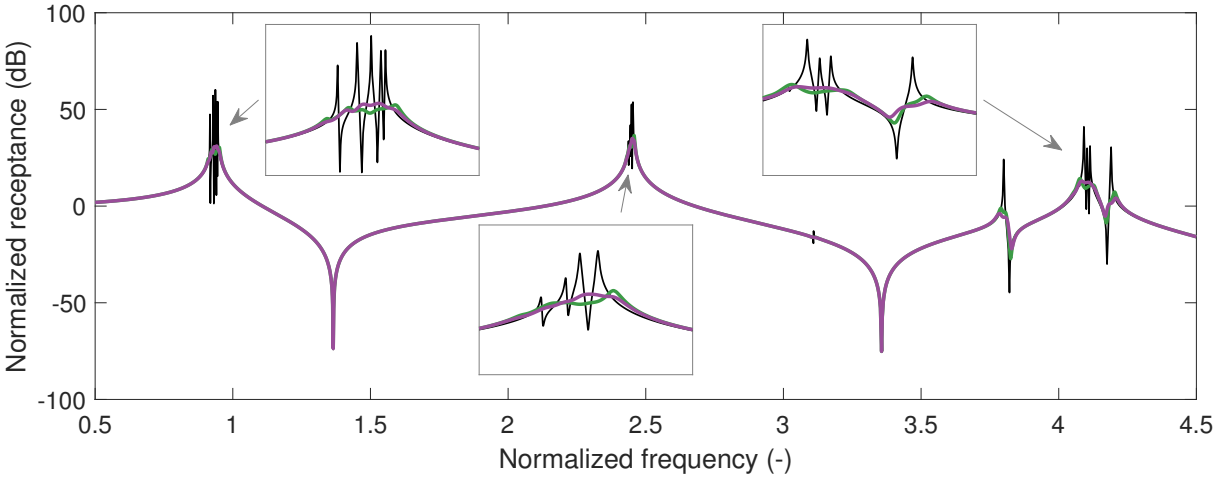

Figure 6.16: Driving-point receptance of the first blade tip with patches in short circuit (—), connected to multimodal shunts (—), and connected to a network (—).

network is identical in both cases with seventeen resonances. However, the order of each shunt circuit goes from seventeen to five when the hybrid strategy is used.

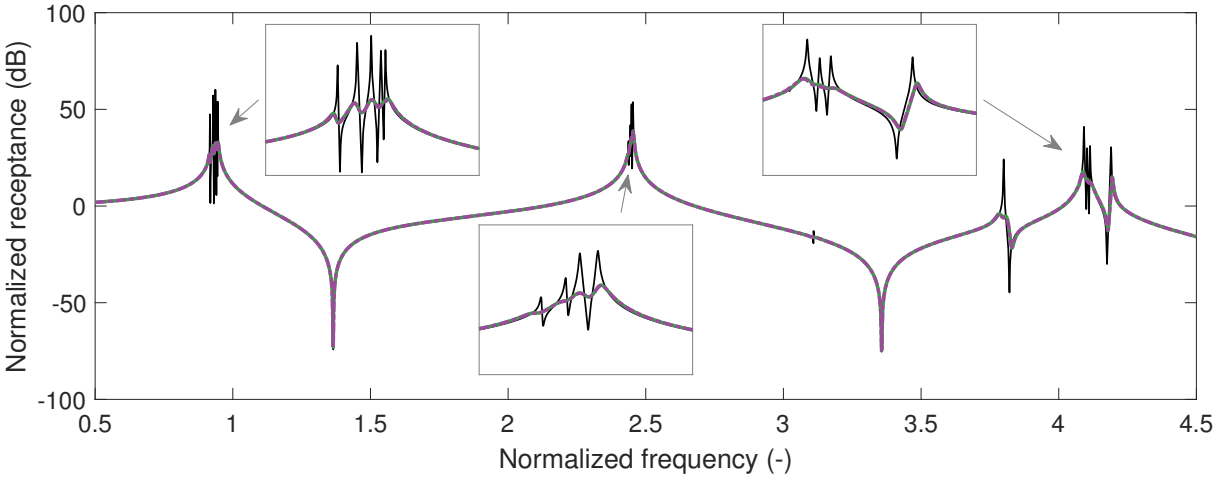

Figure 6.17: Driving-point receptance of the first blade tip with patches in short circuit (—), connected to multimodal shunts tuned with the hybrid strategy (—), and connected to a network tuned with the hybrid strategy (-·-).

The robustness of each strategy can be assessed in Figure 6.18. The isolated-mode and hybrid strategies allow for better performance and robustness, respectively. In Figure 6.18(c), the dip appearing near a frequency factor of 0.93 is due to the action of the electrical resonance tuned to the twelfth (isolated) mechanical mode.

Finally, it should be noted that an approach with similar performance was proposed in [251]. The approach proposed herein is substantially simpler and implementable experimentally since it does not require the decomposition of the structure into multiple sectors. It also accurately captures the dynamics of the host which allows for the control of support-dominated modes, unlike the ROM-based method therein.

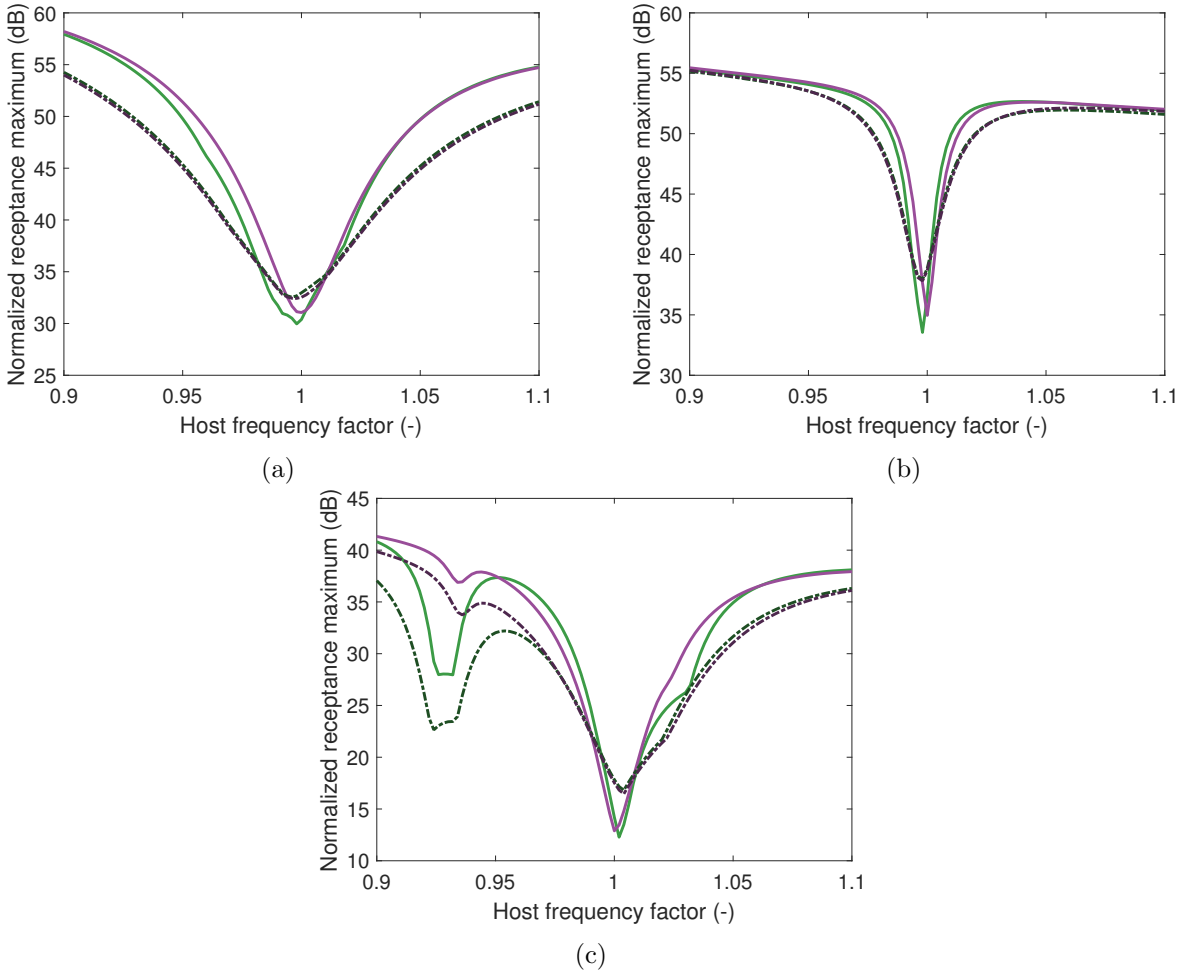

Figure 6.18: Maximum driving-point receptance magnitude of the first blade tip near the first (a), second (b) and third (c) modes families with patches connected to multimodal shunts tuned with the isolated-mode (—) and hybrid (- - -) strategies, and patches connected to a network tuned with the isolated-mode (—) and hybrid (- - -) strategies.

6.6 Damping of a bladed drum

6.6.1 BluM with piezoelectric patches

As stated in Section 6.1.2, the BluM can be endowed with 28 piezoelectric patches distributed on the rim, on the underside of the blades, as in [54]. A superelement was created from a FE model of the BluM, retaining mechanical DoFs on the blades tip at the leading edge (similarly to Figure 6.12(a)), the piezoelectric voltages, and 160 CNMs. Modal damping of 0.01% was added to each mode of this ROM.

The introduction of the patches disrupts the cyclic symmetry of the BluM. The piezoelectric structure is still cyclic symmetric, but the reference sector with patches is now one quarter of the structure. Because the mass and stiffness properties of the patches are small compared to those of the BluM, the former may be seen as a perturbation of the latter. Thus, some of the modes of the piezoelectric structure may be seen as perturbed versions of the modes with nodal diameters of the BluM alone (cf. Section 6.2). For

modes with a high number of nodal diameters in the nominal structure, this disruption is more pronounced and the introduction of patches has a more significant impact.

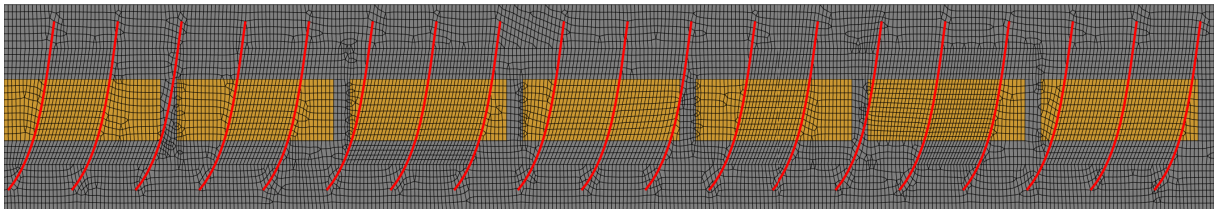

Figure 6.19: FE mesh of a quarter of the BluM's rim (in gray) with piezoelectric patches (in orange). The blade roots are indicated in red.

It should also be noted that the FE mesh and algorithm for modal analysis introduce mistuning by themselves. Indeed, the mesh needs to adapt to the geometry of the patches and the blades, which makes it significantly irregular in some regions, as shown in Figure 6.19. As a consequence, the cyclic symmetry of the structure with 78 sectors is lost when using this mesh, even when the piezoelectric patches are not incorporated in the model. This numerical effect is a signature of the strong sensitivity of cyclic symmetric structures to mistuning. The algorithm for modal analysis (a block Lanczos algorithm [140]) also struggles with the numerous close eigenvalues. Since it is rather difficult to remedy this numerical issue and since it can be used to represent unintentional mistuning, it was decided to keep this effect in the model.

6.6.2 Blade tip receptance

At first the driving-point receptance of a blade tip at the leading edge is used to analyze the dynamics of the structure and assess the effectiveness of the control system. It is shown in Figure 6.20 when the patches are all short-circuited. At low frequencies, isolated modes that correspond to the drum-dominated modes illustrated in Figure 6.8 are visible, whereas a zone of high modal density is observable near $\bar{\omega} = 0.9$, which corresponds to the 1B family of modes.

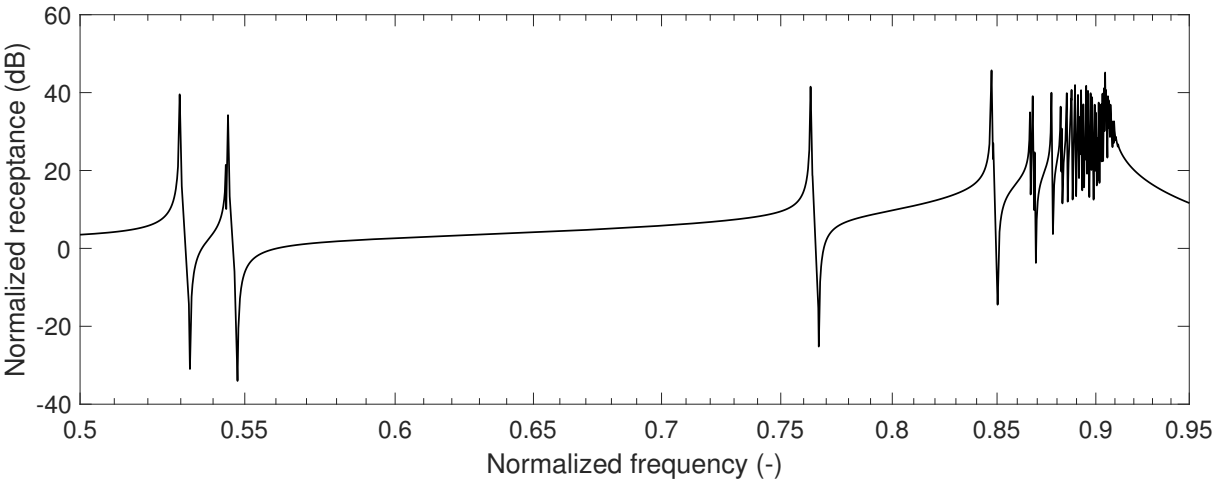

Figure 6.20: Driving-point receptance of a blade tip with patches in short circuit.

The driving-point receptance is not the most representative for an operational excitation of the structure, but would be easier to obtain experimentally (because it requires the

excitation of a single blade). Moreover, nearly all modes are excited by this configuration, which eases the assessment of the control strategy.

To mitigate the resonances of the BluM, three control strategies are considered:

1. 28 individual shunts with ideal Norton's admittance.
2. 7 decentralized networks interconnecting 4 patches distributed in an alternate way.
3. A centralized network interconnecting the 28 patches.

The second strategy was considered because the third one would require a MCU with 28 analog I/O pins, which may not be easy to find. From the results of Section 3.8.4, decentralized networks with an alternate patch distribution may be advantageous as they could exhibit better performance than mere shunts. Moreover, this could be a practical alternative where the MCUs have a realistic number of I/O pins and are in limited number. The patches interconnections for each strategy are depicted in Figure 6.21. In each strategy, the relative control authority on each mode is balanced, i.e., unit (global) relative scaling factors were assigned to each mode.

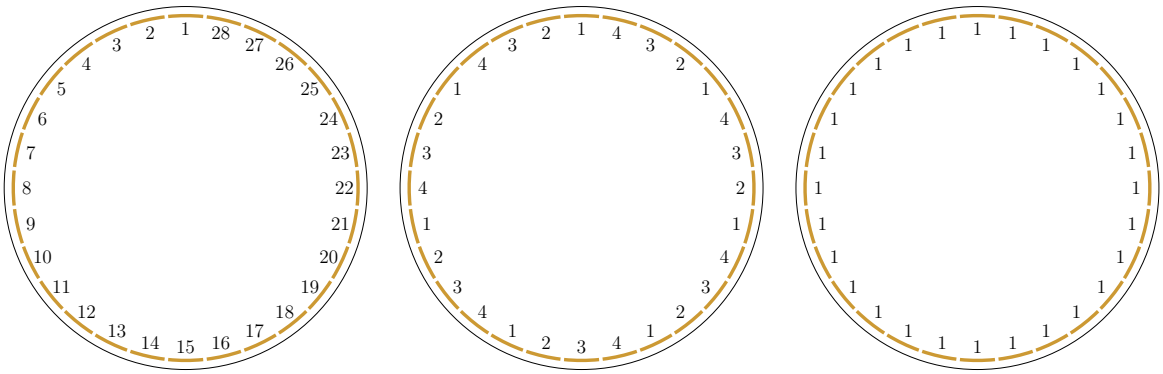

Figure 6.21: Connection of the patches to the circuits/networks used in strategies 1 (a), 2 (b) and 3 (c) (numbers indicate the circuit/network a patch is connected to).

The modes with frequencies lower than or equal to that of the last mode of the 1B family are targeted for vibration mitigation. It should be noted that this may not be a choice that would be made in practice, and only a subset of these modes would probably be targeted, as will be made in Section 6.6.3. The results of this section are therefore presented to demonstrate what one *can* do but not necessarily what one *should* do.

A hybrid strategy is adopted in order to simplify the circuits/networks. The first four peaks in Figure 6.20 (which correspond to modes with 3, 2, 4 and 5 nodal diameters) are targeted as isolated modes, and the resonances in the high modal density frequency region are targeted with a mean shunt.

Figure 6.22 features the driving-point receptance of the blade with the different control strategies. They all are effective on the isolated modes, and, as expected, the centralized network exhibits the best performance, followed by the decentralized networks. In the high modal density region, all three approaches are globally equivalent and control remarkably well most of the resonances with limited controller complexity thanks to the hybrid strategy. Near the highest frequencies, performance degrades

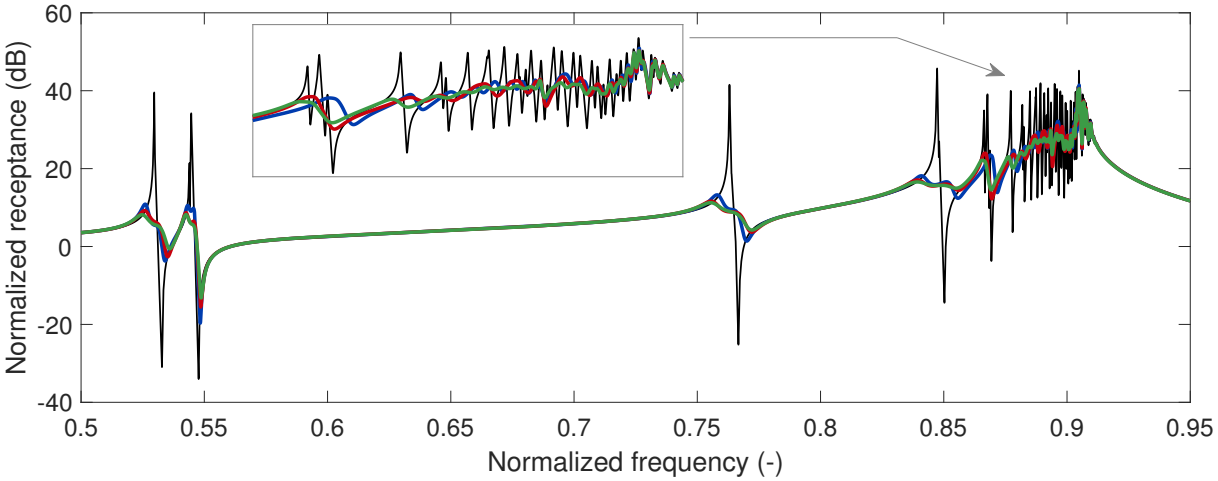

Figure 6.22: Driving-point receptance of a blade tip with patches in short circuit (—) and connected to multimodal shunt circuits (—), decentralized networks (—) and a centralized network (—) tuned with a hybrid strategy.

because the associated modes have a high number of nodal diameters, imparting partial charge cancellation on the 28 patches. This results in low EEMCFs with those modes and eventually limited vibration reduction.

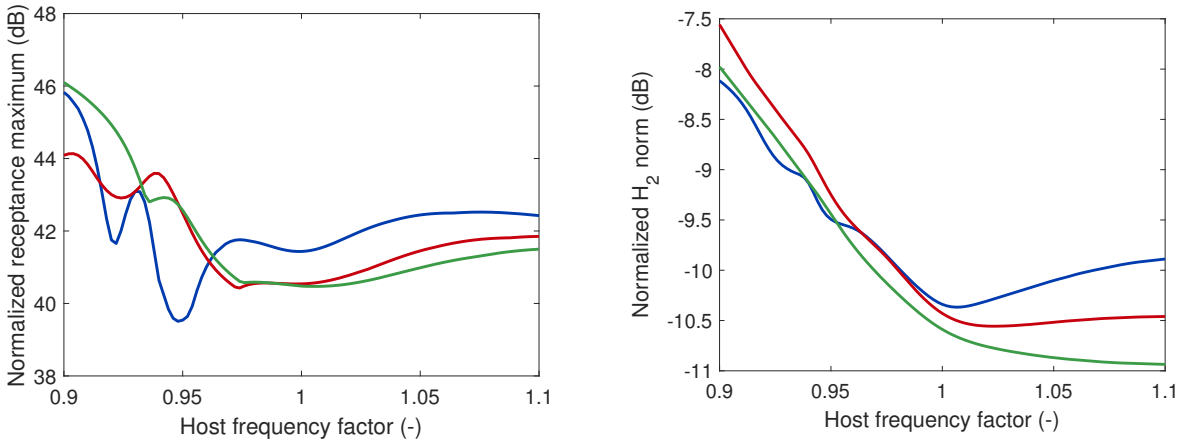

(a) (b)

Figure 6.23: Maximum normalized driving-point receptance (a) and normalized H_2 norm (b) with patches connected to multimodal shunt circuits (—), decentralized networks (—) and a centralized network (—) tuned with a hybrid strategy.

Figure 6.23(a) assesses the robustness of the proposed strategies when the frequencies of the host are modified by multiplication with a scalar factor f_{fr}. The small effect of this factor is due to the fact that the receptance maximum is determined by the highest-amplitude peak which is near the end of the region of high modal density (cf. Figure 6.22). Since the peaks around these frequencies are associated to modes exhibiting small electromechanical couplings, the receptance amplitudes in the uncontrolled and controlled systems are close, and the controllers have a small influence on these amplitudes.

To obtain a clearer picture of the robustness of the proposed strategies in terms of broadband control, the H_2 norm evaluated in the frequency range $\overline{\omega} = [0.5f_{fr}, 0.95f_{fr}]$ can be analyzed. This H_2 norm divided by that of the uncontrolled structure is shown in

Figure 6.23(b). The asymmetric character of this function with respect to the frequency factor is due to the ability of parallel RL shunts to partially control higher-frequency modes (as discussed in Chapters 2 and 4). Hence, when the host frequency is underestimated in the tuning procedure ($f_{fr} > 1$), the controllers are able to maintain (and even enhance in the centralized network case) performance in terms of the H_2 norm. This norm is mostly determined by control performance in the high modal density region, and the apparent robustness is due to the robustness of the mean shunt approach. However, it should be noted that the robustness concerning isolated modes is similar to the case of a single parallel RL shunt (i.e., the controllers can quickly be detuned from these modes).

6.6.3 Engine order excitation

A more representative excitation is the engine order one. In a cylindrical reference frame linked to the axis of rotation with radial, circumferential and axial coordinates r_c, θ_c and z_c, respectively, it can be expressed as

$$\begin{aligned}\mathbf{f}_{N_{EO}}(r_c, \theta_c, z_c, t) &= \mathbf{f}_0(r_c, z_c)\cos(N_{EO}\,(\theta_c - \Omega_{rot}t)) \\ &= \mathbf{f}_0(r_c, z_c)\,(\cos(N_{EO}\theta_c)\cos(N_{EO}\Omega_{rot}t) + \sin(N_{EO}\theta_c)\sin(N_{EO}\Omega_{rot}t))\,, \end{aligned} \quad (6.42)$$

where $\mathbf{f}_0(r_c, z_c)$ is an arbitrary force field which is circumferentially modulated. This relation indicates that the rotating excitation can equivalently be represented by the sum of two orthogonal spatial harmonic distributions, respectively modulated by two harmonic time signals in quadrature. The harmonic response of the BluM to a rotating excitation can thus be evaluated with the sum of two FRFs.

The responses of a blade to an engine order excitation N_{EO} varying from 6 to 9 were assessed. The frequencies of the modes with compatible number of nodal diameters (Equation (6.3)) are all in the high modal density region, and can thus be targeted by a mean shunt. In this case, all three strategies yield identical results.

Figure 6.24 shows the results. The fact that multiple, closely-spaced resonances appear in these responses comes from the mistuning in the structure, but a dominant mode is clearly observable in each case. This dominant mode is the counterpart of the modes in the cyclic symmetric structure with 6 to 9 nodal diameters. When the patches are shunted with a mean shunt, these resonances are effectively mitigated.

In an experimental setup, if the mistuning present in the BluM is large enough to make these engine orders excite isolated modes, the hybrid strategy adopted in Section 6.6.2 can be used to mitigate them as well.

The satisfactory performance exhibited by the mean shunt strategy on all these engine orders is due to the electromechanical coupling with the targeted modes. With an experimental setup, this coupling may be lower since the assumptions of the FE model may not be respected, e.g. regarding the material properties or imperfect adhesion to the structure due to the bonding layer [79]. To investigate the effect of a potential overestimation of the EEMCFs, the piezoelectric coupling matrix was multiplied by a factor smaller than one (resulting on the same factor applied to the EEMCFs) to artificially decrease the electromechanical coupling. Figure 6.25 features the response of the blade using arbitrary factors 0.25 and 0.5. As can be expected, performance is deteriorated if the EEMCFs are smaller than the nominal case. Thus, if the experimental

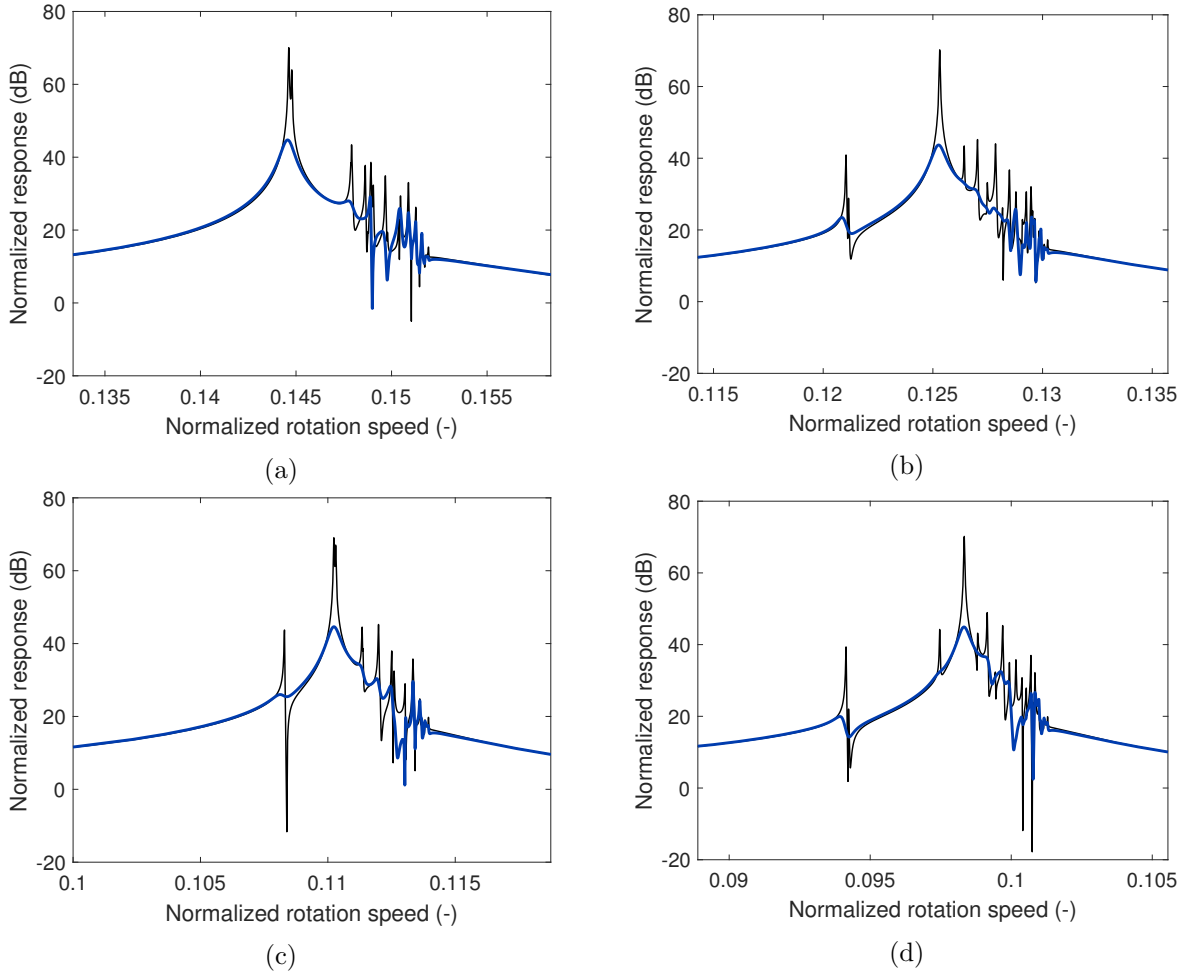

Figure 6.24: Normalized response of a blade tip under an engine order excitation ($N_{EO} = 6$ (a), $N_{EO} = 7$ (b), $N_{EO} = 8$ (c), $N_{EO} = 9$ (d)) with patches in short-circuit (—) and shunted with a mean shunt (—).

setup exhibits very low EEMCFs, an active control strategy with a negative capacitance to enhance electromechanical coupling could be considered.

6.7 Conclusion

The main dynamical features of bladed assemblies, namely modes with nodal diameters, engine-order excitation, and mistuning, were first briefly reviewed. In view of the complexity of the structures at hand, a modified model-order reduction technique tailored to piezoelectric structures was proposed, yielding a ROM of similar type as the original model. The mean shunt strategy was integrated into the approach proposed in Chapter 3 into a hybrid strategy to allow for the control of multiple families of modes.

Piezoelectric vibration damping of bladed structures was then studied with two examples. The first one is a bladed rail with five blades. With this structure, the hybrid strategy proved effective, simple and robust. Next, an industrial BluM was considered. Vibration mitigation of the resonances observed in a driving-point receptance of a blade was obtained using the hybrid strategy. Finally, the response of the structure under engine-order

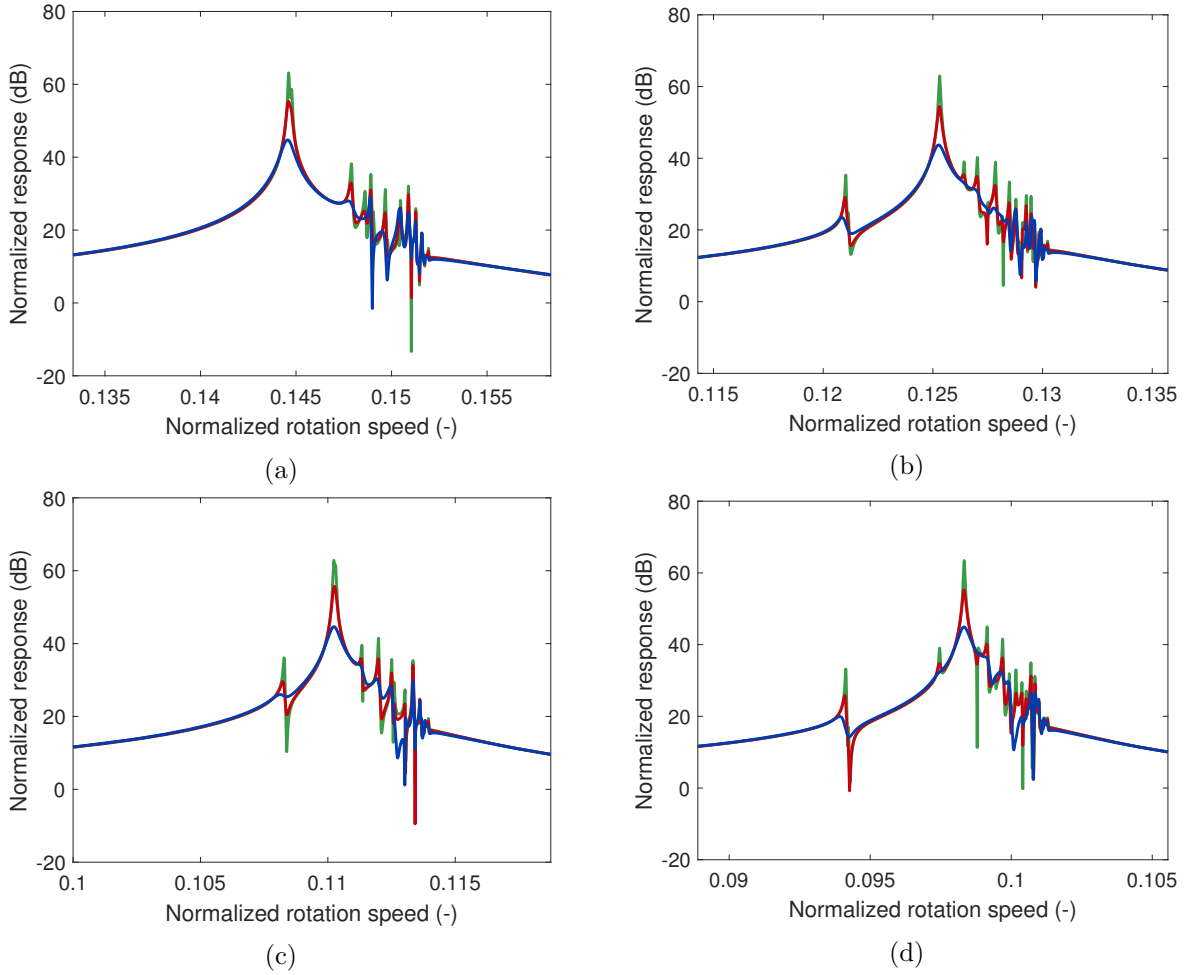

Figure 6.25: Normalized response of a blade tip under an engine order excitation ($N_{EO} = 6$ (a), $N_{EO} = 7$ (b), $N_{EO} = 8$ (c), $N_{EO} = 9$ (d)) with patches shunted with a mean shunt, multiplying the EEMCF by 1 (—), 0.5 (—) and 0.25 (—).

excitation was damped using a mean shunt strategy.

Effective piezoelectric vibration mitigation was thus demonstrated numerically. The next step would be the experimental validation on real bladed structures. This perspective is discussed in the conclusion of this thesis.

Conclusion

This thesis focused on developing vibration mitigation means for complex structures. The core of this work is constituted by tuning methods for multimodal piezoelectric vibration mitigation. These techniques can be implemented either with circuits/networks made up of passive electrical elements, or DVAs, and proved effective on various numerical and experimental examples.

Chapter 1 presented the general architecture of a DVA and demonstrated its equivalence with a piezoelectric shunt. The power consumption of the realized DVA is about 1W, and is mostly determined by quiescent power. Sampling delays were shown to be responsible for instabilities due to the generation of true power in the digital shunt. This aspect is most critical for systems with low electromechanical coupling. A stabilization approach was proposed to solve this issue with simple modifications of the coefficients of the implemented transfer function.

Chapter 2 proposed a three-step passivity-based tuning approach for circuits connected to a single transducer. After identifying the structure, specifications of ideal immittances were derived. These immittances can directly be programmed in a DVA, or used to tune shunt circuits previously proposed in the literature. The method provides effective vibration mitigation of multiple modes and requires limited experimental data.

Chapter 3 extended these concepts to multiple transducers, and proposed a modal-based synthesis of networks interconnecting them. It also established a theoretical framework to compare the three approaches generally used for multimodal piezoelectric damping. One important conclusion of Chapters 2 and 3 is that passive networks can optimally use the control authority of all piezoelectric transducers on all modes simultaneously. By contrast, shunt circuits need to compromise between the modes. At their best, passive shunts achieve the same performance as the case where all transducers are connected to RL shunts targeting a specific mode.

Chapter 4 proposed an efficient algorithm for H_∞ optimization. The approach relies on solving a sequence of problems of increasing complexity through optimization of norms of increasing order. The typical outcome of this algorithm is an all-equal-peak design. Different transfer functions, such as the receptance, mobility, accelerance or even scaled versions of these transfer functions can be optimized.

The detrimental effects of structural nonlinear behaviors on tuned vibration absorbers were studied in Chapter 5. The versatility of the DVA was exploited to develop an experimental piezoelectric nonlinear tuned vibration absorber featuring different nonlinear mathematical forms. This nonlinear absorber was shown to outperform its linear counterpart when acting on a nonlinear structure. The control strategy was also extended to the control of multiple nonlinear resonances.

Chapter 6 then focused on bladed structures. A modified model-order reduction technique tailored for piezoelectric structures was proposed. A new hybrid strategy combining the mean shunt concept with the approach of Chapter 3 was developed. Effective vibration mitigation was finally numerically demonstrated on a bladed rail and an industrial BluM.

This thesis thus contributes to the development of advanced piezoelectric vibration mitigation strategies which can be readily used by practitioners. Specifically, the main achievements of this research work are:

1. A DVA, with linear or nonlinear tuning laws made robust to delay-induced instabilities, was implemented.
2. Four innovative approaches for multimodal vibration damping were developed, namely a passivity-based tuning of piezoelectric shunts, a modal-based synthesis of networks, a fine-tuning methodology based on norm-homotopy optimization and a tuning strategy dedicated to nonlinear systems.
3. The effective control of multiple families of modes of bladed assemblies was realized using a hybrid methodology combining the modal-based synthesis of networks with previous developments in the technical literature. In this context, a modified Craig-Bampton model-order reduction method for piezoelectric structures was also proposed.

Perspectives for future research

Four research directions could be followed to build on the achievements of this thesis. They are based on the limitations highlighted throughout this manuscript.

Placement, sizing and distribution of piezoelectric transducers

Most structures studied in this thesis were either existing experimental setups or numerical structures proposed in the literature, which is why placing and sizing piezoelectric transducers was not tackled herein. It remains nonetheless important and can be quite challenging when multiple transducers are used to target multiple modes. In this regard, an interesting extension to the proposed norm-homotopy algorithm would be to concurrently optimize the position and size of piezoelectric transducers.

Moreover, Chapter 3 briefly discussed the relevance of an appropriate choice of the piezoelectric transducers interconnected with a network, and how this choice could affect performance. The discussion was not carried out in depth, and only exploratory results were shown. A quantitative method guiding the user for the most advantageous interconnections and control emphasis on specific modes could be very helpful. Moreover, the link between the local and global scaling factors should be clarified.

Adaptivity of the absorber

Chapters 1, 5 and 6 underlined the lack of robustness of piezoelectric tuned vibration absorbers, and showed that changes in the resonance frequency of the host could have a dramatic effect on performance. Varying operational conditions such as temperature, wear or boundary conditions can strongly impact the resonance frequencies of a structure.

The methods proposed in Chapters 2 and 3 only require the measurement of the dynamic capacitance or elastance. Since the DVA is endowed with a voltage sensor

and a current source, it is able to measure these transfer functions on its own. Coupled with adequate signal processing, the DVA could therefore be able to achieve *offline adaptivity*. In other words, a DVA connected to an unforced structure before operation could run an initialization routine where it identifies the structural properties by injecting a small current, computes the parameters of its admittance, and then runs as a regular shunt circuit. However, in-operation structural changes would not be detectable with this offline adaptive approach.

Several works proposed to make piezoelectric shunts semi-active, by updating their electrical parameters to stay tuned to the host frequency. For instance, Fleming and Moheimani [252] used a DVA with an adaptation scheme based on the minimization of the root-mean square (RMS) strain in the piezoelectric transducer. Niederberger et al [253] used a relative phase adaptation scheme to guarantee a phase quadrature between the current in the shunt and the velocity of the structure. This technique was shown to be faster than the RMS strain minimization, but it requires an additional sensor on the structure. Recently, Gardonio et al [166] proposed a scheme based on the maximization of dissipated power in the shunt. This approach was also implemented with a DVA, and its advantage is that it only requires the voltage and current in the transducer, which are local and readily-available measurements, especially with a DVA. Thus, an interesting research direction would be to adapt this law to the ideal immittance circuits and even to networks in order to provide the DVA with *online adaptivity*, making the control strategy much more robust.

If provided with the ability to detect structural changes (either offline or online), the DVA could also be used to perform structural health monitoring. In particular, it could deduce the structural resonance frequencies (or equivalent indicators) to inform the operator about the state of the structure.

Active digital vibration absorber

The introduction highlighted three advantages of passive control, namely the absence of power requirements, its fail-safe character, and the guaranteed stability of the controlled system. As shown in Chapter 1, the DVA requires power for operation and thus is not fail safe, and can potentially be unstable. Therefore, the relevance of implementing a passive control law with a DVA for operation may be questionable.

Most of this thesis was focused on passive control, and conditions for the circuits or networks to be realizable as an assembly of passive electrical components were derived. In Chapters 2 and 3, they were shown to limit the extent to which the control authority on several modes could be raised. In particular, it was shown in an example of Chapter 3 (Section 3.6.1) that violating this passivity constraint led to the appearance of an active electrical component, the negative capacitance.

Going beyond the passivity limits in order to increase the performance of a DVA is conceivable, and was pursued in [109]. Nothing seems to prevent the application of the tuning formulas developed in Chapters 2 and 3 without respecting the passivity constraints. This would constitute a tuning approach for a resonant active controller. The passivity constraint would be replaced by other concerns, such as the stability of the closed-loop system or its power consumption and control effort. Unlike in [109], numerical optimization would not be required to tune such an active controller.

The piezoelectric transducer connected to a DVA acts simultaneously as a sensor and as an actuator, and thus allows for a perfect collocated control. This configuration has advantages in terms of closed-loop stability [4]. Another way in which the developments in this thesis could be used in the active control of structures could come from the strong similarity between a series RL piezoelectric shunt and a PPF controller, as noted e.g. in [173].

Development and integration of the absorber in bladed structures

The final milestone of the Maveric project mentioned in the introduction of this thesis is the experimental demonstration of smart vibration absorbers on a BluM. To achieve this, several tasks still need to be undertaken. The first one is the experimental realization of a DVA able to control multiple piezoelectric transducers, or multiple (and potentially interconnected) DVAs. As in Chapter 6, the first candidate host for such a demonstration would be a bladed rail rather than a BluM to deal with complexity incrementally.

Turning now to a possible deployment of such vibration mitigation approaches, the ideal control system should exhibit high performance while being robust, easily integrable and fail-safe. Performance was numerically demonstrated in Chapter 6 but remains to be experimentally validated. If unsatisfactory, an active DVA could be conceived. Robustness issues could be addressed using real-time adaptivity. Regarding the integration, a DVA could be made much smaller and lighter than the two realizations presented in this thesis. It would thus fit easily inside the BluM, but special care would have to be taken to connect it to the piezoelectric patches with strong wires, and to make the whole system balanced. Power consumption would also be an important aspect of the DVA integration. For the application at hand, it was demonstrated by collaborators of the Maveric project that a significant amount of power could be extracted from the rotation with an electromagnetic energy harvesting system. Finally, the DVA is not fail-safe. To remedy this, several options could be explored. An electronic switch which connects the patches to a DVA when power is on, and to a simpler shunt such as a properly-tuned resistor when power is off could be a simple, fail-safe solution. Alternatively, an active DVA could be coupled with a passive shunt to form a fail-safe hybrid control system. Finally, it should be noted that this kind of control strategy could only be applied to the cold parts of the engine (such as the low-pressure compressor) because of the temperature limitations incurred by the use of piezoceramic elements.

Acronyms

ABH acoustic black hole.

ADC analog-to-digital converter.

AFT alternating frequency–time domain.

ANCB augmented nonlinear current blocking.

BLISK bladed disk.

BluM bladed drum.

BoAs basins of attraction.

CB current blocking.

CF current flowing.

CNM component normal mode.

DAC digital-to-analog converter.

DoFs degrees of freedom.

DRC detached resonance curve.

DVA digital vibration absorber.

EEMCF effective electromechanical coupling factor.

FE finite element.

FEM finite element method.

FRF frequency response function.

HBM harmonic balance method.

HV high-voltage.

I/O input-output.

KCL Kirchhoff's current law.

KVL Kirchhoff's voltage law.

LV low-voltage.

MCB modified Craig-Bampton.

MCU microcontroller unit.

MDoF multiple-degree-of-freedom.

MIMO multiple-input multiple-output.

NCB nonlinear current blocking.

NES nonlinear energy sink.

NFR nonlinear frequency response.

NH norm-homotopy.

NLTVA nonlinear tuned vibration absorber.

NPPF nonlinear positive position feedback.

NPTVA nonlinear piezoelectric tuned vibration absorber.

OpAmp operational amplifier.

PCB printed circuit board.

PPF positive position feedback.

PWM pulse width modulation.

QP quasiperiodic.

RMS root-mean square.

ROM reduced-order model.

SDoF single-degree-of-freedom.

SFCF second Foster canonical form.

SHC sample-and-hold circuit.

SISO single-input single-output.

SMW Sherman-Morrison-Woodbury.

SPIS series-parallel impedance structure.

SSDNC synchronized switch damping on negative capacitor.

TMD tuned mass damper.

TRL technology readiness level.

ZOH zero-order hold.

ZPK zero-pole-gain.

Nomenclature

Subscripts

$\cdot_b$	Boundary
$\cdot_d$	Discrete
$\cdot_e$	Electrical
$\cdot_g$	Group
$\cdot_i$	Internal
$\cdot_p$	Piezoelectric
$\cdot_s$	Shunt
$\cdot_0$	Host system characteristic
$\cdot_{<k}$	Non-resonant electrical modes with frequencies lower than that of mode k
$\cdot_{>r}$	Non-resonant mechanical modes with frequencies higher than that of mode r
$\cdot_{avg}$	Average
$\cdot_a$	Absorber
$\cdot_{CC}$	Negative-voltage power supply
$\cdot_{EE}$	Positive-voltage power supply
$\cdot_{in}$	Input
$\cdot_{Max}$	Maximal
$\cdot_{nl}$	Nonlinear
$\cdot_{oc}$	Open-circuit
$\cdot_{opt}$	Optimal
$\cdot_{out}$	Output
$\cdot_Q$	Quiescent
$\cdot_{sc}$	Short-circuit

Superscripts

$\cdot^\epsilon$	Quantity at constant strain
$\cdot^\sigma$	Quantity at constant stress

$.^{E}$ Quantity at constant electric field

$.^{R}$ Resistive shunt

$.^{\star}$ Optimal

$.^{RLP}$ Parallel RL shunt

$.^{RLS}$ Series RL shunt

Operators

$\angle\cdot$ Complex argument

$\cdot \succeq 0$ Positive semidefinite matrix

$.^{*}$ Complex conjugate

$.^{\dagger}$ Pseudoinverse

$.^{H}$ Matrix Hermitian transpose

$.^{T}$ Matrix transpose

$\dot{\cdot}$ Time derivative

$\Im\{\cdot\}$ Imaginary part

$\lambda_{Max}\{\cdot\}$ Maximum eigenvalue

$\Re\{\cdot\}$ Real part

$H_p\{\cdot\}$ p-norm of a transfer function

General notation

$\mathbf{0}$ Zero vector/matrix

$\mathbf{1}$ Vector/matrix filled with ones

$\mathbf{I}$ Identity matrix

$\bar{\cdot}$ Dimensionless/normalized quantity

$\hat{\cdot}$ Effective characteristic around a resonance frequency

t Time

Single-degree-of-freedom piezoelectric structure

Δx Residual deformation

$\epsilon_{kl}^{\varepsilon}$ Entry k,l of the permittivity matrix at constant strain

γ_p Piezoelectric coupling coefficient (Norton's model)

ω_{oc} Open-circuit resonance frequency

ω_{sc} Short-circuit resonance frequency

ψ Piezoelectric flux linkage

σ_k Component k of Voigt's stress vector

θ_p Piezoelectric coupling coefficient (Thévenin's model)

ε_l Component l of Voigt's strain vector

A Area of a piezoelectric rod

$C_p(s)$ Dynamic capacitance

C_p^{σ} Piezoelectric capacitance at constant stress

C_p^{ε} Piezoelectric capacitance at constant strain

c_{kl} Entry k,l of the Hooke's matrix

D_k Component k of the electric displacement field vector

E_p Component p of the electric field vector

$E_p(s)$ Dynamic elastance

e_{kp} Entry k,p of the material piezoelectric coupling matrix

E_{oc} Stored energy under open-circuit condition

E_{sc} Stored energy under short-circuit condition

f External forcing

f_p Force across a piezoelectric rod

h Height of a piezoelectric rod

i Piezoelectric current

K_c Effective electromechanical coupling factor

k_{oc} Stiffness of a piezoelectric structure with open-circuited electrodes

$k_{p,oc}$ Piezoelectric stiffness with open-circuited electrodes

$k_{p,sc}$ Piezoelectric stiffness with short-circuited electrodes

k_{sc} Stiffness of a piezoelectric structure with short-circuited electrodes

q Piezoelectric charge

V Piezoelectric voltage

x Displacement

Piezoelectric shunts

δ Frequency ratio of a series RL shunt

ν Frequency ratio of a parallel RL shunt

ω_e Electrical resonance frequency

ς Electrical damping ratio of a parallel RL shunt

ζ Electrical damping ratio of a series RL shunt

B Reluctance

G Conductance

L Inductance

N_s Number of targeted modes

p (with subscript) pole of a transfer function

R Resistance

r (with subscript) residue

Y Electrical admittance

y_l Influence of capacitively-dominated modes (admittance model)

Y_N Norton's equivalent admittance

y_u Influence of inductively-dominated modes (admittance model)

Z Electrical impedance

z (with subscript) zero of a transfer function

z_l Influence of capacitively-dominated modes (impedance model)

Z_T Thévenin's equivalent impedance

z_u Influence of inductively-dominated modes (impedance model)

Digital vibration absorber

α Voltage division ratio of the DVA

τ Sampling period

g Gain of the DVA

N_{ADC} ADC output value

N_{DAC} DAC input value

P (with subscript) power

R_i Current injector resistance

V (with subscript) voltage

z z transform variable

Transfer functions

ω Angular frequency

f (with subscript) frequency

GM Gain margin

K Gain of a transfer function

PM Phase margin

s Laplace's variable

Multiple-degree-of-freedom piezoelectric structure

$\boldsymbol{\eta}$ Modal coordinates vector

$\boldsymbol{\gamma}_p$ Piezoelectric coupling vector (Norton's model)

$\boldsymbol{\theta}_p$ Piezoelectric coupling vector (Thévenin's model)

$\gamma_{\phi,k}$ k^{th} modal piezoelectric coupling coefficient (Norton's model)

κ_r Influence of higher-frequency mechanical modes

$\boldsymbol{\Gamma}_p$ Piezoelectric coupling matrix (Norton's model)

$\boldsymbol{\Omega}_{oc}$ Mechanical resonance frequencies matrix with open-circuited transducers

$\boldsymbol{\Omega}_{sc}$ Mechanical resonance frequencies matrix with short-circuited transducers

$\boldsymbol{\Phi}_{oc}$ Mechanical mode shapes matrix with open-circuited transducers

$\boldsymbol{\Phi}_{sc}$ Mechanical mode shapes matrix with short-circuited transducers

$\boldsymbol{\Theta}_p$ Piezoelectric coupling matrix (Thévenin's model)

$\mathbf{C}_p(s)$ Dynamic capacitance matrix

$\mathbf{C}_p^{\varepsilon}$ Piezoelectric capacitance matrix at constant strain

$\mathbf{E}_p(s)$ Dynamic elastance matrix

$\mathbf{E}_p^{\varepsilon}$ Piezoelectric elastance matrix at constant strain

$\mathbf{f}$ External forcing

$\mathbf{H}$ Transfer matrix

$\mathbf{K}_{oc}$ Structural stiffness matrix with open-circuited transducers

$\mathbf{K}_{sc}$ Structural stiffness matrix with short-circuited transducers

$\mathbf{M}$ Structural mass matrix

$\mathbf{x}$ Generalized DoFs

$\theta_{\phi,k}$ k^{th} modal piezoelectric coupling coefficient (Thévenin's model)

Networks

α_p Scaling factor of an electrical mode for passivity

$\mathbf{\Gamma}_\Phi$ Modal piezoelectric coupling matrix

$\boldsymbol{\eta}_e$ Electrical modal coordinates vector

$\boldsymbol{\psi}$ Flux linkages vector

$\boldsymbol{\varphi}_p$ Dimensionless electrical mode shape

$\mathbf{\Omega}_e$ Electrical resonance frequencies matrix

$\mathbf{\Phi}_{e,g\mathbf{k}(g)}$ Electrical mode shapes matrix of group g

$\mathbf{\Phi}_e$ Electrical mode shapes matrix

$\mathbf{\Phi}_{p,\mathbf{g}(k)k}$ Electrical mode shapes of all resonant groups on all piezoelectric transducers around the frequency of electrical mode k

$\mathbf{B}$ Reluctance matrix

$\mathbf{C}$ Capacitance matrix (of the overall network)

$\mathbf{C}_e$ Capacitance matrix (of the interconnecting network)

$\mathbf{D}_p$ Scaling factors matrix

$\mathbf{E}_g$ Localization matrix to a group of electrical DoFs

$\mathbf{E}_p$ Piezoelectric localization matrix

$\mathbf{E}_{pg}$ Localization matrix relating the piezoelectric DoFs of a group to those of the whole piezoelectric structure

$\mathbf{G}$ Conductance matrix

$\mathbf{g}(k)$ Vector of resonant groups around the frequency of electrical mode k

$\mathbf{k}(g)$ Electrical resonances vector of group g

$\mathbf{S}$ Schur complement of the short-circuit resonance frequencies matrix

$\mathbf{V}$ Orthogonal basis of the kernel of $\mathbf{\Phi}_p^T$

$\mathbf{W}$ Orthogonal basis of the kernel of $\mathbf{\Phi}_p$

$\mathbf{Y}$ Admittance matrix

$\mathbf{Z}_e$ Electrical damping ratios matrix

$\overline{\mathbf{\Phi}}_p$ Dimensionless electrical mode shapes matrix

$\overline{\mathbf{D}}_p$ Relative scaling factors matrix

$\overline{d}_p$ Relative scaling factor

d_p Scaling factor

I Number of internal electrical DoFs

N_e Number of electrical DoFs

N_g Number of groups of electrical DoFs

P Number of piezoelectric transducers

P_g Number of piezoelectric transducers connected to group g

Norm-homotopy optimization

$\boldsymbol{\xi}$ Vector of optimization variables

χ Scaling factor for a transfer function

$\mathbf{c}$ Set of inequality constraints

$\mathbf{w}_f$ Spatial forcing distribution

$\mathbf{w}_u$ Localization vector

N_ω Scaling factor for a transfer function

Nonlinear systems

$\boldsymbol{\nabla}$ Frequency-domain differential operator

$.^{(i)}$ Quantity at order i of a series expansion

ϵ Series expansion parameter

$\mathbf{b}$ Generalized loadings in the frequency domain

$\mathbf{z}$ Vector of harmonic coefficients

C_2 Quadratic elastance coefficient

C_3 Cubic elastance coefficient

C_5 Quintic elastance coefficient

$C_{p,3}$ Cubic piezoelectric elastance coefficient

k_3 Cubic stiffness coefficient

q_c Fundamental cosine coefficient

q_s Fundamental sine coefficient

$R_{p,3}$ Cubic piezoelectric resistance coefficient

Bladed structures

$\boldsymbol{\eta}_i$ CNMs modal coordinates

$\boldsymbol{\upsilon}_i$ Modified CNMs modal coordinates

$\boldsymbol{\Omega}_i$ Component normal modes resonance frequencies matrix

$\boldsymbol{\Omega}_i$ CNMs resonant frequencies matrix

$\boldsymbol{\Phi}_{c,p}$ Piezoelectric constraint modes

$\boldsymbol{\Phi}_c$ Constraint modes

$\boldsymbol{\Phi}_i$ CNMs mode shapes matrix

$\mathbf{R}_{CB}$ Craig-Bampton reduction matrix

$\mathbf{R}_{MCB}$ Modified Craig-Bampton reduction matrix

Ω_{rot} Angular rotation speed

θ_c Circumferential cylindrical coordinate

$\widehat{\omega}_{sc,\mathbf{r}}$ Average short-circuit resonance frequency (mean shunt strategy)

$\widehat{\omega}^2_{sc,avg}$ Average of the squared resonant short-circuit frequencies

$C_{p,static}$ Static capacitance of the p^{th} transducer

f_{fr} Frequency factor of the host structure

N_{EO} Engine order

N_{ND} Number of nodal diameters

N_{Sec} Number of sectors

r_c Radial cylindrical coordinate

z_c Axial cylindrical coordinate

A Linear algebra

This appendix recapitulates non-trivial linear algebra formulas and properties used throughout this thesis. In each of the formulas used herein, it is assumed that $\mathbf{A}$, $\mathbf{B}$, $\mathbf{C}$, $\mathbf{D}$, $\mathbf{U}$ and $\mathbf{V}$ are matrices and $\mathbf{u}$ and $\mathbf{v}$ are vectors. They are of conformable size in the context in which they are used. The inverted matrices are implicitly assumed to be regular.

A.1 Inverse of rank-updated matrices

A.1.1 Sherman-Morrison formula

The Sherman-Morrison formula allows to compute the inverse of a rank-one updated matrix from the inverse of the non-updated matrix [254], provided it is regular. It is given by

$$\left(\mathbf{A}+\mathbf{u}\mathbf{v}^T\right)^{-1} = \mathbf{A}^{-1} - \frac{1}{1+\mathbf{v}^T\mathbf{A}^{-1}\mathbf{u}}\mathbf{A}^{-1}\mathbf{u}\mathbf{v}^T\mathbf{A}^{-1}. \tag{A.1}$$

A.1.2 Sherman-Morrison-Woodbury formula

The SMW formula is a generalization of the Sherman-Morrison formula for rank-k updates [255]. It is given by

$$\left(\mathbf{A}+\mathbf{U}\mathbf{D}\mathbf{V}^T\right)^{-1} = \mathbf{A}^{-1} - \mathbf{A}^{-1}\mathbf{U}\left(\mathbf{D}^{-1}+\mathbf{V}^T\mathbf{A}^{-1}\mathbf{U}\right)^{-1}\mathbf{V}^T\mathbf{A}^{-1}. \tag{A.2}$$

A.2 Determinants of rank-updated matrices

The matrix determinant lemma for a rank-one update of a matrix [256] results in

$$\det\left(\mathbf{A}+\mathbf{u}\mathbf{v}^T\right) = \left(1+\mathbf{v}^T\mathbf{A}^{-1}\mathbf{u}\right)\det\left(\mathbf{A}\right). \tag{A.3}$$

A rank-k counterpart can also be derived. First, by noting that the determinant of a matrix product is equal to the product of the determinants,

$$\begin{aligned}
\det\left(\mathbf{A}+\mathbf{U}\mathbf{D}\mathbf{V}^T\right) &= \det\left(\mathbf{A}^{1/2}\left(\mathbf{I}+\mathbf{A}^{-1/2}\mathbf{U}\mathbf{D}\mathbf{V}^T\mathbf{A}^{-1/2}\right)\mathbf{A}^{1/2}\right) \\
&= \det\left(\mathbf{A}^{1/2}\right)\det\left(\mathbf{I}+\mathbf{A}^{-1/2}\mathbf{U}\mathbf{D}\mathbf{V}^T\mathbf{A}^{-1/2}\right)\det\left(\mathbf{A}^{1/2}\right) \\
&= \det\left(\mathbf{I}+\mathbf{A}^{-1/2}\mathbf{U}\mathbf{D}^{1/2}\mathbf{D}^{1/2}\mathbf{V}^T\mathbf{A}^{-1/2}\right)\det\left(\mathbf{A}\right).
\end{aligned}$$

According to the Weinstein-Aronszajn formula ([257], Equation (5.47)),

$$\det\left(\mathbf{I}+\mathbf{A}^{-1/2}\mathbf{U}\mathbf{D}^{1/2}\mathbf{D}^{1/2}\mathbf{V}^T\mathbf{A}^{-1/2}\right) = \det\left(\mathbf{I}+\mathbf{D}^{1/2}\mathbf{V}^T\mathbf{A}^{-1/2}\mathbf{A}^{-1/2}\mathbf{U}\mathbf{D}^{1/2}\right)$$

Thus,

$$\begin{aligned}\det\left(\mathbf{A}+\mathbf{UDV}^T\right) &= \det\left(\mathbf{I}+\mathbf{D}^{1/2}\mathbf{V}^T\mathbf{A}^{-1/2}\mathbf{A}^{-1/2}\mathbf{UD}^{1/2}\right)\det\left(\mathbf{A}\right)\\ &= \det\left(\mathbf{D}^{1/2}\left(\mathbf{D}^{-1}+\mathbf{V}^T\mathbf{A}^{-1}\mathbf{U}\right)\mathbf{D}^{1/2}\right)\det\left(\mathbf{A}\right)\\ &= \det\left(\mathbf{D}^{1/2}\right)\det\left(\mathbf{D}^{-1}+\mathbf{U}^T\mathbf{A}^{-1}\mathbf{V}\right)\det\left(\mathbf{D}^{1/2}\right)\det\left(\mathbf{A}\right).\end{aligned}$$

Performing one last simplification on the determinants of $\mathbf{D}^{1/2}$, the rank-k counterpart of Equation (A.3) is obtained as:

$$\det\left(\mathbf{A}+\mathbf{UDV}^T\right) = \det\left(\mathbf{D}^{-1}+\mathbf{V}^T\mathbf{A}^{-1}\mathbf{U}\right)\det\left(\mathbf{A}\right)\det\left(\mathbf{D}\right). \tag{A.4}$$

A.3 Block inversion

A regular matrix defined by blocks can be inverted following

$$\begin{bmatrix}\mathbf{A} & \mathbf{B}\\ \mathbf{C} & \mathbf{D}\end{bmatrix}^{-1} = \begin{bmatrix}\mathbf{A}^{-1}+\mathbf{A}^{-1}\mathbf{B}\left(\mathbf{D}-\mathbf{CA}^{-1}\mathbf{B}\right)^{-1}\mathbf{CA}^{-1} & -\mathbf{A}^{-1}\mathbf{B}\left(\mathbf{D}-\mathbf{CA}^{-1}\mathbf{B}\right)^{-1}\\ -\left(\mathbf{D}-\mathbf{CA}^{-1}\mathbf{B}\right)^{-1}\mathbf{CA}^{-1} & \left(\mathbf{D}-\mathbf{CA}^{-1}\mathbf{B}\right)^{-1}\end{bmatrix}. \tag{A.5}$$

The matrix

$$\mathbf{D}-\mathbf{CA}^{-1}\mathbf{B} \tag{A.6}$$

is called the Schur complement of the block $\mathbf{A}$, and is assumed to be invertible in Equation (A.5).

A.4 Properties of positive definite and positive semidefinite matrices

Property 1 An $n \times n$ symmetric matrix $\mathbf{A}$ which satisfies

$$\mathbf{u}^T\mathbf{Au} \geq 0, \qquad \forall \mathbf{u} \in \mathbb{R}^n \tag{A.7}$$

is said to be positive semidefinite ($\mathbf{A} \succeq 0$). If the equality only holds for $\mathbf{u} = \mathbf{0}$, the matrix is then positive definite ($\mathbf{A} \succ 0$).

Property 2 A positive semidefinite (definite) matrix has positive eigenvalues (strictly positive eigenvalues).

Property 3 Every positive definite matrix is invertible, and its inverse is also positive definite.

Property 4 The sum of two positive semidefinite matrices is also positive semidefinite. The sum of a positive semidefinite and a positive definite matrices is positive definite.

Property 5 If the matrix $\mathbf{A} \succ 0$, so is

$$\mathbf{U}^T\mathbf{A}\mathbf{U} \tag{A.8}$$

provided that $\mathbf{U}$ has more rows than columns or is square, and is full-rank. It is positive semidefinite otherwise.

Property 6 If two matrices $\mathbf{A}$ and $\mathbf{B}$ are such that

$$\mathbf{A} - \mathbf{B} \succeq 0, \tag{A.9}$$

then their inverses verify

$$\mathbf{B}^{-1} - \mathbf{A}^{-1} \succeq 0. \tag{A.10}$$

This can be proven by simultaneously diagonalizing matrices $\mathbf{A}$ and $\mathbf{B}$. Let $\mathbf{V}$ and $\mathbf{D}$ be such that

$$\mathbf{A}\mathbf{V} = \mathbf{B}\mathbf{V}\mathbf{D}, \qquad \mathbf{V}^T\mathbf{A}\mathbf{V} = \mathbf{I}, \qquad \mathbf{V}^T\mathbf{B}\mathbf{V} = \mathbf{D}. \tag{A.11}$$

Pre- and postmultiplying Equation (A.9) by $\mathbf{V}^T$ and $\mathbf{V}$, respectively, yields

$$\mathbf{I} - \mathbf{D} \succeq 0, \tag{A.12}$$

which means that the elements on the diagonal of $\mathbf{D}$ should be less than or equal to one. Using the spectral expansion of the inverse matrices

$$\mathbf{A}^{-1} = \mathbf{V}\mathbf{V}^T, \qquad \mathbf{B}^{-1} = \mathbf{V}\mathbf{D}^{-1}\mathbf{V}^{-T} \tag{A.13}$$

and pre- and postmultiplying Equation (A.10) by $\mathbf{V}^{-1}$ and $\mathbf{V}^{-T}$, respectively, gives

$$\mathbf{D}^{-1} - \mathbf{I} \succeq 0, \tag{A.14}$$

which is satisfied if Equation (A.12) is satisfied (because the elements on the diagonal of $\mathbf{D}^{-1}$ are then larger than or equal to one).

B Appendix to Chapter 1

B.1 Initial estimates for the roots of a delayed system's characteristic equation

Equation (1.102) is recalled here:

$$1 + H(s)\frac{1 - e^{-s\tau}}{s\tau} = 0. \tag{B.1}$$

The goal of this appendix is to find roots of this equation for a given small but finite value of τ, other than those close to the roots of $1 + H(s)$. The nominal open-loop transfer function is expressed as a rational function of s as

$$H(s) = \frac{\sum_{m=0}^{M} b_m s^m}{\sum_{n=0}^{N} a_n s^n}. \tag{B.2}$$

When this transfer function is proper ($N \geq M$), roots emanate from $-\infty$, where the asymptotic behavior of H is given by

$$H(s) \overset{|s|\to\infty}{\to} \frac{b_M}{a_N} s^{M-N} \tag{B.3}$$

The solutions of Equation (B.1) thus satisfy

$$e^{-s\tau} - \left(\frac{s\tau}{H(s)} + 1\right) = 0 \overset{|s|\to\infty}{\to} e^{-s\tau} - \left(\frac{a_N}{b_M} s^{N-M+1}\tau + 1\right) = 0. \tag{B.4}$$

When $N - M + 1 > 0$ (i.e., for proper $H(s)$), the constant 1 becomes negligible, and this equation can be rewritten

$$e^{-s\tau} = Ks^p, \tag{B.5}$$

with $K = \tau a_N / b_M$ and $p = N - M + 1$. This equation is simpler but still transcendental and still challenging to solve as such. We note that

(i) If p is odd and $K < 0$ or if p is even and $K > 0$, this equation has a negative real root.

(ii) If p is even and $K < 0$ or if p is odd and $K < 0$, this equation does not have a negative real root.

Assuming $s = s_r + js_i$, Equation (B.5) is satisfied in magnitude if

$$e^{-s_r\tau} = |K| \left(s_r^2 + s_i^2\right)^{p/2}. \tag{B.6}$$

It is first attempted to locate the roots on or close to the real axis, by assuming that $|s_i| \ll |s_r|$, i.e.,

$$e^{-s_r\tau} \approx |K|\,|s_r|^p\,. \tag{B.7}$$

The logarithm of this equation yields

$$s_r\tau + \log|K| + p\log|s_r| = 0, \tag{B.8}$$

and since a negative value of s_r is sought, this expression can also be rewritten as

$$s_r\tau + \log|K| + p\log(-s_r) = 0. \tag{B.9}$$

The derivative of this expression is

$$\tau + \frac{p}{s_r}, \tag{B.10}$$

which shows that it only has one extremum at

$$s_r = -\frac{p}{\tau}, \tag{B.11}$$

and that it is a concave function. Therefore, if Newton's method is used to solve Equation (B.9) with an initial guess smaller than this value, the method is guaranteed to find the desired root. Expanding Equation (B.9) in a second-order Taylor series around $s_r = -p/\tau$ and taking the smallest root gives an initial guess

$$s_r^{(0)} = -\frac{p}{\tau}\left[1 - \sqrt{2\log\frac{p}{\tau} + \frac{2}{p}\log|K| - \frac{1}{2}}\right] \tag{B.12}$$

which can be iteratively corrected with Newton's method

$$s_r^{(k+1)} = s_r^{(k)} - \frac{s_r^{(k)}\tau + \log|K| + p\log\left(-s_r^{(k)}\right)}{\tau + \dfrac{p}{s_r^{(k)}}}. \tag{B.13}$$

The iterations can stop once Equation (B.9) is solved up to a prescribed tolerance value. The resulting value, noted $s_{r,0}$ gives an estimate of the magnitude of the roots.

Using the estimate $s_{r,0}$ in Equation (B.6) and neglecting the polynomial s_r^p term in front of the exponential one, the following simplified magnitude equation is obtained

$$e^{-\tau s_r} \approx |K|\left(s_{r,0}^2 + s_i^2\right)^{p/2}, \tag{B.14}$$

which allows to express the real part of the roots as an explicit function of their imaginary part

$$s_r(s_i) = -\frac{1}{\tau}\left[\log|K| + \frac{p}{2}\log\left(s_{r,0}^2 + s_i^2\right)\right]. \tag{B.15}$$

To find a suitable initial guess for s_i, the point $s_r(s_i) + js_i$ should be chosen such that Equation (B.5) is satisfied in phase:

$$-\tau s_i = \angle\left(K(s_r(s_i) + js_i)^p\right) \tag{B.16}$$

In case (i)

$$\tan\left(\frac{-\tau s_i + 2k\pi}{p}\right) = \frac{s_i}{s_r(s_i)}, \qquad k \in \mathbb{Z}, \tag{B.17}$$

whereas in case (ii)

$$\tan\left(\frac{-\tau s_i + \pi + 2k\pi}{p}\right) = \frac{s_i}{s_r(s_i)}, \qquad k \in \mathbb{Z}. \tag{B.18}$$

It can be noted that Equations (B.17) and (B.18) are both odd functions of s_i. Substituting s_i for $-s_i$ for simplicity, these equations can be solved approximately using series expansions around specific points, in a similar spirit to [258]. The procedure to solve case (i) is explained hereafter, and a similar approach can be followed for case (ii). Since $-s_i/s_r(-s_i) > 0$, the tangent function must be positive, and thus its argument must be in the interval $[0, \pi/2[$. In these intervals, the tangent function can be approximated by its linearized version around 0 or its linearized inverse around $\pi/2$ as

$$\tan\left(\frac{\tau s_i + 2k\pi}{p}\right) \approx \begin{cases} \dfrac{\tau s_i + 2k\pi}{p}, & \dfrac{\tau s_i + 2k\pi}{p} \in \left[0, \dfrac{\pi}{4}\right[\\ \left(\dfrac{\pi}{2} - \dfrac{\tau s_i + 2k\pi}{p}\right)^{-1}, & \dfrac{\tau s_i + 2k\pi}{p} \in \left[\dfrac{\pi}{4}, \dfrac{\pi}{2}\right[\end{cases}. \tag{B.19}$$

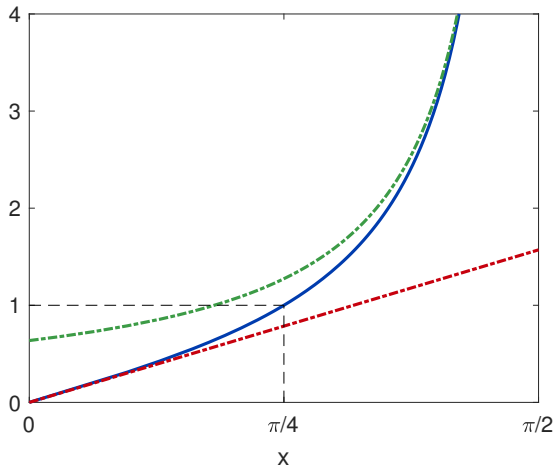

Figure B.1: $\tan(x)$ (—), its approximation for $x \in [0, \pi/4[$ (-·-) and for $x \in [\pi/4, \pi/2[$ (-··-).

Figure B.1 depicts these two possible approximations. To choose which one best represents the tangent function around the sought root, the value of the right-hand side of Equation (B.17) or (B.18) can be computed when the argument of the tangent function is equal to $\pi/4$, i.e.,

$$\tau s_{i,0} = \frac{p\pi}{4} + 2k\pi. \tag{B.20}$$

Then, depending on the value of the right-hand side, the tangent approximation and point $s_{i,1}$ around which the linearization is made are determined by the following conditions:

(a) If $-s_{i,0}/s_r(-s_{i,0}) < \tan(\pi/4) = 1$, the first approximation is the best and one sets $\tau s_{i,1} = 2k\pi$.

(b) If $-s_{i,0}/s_r(-s_{i,0}) > \tan(\pi/4) = 1$, the second approximation is the best and one sets $\tau s_{i,1} = p\pi/2 + 2k\pi$.

The right-hand side of Equation (B.17) can also be linearized. To be consistent with the tangent approximation, a linearized approximation of $-s_i/s_r(-s_i)$ (or $s_r(-s_i)/s_i$) around $s_{i,1}$ is chosen in case (a) (case (b)).

$$-\frac{s_i}{s_r(-s_i)} \approx \begin{cases} -\dfrac{s_{i,1}}{s_r(-s_{i,1})} + (s_i - s_{i,1})\dfrac{\partial}{\partial s_i}\left(-\dfrac{s_i}{s_r(-s_i)}\right)\Big|_{s_i=s_{i,1}}, & \text{case (a)} \\ \left(-\dfrac{s_r(-s_{i,1})}{s_{i,1}} + (s_i - s_{i,1})\dfrac{\partial}{\partial s_i}\left(-\dfrac{s_r(-s_i)}{s_i}\right)\Big|_{s_i=s_{i,1}}\right)^{-1}, & \text{case (b)} \end{cases}. \tag{B.21}$$

By equating Equations (B.19) and (B.21), an initial guess can be found for s_i.

To sum up, the procedure to find an initial guess of the first N_r roots of Equation (B.5) (with positive imaginary parts) goes as follows. For each value of k in $[0, \cdots, N_r - 1]$,

1. Set
$$\tau s_{i,0} = \begin{cases} \dfrac{p\pi}{4} + 2k\pi, & \text{case (i)} \\ \dfrac{p\pi}{4} + \pi + 2k\pi, & \text{case (ii)}. \end{cases} \tag{B.22}$$
2. Compute $f_0 = -s_{i,0}/s_r(-s_{i,0})$ (Equation (B.15)).
   a) If $f_0 < 1$ (case (a)), set
   $$\tau s_{i,1} = \begin{cases} 2k\pi, & \text{case (i)} \\ \pi + 2k\pi, & \text{case (ii)}. \end{cases}, \tag{B.23}$$
   compute $-s_i/s_r(-s_i)$ and its derivative at $s_i = s_{i,1}$, equate Equations (B.19) and (B.21) and solve for s_i
   $$s_i = s_{i,1} - \frac{s_{i,1}}{s_r(-s_{i,1})}\frac{1}{1 + \dfrac{\partial}{\partial s_i}\left(\dfrac{s_i}{s_r(-s_i)}\right)\Big|_{s_i=s_{i,1}}} \tag{B.24}$$
   b) If $f_0 > 1$ (case (b)),set
   $$\tau s_{i,1} = \begin{cases} \dfrac{p\pi}{2} + 2k\pi, & \text{case (i)} \\ \dfrac{p\pi}{2} + \pi + 2k\pi, & \text{case (ii)}. \end{cases}, \tag{B.25}$$
   compute $-s_r(-s_i)/s_i$ and its derivative at $s_i = s_{i,1}$, equate Equations (B.19) and (B.21) and solve for s_i
   $$s_i = s_{i,1} + \frac{s_r(-s_{i,1})}{s_{i,1}}\frac{1}{1 - \dfrac{\partial}{\partial s_i}\left(\dfrac{s_r(-s_i)}{s_i}\right)\Big|_{s_i=s_{i,1}}} \tag{B.26}$$

3. Compute $s_r(s_i)$ and set $s = s_r + js_i$.

4. If needed, correct the initial guess numerically with root-finding techniques, such as the Newton-Raphson method.

Figure B.2 features two examples comparing the initial estimates of the roots obtained with the proposed method to their values obtained by numerically solving Equation (B.5)[1]. These examples show that Equation (B.15) is an excellent approximation to find the real part of the roots. As for the imaginary part, the main source of error comes from the approximation made in Equation (B.19). It is excellent for small and high imaginary parts. For intermediate values, the initial guess is not as accurate, but can nonetheless be corrected with a Newton-Raphson procedure.

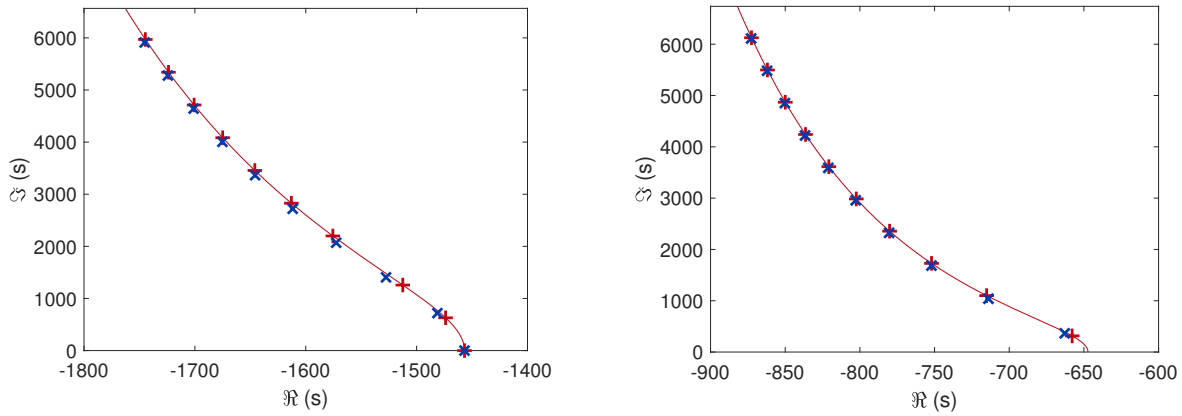

(a) (b)

Figure B.2: Ten roots (with smallest absolute imaginary part) of the transcendental equations $e^{-s\tau} = Ks^p$ for $K = 1$, $\tau = 10^{-2}$ and $p = 1$ (a) and $p = 2$ (b). — : Equation (B.15), +: approximate roots, ×: exact roots.

[1]The logarithm of this equation was solved to avoid bad numerical conditioning.

C Appendix to Chapter 2

C.1 State-space models of multiple-branch circuits

The state variables are chosen as the voltages or flux linkages across the capacitors and the currents through the inductors. Depending on the considered circuit, either an admittance model (voltage input and current output) or an impedance model (current input and voltage output) can be derived.

C.1.1 Hollkamp's circuit

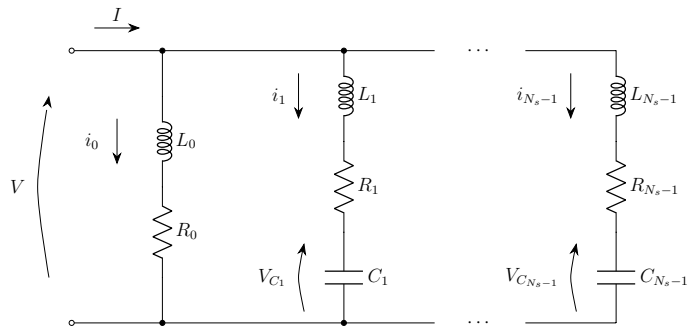

Figure C.1: Hollkamp's shunt circuit.

Figure C.1 depicts the quantities used to build the state-space model of Hollkamp's shunt circuit. The application of KVL to branches 0 and $k > 0$ respectively yields

$$\dot{i}_0 = \frac{1}{L_0}\left(V - R_0 i_0\right) \tag{C.1}$$

and

$$\dot{i}_k = \frac{1}{L_k}\left(V - R_k i_k - V_{C,k}\right), \qquad k = 1, \cdots, N_s - 1. \tag{C.2}$$

The voltage across capacitor k is governed by

$$\dot{V}_{C,k} = \frac{1}{C_k} i_k, \qquad k = 1, \cdots, N_s - 1. \tag{C.3}$$

The output current is finally given by

$$I = \sum_{i=0}^{N_s-1} i_k \tag{C.4}$$

Introducing the matrices of electrical parameters

$$\mathbf{L}_H = \begin{bmatrix} L_0 & & \\ & \ddots & \\ & & L_{N_s-1} \end{bmatrix}, \quad \mathbf{R}_H = \begin{bmatrix} R_0 & & \\ & \ddots & \\ & & R_{N_s-1} \end{bmatrix}, \quad \mathbf{E}_H = \begin{bmatrix} 0 & & & \\ & \frac{1}{C_1} & & \\ & & \ddots & \\ & & & \frac{1}{C_{N_s-1}} \end{bmatrix} \tag{C.5}$$

and the vector of electrical charges

$$\mathbf{q}^T = \begin{bmatrix} q_0 & q_1 & \cdots & q_{N_s-1} \end{bmatrix}, \tag{C.6}$$

the state evolution equations become

$$\begin{bmatrix} \dot{\mathbf{q}} \\ \ddot{\mathbf{q}} \end{bmatrix} = \begin{bmatrix} \mathbf{0} & \mathbf{I} \\ -\mathbf{L}_H^{-1}\mathbf{E}_H & -\mathbf{L}_H^{-1}\mathbf{R}_H \end{bmatrix} \begin{bmatrix} \mathbf{q} \\ \dot{\mathbf{q}} \end{bmatrix} + \begin{bmatrix} \mathbf{0} \\ \mathbf{L}_H^{-1}\mathbf{1}_{N_s\times 1} \end{bmatrix} V \tag{C.7}$$

and the output equation is

$$I = \begin{bmatrix} \mathbf{0}_{1\times N_s} & \mathbf{1}_{1\times N_s} \end{bmatrix} \begin{bmatrix} \mathbf{q} \\ \dot{\mathbf{q}} \end{bmatrix}. \tag{C.8}$$

This circuit does not have a state-space impedance model because its impedance is an improper transfer function.

C.1.2 Current flowing circuit

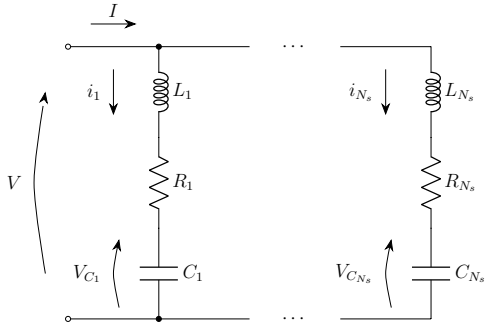

Figure C.2: Current flowing shunt circuit.

Figure C.2 depicts the quantities used to build the state-space model of the CF shunt circuit. Following the same lines as for Hollkamp's shunt circuit, KVL applied to branch k gives

$$\dot{i}_k = \frac{1}{L_k}\left(V - R_k i_k - V_{C,k}\right), \qquad k = 1, \cdots, N_s, \tag{C.9}$$

and the voltage across capacitor k is governed by

$$\dot{V}_{C,k} = \frac{1}{C_k} i_k, \qquad k = 1, \cdots, N_s. \tag{C.10}$$

The output current is finally given by

$$I = \sum_{i=1}^{N_s} i_k \tag{C.11}$$

Introducing the matrices of electrical parameters

$$\mathbf{L}_{CF} = \begin{bmatrix} L_1 & & \\ & \ddots & \\ & & L_{N_s} \end{bmatrix}, \quad \mathbf{R}_{CF} = \begin{bmatrix} R_1 & & \\ & \ddots & \\ & & R_{N_s} \end{bmatrix}, \quad \mathbf{E}_{CF} = \begin{bmatrix} \frac{1}{C_1} & & \\ & \ddots & \\ & & \frac{1}{C_{N_s}} \end{bmatrix} \tag{C.12}$$

and the vector of electrical charges

$$\mathbf{q}^T = \begin{bmatrix} q_1 & \cdots & q_{N_s} \end{bmatrix}, \tag{C.13}$$

the state evolution equations are

$$\begin{bmatrix} \dot{\mathbf{q}} \\ \ddot{\mathbf{q}} \end{bmatrix} = \begin{bmatrix} \mathbf{0} & \mathbf{I} \\ -\mathbf{L}_{CF}^{-1}\mathbf{E}_{CF} & -\mathbf{L}_{CF}^{-1}\mathbf{R}_{CF} \end{bmatrix} \begin{bmatrix} \mathbf{q} \\ \dot{\mathbf{q}} \end{bmatrix} + \begin{bmatrix} \mathbf{0} \\ \mathbf{L}_{CF}^{-1}\mathbf{1}_{N_s \times 1} \end{bmatrix} V \tag{C.14}$$

and the output equation is

$$I = \begin{bmatrix} \mathbf{0}_{1 \times N_s} & \mathbf{1}_{1 \times N_s} \end{bmatrix} \begin{bmatrix} \mathbf{q} \\ \dot{\mathbf{q}} \end{bmatrix}. \tag{C.15}$$

This circuit does not have a state-space impedance model because its impedance is an improper transfer function.

C.1.3 Second Foster canonical form

C.1.3.1 Impedance model

Based on Figure C.3, the application of KCL to the parallel RL circuit gives

$$I = \frac{1}{L_0} \int V_0 dt + \frac{1}{R_0} V_0 = \frac{1}{L_0} \psi_0 + \frac{1}{R_0} \dot{\psi}_0, \tag{C.16}$$

and the application of KCL to the parallel RLC circuits yields

$$I = \frac{1}{L_k} \int V_k dt + \frac{1}{R_k} V_k + C_k \dot{V}_k = \frac{1}{L_k} \psi_k + \frac{1}{R_k} \dot{\psi}_k + C_k \ddot{\psi}_k, \qquad k = 1, \cdots, N_s - 1. \tag{C.17}$$

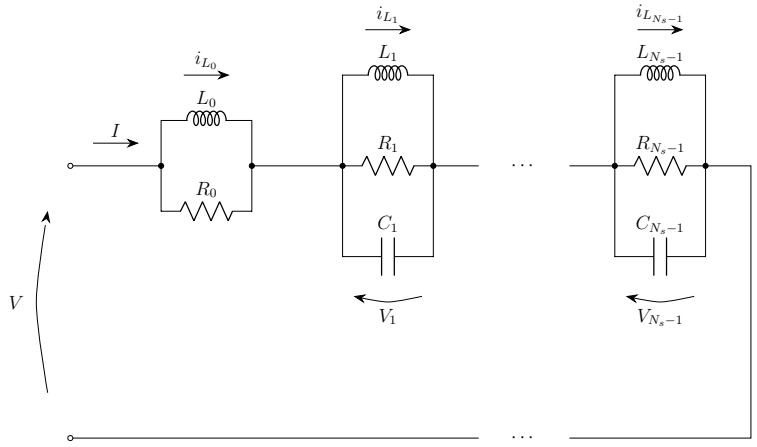

Figure C.3: Second Foster canonical form shunt circuit.

The output voltage is eventually obtained as the sum of all voltages across the parallel circuits as

$$V = \sum_{k=0}^{N_s-1} V_k = \sum_{k=0}^{N_s-1} \dot{\psi}_k. \tag{C.18}$$

Introducing the matrices of electrical parameters

$$\mathbf{B}_{SFCF} = \begin{bmatrix} \dfrac{1}{L_1} & & \\ & \ddots & \\ & & \dfrac{1}{L_{N_s-1}} \end{bmatrix}, \quad \mathbf{G}_{SFCF} = \begin{bmatrix} \dfrac{1}{R_1} & & \\ & \ddots & \\ & & \dfrac{1}{R_{N_s-1}} \end{bmatrix},$$

$$\mathbf{C}_{SFCF} = \begin{bmatrix} C_1 & & \\ & \ddots & \\ & & C_{N_s-1} \end{bmatrix} \tag{C.19}$$

and the vector of flux linkages

$$\boldsymbol{\psi}^T = \begin{bmatrix} \psi_1 & \cdots & \psi_{N_s-1} \end{bmatrix}, \tag{C.20}$$

the state evolution equations become

$$\begin{bmatrix} \dot{\boldsymbol{\psi}} \\ \dot{\psi}_0 \\ \ddot{\boldsymbol{\psi}} \end{bmatrix} = \begin{bmatrix} \mathbf{0} & \mathbf{0} & \mathbf{I} \\ \mathbf{0} & -\dfrac{R_0}{L_0} & \mathbf{0} \\ -\mathbf{C}_{SFCF}^{-1}\mathbf{B}_{SFCF} & \mathbf{0} & -\mathbf{C}_{SFCF}^{-1}\mathbf{G}_{SFCF} \end{bmatrix} \begin{bmatrix} \boldsymbol{\psi} \\ \psi_0 \\ \dot{\boldsymbol{\psi}} \end{bmatrix} + \begin{bmatrix} \mathbf{0} \\ R_0 \\ \mathbf{C}_{SFCF}^{-1}\mathbf{1}_{(N_s-1)\times 1} \end{bmatrix} I \tag{C.21}$$

and the output equation is

$$V = \begin{bmatrix} \mathbf{0}_{1\times(N_s-1)} & -\dfrac{R_0}{L_0} & \mathbf{1}_{1\times(N_s-1)} \end{bmatrix} \begin{bmatrix} \boldsymbol{\psi} \\ \psi_0 \\ \dot{\boldsymbol{\psi}} \end{bmatrix} + R_0 I. \tag{C.22}$$

C.1.3.2 Admittance model

An admittance model can be derived directly from the impedance model, using the same state variables. From Equation (C.22), the output current is expressed as

$$I = \begin{bmatrix} \mathbf{0}_{1\times(N_s-1)} & \dfrac{1}{L_0} & -\dfrac{1}{R_0}\mathbf{1}_{1\times(N_s-1)} \end{bmatrix} \begin{bmatrix} \boldsymbol{\psi} \\ \psi_0 \\ \dot{\boldsymbol{\psi}} \end{bmatrix} + \frac{1}{R_0} V, \tag{C.23}$$

which gives the output equation. The state evolution equation can be found by inserting this relation in Equation (C.21), yielding

$$\begin{bmatrix} \dot{\boldsymbol{\psi}} \\ \dot{\psi}_0 \\ \ddot{\boldsymbol{\psi}} \end{bmatrix} = \left(\begin{bmatrix} \mathbf{0} & \mathbf{0} & \mathbf{I} \\ \mathbf{0} & -\dfrac{R_0}{L_0} & \mathbf{0} \\ -\mathbf{C}_{SFCF}^{-1}\mathbf{B}_{SFCF} & \mathbf{0} & -\mathbf{C}_{SFCF}^{-1}\mathbf{G}_{SFCF} \end{bmatrix} + \begin{bmatrix} \mathbf{0} \\ R_0 \\ \mathbf{C}_{SFCF}^{-1}\mathbf{1}_{(N_s-1)\times 1} \end{bmatrix} \begin{bmatrix} \mathbf{0}_{(N_s-1)\times 1} \\ \dfrac{1}{L_0} \\ -\dfrac{1}{R_0}\mathbf{1}_{(N_s-1)\times 1} \end{bmatrix}^T \right) \begin{bmatrix} \boldsymbol{\psi} \\ \psi_0 \\ \dot{\boldsymbol{\psi}} \end{bmatrix} + \begin{bmatrix} \mathbf{0} \\ 1 \\ \dfrac{1}{R_0}\mathbf{C}_{SFCF}^{-1}\mathbf{1}_{(N_s-1)\times 1} \end{bmatrix} V. \tag{C.24}$$

C.1.4 Series-parallel impedance structure

Following the same lines as for the impedance model of the SFCF circuit, the application of KCL to the parallel RLC circuits yields

$$I = \frac{1}{L_k}\int V_k dt + \frac{1}{R_k} V_k + C_k \dot{V}_k = \frac{1}{L_k}\psi_k + \frac{1}{R_k}\dot{\psi}_k + C_k \ddot{\psi}_k, \qquad k = 1, \cdots, N_s, \tag{C.25}$$

and the output voltage is obtained as the sum of all voltages across the parallel circuits as

$$V = \sum_{k=1}^{N_s} V_k = \sum_{k=1}^{N_s} \dot{\psi}_k. \tag{C.26}$$

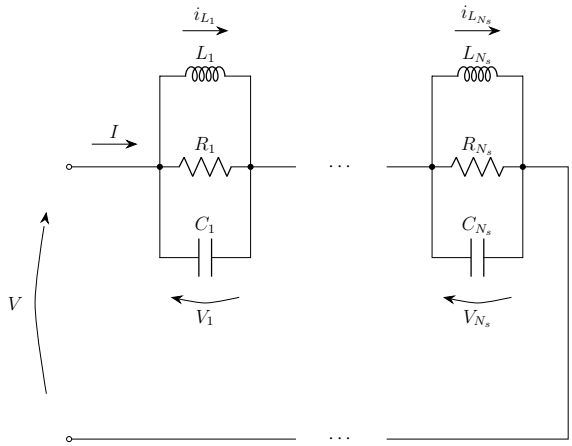

Figure C.4: Series-parallel impedance structure shunt circuit.

Introducing the matrices of electrical parameters

$$\mathbf{B}_{SPIS} = \begin{bmatrix} \frac{1}{L_1} & & \\ & \ddots & \\ & & \frac{1}{L_{N_s}} \end{bmatrix}, \quad \mathbf{G}_{SPIS} = \begin{bmatrix} \frac{1}{R_1} & & \\ & \ddots & \\ & & \frac{1}{R_{N_s}} \end{bmatrix}, \quad \mathbf{C}_{SPIS} = \begin{bmatrix} C_1 & & \\ & \ddots & \\ & & C_{N_s} \end{bmatrix} \tag{C.27}$$

and the vector of flux linkages

$$\boldsymbol{\psi}^T = \begin{bmatrix} \psi_1 & \cdots & \psi_{N_s} \end{bmatrix}, \tag{C.28}$$

the state evolution equation becomes

$$\begin{bmatrix} \dot{\boldsymbol{\psi}} \\ \ddot{\boldsymbol{\psi}} \end{bmatrix} = \begin{bmatrix} \mathbf{0} & \mathbf{I} \\ -\mathbf{C}_{SPIS}^{-1}\mathbf{B}_{SPIS} & -\mathbf{C}_{SPIS}^{-1}\mathbf{G}_{SPIS} \end{bmatrix} \begin{bmatrix} \boldsymbol{\psi} \\ \dot{\boldsymbol{\psi}} \end{bmatrix} + \begin{bmatrix} \mathbf{0} \\ \mathbf{C}_{SPIS}^{-1}\mathbf{1}_{N_s\times 1} \end{bmatrix} I \tag{C.29}$$

and the output equation is

$$V = \begin{bmatrix} \mathbf{0}_{1\times N_s} & \mathbf{1}_{1\times N_s} \end{bmatrix} \begin{bmatrix} \boldsymbol{\psi} \\ \dot{\boldsymbol{\psi}} \end{bmatrix}. \tag{C.30}$$

This circuit does not have a state-space admittance model because its admittance is an improper transfer function.

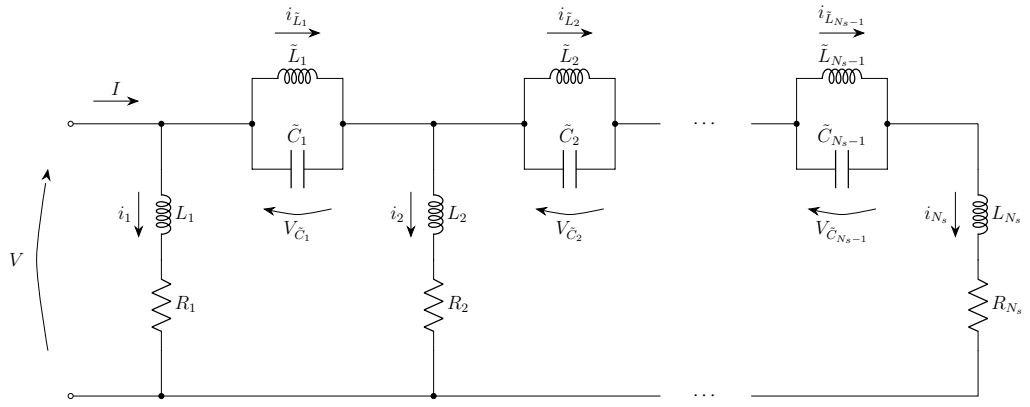

Figure C.5: Current blocking circuit with series RL shunts.

C.1.5 Current blocking circuit

C.1.5.1 Circuit with series RL shunts

The currents flowing through the filter inductors are governed by

$$\dot{i}_{\tilde{L}_k} = \frac{1}{\tilde{L}_k} V_{\tilde{C}_k} \tag{C.31}$$

while the voltages across the filter capacitors are governed by

$$\dot{V}_{\tilde{C}_k} = \frac{1}{\tilde{C}_k} \left(\tilde{i}_k - i_{\tilde{L}_k} \right), \tag{C.32}$$

where $\tilde{i}_k$ is the total current going through the filter. The currents flowing through the shunt inductors are given by

$$\dot{i}_k = -\frac{R_k}{L_k} i_k + \frac{1}{L_k} V_k \tag{C.33}$$

Using KVL, the voltage across each shunt is given by

$$V_k = V - \sum_{i=1}^{k-1} V_{\tilde{C}_i} \tag{C.34}$$

and using KCL, the currents through the filters are found as

$$\tilde{i}_k = \sum_{i=k+1}^{N} i_i. \tag{C.35}$$

Finally, the output equation is

$$I = \sum_{i=1}^{N} i_i. \tag{C.36}$$

Introducing the vectors of electrical charges and currents

$$\mathbf{q}^T = \begin{bmatrix} q_1 & \cdots & q_{N_s} \end{bmatrix}, \qquad \mathbf{q}_{\tilde{C}}^T = \begin{bmatrix} q_{\tilde{C}_1} & \cdots & q_{\tilde{C}_{N_s-1}} \end{bmatrix}, \qquad \dot{\mathbf{q}}_{\tilde{L}}^T = \begin{bmatrix} \dot{q}_{\tilde{L}_1} & \cdots & \dot{q}_{\tilde{L}_{N_s-1}} \end{bmatrix}, \tag{C.37}$$

the matrices of electrical parameters

$$\mathbf{L}_{CB} = \begin{bmatrix} L_1 & & \\ & \ddots & \\ & & L_{N_s} \end{bmatrix}, \qquad \mathbf{R}_{CB} = \begin{bmatrix} R_1 & & \\ & \ddots & \\ & & R_{N_s} \end{bmatrix}, \tag{C.38}$$

$$\tilde{\mathbf{L}}_{CB} = \begin{bmatrix} \tilde{L}_1 & & \\ & \ddots & \\ & & \tilde{L}_{N_s-1} \end{bmatrix}, \qquad \tilde{\mathbf{E}}_{CB} = \begin{bmatrix} \dfrac{1}{\tilde{C}_1} & & \\ & \ddots & \\ & & \dfrac{1}{\tilde{C}_{N_s-1}} \end{bmatrix}, \tag{C.39}$$

and the upper triangular matrix $\mathbf{T}_{CB}$ given by

$$\mathbf{T}_{CB} = \begin{bmatrix} 0 & 1 & 1 & \cdots & 1 \\ 0 & 0 & 1 & \cdots & 1 \\ \vdots & \vdots & \ddots & \ddots & \vdots \\ 0 & 0 & 0 & \cdots & 1 \end{bmatrix}, \tag{C.40}$$

the state evolution equations read

$$\begin{bmatrix} \dot{\mathbf{q}} \\ \ddot{\mathbf{q}} \\ \dot{\mathbf{q}}_{\tilde{C}} \\ \ddot{\mathbf{q}}_{\tilde{L}} \end{bmatrix} = \begin{bmatrix} \mathbf{0} & \mathbf{I} & \mathbf{0} & \mathbf{0} \\ \mathbf{0} & -\mathbf{L}_{CB}^{-1}\mathbf{R}_{CB} & -\mathbf{L}_{CB}^{-1}\mathbf{T}_{CB}^{T}\tilde{\mathbf{E}}_{CB} & \mathbf{0} \\ \mathbf{0} & \mathbf{T}_{CB} & \mathbf{0} & -\mathbf{I} \\ \mathbf{0} & \mathbf{0} & \tilde{\mathbf{L}}_{CB}^{-1}\tilde{\mathbf{E}}_{CB} & \mathbf{0} \end{bmatrix} \begin{bmatrix} \mathbf{q} \\ \dot{\mathbf{q}} \\ \mathbf{q}_{\tilde{C}} \\ \dot{\mathbf{q}}_{\tilde{L}} \end{bmatrix} + \begin{bmatrix} \mathbf{0} \\ \mathbf{L}_{CB}^{-1}\mathbf{1}_{N_s\times 1} \\ \mathbf{0} \\ \mathbf{0} \end{bmatrix} V \tag{C.41}$$

and the output equation reads

$$I = \begin{bmatrix} \mathbf{0}_{1\times N_s} & \mathbf{1}_{1\times N_s} & \mathbf{0}_{1\times(N_s-1)} & \mathbf{0}_{1\times(N_s-1)} \end{bmatrix} \begin{bmatrix} \mathbf{q} \\ \dot{\mathbf{q}} \\ \mathbf{q}_{\tilde{C}} \\ \dot{\mathbf{q}}_{\tilde{L}} \end{bmatrix}. \tag{C.42}$$

This circuit does not have a state-space impedance model because its impedance is an improper transfer function.

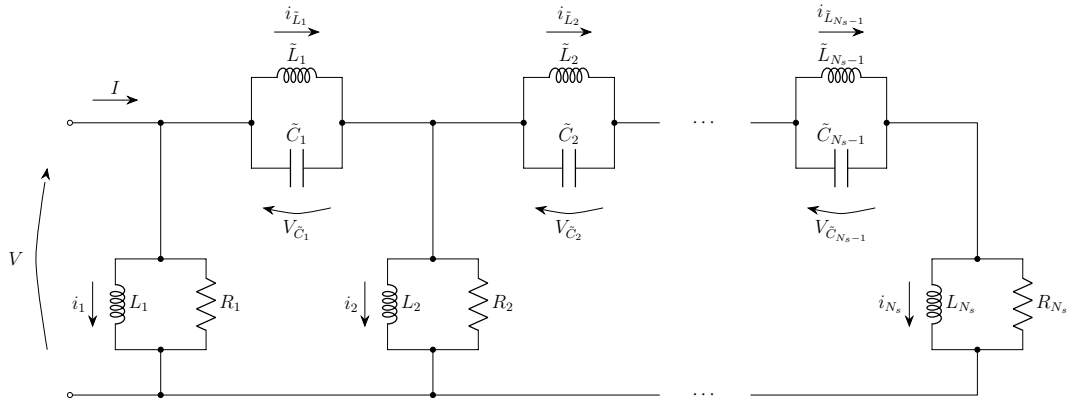

Figure C.6: Current blocking circuit with parallel RL shunts.

C.1.5.2 Circuit with parallel RL shunts

Similarly to the CB with series RL shunts, the filters dynamics are governed by

$$\dot{i}_{\tilde{L}_k} = \frac{1}{\tilde{L}_k} V_{\tilde{C}_k} \tag{C.43}$$

and

$$\dot{V}_{\tilde{C}_k} = \frac{1}{\tilde{C}_k} \left(\tilde{i}_k - i_{\tilde{L}_k} \right), \tag{C.44}$$

where $\tilde{i}_k$ is the total current going through the filter. Using KVL, the voltage across each shunt is given by

$$V_k = V - \sum_{i=1}^{k-1} V_{\tilde{C}_i}, \tag{C.45}$$

and the current in the shunt inductor is this time governed by

$$\dot{i}_k = \frac{V_k}{L_k} = \frac{1}{L_k} \left(V - \sum_{i=1}^{k-1} V_{\tilde{C}_i} \right). \tag{C.46}$$

The total current going through the shunts can also be determined by

$$i_k + \frac{V_k}{R_k} = i_k + \frac{1}{R_k} \left(V - \sum_{i=1}^{k-1} V_{\tilde{C}_i} \right) \tag{C.47}$$

Using KCL, the currents through the filters are found as

$$\tilde{i}_k = \sum_{i=k+1}^{N_s} \left(i_i + \frac{1}{R_i} \left(V - \sum_{l=1}^{i-1} V_{\tilde{C}_l} \right) \right). \tag{C.48}$$

Combining these relations, the state evolution equations read

$$\begin{bmatrix} \dot{\mathbf{q}} \\ \ddot{\mathbf{q}} \\ \dot{\mathbf{q}}_{\tilde{C}} \\ \ddot{\mathbf{q}}_{\tilde{L}} \end{bmatrix} = \begin{bmatrix} \mathbf{0} & \mathbf{I} & \mathbf{0} & \mathbf{0} \\ \mathbf{0} & \mathbf{0} & -\mathbf{L}_{CB}^{-1} \mathbf{T}_{CB}^T \tilde{\mathbf{E}}_{CB} & \mathbf{0} \\ \mathbf{0} & \mathbf{T}_{CB} & -\mathbf{T}_{CB} \mathbf{R}_{CB}^{-1} \mathbf{T}_{CB}^T \tilde{\mathbf{E}}_{CB} & -\mathbf{I} \\ \mathbf{0} & \mathbf{0} & \tilde{\mathbf{L}}_{CB}^{-1} \tilde{\mathbf{E}}_{CB} & \mathbf{0} \end{bmatrix} \begin{bmatrix} \mathbf{q} \\ \dot{\mathbf{q}} \\ \mathbf{q}_{\tilde{C}} \\ \dot{\mathbf{q}}_{\tilde{L}} \end{bmatrix} + \begin{bmatrix} \mathbf{0} \\ \mathbf{L}_{CB}^{-1} \mathbf{1}_{N_s \times 1} \\ \mathbf{T}_{CB} \mathbf{R}_{CB}^{-1} \mathbf{1}_{N_s \times 1} \\ \mathbf{0} \end{bmatrix} V \tag{C.49}$$

and the output equation reads

$$I = \begin{bmatrix} \mathbf{0}_{1\times N_s} & \mathbf{1}_{1\times N_s} & \mathbf{1}_{1\times N_s}\mathbf{R}_{CB}^{-1}\mathbf{T}_{CB}^{T}\tilde{\mathbf{E}}_{CB} & \mathbf{0}_{1\times(N_s-1)} \end{bmatrix} \begin{bmatrix} \mathbf{q} \\ \dot{\mathbf{q}} \\ \mathbf{q}_{\tilde{C}} \\ \dot{\mathbf{q}}_{\tilde{L}} \end{bmatrix} + \mathbf{1}_{1\times N_s}\mathbf{R}_{CB}^{-1}\mathbf{1}_{N_s\times 1} V. \quad \text{(C.50)}$$

An impedance model can also be derived directly from this admittance model following the same procedure as in Section C.1.3.2. The global resistance of the CB circuit with parallel shunts is expressed as

$$R_{CBP} = \frac{1}{\mathbf{1}_{1\times N_s}\mathbf{R}_{CB}^{-1}\mathbf{1}_{N_s\times 1}} \quad \text{(C.51)}$$

From Equation (C.50) the output voltage is expressed as

$$V = -R_{CBP} \begin{bmatrix} \mathbf{0}_{1\times N_s} & \mathbf{1}_{1\times N_s} & \mathbf{1}_{1\times N_s}\mathbf{R}_{CB}^{-1}\mathbf{T}_{CB}^{T}\tilde{\mathbf{E}}_{CB} & \mathbf{0}_{1\times(N_s-1)} \end{bmatrix} \begin{bmatrix} \mathbf{q} \\ \dot{\mathbf{q}} \\ \mathbf{q}_{\tilde{C}} \\ \dot{\mathbf{q}}_{\tilde{L}} \end{bmatrix} + R_{CBP} I. \quad \text{(C.52)}$$

Inserting this relation in Equation (C.49) eventually yields

$$\begin{bmatrix} \dot{\mathbf{q}} \\ \ddot{\mathbf{q}} \\ \dot{\mathbf{q}}_{\tilde{C}} \\ \ddot{\mathbf{q}}_{\tilde{L}} \end{bmatrix} = \left(\begin{bmatrix} \mathbf{0} & \mathbf{I} & \mathbf{0} & \mathbf{0} \\ \mathbf{0} & \mathbf{0} & -\mathbf{L}_{CB}^{-1}\mathbf{T}_{CB}^{T}\tilde{\mathbf{E}}_{CB} & \mathbf{0} \\ \mathbf{0} & \mathbf{T}_{CB} & -\mathbf{T}_{CB}\mathbf{R}_{CB}^{-1}\mathbf{T}_{CB}^{T}\tilde{\mathbf{E}}_{CB} & -\mathbf{I} \\ \mathbf{0} & \mathbf{0} & \tilde{\mathbf{L}}_{CB}^{-1}\tilde{\mathbf{E}}_{CB} & \mathbf{0} \end{bmatrix} - R_{CBP} \begin{bmatrix} \mathbf{0} \\ \mathbf{L}_{CB}^{-1}\mathbf{1}_{N_s\times 1} \\ \mathbf{T}_{CB}\mathbf{R}_{CB}^{-1}\mathbf{1}_{N_s\times 1} \\ \mathbf{0} \end{bmatrix} \begin{bmatrix} \mathbf{0}_{N_s\times 1} \\ \mathbf{1}_{N_s\times 1} \\ \tilde{\mathbf{E}}_{CB}\mathbf{T}_{CB}\mathbf{R}_{CB}^{-1}\mathbf{1}_{N_s\times 1} \\ \mathbf{0}_{(N_s-1)\times 1} \end{bmatrix}^{T} \right) \begin{bmatrix} \mathbf{q} \\ \dot{\mathbf{q}} \\ \mathbf{q}_{\tilde{C}} \\ \dot{\mathbf{q}}_{\tilde{L}} \end{bmatrix} + R_{CBP} \begin{bmatrix} \mathbf{0} \\ \mathbf{L}_{CB}^{-1}\mathbf{1}_{N_s\times 1} \\ \mathbf{T}_{CB}\mathbf{R}_{CB}^{-1}\mathbf{1}_{N_s\times 1} \\ \mathbf{0} \end{bmatrix} I. \quad \text{(C.53)}$$

D Appendix to Chapter 3

D.1 Evaluation of the electromechanical coupling factor

Often, the resonance frequencies of one type only (short-circuit or open-circuit) are known. It would thus be interesting to derive the other type of frequencies without performing another eigenvalue analysis or a measurement of the dual electrical transfer function. It is now assumed that the short-circuit modal characteristics are known. They can be split into a resonant mode (identified by the subscript r) and non-resonant modes (identified by the subscript nr) as

$$\boldsymbol{\eta}_{sc}^T = \left[\eta_{sc,r}\ \boldsymbol{\eta}_{sc,nr}^T\right], \qquad \boldsymbol{\Phi}_{sc} = \left[\boldsymbol{\phi}_{sc,r}\ \boldsymbol{\Phi}_{sc,nr}\right]. \tag{D.1}$$

For an unforced structure and imposing open-circuit conditions on the transducers, Equation (3.4) becomes

$$\begin{cases} \left(s^2 + \omega_{sc,r}^2\right)\eta_{sc,r} + \boldsymbol{\phi}_{sc,r}^T\boldsymbol{\Gamma}_p\mathbf{V} = 0 \\ \left(s^2\mathbf{I} + \boldsymbol{\Omega}_{sc,nr}^2\right)\boldsymbol{\eta}_{sc,nr} + \boldsymbol{\Phi}_{sc,nr}^T\boldsymbol{\Gamma}_p\mathbf{V} = \mathbf{0} \\ \boldsymbol{\Gamma}_p^T\boldsymbol{\Phi}_{sc,nr}\boldsymbol{\eta}_{sc,nr} + \boldsymbol{\Gamma}_p^T\boldsymbol{\phi}_{sc,r}\eta_{sc,r} - \mathbf{C}_p^\varepsilon\mathbf{V} = \mathbf{0} \end{cases}. \tag{D.2}$$

If the non-resonant modes are neglected, i.e., if $\boldsymbol{\eta}_{sc,nr} = \mathbf{0}$, Equation (D.2) becomes equivalent to Equation (1.6). Approximations of the open-circuit resonance frequency and of the EEMCF are thus given by

$$\omega_{oc,r}^2 \approx \omega_{sc,r}^2 + \boldsymbol{\phi}_{sc,r}^T\boldsymbol{\Gamma}_p\left(\mathbf{C}_p^\varepsilon\right)^{-1}\boldsymbol{\Gamma}_p^T\boldsymbol{\phi}_{sc,r} \tag{D.3}$$

and

$$K_{c,r}^2 \approx \frac{1}{\omega_{sc,r}^2}\boldsymbol{\phi}_{sc,r}^T\boldsymbol{\Gamma}_p\left(\mathbf{C}_p^\varepsilon\right)^{-1}\boldsymbol{\Gamma}_p^T\boldsymbol{\phi}_{sc,r}, \tag{D.4}$$

respectively. The approximation for the EEMCF is classically made in the literature [137, 259]. A more accurate estimate can be obtained by expressing the non-resonant modal amplitudes as a sole function of the voltages

$$\boldsymbol{\eta}_{sc,nr} = -\left(s^2\mathbf{I} + \boldsymbol{\Omega}_{sc,nr}^2\right)^{-1}\boldsymbol{\Phi}_{sc,nr}^T\boldsymbol{\Gamma}_p\mathbf{V}. \tag{D.5}$$

Inserting this relation into the electrical equation,

$$\boldsymbol{\Gamma}_p^T\boldsymbol{\phi}_{sc,r}\eta_{sc,r} = \left[\boldsymbol{\Gamma}_p^T\boldsymbol{\Phi}_{sc,nr}\left(s^2\mathbf{I} + \boldsymbol{\Omega}_{sc,nr}^2\right)^{-1}\boldsymbol{\Phi}_{sc,nr}^T\boldsymbol{\Gamma}_p + \mathbf{C}_p^\varepsilon\right]\mathbf{V}. \tag{D.6}$$

The right-hand side of this equation features a frequency-dependent matrix, which means that the voltages are dynamically related to the resonant modal coordinate. To simplify

the problem, a simple relation can be retrieved if only the static contribution from non-resonant modes is retained. For $s \approx j\omega_{sc,r}$, the diagonal matrix

$$\left(s^2\mathbf{I} + \mathbf{\Omega}_{sc,nr}^2\right)^{-1} \approx \begin{bmatrix} \mathbf{0} & \mathbf{0} \\ \mathbf{0} & \mathbf{\Omega}_{sc,>r}^{-2} \end{bmatrix}, \tag{D.7}$$

where $\mathbf{\Omega}_{sc,>r}$ is a diagonal matrix containing the short-circuit frequencies greater than $\omega_{sc,r}$. Inserting this approximation into Equation (D.6) and back into the resonant mechanical part of Equation (D.2), approximations of the open-circuit resonance frequency and of the EEMCF are obtained as

$$\omega_{oc,r}^2 \approx \omega_{sc,r}^2 + \boldsymbol{\phi}_{sc,r}^T \mathbf{\Gamma}_p \left[\mathbf{\Gamma}_p^T \mathbf{\Phi}_{sc,>r} \mathbf{\Omega}_{sc,>r}^{-2} \mathbf{\Phi}_{sc,>r}^T \mathbf{\Gamma}_p + \mathbf{C}_p^\varepsilon\right]^{-1} \mathbf{\Gamma}_p^T \boldsymbol{\phi}_{sc,r} \tag{D.8}$$

and

$$K_{c,r}^2 \approx \frac{1}{\omega_{sc,r}^2} \boldsymbol{\phi}_{sc,r}^T \mathbf{\Gamma}_p \left[\mathbf{\Gamma}_p^T \mathbf{\Phi}_{sc,>r} \mathbf{\Omega}_{sc,>r}^{-2} \mathbf{\Phi}_{sc,>r}^T \mathbf{\Gamma}_p + \mathbf{C}_p^\varepsilon\right]^{-1} \mathbf{\Gamma}_p^T \boldsymbol{\phi}_{sc,r}, \tag{D.9}$$

respectively.

If instead the open-circuit modal characteristics are known, the short-circuit resonance frequencies can be approximated by

$$\omega_{sc,r}^2 \approx \omega_{oc,r}^2 - \boldsymbol{\phi}_{oc,r}^T \mathbf{\Theta}_p \left[\mathbf{E}_p^\varepsilon - \mathbf{\Theta}_p^T \mathbf{\Phi}_{oc,>r} \mathbf{\Omega}_{oc,>r}^{-2} \mathbf{\Phi}_{oc,>r}^T \mathbf{\Theta}_p\right]^{-1} \mathbf{\Theta}_p^T \boldsymbol{\phi}_{oc,r}, \tag{D.10}$$

and the EEMCF is approximated by

$$K_{c,r}^2 \approx \frac{\boldsymbol{\phi}_{oc,r}^T \mathbf{\Theta}_p \left[\mathbf{E}_p^\varepsilon - \mathbf{\Theta}_p^T \mathbf{\Phi}_{oc,>r} \mathbf{\Omega}_{oc,>r}^{-2} \mathbf{\Phi}_{oc,>r}^T \mathbf{\Theta}_p\right]^{-1} \mathbf{\Theta}_p^T \boldsymbol{\phi}_{oc,r}}{\omega_{oc,r}^2 - \boldsymbol{\phi}_{oc,r}^T \mathbf{\Theta}_p \left[\mathbf{E}_p^\varepsilon - \mathbf{\Theta}_p^T \mathbf{\Phi}_{oc,>r} \mathbf{\Omega}_{oc,>r}^{-2} \mathbf{\Phi}_{oc,>r}^T \mathbf{\Theta}_p\right]^{-1} \mathbf{\Theta}_p^T \boldsymbol{\phi}_{oc,r}}. \tag{D.11}$$

A similar approximation was proposed by Fan et al [260], where the static contribution from all modes was taken into account (through the inversion of the stiffness matrix).

D.2 Optimal electrical mode shapes accounting for background contributions

From Equation (3.34) and using Equation (3.50), the EEMCF is expresed as

$$\widehat{K}_{c,rk}^2 = \frac{\left(\boldsymbol{\phi}_{sc,r}^T \mathbf{\Gamma}_p \left(\mathbf{C}_p^\varepsilon\right)^{-1/2} \boldsymbol{\varphi}_p\right)^2}{\left(1 + \boldsymbol{\varphi}_p^T \left(\mathbf{C}_p^\varepsilon\right)^{-1/2} \left(\widehat{\mathbf{C}}_{p,r}^\varepsilon - \mathbf{C}_p^\varepsilon\right) \left(\mathbf{C}_p^\varepsilon\right)^{-1/2} \boldsymbol{\varphi}_p\right) \omega_{sc,r}^2} = \frac{\left(\mathbf{u}_r^T \boldsymbol{\varphi}_p\right)^2}{\left(1 + \boldsymbol{\varphi}_p^T \mathbf{A}_r \boldsymbol{\varphi}_p\right) \omega_{sc,r}^2}, \tag{D.12}$$

where

$$\widehat{\mathbf{C}}_{p,r}^\varepsilon = \mathbf{C}_p^\varepsilon + \mathbf{\Gamma}_p^T \mathbf{\Phi}_{sc,>r} \mathbf{\Omega}_{sc,>r}^{-2} \mathbf{\Phi}_{sc,>r}^T \mathbf{\Gamma}_p. \tag{D.13}$$

is the effective capacitance matrix accounting for the influence of non-resonant mechanical modes.

When $\mathbf{A}_r = 0$, the optimal solution is given in Section 3.5.2.1 as

$$\boldsymbol{\varphi}_p^\star = \frac{\mathbf{u}_r}{||\mathbf{u}_r||} \tag{D.14}$$

When $\mathbf{A}_r \to \infty$, the EEMCF in Equation (D.12) can be approximated by

$$\widehat{K}^2_{c,rk} \approx \frac{\left(\mathbf{u}_r^T \boldsymbol{\varphi}_p\right)^2}{\boldsymbol{\varphi}_p^T \mathbf{A}_r \boldsymbol{\varphi}_p \omega^2_{sc,r}} = \frac{\boldsymbol{\varphi}_p^T \mathbf{u}_r \mathbf{u}_r^T \boldsymbol{\varphi}_p}{\boldsymbol{\varphi}_p^T \mathbf{A}_r \boldsymbol{\varphi}_p \omega^2_{sc,r}}, \tag{D.15}$$

which is a Rayleigh quotient. This quotient is stationary if $\boldsymbol{\varphi}_p$ is given by

$$\boldsymbol{\varphi}_p^\star = \mathbf{v}_r, \tag{D.16}$$

where $\mathbf{v}_r$ is an eigenvector of the generalized eigenvalue problem

$$\lambda_r \mathbf{A}_r \mathbf{v}_r = \mathbf{u}_r \mathbf{u}_r^T \mathbf{v}_r, \qquad ||\mathbf{v}_r|| = 1. \tag{D.17}$$

To maximize the EEMCF, this vector should be associated with the maximum generalized eigenvalue λ_r.

To simplify the optimization problem, it is proposed to consider that the optimal solution for finite $\mathbf{A}_r$ is a combination of these two asymptotic solutions

$$\boldsymbol{\varphi}_p^\star = c_1 \frac{\mathbf{u}_r}{||\mathbf{u}_r||} + c_2 \mathbf{v}_r. \tag{D.18}$$

The constants c_1 and c_2 should be chosen to optimize the EEMCF, but should also verify the passivity constraint (Equation (3.53))

$$c_1^2 + c_2^2 + 2c_1 c_2 \frac{\mathbf{u}_r^T \mathbf{v}_r}{||\mathbf{u}_r||} \leq 1. \tag{D.19}$$

This constrained optimization problem can be solved using Lagrangian methods for constrained optimization [167]. The Lagrangian can be formed as

$$\begin{aligned}\mathcal{L} = &\frac{\left(\mathbf{u}_r^T \left(c_1 \frac{\mathbf{u}_r}{||\mathbf{u}_r||} + c_2 \mathbf{v}_r\right)\right)^2}{\left(1 + \left(c_1 \frac{\mathbf{u}_r}{||\mathbf{u}_r||} + c_2 \mathbf{v}_r\right)^T \mathbf{A}_r \left(c_1 \frac{\mathbf{u}_r}{||\mathbf{u}_r||} + c_2 \mathbf{v}_r\right)\right) \omega^2_{sc,r}} \\ &- \mu_r \left(c_1^2 + c_2^2 + 2c_1 c_2 \frac{\mathbf{u}_r^T \mathbf{v}_r}{||\mathbf{u}_r||} - 1\right) = \frac{n_r\left(c_1, c_2\right)}{d_r\left(c_1, c_2\right)} - \mu_r c_r\left(c_1, c_2\right),\end{aligned} \tag{D.20}$$

where μ_r is a Lagrangian multiplier. The optimal solution is given by the stationary points of the Lagrangian.

$$\frac{\partial \mathcal{L}}{\partial c_1} = \frac{\frac{\partial n_r\left(c_1, c_2\right)}{\partial c_1} d_r\left(c_1, c_2\right) - n_r\left(c_1, c_2\right) \frac{\partial d_r\left(c_1, c_2\right)}{\partial c_1}}{d_r^2\left(c_1, c_2\right)} - \mu_r \frac{\partial c_r\left(c_1, c_2\right)}{\partial c_1} = 0 \tag{D.21}$$

$$\frac{\partial \mathcal{L}}{\partial c_2} = \frac{\frac{\partial n_r\left(c_1, c_2\right)}{\partial c_2} d_r\left(c_1, c_2\right) - n_r\left(c_1, c_2\right) \frac{\partial d_r\left(c_1, c_2\right)}{\partial c_2}}{d_r^2\left(c_1, c_2\right)} - \mu_r \frac{\partial c_r\left(c_1, c_2\right)}{\partial c_2} = 0 \tag{D.22}$$

$$\frac{\partial \mathcal{L}}{\partial \mu_r} = c_r\left(c_1, c_2\right) = 0 \tag{D.23}$$

The Lagrangian multiplier μ_r can be eliminated by combining Equations (D.21) and (D.22), yielding the relation

$$\left(\frac{\partial n_r\left(c_1,c_2\right)}{\partial c_1}d_r\left(c_1,c_2\right)-n_r\left(c_1,c_2\right)\frac{\partial d_r\left(c_1,c_2\right)}{\partial c_1}\right)\frac{\partial c_r\left(c_1,c_2\right)}{\partial c_2} = \left(\frac{\partial n_r\left(c_1,c_2\right)}{\partial c_2}d_r\left(c_1,c_2\right)-n_r\left(c_1,c_2\right)\frac{\partial d_r\left(c_1,c_2\right)}{\partial c_2}\right)\frac{\partial c_r\left(c_1,c_2\right)}{\partial c_1}. \quad \text{(D.24)}$$

From there on, the procedure only consists in a series of basic algebraic operations and the use of Equation (D.23) to simplify the expressions. This equality can be shown to yield the following relation between c_1 and c_2:

$$c_2 = \frac{\cos\left(\theta_r\right)\left(b_r-\dfrac{1}{\lambda_r}\right)}{\left(1-\cos\left(\theta_r\right)\right)a_r}c_1, \quad \text{(D.25)}$$

where

$$\cos\left(\theta_r\right)=\frac{\mathbf{u}_r^T\mathbf{v}_r}{||\mathbf{u}_r||}, \qquad a_r=\frac{1}{||\mathbf{u}_r||^2}, \qquad b_r=\frac{\mathbf{u}_r^T\mathbf{A}_r\mathbf{u}_r}{||\mathbf{u}_r||^4}. \quad \text{(D.26)}$$

Inserting this relation in Equation (D.23) leads to the optimal value of c_1

$$c_1 = \frac{\left(1-\cos\left(\theta_r\right)\right)a_r}{\sqrt{\left(1-\cos\left(\theta_r\right)\right)^2a_r^2+\cos^2\left(\theta_r\right)\left(b_r-\dfrac{1}{\lambda_r}\right)^2+2\cos^2\left(\theta_r\right)\left(1-\cos\left(\theta_r\right)\right)a_r\left(b_r-\dfrac{1}{\lambda_r}\right)}}, \quad \text{(D.27)}$$

which inserted into Equation (D.25) gives the optimal value of c_2, and eventually the optimal dimensionless electrical mode shape using Equation (D.18).

D.3 Dimensionless modes orthogonality and scaling factors

In the case where there are two piezoelectric transducers and two targeted modes, a necessary condition to satisfy Equation (3.72) is

$$\det\left(\begin{bmatrix}\dfrac{1}{d_{p,1}^2}-1 & -\cos\theta\\ -\cos\theta & \dfrac{1}{d_{p,2}^2}-1\end{bmatrix}\right)\geq 0 \quad \text{(D.28)}$$

where θ is the angle between the two dimensionless electrical mode shapes. Considering the equality yields a relation between the scaling factors

$$d_{p,2}^2\left(d_{p,1}^2\right)=\frac{1-d_{p,1}^2}{1-\left(1-\cos^2\theta\right)d_{p,1}^2}. \quad \text{(D.29)}$$

This relation is plotted in Figure D.1 for various values of $\cos\theta$. The values of scaling factors satisfying the passivity constraint are not unique, but can be chosen to optimize

some metric. For instance, it can be sought to optimize the sum of their squares. A necessary condition to find the optimum is then

$$\frac{\partial}{\partial d_{p,1}^2}\left(d_{p,1}^2 + d_{p,2}^2\left(d_{p,1}^2\right)\right) = 0. \tag{D.30}$$

This equation is satisfied if the scaling factors are equal and satisfy

$$d_{p,1}^2 = d_{p,2}^2 = \frac{1}{1+|\cos\theta|}. \tag{D.31}$$

Figure D.1 depicts this optimal solution for various values of $\cos\theta$.

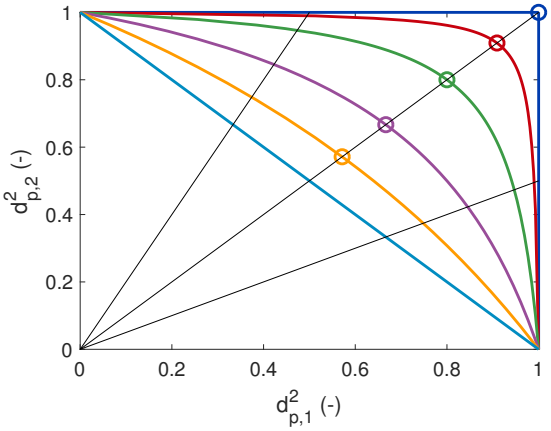

Figure D.1: Passivity constraint on the scaling factors: $\cos\theta = 0$ (—), $\cos\theta = 0.1$ (—), $\cos\theta = 0.25$ (—), $\cos\theta = 0.5$ (—), $\cos\theta = 0.75$ (—) and $\cos\theta = 1$ (—). The corresponding optimal scaling factors are indicated as well (∘). Black lines indicate $d_{p,2}^2 = 0.5d_{p,1}^2$, $d_{p,2}^2 = d_{p,1}^2$ and $d_{p,2}^2 = 2d_{p,1}^2$.

Choosing identical scaling factors is the optimal solution for each value of θ is this case. It can be observed in Figure D.1 that when the modes are almost aligned ($\cos\theta$ close to one), the objective function is not largely affected by choosing a scaling factor different than the other one. In the limit case when they are aligned, this objective function is constant whatever their relative values. However, for nearly-orthogonal modes ($\cos\theta$ close to zero), choosing different scaling factors can seriously impact the objective function. For instance, in the case $\cos\theta = 0.1$, the optimal solution is $d_{p,1}^2 = d_{p,2}^2 = 0.91$. Choosing $d_{p,1}^2 = 0.5d_{p,2}^2$ while respecting the passivity constraint leads to $d_{p,1}^2 = 0.495$ and $d_{p,2}^2 = 0.99$, i.e., a substantial decrease in $d_{p,1}$ and a marginal increase in $d_{p,2}$. In the limit case where the modes are truly orthogonal, the two scaling factors can be chosen independently, but the optimal choice is still $d_{p,1} = d_{p,2} = 1$.

For more than two modes and/or two transducers, the relations are more complicated. Nevertheless, this simple example highlights two guidelines that should be respected when choosing the scaling factors.

1. Choosing identical scaling factors leads to a solution which optimizes or nearly optimizes the sum of scaling factors squared.

2. When modes are nearly orthogonal, choosing different relative scaling factors can drastically reduce the objective function. For modes which are nearly aligned, these relative scaling factors can be chosen with more freedom without significantly affecting the objective function.

D.4 Limits on the electromechanical coupling factors attainable with passive networks

Using $\mathbf{E}_p^T \boldsymbol{\Phi}_{e,k} = \boldsymbol{\Phi}_{p,k} = d_{p,k} \boldsymbol{\Phi}_{p,k}^\star$ (Equation (3.57)), the EEMCF given in Equation (3.30) becomes

$$\widehat{K}_{c,rk}^2 = \frac{d_{p,k}^2 \boldsymbol{\Phi}_{sc,r}^T \boldsymbol{\Gamma}_p \boldsymbol{\Phi}_{p,k}^\star \left(\boldsymbol{\Phi}_{p,k}^\star\right)^T \boldsymbol{\Gamma}_p^T \boldsymbol{\Phi}_{sc,r}}{\omega_{sc,r}^2} = d_{p,k}^2 \frac{\boldsymbol{\Phi}_{sc,r}^T \boldsymbol{\Gamma}_p \left(\mathbf{C}_p^\varepsilon\right)^{-1} \boldsymbol{\Gamma}_p^T \boldsymbol{\Phi}_{sc,r}}{\omega_{sc,r}^2}, \tag{D.32}$$

which is exactly identical to that given in Equation (D.4) when $d_{p,k} = 1$. Thus, the network can attain an EEMCF as high as that of the structure only when the scaling factor of the electrical mode is equal to one, and may have a lower performance when passivity requirement constrains this scaling factor to be smaller than one.

D.4.1 Comparison of the coupling factors accounting for background contributions

It can also be shown that

$$K_{c,r}^2 - \widehat{K}_{c,rk}^2 \geq 0 \tag{D.33}$$

when these EEMCFs are evaluated accounting for the background contribution of non-resonant modes (Equations (D.9) and (3.45)), and when the considered mode shape is optimized, i.e.,

$$\boldsymbol{\Phi}_{p,k} = \boldsymbol{\Phi}_{p,k}^\star, \tag{D.34}$$

as defined by Equation (3.57). Considering the discussion in Section 3.5.6.1, the dimensionless mode shapes associated to non-resonant electrical modes have to be orthogonal to the resonant one

$$\boldsymbol{\varphi}_{p,l}^T \boldsymbol{\varphi}_{p,k} = 0, \qquad \forall l \neq k. \tag{D.35}$$

In terms of capacitance-normalized electrical mode shapes, using Equation (3.50), this means that the non-resonant electrical mode shapes should also verify

$$\boldsymbol{\Phi}_{p,l}^T \mathbf{C}_p^\varepsilon \boldsymbol{\Phi}_{p,k} = 0, \qquad \forall l \neq k. \tag{D.36}$$

Using Equation (3.57), this translates to

$$\boldsymbol{\Phi}_{p,l}^T \boldsymbol{\Gamma}_p^T \boldsymbol{\Phi}_{sc,r} = 0, \tag{D.37}$$

which means that, using the notations of Section 3.4.3.3,

$$\boldsymbol{\gamma}_{\boldsymbol{\Phi},r<k} = \mathbf{0}, \tag{D.38}$$

and hence, with Equations (3.41) and (3.42)

$$\widehat{\omega}_{sc,r}^2 = \omega_{sc,r}^2, \qquad . \tag{D.39}$$

and

$$\widehat{\gamma}_{\mathbf{\Phi},rk} = \gamma_{\mathbf{\Phi},rk} = \left(\boldsymbol{\phi}_{sc,r}^T \mathbf{\Gamma}_p^T \boldsymbol{\phi}_{p,k}\right)^2 = \boldsymbol{\phi}_{sc,r}^T \mathbf{\Gamma}_p \left(\mathbf{C}_p^\varepsilon\right)^{-1} \mathbf{\Gamma}_p^T \boldsymbol{\phi}_{sc,r}. \tag{D.40}$$

Using the SMW formula (Equation (A.2)) in Equation (D.9), the EEMCF of the structure is expressed as

$$K_{c,r}^2 = \frac{1}{\omega_{sc,r}^2}\left[\gamma_{\mathbf{\Phi},rk}^2 - \mathbf{u}_r^T \left(\mathbf{\Omega}_{sc,>r}^{-2} + \mathbf{\Phi}_{sc,>r}^T \mathbf{\Gamma}_p \left(\mathbf{C}_p^\varepsilon\right)^{-1} \mathbf{\Gamma}_p^T \mathbf{\Phi}_{sc,>r}\right)^{-1} \mathbf{u}_r\right], \tag{D.41}$$

where $\mathbf{u}_r$ is given by

$$\mathbf{u}_r = \mathbf{\Phi}_{sc,>r}^T \mathbf{\Gamma}_p \left(\mathbf{C}_p^\varepsilon\right)^{-1} \mathbf{\Gamma}_p^T \boldsymbol{\phi}_{sc,r}. \tag{D.42}$$

The EEMCF of the network, as given by Equation (3.45), is not easy to work with in this proof. Alternatively, it can be obtained by considering the effective open-circuit resonance frequency of the system in Equation (3.35). This effective frequency is obtained by imposing $\omega_{e,k} = 0$, making the dynamics of the resonant electrical mode identical to the non-resonant ones. These dynamics are thus described by

$$\begin{bmatrix} \mathbf{\Omega}_{sc,>r}^2 & \mathbf{\Gamma}_{\mathbf{\Phi},>r\leq k} \\ -\mathbf{\Gamma}_{\mathbf{\Phi},>r\leq k}^T & \mathbf{I} \end{bmatrix} \begin{bmatrix} \boldsymbol{\eta}_{sc,>r} \\ s\boldsymbol{\eta}_{e,\leq k} \end{bmatrix} = \begin{bmatrix} 0 \\ \boldsymbol{\gamma}_{\mathbf{\Phi},r\leq k}^T \eta_{sc,r} \end{bmatrix}, \tag{D.43}$$

where the subscript $\leq k$ indicates electrical modes with index $i \leq k$. Only $s\boldsymbol{\eta}_{e,\leq k}$ has to be solved for, as it is the only term that appears in the first line of Equation (3.35). Using a block inversion formula (Equation (A.5)), it is given by

$$s\boldsymbol{\eta}_{e,\leq k} = \left(\mathbf{I} + \mathbf{\Gamma}_{\mathbf{\Phi},>r\leq k}^T \mathbf{\Omega}_{sc,>r}^{-2} \mathbf{\Gamma}_{\mathbf{\Phi},>r\leq k}\right)^{-1} \boldsymbol{\gamma}_{\mathbf{\Phi},r\leq k}^T \eta_{sc,r}. \tag{D.44}$$

Reinserting this relation into the first line of Equation (3.35) gives the effective open-circuit resonance frequency

$$\widehat{\omega}_{oc,r}^2 = \omega_{sc,r}^2 + \boldsymbol{\gamma}_{\mathbf{\Phi},r\leq k} \left(\mathbf{I} + \mathbf{\Gamma}_{\mathbf{\Phi},>r\leq k}^T \mathbf{\Omega}_{sc,>r}^{-2} \mathbf{\Gamma}_{\mathbf{\Phi},>r\leq k}\right)^{-1} \boldsymbol{\gamma}_{\mathbf{\Phi},r\leq k}^T \tag{D.45}$$

An EEMCF can thus be estimated by

$$\widehat{K}_{c,rk}^2 = \frac{\widehat{\omega}_{oc,r}^2 - \widehat{\omega}_{sc,r}^2}{\widehat{\omega}_{sc,r}^2} = \frac{1}{\omega_{sc,r}^2} \boldsymbol{\gamma}_{\mathbf{\Phi},r\leq k} \left(\mathbf{I} + \mathbf{\Gamma}_{\mathbf{\Phi},>r\leq k}^T \mathbf{\Omega}_{sc,>r}^{-2} \mathbf{\Gamma}_{\mathbf{\Phi},>r\leq k}\right)^{-1} \boldsymbol{\gamma}_{\mathbf{\Phi},r\leq k}^T. \tag{D.46}$$

It is possible (but tedious) to show that this expression is identical to that given in Equation (3.45), because they were both obtained with the same assumptions. Using the SMW formula (Equation (A.2)), this equation becomes

$$\begin{aligned} \widehat{K}_{c,rk}^2 = \frac{1}{\omega_{sc,r}^2} \boldsymbol{\phi}_{sc,r}^T \mathbf{\Gamma}_p^T \Big[& \mathbf{\Phi}_{p,\leq k} \mathbf{\Phi}_{p,\leq k}^T - \mathbf{\Phi}_{p,\leq k} \mathbf{\Phi}_{p,\leq k}^T \mathbf{\Gamma}_p^T \mathbf{\Phi}_{sc,>r} \\ & \left(\mathbf{\Omega}_{sc,>r}^{-2} + \mathbf{\Phi}_{sc,>r}^T \mathbf{\Gamma}_p \mathbf{\Phi}_{p,\leq k} \mathbf{\Phi}_{p,\leq k}^T \mathbf{\Gamma}_p^T \mathbf{\Phi}_{sc,>r}\right)^{-1} \mathbf{\Phi}_{sc,>r}^T \mathbf{\Gamma}_p \mathbf{\Phi}_{p,\leq k} \mathbf{\Phi}_{p,\leq k}^T \Big] \mathbf{\Gamma}_p^T \boldsymbol{\phi}_{sc,r} \end{aligned} \tag{D.47}$$

Equation (D.37) implies that

$$\boldsymbol{\phi}_{sc,r}^T \mathbf{\Gamma}_p^T \mathbf{\Phi}_{p,\leq k} \mathbf{\Phi}_{p,\leq k}^T = \boldsymbol{\phi}_{sc,r}^T \mathbf{\Gamma}_p^T \boldsymbol{\phi}_{p,k} \boldsymbol{\phi}_{p,k}^T, \tag{D.48}$$

which allows for a simplification of Equation (D.47)

$$\widehat{K}^2_{c,rk} = \frac{1}{\omega^2_{sc,r}} \left[\gamma^2_{\mathbf{\Phi},rk} - \mathbf{u}_r^T \left(\mathbf{\Omega}^{-2}_{sc,>r} + \mathbf{\Phi}^T_{sc,>r} \mathbf{\Gamma}_p \mathbf{\Phi}_{p,\leq k} \mathbf{\Phi}^T_{p,\leq k} \mathbf{\Gamma}_p^T \mathbf{\Phi}_{sc,>r} \right)^{-1} \mathbf{u}_r \right]. \tag{D.49}$$

By comparing Equations (D.41) and (D.49), it is observed that the EEMCFs are given by a sum of two terms. In both equations, the first term is identical. The second term, which represents the background contributions from non-resonant modes, is a quadratic form. The difference of the EEMCFs is thus given by

$$\begin{aligned} K^2_{c,r} - \widehat{K}^2_{c,rk} = \frac{1}{\omega^2_{sc,r}} \mathbf{u}_r^T \Big[&\left(\mathbf{\Omega}^{-2}_{sc,>r} + \mathbf{\Phi}^T_{sc,>r} \mathbf{\Gamma}_p \mathbf{\Phi}_{p,\leq k} \mathbf{\Phi}^T_{p,\leq k} \mathbf{\Gamma}_p^T \mathbf{\Phi}_{sc,>r} \right)^{-1} \\ &- \left(\mathbf{\Omega}^{-2}_{sc,>r} + \mathbf{\Phi}^T_{sc,>r} \mathbf{\Gamma}_p \left(\mathbf{C}_p^{\varepsilon} \right)^{-1} \mathbf{\Gamma}_p^T \mathbf{\Phi}_{sc,>r} \right)^{-1} \Big] \mathbf{u}_r \end{aligned} \tag{D.50}$$

The matrix involved in this quadratic form is positive semidefinite. To demonstrate this, it can be observed that

$$\begin{aligned} &\mathbf{\Omega}^{-2}_{sc,>r} + \mathbf{\Phi}^T_{sc,>r} \mathbf{\Gamma}_p \left(\mathbf{C}_p^{\varepsilon} \right)^{-1} \mathbf{\Gamma}_p^T \mathbf{\Phi}_{sc,>r} - \left(\mathbf{\Omega}^{-2}_{sc,>r} + \mathbf{\Phi}^T_{sc,>r} \mathbf{\Gamma}_p \mathbf{\Phi}_{p,\leq k} \mathbf{\Phi}^T_{p,\leq k} \mathbf{\Gamma}_p^T \mathbf{\Phi}_{sc,>r} \right) \\ &\qquad = \mathbf{\Phi}^T_{sc,>r} \mathbf{\Gamma}_p \left(\left(\mathbf{C}_p^{\varepsilon} \right)^{-1} - \mathbf{\Phi}_{p,\leq k} \mathbf{\Phi}^T_{p,\leq k} \right) \mathbf{\Gamma}_p^T \mathbf{\Phi}_{sc,>r} \succeq 0 \end{aligned} \tag{D.51}$$

because of the passivity constraints (Equation (3.49)). Thus, by Property 6 of positive semidefinite matrices,

$$\left(\mathbf{\Omega}^{-2}_{sc,>r} + \mathbf{\Phi}^T_{sc,>r} \mathbf{\Gamma}_p \mathbf{\Phi}_{p,\leq k} \mathbf{\Phi}^T_{p,\leq k} \mathbf{\Gamma}_p^T \mathbf{\Phi}_{sc,>r} \right)^{-1} - \left(\mathbf{\Omega}^{-2}_{sc,>r} + \mathbf{\Phi}^T_{sc,>r} \mathbf{\Gamma}_p \left(\mathbf{C}_p^{\varepsilon} \right)^{-1} \mathbf{\Gamma}_p^T \mathbf{\Phi}_{sc,>r} \right)^{-1} \succeq 0, \tag{D.52}$$

which means that the difference in the EEMCFs is positive or zero, i.e., that Equation (D.33) is verified. Therefore, the background contributions from non-resonant modes can limit the EEMCF of the network to a lower value than that of the structure, but in no case can the former be larger than the latter with a passive network.

E Appendix to Chapter 4

E.1 Parametrization of electrical matrices

A parametrization of the electrical matrices $\mathbf{C}_e$, $\mathbf{G}$ and $\mathbf{B}$ is detailed here. These matrices need to be symmetric positive semidefinite. The symmetry constraint reduces the number of free parameters for each matrix to $N_e(N_e+1)/2$ (which is the number of entries on its upper triangular part). These parameters are constrained by N_e inequalities on the eigenvalues of the matrix, which should be positive.

Working directly with the entries of the matrices is not efficient, because the constraints on the eigenvalues leads to complex nonlinear inequalities. This is why a parametrization based on the eigenstructure of these matrices is proposed here. The N_e eigenvalues are explicitly taken as parameters, which allows for the use of simple linear inequality constraints. The remaining $N_e(N_e-1)/2$ free parameters are Givens rotation angles, which are used to parametrize the eigenvectors.

In the sequel, $\mathbf{C}_e$ is taken as an example, and the extension to $\mathbf{G}$ and $\mathbf{B}$ is straightforward.

E.1.1 Direct parametrization

$\mathbf{C}_e$ is guaranteed to be symmetric if it is built using its eigenvalue decomposition, i.e.,

$$\mathbf{C}_e = \mathbf{U}_C \mathbf{\Lambda}_C \mathbf{U}_C^T, \tag{E.1}$$

where $\mathbf{U}_C$ and $\mathbf{\Lambda}_C$ are the orthogonal matrix of eigenvectors and diagonal matrix of eigenvalues of $\mathbf{C}_e$, respectively. Every element on the diagonal of $\mathbf{\Lambda}_C$ must be equal to or greater than zero. The eigenvalues constitute a set of N_e parameters. The remaining $N_e(N_e-1)/2$ free parameters of $\mathbf{C}_e$ can be used to parametrize $\mathbf{U}_C$.

A simple way to build an orthogonal matrix $\mathbf{U}_C$ is to use Givens rotations [261]. For a set of $N_e(N_e-1)/2$ rotation angles $\theta_{C,i}$, it is built by

$$\mathbf{U}_C = \prod_{i=1}^{N_e(N_e-1)/2} \mathbf{G}_i(\theta_{C,i}), \tag{E.2}$$

where $\mathbf{G}_i(\theta_i)$ are Givens rotation matrices

$$\mathbf{G}_i(\theta_i) = \mathbf{I} + \begin{bmatrix} \mathbf{e}_{i1(i)} & \mathbf{e}_{i2(i)} \end{bmatrix} \begin{bmatrix} \cos\theta_{C,i} - 1 & -\sin\theta_{C,i} \\ \sin\theta_{C,i} & \cos\theta_{C,i} - 1 \end{bmatrix} \begin{bmatrix} \mathbf{e}_{i1(i)} & \mathbf{e}_{i2(i)} \end{bmatrix}^T. \tag{E.3}$$

$\mathbf{e}_k$ is a unit column vector filled with zeros except for its k^{th} entry which is one. The numbers $i1(i)$ and $i2(i)$ are found by taking each $i1 \in \begin{bmatrix} 1 & \dots & N_e \end{bmatrix}$ and $i2 \in \begin{bmatrix} i1+1 & \dots & N_e \end{bmatrix}$, and incrementing i each times the index $i1$ or $i2$ is changed.

The matrix $\mathbf{C}_e$ is thus parametrized by the set of $N_e(N_e+1)/2$ parameters

$$\boldsymbol{\xi}_C = \begin{bmatrix} \lambda_{C,1} & \cdots & \lambda_{C,N_e} & \theta_{C,1} & \cdots & \theta_{C,N_e(N_e-1)/2} \end{bmatrix}^T \tag{E.4}$$

The derivative of the matrix with respect to the parameters can also be computed. For the eigenvalues, it is simply given by

$$\frac{\partial \mathbf{C}_e}{\partial \lambda_i} = \mathbf{U}_C \mathbf{e}_i \mathbf{e}_i^T \mathbf{U}_C^T. \tag{E.5}$$

For the Givens rotation angles, the derivative of the eigenvectors is first computed as

$$\frac{\partial \mathbf{U}_C}{\partial \theta_k} = \left(\prod_{i=1}^{k} \mathbf{G}_i(\theta_{C,i}) \right) \frac{\partial \mathbf{G}_k(\theta_{C,k})}{\partial \theta_{C,k}} \left(\prod_{i=k+1}^{N_e(N_e-1)/2} \mathbf{G}_i(\theta_{C,i}) \right), \tag{E.6}$$

where

$$\frac{\partial \mathbf{G}_k(\theta_{C,k})}{\partial \theta_{C,k}} = \begin{bmatrix} \mathbf{e}_{i1(i)} & \mathbf{e}_{i2(i)} \end{bmatrix} \begin{bmatrix} -\sin\theta_{C,i} & -\cos\theta_{C,i} \\ \cos\theta_{C,i} & -\sin\theta_{C,i} \end{bmatrix} \begin{bmatrix} \mathbf{e}_{i1(i)} & \mathbf{e}_{i2(i)} \end{bmatrix}^T. \tag{E.7}$$

The derivative of $\mathbf{C}_e$ is finally found as

$$\frac{\partial \mathbf{C}_e}{\partial \theta_i} = \frac{\partial \mathbf{U}_C}{\partial \theta_i} \boldsymbol{\Lambda}_C \mathbf{U}_C^T + \mathbf{U}_C \boldsymbol{\Lambda}_C \frac{\partial \mathbf{U}_C^T}{\partial \theta_i}. \tag{E.8}$$

For decentralized networks, the block-diagonal structure of the matrices in Equation (3.85) enforces some angles to zero. These angles are associated to line and column indices ($i1$ and $i2$, respectively) of elements that to not belong to the blocks on the diagonal. These elements should thus be forced to zero during the optimization process.

E.1.2 Inverse parametrization

An initial guess of electrical matrices is required to start the NH optimization algorithm. To find the parameters associated to these matrices, it is first required to compute their eigenvalues and eigenvectors (Equation (E.1)). The diagonal elements of $\boldsymbol{\Lambda}_C$ are the eigenvalues, which constitute the first N_e parameters. For the Givens rotation angles, the construction algorithm of $\mathbf{U}_C$ must be run backward. The algorithm is initialized by taking $\mathbf{U}_C^{(1)} = \mathbf{U}_C$. The indices $i1$ and $i2$ are covered by taking an inverse order, $i1 \in \begin{bmatrix} N_e & \cdots & 1 \end{bmatrix}$ and $i2 \in \begin{bmatrix} N_e & \cdots & i1+1 \end{bmatrix}$. The rotation angle θ_i can be found as

$$\theta_i = \arctan\left(\frac{\mathbf{e}_{i2}^T \mathbf{U}_C^{(i)} \mathbf{e}_{i1}}{\mathbf{e}_{i2}^T \mathbf{U}_C^{(i)} \mathbf{e}_{i2}} \right). \tag{E.9}$$

An inverse rotation is performed to update the matrix $\mathbf{U}_C$,

$$\mathbf{U}_C^{(i+1)} = \mathbf{U}_C^{(i)} \left(\mathbf{I} + \begin{bmatrix} \mathbf{e}_{i1(i)} & \mathbf{e}_{i2(i)} \end{bmatrix} \begin{bmatrix} \cos\theta_{C,i} - 1 & \sin\theta_{C,i} \\ -\sin\theta_{C,i} & \cos\theta_{C,i} - 1 \end{bmatrix} \begin{bmatrix} \mathbf{e}_{i1(i)} & \mathbf{e}_{i2(i)} \end{bmatrix}^T \right) \tag{E.10}$$

and i can be incremented, until it reaches $N_e(N_e - 1)/2$.

It should be noted that this parametrization works if the eigenvectors matrix is equivalent to a compound rotation matrix, i.e., if it has a unit determinant. General eigenvalues calculators do not guarantee this, and eigenvectors matrices with negative unit determinant are also possible. This case can easily be treated, either by swapping two columns of the eigenvectors matrix (and swapping the associated eigenvalues correspondingly), or by multiplying one of the eigenvectors by -1.

F Appendix to Chapter 5

F.1 State-space models of nonlinear piezoelectric structures

The equations of motion of a nonlinear piezoelectric structure can generally be expressed by [205]

$$\mathbf{M}_0\ddot{\mathbf{x}} + \mathbf{C}_0\dot{\mathbf{x}} + \mathbf{K}_0\mathbf{x} - \boldsymbol{\Theta}\mathbf{q} + \mathbf{f}_{nl}(\mathbf{x}) = \mathbf{f}. \tag{F.1}$$

This set of nonlinear second-order ordinary differential equations can be cast to the equivalent first-order system

$$\begin{bmatrix} \dot{\mathbf{x}} \\ \ddot{\mathbf{x}} \end{bmatrix} = \begin{bmatrix} \mathbf{0} & \mathbf{I} \\ -\mathbf{M}_0^{-1}\mathbf{K}_0 & -\mathbf{M}_0^{-1}\mathbf{C}_0 \end{bmatrix} \begin{bmatrix} \mathbf{x} \\ \dot{\mathbf{x}} \end{bmatrix} + \begin{bmatrix} \mathbf{0} & \mathbf{0} \\ \mathbf{M}_0^{-1} & \mathbf{M}_0^{-1}\boldsymbol{\Theta} \end{bmatrix} \begin{bmatrix} \mathbf{f} \\ \mathbf{q} \end{bmatrix} + \begin{bmatrix} \mathbf{0} \\ -\mathbf{M}_0^{-1}\mathbf{f}_{nl}(\mathbf{x}) \end{bmatrix}, \tag{F.2}$$

and the voltages across the electrodes of the piezoelectric transducers are given by

$$\mathbf{V} = \boldsymbol{\Theta}^T\mathbf{x} - \mathbf{E}_p^{\varepsilon}\mathbf{q}. \tag{F.3}$$

The electrical circuits or networks that are connected to the piezoelectric transducers are assumed to be governed by the following state-space model

$$\dot{\mathbf{x}}_e = \mathbf{A}_e\mathbf{x}_e + \mathbf{B}_e\mathbf{V} + \mathbf{f}_{nl,e}(\mathbf{x}_e) \tag{F.4}$$

and the output equation

$$\mathbf{q} = \mathbf{C}_e\mathbf{x}_e. \tag{F.5}$$

Inserting Equation (F.5) into Equation (F.3), and inserting this back into Equation (F.4) allows for the elimination of the voltages in the electrical state-space equation:

$$\dot{\mathbf{x}}_e = \mathbf{A}_e\mathbf{x}_e + \mathbf{B}_e\left(\boldsymbol{\Theta}^T\mathbf{x} - \mathbf{E}_p^{\varepsilon}\mathbf{C}_e\mathbf{x}_e\right) + \mathbf{f}_{nl,e}(\mathbf{x}_e). \tag{F.6}$$

Combining Equations (F.2), (F.5) and (F.6) yields the state-space evolution equation of the nonlinear coupled electromechanical system

$$\begin{bmatrix} \dot{\mathbf{x}} \\ \ddot{\mathbf{x}} \\ \dot{\mathbf{x}}_e \end{bmatrix} = \begin{bmatrix} \mathbf{0} & \mathbf{I} & \mathbf{0} \\ -\mathbf{M}_0^{-1}\mathbf{K}_0 & -\mathbf{M}_0^{-1}\mathbf{C}_0 & \mathbf{M}_0^{-1}\boldsymbol{\Theta}\mathbf{C}_e \\ \mathbf{B}_e\boldsymbol{\Theta}^T & \mathbf{0} & \mathbf{A}_e - \mathbf{B}_e\mathbf{E}_p^{\varepsilon}\mathbf{C}_e \end{bmatrix} \begin{bmatrix} \mathbf{x} \\ \dot{\mathbf{x}} \\ \mathbf{x}_e \end{bmatrix} + \begin{bmatrix} \mathbf{0} \\ \mathbf{M}_0^{-1} \\ \mathbf{0} \end{bmatrix} \begin{bmatrix} \mathbf{f} \end{bmatrix} + \begin{bmatrix} \mathbf{0} \\ -\mathbf{M}_0^{-1}\mathbf{f}_{nl}(\mathbf{x}) \\ \mathbf{f}_{nl,e}(\mathbf{x}_e) \end{bmatrix}, \tag{F.7}$$

which is in the form of Equation (5.2).

F.2 Models of nonlinear shunt circuits

F.2.1 Nonlinear Hollkamp's shunt circuit

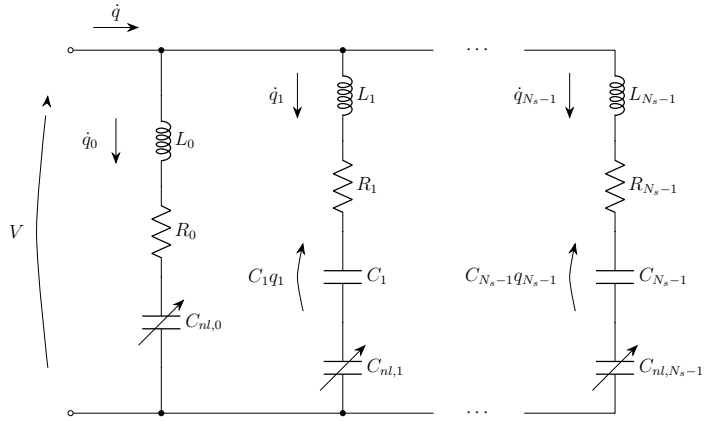

Figure F.1: Nonlinear Hollkamp's shunt circuit.

The current in the inductors and the charges in the linear capacitors are used as state variables. From Figure F.1, the application of KVL to branches 0 and $k > 0$ respectively yields

$$\ddot{q}_0 = \frac{1}{L_0}\left(V - R_0\dot{q}_0 - C_{nl,0}q_0^3\right) \tag{F.8}$$

and

$$\ddot{q}_k = \frac{1}{L_k}\left(V - \frac{1}{C_k}q_k - R_k\dot{q}_k - C_{nl,k}q_k^3\right). \tag{F.9}$$

Using the same notation as Section C.1.1 and introducing the vector of nonlinear voltages

$$\mathbf{V}_{nl} = \begin{bmatrix} C_{nl,0}q_0^3 \\ \vdots \\ C_{nl,N_s-1}q_{N_s-1}^3 \end{bmatrix}, \tag{F.10}$$

the state evolution equations become

$$\begin{bmatrix} \dot{\mathbf{q}} \\ \ddot{\mathbf{q}} \end{bmatrix} = \begin{bmatrix} \mathbf{0} & \mathbf{I} \\ -\mathbf{L}_H^{-1}\mathbf{E}_H & -\mathbf{L}_H^{-1}\mathbf{R}_H \end{bmatrix} \begin{bmatrix} \mathbf{q} \\ \dot{\mathbf{q}} \end{bmatrix} + \begin{bmatrix} \mathbf{0} \\ \mathbf{L}_H^{-1}\mathbf{1}_{N_s\times 1} \end{bmatrix} V + \begin{bmatrix} \mathbf{0} \\ -\mathbf{L}_H^{-1}\mathbf{V}_{nl} \end{bmatrix} \tag{F.11}$$

and the output equation is

$$q = \begin{bmatrix} \mathbf{1} & \mathbf{0} \end{bmatrix} \begin{bmatrix} \mathbf{q} \\ \dot{\mathbf{q}} \end{bmatrix}. \tag{F.12}$$

F.2.2 Nonlinear and augmented nonlinear current blocking shunt circuit

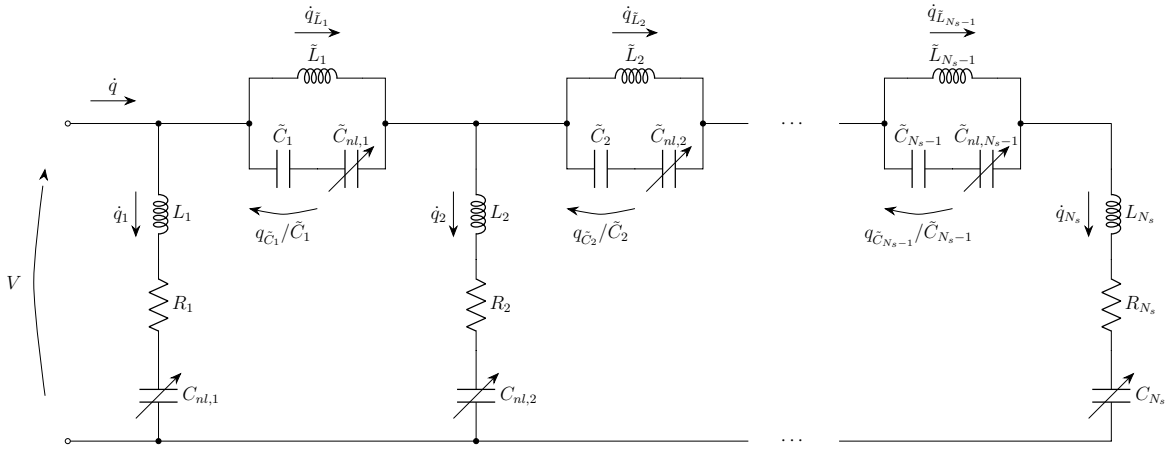

Figure F.2: Augmented nonlinear current blocking circuit with series RL shunts.

The model of an ANCB circuit is derived hereafter, and that of an NCB circuit can readily be derived from it. The charges and currents through the shunts, the currents through the filter inductors and the charge through the filter capacitors are used as state variables. From Figure F.2, the currents flowing through the filter inductors are governed by

$$\ddot{q}_{\tilde{L}_k} = \frac{1}{\tilde{L}_k}\left(\frac{1}{\tilde{C}_k}q_{\tilde{C}_k} + \tilde{C}_{nl,k}q_{\tilde{C}_k}^3\right) \tag{F.13}$$

while the current through the filter capacitors are given by

$$\dot{q}_{\tilde{C}_k} = \dot{\tilde{q}}_k - \dot{q}_{\tilde{L}_k}, \tag{F.14}$$

where $\dot{\tilde{q}}_k$ is the total current going through the filter. The current flowing through the shunt inductor is governed by

$$\ddot{q}_k = -\frac{R_k}{L_k}\dot{q}_k - \frac{C_{nl,k}}{L_k}q_k^3 + \frac{1}{L_k}V_k. \tag{F.15}$$

Using KVL, the voltage across each shunt is given by

$$V_k = V - \sum_{i=1}^{k-1}\left(\frac{1}{\tilde{C}_i}q_{\tilde{C}_i} + \tilde{C}_{nl,i}q_{\tilde{C}_i}^3\right) \tag{F.16}$$

and using KCL, the currents through the filter are found as

$$\dot{\tilde{q}}_k = \sum_{i=k+1}^{N}\dot{q}_i. \tag{F.17}$$

Using the same notations as Section C.1.5.1 and introducing the vectors of nonlinear voltages

$$\mathbf{V}_{nl} = \begin{bmatrix} C_{nl,1}q_1^3 \\ \vdots \\ C_{nl,N_s}q_{N_s}^3 \end{bmatrix}, \qquad \tilde{\mathbf{V}}_{nl} = \begin{bmatrix} \tilde{C}_{nl,1}q_{\tilde{C}_1}^3 \\ \vdots \\ \tilde{C}_{nl,N_s-1}q_{\tilde{C}_{N_s-1}}^3 \end{bmatrix}, \tag{F.18}$$

the state evolution equations read

$$\begin{bmatrix} \dot{\mathbf{q}} \\ \ddot{\mathbf{q}} \\ \dot{\mathbf{q}}_{\tilde{C}} \\ \ddot{\mathbf{q}}_{\tilde{L}} \end{bmatrix} = \begin{bmatrix} \mathbf{0} & \mathbf{I} & \mathbf{0} & \mathbf{0} \\ \mathbf{0} & -\mathbf{L}_{CB}^{-1}\mathbf{R}_{CB} & -\mathbf{L}_{CB}^{-1}\mathbf{T}^T\tilde{\mathbf{E}}_{CB} & \mathbf{0} \\ \mathbf{0} & \mathbf{T} & \mathbf{0} & -\mathbf{I} \\ \mathbf{0} & \mathbf{0} & \tilde{\mathbf{L}}_{CB}^{-1}\tilde{\mathbf{E}}_{CB} & \mathbf{0} \end{bmatrix} \begin{bmatrix} \mathbf{q} \\ \dot{\mathbf{q}} \\ \mathbf{q}_{\tilde{C}} \\ \dot{\mathbf{q}}_{\tilde{L}} \end{bmatrix} + \begin{bmatrix} \mathbf{0} \\ \mathbf{L}_{CB}^{-1}\mathbf{1}_{N_s\times 1} \\ \mathbf{0} \\ \mathbf{0} \end{bmatrix} V + \begin{bmatrix} \mathbf{0} \\ -\mathbf{L}_{CB}^{-1}\left(\mathbf{V}_{nl} + \mathbf{T}^T\tilde{\mathbf{V}}_{nl}\right) \\ \mathbf{0} \\ \tilde{\mathbf{L}}_{CB}^{-1}\tilde{\mathbf{V}}_{nl} \end{bmatrix}, \quad \text{(F.19)}$$

and the output equation reads

$$q = \begin{bmatrix} \mathbf{1} & \mathbf{0} & \mathbf{0} & \mathbf{0} \end{bmatrix} \begin{bmatrix} \mathbf{q} \\ \dot{\mathbf{q}} \\ \mathbf{q}_{\tilde{C}} \\ \dot{\mathbf{q}}_{\tilde{L}} \end{bmatrix}. \quad \text{(F.20)}$$

The model of the NCB can be obtained by setting $\tilde{\mathbf{V}}_{nl} = \mathbf{0}$.

The state evolution matrix in Equation (F.19) is singular (this stems from the fact that the charges in the shunts are not uniquely defined under a static voltage). Depending on the implementation of the solver for the nonlinear equations, this may be an issue. In this case, the second line of this system of equations may be replaced by

$$\ddot{\mathbf{q}} = -\mathbf{L}_{CB}^{-1}\mathbf{E}_{CB}\mathbf{q} - \mathbf{L}_{CB}^{-1}\mathbf{R}_{CB}\dot{\mathbf{q}} - \mathbf{L}_{CB}^{-1}\mathbf{T}^T\tilde{\mathbf{E}}_{CB}\mathbf{q}_{\tilde{C}} + \mathbf{L}_{CB}^{-1}\mathbf{1}_{N_s\times 1}V - \mathbf{L}_{CB}^{-1}\left(\mathbf{V}_{nl} + \mathbf{T}^T\tilde{\mathbf{V}}_{nl}\right), \quad \text{(F.21)}$$

where $\mathbf{E}_{CB}$ is a diagonal regularization matrix. Physically, it is equivalent to adding capacitors in series with the RL shunts. The values on the diagonal should be small with respect to $1/C_p^\varepsilon$ (typically, $\mathbf{E}_{CB} = 10^{-6}\mathbf{I}/C_p^\varepsilon$ can be used) in order to accurately represent the dynamics of the CB circuit.

G Appendix to Chapter 6

G.1 Modified Craig-Bampton reduced-order model

Accounting for internal electrical DoFs, Equation (6.4) reads

$$\begin{bmatrix} \mathbf{M}_{bb} & \mathbf{M}_{bi} & \mathbf{0} & \mathbf{0} \\ \mathbf{M}_{ib} & \mathbf{M}_{ii} & \mathbf{0} & \mathbf{0} \\ \mathbf{0} & \mathbf{0} & \mathbf{0} & \mathbf{0} \\ \mathbf{0} & \mathbf{0} & \mathbf{0} & \mathbf{0} \end{bmatrix} \begin{bmatrix} \ddot{\mathbf{x}}_b \\ \ddot{\mathbf{x}}_i \\ \ddot{\mathbf{V}}_b \\ \ddot{\mathbf{V}}_i \end{bmatrix} + \begin{bmatrix} \mathbf{K}_{bb} & \mathbf{K}_{bi} & \boldsymbol{\Gamma}_{bb} & \boldsymbol{\Gamma}_{bi} \\ \mathbf{K}_{ib} & \mathbf{K}_{ii} & \boldsymbol{\Gamma}_{ib} & \boldsymbol{\Gamma}_{ii} \\ \boldsymbol{\Gamma}_{bb}^T & \boldsymbol{\Gamma}_{ib}^T & -\mathbf{C}_{p,bb}^{\varepsilon} & -\mathbf{C}_{p,bi}^{\varepsilon} \\ \boldsymbol{\Gamma}_{bi}^T & \boldsymbol{\Gamma}_{ii}^T & -\mathbf{C}_{p,ib}^{\varepsilon} & -\mathbf{C}_{p,ii}^{\varepsilon} \end{bmatrix} \begin{bmatrix} \mathbf{x}_b \\ \mathbf{x}_i \\ \mathbf{V}_b \\ \mathbf{V}_i \end{bmatrix} = \begin{bmatrix} \mathbf{f}_b \\ \mathbf{f}_i \\ \mathbf{q}_b \\ \mathbf{q}_i \end{bmatrix}, \tag{G.1}$$

where $\mathbf{V}_b$ ($\mathbf{q}_b$) and $\mathbf{V}_i$ ($\mathbf{q}_i$) are the voltage (charges) associated to electrode DoFs and internal electrical DoFs, respectively. Assuming $\mathbf{f}_i = \mathbf{0}$ and $\mathbf{q}_i = \mathbf{0}$, the internal voltages are statically determined by the other variables. Since the Craig-Bampton reduction method is statically exact, the effect of the internal voltages is exactly represented in the ROM whatever the retained internal DoFs. This statement is further supported by the fact that the CNM shape matrix (obtained by solving the generalized eigenvalue problem associated to Equation (G.1) with $\mathbf{x}_b = \mathbf{V}_b = \mathbf{0}$) is given by

$$\begin{bmatrix} \boldsymbol{\Phi}_i & \mathbf{0} \\ \left(\mathbf{C}_{p,ii}^{\varepsilon}\right)^{-1} \boldsymbol{\Gamma}_{ii}^T \boldsymbol{\Phi}_i & \boldsymbol{\Phi}_{e,i} \end{bmatrix} \tag{G.2}$$

where

$$\left(\mathbf{K}_{ii} + \boldsymbol{\Gamma}_{ii} \left(\mathbf{C}_{p,ii}^{\varepsilon}\right)^{-1} \boldsymbol{\Gamma}_{ii}^T\right) \boldsymbol{\Phi}_i = \mathbf{M}_{ii} \boldsymbol{\Phi}_i \boldsymbol{\Omega}_i^2. \tag{G.3}$$

and $\boldsymbol{\Phi}_{e,i}$ can be chosen arbitrarily to span the full space of internal electrical DoFs. Hence, if a classical Craig-Bampton approach is used, the internal DoFs can be expressed with the boundary DoFs and the CNM modal coordinates $\boldsymbol{\eta}_i$ (associated to the first block of columns in Equation (G.2)) and $\boldsymbol{\eta}_{e,i}$ (associated to the second block of columns in Equation (G.2)) as

$$\begin{bmatrix} \mathbf{x}_b \\ \mathbf{V}_b \\ \mathbf{x}_i \\ \mathbf{V}_i \end{bmatrix} = \begin{bmatrix} \mathbf{I} & \mathbf{0} & \mathbf{0} & \mathbf{0} \\ \mathbf{0} & \mathbf{I} & \mathbf{0} & \mathbf{0} \\ \boldsymbol{\Phi}_c & \boldsymbol{\Phi}_{c,p} & \boldsymbol{\Phi}_i & \mathbf{0} \\ \left(\mathbf{C}_{p,ii}^{\varepsilon}\right)^{-1} \boldsymbol{\Gamma}_{ib} & -\left(\mathbf{C}_{p,ii}^{\varepsilon}\right)^{-1} \mathbf{C}_{p,ib}^{\varepsilon} & \left(\mathbf{C}_{p,ii}^{\varepsilon}\right)^{-1} \boldsymbol{\Gamma}_{ii}^T \boldsymbol{\Phi}_i & \boldsymbol{\Phi}_{e,i} \end{bmatrix} \begin{bmatrix} \mathbf{x}_b \\ \mathbf{V}_b \\ \boldsymbol{\eta}_i \\ \boldsymbol{\eta}_{e,i} \end{bmatrix} = \mathbf{R}_{CB} \begin{bmatrix} \mathbf{x}_b \\ \mathbf{V}_b \\ \boldsymbol{\eta}_i \\ \boldsymbol{\eta}_{e,i} \end{bmatrix} \tag{G.4}$$

With this transformation matrix, it can be shown that the reduced mass matrix becomes

$$\mathbf{M}_{CB} = \mathbf{R}_{CB}^{T}\mathbf{M}\mathbf{R}_{CB} = \begin{bmatrix} \widetilde{\mathbf{M}}_{bb} & \widetilde{\mathbf{M}}_{bi} & \widetilde{\mathbf{M}}_{be} & \mathbf{0} \\ \widetilde{\mathbf{M}}_{ib} & \mathbf{I} & \widetilde{\mathbf{M}}_{ie} & \mathbf{0} \\ \widetilde{\mathbf{M}}_{eb} & \widetilde{\mathbf{M}}_{ei} & \widetilde{\mathbf{M}}_{ee} & \mathbf{0} \\ \mathbf{0} & \mathbf{0} & \mathbf{0} & \mathbf{0} \end{bmatrix}. \tag{G.5}$$

The non-zero block is identical to the reduced mass matrix in Equation (6.10). Identical transformations and approximations to Section 6.3 can thus be used to retrieve a ROM having matrices with the same structure as Equation (3.1). Furthermore, the reduction approach does not need to retain purely electrical CNMs ($\mathbf{\Phi}_{e,i}$), because they only have a static effect and their influence is thus captured exactly by the Craig-Bampton reduction method. This is naturally performed when the CNMs are selected in ascending order of frequency, since the frequencies associated to these purely electrical CNMs are infinite.

Bibliography

[1] M. Darecki, C. Edelstenne, T. Enders, E. Fernandez, P. Hartman, J.-P. Herteman, M. Kerkloh, I. King, P. Ky, M. Mathieu, G. Orsi, G. Schotman, C. Smith, and J.-D. Wörner, "Flightpath 2050 Europe's vision for aviation," European commission, Brussels, Tech. Rep., 2011.

[2] Airbus, "Airbus reveals new zero-emission concept aircraft," 2020.

[3] "Waypoint 2050," Air Transport Action Group, Tech. Rep. September, 2020.

[4] A. Preumont, *Vibration Control of Active Structures*, 3rd ed., ser. Solid Mechanics and Its Applications, G. Gladwell, Ed. Dordrecht: Springer Netherlands, 2011, vol. 179.

[5] H. Frahm, "Device for Damping Vibrations of Bodies," 1911.

[6] J. Ormondroyd and J. Den Hartog, "Theory of the dynamic vibration absorber," *Journal of Applied Mechanics*, vol. 50, no. 7, pp. 11–22, 1928.

[7] J. E. Brock, "A Note on the Damped Vibration Absorber," *Transactions of the ASME, Journal of Applied Mechanics*, vol. 13, no. 4, pp. A–284, 1946.

[8] J. P. Den Hartog, *Mechanical Vibrations*. Courier Corporation, 1985.

[9] O. Nishihara and T. Asami, "Closed-Form Solutions to the Exact Optimizations of Dynamic Vibration Absorbers (Minimizations of the Maximum Amplitude Magnification Factors)," *Journal of Vibration and Acoustics*, vol. 124, no. 4, p. 576, 2002.

[10] M. Gutierrez Soto and H. Adeli, "Tuned Mass Dampers," *Archives of Computational Methods in Engineering*, vol. 20, no. 4, pp. 419–431, dec 2013.

[11] S. Elias and V. Matsagar, "Research developments in vibration control of structures using passive tuned mass dampers," *Annual Reviews in Control*, vol. 44, pp. 129–156, 2017.

[12] R. L. Forward, "Electronic damping of vibrations in optical structures," *Applied Optics*, vol. 18, no. 5, p. 690, mar 1979.

[13] N. Hagood and A. von Flotow, "Damping of structural vibrations with piezoelectric materials and passive electrical networks," *Journal of Sound and Vibration*, vol. 146, no. 2, pp. 243–268, apr 1991.

[14] S. O. R. Moheimani and A. J. Fleming, *Piezoelectric Transducers for Vibration Control and Damping*, ser. Advances in Industrial Control. London: Springer-Verlag, 2006.

[15] N. W. Hagood and E. F. Crawley, "Experimental investigation into passive damping enhancement for space structures," *Journal of Guidance, Control, and Dynamics*, vol. 14, no. 6, pp. 1100–1109, nov 1991.

[16] A. Agneni, F. Mastroddi, and G. Polli, "Shunted piezoelectric patches in elastic and aeroelastic vibrations," *Computers & Structures*, vol. 81, no. 2, pp. 91–105, feb 2003.

[17] C.-Y. Yun and S.-J. Kim, "Improvement of aeroelastic stability of hingeless helicopter rotor blade by passive piezoelectric damping," *International Journal of Aeronautical and Space Sciences*, vol. 7, no. 1, pp. 54–64, jun 2006.

[18] D. Alaluf, B. Mokrani, K. Wang, and A. Preumont, "Damping of piezoelectric space instruments: application to an active optics deformable mirror," *CEAS Space Journal*, vol. 11, no. 4, pp. 543–551, dec 2019.

[19] S.-Y. Wu, "Piezoelectric shunts with a parallel R-L circuit for structural damping and vibration control," in *Spie*, C. D. Johnson, Ed., vol. 2720, no. Lc, may 1996, pp. 259–269.

[20] S. Moheimani, "A survey of recent innovations in vibration damping and control using shunted piezoelectric transducers," *IEEE Transactions on Control Systems Technology*, vol. 11, no. 4, pp. 482–494, jul 2003.

[21] B. Yan, K. Wang, Z. Hu, C. Wu, and X. Zhang, "Shunt Damping Vibration Control Technology: A Review," *Applied Sciences*, vol. 7, no. 5, p. 494, 2017.

[22] J. Gripp and D. Rade, "Vibration and noise control using shunted piezoelectric transducers: A review," *Mechanical Systems and Signal Processing*, vol. 112, pp. 359–383, nov 2018.

[23] B. Lossouarn, M. Aucejo, J.-F. Deü, and B. Multon, "Design of inductors with high inductance values for resonant piezoelectric damping," *Sensors and Actuators A: Physical*, vol. 259, pp. 68–76, jun 2017.

[24] C. H. Park and D. J. Inman, "Enhanced Piezoelectric Shunt Design," *Shock and Vibration*, vol. 10, no. 2, pp. 127–133, 2003.

[25] A. Fleming, S. Behrens, and S. Moheimani, "Synthetic impedance for implementation of piezoelectric shunt-damping circuits," *Electronics Letters*, vol. 36, no. 18, p. 1525, 2000.

[26] Y. Fujino, L. Sun, B. M. Pacheco, and P. Chaiseri, "Tuned Liquid Damper (TLD) for Suppressing Horizontal Motion of Structures," *Journal of Engineering Mechanics*, vol. 118, no. 10, pp. 2017–2030, oct 1992.

[27] M. D. Rao, "Recent applications of viscoelastic damping for noise control in automobiles and commercial airplanes," *Journal of Sound and Vibration*, vol. 262, no. 3, pp. 457–474, may 2003.

[28] A. F. Vakakis, O. V. Gendelman, L. A. Bergman, D. M. McFarland, G. Kerschen, and Y. S. Lee, *Nonlinear Targeted Energy Transfer in Mechanical and Structural Systems*, ser. Solid Mechanics and Its Applications. Dordrecht: Springer Netherlands, 2009, vol. 156.

[29] T. Zhou and L. Cheng, "A resonant beam damper tailored with Acoustic Black Hole features for broadband vibration reduction," *Journal of Sound and Vibration*, vol. 430, pp. 174–184, sep 2018.

[30] S. Behrens, A. Fleming, and S. Moheimani, "Passive Vibration Control via Electromagnetic Shunt Damping," *IEEE/ASME Transactions on Mechatronics*, vol. 10, no. 1, pp. 118–122, feb 2005.

[31] Z. Deng and M. J. Dapino, "Review of magnetostrictive materials for structural vibration control," *Smart Materials and Structures*, vol. 27, no. 11, p. 113001, nov 2018.

[32] C. L. Davis and G. A. Lesieutre, "An Actively Tuned Solid-State Vibration Absorber using Capacitive Shunting of Piezoelectric Stiffness," *Journal of Sound and Vibration*, vol. 232, no. 3, pp. 601–617, may 2000.

[33] G. F. Franklin, J. D. Powell, and M. L. Workman, *Digital Control of Dynamic Systems*, 3rd ed. Addison-wesley Reading, MA, 1998.

[34] M. J. Balas, "Direct Velocity Feedback Control of Large Space Structures," *Journal of Guidance and Control*, vol. 2, no. 3, pp. 252–253, may 1979.

[35] C. J. Goh and T. K. Caughey, "On the stability problem caused by finite actuator dynamics in the collocated control of large space structures," *International Journal of Control*, vol. 41, no. 3, pp. 787–802, mar 1985.

[36] G. Zhao, A. Paknejad, G. Raze, A. Deraemaeker, G. Kerschen, and C. Collette, "Nonlinear

positive position feedback control for mitigation of nonlinear vibrations," *Mechanical Systems and Signal Processing*, vol. 132, pp. 457–470, oct 2019.

[37] A. Paknejad, G. Zhao, M. Osée, A. Deraemaeker, F. Robert, and C. Collette, "A novel design of positive position feedback controller based on maximum damping and H_2 optimization," *Journal of Vibration and Control*, vol. 26, no. 15-16, pp. 1155–1164, aug 2020.

[38] A. Preumont, J.-P. Dufour, and C. Malekian, "Active damping by a local force feedback with piezoelectric actuators," *Journal of Guidance, Control, and Dynamics*, vol. 15, no. 2, pp. 390–395, mar 1992.

[39] G. Zhao, A. Paknejad, A. Deraemaeker, and C. Collette, "H_∞ optimization of an integral force feedback controller," *Journal of Vibration and Control*, vol. 25, no. 17, pp. 2330–2339, sep 2019.

[40] C. Collette and S. Chesné, "Robust hybrid mass damper," *Journal of Sound and Vibration*, vol. 375, pp. 19–27, aug 2016.

[41] G. S. Agnes, "Active/passive piezoelectric vibration suppression," in *Journal of Intelligent Materials, Systems, and Structures*, C. D. Johnson, Ed., vol. 6, may 1994, pp. 24–34.

[42] M. Tsai and K. Wang, "On the Structural Damping Characteristics of Active Piezoelectric Actuators with Passive Shunt," *Journal of Sound and Vibration*, vol. 221, no. 1, pp. 1–22, mar 1999.

[43] K. W. Wang and J. Tang, *Adaptive Structural Systems with Piezoelectric Transducer Circuitry*. Boston, MA: Springer US, 2008.

[44] A. Paknejad, G. Raze, G. Zhao, M. Osée, A. Deraemaeker, F. Robert, G. Kerschen, and C. Collette, "Hybridization of Active Control and Pasive Resonant Shunt," in *Proceedings of the 9th ECCOMAS Thematic Conference on Smart Structures and Materials*. Paris: International Centre for Numerical Methods in Engineering (CIMNE), 2019, pp. 930–941.

[45] A. Paknejad, G. Zhao, S. Chesné, A. Deraemaeker, and C. Collette, "Hybrid Electromagnetic Shunt Damper for Vibration Control," *Journal of Vibration and Acoustics*, vol. 143, no. 2, pp. 1–11, apr 2021.

[46] CFM56 turbofan aircraft engine Cutaway Drawing. https://conceptbunny.com/cfm56-turbofan-aircraft-engine/, accessed: 2021/01/17.

[47] A. Kermanpur, H. Sepehri Amin, S. Ziaei-Rad, N. Nourbakhshnia, and M. Mosaddeghfar, "Failure analysis of Ti6Al4V gas turbine compressor blades," *Engineering Failure Analysis*, vol. 15, no. 8, pp. 1052–1064, dec 2008.

[48] A. Mateo, "On the feasibility of BLISK produced by linear friction welding," *Revista de Metalurgia*, vol. 50, no. 3, p. e023, aug 2014.

[49] D. Ewins, "Control of vibration and resonance in aero engines and rotating machinery – An overview," *International Journal of Pressure Vessels and Piping*, vol. 87, no. 9, pp. 504–510, sep 2010.

[50] M. P. Castanier and C. Pierre, "Modeling and Analysis of Mistuned Bladed Disk Vibration: Current Status and Emerging Directions," *Journal of Propulsion and Power*, vol. 22, no. 2, pp. 384–396, mar 2006.

[51] M. Krack, L. Salles, and F. Thouverez, "Vibration Prediction of Bladed Disks Coupled by Friction Joints," *Archives of Computational Methods in Engineering*, vol. 24, no. 3, pp. 589–636, jul 2017.

[52] D. Laxalde, "Étude d'amortisseurs non-linéaires appliqués aux roues aubagées et aux systèmes multi-étages," Ph.D. dissertation, École Centrale de Lyon, 2007.

[53] N. Nguyen, "Blading system and method for controlling structural vibrations," 2000.

[54] B. Mokrani, "Piezoelectric Shunt Damping of Rotationally Periodic Structures," Ph.D. dissertation, Université Libre de Bruxelles, 2015.

[55] A. J. Fleming, "Synthesis and Implementation of Sensor-less Shunt Controllers for Piezoelectric and Electromagnetic Vibration Control," Ph.D. dissertation, University of Newcastle, 2004.

[56] A. J. Fleming, S. Behrens, and S. O. R. Moheimani, "An autonomous piezoelectric shunt damping system," G. S. Agnes and K.-W. Wang, Eds., vol. 5052, jul 2003, pp. 207–216.

[57] Z. Plíva, M. Kolář, P. Došek, and T. Sluka, "A Piezoelectric Elements and Their Electronics Driving with Help of FPGA Circuits," *Ferroelectrics*, vol. 351, no. 1, pp. 187–195, jun 2007.

[58] I. Giorgio, "Multimode Collocated Vibration Control with Multiple Piezoelectric Transducers," Ph.D. dissertation, Università degli studi di Roma, 2008.

[59] G. Rosi, "Control of sound radiation and transmission by means of passive piezoelectric networks : modelling , optimization and experimental implementation," Ph.D. dissertation, Université Pierre et Marie Curie - Paris VI, 2010.

[60] G. Matten, M. Collet, S. Cogan, and E. Sadoulet-Reboul, "Synthetic Impedance for Adaptive Piezoelectric Metacomposite," *Procedia Technology*, vol. 15, pp. 84–89, 2014.

[61] G. Matten, "Conception robuste d'actionneurs électromécaniques distribués pour le contrôle vibroacoustique de structures," Ph.D. dissertation, Université de Franche-Comté, apr 2016.

[62] J. Nečásek, J. Václavík, and P. Marton, "Digital synthetic impedance for application in vibration damping," *Review of Scientific Instruments*, vol. 87, no. 2, p. 024704, feb 2016.

[63] J. Necasek, J. Vaclavik, and P. Marton, "Comparison of analog front-ends for digital synthetic impedance device," in *2017 IEEE International Workshop of Electronics, Control, Measurement, Signals and their Application to Mechatronics (ECMSM)*. IEEE, may 2017, pp. 1–4.

[64] T. M. P. Silva, "Vibration attenuation in linear and nonlinear flexible structures via nonlinear piezoelectric shunt circuits," Ph.D. dissertation, University of São Paulo, 2018.

[65] L. Dal Bo, P. Gardonio, D. Casagrande, and S. Saggini, "Smart panel with sweeping and switching piezoelectric patch vibration absorbers: Experimental results," *Mechanical Systems and Signal Processing*, vol. 120, pp. 308–325, apr 2019.

[66] C. Sugino, S. Leadenham, M. Ruzzene, and A. Erturk, "Metamaterial piezoelectric beam with synthetic impedance shunts," in *Active and Passive Smart Structures and Integrated Systems 2017*, G. Park, Ed., vol. 10164, apr 2017, p. 1016410.

[67] K. Yi, G. Matten, M. Ouisse, E. Sadoulet-Reboul, M. Collet, and G. Chevallier, "Programmable metamaterials with digital synthetic impedance circuits for vibration control," *Smart Materials and Structures*, vol. 29, no. 3, p. 035005, mar 2020.

[68] A. Meitzler, H. Tiersten, A. Warner, D. Berlincourt, G. Coquin, and F. Welsh III, "IEEE Standard on Piezoelectricity," *ANSI/IEEE Std 176-1987*, 1988.

[69] C. K. Alexander and M. N. O. Sadiku, *Fundamentals of Electric Circuits*. Cambridge: McGraw-Hill Education, 2000.

[70] G. A. Lesieutre and C. L. Davis, "Can a Coupling Coefficient of a Piezoelectric Device be Higher Than Those of Its Active Material?" *Journal of Intelligent Material Systems and Structures*, vol. 8, no. 10, pp. 859–867, oct 1997.

[71] A. F. Ulitko, "Theory of electromechanical energy conversion in nonuniformly deformable piezoceramics," *Soviet Applied Mechanics*, vol. 13, no. 10, pp. 1055–1062, oct 1977.

[72] K.-D. Wolf, "Electromechanical Energy Conversion in asymmetric Piezoelectric Bending Actuators," Ph.D. dissertation, Technischen Universität Darmstadt, 2000.

[73] M. Neubauer, "Optimal Design of Piezoelectric Actuators for Shunt Damping Techniques," *Archives of Acoustics*, vol. 39, no. 4, pp. 615–622, mar 2015.

[74] K. Yamada, H. Matsuhisa, H. Utsuno, and K. Sawada, "Optimum tuning of series and parallel LR circuits for passive vibration suppression using piezoelectric elements," *Journal of Sound and Vibration*, vol. 329, no. 24, pp. 5036–5057, nov 2010.

[75] O. Thomas, J. Ducarne, and J.-F. Deü, "Performance of piezoelectric shunts for vibration reduction," *Smart Materials and Structures*, vol. 21, no. 1, p. 015008, jan 2012.

[76] J. Ducarne, O. Thomas, and J.-F. Deü, "Placement and dimension optimization of shunted piezoelectric patches for vibration reduction," *Journal of Sound and Vibration*, vol. 331, no. 14, pp. 3286–3303, jul 2012.

[77] M. Berardengo, O. Thomas, C. Giraud-Audine, and S. Manzoni, "Improved resistive shunt by means of negative capacitance: New circuit, performances and multi-mode control," *Smart Materials and Structures*, vol. 25, no. 7, pp. 1–23, 2016.

[78] E. Crawley and J. De Luis, "Use of piezo-ceramics as distributed actuators in large space structures," in *26th Structures, Structural Dynamics, and Materials Conference*. Reston, Virigina: American Institute of Aeronautics and Astronautics, apr 1985, p. 626.

[79] A. R. de Faria, "The impact of finite-stiffness bonding on the sensing effectiveness of piezoelectric patches," *Smart Materials and Structures*, vol. 12, no. 4, pp. N5–N8, aug 2003.

[80] C. Maurini, J. Pouget, and F. Dell'Isola, "Extension of the Euler–Bernoulli model of piezoelectric laminates to include 3D effects via a mixed approach," *Computers & Structures*, vol. 84, no. 22-23, pp. 1438–1458, sep 2006.

[81] T. Ikegame, K. Takagi, and T. Inoue, "Exact Solutions to H∞ and H2 Optimizations of Passive Resonant Shunt Circuit for Electromagnetic or Piezoelectric Shunt Damper," *Journal of Vibration and Acoustics*, vol. 141, no. 3, p. 031015, jun 2019.

[82] J. Høgsberg and S. Krenk, "Balanced calibration of resonant shunt circuits for piezoelectric vibration control," *Journal of Intelligent Material Systems and Structures*, vol. 23, no. 17, pp. 1937–1948, nov 2012.

[83] P. Soltani, G. Kerschen, G. Tondreau, and A. Deraemaeker, "Piezoelectric vibration damping using resonant shunt circuits: an exact solution," *Smart Materials and Structures*, vol. 23, no. 12, p. 125014, dec 2014.

[84] C. H. Park and D. J. Inman, "Uniform model for series R-L and parallel R-L shunt circuits and power consumption," N. M. Wereley, Ed., vol. 3668, no. March, jun 1999, pp. 797–804.

[85] G. Caruso, "A critical analysis of electric shunt circuits employed in piezoelectric passive vibration damping," *Smart Materials and Structures*, vol. 10, no. 5, pp. 1059–1068, oct 2001.

[86] X. Tang, Y. Liu, W. Cui, and L. Zuo, "Analytical Solutions to H2 and H∞ Optimizations

of Resonant Shunted Electromagnetic Tuned Mass Damper and Vibration Energy Harvester," *Journal of Vibration and Acoustics*, vol. 138, no. 1, feb 2016.

[87] R. L. Forward, "Electromechanical transducer-coupled mechanical structure with negative capacitance compensation circuit," 1979.

[88] M. Berardengo, O. Thomas, C. Giraud-Audine, and S. Manzoni, "Improved resistive shunt by means of negative capacitance: new circuit, performances and multi-mode control," *Smart Materials and Structures*, vol. 25, no. 7, p. 075033, jul 2016.

[89] M. Berardengo, S. Manzoni, O. Thomas, and M. Vanali, "Piezoelectric resonant shunt enhancement by negative capacitances: Optimisation, performance and resonance cancellation," *Journal of Intelligent Material Systems and Structures*, vol. 29, no. 12, pp. 2581–2606, 2018.

[90] C. Richard, D. Guyomar, D. Audigier, and G. Ching, "Semi-passive damping using continuous switching of a piezoelectric device," in *Smart Structures and Materials 1999: Passive Damping and Isolation*, T. T. Hyde, Ed., vol. 3672, no. March, jun 1999, pp. 104–111.

[91] W. W. Clark, "Vibration Control with State-Switched Piezoelectric Materials," *Journal of Intelligent Material Systems and Structures*, vol. 11, no. 4, pp. 263–271, apr 2000.

[92] C. Richard, D. Guyomar, D. Audigier, and H. Bassaler, "Enhanced semi-passive damping using continuous switching of a piezoelectric device on an inductor," T. T. Hyde, Ed., vol. 3989, apr 2000, pp. 288–299.

[93] H. Ji, J. Qiu, J. Cheng, and D. Inman, "Application of a Negative Capacitance Circuit in Synchronized Switch Damping Techniques for Vibration Suppression," *Journal of Vibration and Acoustics*, vol. 133, no. 4, pp. 1–10, aug 2011.

[94] E. Lefeuvre, A. Badel, L. Petit, C. Richard, and D. Guyomar, "Semi-passive Piezoelectric Structural Damping by Synchronized Switching on Voltage Sources," *Journal of Intelligent Material Systems and Structures*, vol. 17, no. 8-9, pp. 653–660, sep 2006.

[95] D. Niederberger and M. Morari, "An autonomous shunt circuit for vibration damping," *Smart Materials and Structures*, vol. 15, no. 2, pp. 359–364, apr 2006.

[96] J. Ducarne, "Modélisation et optimisation de dispositifs non-linéaires d'amortissement de structures par systèmes piézoélectriques commutés," Ph.D. dissertation, Conservatoire National des Arts et Métiers, 2009.

[97] B. Lossouarn, "Multimodal vibration damping of structures coupled to their analogous piezoelectric networks," Ph.D. dissertation, Conservatoire national des arts et metiers - CNAM, 2016.

[98] R. Darleux, "Development of analogous piezoelectric networks for the vibration damping of complex structures," Ph.D. dissertation, HESAM Université, 2020.

[99] R. Riordan, "Simulated inductors using differential amplifiers," *Electronics Letters*, vol. 3, no. 2, p. 50, 1967.

[100] A. Antoniou, "Realisation of gyrators using operational amplifiers, and their use in RC-active-network synthesis," *Proceedings of the Institution of Electrical Engineers*, vol. 116, no. 11, p. 1838, 1969.

[101] C. Newcomb and I. Flinn, "Improving the linearity of piezoelectric ceramic actuators," *Electronics Letters*, vol. 18, no. 11, p. 442, 1982.

[102] G. C. Goodwin, S. F. Graebe, and M. E. Salgado, *Control System Design*. Upper Saddle River, NJ: Prentice Hall, 2001.

[103] P. Horowitz and W. Hill, *The Art of Electronics*, 3rd ed. Cambridge University Press, 2015.

[104] B. Lossouarn, J.-F. Deü, and G. Kerschen, "A fully passive nonlinear piezoelectric vibration absorber," *Philosophical Transactions of the Royal Society A: Mathematical, Physical and Engineering Sciences*, vol. 376, no. 2127, p. 20170142, aug 2018.

[105] "OPA454 High-Voltage (100-V), High-Current (50-mA) Operational Amplifiers, G = 1 Stable," 2016.

[106] O. Brune, "Synthesis of a finite two-terminal network whose driving-point impedance is a prescribed function of frequency," Ph.D. dissertation, Massachusetts Institute of Technology, 1931.

[107] J. Gannett and L. Chua, "Frequency Domain Passivity Conditions for Linear Time-Invariant Lumped Networks," EECS Department, University of California, Berkeley, Berkeley, Tech. Rep. Technical Report No. UCB/ERL M78/21, 1978.

[108] S. O. R. Moheimani, A. J. Fleming, and S. Behrens, "On the feedback structure of wideband piezoelectric shunt damping systems," *Smart Materials and Structures*, vol. 12, no. 1, pp. 49–56, feb 2003.

[109] A. Fleming and S. Moheimani, "Control orientated synthesis of high-performance piezoelectric shunt impedances for structural vibration control," *IEEE Transactions on Control Systems Technology*, vol. 13, no. 1, pp. 98–112, jan 2005.

[110] J. M. Cardoso, J. G. F. Coutinho, and P. C. Diniz, *Embedded Computing for High Performance*. Elsevier, 2017.

[111] A. Sarwar, "CMOS Power Consumption and C_{pd} Calculation," 1997.

[112] I. Williams, "TI Precision Labs - Op Amps: Power and Temperature," 2015.

[113] A. Tustin, "A method of analysing the behaviour of linear systems in terms of time series," *Journal of the Institution of Electrical Engineers - Part IIA: Automatic Regulators and Servo Mechanisms*, vol. 94, no. 1, pp. 130–142, may 1947.

[114] X. Xu, N. Ozay, and V. Gupta, "Passivity-Based Analysis of Sampled and Quantized Control Implementations," *Automatica*, vol. 119, p. 109064, oct 2020.

[115] A. E.-N. Gene F. Franklin, J. David Powell, *Feedback Control of Dynamic Systems*. Pearson London, 2015.

[116] K. Walton and J. Marshall, "Direct method for TDS stability analysis," *IEE Proceedings D Control Theory and Applications*, vol. 134, no. 2, p. 101, 1987.

[117] G. Raze, A. Paknejad, G. Zhao, V. Broun, C. Collette, and G. Kerschen, "Suppression of delay-induced instabilities of digital piezoelectric vibration absorbers," in *Proceedings of the 9th ECCOMAS Thematic Conference on Smart Structures and Materials - SMART 2019*, A. Benjeddou, N. Mechbal, and J.-F. Deü, Eds. International Centre for Numerical Methods in Engineering (CIMNE), 2019, pp. 991–1001.

[118] B. D. Marneffe, "Active and Passive Vibration Isolation and Damping via Shunted Transducers," Ph.D. dissertation, Universite Libre de Bruxelles, 2007.

[119] J. Høgsberg and S. Krenk, "Calibration of piezoelectric RL shunts with explicit residual mode correction," *Journal of Sound and Vibration*, vol. 386, pp. 65–81, 2017.

[120] P. Gardonio and D. Casagrande, "Shunted piezoelectric patch vibration absorber on two-dimensional thin structures: Tuning considerations," *Journal of Sound and Vibration*, vol. 395, pp. 26–47, 2017.

[121] J. F. Toftekær, A. Benjeddou, J. Høgsberg, and S. Krenk, "Optimal piezoelectric

resistive–inductive shunt damping of plates with residual mode correction," *Journal of Intelligent Material Systems and Structures*, vol. 29, no. 16, pp. 3346–3370, sep 2018.

[122] F. A. C. Viana and V. Steffen, Jr, "Multimodal vibration damping through piezoelectric patches and optimal resonant shunt circuits," *Journal of the Brazilian Society of Mechanical Sciences and Engineering*, vol. 28, no. 3, pp. 293–310, sep 2006.

[123] S. Alessandroni, F. Dell'Isola, and M. Porfiri, "A revival of electric analogs for vibrating mechanical systems aimed to their efficient control by PZT actuators," *International Journal of Solids and Structures*, vol. 39, no. 20, pp. 5295–5324, oct 2002.

[124] I. Giorgio, L. Galantucci, A. Della Corte, and D. Del Vescovo, "Piezo-electromechanical smart materials with distributed arrays of piezoelectric transducers: Current and upcoming applications," *International Journal of Applied Electromagnetics and Mechanics*, vol. 47, no. 4, pp. 1051–1084, jun 2015.

[125] D. L. Edberg, A. S. Bicos, and J. S. Fechter, "On piezoelectric energy conversion for electronic passive damping enhancement," in *Proceedings of Damping*, 1991, pp. 717–724.

[126] J. J. Hollkamp, "Multimodal Passive Vibration Suppression with Piezoelectric Materials and Resonant Shunts," *Journal of Intelligent Material Systems and Structures*, vol. 5, no. 1, pp. 49–57, jan 1994.

[127] S.-Y. Wu, "Method for multiple-mode shunt damping of structural vibration using a single PZT transducer," L. P. Davis, Ed., vol. 3327, no. 1, jun 1998, pp. 159–168.

[128] S. Behrens, S. Moheimani, and A. Fleming, "Multiple mode current flowing passive piezoelectric shunt controller," *Journal of Sound and Vibration*, vol. 266, no. 5, pp. 929–942, oct 2003.

[129] A. J. Fleming, S. Behrens, and S. O. R. Moheimani, "Reducing the inductance requirements of piezoelectric shunt damping systems," *Smart Materials and Structures*, vol. 12, no. 1, pp. 57–64, feb 2003.

[130] A. Agneni, M. Del Sorbo, F. Mastroddi, and G. M. Polli, "Multi-modal damping by shunted piezo-patches: Possible aeroelastic applications," *International Journal of Applied Electromagnetics and Mechanics*, vol. 24, no. 1-2, pp. 1–24, dec 2006.

[131] A. L. Goldstein, "Self-Tuning Multimodal Piezoelectric Shunt Damping," *Journal of the Brazilian Society of Mechanical Sciences and Engineering*, vol. 33, no. 4, pp. 428–436, dec 2011.

[132] G. Raze, A. Jadoul, V. Broun, and G. Kerschen, "A Simplified Current Blocking Piezoelectric Shunt Circuit for Multimodal Vibration Mitigation," in *Conference Proceedings of the Society for Experimental Mechanics Series*, 2020, vol. 5, pp. 23–25.

[133] G. Raze, A. Paknejad, G. Zhao, C. Collette, and G. Kerschen, "Multimodal vibration damping using a simplified current blocking shunt circuit," *Journal of Intelligent Material Systems and Structures*, vol. 31, no. 14, pp. 1731–1747, aug 2020.

[134] N. W. Hagood, W. H. Chung, and A. Von Flotow, "Modelling of Piezoelectric Actuator Dynamics for Active Structural Control," *Journal of Intelligent Material Systems and Structures*, vol. 1, no. 3, pp. 327–354, jul 1990.

[135] A. Benjeddou, "Advances in piezoelectric finite element modeling of adaptive structural elements: a survey," *Computers & Structures*, vol. 76, no. 1-3, pp. 347–363, jun 2000.

[136] V. Piefort, "Finite Element Modelling of Piezoelectric Active Structures," Ph.D. dissertation, Université Libre de Bruxelles, 2001.

[137] O. Thomas, J.-F. Deü, and J. Ducarne, "Vibrations of an elastic structure with shunted piezoelectric patches: efficient finite element formulation and electromechanical coupling coefficients," *International Journal for Numerical Methods in Engineering*, vol. 80, no. 2, pp. 235–268, oct 2009.

[138] E. Balmes and A. Deraemaeker, "Modeling structures with piezoelectric materials. Theory and SDT turorial," p. 71, 2014.

[139] J. F. Toftekær and J. Høgsberg, "Multi-mode piezoelectric shunt damping with residual mode correction by evaluation of modal charge and voltage," *Journal of Intelligent Material Systems and Structures*, vol. 31, no. 4, pp. 570–586, mar 2020.

[140] M. Géradin and D. J. Rixen, *Mechanical vibrations: theory and application to structural dynamics*. John Wiley & Sons, 2014.

[141] R. M. Foster, "A Reactance Theorem," *Bell System Technical Journal*, vol. 3, no. 2, pp. 259–267, apr 1924.

[142] W.-K. Chen, *Passive, Active, and Digital Filters*. CRC Press, oct 2018.

[143] S. Moheimani and S. Behrens, "Multimode Piezoelectric Shunt Damping With a Highly Resonant Impedance," *IEEE Transactions on Control Systems Technology*, vol. 12, no. 3, pp. 484–491, may 2004.

[144] M. Berardengo, S. Manzoni, M. Vanali, and R. Bonsignori, "Enhancement of the broadband vibration attenuation of a resistive piezoelectric shunt," *Journal of Intelligent Material Systems and Structures*, in press.

[145] G. Raze, B. Lossouarn, A. Paknejad, G. Zhao, J. F. Deü, C. Collette, and G. Kerschen, "A multimodal nonlinear piezoelectric vibration absorber," in *Proceedings of ISMA 2018 - International Conference on Noise and Vibration Engineering and USD 2018 - International Conference on Uncertainty in Structural Dynamics*, 2018, pp. 63–77.

[146] A. Cigada, S. Manzoni, M. Redaelli, and M. Vanali, "Optimization of the current flowing technique aimed at semi-passive multi-modal vibration reduction," *Journal of Vibration and Control*, vol. 18, no. 2, pp. 298–312, feb 2012.

[147] A. Fleming, S. Behrens, and S. Reza Moheimani, "Optimization and implementation of multimode piezoelectric shunt damping systems," *IEEE/ASME Transactions on Mechatronics*, vol. 7, no. 1, pp. 87–94, mar 2002.

[148] C. Davis and G. Lesieutre, "A modal strain energy approach to the prediction of resistively shunted piezoceramic damping," *Journal of Sound and Vibration*, vol. 184, no. 1, pp. 129–139, jul 1995.

[149] K. M. Guo and J. Jiang, "Independent modal resonant shunt for multimode vibration control of a truss-cored sandwich panel," *International Journal of Dynamics and Control*, vol. 2, no. 3, pp. 326–334, sep 2014.

[150] F. Dell'Isola and S. Vidoli, "Continuum modelling of piezoelectromechanical truss beams: an application to vibration damping," *Archive of Applied Mechanics (Ingenieur Archiv)*, vol. 68, no. 1, pp. 1–19, feb 1998.

[151] S. Vidoli and F. Dell'Isola, "Modal coupling in one-dimensional electromechanical structured continua," *Acta Mechanica*, vol. 141, no. 1-2, pp. 37–50, mar 2000.

[152] C. Maurini, F. Dell'Isola, and D. Del Vescovo, "Comparison of piezoelectronic networks acting as distributed vibration absorbers," *Mechanical Systems and Signal Processing*, vol. 18, no. 5, pp. 1243–1271, sep 2004.

[153] M. Porfiri, F. Dell'Isola, and F. M. Frattale Mascioli, "Circuit analog of a beam

and its application to multimodal vibration damping, using piezoelectric transducers," *International Journal of Circuit Theory and Applications*, vol. 32, no. 4, pp. 167–198, jul 2004.

[154] B. Lossouarn, M. Aucejo, and J.-F. Deü, "Multimodal coupling of periodic lattices and application to rod vibration damping with a piezoelectric network," *Smart Materials and Structures*, vol. 24, no. 4, p. 045018, apr 2015.

[155] B. Lossouarn, J. F. Deü, and M. Aucejo, "Multimodal vibration damping of a beam with a periodic array of piezoelectric patches connected to a passive electrical network," *Smart Materials and Structures*, vol. 24, no. 11, p. 115037, nov 2015.

[156] B. Lossouarn, J.-F. Deü, M. Aucejo, and K. A. Cunefare, "Multimodal vibration damping of a plate by piezoelectric coupling to its analogous electrical network," *Smart Materials and Structures*, vol. 25, no. 11, p. 115042, nov 2016.

[157] R. Darleux, B. Lossouarn, and J.-f. Deü, "Broadband vibration damping of non-periodic plates by piezoelectric coupling to their electrical analogues," *Smart Materials and Structures*, vol. 29, no. 5, p. 054001, may 2020.

[158] I. Giorgio, A. Culla, and D. Del Vescovo, "Multimode vibration control using several piezoelectric transducers shunted with a multiterminal network," *Archive of Applied Mechanics*, vol. 79, no. 9, pp. 859–879, sep 2009.

[159] J. J. Grainger and W. D. J. Stevenson, *Power System Analysis*. McGraw-Hill Education, 1994.

[160] M. Porfiri, C. Maurini, and J. Pouget, "Identification of electromechanical modal parameters of linear piezoelectric structures," *Smart Materials and Structures*, vol. 16, no. 2, pp. 323–331, apr 2007.

[161] K. Swamy, "On Sylvester's criterion for positive-semidefinite matrices," *IEEE Transactions on Automatic Control*, vol. 18, no. 3, pp. 306–306, jun 1973.

[162] G. Raze and G. Kerschen, "H_∞ optimization of multiple tuned mass dampers for multimodal vibration control," *Computers & Structures*, vol. 248, p. 106485, may 2021.

[163] V. Steffen and D. J. Inman, "Optimal Design of Piezoelectric Materials for Vibration Damping in Mechanical Systems," *Journal of Intelligent Material Systems and Structures*, vol. 10, no. 12, pp. 945–955, dec 1999.

[164] J.-Y. Jeon, "Passive vibration damping enhancement of piezoelectric shunt damping system using optimization approach," *Journal of Mechanical Science and Technology*, vol. 23, no. 5, pp. 1435–1445, may 2009.

[165] M. Berardengo, S. Manzoni, and A. M. Conti, "Multi-mode passive piezoelectric shunt damping by means of matrix inequalities," *Journal of Sound and Vibration*, vol. 405, pp. 287–305, 2017.

[166] P. Gardonio, M. Zientek, and L. D. Bo, "Panel with self-tuning shunted piezoelectric patches for broadband flexural vibration control," *Mechanical Systems and Signal Processing*, vol. 134, pp. 1–32, 2019.

[167] J. Nocedal and S. J. J. Wright, *Numerical Optimization*, ser. Springer Series in Operations Research and Financial Engineering. Springer New York, 2006, vol. 43, no. 2.

[168] J. Ren and Q. Zhang, "Structural Reanalysis Based on FRFs Using Sherman–Morrison–Woodbury Formula," *Shock and Vibration*, vol. 2020, pp. 1–12, jul 2020.

[169] M. Berardengo, J. Høgsberg, S. Manzoni, M. Vanali, A. Brandt, and T. Godi,

"LRLC-shunted piezoelectric vibration absorber," *Journal of Sound and Vibration*, vol. 474, p. 115268, may 2020.

[170] R. E. Roberson, "Synthesis of a nonlinear dynamic vibration absorber," *Journal of the Franklin Institute*, vol. 254, no. 3, pp. 205–220, sep 1952.

[171] R. Ibrahim, "Recent advances in nonlinear passive vibration isolators," *Journal of Sound and Vibration*, vol. 314, no. 3-5, pp. 371–452, jul 2008.

[172] R. Viguie, "Tuning Methodology of Nonlinear Vibration Absorbers Coupled to Nonlinear Mechanical Systems," Ph.D. dissertation, University of Liège, 2010.

[173] G. S. Agnes, "Performance of Nonlinear Mechanical, Resonant-Shunted Piezoelectric, and Electronic Vibration Absorbers for Multi-Degree-of-Freedom Structures," Ph.D. dissertation, Virginia Polytechnic Institute and State University, 1997.

[174] G. S. Agnes and D. J. Inman, "Nonlinear piezoelectric vibration absorbers," *Smart Materials and Structures*, vol. 5, no. 5, pp. 704–714, oct 1996.

[175] B. Zhou, F. Thouverez, and D. Lenoir, "Essentially nonlinear piezoelectric shunt circuits applied to mistuned bladed disks," *Journal of Sound and Vibration*, vol. 333, no. 9, pp. 2520–2542, apr 2014.

[176] F. Petit, M. Loccufier, and D. Aeyels, "The energy thresholds of nonlinear vibration absorbers," *Nonlinear Dynamics*, vol. 74, no. 3, pp. 755–767, nov 2013.

[177] R. Viguié and G. Kerschen, "Nonlinear vibration absorber coupled to a nonlinear primary system: A tuning methodology," *Journal of Sound and Vibration*, vol. 326, no. 3-5, pp. 780–793, oct 2009.

[178] G. Habib and G. Kerschen, "A principle of similarity for nonlinear vibration absorbers," *Physica D: Nonlinear Phenomena*, vol. 332, pp. 1–8, oct 2016.

[179] G. Habib, T. Detroux, R. Viguié, and G. Kerschen, "Nonlinear generalization of Den Hartog's equal-peak method," *Mechanical Systems and Signal Processing*, vol. 52-53, no. 1, pp. 17–28, 2015.

[180] T. Detroux, G. Habib, L. Masset, and G. Kerschen, "Performance, robustness and sensitivity analysis of the nonlinear tuned vibration absorber," *Mechanical Systems and Signal Processing*, vol. 60, pp. 799–809, 2015.

[181] P. Soltani and G. Kerschen, "The nonlinear piezoelectric tuned vibration absorber," *Smart Materials and Structures*, vol. 24, no. 7, p. 075015, jul 2015.

[182] G. Habib and G. Kerschen, "Linearization of nonlinear resonances: Isochronicity and force-displacement proportionality," *Journal of Sound and Vibration*, vol. 457, pp. 227–239, sep 2019.

[183] G. Zhao, G. Raze, A. Paknejad, A. Deraemaeker, G. Kerschen, and C. Collette, "Active nonlinear inerter damper for vibration mitigation of Duffing oscillators," *Journal of Sound and Vibration*, vol. 473, p. 115236, may 2020.

[184] X. Sun, J. Xu, F. Wang, and L. Cheng, "Design and experiment of nonlinear absorber for equal-peak and de-nonlinearity," *Journal of Sound and Vibration*, vol. 449, pp. 274–299, jun 2019.

[185] T. Detroux, J.-P. Noël, and G. Kerschen, "Tailoring the resonances of nonlinear mechanical systems," *Nonlinear Dynamics*, oct 2020.

[186] P. Pai, B. Wen, A. Naser, and M. Schulz, "Structural Vibration Control using PZT Patches and Non-Linear Phenomena," *Journal of Sound and Vibration*, vol. 215, no. 2, pp. 273–296, aug 1998.

[187] S. S. Oueini and A. H. Nayfeh, "Analysis and Application of a Nonlinear Vibration Absorber," *Journal of Vibration and Control*, vol. 6, no. 7, pp. 999–1016, oct 2000.

[188] T. M. Silva, M. A. Clementino, C. De Marqui, and A. Erturk, "An experimentally validated piezoelectric nonlinear energy sink for wideband vibration attenuation," *Journal of Sound and Vibration*, vol. 437, pp. 68–78, dec 2018.

[189] S. Lo Feudo, C. Touzé, J. Boisson, and G. Cumunel, "Nonlinear magnetic vibration absorber for passive control of a multi–storey structure," *Journal of Sound and Vibration*, vol. 438, pp. 33–53, jan 2019.

[190] G. Kerschen, J. J. Kowtko, D. M. Mcfarland, L. A. Bergman, and A. F. Vakakis, "Theoretical and Experimental Study of Multimodal Targeted Energy Transfer in a System of Coupled Oscillators," *Nonlinear Dynamics*, vol. 47, no. 1-3, pp. 285–309, dec 2006.

[191] K. Dekemele, R. De Keyser, and M. Loccufier, "Performance measures for targeted energy transfer and resonance capture cascading in nonlinear energy sinks," *Nonlinear Dynamics*, vol. 93, no. 2, pp. 259–284, 2018.

[192] B. Lossouarn, J.-F. Deü, and G. Kerschen, "Multimodal Damping of a Nonlinear Structure with a Passive Piezoelectric Network," in *Special Topics in Structural Dynamics, Volume 5*, N. Dervilis, Ed. Cham: Springer International Publishing, 2019, pp. 161–163.

[193] G. Raze, S. Guichaux, A. Jadoul, V. Broun, and G. Kerschen, "Mitigation of nonlinear vibrations with a digital piezoelectric tuned vibration absorber," in *Seventh International Conference on Nonlinear vibrations, Localization and Energy transfer*, Marseille, 2019.

[194] G. Raze, S. Guichaux, A. Jadoul, V. Broun, and G. Kerschen, "A Digital Absorber for Nonlinear Vibration Mitigation," in *Conference Proceedings of the Society for Experimental Mechanics Series*, 2021, vol. 1, pp. 105–108.

[195] G. Raze, A. Jadoul, S. Guichaux, V. Broun, and G. Kerschen, "A digital nonlinear piezoelectric tuned vibration absorber," *Smart Materials and Structures*, vol. 29, no. 1, p. 015007, jan 2020.

[196] G. Raze and G. Kerschen, "A Multimodal Nonlinear Tuned Vibration Absorber," in *IUTAM Bookseries*. Springer International Publishing, 2020, vol. 37, pp. 235–247.

[197] G. Raze and G. Kerschen, "Multimodal vibration damping of nonlinear structures using multiple nonlinear absorbers," *International Journal of Non-Linear Mechanics*, vol. 119, p. 103308, mar 2020.

[198] S. H. Strogatz, *Nonlinear Dynamics and Chaos*. CRC Press, may 2018.

[199] A. H. Nayfeh and P. F. Pai, *Linear and Nonlinear Structural Mechanics*. Wiley, aug 2004.

[200] A. Lazarus, O. Thomas, and J.-F. Deü, "Finite element reduced order models for nonlinear vibrations of piezoelectric layered beams with applications to NEMS," *Finite Elements in Analysis and Design*, vol. 49, no. 1, pp. 35–51, feb 2012.

[201] H. Kaizuka and B. Siu, "A simple way to reduce hysteresis and creep when using piezoelectric actuators," *Japanese Journal of Applied Physics*, vol. 27, no. 5A, pp. L773–L776, 1988.

[202] J. Rodriguez-Fortun, J. Orus, J. Alfonso, F. Buil, and J. Castellanos, "Hysteresis in Piezoelectric Actuators: Modeling and Compensation," *IFAC Proceedings Volumes*, vol. 44, no. 1, pp. 5237–5242, jan 2011.

[203] I. Kovacic and M. J. Brennan, *The Duffing Equation*. Chichester, UK: John Wiley & Sons, Ltd, mar 2011.

[204] R. Seydel, *Practical Bifurcation and Stability Analysis*, ser. Interdisciplinary Applied Mathematics. New York, NY: Springer New York, 2010, vol. 5.

[205] T. Detroux, L. Renson, L. Masset, and G. Kerschen, "The harmonic balance method for bifurcation analysis of large-scale nonlinear mechanical systems," *Computer Methods in Applied Mechanics and Engineering*, vol. 296, pp. 18–38, nov 2015.

[206] T. Detroux, "Performance and Robustness of Nonlinear Systems Using Bifurcation Analysis," Ph.D. dissertation, Université de Liège, 2016.

[207] M. Krack and J. Gross, *Harmonic Balance for Nonlinear Vibration Problems*, ser. Mathematical Engineering. Cham: Springer International Publishing, 2019.

[208] T.-C. Yuan, J. Yang, and L.-Q. Chen, "A harmonic balance approach with alternating frequency/time domain progress for piezoelectric mechanical systems," *Mechanical Systems and Signal Processing*, vol. 120, pp. 274–289, apr 2019.

[209] T. M. Cameron and J. H. Griffin, "An Alternating Frequency/Time Domain Method for Calculating the Steady-State Response of Nonlinear Dynamic Systems," *Journal of Applied Mechanics*, vol. 56, no. 1, pp. 149–154, mar 1989.

[210] B. Zhou, F. Thouverez, and D. Lenoir, "A variable-coefficient harmonic balance method for the prediction of quasi-periodic response in nonlinear systems," *Mechanical Systems and Signal Processing*, vol. 64-65, pp. 233–244, dec 2015.

[211] A. Renault, O. Thomas, and H. Mahé, "Numerical antiresonance continuation of structural systems," *Mechanical Systems and Signal Processing*, vol. 116, pp. 963–984, feb 2019.

[212] "PA78 Power Operational Amplifier," 2012.

[213] J.-J. E. Slotine and W. Li, *Applied Nonlinear Control*. Prentice hall Englewood Cliffs, NJ, 1991.

[214] M. Guskov and F. Thouverez, "Harmonic Balance-Based Approach for Quasi-Periodic Motions and Stability Analysis," *Journal of Vibration and Acoustics*, vol. 134, no. 3, p. 031003, jun 2012.

[215] J. H. Griffin, "A Review of Friction Damping of Turbine Blade Vibration," *International Journal of Turbo and Jet Engines*, vol. 7, no. 3-4, pp. 297–308, jan 1990.

[216] M. L. Stangeland, R. E. Berenson, G. A. Davis, and E. J. Krie, "Turbine blisk rim friction finger damper," 2002.

[217] A. Lupini, M. Mitra, and B. I. Epureanu, "Application of Tuned Vibration Absorber Concept to Blisk Ring Dampers: A Nonlinear Study," *Journal of Engineering for Gas Turbines and Power*, vol. 141, no. 10, pp. 1–8, oct 2019.

[218] E. P. Petrov and D. J. Ewins, "Analytical Formulation of Friction Interface Elements for Analysis of Nonlinear Multi-Harmonic Vibrations of Bladed Disks," *Journal of Turbomachinery*, vol. 125, no. 2, pp. 364–371, apr 2003.

[219] D. Laxalde, F. Thouverez, and J.-P. Lombard, "Forced Response Analysis of Integrally Bladed Disks With Friction Ring Dampers," *Journal of Vibration and Acoustics*, vol. 132, no. 1, pp. 0 110 131–0 110 139, feb 2010.

[220] S. Filippi, E. B. Rodrigues, and M. M. Gola, "Experimental Characterization of Contact Hysteresis at High Temperatures," in *Volume 5: Marine; Microturbines and Small Turbomachinery; Oil and Gas Applications; Structures and Dynamics, Parts A and B*. ASMEDC, jan 2006, pp. 893–902.

[221] L. Salles, L. Blanc, F. Thouverez, and A. Gouskov, "Dynamic analysis of fretting-wear in friction contact interfaces," *International Journal of Solids and Structures*, vol. 48, no. 10,

pp. 1513–1524, may 2011.

[222] A. Fantetti, L. Tamatam, M. Volvert, I. Lawal, L. Liu, L. Salles, M. Brake, C. Schwingshackl, and D. Nowell, "The impact of fretting wear on structural dynamics: Experiment and Simulation," *Tribology International*, vol. 138, no. February, pp. 111–124, oct 2019.

[223] D. Laxalde, C. Gibert, and F. Thouverez, "Experimental and Numerical Investigations of Friction Rings Damping of Blisks," in *Volume 5: Structures and Dynamics, Parts A and B.* ASMEDC, jan 2008, pp. 469–479.

[224] K. R. Cross, J. R. Cavanagh, and R. L. Newman, "Vibration damping coatings," 1973.

[225] J. Sun and L. Kari, "Coating Methods to Increase Material Damping of Compressor Blades: Measurements and Modeling," in *Volume 6: Structures and Dynamics, Parts A and B.* ASMEDC, oct 2010, pp. 1157–1165.

[226] A. Motherwell, "Hollow component with internal damping," 2005.

[227] J. Tang and K. W. Wang, "Vibration Control of Rotationally Periodic Structures Using Passive Piezoelectric Shunt Networks and Active Compensation," *Journal of Vibration and Acoustics*, vol. 121, no. 3, pp. 379–390, jul 1999.

[228] H. Yu and K. W. Wang, "Piezoelectric Networks for Vibration Suppression of Mistuned Bladed Disks," *Journal of Vibration and Acoustics*, vol. 129, no. 5, pp. 559–566, oct 2007.

[229] H. Yu and K. W. Wang, "Vibration Suppression of Mistuned Coupled-Blade-Disk Systems Using Piezoelectric Circuitry Network," *Journal of Vibration and Acoustics*, vol. 131, no. 2, pp. 0 210 081–02 100 812, apr 2009.

[230] J. Liu, L. Li, P. Deng, and C. Li, "A Comparative Study on the Dynamic Characteristics of Bladed Disks With Piezoelectric Network and Piezoelectric Shunt Circuit," in *Volume 7A: Structures and Dynamics*, vol. 7A-2016, no. March. American Society of Mechanical Engineers, jun 2016.

[231] L. Li, P. Deng, and Y. Fan, "Dynamic characteristics of a cyclic-periodic structure with a piezoelectric network," *Chinese Journal of Aeronautics*, vol. 28, no. 5, pp. 1426–1437, oct 2015.

[232] P. Bisegna and G. Caruso, "Optimization of a passive vibration control scheme acting on a bladed rotor using an homogenized model," *Structural and Multidisciplinary Optimization*, vol. 39, no. 6, pp. 625–636, dec 2009.

[233] A. Sénéchal, "Réduction de vibrations de structure complexe par shunts piézoélectriques : application aux turbomachines," Ph.D. dissertation, Conservatoire National des Arts et Métiers, 2011.

[234] J. L. Kauffman and G. A. Lesieutre, "Piezoelectric-Based Vibration Reduction of Turbomachinery Bladed Disks via Resonance Frequency Detuning," *AIAA Journal*, vol. 50, no. 5, pp. 1137–1144, may 2012.

[235] S. M. Schwarzendahl, J. Szwedowicz, M. Neubauer, L. Panning, and J. Wallaschek, "On Blade Damping Technology Using Passive Piezoelectric Dampers," in *Volume 7: Structures and Dynamics, Parts A and B.* American Society of Mechanical Engineers, jun 2012, pp. 1205–1215.

[236] J. L. Szwedowicz, W. Kappis, L. Panning, S. M. Schwarzendahl, M. Neubauer, A. Hohl, and J. Wallaschek, "Method for influencing, damping, or suppressing mechanical vibrations occurring during operation in a turbomachine blade, a turbomachine blade useful for carrying out the method, and a piezoelectric damping element," 2013.

[237] B. Zhou, F. Thouverez, and D. Lenoir, "Vibration Reduction of Mistuned Bladed Disks by Passive Piezoelectric Shunt Damping Techniques," *AIAA Journal*, vol. 52, no. 6, pp. 1194–1206, jun 2014.

[238] R. Viguié, D. Verhelst, A. Preumont, B. Mokrani, and R. Bastaits, "Piezoelectric damper system for an axial turbomachine rotor," 2015.

[239] B. Mokrani, R. Bastaits, M. Horodinca, I. Romanescu, I. Burda, R. Viguié, and A. Preumont, "Parallel Piezoelectric Shunt Damping of Rotationally Periodic Structures," *Advances in Materials Science and Engineering*, vol. 2015, pp. 1–12, 2015.

[240] B. Mokrani and A. Preumont, "A numerical and experimental investigation on passive piezoelectric shunt damping of mistuned blisks," *Journal of Intelligent Material Systems and Structures*, vol. 29, no. 4, pp. 610–622, mar 2018.

[241] J. Liu, L. Li, and Y. Fan, "A comparison between the friction and piezoelectric synchronized switch dampers for blisks," *Journal of Intelligent Material Systems and Structures*, vol. 29, no. 12, pp. 2693–2705, jul 2018.

[242] Y. Wu, L. Li, Y. Fan, S. Zucca, C. Gastaldi, and H. Ma, "Design of dry friction and piezoelectric hybrid ring dampers for integrally bladed disks based on complex nonlinear modes," *Computers & Structures*, vol. 233, p. 106237, jun 2020.

[243] J. Laborenz, C. Siewert, L. Panning, J. Wallaschek, C. Gerber, and P.-A. Masserey, "Eddy Current Damping: A Concept Study for Steam Turbine Blading," *Journal of Engineering for Gas Turbines and Power*, vol. 132, no. 5, pp. 1–7, may 2010.

[244] K. P. Duffy, G. V. Brown, and R. I. Bagley, "Self-tuning impact damper for rotating blades," 2004.

[245] E. Bowyer and V. Krylov, "Damping of flexural vibrations in turbofan blades using the acoustic black hole effect," *Applied Acoustics*, vol. 76, pp. 359–365, feb 2014.

[246] D. L. Thomas, "Dynamics of rotationally periodic structures," *International Journal for Numerical Methods in Engineering*, vol. 14, no. 1, pp. 81–102, 1979.

[247] F. Nyssen, "Numerical Modeling and Experimental Identification of Mistuned Multi-Stage Bladed Assemblies," Ph.D. dissertation, University of Liège, 2016.

[248] D. J. Ewins, "Vibration Characteristics of Bladed Disc Assemblies," *Journal of Mechanical Engineering Science*, vol. 15, no. 3, pp. 165–186, jun 1973.

[249] R. R. Craig and M. C. C. Bampton, "Coupling of substructures for dynamic analyses." *AIAA Journal*, vol. 6, no. 7, pp. 1313–1319, jul 1968.

[250] D.-M. Tran, "Component mode synthesis methods using interface modes. Application to structures with cyclic symmetry," *Computers & Structures*, vol. 79, no. 2, pp. 209–222, jan 2001.

[251] G. Raze, J. Dietrich, A. Paknejad, B. Lossouarn, G. Zhao, A. Deraemaeker, C. Collette, and G. Kerschen, "Passive control of a periodic structure using a network of periodically-coupled piezoelectric shunt circuits," in *Proceedings of ISMA 2020-International Conference on Noise and Vibration Engineering and USD 2020-International Conference on Uncertainty in Structural Dynamics*, 2020, pp. 145–160.

[252] A. J. Fleming and S. O. R. Moheimani, "Adaptive piezoelectric shunt damping," *Smart Materials and Structures*, vol. 12, no. 1, pp. 36–48, feb 2003.

[253] D. Niederberger, A. Fleming, S. O. R. Moheimani, and M. Morari, "Adaptive multi-mode resonant piezoelectric shunt damping," *Smart Materials and Structures*, vol. 13, no. 5, pp.

1025–1035, oct 2004.

[254] J. Sherman and W. J. Morrison, "Adjustment of an Inverse Matrix Corresponding to a Change in One Element of a Given Matrix," *The Annals of Mathematical Statistics*, vol. 21, no. 1, pp. 124–127, mar 1950.

[255] M. A. Woodbury, "Inverting modified matrices," *Memorandum report*, vol. 42, no. 106, p. 336, 1950.

[256] J. Ding and A. Zhou, "Eigenvalues of rank-one updated matrices with some applications," *Applied Mathematics Letters*, vol. 20, no. 12, pp. 1223–1226, dec 2007.

[257] A. Chervov, G. Falqui, and V. Rubtsov, "Algebraic properties of Manin matrices 1," *Advances in Applied Mathematics*, vol. 43, no. 3, pp. 239–315, sep 2009.

[258] S. Frankel, "Complete Approximate Solutions of the Equation x = tan x," *National Mathematics Magazine*, vol. 11, no. 4, p. 177, jan 1937.

[259] M. Trindade and A. Benjeddou, "Effective Electromechanical Coupling Coefficients of Piezoelectric Adaptive Structures: Critical Evaluation and Optimization," *Mechanics of Advanced Materials and Structures*, vol. 16, no. 3, pp. 210–223, apr 2009.

[260] Y. Fan, M. Collet, M. Ichchou, O. Bareille, and L. Li, "Wave Electromechanical Coupling Factor for the Guided Waves in Piezoelectric Composites," *Materials*, vol. 11, no. 8, p. 1406, aug 2018.

[261] J. C. Pinheiro and D. M. Bates, "Unconstrained parametrizations for variance-covariance matrices," *Statistics and Computing*, vol. 6, no. 3, pp. 289–296, sep 1996.

[262] G. Zhao, G. Raze, A. Paknejad, A. Deraemaeker, G. Kerschen, and C. Collette, "Active tuned inerter-damper for smart structures and its H_∞ optimisation," *Mechanical Systems and Signal Processing*, vol. 129, pp. 470–478, 2019.

[263] G. Zhao, G. Raze, A. Paknejad, A. Deraemaeker, G. Kerschen, and C. Collette, "Active nonlinear energy sink using force feedback under transient regime," *Nonlinear Dynamics*, vol. 102, no. 3, pp. 1319–1336, nov 2020.

[264] G. Zhao, A. Paknejad, G. Raze, G. Kerschen, and C. Collette, "H_∞ optimization of an enhanced force feedback controller for mitigation of nonlinear vibrations," in *7th World Conference on Structural Vibration Control*, Qingdao, 2018.

[265] G. Zhao, A. Paknejad, G. Raze, G. Kerschen, and C. Collette, "H_∞ optimization of positive position feedback control for mitigation of nonlinear vibrations," in *Proceedings of ISMA 2018 - International Conference on Noise and Vibration Engineering and USD 2018 - International Conference on Uncertainty in Structural Dynamics*, W. Desmet, B. Pluymers, D. Moens, and W. Rottiers, Eds. Leuven: KU Leuven, 2018, pp. 143–151.

[266] G. Zhao, G. Raze, A. Paknejad, A. Deraemaeker, G. Kerschen, and C. Collette, "Active nonlinear energy sink using integral force feedback," in *Proceedings of the International Modal Analysis Conference (IMAC) XXXVIII*, 2020.

[267] A. Paknejad, G. Raze, G. Zhao, A. Deraemaeker, G. Kerschen, and C. Collette, "Active vibration damping of bladed structures," in *Proceedings of ISMA 2020-International Conference on Noise and Vibration Engineering and USD 2020-International Conference on Uncertainty in Structural Dynamics*, 2020, pp. 105–114.

Publications associated with this thesis

The complete list of the author's publications is available in the institutional repository ORBi.

Journal articles

G. Raze and G. Kerschen, "Multimodal vibration damping of nonlinear structures using multiple nonlinear absorbers," *International Journal of Non-Linear Mechanics*, vol. 119, p. 103308, mar 2020.

G. Raze, A. Jadoul, S. Guichaux, V. Broun, and G. Kerschen, "A digital nonlinear piezoelectric tuned vibration absorber," *Smart Materials and Structures*, vol. 29, no. 1, p. 015007, jan 2020.

G. Raze, A. Paknejad, G. Zhao, C. Collette, and G. Kerschen, "Multimodal vibration damping using a simplified current blocking shunt circuit," *Journal of Intelligent Material Systems and Structures*, vol. 31, no. 14, pp. 1731–1747, aug 2020.

G. Raze and G. Kerschen, "H_∞ optimization of multiple tuned mass dampers for multimodal vibration control," *Computers & Structures*, vol. 248, p. 106485, may 2021.

G. Zhao, G. Raze, A. Paknejad, A. Deraemaeker, G. Kerschen, and C. Collette, "Active tuned inerter-damper for smart structures and its H_∞ optimisation," *Mechanical Systems and Signal Processing*, vol. 129, pp. 470–478, 2019.

G. Zhao, A. Paknejad, G. Raze, A. Deraemaeker, G. Kerschen, and C. Collette, "Nonlinear positive position feedback control for mitigation of nonlinear vibrations," *Mechanical Systems and Signal Processing*, vol. 132, pp. 457–470, oct 2019.

G. Zhao, G. Raze, A. Paknejad, A. Deraemaeker, G. Kerschen, and C. Collette, "Active nonlinear inerter damper for vibration mitigation of Duffing oscillators," *Journal of Sound and Vibration*, vol. 473, p. 115236, may 2020.

G. Zhao, G. Raze, A. Paknejad, A. Deraemaeker, G. Kerschen, and C. Collette, "Active nonlinear energy sink using force feedback under transient regime," *Nonlinear Dynamics*, vol. 102, no. 3, pp. 1319–1336, nov 2020.

Conference articles and presentations

G. Raze and G. Kerschen, "A Multimodal Nonlinear Tuned Vibration Absorber," in *IUTAM Bookseries*. Springer International Publishing, 2020, vol. 37, pp. 235–247.

G. Raze, B. Lossouarn, A. Paknejad, G. Zhao, J. F. Deü, C. Collette, and G. Kerschen, "A multimodal nonlinear piezoelectric vibration absorber," in *Proceedings of ISMA 2018 - International Conference on Noise and Vibration Engineering and USD 2018 - International Conference on Uncertainty in Structural Dynamics*, 2018, pp. 63–77.

G. Raze, A. Jadoul, V. Broun, and G. Kerschen, "A Simplified Current Blocking Piezoelectric Shunt Circuit for Multimodal Vibration Mitigation," in *Conference Proceedings of the Society for Experimental Mechanics Series*, 2020, vol. 5, pp. 23–25.

G. Raze, S. Guichaux, A. Jadoul, V. Broun, and G. Kerschen, "Mitigation of nonlinear vibrations with a digital piezoelectric tuned vibration absorber," in *Seventh International Conference on Nonlinear vibrations, Localization and Energy transfer*, Marseille, 2019.

G. Raze, A. Paknejad, G. Zhao, V. Broun, C. Collette, and G. Kerschen, "Suppression of delay-induced instabilities of digital piezoelectric vibration absorbers," in *Proceedings of the 9th ECCOMAS Thematic Conference on Smart Structures and Materials - SMART 2019*, A. Benjeddou, N. Mechbal, and J.-F. Deü, Eds. International Centre for Numerical Methods in Engineering (CIMNE), 2019, pp. 991–1001.

G. Raze, S. Guichaux, A. Jadoul, V. Broun, and G. Kerschen, "A Digital Absorber for Nonlinear Vibration Mitigation," in *Conference Proceedings of the Society for Experimental Mechanics Series*, 2021, vol. 1, pp. 105–108.

G. Raze, J. Dietrich, A. Paknejad, B. Lossouarn, G. Zhao, A. Deraemaeker, C. Collette, and G. Kerschen, "Passive control of a periodic structure using a network of periodically-coupled piezoelectric shunt circuits," in *Proceedings of ISMA 2020-International Conference on Noise and Vibration Engineering and USD 2020-International Conference on Uncertainty in Structural Dynamics*, 2020, pp. 145–160.

G. Zhao, A. Paknejad, G. Raze, G. Kerschen, and C. Collette, "H_∞ optimization of an enhanced force feedback controller for mitigation of nonlinear vibrations," in *7th World Conference on Structural Vibration Control*, Qingdao, 2018.

G. Zhao, A. Paknejad, G. Raze, G. Kerschen, and C. Collette, "H_∞ optimization of positive position feedback control for mitigation of nonlinear vibrations," in *Proceedings of ISMA 2018 - International Conference on Noise and Vibration Engineering and USD 2018 - International Conference on Uncertainty in Structural Dynamics*, W. Desmet, B. Pluymers, D. Moens, and W. Rottiers, Eds. Leuven: KU Leuven, 2018, pp. 143–151.

A. Paknejad, G. Raze, G. Zhao, M. Osée, A. Deraemaeker, F. Robert, G. Kerschen, and C. Collette, "Hybridization of Active Control and Pasive Resonant Shunt," in *Proceedings of the 9th ECCOMAS Thematic Conference on Smart Structures and Materials*. Paris: International Centre for Numerical Methods in Engineering (CIMNE), 2019, pp. 930–941.

G. Zhao, G. Raze, A. Paknejad, A. Deraemaeker, G. Kerschen, and C. Collette, "Active nonlinear energy sink using integral force feedback," in *Proceedings of the International Modal Analysis Conference (IMAC) XXXVIII*, 2020.

A. Paknejad, G. Raze, G. Zhao, A. Deraemaeker, G. Kerschen, and C. Collette, "Active vibration damping of bladed structures," in *Proceedings of ISMA 2020-International Conference on Noise and Vibration Engineering and USD 2020-International Conference on Uncertainty in Structural Dynamics*, 2020, pp. 105–114.